Journal of Heat Transfer

Published Monthly by ASME

VOLUME 129 • NUMBER 10 • OCTOBER 2007 (pp. 1309-1463)

Editor, **YOGESH JALURIA (2010)**
Assistant to the Editor, **S. PATEL**

Associate Editors
Gautam Biswas, Indian Inst. of Tech., Kanpur (2009)
Louis C. Burmeister, Univ. of Kansas (2008)
Minking Chyu, Univ. of Pittsburgh (2009)
Suresh V. Garimella, Purdue Univ. (2007)
A. Haji-Sheikh, Univ. of Texas at Arlington (2008)
Anthony M. Jacobi, Univ. of Illinois (2008)
Yogendra Joshi, Georgia Inst. of Tech. (2008)
Satish G. Kandlikar, Rochester Inst. of Tech. (2007)
Jay M. Khodadadi, Auburn Univ. (2007)
Sai C. Lau, Texas A&M Univ. (2009)
Ben Q. Li, Univ. of Michigan, Dearborn (2009)
Raj M. Manglik, Univ. of Cincinnati (2009)
Chang H. Oh, Idaho National Lab. (2007)
Ranga Pitchumani, Univ. of Connecticut (2007)
Ramendra P. Roy, Arizona State Univ. (2007)
Jamal Seyed-Yagoobi, Illinois Inst. of Tech. (2009)
Bengt Sunden, Lund Inst. of Tech., Sweden (2008)
Walter W. Yuen, Univ. of California–Santa Barbara (2008)

Past Editors
V. DHIR
J. R. HOWELL
R. VISKANTA
G. M. FAETH
K. T. YANG
E. M. SPARROW

HEAT TRANSFER DIVISION
Chair, **R. W. DOUGLASS**
Vice Chair, **T. W. TONG**
Past Chair, **M. K. JENSEN**

PUBLICATIONS COMMITTEE
Chair, **BAHRAM RAVANI**

OFFICERS OF THE ASME
President, **SAM Y. ZAMRIK**
Executive Director,
VIRGIL R. CARTER
Treasurer,
THOMAS D. PESTORIUS

PUBLISHING STAFF

Managing Director, Publishing
PHILIP DI VIETRO

Manager, Journals
COLIN McATEER

Production Coordinator
JUDITH SIERANT

Transactions of the ASME, Journal of Heat Transfer (ISSN 0022-1481) is published monthly by The American Society of Mechanical Engineers, Three Park Avenue, New York, NY 10016. Periodicals postage paid at New York, NY and additional mailing offices.
POSTMASTER: Send address changes to Transactions of the ASME, Journal of Heat Transfer, c/o THE AMERICAN SOCIETY OF MECHANICAL ENGINEERS, 22 Law Drive, Box 2300, Fairfield, NJ 07007-2300.
CHANGES OF ADDRESS must be received at Society headquarters seven weeks before they are to be effective. Please send old label and new address.

STATEMENT from By-Laws. The Society shall not be responsible for statements or opinions advanced in papers or ... printed in its publications (B7.1, Para. 3).
COPYRIGHT © 2007 by The American Society of Mechanical Engineers. For authorization to photocopy material for internal or personal use under those circumstances not falling within the fair use provisions of the Copyright Act, contact the Copyright Clearance Center (CCC), 222 Rosewood Drive, Danvers, MA 01923, tel: 978-750-8400, www.copyright.com. Request for special permission or bulk copying should be addressed to Reprints/Permission Department.

Canadian Goods & Services Tax Registration #126148048

TECHNICAL PAPERS

Conduction

Evaporation, Boiling, and Condensation

Experimental Techniques

Heat and Mass Transfer

Natural and Mixed Convection

Porous Media

Radiative Heat Transfer

Heat Exchangers

(Contents continued on inside back cover)

This journal is printed on acid-free paper, which exceeds the ANSI Z39.48-1992 specification for permanence of paper and library materials. ∞™
♲ 85% recycled content, including 10% post-consumer fibers.

(**Contents continued**)

Journal of Heat Transfer **Volume 129, Number 10** **OCTOBER 2007**

Electronic Cooling

TECHNICAL BRIEFS

The ASME Journal of Heat Transfer is abstracted and indexed in the following:

Applied Science and Technology Index, Chemical Abstracts, Chemical Engineering and Biotechnology Abstracts (Electronic equivalent of Process and Chemical Engineering), Civil Engineering Abstracts, Compendex (The electronic equivalent of Engineering Index), Corrosion Abstracts, Current Contents, E & P Health, Safety, and Environment, Ei EncompassLit, Engineered Materials Abstracts, Engineering Index, Enviroline (The electronic equivalent of Environment Abstracts), Environment Abstracts, Environmental Engineering Abstracts, Environmental Science and Pollution Management, Fluidex, Fuel and Energy Abstracts, Index to Scientific Reviews, INSPEC, International Building Services Abstracts, Mechanical & Transportation Engineering Abstracts, Mechanical Engineering Abstracts, METADEX (The electronic equivalent of Metals Abstracts and Alloys Index), Petroleum Abstracts, Process and Chemical Engineering, Referativnyi Zhurnal, Science Citation Index, SciSearch (The electronic equivalent of Science Citation Index), Theoretical Chemical Engineering

Combined Parameter and Function Estimation With Application to Thermal Conductivity and Surface Heat Flux

Tahar Loulou
Centre de Recherche,
Université de Bretagne Sud,
LET2E,
Rue Saint Maude,
F-56321 Lorient Cedex, France
e-mail: tahar.loulou@univ-ubs.fr

This is a numerical and experimental study on the combined parameter and function estimation. The determination of thermal conductivity and the surface heat flux is an illustration of combined estimation of one parameter and one function by means of the conjugate gradient method with vectorial descent parameter. The experimental example developed herein uses one set of good data obtained by Beck and Arnold (1977, Parameter Estimation in Engineering and Science, Wiley, New York). For this case, two measured temperatures in the solid are used to illustrate combined estimation. The unknown boundary condition and thermal conductivity of this solid were satisfactorily reconstructed and a good enough comparison is demonstrated between the known and estimated unknowns. The temperature data of Beck and Arnold are found to be excellent. Also, it is shown that the developed approach is general, stable, powerful, and able to process a wide variety of heat transfer problems where a simultaneous estimation is unavoidable. [DOI: 10.1115/1.2755064]

Keywords: combined estimation, inverse heat conduction problem, thermal conductivity, function and/or parameter estimation, conjugate gradient method, regularization

Introduction

The subject of inverse problem has been an active area of research for the past several decades. This exciting field has found application in almost all disciplines of science and technology, in general, and in heat transfer, in particular. Different techniques have been used to solve inverse problems including the conjugate gradient method [1,2], the function specification method and the general ordinary least squares [3,4], the mollification method [5], and several other methods [6]. To date, the most commonly considered inverse problem by the heat transfer community is the inverse heat conduction problem, which is a problem of function estimation.

Two general classes of inverse problem are parameter and function estimation. By parameter estimation, we mean the identification of a constant parameter such as thermal diffusivity, heat transfer coefficient or thermal conductance, thermal conductivity, emissivity, specific heat, and many other constant thermal properties. The function estimation designates the estimation of any thermal function of time and/or space or temperature such as surface heat flux, temperature dependent thermal conductivity, thermal source, initial temperature distribution, solidification front, and many other thermal functions.

In many cases, when a parametric representation is used to approximate an unknown thermal function, the distinction between parameter and function is blurred. In function estimation, the parametric form is used to alleviate the identification procedure, but the final goal is always the reconstruction of the unknown function. This paper discusses problems that have aspects of combined estimation of parameter and function. Beck provides an excellent and comprehensive review on this subject [7].

The presented work is built around an example of simultaneous estimation of thermal conductivity of a solid and one of its boundary condition from transient temperature measurements recorded within the solid region. The determination of thermal conductivity and the surface heat flux is a combined estimation of one parameter and one function. Similar work can be found in Ref. [8]. As experimental data, we will use a set of very good data obtained by Beck and Arnold [3]. Originally, these temperature measurements were predestined to estimate thermal conductivity k and volumetric specific heat c of a given metallic alloy, the surface heat flux being known. To check the efficiency of the proposed method, we suppose that the volumetric specific heat c estimated by Beck and Arnold is good enough and can be supposed to be known exactly but thermal conductivity and surface heat flux are both unknowns. Then, our goal is the combined estimation of thermal conductivity k and applied surface heat flux $q(t)$ from the temperature measurements within the solid. As these thermophysical properties and the boundary conditions are known by means of other methods, the proposed experimental example helps us to qualify this new approach.

To the best knowledge of the author, this is the first time where thermal conductivity and applied heat flux of solid are estimated jointly at the same time. The only literature work revealing the importance of such approach is due to Dowding et al. [9] where they mentioned the valuable insight that can provide. They have adopted another way, which consists in determining the thermal properties of a solid with known heat flux and temperature histories. Then, the inverse heat conduction problem (IHCP) of recovering the heat flux history is solved using the estimated values for the thermal properties and temperature histories recorded within the solid. They have shown the feasibility of such a resolution and stated the nontriviality of such an exercise looking the ill-posedness character of the IHCP. In their work, thermal properties were correctly estimated and a good agreement between the esti-

---

Contributed by the Heat Transfer Division of ASME for publication in the Journal of Heat Transfer. Manuscript received December 1, 2005; final manuscript received February 9, 2007. Review conducted by Yogendra Joshi.

mated and measured heat flux histories was demonstrated. By doing so, Dowding et al. have estimated in the first step the thermal properties of a solid and then verified the applied surface heat flux in the second step. This approach is quite different from the one adopted here where thermal conductivity and applied heat flux are considered as two unknowns and should be estimated at the same time when the volumetric specific heat of the solid is supposed available.

Inverse Problem Formulation

Generally, IHCPs are solved by minimizing a residual functional $S(\mathbf{U})$ based on the ordinary least squares norm and coupled with some stabilizing technique used in the iterative procedure. The sum of the squared residuals between the measured data and the responses of model simulating the physical problem under investigation defines the least squares norm. For continuous measured data, the residual functional is written as follows:

$$S(\mathbf{U}) = \sum_{i=1}^{I} \int_{0}^{t_f} [T(x_i,t;\mathbf{U}) - Y(x_i,t)]^2 dt \tag{1}$$

where $T(x_i,t;\mathbf{U})$ and $Y(x_i,t)$ are, respectively, the computed and the measured temperature at the location x_i and over the time period $[0,t_f]$ corresponding to the duration of the experiment.

The investigated example in this paper is a slab of thickness L, which is initially at uniform temperature T_0. For time $t>0$, the boundary surface at $x=L$ is kept insulated, while that at $x=0$ is subjected to prescribed heat flux $q(t)$. The mathematical model for this one-dimensional transient heat conduction problem, with constant physical properties k and c, is given as follows:

$$c\frac{\partial T(x,t)}{\partial t} = k\frac{\partial^2 T(x,t)}{\partial x^2} \quad 0<x<L \quad 0<t\leqslant t_f \tag{2}$$

$$-k\frac{\partial T(x,t)}{\partial x} = q(t) \quad x=0 \quad 0<t\leqslant t_f \tag{3}$$

$$\frac{\partial T(x,t)}{\partial x} = 0 \quad x=L \quad 0<t\leqslant t_f \tag{4}$$

$$T(x,0) = T_0 \quad 0\leqslant x\leqslant L \tag{5}$$

Our objective is to estimate the unknown parameter k and the function $q(t)$ from the transient temperature histories taken at two known sensor locations inside the slab, i.e., $x_1=0$ and $x_2=L$.

Configuration $\mathcal{C}_1$. For combined estimation of thermal conductivity k and transient heat flux $q(t)$, one way to construct the vector $\mathbf{U}$ is to choose the unknown as

$$\mathbf{U}^T = [k,\hat{q}_1,\hat{q}_2,\ldots,\hat{q}_J] \tag{6}$$

where the superscript T denotes the transpose and $\hat{q}_j$ is the surface heat flux component at time t_j, $\hat{q}_j=q(t_j)$, $j=1,\ldots J$, J being the total number of time steps. By doing so, we are estimating the heat flux at each time step, which is known as grid time representation of surface heat flux (grid function). Also, this approach is named infinite-dimensional form and allows the use of variational methods to calculate the gradient of the functional to be minimized. Then, the total number of $\mathbf{U}$ components is $M=1+J$. The use of two sensors ensures the feasibility of the inversion because the number of measurements is greater than the unknowns to be recovered in this configuration.

Configuration $\mathcal{C}_2$. If the unknown heat flux $q(t)$ has a smooth evolution or a special profile such as sinus, polynomial function, piecewise linear function, step variation, tooth function variation, etc., parametric representation can be introduced in the goal to reduce the heat flux unknowns to be recovered jointly with k. It assumes available some information concerning the functional form of the unknown heat flux. The parametrization of $q(t)$ has an another benefit, which consists in introducing some regularizing effect in the solution of the inverse problem. It reduces the ill conditioning of the inverse problem and allows the refining of temporal grid size, which results in a significant increase of the computation accuracy. Then, the unknown heat flux can be written in general form as

$$q(t) = \sum_{i=1}^{m} \hat{q}_i \mathcal{B}_i(t) \tag{7}$$

where the functions $\mathcal{B}_i(t)$ are any basis functions on time (polynomials, B splines, cosine, etc.,), used to approximate the unknown function form of the heat flux $q(t)$. There are m constants (or parameters) to describe the unknown $q(t)$. In this special case, the total number of parameters to be recovered by the solution of the inverse problem is $M=1+m$, where m is the number of parameters in the above parametrization. The vector $\mathbf{U}$ is written as

$$\mathbf{U}^T = [k,\hat{q}_1,\hat{q}_2,\ldots,\hat{q}_m] \tag{8}$$

In this case, the total number of unknowns of the inverse problem to be recovered can be less than the measurements taken at one sensor and the use of one sensor could be investigated.

Also, for conciseness and the sake of brevity, the parameter estimation and function estimation theories are not repeated. For a background in parameter estimation, see Ref. [3], in function estimation, see Ref. [4] for the function specification method, and Ref. [10] for the iterative regularization method (IRM). The IRM uses the conjugate gradient method as support for the iterative process and the discrepancy principle to terminate iteration [11]. The gradient of the functional to be minimized with respect to the sought unknowns is computed by means of the adjoint problem. A whole description on the development and application of the method can be found in Ref. [12].

In the absence of noise, the iterative process is repeated until each component of the vector $\mathbf{U}$ satisfies the following stopping criteria:

$$\left|\frac{u_i^{s+1} - u_i^s}{u_i^{s+1}}\right| \leqslant \epsilon \quad i=1,\ldots,M \tag{9}$$

where ϵ is a small number $(10^{-4}-10^{-6})$. In the event that the input temperatures are given with errors, the iterative process is stopped in accordance with the discrepancy principle criterion [1,11], i.e., upon fulfillment of the following condition:

$$S(\mathbf{U}) = \sum_{i=1}^{I} \int_{0}^{t_f} [T(x_i,t;\mathbf{U}) - Y(x_i,t)]^2 dt \approx \sum_{i=1}^{I} \int_{0}^{t_f} \sigma_i^2(t) dt \approx \delta \tag{10}$$

where δ is the integrated error of the measured data at location x_i and having $\sigma_i(t)$ as standard deviation. If the standard deviation is assumed to be the same for all temperature measurements, then the integrated error will have the following expression:

$$\delta = I\sigma^2 t_f \tag{11}$$

Numerical Simulations

Basic numerical simulations are conducted by using the theoretical model of the experimental setup presented in the remaining part of this paper. A slab of thickness $L=0.0254$ m is initially at uniform temperature $T_0=27.5$°C. For time $t>0$, the boundary surface at $x=L$ is kept insulated, while that at $x=0$ is subjected to prescribed heat flux $q(t)$ expressed by

Table 1 Summary of obtained results with configurations $\mathcal{C}_1$ and $\mathcal{C}_2$ and with exact and noised temperatures. The noise level is taken bigger than the one observed in the experience, i.e., $\sigma = 0.1667°\text{C}$, which corresponds to 2.25% of the temperature rise on the heated surface. With $\mathcal{C}_2$, the unknown heat flux is parametrized with three piecewise constant functions ($m=3$). The displayed value of residual function corresponds to the last iteration where the discrepancy principle is fulfilled.

Measurement type			Exact data		Noised data	
Configuration			$\mathcal{C}_1$	$\mathcal{C}_2$	$\mathcal{C}_1$	$\mathcal{C}_2$
Stopping criterion	δ	°C^2 s	⋯	⋯	1.6697	1.6697
Iteration number	it	#	74	25	9	9
Residual function	$S(\mathbf{U})$	°C^2 s	0.0000	0.0000	1.6581	1.6549
Thermal conductivity	k	W/m K	75.014	75.014	75.368	74.779
Estimation error	ε_k	%	0.00	0.00	0.47	0.31
Heat flux rms	ϱ_q	W/m^2	0.0474	0.0020	2752.38	269.50
Estimation error	ε_q	%	0.00	0.00	1.61	0.01
Temperature rms	ϱ_t	°C	0.0000	0.0000	0.1667	0.1665

$$q(t) = \begin{cases} 0 & \text{for } t < 3.3 \text{ s} \\ 30{,}300 \text{ W/m}^2 & \text{for } 3.3 \leqslant t \leqslant 18.6 \text{ s} \\ 0 & \text{for } t > 18.6 \text{ s} \end{cases} \tag{12}$$

which represents a step change with time. These simulations are conducted by using thermophysical properties estimated by Beck, k and c, and by taking 51 nodes in space and 100 time steps. Initial guesses for k and $q(t)$ were taken as 0.1 W/m K and 1.0 W/m^2 for all presented tests. Table 1 summarizes the investigation results with exact data and data corrupted with additive errors having a normal distribution, zero mean, constant variance, and uncorrelated. As the relative error between the analytical and numerical solutions of this problem is about 1.60%, the true temperatures used in simulation are computed numerically. Random errors are generated with routines in IMSL library [13].

A measure of the difference between the measured and computed temperature and heat flux is introduced to qualify the estimation efficiency. For temperature, it should be analogous to the standard deviation of measurements, which is known in the present case. An expression for the estimated standard deviation of temperature is

$$\varrho_t = \left[\frac{1}{I(J-1)} \sum_{i=1}^{I} \sum_{j=1}^{J} [Y_i^j - T_i^j]^2 \right]^{1/2} \quad (°\text{C}) \tag{13}$$

where the computed and measured temperatures are, respectively, $T_i^j = T(x_i, t_j)$ and $Y_i^j = Y(x_i, t_j)$. In the same manner to Eq. (13), the root mean square criterion is introduced for the heat flux estimation, that is,

$$\varrho_q = \left[\frac{1}{J} \sum_{j=1}^{J} [\tilde{q}_j - q_j]^2 \right]^{1/2} \quad (\text{W/m}^2) \tag{14}$$

where $\tilde{q}_j$ and q_j are, respectively, the calculated and the exact heat flux at time t_j. As the exact heat flux profile is known, another qualifying error criterion is introduced denoted as

$$\varepsilon_q = 100 \frac{\displaystyle\int_0^{t_f} [\tilde{q}(t) - q(t)]^2 dt}{\displaystyle\int_0^{t_f} [q(t)]^2 dt} \quad (\%) \tag{15}$$

where $\tilde{q}(t)$ and $q(t)$ are, respectively, the calculated and the exact heat flux. There is a significant difference in the interpretation of Eqs. (13) and (14), see Ref. [14] for more details. By considering the recovered thermal conductivity, by Beck, as a reference value k_r, a relative comparison coefficient is introduced in the analysis of obtained results and is defined as

$$\varepsilon_k = 100 \left| \frac{k_r - k}{k_r} \right| \quad (\%) \tag{16}$$

where k is the thermal conductivity estimated by the present method and the reference value of thermal conductivity was taken as $k_r = 75.014$ W/m K.

By using exact data, both unknowns are recovered exactly and the only difference between $\mathcal{C}_1$ and $\mathcal{C}_2$ lies in the number of iterations required to satisfy the stopping criteria. With theoretical temperatures, the estimation results are still comparable between $\mathcal{C}_1$ and $\mathcal{C}_2$ and the estimation errors are nearly equal to zero.

As usually observed with the IRM when it is used without and with noised data, the iteration number drops from 74 to 9 for $\mathcal{C}_1$ and from 25 to 9 for $\mathcal{C}_2$ for this example. On the other hand, the estimation errors depicted in Table 1 are low and acceptable with respect to the level of added noise. For both configurations, the resulting temperature rms is of the same order and equal to the level of added noise. With $\mathcal{C}_1$ and $\mathcal{C}_2$, the k estimate is obtained with an error less than 1%. The heat flux is reconstructed faithfully for both models with a slight advantage to $\mathcal{C}_2$ case.

Experimental Setup

The set of data used in this paper was obtained by Beck and Arnold [3]. The developed experiment is well detailed and commented in Ref. [3] and is briefly discussed in this section. Initially, the primary objective of this experimental work was the estimation of thermophysical properties (thermal conductivity k and volumetric specific heat c) of a metallic alloy. In this experiment, two adjacent, identical Armaco iron cylindrical specimens of 0.0254 m in thickness and 0.0762 m in external diameter were heated by a single flat heater placed between them. The heat flow was one dimensional in the axial direction of each cylinder. All surfaces except those where the heating electrical resistance was located were insulated. Four thermocouples numbered 5, 6, 7, and 8 were carefully attached to the heated surface of each specimen. In the same manner, four sensors numbered 1, 2, 3, and 4 were placed in the opposite flat insulated surfaces at the same angular distribution of the heat side. Indeed, the sensors were located at angles 0, 90, 180, and 270 deg of each considered face. This then provided eight temperature histories with four being at a heated surface and four being at the insulated surface.

The applied surface heat flux $q(t)$ follows a time step variation. It was zero until $t=3.3$ s and was zero after $t=18.6$ s. The value of $q(t)$ in the interval $3.3 \leqslant t \leqslant 18.6$ s (heating period) was set to 30,300 W/m^2. The obtained experimental measurements of all temperature sensors are reported in Ref. [3], page 402. One mistake should be corrected on the reported data and it concerns thermocouples Tc_2, Tc_3, and Tc_4 at time 21.3 s. The recorded

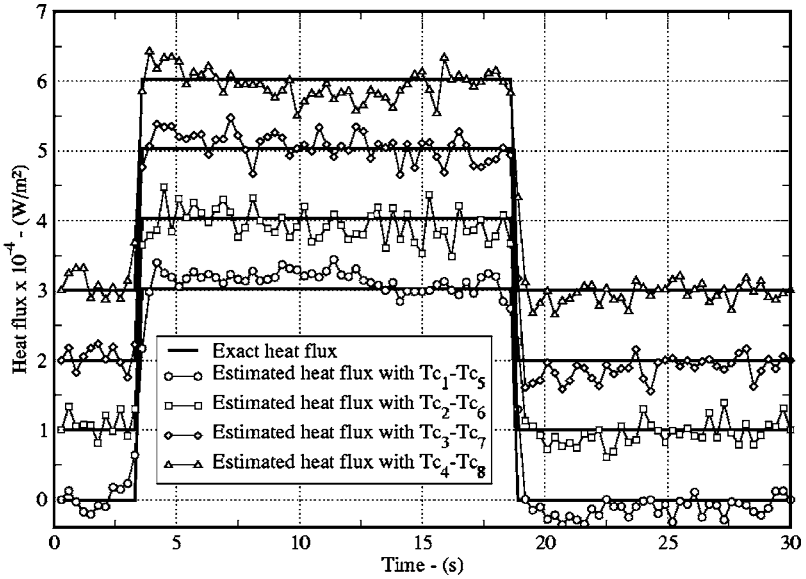

Fig. 1 Configuration $\mathcal{C}_1$. Recovered surface heat flux for the four combinations of sensors: Tc_1-$Tc_5, \ldots, Tc_4$-Tc_8. To alleviate the presentation of all heat flux profiles, the results are shifted one by one toward the top.

temperatures should be 88.31, 88.79, and 88.55°F instead of 89.31, 89.79, and 89.55°F. These corrections are expressed in °F to respect the original data given in Ref. [3]. The measured data were converted to °C before their use in the present work. As reported in Ref. [3], the final time of experiment and the time step acquisition were taken as $t_f=30$ and $\Delta t=0.3$ s. The initial temperature distribution in the sample was constant and taken as $T(x,0)=T_0=27.5\,°\mathrm{C}$.

Experimental Results

Although simulated measurements provide some insight into understanding the behavior of the method, the absolute and true test is with experimental data provided that they were carefully carried out. IRM (conjugate gradient method coupled to discrepancy principle) is extensively studied and applied in the literature to solve many kinds of inverse problems in various fields such as heat transfer, acoustic and vibration, ground water and hydrology, tomography, etc. However, relatively few of these investigations have been done with experimental data.

The finite difference method, with a pure implicit time scheme, is used in solving the established *direct*, *adjoint* and *variation* problems. A mesh grid with 51 nodes in space and 100 steps in time is used for all the results presented below. Indeed, the time step of resolution was taken equal to the experimental time step (sampling rate) to avoid any interpolation of measured data. In Ref. [3], temperature histories resulting from an average of the eight thermocouple combinations, Tc_1-Tc_5, Tc_2-Tc_6, Tc_3-Tc_7, and Tc_4-Tc_8, were used to estimate thermophysical properties of metallic sample, and give, respectively, $k=75.014$ W/m K and $c=3728.6$ kJ/m^3 K. In the remaining part of this section, c is assumed known, that is, estimated with sufficient accuracy in Ref. [3], but k and $q(t)$ are to be recovered by the proposed inverse analysis from the experimental measurements of Beck and Arnold.

Many regularizing techniques were proposed in the literature [1,4,10,15] to reduce the inherent ill-posedness character of inverse problems. The IRM proposed by Alifanov et al. is used in this paper [1,10]. It consists in stopping the iterative process of the conjugate gradient method according to the discrepancy principle [11]. This method requires the knowledge of the measurement error level, i.e., the standard deviation σ, which is given in Ref. [3] as 0.06°C for the used experimental data. Then, the stopping criterion can be computed according to the residual principle [11]. The magnitude of σ is less than 1% of the temperature rise of sensor Tc_1-Tc_5, which is approximately 8.5°C.

Configuration $\mathcal{C}_1$. The first configuration of building the unknown components of vector $\mathbf{U}$ is $\mathcal{C}_1$. Hence, the vector $\mathbf{U}$ contains k as a first component and as many other $\hat{q}_i$ components ($\hat{q}_i=q(t_i)$) as time steps considered in solving the direct problem, i.e., 100 time steps. The total number of $\mathbf{U}$ components is $M=1+J=101$. The initial guesses ($s=0$) of the unknown components were taken as $k^{(0)}=0.1$ and $\hat{q}_j^{(0)}=1$, $j=1,\ldots,J$ for the first configuration and all investigated tests.

Figure 1 shows the estimated heat flux results of the IRM by using separately the four combinations of temperature sensors Tc_1-$Tc_5,\ldots, Tc_4$-Tc_8. Also, the exact heat flux profile is depicted in the same figure. For all combinations of sensors, the obtained results look good enough and not greatly affected by the abrupt changes near 3.3 and 18.6 s. The major time behavior of heat flux (step variation) is reconstructed faithfully and among the presented results, measurements of sensors Tc_2-Tc_6 and Tc_3-Tc_7 give the better estimates of $q(t)$. Indeed, the reconstructed heat flux values are well spread out around the exact profile, which result in small values of ϱ_q for the two cases. The minimum rms value is observed for the sensor combination Tc_3-Tc_7 with the others slightly larger. For all studied cases, the ϱ_q values shown in Table 2 are less than 8.5% of the maximum value of $q(t)$, which is 30,300 W/m^2. We observe that just after heating stops, estimated heat flux has a tendency to be negative near and after the time of 18.6 s. The absence of instabilities (abrupt changes) of heat flux around 3.3 and 18.6 s is due in great part to the sensor location on the heated surface. This means that we are dealing with a relatively easy inverse problem with respect to unknown heat flux. The estimation error, as defined in Eq. (15), is quite acceptable and is approximately the same for all cases with a slightly larger value for combination Tc_2-Tc_6. The minimum errors ε_q and rms ϱ_q are observed when the averaged measurements are used, which seems consistent with the physics of the problem and our expectations.

Table 2 summarizes the estimation errors. The data displayed in this table were obtained for five considered experiments with the

Table 2 Summary of obtained results with different sensor combinations and configuration $\mathcal{C}_1$. Average means that rather than using four separate values, an average of these readings on each side of solid and each time step was used.

Sensor combination			Tc_1-Tc_5	Tc_2-Tc_6	Tc_3-Tc_7	Tc_4-Tc_8	Average
Stopping criterion	δ	°C^2 s	0.2160	0.2160	0.2160	0.2160	0.2160
Iteration number	it	#	14	42	57	12	16
Residual function	$S(\mathbf{U})$	°C^2 s	0.1981	1.3175	0.2692	0.1958	0.2157
Thermal conductivity	k	W/m K	76.510	73.669	72.169	73.208	73.975
Estimation error	ε_k	%	1.99	1.79	3.79	2.40	1.38
Heat flux rms	ϱ_q	W/m^2	2414.05	2497.74	2272.51	2421.97	1789.01
Estimation error	ε_q	%	1.24	1.33	1.10	1.25	0.68
Temperature rms	ϱ_t	°C	0.0577	0.1485	0.0677	0.0583	0.0603

following sensor combinations: Tc_1-Tc_5, Tc_2-Tc_6, Tc_3-Tc_7, Tc_4-Tc_8, and average. The combination average uses all temperatures, i.e., measurements were averaged on each side of the solid. Also displayed in this table are the stopping criterion δ, the required iteration number s for fulfillment of discrepancy principle, estimation error of $q(t)$, estimation error of k, and the heat flux and temperature root mean squares ϱ_q and ϱ_t.

Values of estimated thermal conductivity are of the same order of magnitude but slightly lower than those obtained by Beck [3], except for the first sensor combination Tc_1-Tc_5. The computed values of thermal conductivity belong to the interval [72.169,76.510] (W/m K), which contains the reference value k_r too. The maximum comparative error (difference with Beck's results) ε_k is observed with the third sensor combination Tc_3-Tc_7 and corresponds to the lowest estimated value in these configurations. Conversely, this sensor combination gives the best estimates for heat flux $q(t)$ following the obtained estimation error ε_q and root mean square ϱ_q. On the other hand, the smallest difference with the reference value k_r is due to the second sensor combination Tc_2-Tc_6.

Figure 2 represents the temperature residuals of the presented estimates. According to this figure, the better estimates are those obtained with sensor combinations Tc_1-Tc_5 and Tc_4-Tc_8. For both of them, the residual amplitude is less than 0.2°C and is acceptable despite a weak deviation from the null mean value during the first stages of heating and cooling. Maybe, some correlation between measurements is at the origin of this deviation. On the other hand, the rms temperature values are of the same order of magnitude of standard deviation of measurements for all cases with an overestimated value with configuration Tc_2-Tc_6. This result confirms the efficiency of the inverse analysis and its ability in recovering simultaneously k and $q(t)$, even with a wider deviation in their initial guesses.

Combinations Tc_1-Tc_5 and Tc_4-Tc_8 need only 14 and 12 iterations to evaluate heating flux and thermal conductivity. On the other hand, combinations Tc_2-Tc_6 and Tc_3-Tc_7 need much more, about 42 and 57 iterations (three and four times more). Indeed, the results obtained in these two cases were obtained without discrepancy principle. The value δ=0.2160 of integrated measurement errors is never reached by the iterative process and it did not stop according to the residual principle (Eq. (10)). The functional $S(\mathbf{U})$ reaches the value of 1.3175 after 42 iterations for Tc_2-Tc_6 combination and 0.2692 after 57 iterations for Tc_3-Tc_7 combination. At this iteration level, all $\mathbf{U}$ components have satisfied Eq. (9) with $\epsilon=10^{-5}$ and computed temperatures follow detailed changes in measured ones on the heated surface of the solid (x=0). This behavior of IRM is due to a big deviation of measured temperatures from the expected exact profile on the insulated interface (x=L). This is well demonstrated by analyzing carefully the re-

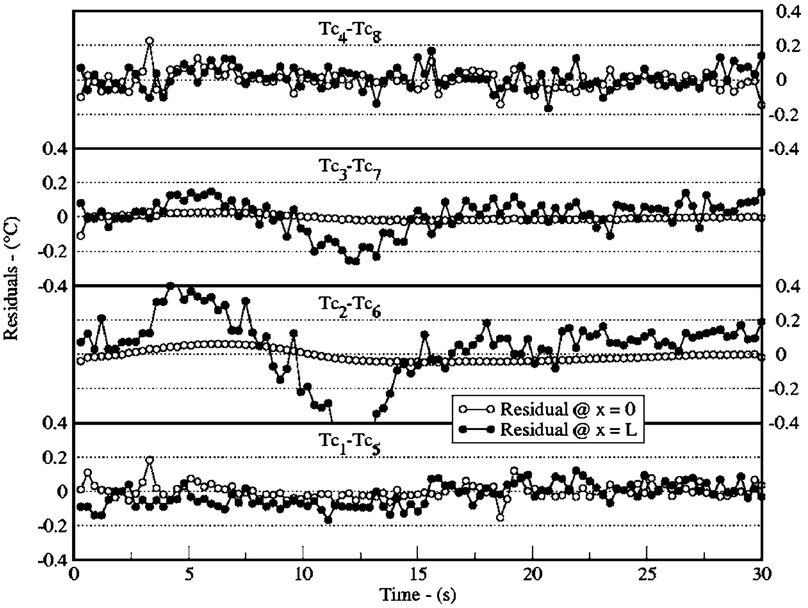

Fig. 2 Temperature residuals of the obtained results with the four combinations of sensors: Tc_1-Tc_5, Tc_2-Tc_6, Tc_3-Tc_7, and Tc_4-Tc_8 and in the case of configuration $\mathcal{C}_1$

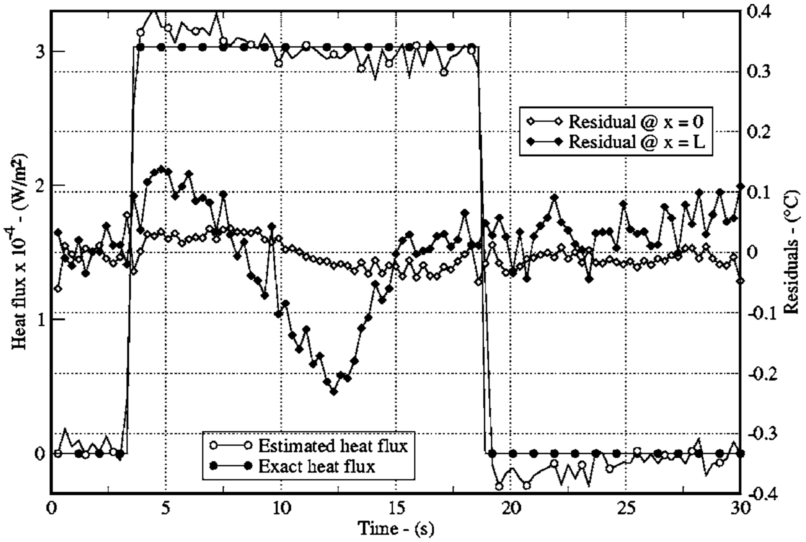

Fig. 3 Recovered surface heat flux by using all measurements and resulting temperature residuals in the case of configuration $\mathcal{C}_1$. All measurements mean that temperatures were averaged on each side of the solid.

siduals depicted in Fig. 2. Sensor combinations Tc_2-Tc_6 and Tc_3-Tc_7 show high residuals on the insulated side of specimen while approximately null and smooth residuals on the heated side. For both cases, this smoothness is explained by the fact that the computed temperatures are matching precisely (exactly) the measured temperatures at $x=0$ and the waving phenomenon around the time axis explains some deficiency of the model during heating and cooling periods (model adequacy or inconstancy to experiment). No notable instabilities were observed in these two sensor configurations because the temperature measurements were of high quality (weak measurement noise).

Figure 3 depicts the estimated surface heat flux obtained with all measurements (averaged measurements). The last column of Table 2 exhibits the estimation parameters. In this case, temperature measurements were averaged on each side of the solid. After 16 iterations, the recomputed heat flux agrees in a good manner with the exact profile and shown less instabilities. Among the presented cases, the lowest rms ϱ_q and estimation error ε_q are observed with this example. As for the temperature rms, it coincides quasiperfectly with the standard deviation of measurements. During the first third part of heating period, the estimated heat flux is slightly overestimated. Then, it stabilizes around the exact heat flux profile during the second third part and becomes underestimated in the last third part. After heating stops, the estimated values of $q(t)$ become negative, which has no physical sense and expresses some inconsistency of the model. This case gives the closest thermal conductivity k to reference value k_r, i.e., the lowest estimation error for thermal conductivity k.

Also, Fig. 3 presents the temperature residuals for the average case. These residuals are correlated and the biggest variation is observed with the sensor installed at $x=L$ during the first two-thirds of the heating period, i.e., from 3 s to 15 s. The maximum observed residual magnitude is approximately 0.2°C, which represents 5% of the temperature rise on the insulated surface. For both sensors, the residuals are positive in the first stages of heating period and become negative in the middle of this period. This outcome is the signature that some inconsistency exists in the model (theoretical and/or experimental) or that some small effects are neglected (heat losses, for example) or biased measurement errors.

Figure 4 shows the computed and measured temperatures on both faces of the sample. The best agreement is observed with sensor installed on the heated surface where measurements match the model response perfectly.

On the other hand, a significant difference is observed between the measured temperatures and the computed ones on the insulated surface and especially in the first half of heating period. By inspecting separately each combination of measured temperature profiles, this indentation is mainly due to the important deviation observed with thermocouple Tc_2 (see the original data of Beck [3]). An attempt of estimating k and $q(t)$ should be conducted, without temperatures of Tc_2-Tc_6 sensors, to elucidate the effect and influence of these data on the estimation quality.

To bring some insight in understanding the behavior of IRM with cases Tc_2-Tc_6 and Tc_3-Tc_7 presented above, a special experimental test was conducted. Indeed, Fig. 5 shows two estimated heat flux profiles obtained by considering, respectively, the two stopping criteria. Data of sensors Tc_4-Tc_8 were used in this experimental test. The first run means that no regularization is considered and the iterative process was spotted according to Eq. (9) (regularization off), whereas the second one shows the application of the discrepancy principle, i.e., application of Eq. (10) (regularization on) in stopping the iterative process. The only difference between shown profiles resides in their smoothness with a marked advantage to the regularized profile. If the estimation is performed with criterion (10), the residuals will be less pronounced because the computed temperatures are "pushed" to follow as close as possible the measured ones (the temperature rms would be very small). Hence, the obtained results with this criterion should be seriously disturbed and highly instable. Fortunately and even the regularization is totally skipped, the first profile looks pretty good and this difference is appreciated with difficulty by human eye. Here again, this remark attests and demonstrates the quality of the temperature measurements used herein and the large signal-to-noise ratio achieved in this experiment. Without regularization, iterative process stopped after 38 iterations, instead of 12, giving the following estimation values: $S(\mathbf{U})=0.1168\,°\mathrm{C\,s}^2$, $\varrho_q=2901.51\ \mathrm{W/m}^2$, $\varrho_t=0.045\,°\mathrm{C}$, $\varepsilon_q=1.79\%$, $k=73.135\ \mathrm{W/m\,K}$, and $\varepsilon_k=2.50\%$. As expected, these values confirm the regularizing character of the discrepancy principle and an appreciable difference between these new values and those listed before in the last column of Table 2 can be observed. The zoom presented in Fig. 5 allows a better visualization for the human eye between heat flux profiles estimated with and without regularization. This simple numerical experience provides considerable insight in understand-

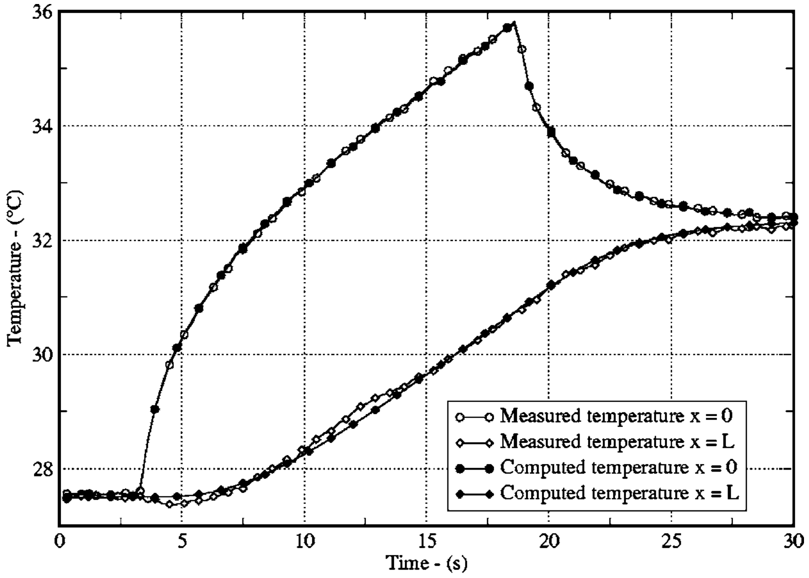

Fig. 4 Measured and calculated temperatures for averaged measurement example in the case of configuration $\mathcal{C}_1$

ing the IRM concept.

Sequential estimation of k. Generally, the sequential estimates demonstrate how the estimated properties vary as additional measurements are considered and hence allow the qualification of the estimation accuracy and the experimental procedure. Figure 6 depicts the sequential estimation of thermal conductivity k, that is, the data for only part of the interval experimental time $[0.3,30]$ s have been used. The sequential estimation started at time 6 s and was increased by one time step at each new estimation. In other words, the data are analyzed by adding a couple of data at each time (two sensors); it shows how the estimated properties change as two more measurements are added to the analysis. Starting at $t=6$ s means we analyzed only the first 6 s of the experiment, which corresponds to $2\times 20=40$ temperature measurements.

Five sequential estimates of k are displayed in Fig. 6 corresponding to the five sensor combinations. All estimates present approximately the same time evolution except the result of combination Tc_1-Tc_5. The typical sequential estimation starts at low values, grows rapidly until a maximum value, at 12–13 s, before a slow decrease, and finally stabilizes around an acceptable value in the last third time interval. Indeed, as more data are considered, the thermal conductivity estimate approaches constant values and shows an asymptotical tendency. Meaning, if the experiment is ended at 20 s, the estimated k would not differ significantly from the property estimated at 30 s. Usually, with an excellent estimation procedure and well designed experiment, the sequential estimates converge to a constant value and are fairly steady with experimental time. For all cases and at short experimental time, the values of estimated thermal conductivity are widely spread out starting at low values of 40–50 W/m K. With short time interval, the sequential estimates vary significantly because of the lack of information in the temperature measurements. A similar behavior of sequential estimation of k and c was observed by Beck in his initial work [3]. For times greater than 20 s, the sequential esti-

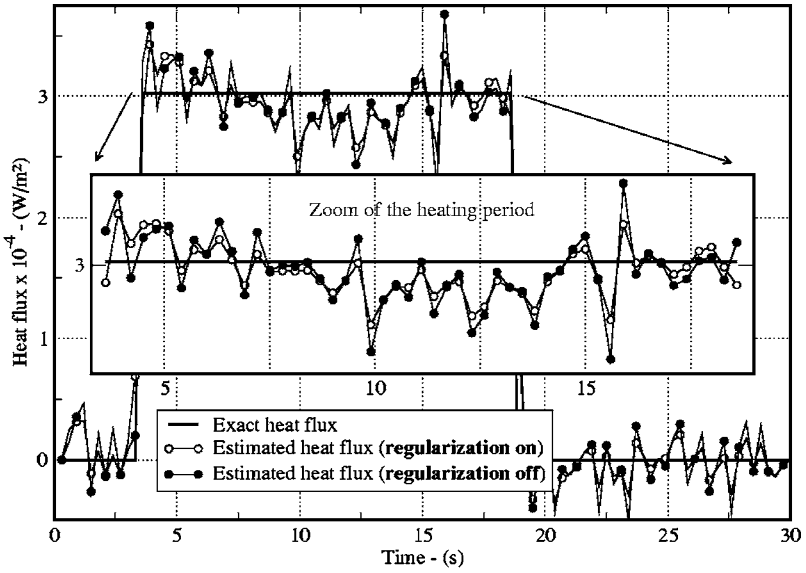

Fig. 5 Recovered heat surface flux with and without regularization in the case of configuration $\mathcal{C}_1$ obtained with sensor combination Tc_4-Tc_8

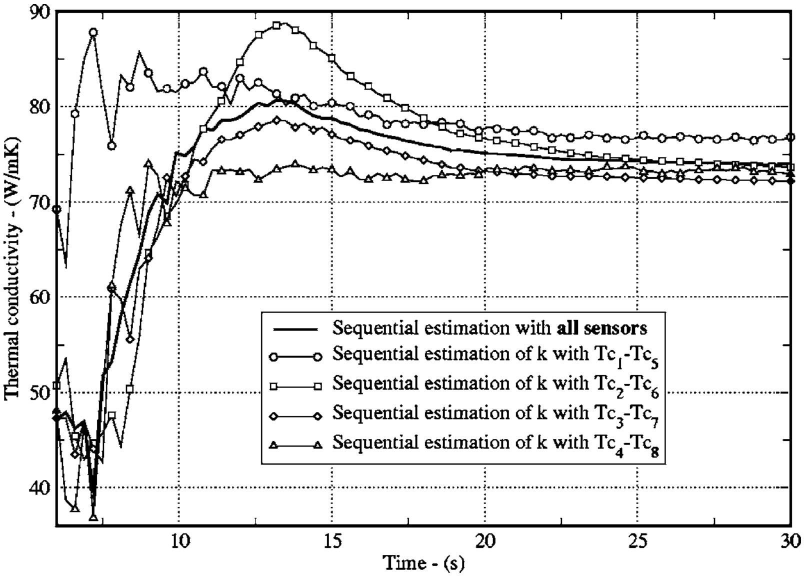

Fig. 6 Sequential estimation of thermal conductivity with averaged measurements in the case of configuration $\mathcal{C}_1$

mates of k change by 1–1.5%. This small change is completely drowned in the confidence region predicted later in this paper. For all displayed results, the final value presents a difference less than 4% with respect to the reference value recovered by Beck [3]. For the average case, there is no notable difference between the sequential estimates of k obtained with and without regularization, which underlines the high quality of used measurements. Finally, k values obtained with regularization are a little bit spread around those obtained without regularization and it seems that the best parameter estimates are obtained when all the data are used.

Some particular sequential estimates of k are displayed in Table 3. These values were obtained by considering four experiments with the following final times: 6, 12, 18, and 24 s. This table shows the obtained thermal conductivity, the heat flux and temperature rms, the estimation error, and the required iteration number. These results were obtained by using the discrepancy principle as stopping criterion in the conjugate gradient method and with the average sensor combination. As shown in Table 3, the last two runs do not comply with the discrepancy principle. The biggest change in thermal conductivity error is observed between 6 s and 12 s. Even though there is a little change in the heat flux rms between experiments, the heat flux error seems to be less sensitive to the sequential estimation, which is correct and logical with the global character of the IRM.

Figure 7 displays the sequential estimated heat flux for $t_f=6$, 12, 18, and 20 s. All reconstructed heat fluxes are in excellent agreement with the exact profile with a slight disadvantage for the first time period. The heat flux rms ϱ_q is of the same order for all considered discrete time intervals. As expected, the estimation error of $q(t)$ does not depend on the final experimental time. The temperature rms ϱ_t is approximately equal to the standard deviation of used data, which is a good indicator on the quality of the estimation.

Figure 8 depicts the residuals for the sequential estimations presented in Table 3. As the time increases, the residuals of insulated surface get more pronounced while the residuals of the opposite side still have the same amplitude. The corresponding measured and calculated temperatures not displayed here present a relatively high matching between the two data. The computed temperatures are smoother than the measured ones but are still indistinguishable for the human eye.

Configuration $\mathcal{C}_2$. The second configuration of building the unknown components of vector $\mathbf{U}$ is $\mathcal{C}_2$. Hence, the vector $\mathbf{U}$ contains k as a first component and as many other $\hat{q}_i$ components as parameters considered in building the parametric form of $q(t)$. The total number of $\mathbf{U}$ components is $M=1+m=4$. The initial guess ($s=0$) of the components was taken as $k^{(0)}=0.1$ and $q_i^{(0)}=12$. By using a priori information on the heat flux evolution, B-spline functions of the first order (constant) were chosen as basis function to approximate the heat flux, see Ref. [16]. The problem is reduced to estimate four constants, the first one corresponds to conductivity k and the remaining ones represent the parameters of heat flux approximation. The following test was performed with the five sets of experimental data Tc_1-Tc_5,

Table 3 Results of sequential estimation at different final experimental times in the case of configuration $\mathcal{C}_1$ and using average combination of measurements

Time of experiment	t_f	s	6	12	18	24
Thermal conductivity	k	W/m K	54.453	79.118	76.070	74.390
Estimation error	ε_k	%	27.40	5.47	1.40	0.83
Stopping criterion	δ	°C^2 s	0.0432	0.0864	0.1296	0.1728
Residual function	$S(\mathbf{U})$	°C^2 s	0.0321	0.0861	0.1439	0.1840
Iteration number	it	#	12	20	39	47
Temperature rms	ϱ_t	°C	0.057	0.061	0.064	0.062
Heat flux rms	ϱ_q	W/m^2	2568.35	1758.342	1284.59	1920.40
Estimation error	ε_q	%	1.69	0.47	0.22	0.63

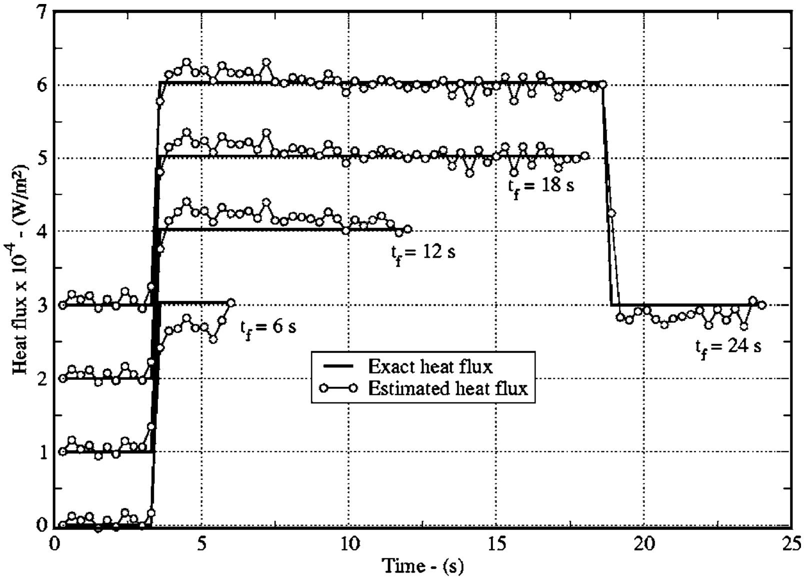

Fig. 7 Recovered surface heat flux for different experimental times in the case of configuration $\mathcal{C}_1$ and using average combination of measurements. The displayed profiles are shifted up one by one to get a better graphical presentation.

Tc_2-Tc_6, Tc_3-Tc_7, Tc_4-Tc_8, and average combination.

Table 4 summarizes the obtained estimates. The estimates of thermal conductivity are contained in the interval [72.228,76.691](W/m K) and remain of the same order of magnitude in comparison with the previous values computed in configuration $\mathcal{C}_1$. Also, the estimation error with respect to Beck's reference value is still acceptable. In all presented cases, the estimation was performed with an acceptable number of iterations.

In the above table, one can observe that the iterative process never reaches the integrated error and stops widely before its numerical value (see rows 2 and 4). In these cases, the termination of iteration obeys Eq. (9) instead of Eq. (10). The chosen parametric form of the heat flux reduces tremendously the variation or the flexibility of unknown heat flux with respect to time, restoring the accomplishment of the discrepancy principle impossible. For all presented sensor combinations, the estimation error of heat flux is less than 1%, which reflects the power of parametric representation when a priori information on unknown heat flux is used. Indeed, in this kind of experiment, one can have enough information about the sequence of experimental procedure and take advantage of this information to get the best improvement into the estimation results. Knowing the total experience time, the beginning and the end of heating period, and the time variation of applied heat flux, one can specify the right parametric form for $q(t)$ to increase the estimation accuracy.

With the parametric form, we obtain the smallest heat flux rms among all presented results in this paper, $\varrho_q=669.24\ \mathrm{W/m^2}$ compared with the maximum value of $30,300\ \mathrm{W/m^2}$. It represents less than 2.5% of the maximum heat flux value. Indeed, in the

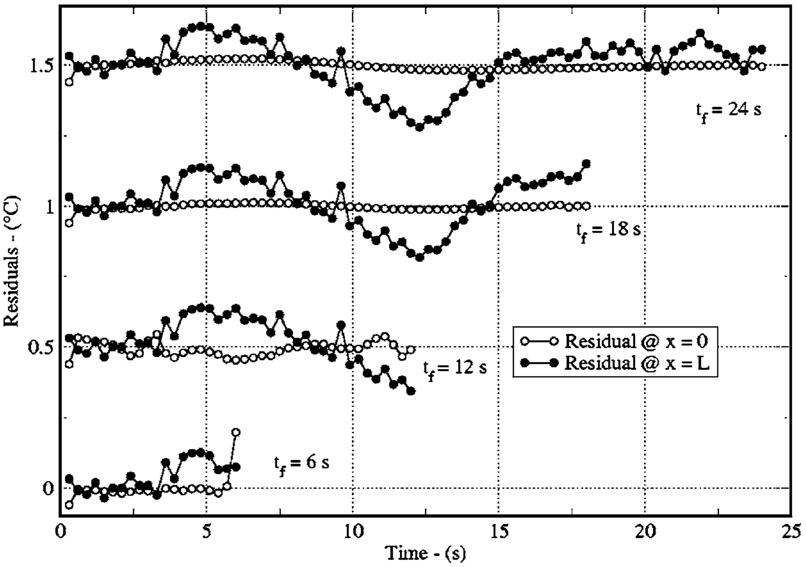

Fig. 8 Temperature residuals for different experimental times in the case of configuration $\mathcal{C}_1$ and using average combination of measurements. For the sake of clarity, residuals are shifted up one by one.

Table 4 Summary of obtained results with different sensor combinations and with configuration $\mathcal{C}_2$. Average means that rather than using four separate values, an average of these readings on each side of solid and each time step was used. The unknown heat flux is parametrized with three piecewise constant functions. The displayed value of residual function corresponds to the last iteration.

Sensor combination			Tc_1-Tc_5	Tc_2-Tc_6	Tc_3-Tc_7	Tc_4-Tc_8	Average
Stopping criterion	δ	°C^2 s	0.2160	0.2160	0.2160	0.2160	0.2160
Iteration number	it	#	25	17	27	21	17
Residual function	$S(\mathbf{U})$	°C^2 s	0.3711	1.5935	0.5360	0.5956	0.3851
Thermal conductivity	k	W/m K	76.691	73.667	72.228	73.170	73.929
Estimation error	ε_k	%	2.23	1.79	3.71	2.45	1.44
Heat flux rms	ϱ_q	W/m^2	1167.52	806.61	946.70	1094.47	669.24
Estimation error	ε_q	%	0.289	0.136	0.187	0.248	0.092
Temperature rms	ϱ_t	°C	0.0789	0.1634	0.0952	0.1003	0.0806

average case, the estimation error was less than 0.10%. As is displayed in Fig. 9, the heat flux matches quasiperfectly the exact profile over the heating period. After an abrupt change at time 18.6 s, the heat flux has a tendency to be negative, which represents an inherent deficiency of the IRM with this type of time profile [14].

By using the parametrization concept, the residuals tend to be more correctly distributed around the zero mean value for the first sensor (heated surface) than the second one (insulated surface) but both are correlated. Indeed, the second thermocouple shows considerable deviation between measurements and model response during the heating period. The model adequacy with the experience may be at the origin of this difference, i.e., the experience does not reflect the theoretical model perfectly (model inconsistency, omission of some effects such as heat losses, etc.). For both thermocouples, the magnitude of the residuals is approximately 0.20°C, which represents 2–3% of the temperature rise on the heated surface and 4–5% of the temperature rise on the insulated surface. In this form, the estimated heat flux is "pushed" to produce the smallest distance between measurements and computed temperatures. The noise amplitude is still of the same order of magnitude as in the previously presented cases without parameterization.

The measured and calculated temperature profiles are presented in Fig. 10. With the parametric form of heat flux, the best resulting temperature rms is obtained with the first and the last sensor combination (Tc_1-Tc_5 and average) and is still comparable to measurement standard deviation. However, one should be careful in the parametrization of unknowns because this procedure can hide useful details on the experiment drift when there is an important deviation between measurements and model response. This omission is mainly due to overregularizing effect introduced by this procedure.

All previous results (for $\mathcal{C}_1$ and $\mathcal{C}_2$ configurations) were obtained iteratively with the conjugate gradient method, which uses a descent parameter in vectorial form, i.e., each unknown, k or $q(t)$, has its own descent parameter. The details showing the derivation of this descent vector (two components) are presented in Ref. [12]. On the other hand, several runs were conducted using a common descent parameter to k and $q(t)$ but all of them ended in failure even with very close initial guesses to the exact values for both unknowns. These computations are not reported here for the sake of brevity.

Experimental Uncertainty. The estimated thermal conductivity is presented without confidence interval due to the nature of the IRM. The IRM does not allow the computation of confidence interval like the ordinary least squares method. To give an idea on the estimation error, we use the approach developed by Moffat [17,18], which consists in a parametric investigation to quantify the experimental uncertainty, i.e., if the parameter β changes by x%, the results vary by y%. The uncertainty in the estimated k, based on the uncertainty in the experimental parameters, is calculated as follows:

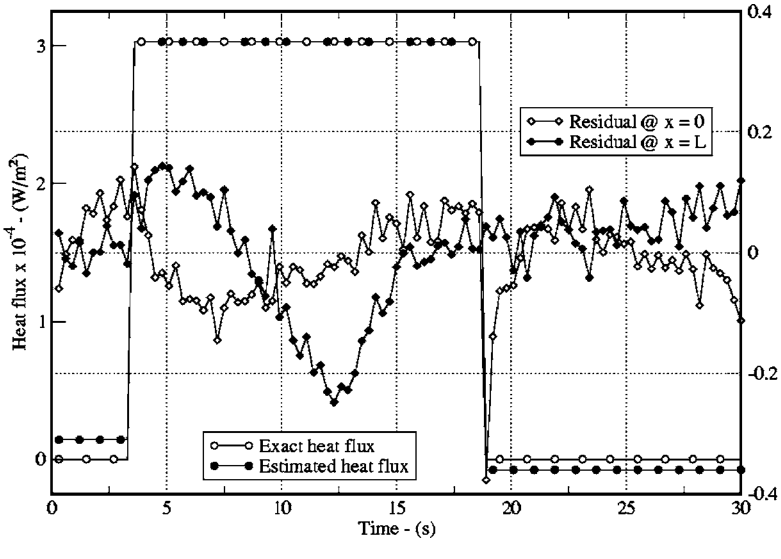

Fig. 9 Recovered surface heat flux and temperature residuals by using parametric form and averaged measurements

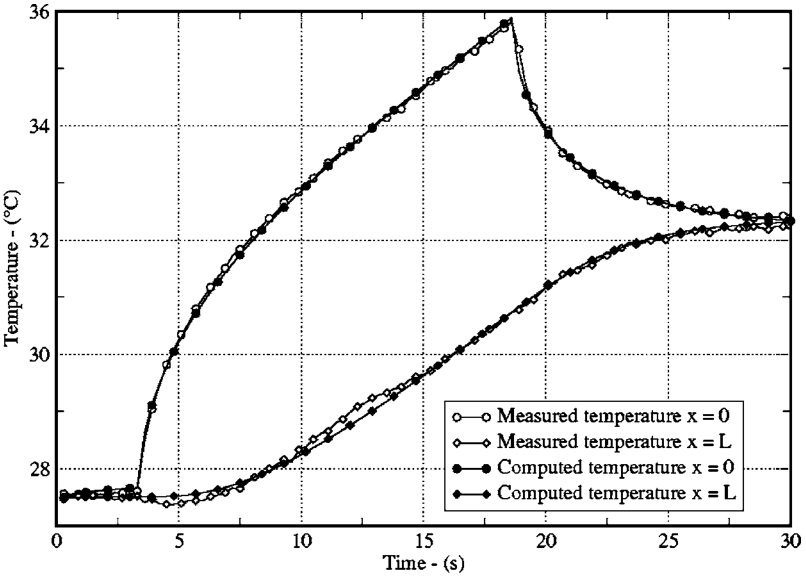

Fig. 10 Measured and recomputed temperatures when the parametric form of $q(t)$ is used

$$\Delta k = \left[\left(\frac{\partial k}{\partial \beta_1} \Delta \beta_1 \right)^2 + \left(\frac{\partial k}{\partial \beta_2} \Delta \beta_2 \right)^2 + \cdots \right]^{1/2} \tag{17}$$

where $\beta_1, \beta_2, \ldots$ are other measurable experiment parameters such as thickness of sample, heating heat flux, known thermophysical properties, etc.

Only experimental uncertainty of volumetric specific heat c and sample thickness L and their contribution to the total uncertainty in the estimated k are given in Table 5. The thickness error could be interpreted as sensor location error because thermocouples are installed on both sides $x=0$ and $x=L$. The effects of an absolute error of 0.0005 m on the sample thickness and 149,144 $\mathrm{J/m^3\,^\circ C}$ on the volumetric specific heat, corresponding, respectively, to 1.0% and 4.0%, are investigated for both developed configurations. Impact of other parameters, such as insulation, heating power, etc., can be analyzed by using the same approach. This high level of relative error on c and L was deliberately exaggerated to identify the dominant term.

Hence, the confidence interval of estimated thermal conductivity is given by 73.975 ± 3.249 W/m K for the first configuration $\mathcal{C}_1$ and 73.929 ± 3.324 W/m K for the second configuration $\mathcal{C}_2$. For both configurations, the uncertainty represents a maximum error of 4.50%. The dominant term on k error is observed with the sample thickness, which underlines the high precaution to be observed in measuring this quantity. On the other hand, the error of specific heat seems to have less influence on k estimate. Finally, during this error analysis, it is noticed that the measurement error on L and c has a non-negligible effect on the estimation error of $q(t)$ and the most important effect was observed with c error.

Conclusion

We have shown in this paper the application of the conjugate gradient method coupled with discrepancy principle for estimating simultaneously one parameter and one function by using experimental data. This example involves the estimation of thermal conductivity (one parameter) of a solid and one of its unknown boundary conditions at $x=0$ (heat flux function). The obtained results illustrate the efficiency of the above method when it is applied with a vectorial descent parameter and experimental data.

The temperature data of Beck and Arnold are found to be excellent. The estimated thermal conductivity is close to the result of Beck. Moreover, the reconstructed unknown heat flux is estimated with an acceptable accuracy in comparison with the error level of measurements and the known exact profile. As reported by Beck, uncertainty in experimental procedure accounts for the small observed discrepancy between the model outcome and the measured temperatures.

By using a priori information on the time evolution of heat flux, the estimation could be greatly increased by introducing the parametrization concept. When a piecewise constant function is used for the parametrization of unknown heat flux, the estimation results are in excellent agreement with the exact ones.

Generally, the comparison of the recovered data with the exact model showed good agreement. The obtained results underline the feasibility of the procedure and its capabilities to recover simultaneously thermal conductivity and surface heat flux without using any a priori information on both of them. This represents a noted benefit for this iterative method.

Table 5 Experimental uncertainty analysis of estimated thermal conductivity k for both developed configurations $\mathcal{C}_1$ and $\mathcal{C}_2$. Averaged temperature measurements are used in this error analysis.

Parameter	Unit	Uncertainty	(%)	Contribution with $\mathcal{C}_1$	Contribution with $\mathcal{C}_2$
β_i	—	$\Delta\beta_i$	—	$(\partial k/\partial\beta_i)\Delta\beta_i$	$(\partial k/\partial\beta_i)\Delta\beta_i$
c	$\mathrm{J/^\circ C\,m^3}$	149,144	4	2.847	2.965
L	m	2.54×10^{-4}	1	1.567	1.504
Total error	W/m °C	Δk	—	3.249	3.324

As underlined in Ref. [7], the proposed combined parameter and function estimation procedure is based on common framework, complies with Beck's requirements, and can then be applied to many other inverse problems not elucidated yet. The concept of the proposed method is quite general, owns a solid mathematical background, has wide applications in the analysis of experimental data, and could be considered as a complementary tool to the previous study presented in Ref. [7]. This approach is ready to be extended and employed in many new challenging problems in conduction, convection, radiation, or any combination of all heat transfer modes.

Acknowledgment

The author would like to express his deep acknowledgments to Professor J. V. Beck for his invaluable help by providing him with his excellent experimental data, published in Beck and Arnold [3].

Nomenclature

c = specific heat
I = number of sensors
J = number of time step
k = thermal conductivity
M = number of unknowns
q_i = component of unknown heat flux vector
$q(t)$ = unknown heat flux
$S(\mathbf{U})$ = residual functional
$T(x,t)$ = computed temperature
T_0 = initial temperature
$\mathbf{U}$ = unknown vector
u_i = unknown vector component
$Y(x_i,t)$ = measured temperature

Greek Symbols

δ = integrated measurement error
ϵ = precision
ε_k = estimation error of k
ε_q = estimation error of $q(t)$
ϱ_q = root mean square of heat flux $q(t)$
ϱ_t = root mean square of temperature
σ = standard deviation of measurement

References

[1] Alifanov, O. M., 1994, *Inverse Heat Transfer Problems*, Springer-Verlag, Berlin.
[2] Ozisik, M. N., and Orlande, H. R. B., 2000, *Inverse Heat Transfer: Fundamentals and Applications*, Taylor & Francis, Philadelphia, PA.
[3] Beck, J. V., and Arnold, K. J., 1977, *Parameter Estimation in Engineering and Science*, Wiley, New York.
[4] Beck, J. V., Blackwell, B., and St-Clair, C. R., 1985, *Inverse Heat Conduction. Ill Posed Problems*, Wiley, New York.
[5] Murio, D. A., 1993, *The Mollification Method and the Numerical Solution of the Ill-Posed Problems*, Wiley Interscience, New York.
[6] Hensel, E., 1991, *Inverse Theory and Applications for Engineers*, Prentice-Hall, Englewood Cliffs, NJ.
[7] Beck, J. V., 1988, "Combined Parameter and Function Estimation in Heat Transfer With Application to Contact Conductance," J. Heat Transfer, **110**, pp. 1046–1058.
[8] Martin, T. J., and Dulikravicz, G. S., 2000, "Inverse Determination of Temperature-Dependent Thermal Conductivity Using Steady Surface Data on Arbitrary Objects," ASME J. Heat Transfer, **122**, pp. 450–459.
[9] Dowding, K. J., Beck, J. V., Ulbrich, A., Blackwell, B., and Hayes, J., 1995, "Estimation of Thermal Properties and Surface Heat Flux in Carbon-Carbon Composite," J. Thermophys. Heat Transfer, **9**(2), pp. 345–351.
[10] Alifanov, O. M., Artyukhin, E. A., and Rumyantsev, S. V., 1995, *Extreme Methods of Solving Ill-Posed Problems and Their Applications to Inverse Heat Transfer Problems*, Begell House, New York.
[11] Morozov, V. A., 1984, *Methods for Solving Incorrectly Posed Problems*, Springer-Verlag, Berlin.
[12] Loulou, T., and Artioukhine, E. A., 2003, "Optimal Choice of Descent Steps in Gradient Type Methods When Applied to Combined Parameter and/or Function Estimation," Inverse Probl. Eng., **11**(4), pp. 273–288.
[13] IMSL, Library edition 10.0, User's Manual, Houston, TX, 1987.
[14] Beck, J. V., Blackwell, B., and Haji-Sheikh, A., 1996, "Comparison of Some Inverse Heat Conduction Methods Using Experimental Data," Int. J. Heat Mass Transfer, **139**(17), pp. 3649–3657.
[15] Tikhonov, A. N., and Arsenin, V. Y., 1977, *Solution of Ill-Posed Problems*, Winston, Washington DC.
[16] de Boor, C., 1981, *A Practical Guide to Splines*, Springer-Verlag, Berlin.
[17] Moffat, R. J., 1982, "Contribution to the Theory of Single-Sample Uncertainty Analysis," J. Fluids Eng., **104**, pp. 250–260.
[18] Moffat, R. J., 1985, "Using Uncertainty Analysis in the Planning of an Experiment," J. Fluids Eng., **107**, pp. 173–178.

Flow Boiling Heat Transfer in Microchannels

Dong Liu[1]
e-mail: dongliu@ecn.purdue.edu

Suresh V. Garimella
e-mail: sureshg@ecn.purdue.edu

Cooling Technologies Research Center,
School of Mechanical Engineering,
Purdue University,
West Lafayette, IN 47907-2088

Flow boiling heat transfer to water in microchannels is experimentally investigated. The dimensions of the microchannels considered are 275×636 *and* $406\times 1063\ \mu\mathrm{m}^2$*. The experiments are conducted at inlet water temperatures in the range of* $67-95^{\circ}\mathrm{C}$ *and mass fluxes of* $221-1283\ \mathrm{kg/m^2\,s}$*. The maximum heat flux investigated in the tests is* $129\ \mathrm{W/cm^2}$ *and the maximum exit quality is 0.2. Convective boiling heat transfer coefficients are measured and compared to predictions from existing correlations for larger channels. While an existing correlation was found to provide satisfactory prediction of the heat transfer coefficient in subcooled boiling in microchannels, saturated boiling was not well predicted by the correlations for macrochannels. A new superposition model is developed to correlate the heat transfer data in the saturated boiling regime in microchannel flows. In this model, specific features of flow boiling in microchannels are incorporated while deriving analytical solutions for the convection enhancement factor and nucleate boiling suppression factor. Good agreement with the experimental measurements indicates that this model is suitable for use in analyzing boiling heat transfer in microchannel flows.* [DOI: 10.1115/1.2754944]

Keywords: microchannels, boiling, high heat flux, heat sink

1 Introduction

Boiling heat transfer in microchannel heat sinks has attracted significant interest due to its capability for dissipating the high heat fluxes encountered in the thermal management of microelectronics [1,2]. However, the complex nature of convective flow boiling and two-phase flow in microchannels is still not well understood and has impeded the practical implementation of microchannel heat sinks with two-phase flow [3–5]. Among the unresolved issues of particular importance is the quantitative prediction of the boiling heat transfer coefficient in microchannels over a wide range of conditions, from subcooled to saturated boiling. A limited number of studies in the literature [6–17] have addressed this issue, as summarized in Table 1. A survey of this literature reveals a lack of consensus on the understanding and prediction of boiling heat transfer and two-phase flow in microchannels. In particular, although flow-pattern-based models [18,19] have been proposed to correlate boiling data, these models are typically applicable over a narrow range of experimental conditions. There is thus a clear need for additional systematic studies, which carefully address the experimental characterization and modeling of boiling heat transfer in microchannel flows.

The objective of the present work is to conduct a comprehensive experimental investigation of flow boiling heat transfer in microchannel heat sinks, covering a range of subcooled and saturated boiling conditions. The subcooled and saturated boiling regimes are studied in the lower quality range (up to 20%). Heat flux, temperature, and pressure drop measurements are used to construct boiling curves. Boiling heat transfer correlations developed for conventional-sized channels are critically appraised for their applicability to the prediction of flow boiling in microchannels. A heat transfer correlation suitable for prediction of heat transfer coefficients in the subcooled boiling regime is identified. A new superposition model is developed as a modification to the model of Chen and co-workers [20,21] to correlate the results in the saturated boiling regime; the proposed model incorporates the unique flow features of microchannel flows. The model predictions are validated against the experimental results.

2 Experiments

2.1 Experimental Setup. Figure 1(*a*) shows the test loop assembled for the experimental investigation of convective flow boiling in microchannels. A variable-speed gear pump is used to circulate the working fluid (de-ionized water) through the test loop. Two turbine flowmeters are arranged in parallel to measure flow rates in different ranges during the tests. A water bath adjusts the degree of subcooling in the fluid prior to entering the microchannel heat sink. A liquid-to-air heat exchanger is employed to condense the vapor in the two-phase mixture before the fluid returns to the reservoir. The absolute pressures in the entrance and exit manifolds of the microchannel test section are measured. The experimental data are read into a data acquisition system for processing.

The microchannel test section consists of a copper test block, an insulating G10 housing piece, and a G7 fiberglass cover, as shown in Figs. 1(*b*) and 1(*c*). Twenty-five microchannels were cut into the top surface of the copper block, which has an area of $25.4\times 25.4\ \mathrm{mm}^2$ using a precision sawing technique. Test pieces with two different microchannel dimensions were tested. The first test piece (microchannel I) contains microchannels that are $275\ \mu\mathrm{m}$ in width (w_c) and $636\ \mu\mathrm{m}$ in height (H_c), with an intervening fin thickness (w_w) of $542\ \mu\mathrm{m}$, while the second test piece (microchannel II) contains microchannels that are $406\ \mu\mathrm{m}$ in width and $1063\ \mu\mathrm{m}$ in height, with an intervening fin thickness of $597\ \mu\mathrm{m}$. Eight cartridge heaters embedded in the copper block provide a maximum power input of 1600 W. As indicated in Fig. 1(*c*), three Copper-Constantan (type-T) thermocouples (T_1-T_3) made from 36-gauge wire were inserted just below the microchannels at a distance of 3.17 mm from the base. Microchannel wall temperatures at the three streamwise locations are obtained by extrapolation from these three thermocouple readings. Four more thermocouples (T_1-T_3) were embedded in the copper block at 6.35 mm axial intervals for measurement of the average heat flux. The inlet and outlet fluid temperatures ($T_{f,\mathrm{in}}$ and $T_{f,\mathrm{out}}$) were measured at locations immediately upstream and downstream of the

---

[1] Corresponding author.

Contributed by the Heat Transfer Division of ASME for publication in the JOURNAL OF HEAT TRANSFER. Manuscript received August 21, 2006; final manuscript received December 14, 2006. Review conducted by Satish G. Kandlikar. Paper presented at the 2005 ASME International Engineering Congress (IMECE2005), Orlando, FL, November 5–11, 2005.

Table 1 Studies of flow boiling in microchannels in the literature

Reference	Dimension	Fluid	Parameter range	Key observations	Heat transfer correlation
Lazarek and Black [6]	D_h=3.15 mm	R-113	G: 140–740 kg/s m^2	Heat transfer coefficient relatively independent of vapor quality, and function of Nu, Re, and Bo	$\text{Nu}=30\,\text{Re}^{0.857}\,\text{Bo}^{0.714}$
			x: 0–0.8	Nucleate boiling dominates	
Wambsganss et al. [7]	D_h=2.92 mm	R-113	G: 50–300 kg/s m^2	Nucleate boiling dominates	
			x: 0–0.9	Heat transfer coefficient strongly dependent on heat flux and weakly dependent on mass flux and quality	
Tran et al. [8]	D_h=2.4 mm	R-12	G: 44–832 kg/s m^2	Nucleate boiling dominates	$\text{Nu}=770(\text{Re}_{Lo}\,\text{Co}\,\text{Bo})^{0.62}\left(\frac{\rho_g}{\rho_l}\right)^{0.297}$
			x: 0–0.94	Heat transfer coefficient independent of quality for $x>0.2$ and has no mass flux dependence	
Kew and Cornwell [9]	D_h=1.39–3.69 mm	R-141b		Heat transfer coefficient shows different trends for high and low mass flux	
Yan and Lin [10]	D_h=2 mm	R-134a	G: 50–200 kg/s m^2	Variation of heat transfer coefficient with quality is not consistent and depends on heat flux, saturation temperature, and mass flux	$h_{\text{tp}}=(C_1\text{Co}^{C_2}+C_3\text{Bo}^{C_4}\,\text{Fr}_{lo})(1-X_m)^{0.8}h_l$
			x: 0–0.9		
Bao et al. [11]	D_h=1.95 mm	R11	G: 50–1800 kg/s m^2	Nucleate boiling dominates	$h=C_1q''^{C_2}$
		HCFC123	x: 0–0.9	Heat transfer coefficient independent of mass flux and vapor quality and increases with heat flux and system pressure for saturated regime	
Lee and Lee [12]	20×0.4–2 mm	R-113	G: 50–200 kg/s m^2	Heat transfer dominated by convection	Film-flow model applicable for low flow rate; Kandlikar correlation applicable for high flow rate
			x: 0.15–0.75	Heat transfer coefficient independent of heat flux and increases with mass flux and vapor quality.	
Yu et al. [13]	D_h=2.98 mm	Water	G: 50–200 kg/s m^2	Nucleate boiling dominates over a large mass flux and quality range	$h=6{,}400{,}000(\text{Bo We})^{0.27}\left(\frac{\rho_l}{\rho_v}\right)^{-0.2}$
			x: 0–0.9		
Qu and Mudawar [14]	$231\times713\ \mu\text{m}^2$	Water	G: 134–402 kg/s m^2	Forced convection heat transfer dominant in saturated boiling	Annular model proposed
			x: 0–0.2		
Haynes and Fletcher [15]	D_h=0.92 mm	R11	G: 110–1840 kg/s m^2	Nucleate boiling dominates as subcooled liquid approaches saturation	$h=h_{\text{conv}}+h_{\text{pb}}(q_{\text{nb}})\frac{T_w-T_{\text{sat}}}{T_w-T_{\text{mean}}}$
	1.95 mm	HCFC123	x: −0.35–1.0	No suppression of nucleate boiling if $\text{Re}_{\text{LO}}<10^4$ h_{conv} for larger than single-phase value, strongly correlated with nucleate boiling	
Warrier et al. [16]	D_h=0.75 mm	FC-84	G: 557–1600 kg/s m^2	No significant maldistribution for five-channel configuration	Subcooled region $\frac{h_{\text{tp}}}{h_{\text{sp\_FD}}}=1+6.0\text{Bo}^{1/16}+290(1-855\text{Bo})\text{Sc}^{4.15}$
			x: 0–0.2	Flow pattern develops quickly into annular flow	Saturated region $\frac{h_{\text{tp}}}{h_{\text{sp\_FD}}}=1+6.0\text{Bo}^{1/16}-5.3(1-855\text{Bo})X^{0.65}$
Chen and Garimella [17]	$504\times2500\ \mu\text{m}^2$	FC-77		Nucleate boiling heat transfer dominant	

microchannels, respectively. The power input to the cartridge heaters was regulated by a digitally controlled dc power supply unit.

2.2 Test Procedure. Prior to each experiment, the working fluid was degassed by violently boiling the water for approximately 1 h. The amount of dissolved gas in the water was monitored with an in-line oxygen sensor and the water was considered degassed when the concentration was less than 4 ppm; at this concentration, the effects of dissolved gas on the boiling heat transfer may be neglected [22].

In each experiment, the heater power supply was switched on and set to the desired value after the fluid inlet temperature was stabilized. A steady state was reached when readings from all thermocouples remained unchanged (within ±0.1°C) over a 2 min period. Each steady-state value was calculated as an average of 300 readings for all power, temperature, pressure, and flow rate measurements. The heat flux was then increased for the next test, and the procedure repeated for subsequent tests. The fluid inlet velocity and temperature were varied to achieve different testing conditions, as summarized for both microchannel dimensions in Tables 2 and 3. The maximum heat flux in the experiments was 128.8 W/cm^2. The inlet temperature of water is adjusted as a parameter, and varies between 66.6 and 94.9°C for microchannel I and 78.8 and 95.4°C for microchannel II. If the fluid were introduced at near-saturated conditions, the distribution of the two-phase mixture in the microchannels would be heavily affected by the entrance manifold, with the flow boiling patterns in the microchannels being a function of the particular entrance conditions used.

2.3 Data Reduction. The heat loss to the ambient from the test section is estimated from the difference between the total power input q_{input} and the sensible heat gain by the fluid under single-phase heat transfer conditions as

$$q_{\text{loss}}=q_{\text{input}}-\dot{m}c_p(T_{f,\text{out}}-T_{f,\text{in}}) \tag{1}$$

and is correlated as a function of the average wall temperature $q_{\text{loss}}=q_{\text{loss}}(T_{w,m})$ for each inlet condition, which is then used in calculating heat loss under boiling conditions. Once boiling commences, between 87% and 98% of the input power was transferred to the water under the range of experimental conditions considered, depending on the heat flux and flow rate.

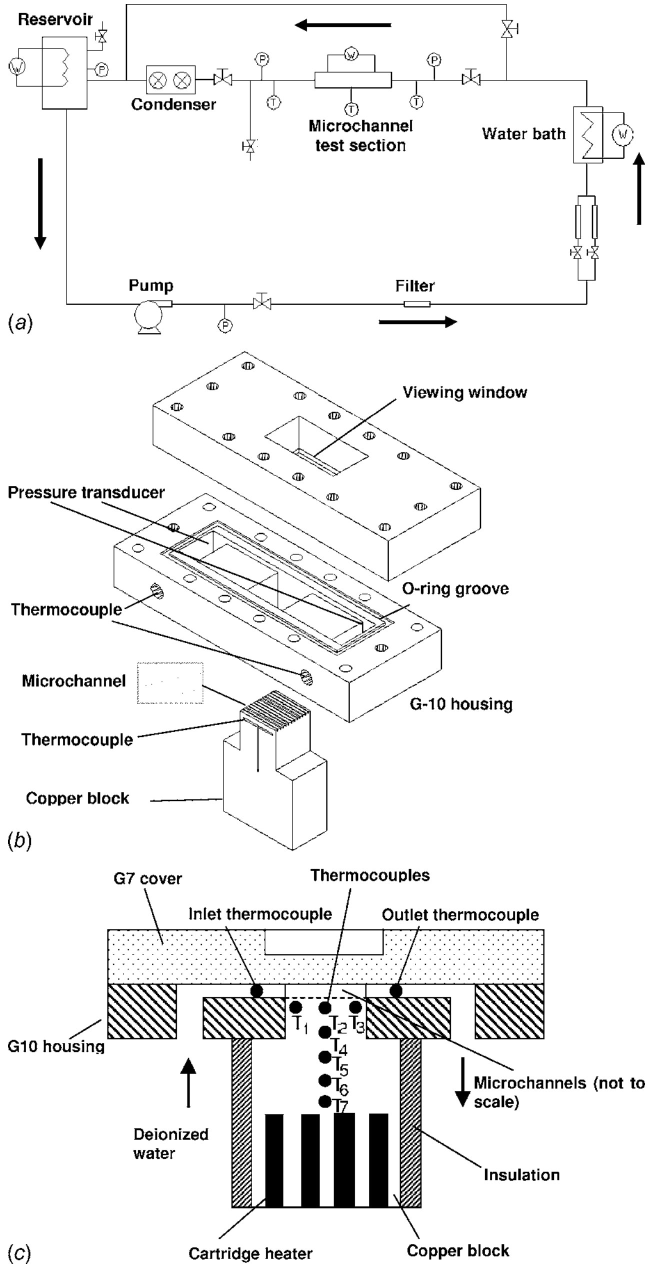

Fig. 1 Experimental setup for studying flow boiling in a microchannel heat sink: (*a*) test loop, (*b*) test piece assembly, and (*c*) cross-sectional view of the microchannel test piece

The applied heat flux q'' is calculated using the base area of the copper block, $A_b = WL$, and represents the heat dissipation rate of the heat sink,

$$q'' = (q_{\text{input}} - q_{\text{loss}})/A_b \tag{2}$$

The effective wall heat flux is defined as

$$q''_w = (q_{\text{input}} - q_{\text{loss}})/A_t \tag{3}$$

where A_t $(=n(w_c+2\eta H_c L))$ is the total heat transfer area of the microchannels.

The microchannel length can be divided into two regions according to the local thermodynamic quality:

Table 2 Test matrix for microchannel flow boiling experiments: microchannel I

Case	u_0 (m/s)	G (kg/s m^2)	$T_{f,\text{in}}$ (°C)	q''_{max} (W/cm^2)	$x_{\text{exit,max}}$
I-1	0.33	324	66.6	111.1	0.16
I-2	0.34	327	77.9	116.1	0.19
I-3	0.33	319	78.7	106.5	0.18
I-4	0.33	323	84.8	119.7	0.20
I-5	0.33	322	89.2	115.4	0.20
I-6	0.33	321	94.9	106.1	0.19
I-7	0.68	663	66.5	117.8	0.05
I-8	0.67	651	77.6	99.1	0.05
I-9	0.68	655	85.7	111.2	0.07
I-10	0.68	661	89.2	118.0	0.08
I-11	0.68	662	78.9	112.7	0.06
I-12	0.68	652	94.8	96.4	0.07
I-13	0.95	921	78.3	104.3	0.03
I-14	0.95	919	85.6	117.1	0.05
I-15	0.96	926	93.2	115.1	0.06
I-16	1.33	1283	87.8	114.7	0.03

$$x = \frac{i_f - i_{\text{sat},0}}{h_{\text{fg}}} \tag{4}$$

The subcooled region covers the portion of the channel over which the thermodynamic quality takes negative values. In terms of flow regimes, it includes both the single-phase and subcooled boiling regions. The length of the subcooled region can be calculated from the following energy balance:

$$L_{\text{sp}} + L_{\text{sub}} = \frac{\dot{m}c_p(T_{\text{sat},0} - T_{f,\text{in}})}{q''W} \tag{5}$$

in which $T_{\text{sat},0}$ is the local saturation temperature, and L_{sp} and L_{sub} are the lengths of the single-phase and subcooled boiling regions, respectively. In the saturated region that follows, the temperature of the vapor-liquid mixture remains at the local saturation point and the quality increases from zero as the fluid picks up more heat, adding to the vapor content of the flow.

The boiling heat transfer coefficient is determined from

$$\bar{h}_{\text{tp}} = \frac{q''_w}{T_w - T_f} \tag{6}$$

in which T_w is the average temperature of the channel wall and T_f is the mean fluid temperature.

Temperature-dependent thermophysical properties of water were used for both the liquid and vapor phases in the data analysis. The saturation temperatures at the inlet and outlet were determined from the pressure measurements. Then, following the ap-

Table 3 Test matrix for microchannel flow boiling experiments: microchannel II

Case	u_0 (m/s)	G (kg/s m^2)	$T_{f,\text{in}}$ (°C)	q''_{max} (W/cm^2)	$x_{\text{exit,max}}$
II-1	0.23	224	79.7	120.9	0.093
II-2	0.23	221	91.7	116.9	0.112
II-3	0.23	224	94.5	122.2	0.116
II-4	0.25	241	94.8	126	0.113
II-5	0.31	299	80.8	121.4	0.062
II-6	0.31	299	85.9	117.3	0.067
II-7	0.31	297	91.9	121.9	0.082
II-8	0.31	297	94.7	108.6	0.07
II-9	0.34	332	78.8	118.3	0.049
II-10	0.34	330	92.1	112.5	0.06
II-11	0.34	328	95.1	118.9	0.069
II-12	0.37	360	79.8	120.2	0.044
II-13	0.37	361	91.8	128.8	0.068
II-14	0.37	357	94.5	114.9	0.059
II-15	0.37	357	95.4	125.4	0.067

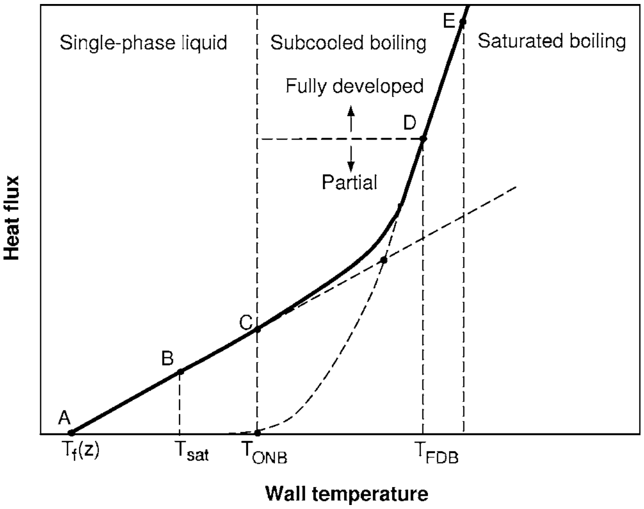

Fig. 2 Boiling curve: variation of wall temperature and heat flux during flow boiling in channels

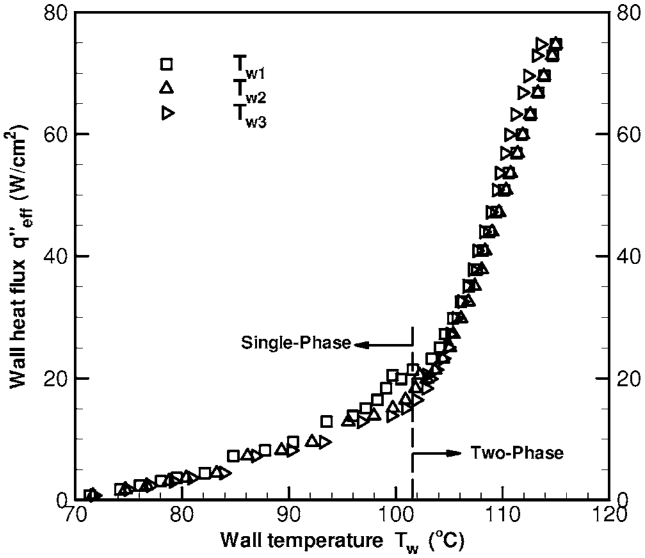

Fig. 3 Boiling curve, case I-1 (G=324 kg/m^2 s, $T_{f,\mathrm{in}}$=66.6°C)

proach of Collier [23], a linear profile is assumed for the local saturation temperature between the inlet and outlet, and the local saturation temperature $T_{\mathrm{sat},0}$ in Eq. (5) is obtained as its intersection point with the single-phase temperature curve.

2.4 Measurement Uncertainties. The uncertainty in temperature measurements was estimated to be ±0.3°C with the T-type thermocouples employed. The flowmeter was calibrated with a weighing method, yielding a maximum uncertainty of 2.4%. The measurement error for the pressure transducer was 0.25% of full scale (1 atm). Uncertainty associated with the heat flux measurement was in the range of 3.1–7.5%. A standard error analysis [24] revealed uncertainties in the reported heat transfer coefficient to be in the range of 5–9.4%. Experiments conducted over a period of months showed good repeatability.

3 Experimental Results

Experimental measurements of wall temperature and pressure drop are presented in this section to characterize the boiling heat transfer features in the microchannel flows tested.

The boiling curve shown in Fig. 2 schematically illustrates the wall temperature variation as a function of heat flux. The fluid enters the channel at point A as subcooled single-phase liquid. The heat transfer mode is single-phase convective heat transfer until location C, at which point the wall temperature exceeds the threshold value for the onset of nucleate boiling (ONB). From this point onward, both single-phase convection and nucleate boiling contribute to the total heat transfer. The convective component is then swamped by boiling heat transfer from point D when the fully developed boiling region (FDB) starts. The intermediate region (C–D) is defined as the partial boiling regime. As fluid continues to absorb heat, saturated boiling is established at location E, when the bulk temperature reaches the local saturation temperature. Beyond this point, the vapor content increases steadily until dryout occurs. In the present work, the subcooled and the saturated boiling regimes are studied.

Figure 3 shows representative boiling curves measured in the experiments at the three streamwise locations for case I-1 (details as in Table 2). The ONB can be clearly identified in the figure as the point where the wall temperature exhibits a change in slope from the single-phase dependence. In the two-phase regime, the rise in wall temperature over a wide range of wall heat flux is modest as expected. At a sufficiently high heat flux in the two-phase regime, the wall temperature near the channel exit (T_3) drops below that at the upstream locations. This is caused in part by the reduction in local saturation temperature of water when saturated boiling occurs.

The effects of inlet fluid temperature and velocity on the boiling curves are shown in Figs. 4 and 5. The wall temperatures shown in these figures are those measured near the exit of the microchannel, i.e., from thermocouple T_{w3}. It is observed that in the single-phase region the fluid with lower inlet temperature or velocity is able to dissipate higher heat fluxes while maintaining the same wall superheat. However, after the ONB, all boiling curves collapse onto a single curve irrespective of the inlet conditions, indicating the dominance of nucleate boiling over convective heat transfer.

The measured pressure drop across the microchannel heat sink as the flow transitions from single-phase to two-phase operation is shown in Fig. 6; the pressure drop is measured between the two manifolds upstream and downstream and inlet/exit losses are corrected for as recommended in Ref. [25]. In the single-phase region, the pressure drop slightly decreases as the heat flux in-

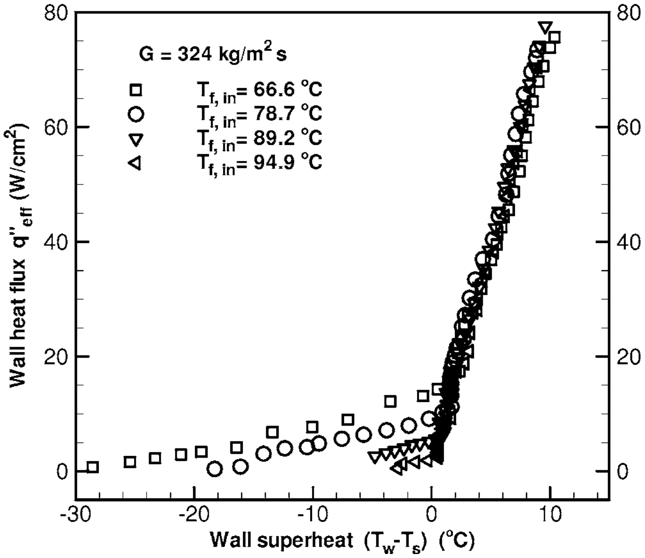

Fig. 4 Effect of inlet temperature on the boiling curves (wall temperature measured for microchannel I at $T_{w,3}$)

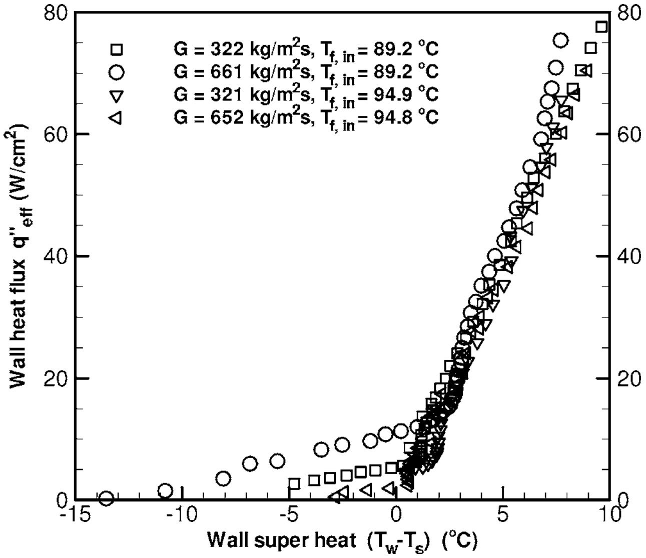

Fig. 5 Effect of inlet velocity on boiling curves (wall temperature measured for microchannel I)

creases due to the reduced viscosity of water at higher temperatures. After the ONB, the pressure drop increases rapidly when the acceleration effect of the vapor content becomes pronounced. It may be noted that both Figs. 3 and 6 provide consistent predictions of the incipience heat flux for the ONB, i.e., at $q''=15\ \text{W/cm}^2$.

The experimental results are discussed further after a presentation of the development of predictive models for flow boiling heat transfer.

4 Modeling of the Flow Boiling Heat Transfer Coefficient

Flow boiling heat transfer is strongly influenced by the morphological structure of the liquid-vapor mixture, i.e., the flow pattern [26]. Flow-pattern-based models are thus capable of providing more accurate predictions of local boiling heat transfer coefficient [18,19]. However, the purpose of the present study is to offer easy-to-use predictive tools that capture the global heat transfer behavior and can be applied to the design of two-phase microchannel heat sinks. Therefore, a correlation-based approach is adopted in this study for modeling the flow boiling heat transfer coefficient. Detailed flow-pattern-based modeling of bubbly, slug, and annular flows is the subject of ongoing work.

Correlation-based models for the flow boiling heat transfer coefficient, in both subcooled and saturated boiling, have been classified into two categories [27,28]: the extrapolation type (termed "enhancement type" in Ref. [28]) and the superposition type (further divided into superposition and asymptotic types in Ref. [28]). The first of these involves extrapolating single-phase convection data into the boiling regime by correlating the heat transfer coefficient as a function of the boiling number (Bo) and the convection number (Co), and relying on experimental databases (subcooled boiling [27,29–32] and saturated boiling [6,8,13,33–35]). This approach is expected to work reasonably well in the subcooled boiling regime, where heat transfer is primarily due to singe-phase convection and a modification factor using dimensionless groups is adequate for representing the enhancement due to nucleate boiling. However, when applied beyond regions for which they were proposed, the extrapolation approach is of limited value. Further, the functional form of the nondimensional groups involved may not adequately represent the most important parameters of the boiling process. In contrast, the second approach, superposition, deals with both single-phase and nucleate boiling heat transfer modes that are present in the two-phase flows, and treats the total heat transfer as either a linear or a power-type superposition of single-phase convection and nucleate boiling components (subcooled boiling [36–38] and saturated boiling [20,21,36,37,39]). This approach is more physically sound and may be tailored to different flow and heat transfer situations, such as laminar versus turbulent flows. A superposition-type approach is, therefore, used in this work for the development of a model for saturated boiling.

In the following, boiling regimes are first analyzed to set the context for assessing the applicability of selected heat transfer correlations in predicting boiling heat transfer in microchannel flow. It will be shown that Shah's correlation [38] from the literature is suitable for the subcooled boiling regime, and therefore, the emphasis here is placed on developing a new model for the saturated boiling regime as a modification to an earlier model [20], which incorporates some of the specific features of flow boiling in microchannels.

4.1 Models for Different Heat Transfer Regions. Under commonly encountered flow conditions, the fluid enters the microchannel with some degree of subcooling and exits as a saturated liquid-vapor mixture. Thus, three regions—single-phase flow, subcooled boiling, and saturated boiling—can exist along the microchannel length. The single-phase length L_{sp} can be calculated from Eq. (5), which, combined with the ONB model developed in Ref. [40],

$$\sqrt{T_{f,\text{in}} + \frac{q''Wz_{\text{ONB}}}{\rho_f c_p u_0(nw_cH_c)} + \frac{\{[\alpha/(1+2\eta\alpha)][(w_c+w_w)/H_c]\}q''}{(Nu_z k_f)/D_h}} - \sqrt{T_s} = \sqrt{\frac{2\sigma C}{\rho_v h_{fg}}\frac{\{[\alpha/(1+2\eta\alpha)][(w_c+w_w)/H_c]\}q''}{k_f}} \qquad (7)$$

yields the subcooled boiling length L_{sub}. Figure 7 illustrates the variation of length ratio of the different boiling regions as the heat input changes. At very low heat input, the fluid in the entire microchannel remains a single-phase liquid, shown as region I. As the heat input increases, nucleate boiling occurs first at the exit of the microchannel and then shifts upstream. The shift of the boiling front is very rapid, and with a slight increase in heat input, the subcooled boiling regime occupies an appreciable portion of the microchannel length, as indicated by region II. Further increasing the heat input results in saturated boiling in the microchannel (as

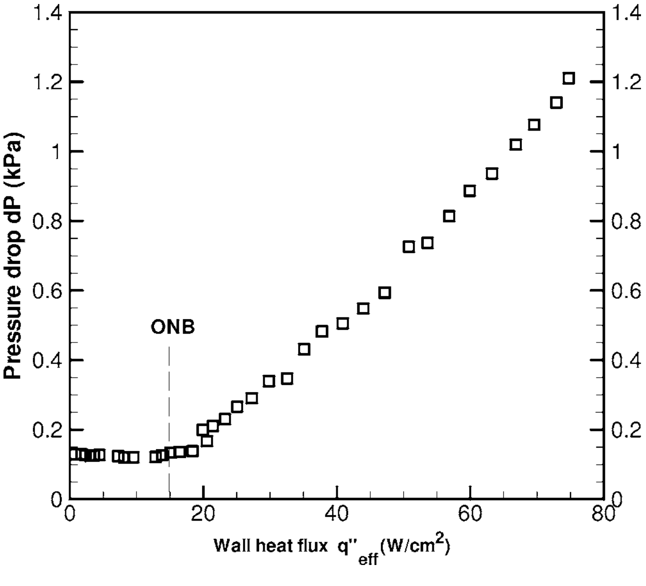

Fig. 6 Pressure drop, case I-1 ($G=324\ \text{kg/m}^2\ \text{s}$, $T_{f,\text{in}}=66.6°\text{C}$)

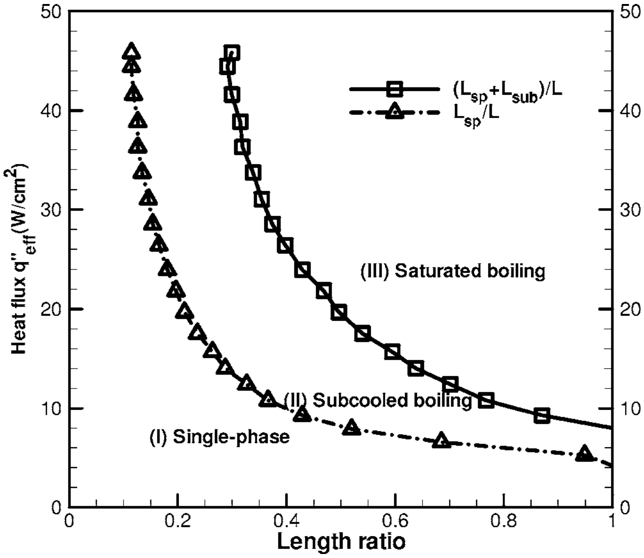

Fig. 7 Three boiling regimes in a microchannel, case II-10 (G =330 kg/m^2 s, $T_{f,\mathrm{in}}$=92.1°C)

shown in region III).

In view of the existence of the three heat transfer regions, it is reasonable to define the average boiling heat transfer as

$$\bar{h} = (h_{\mathrm{sp}}L_{\mathrm{sp}} + h_{\mathrm{sub}}L_{\mathrm{sub}} + h_{\mathrm{sat}}L_{\mathrm{sat}})/L \qquad (8)$$

This definition describes the overall heat transfer in microchannel flows, independent of specific flow patterns. It now remains to obtain the heat transfer coefficients for the respective regions in Eq. (8) as follows.

Single-Phase Regime. The selection of the correlation for predicting single-phase heat transfer plays an important role in the success of any proposed equation for analyzing flow boiling. The Dittus-Boelter correlation for turbulent flow [41] has been widely adopted for this purpose [20,30,34,38]. However, its applicability to microchannel transport is questionable since laminar flow is typically encountered in microchannels ($\mathrm{Re}_f < 1600$ in the present work). Thus, laminar correlations should be employed instead, for instance, the Sieder–Tate correlation [42] for simultaneously developing flow or the Shah–London correlation [43] for thermally developing flow, depending on the thermal and hydrodynamic boundary conditions. Lee et al. [44] pointed out that a full computational heat transfer analysis is necessary for an accurate description of the heat transfer in microchannels. However, the foregoing equations are reasonable approximations, which are useful for correlating the boiling data due to their simple functional forms.

Subcooled Boiling Regime. Among the subcooled boiling heat transfer correlations in the literature, the one proposed by Shah [38] is among the more often cited:

$$h_{\mathrm{tp}} = h_{\mathrm{sp}}\left[1 + (\psi_0 - 1)\frac{T_w - T_s}{T_w - T_f}\right] \qquad (9)$$

In Eq. (9), ψ_0 is the contribution from the limiting case of subcooled cooling, i.e., saturated boiling with zero subcooling and zero quality. The following expressions have been suggested in Ref. [38] for this term:

$$\psi_0 = \begin{cases} 230\mathrm{Bo}^{0.5} & (\mathrm{Bo} > 3 \times 10^{-5}) \\ 1 + 46\mathrm{Bo}^{0.5} & (\mathrm{Bo} < 3 \times 10^{-5}) \end{cases} \qquad (10)$$

It will be shown that predictions from this correlation show good agreement with the experimental measurements for microchannels in the present work. Two other commonly cited correlations, due to Moles–Shaw [27] and Kandlikar [32], are also considered in the comparisons with the experimental results in Sec. 5.

Saturated Boiling Regime. In superposition-type models, starting from that of Rohsenow [45], it is postulated that convective heat transfer is promoted as the flow is agitated by bubble nucleation and growth, while nucleate boiling is suppressed owing to the reduced superheat in the near-wall region caused by the bulk fluid flow. The simplest form of the superposition approach uses a linear addition as in the model of Chen and co-workers [20,21,46]:

$$h_{\mathrm{tp}} = h_{\mathrm{conv}} + h_{\mathrm{boiling}} = Fh_{\mathrm{sp}} + Sh_{\mathrm{nb}} \qquad (11)$$

in which the enhancement factor F for convection and the suppression factor S for nucleate boiling are given by

$$F = \phi_{f,\mathrm{tt}}{}^{0.89} = (1 + X_{\mathrm{tt}}^{-0.5})^{1.78} \qquad (12)$$

$$S = 0.9622 - 0.5822\left[\tan^{-1}\left(\frac{\mathrm{Re}_f F^{1.25}}{6.18 \times 10^4}\right)\right] \qquad (13)$$

and $\phi_{f,\mathrm{tt}}$ is the two-phase multiplier for turbulent-turbulent flows and X_{tt} is the corresponding Martinelli parameter. In Ref. [20], the single-phase heat transfer coefficient was represented by the Dittus–Boelter correlation for turbulent flow, and the Forster–Zuber correlation [47] was used to estimate the nucleate boiling heat transfer coefficient.

More recently, a modification of the model of Chen and co-workers has been proposed for flow boiling in microchannels [48,49]. Two alternative approaches were suggested to amend the enhancement factor F for microchannel flows. The first approach [48] is essentially a curve-fitting technique that forces the enhancement factor F to be linearly related to the two-phase friction multiplier, i.e., $F = 0.64\phi_{f,\mathrm{tt}}$, in contrast to Eq. (12). This functional form is then generalized to the two-phase multipliers for other flow conditions, including the laminar-laminar flow in microchannels. In the second approach [49], a boiling heat transfer coefficient was derived for annular flow and used as the convective component h_{conv} in Eq. (11); however, such a substitution does not derive from the flow physics and is somewhat arbitrary. Although predictions from this model showed reasonable agreement with the experimental data the authors compiled from different studies in the literature, a more physically sound model is desired to capture the important features of flow boiling in microchannels.

4.2 New Model Development for Saturated Boiling.

The superposition-type approach above is modified here to account for the specific features of flow through microchannels. New correlations for the enhancement factor F and suppression factor S are derived following Chen [20] and Bennett et al. [50].

Enhancement Factor F. It is assumed that the convective component in Eq. (11) can still be written in the form of the Sieder–Tate correlation [42] even in two-phase flow:

$$h_{\mathrm{conv}} = 1.86(\mathrm{Re}_{\mathrm{tp}}\mathrm{Pr}_{\mathrm{tp}}D_h/L)^{1/3}\left(\frac{\mu_{\mathrm{tp}}}{\mu_w}\right)^{0.14}\left(\frac{k_{\mathrm{tp}}}{D_h}\right) \qquad (14)$$

Here, the two-phase Reynolds number $\mathrm{Re}_{\mathrm{tp}}$ is an unknown and is introduced in order to retain the functional form of Eq. (14):

$$\mathrm{Re}_{\mathrm{tp}} = \frac{\rho_f V_{\mathrm{tp}} D_h}{\mu_f} \qquad (15)$$

in which V_{tp} is a nominal two-phase velocity. Comparing Eq. (14) with the original Sieder–Tate correlation leads to

$$h_{\mathrm{conv}} = h_{\mathrm{sp}}\left(\frac{\mathrm{Re}_{\mathrm{tp}}}{\mathrm{Re}_f}\right)^{1/3}\left(\frac{\mu_{\mathrm{tp}}}{\mu_f}\right)^{0.14}\left(\frac{k_{\mathrm{tp}}}{k_f}\right) \qquad (16)$$

where the liquid Reynolds number Re_f is based on the liquid velocity V_f, for only liquid flowing in the channel, and is given by

$$\mathrm{Re}_f = \frac{G(1-x)D_h}{\mu_f} = \frac{\rho_f V_f D_h}{\mu_f} \qquad (17)$$

The enhancement factor F can then be obtained as

$$F=\frac{h_{\mathrm{conv}}}{h_{\mathrm{sp}}}=\left(\frac{\mathrm{Re}_{\mathrm{tp}}}{\mathrm{Re}_f}\right)^{1/3}\left(\frac{\mu_{\mathrm{tp}}}{\mu_f}\right)^{0.14}\left(\frac{k_{\mathrm{tp}}}{k_f}\right)\left(\frac{\mathrm{Pr}_{\mathrm{tp}}}{\mathrm{Pr}_f}\right)^{1/3} \tag{18}$$

Following Reynolds analogy, if it is assumed that the shear stress and heat flux profiles are similar, so that

$$\frac{q''(y)}{q''_w|_{y=0}}=\frac{\tau(y)}{\tau_w|_{y=0}}=f(y) \tag{19}$$

Using the definitions of shear stress and heat flux, Eq. (19) can be rearranged as

$$q''_w|_{y=0}du=-\frac{k}{\mu}\,\tau_w|_{y=0}dT \tag{20}$$

Assuming that the nominal velocity V_{tp} corresponds to the velocity at a distance from the wall where the local temperature T reaches the bulk mean value T_b, Eq. (20) can be integrated as

$$\int_0^{V_{\mathrm{tp}}}q''_w du=-\int_{T_w}^{T_b}\frac{k}{\mu}\tau_w dT \tag{21}$$

which yields

$$q''_w V_{\mathrm{tp}}=\frac{k}{\mu}\tau_w(T_w-T_b) \tag{22}$$

Recalling the definition of boiling heat transfer coefficient, the following expression is obtained:

$$h_{\mathrm{conv}}=\frac{q''_w}{T_w-T_b}=\frac{k}{\mu}\frac{\tau_w}{V_{\mathrm{tp}}}=\frac{\tau_w c_p}{\mathrm{Pr}_{\mathrm{tp}}V_{\mathrm{tp}}} \tag{23}$$

For the liquid phase flowing alone in the channel, a similar expression can be derived

$$h_{\mathrm{sp}}=\frac{\tau_{w,f}c_{p,f}}{\mathrm{Pr}_f\,V_f} \tag{24}$$

Therefore, the ratio of boiling convection to single-phase convection defines the enhancement factor F:

$$\frac{h_{\mathrm{conv}}}{h_{\mathrm{sp}}}=\left(\frac{\tau_{w,\mathrm{tp}}}{\tau_{w,f}}\right)\left(\frac{\mathrm{Re}_f}{\mathrm{Re}_{\mathrm{tp}}}\right)\left(\frac{c_{p,\mathrm{tp}}}{c_{p,f}}\right)\left(\frac{\mathrm{Pr}_f}{\mathrm{Pr}_{\mathrm{tp}}}\right)=F \tag{25}$$

Combining with Eq. (18) and solving for $(\mathrm{Re}_{\mathrm{tp}}/\mathrm{Re}_f)$ yield

$$\left(\frac{\mathrm{Re}_{\mathrm{tp}}}{\mathrm{Re}_f}\right)=\left[\left(\frac{\tau_{w,\mathrm{tp}}}{\tau_{w,\mathrm{sp}}}\right)\left(\frac{\mu_f}{\mu_{\mathrm{tp}}}\right)^{0.14}\left(\frac{k_f}{k_{\mathrm{tp}}}\right)\left(\frac{\mathrm{Pr}_f}{\mathrm{Pr}_{\mathrm{tp}}}\right)^{4/3}\left(\frac{c_{p,\mathrm{tp}}}{c_{p,f}}\right)\right]^{3/4} \tag{26}$$

In Eq. (26), the shear stress term is linked to the two-phase multiplier ϕ_f as

$$\frac{\tau_{w,\mathrm{tp}}}{\tau_{w,f}}=\frac{[(dp/dz)F]_{\mathrm{tp}}}{[(dp/dz)F]_f}=\phi_f^2 \tag{27}$$

The expression for enhancement factor F is then obtained as

$$F=(\phi_f^2)^{1/4}\left(\frac{\mu_{\mathrm{tp}}}{\mu_f}\right)^{0.105}\left(\frac{c_{p,\mathrm{tp}}}{c_{p,f}}\right)^{1/4}\left(\frac{k_{\mathrm{tp}}}{k_f}\right)^{3/4} \tag{28}$$

To account for the asymptotic behavior of two-phase convective heat transfer at the beginning of saturated flow boiling, an adjustable parameter ζ is now introduced. In the present study, ζ takes a value of 2, which gives a better fit to the experimental data than the value of 0.64 used in Ref. [49]. The reason for not choosing a value of unity for ζ (which would imply that F reduces to unity at zero quality and the convection contribution is simply represented by the single-phase component) is that the interactions between the bubble and fluid occur well before the flow reaches saturated boiling and the agitation of the fluid due to the bubble dynamics enhances convection even prior to reaching saturation. In addition, the use of a correction factor $\mathrm{Pr}_f^{0.167}$ was suggested by Benett and Chen [46] when applying the Reynolds analogy to fluids with Prandtl number not equal to unity. The final form of enhancement factor F is

Table 4 Values of the constant C in Eq. (30) [51]

Liquid	Vapor	Re_f	Re_g	Abbr.	C
Turbulent	Turbulent	>2000	>2000	tt	20
Viscous	Turbulent	<1000	>2000	vt	12
Turbulent	Viscous	>2000	<1000	tv	10
Viscous	Viscous	<1000	<1000	vv	5

$$F=\zeta(\phi_f^2)^{1/4}\left(\frac{\mu_{\mathrm{tp}}}{\mu_f}\right)^{0.105}\left(\frac{c_{p,\mathrm{tp}}}{c_{p,f}}\right)^{1/4}\left(\frac{k_{\mathrm{tp}}}{k_f}\right)^{3/4}\mathrm{Pr}_f^{0.167} \tag{29}$$

The two-phase multiplier can be related to the Martinelli parameter as [51]

$$\phi_f^2=1+\frac{C}{X}+\frac{1}{X^2} \tag{30}$$

in which the constant C is determined from Ref. [51] and Table 4, depending on the flow regimes of the liquid and vapor phases in microchannels. For the laminar flows (in both liquid and vapor phases) present in this study, the Martinelli parameter is

$$X^2=\frac{[(dp/dz)F]_f}{[(dp/dz)F]_v}=\left(\frac{1-x}{x}\right)\left(\frac{\rho_v}{\rho_f}\right)\left(\frac{\mu_f}{\mu_v}\right) \tag{31}$$

Thus, Eqs. (29)–(31) can be used to determine the enhancement factor F for microchannel flow boiling. The two-phase thermophysical properties in the model can be estimated as the arithmetic mean of those of the liquid and vapor phases weighted by quality x:

$$\psi_{\mathrm{tp}}=x\psi_v+(1-x)\psi_f \tag{32}$$

in which ψ is any thermophysical property. In the low-quality region, the differences in properties between single- and two-phase flows can be neglected as a first-order approximation. Under this approximation, the two-phase Reynolds number $\mathrm{Re}_{\mathrm{tp}}$ can be derived from Eq. (18) as

$$\mathrm{Re}_{\mathrm{tp}}=\mathrm{Re}_f\,F^3 \tag{33}$$

Suppression Factor S. The suppression factor S is usually obtained from regression analysis once the enhancement factor F is known [20]. Although this approach will also be used here, it is first desired to develop an analytical model for the suppression factor S that is independent of particular experimental data sets. Chen [20] pointed out that nucleate boiling during convective flow is governed by an effective superheat that is less than the wall superheat, which gives rise to a suppression of nucleate boiling heat transfer. Bennett et al. [50] proposed a theoretical approach to estimate the effective superheat for flow boiling in various types of boiling geometries. In the following, this approach will be modified to incorporate specific features of microchannel flow boiling.

It is postulated in this work that the fluid temperature varies linearly in the vicinity of the channel wall and is given by

$$T_f(y)=T_w+Ay \tag{34}$$

Considering the boundary condition $-k_f\partial T_f/\partial y|_{y=0}=\mathrm{h}_{\mathrm{conv}}(T_w-T_b)$, the temperature profile becomes

$$T_f(y)=T_w-\frac{h_{\mathrm{conv}}}{k_f}(T_w-T_b)y \tag{35}$$

It is further assumed that the effective superheat within a distance y_0 from the wall, given by the following expression, is the driving force that governs nucleate boiling heat transfer:

$$\Delta T_s|_{y_0} = \frac{1}{y_0}\int_0^{y_0} [T_f(y) - T_b]dy \tag{36}$$

The suppression factor is then defined as the ratio of effective superheat $\Delta T_s|_{y_0}$ to the wall superheat $\Delta T_s(=T_w-T_b)$,

$$S = \frac{\Delta T_s|_{y_0}}{\Delta T_s} = 1 - \frac{h_{\text{conv}}y_0}{2k_f} \tag{37}$$

in which the two-phase convection heat transfer coefficient h_{conv} is obtained from Eq. (14).

The only unknown in Eq. (37), y_0, the thickness of the effective nucleate boiling region, can be approximated as the departure size of the bubble. In flow boiling, the departure size is determined by a balance of the forces acting on the vapor bubble. Due to the small bubble size in microchannel flows, surface tension and shear are the dominant forces (over inertia and buoyancy forces). According to Levy [52], the surface tension force F_s and shear force F_f are given by

$$F_s = C_s r_b \sigma \tag{38}$$

$$F_f = C_F \frac{\tau_w}{D_h} r_b^3 \tag{39}$$

Therefore, the bubble departure radius can be solved from a force balance, $F_s=F_f$, which yields

$$r_b = \sqrt{\frac{C_s\sigma}{C_F(\tau_w/D_h)}} \tag{40}$$

The thickness of the effective nucleate boiling region is then estimated as

$$y_0 = C\left(\frac{\sigma D_h}{\tau_w}\right)^{1/2} \tag{41}$$

where the empirical constant C is taken to be 0.35 in the present model. Compared to other values used in the literature [50,52], this value predicts a more reasonable bubble departure radius for water flow in microchannels [53]. The wall shear stress τ_w can be calculated from

$$\tau_w = 2f\frac{G^2}{\rho_f}$$

and

$$f = 96/\text{Re}_f(1 - 1.3553/\alpha + 1.9467/\alpha^2 - 1.7012/\alpha^3 + 0.9564/\alpha^4 - 0.2537/\alpha^5)$$

Further, the nucleate boiling coefficient in Eq. (11) is evaluated according to Gorenflo [54]:

$$h_{\text{nb}} = h_0 F_{\text{PF}}\left(\frac{q''}{q''_0}\right)^n \left(\frac{R_p}{R_{p0}}\right)^{0.133} \tag{42}$$

where the pressure correction factor F_{PF} for water is

$$F_{\text{PF}} = 1.73p_r^{0.27} + \left(6.1 + \frac{0.68}{1-p_r}\right)p_r^2$$

and p_r is the reduced pressure. The exponent n for the heat flux term is $n=0.9-0.3p_r^{0.15}$, and the reference values are $p_{r0}=0.1$, $q''_0=20{,}000$ W/m², $R_{p0}=0.4$ μm, and $h_0=5600$ W/m² K [54]. The measured surface roughness at the bottom of the channel is approximately 1.5 μm, and the sidewalls are expected to be smoother, because of the method of fabrication. A value of 1 μm is sufficiently accurate for use in Eq. (42).

The suppression factor can also be derived through a regression analysis, as stated earlier. In this approach, S is correlated with the two-phase Reynolds number Re_{tp} as

$$S = \frac{h_{\text{tp,exp}} - Fh_{\text{sp}}}{h_{\text{nb}}} \propto \text{func}(\text{Re}_{\text{tp}}) \tag{43}$$

In Eq. (43), $h_{\text{tp,expt}}$ is the measured boiling heat transfer coefficient and h_{nb} is a selected correlation for the nucleate boiling heat transfer coefficient. Using this approach and the experimental data obtained in the present work, a new empirical correlation for suppression factor S is proposed for saturated flow boiling in microchannels:

$$S = \exp[36.57 - 55746/(\text{Re}_f F^3) - 3.4\ln(\text{Re}_f F^3)] \tag{44}$$

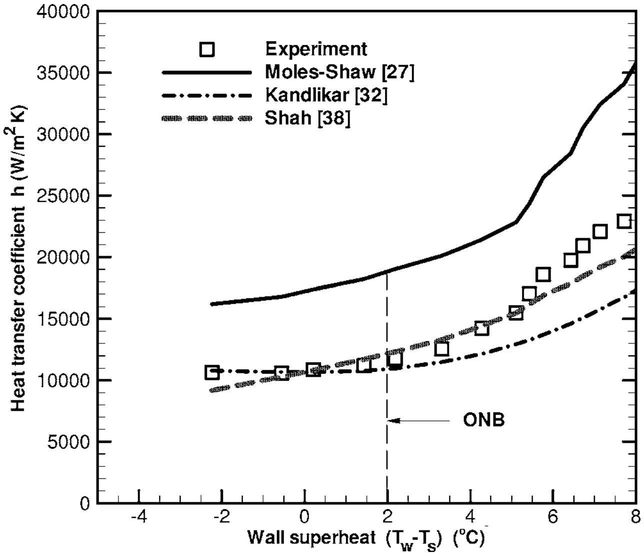

Fig. 8 Subcooled boiling heat transfer coefficient, case I-13 (G=921 kg/m² s, $T_{f,\text{in}}$=78.3°C)

5 Model Validation

5.1 Subcooled Boiling Regime. In the subcooled boiling regime, Eq. (8) reduces to

$$\bar{h} = [h_{\text{sp}}L_{\text{sp}} + h_{\text{sub}}(L - L_{\text{sp}})]/L \tag{45}$$

Figure 8 shows a comparison of the measured heat transfer coefficient, as defined in Eq. (6), with predictions using h_{sub} from various subcooled boiling correlations. In the regime following the occurrence of ONB, it is seen that the Shah correlation for subcooled boiling [38] offers very good predictions of the experimental data, while those of Moles–Shaw [27] and Kandlikar [32] overpredict and underpredict the heat transfer coefficient, respectively. It should be noted that the parameter ψ_0 used in Eq. (10) was originally developed for turbulent flow conditions, which is somewhat inconsistent with the laminar nature of microchannel flows. However, the Shah correlation is still recommended due to its agreement with the measured experimental data.

5.2 Saturated Boiling Regime. Figure 9 shows the predicted enhancement factor F calculated from Eq. (29) over the range of experimental conditions of the present work. The enhancement factor increases monotonically with the reciprocal of the Martinelli parameter, $1/X_{\text{vv}}$, which is proportional to the thermodynamic equilibrium quality. This suggests that the two-phase convective heat transfer is gradually augmented as more liquid is vaporized. Physically, the enhancement process may take place through different mechanisms. During the initial stage of boiling, two-phase flow usually appears in discrete bubbly form without significant interaction of adjacent nucleate bubbles. Individual bubble behavior, such as bubble departure and subsequent sliding on the channel surface [53], contributes in enhancement of the

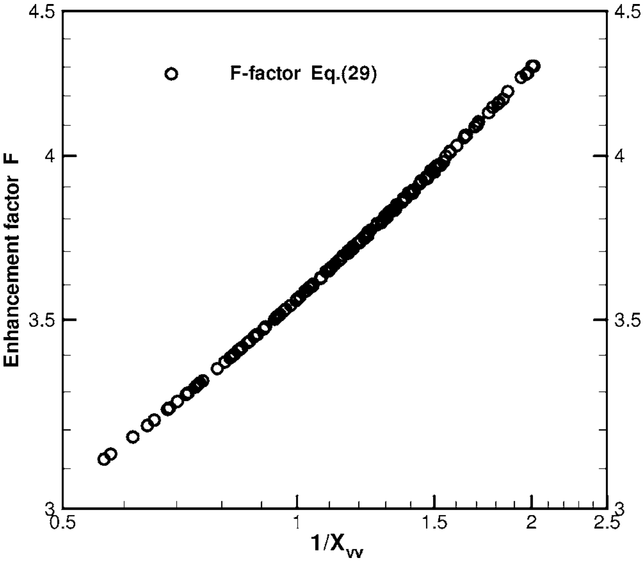

Fig. 9 Convective enhancement factor *F* as a function of laminar Martinelli parameter

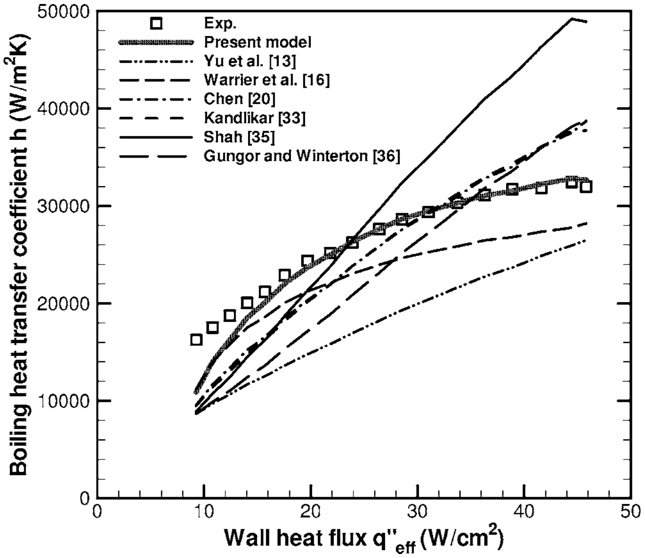

Fig. 11 Saturated boiling heat transfer coefficient, case II-2 (G=221 kg/m^2 s, $T_{f,\mathrm{in}}$=91.7°C)

convective heat transfer by agitating the liquid in the thermal boundary layer. At higher qualities, the microchannel cross section is mostly occupied by the vapor phase due to the dramatic difference in the liquid and vapor densities. The liquid phase is then confined to a small portion of the microchannel cross section, either in a thin film around the channel periphery in annular flows or in short liquid slugs in slug flows. To ensure mass conservation, the effective velocity of the liquid phase is greater than the nominal value calculated by averaging over the entire cross section. In the proposed model, this effect is represented by the two-phase Reynolds number $\mathrm{Re}_{\mathrm{tp}}$ defined in Eq. (33).

Figure 10 shows the predicted suppression factor S calculated from Eq. (44) using the regression analysis, which illustrates the decreasing trend of the suppression factor S as the two-phase Reynolds number $\mathrm{Re}_{\mathrm{tp}}$ increases. This is caused by the intensified forced convection at high $\mathrm{Re}_{\mathrm{tp}}$ that effectively reduces the superheat in the near-wall region. Alternatively, the suppression factor S may also be obtained analytically using Eq. (37).

Predictions of the boiling heat transfer coefficient from three widely cited saturated boiling models for conventional-sized channels [20,33,35], as well as from the correlation developed in the present work using the regression analysis result for S factor, are compared in Fig. 11 against the experimental measurements. Also shown are predictions from three correlation models for mini- and microchannel flows from the literature [13,16,36]. It is clear that the proposed correlation achieves the best agreement in the range of heat flux considered (for case II-2 shown in the figure), while most of the other models underpredict the experimental data at low heat flux and some [20,35,36] tend to overpredict the boiling heat transfer coefficient at high heat flux.

The validity of the proposed analytical model is further examined by comparing predictions for all the test cases in the experiments listed in Tables 2 and 3, as shown in Fig. 12. The agreement over the majority of the experiments is within ±35%. Model predictions using the suppression factor S from the regression analy-

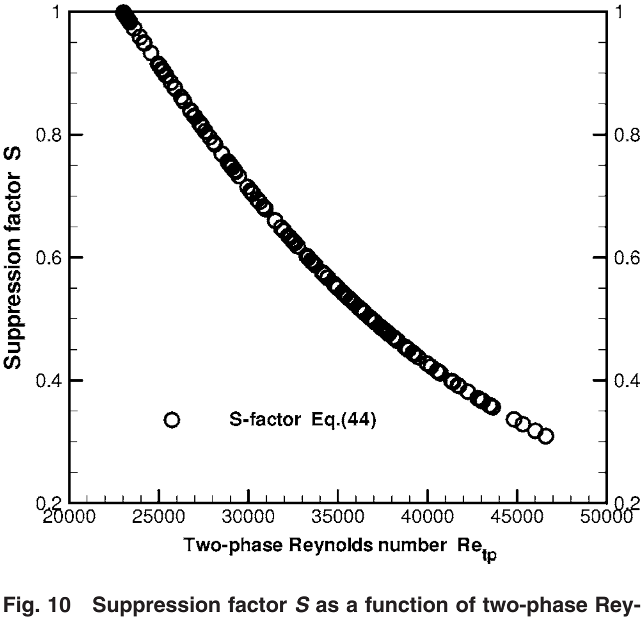

Fig. 10 Suppression factor *S* as a function of two-phase Reynolds number

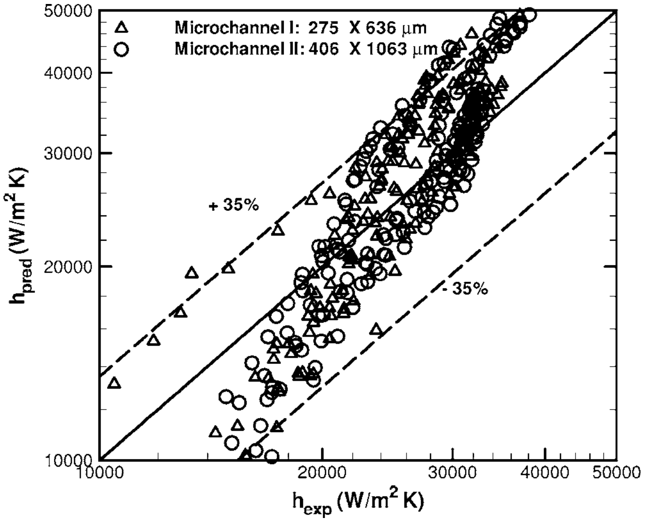

Fig. 12 Comparison of measured boiling heat transfer coefficients with those predicted with *S* factor obtained from analytical approach (Eq. (37)) (G=221–1283 kg/m^2 s, $T_{f,\mathrm{in}}$ =66.6–95.4°C)

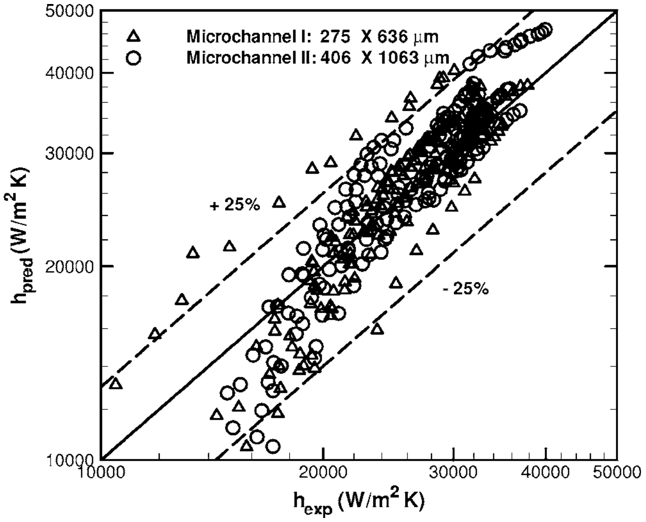

Fig. 13 Comparison of measured boiling heat transfer coefficients with those predicted with S factor obtained from regression analysis (Eq. (44)) (G=221–1283 kg/m^2 s, $T_{f,\mathrm{in}}$ =66.6–95.4°C)

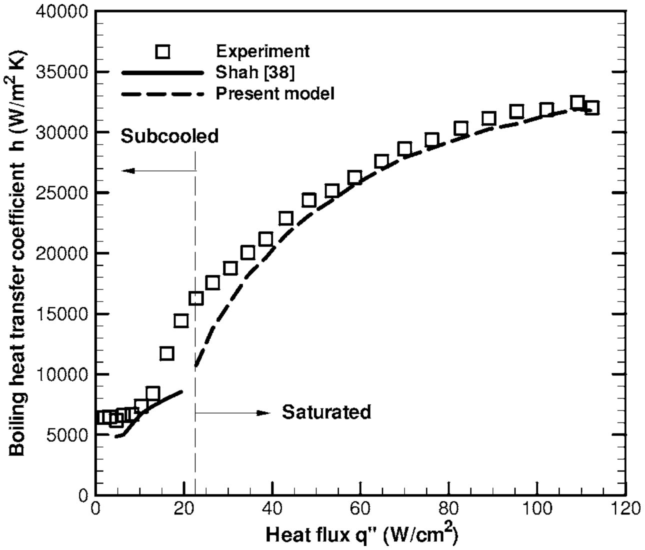

Fig. 14 Boiling heat transfer coefficient over subcooled and saturated regimes, case II-2

Table 5 Comparison with experiments of predictions from the present model (with S obtained both from analysis and regression) and other models in the literature

Model	Present (analytical)	Present (regression analysis)	Yu et al. [13]	Warrier et al. [16]	Chen [20]	Kandlikar [33]	Shah [35]	Gungor and Winterton [36]
MAE[a] (%)	16.7	10.9	32.0	14.1	22.7	20.5	34.6	25.7

[a](Mean absolute error is defined as $(1/N)\Sigma|h_{\mathrm{expt}}-h_{\mathrm{pred}}|/h_{\mathrm{expt}}$)

sis approach (Eq. (37)) are plotted in Fig. 13, which shows better agreement with the experiments, within ±25%. The mean absolute errors (MAEs) associated with all models are calculated and listed in Table 5. The agreement of the proposed analytical model is significantly better than for predictions from almost any of the correlations in the literature for the present experimental data set, except for an empirical model in Ref. [16]. Considering the fact that there is still a systematic tendency to underpredict the heat transfer coefficient at the low range and overpredict it at the high range, more accurate predictions are being sought from detailed flow-pattern-based models.

5.3 Suggested Correlations. Based on the observations from the present study, the Shah correlation [38] is recommended for prediction of the boiling heat transfer coefficient in microchannels in the subcooled boiling regime, while the new correlations developed in the present work, Eq. (29) for enhancement factor F and Eq. (37) and (44) for suppression factor S, are recommended for the saturated boiling regime; this recommendation is illustrated for one representative case in Fig. 14.

6 Conclusions

Flow boiling of water in microchannels is experimentally investigated. The fluid and microchannel wall temperatures and the pressure drop across the microchannel were measured. The boiling heat transfer coefficients for subcooled and saturated boiling regimes were determined. Heat transfer correlations in the literature were assessed critically for applicability to microchannels. A new correlation suitable for the saturated boiling regime is developed. Suitable correlations to be used in the design of microchannel heat sinks in subcooled and saturated boiling at low qualities are suggested.

Key findings from this work are summarized as follows.

(1) The fluid inlet conditions, i.e., degree of subcooling and velocity, affect the onset of nucleate boiling, but have little impact on the boiling curve once the ONB has occurred.
(2) A critical review of conventional correlations in the literature suggests that the superposition-type heat transfer correlations are superior to the extrapolation-type in predicting the flow boiling heat transfer coefficient.
(3) The Shah correlation [38] provides satisfactory prediction of heat transfer coefficient in the subcooled boiling regime.
(4) A new heat transfer correlation is developed to predict the saturated boiling data, based on the model of Chen and co-workers [20,50]. Good agreement with the present experimental measurements indicates that this correlation is suitable for the design of two-phase microchannel heat sinks. Comparison with a larger database in the future is recommended.

Acknowledgment

The authors acknowledge the financial support from members of the Cooling Technologies Research Center, a National Science Foundation Industry/University Cooperative Research Center at Purdue University.

Nomenclature

A_b = area of microchannel heat sink, m^2
Bo = boiling number, Bo=q''/Gh_{fg}
Co = convection number, Co=$[(1-x)/x]^{0.8}(\rho_v/\rho_f)^{0.5}$
c_p = specific heat, kJ/kg °C
D_h = hydraulic diameter, μm
Fr = Froude number, Fr=$G^2/\rho_f^2 g D_h$
G = mass flux, kg/s m^2

h = heat transfer coefficient, $\mathrm{W/cm^2\,K}$
h_{fg} = latent heat, J/kg
H_c = microchannel height, μm
i = enthalpy, J/kg
L = channel length, m
$\dot{m}$ = mass flow rate, kg/s
n = number of microchannels
p = pressure, Pa
Pr = Prandtl number
q'' = applied heat flux, $\mathrm{W/cm^2}$
q''_w = effective heat flux, $\mathrm{W/cm^2}$
Re = Reynolds number, $\mathrm{Re}=GD_h\mu$
T = temperature, °C
u_0 = fluid inlet velocity, m/s
w_c = microchannel width, μm
w_w = microchannel fin thickness, μm
x = vapor quality
X = Martinelli parameter, $X^2=[(dp/dz)F]_f/[(dp/dz)F]_v$

Greek Symbols

α = microchannel aspect ratio
ϕ = two-phase multiplier
η = fin efficiency
ρ = density, $\mathrm{kg/m^3}$
σ = surface tension, N/m

Subscripts

f = fluid
in = inlet
out = outlet
sat = saturated
sp = single phase
sub = subcooling
tp = two phase
v = vapor
w = wall

References

[1] Garimella, S. V., and Sobhan, C. B., 2003, "Transport in Microchannels—A Critical Review," Annu. Rev. Heat Transfer, **13**, pp. 1–50.

[2] Garimella, S. V., Singhal, V., and Liu, D., 2006, "On-Chip Thermal Management With Microchannel Heat Sinks and Integrated Micropumps," Proc. IEEE, **94**, pp. 1534–1548.

[3] Kandlikar, S. G., 2002, "Fundamental Issues Related to Flow Boiling in Minichannels and Microchannels," Exp. Therm. Fluid Sci., **26**, pp. 389–407.

[4] Bergles, A. E., Lienhard, V. J. H., Kendall, G. E., and Griffith, P., 2003, "Boiling and Evaporation in Small Diameter Channels," Heat Transfer Eng., **24**, pp. 18–40.

[5] Thome, J. R., 2004, "Boiling in Microchannels: A Review of Experiment and Theory," Int. J. Heat Fluid Flow, **25**, pp. 128–139.

[6] Lazarek, G. M., and Black, S. H., 1982, "Evaporative Heat Transfer, Pressure Drop and Critical Heat Flux in a Small Vertical Tube With R-113," Int. J. Heat Mass Transfer, **25**, pp. 945–960.

[7] Wambsganss, M. W., France, D. M., Jendrzejczyk, J. A., and Tran, T. N., 1993, "Boiling Heat Transfer in a Horizontal Small-Diameter Tube," J. Heat Transfer, **115**, pp. 963–972.

[8] Tran, T. N., Wambsganss, M. W., and France, D. M., 1996, "Small Circular- and Rectangular-Channel Boiling With Two Refrigerants," Int. J. Multiphase Flow, **5**, pp. 485–498.

[9] Kew, A. P., and Cornwell, K., 1997, "Correlations for the Prediction of Boiling Heat Transfer in Small-Diameter Channels," Appl. Therm. Eng., **17**, pp. 705–715.

[10] Yan, Y. Y., and Lin, T. F., 1998, "Evaporation Heat Transfer and Pressure of Refrigerant R-134a in A Small Pipe," Int. J. Heat Mass Transfer, **41**, pp. 4183–4194.

[11] Bao, Z. Y., Fletcher, D. F., and Haynes, B. S., 2000, "Flow Boiling Heat Transfer of Freon R11 and HCFC123 in Narrow Passages," Int. J. Heat Mass Transfer, **43**, pp. 3347–3358.

[12] Lee, H. J., and Lee, S. Y., 2001, "Heat Transfer Correlation for Boiling Flows in Small Rectangular Horizontal Channels With Low Aspect Ratios," Int. J. Multiphase Flow, **27**, pp. 2043–2062.

[13] Yu, W., France, D. M., Wambsganss, M. W., and Hull, J. R., 2002, "Two-Phase Pressure Drop, Boiling Heat Transfer, and Critical Heat Flux to Water in a Small-Diameter Horizontal Tube," Int. J. Multiphase Flow, **28**, pp. 927–941.

[14] Qu, W., and Mudawar, I., 2003, "Flow Boiling Heat Transfer in Two-Phase Microchannel Heat Sinks—I. Experimental Investigation and Assessment of Correlation Methods," Int. J. Heat Mass Transfer, **46**, pp. 2755–2771.

[15] Haynes, B. S., and Fletcher, D. F., 2003, "Subcooled Boiling Heat Transfer in Narrow Passages," Int. J. Heat Mass Transfer, **46**, pp. 3673–3682.

[16] Warrier, G. R., Dhir, V. K., and Momoda, L. A., 2002, "Heat Transfer and Pressure Drop in Narrow Rectangular Channels," Exp. Therm. Fluid Sci., **26**, pp. 53–64.

[17] Chen, T., and Garimella, S. V., 2007, "Flow Boiling Heat Transfer to a Dielectric Coolant in a Microchannel Heat Sink," IEEE Trans. Compon. Packag. Technol., **30**, pp. 24–31.

[18] Qu, W., and Mudawar, I., 2003, "Flow Boiling Heat Transfer in Two-Phase Microchannel Heat Sinks—Part II: Annular Two-Phase Flow Model," Int. J. Heat Mass Transfer, **46**, pp. 2773–2784.

[19] Thome, J. R., Dupont, V., and Jacobi, A. M., 2004, "Heat Transfer Model for Evaporation in Microchannels. Part I: Presentation of the Model," Int. J. Heat Mass Transfer, **47**, pp. 3375–3385.

[20] Chen, J. C., 1966, "Correlation for Boiling Heat Transfer to Saturated Fluids in Convective Flow," I&EC Process Des. Dev., **5**, pp. 322–329.

[21] Edelstein, S., Perez, A. J., and Chen, J. C., 1984, "Analytical Representation of Convective Boiling Functions," AIChE J., **30**, pp. 840–841.

[22] Steinke, M. E., and Kandlikar, S. G., 2004, "Control and Effect of Dissolved Air in Water During Flow Boiling in Microchannels," Int. J. Heat Mass Transfer, **47**, pp. 1925–1935.

[23] Collier, J. G., 1981, "Forced Convective Boiling," *Two-Phase Flow and Heat Transfer in the Power and Process Industries*, Hemisphere, Washington, DC, pp. 227–255.

[24] Taylor, J. R., 1997, *An Introduction to Error Analysis*, University Science Books, New York.

[25] Collier, J. G., and Thome, J. R., 1994, *Convective Boiling and Condensation*, Oxford University Press, Oxford, UK.

[26] Chen, T., and Garimella, S. V., 2006, "Measurements and High-Speed Visualizations of Flow Boiling of a Dielectric Fluid in a Silicon Microchannel Heat Sink," Int. J. Multiphase Flow, **32**, pp. 957–971.

[27] Moles, F. D., and Shaw, J. F. G., 1972, "Boiling Heat Transfer to Subcooled Liquids Under Conditions of Forced Convection," Trans. Inst. Chem. Eng., **50**, pp. 76–84.

[28] Webb, R. L., and Gupte, N. S., 1992, "A Critical Review of Correlations for Convective Vaporization in Tubes and Tube Banks," Heat Transfer Eng., **13**, pp. 58–81.

[29] Kutateladze, S. S., 1964, "Boiling Heat Transfer," Int. J. Heat Mass Transfer, **4**, pp. 31–45.

[30] Kandlikar, S. G., 1991, "Development of a Flow Boiling Map for Subcooled and Saturated Flow Boiling of Different Fluids Inside Circular Tubes," J. Heat Transfer, **113**, pp. 190–200.

[31] Papell, S. S., 1963, "Subcooled Boiling Heat Transfer Under Forced Convection in a Heated Tube," NASA-TN-D-1583.

[32] Kandlikar, S. G., 1997, "Heat Transfer Characteristics in Partial Boiling, Fully Developed Boiling, and Significant Void Flow Regions of Subcooled Flow Boiling," J. Heat Transfer, **102**, pp. 395–401.

[33] Kandlikar, S. G., 1990, "A General Correlation for Saturated Two-Phase Flow Boiling Heat Transfer Inside Horizontal and Vertical Tubes," J. Heat Transfer, **112**, pp. 219–228.

[34] Shah, M. M., 1976, "A New Correlation for Heat Transfer During Boiling Flow Through Pipes," ASHRAE Trans., **82**, pp. 66–86.

[35] Shah, M. M., 1982, "Chart Correlation for Saturated Boiling Heat Transfer: Equations and Further Study," ASHRAE Trans., **88**, pp. 185–196.

[36] Gungor, K. E., and Winterton, R. H. S., 1986, "A General Correlation for Flow Boiling in Tubes and Annuli," Int. J. Heat Mass Transfer, **29**, pp. 351–358.

[37] Liu, Z., and Winterton, R. H. S., 1991, "A General Correlation for Saturated and Subcooled Flow Boiling in Tubes and Annuli Based on a Nucleate Pool Boiling Equation," Int. J. Heat Mass Transfer, **34**, pp. 2759–2766.

[38] Shah, M. M., 1977, "A General Correlation for Heat Transfer During Subcooled Boiling in Pipes and Annuli," ASHRAE Trans., **83**, pp. 202–217.

[39] Steiner, D., and Taborek, J., 1992, "Flow Boiling Heat Transfer in Vertical Tubes Correlated by an Asymptotic Model," Heat Transfer Eng., **13**, pp. 43–68.

[40] Liu, D., Lee, P. S., and Garimella, S. V., 2005, "Prediction of the Onset of Nucleate Boiling in Microchannel Flow," Int. J. Heat Mass Transfer, **48**, pp. 5134–5149.

[41] Dittus, F. W., and Boelter, L. M. K., 1930, *Heat Transfer in Automobile Radiators of the Tubular Type*, University of California Publications of Engineering, University of California Press, Vol. 2, pp. 443–461.

[42] Sieder, E. N., and Tate, G. E., 1936, "Heat Transfer and Pressure Drop of Liquids in Tubes," Ind. Eng. Chem., **28**, pp. 1429–1436.

[43] Shah, R. K., and London, A. L., 1978, "Laminar Flow Forced Convection in Ducts," *Advances in Heat Transfer*.

[44] Lee, P. S., Garimella, S. V., and Liu, D., 2005, "Experimental Investigation of Heat Transfer in Microchannels," Int. J. Heat Mass Transfer, **48**, pp. 1688–1704.

[45] Rohsenow, W. M., 1952, "A Method of Correlating Heat Transfer Data for Surface Boiling of Liquids," Trans. ASME, **74**, pp. 969–976.

[46] Bennett, L., and Chen, J. C., 1980, "Forced Convective Boiling in Vertical Tubes for Saturated Components and Binary Mixtures," AIChE J., **26**, pp. 454–461.

[47] Forster, H. K., and Zuber, N., 1955, "Dynamics of Vapor Bubbles and Boiling Heat Transfer," AIChE J., **1**, pp. 531–535.

[48] Zhang, W., Hibiki, T., and Mishima, K., 2004, “Correlation for Flow Boiling Heat Transfer in Mini-Channels,” Int. J. Heat Mass Transfer, **47**, pp. 5749–5763.

[49] Zhang, W., Hibiki, T., and Mishima, K., 2005, “Correlation for Flow Boiling Heat Transfer at Low Liquid Reynolds Number in Small Diameter Channels,” J. Heat Transfer, **127**, pp. 1214–1221.

[50] Bennett, D. L., Davis, M. W., and Hertzler, B. L., 1980, “The Suppression of Saturated Nucleate Boiling by Forced Convective Flow,” AIChE Symp. Ser., **199**, pp. 91–103.

[51] Delhaye, J. M., 1981, “Frictional Pressure Drops,” *Two-Phase Flow and Heat Transfer in the Power and Process Industries*, Hemisphere, Washington, DC, pp. 98–150.

[52] Levy, S., 1967, “Forced Convection Subcooled Boiling Prediction of Vapor Volumetric Fraction,” Int. J. Heat Mass Transfer, **10**, pp. 951–965.

[53] Liu, D., Lee, P. S., and Garimella, S. V., 2005, “Nucleate Boiling in Microchannels,” J. Heat Transfer, **127**, p. 803.

[54] Gorenflo, D., 1993, *Pool Boiling: VDI-Heat Atlas*, VDI, Dusseldorf.

Homogeneous Nucleation of Vapor at Preferred Sites During Rapid Transient Heating of Liquid in Micropassages

Van P. Carey
e-mail: vcarey@me.berkeley.edu

Jorge Padilla

Yu Gan

Mechanical Engineering Department,
University of California Berkeley,
Berkeley, CA 94720-1776

Rapid heating of a liquid at the wall of a micropassage may produce homogeneous nucleation of vapor in the liquid in contact with the surface. In such circumstances, nucleation is generally expected to be most likely to occur in the hottest liquid closest to the surface. It is known, however, that in many cases, the liquid molecules closest to the surface will experience long-range attractive forces to molecules in the solid, with the result that the equation of state for the liquid near the surface will differ from that for the bulk liquid. In micro- and nanopassages, this wall-affected region may be a significant fraction of the passage interior volume. Recent investigations of wall force effects on the liquid indicate that these forces increase the spinodal temperature in the near-surface region. The results of these previous investigations suggest that for heated surfaces with nanoscale roughness, protrusion of bulk fluid into crevices in the surface may make them preferred sites for homogeneous nucleation during rapid heating. A detailed model analysis of the heat transfer in a model conical crevice is developed and used to explore the plausibility and apparent mechanisms of preferred-site homogeneous nucleation. The analysis predicts that protrusion of bulk liquid into a conical cavity does, under some conditions, make the cavity a preferred site for the first occurrence of homogeneous nucleation. The analysis is used to examine the range of conditions under which a crevice will be a preferred site. The implications for nucleation near a solid surface during rapid heating are also explored for circumstances similar to those for bubble nucleation adjacent to heaters in microheater reservoirs in inkjet printer heads.

[DOI: 10.1115/1.2754989]

Keywords: homogeneous nucleation, rapid transient heating, boiling onset, micropassage

Introduction

Transient boiling is important in numerous situations of technological interest, many of which involve micropassages. These include the transient initiation of a steady boiling process in microchannel evaporators, and the rapid heating to produce nucleation and bubble growth in the micropassages of inkjet printer droplet generators and microelectromechanical system (MEMS) bubble pumps. In general, heating the passage wall above the saturation temperature may give rise to heterogeneous nucleation or homogeneous nucleation of bubbles at the interface between the liquid and the solid wall. However, observations during previous experimental investigations indicate that homogeneous nucleation often occurs first in rapid transient heating.

Skripov [1] and Asai [2] observed that under extremely high heat flux pulse heating, the dominant bubble generation mechanism is the spontaneous nucleation due to the thermal motion of liquid molecules (homogeneous nucleation). Andrews and O'Horo [3,4] concluded from their experiments that rapid transient heating of a film heater in contact with liquid produced some bubbles by heterogeneous nucleation and some bubbles by homogeneous nucleation. Lin et al. [5] concluded that sudden energizing of polysilicon microresistors in Fluorinert liquids also resulted in the formation of a bubble by homogeneous nucleation. For water in contact with pulse-heated metal films, Balss et al. [6] and Avedisian et al. [7,8] observed onset of bubble nucleation at surface temperatures close to the superheat limit, suggesting that homogeneous nucleation was the mechanism of onset.

A particularly interesting result of the investigation by Andrews and O'Horo [3] is that they reported that bubble formation by homogeneous nucleation appeared to occur on or near the heater surface during the heating transient. The occurrence of homogeneous nucleation away from the surface would seem to contradict the expectation that homogeneous nucleation, if it occurs, will take place first at the surface itself where the liquid is superheated the most.

For this observation to be correct, there would have to be a mechanism that suppresses homogeneous nucleation very near the wall or makes it more likely some distance away from it. One possibility is that force interactions between molecules of the liquid and molecules in the solid surface are affecting the state of the fluid in a way that modifies the intrinsic stability limit. The effects of long-range force interactions between molecules in a fluid phase and the molecules in a nearby solid wall have been widely studied [9]. Wall-fluid attractive forces facilitate the formation of adsorbed liquid films on solid surfaces and disjoining pressure effects in ultrathin liquid films.

The effects of wall-fluid attractive forces on the fluid state near the wall have been explored in investigations by Gerweck and Yadigaroglu [10] and Carey and Wemhoff [11]. Both of these investigations indicated that wall-fluid attractive forces result in a rise in pressure very near the solid surface. Another interesting prediction of the model of Carey and Wemhoff [11] is that as the

---

Contributed by the Heat Transfer Division of ASME for publication in the Journal of Heat Transfer. Manuscript received September 8, 2006; final manuscript received December 9, 2006. Review conducted by Satish G. Kandlikar. Paper presented at the Fourth International Conference on Nanochannels, Microchannels and Minichannels (ICNMM2006), Limerick, Ireland, Jun. 19–21, 2006.

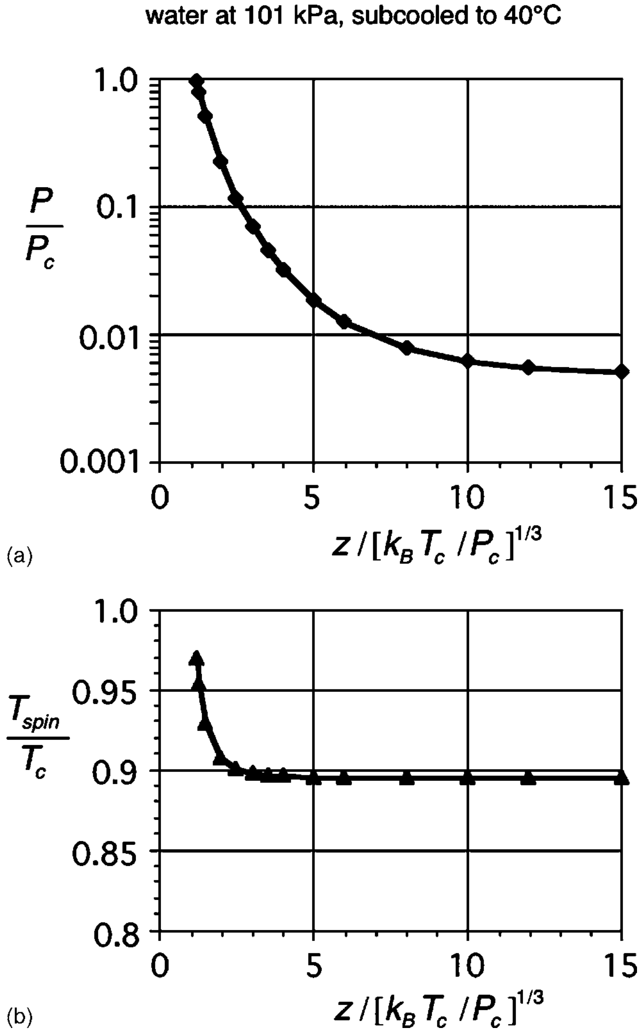

Fig. 1 Prediction of reduced pressure and spinodal temperature with distance from the wall predicted by the model of Carey and Wemhoff [11]. The wall is a gold (metal) surface.

wall is approached, the local spinodal temperature T_{spin} increases rapidly in the region within a few nanometers of the wall. Their results imply that the wall region near the solid surface is a region of high T_{spin} fluid because the pressure is elevated there and the value of T_{spin} for the local pressure (determined from the equation of state) is higher than the local T_{spin} for bulk fluid outside the wall region where wall-fluid attractive forces are negligible. For water at a bulk pressure of 1 atm and 40°C, the variation of pressure and spinodal temperature with distance from a gold (metallic) surface predicted by this model is shown in Fig. 1.

The near-wall property model and flat-surface heat transfer analysis developed by Carey and Wemhoff [11] predicts that during rapid transient pulse heating, the spinodal condition will be first achieved at a location a few nanometers away from the surface. Modeling the heat transfer for sudden delivery of a constant heat flux q_l'' to a planar solid surface, the transient temperature field near the surface was determined to be [11]

$$T = T_\infty + \frac{2q_l''}{k_l}\sqrt{\frac{\alpha_l t}{\pi}} - \frac{q_l'' z}{k_l} + \frac{z^3}{6\sqrt{\pi\alpha_l t}} + \cdots \qquad (1)$$

This implies that the temperature profile will ramp up over time, as shown in Fig. 2, and homogeneous nucleation occurs slightly away from the surface when the temperature profile intersects the spinodal temperature curve.

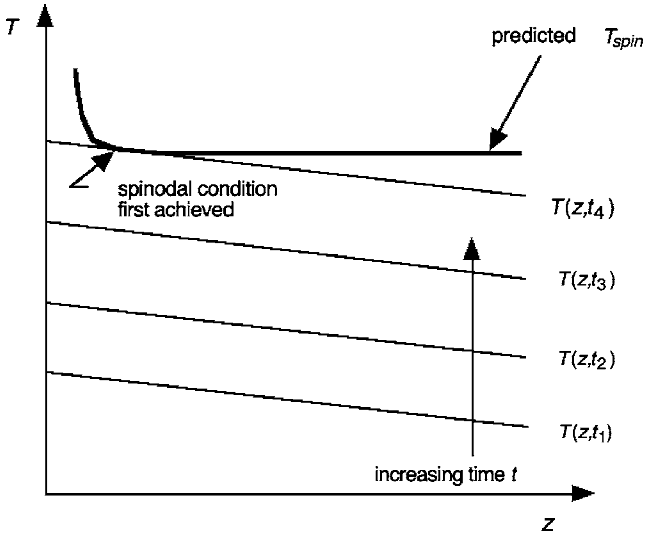

Fig. 2 Schematic of near-wall temperature variation and the approach to the spinodal condition

For rapid transient heating processes in inkjet printers, this appears to enhance the tendency for initiation of homogeneous nucleation in a liquid layer a few nanometers away from the solid heater and the subsequent vapor blanketing and explosive vaporization over the surface. The theoretical analysis of the rapid transient heating of water presented by Carey and Wemhoff [11], including the predicted variation of the spinodal temperature due to wall effects, is consistent with the observed onset and explosive vaporization in the experiments of Rembe et al. [12].

The analysis of Carey and Wemhoff [11] indicates that, in most systems of interest, near-wall effects on nucleation and boiling are confined to the region within a few nanometers of the surface. In many systems, the surface roughness has a scale much larger than this (on the scale of microns, typically), implying that the wall interaction effects would be difficult to separate from roughness effects. This suggests, however, that wall interactions may play a distinct role in micro- and nanoscale systems in which surface geometries may be defined to smaller resolutions. Even a surface manufactured with nanoscale precision could have a roughness level that is comparable to or larger than the thickness of the wall-affected region. In such a circumstance, the wall-affected region presumably would follow the contours of the surface, as depicted in Fig. 3. The analysis of Carey and Wemhoff [11] implies that the spinodal temperature T_{spin} in the bulk liquid is lower than in the wall-affected region, and in deep cavities in the surface, like location A in Fig. 3, a protrusion of low T_{spin} bulk fluid may extend down into the cavity. Sudden initiation of heat generation in the solid will initiate transient conduction of heat into the adjacent liquid. Because the protrusion of low T_{spin} fluid in the cavity is nearly surrounded by solid surface, the tip of this protrusion may be heated to a temperature above T_{spin} before the temperature of fluid at other locations reaches the spinodal temperature. This suggests that a small cavity containing a protrusion of low T_{spin} fluid would be a preferred homogeneous nucleation site in rapid transient heating.

For repeated rapid pulse heating of liquids on thin metallic films, O'Horo and Andrews [4], Rembe et al. [12], Balss et al. [6], and Avedisian et al. [8] reported observing repeated early nucleation at specific locations on the surface. The experimental observations of Balss et al. [6] and Avedisian et al. [8] indicate that these repeated first nucleation events occurred at specific sites with surface temperatures close to the superheat limit, suggesting that homogeneous nucleation was the onset mechanism. Repeated nucleation at a fixed location is often attributed to heterogeneous nucleation. The results of the analysis of Carey and Wemhoff [11]

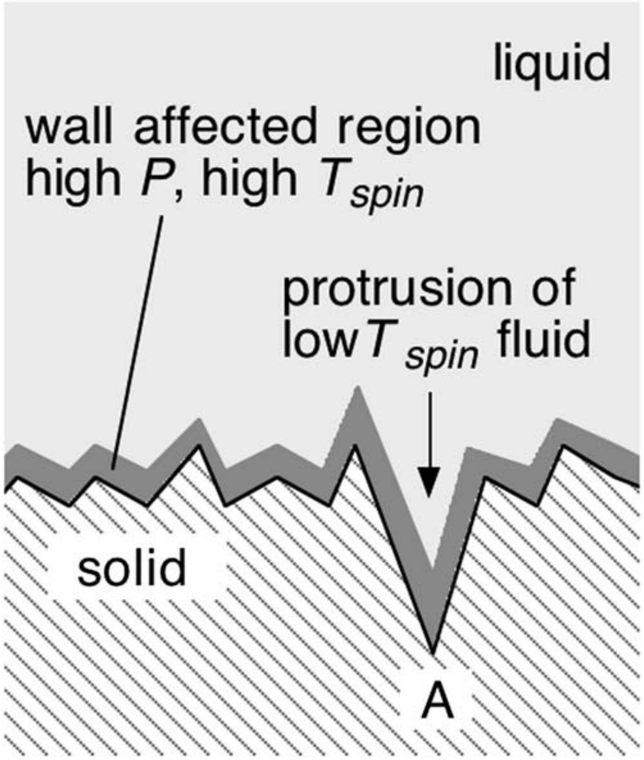

Fig. 3 Schematic of the wall-affected region near a rough surface

suggest a possible mechanism for homogeneous nucleation at preferred sites on a surface subjected to rapid transient heating. The observed repeated early nucleation at fixed locations may be a consequence of homogeneous nucleation at preferred sites where bulk fluid with a lower spinodal temperature (T_{spin}) penetrates into a deep surface cavity.

The investigation summarized here developed a model analysis of transient heat transfer in a liquid-filled conical surface cavity to explore the plausibility and apparent mechanisms of the preferred-site homogeneous nucleation that is suggested by the model analysis of Carey and Wemhoff [11]. The heat transfer model and its predictions are described in the following sections.

Transient Heat Transfer Analysis

To explore the effect of wall attractive forces on the onset of nucleation during rapid transient heating, the liquid-filled conical crevice depicted in Fig. 4 was considered as an idealized model. The cone half-angle is θ_w and the sidewall length is $r=r_c$. Conduction heat transfer in the liquid inside the cone is modeled using the transient conduction equation in spherical coordinates:

$$\frac{\partial T}{\partial t}=\left(\frac{\alpha_l}{r^2}\right)\frac{\partial}{\partial r}\left(r^2\frac{\partial T}{\partial r}\right)+\left(\frac{\alpha_l}{r^2\sin\theta}\right)\frac{\partial}{\partial\theta}\left(\sin\theta\frac{\partial T}{\partial\theta}\right) \tag{2}$$

Initially, the entire system is at uniform temperature T_∞. At time $t=0$, a constant heat flux q_l'' is delivered to the liquid at the solid surface. The computational domain for the fluid in the crevice is the region ABCDA in Fig. 4. In this study, the geometry of the cavity was arbitrarily specified such that $r_b=(1/5)r_c$ and $r_{\text{match}}=(4/3)r_c$.

In this model, the boundary conditions are obtained by matching the temperature field to that associated with delivery of a uniform heat flux to the adjacent flat surface (at location B–F). In the solid heater material, a constant temperature gradient is assumed to exist to transport heat to the flat surface at F. This gradient remains constant as the solid surface temperature along B–F

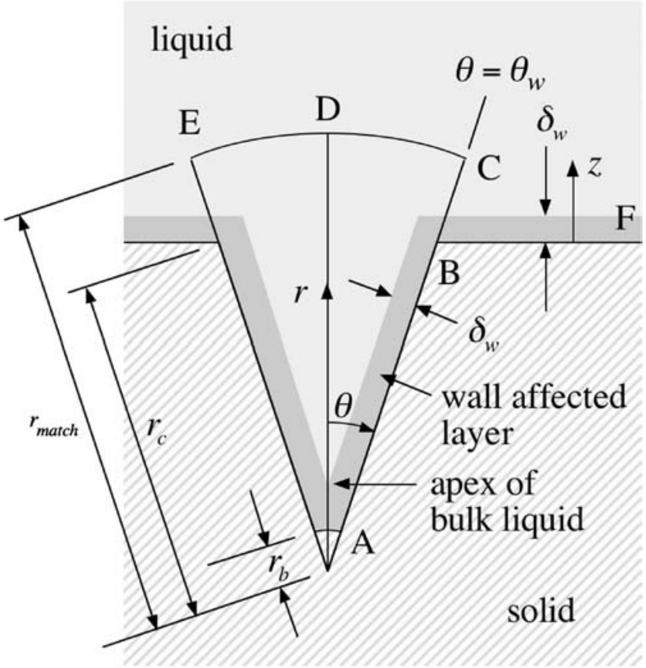

Fig. 4 Computational domain and adjacent regions

ramps up according to the flat-surface transient given by Eq. (1). The liquid adjacent to the flat solid surface B–F is assumed to follow the transient solution for a semi-infinite region of liquid, which, in the near-wall region, can be approximated by the first two terms of the expansion (1). Boundary conditions along B and C and C and D are therefore established by matching this solution along these domain boundaries. At the axis of the cone ($\theta=0$), symmetry dictates that $\partial T/\partial\theta=0$. These considerations yield the following boundary conditions: along A-B: for $(1/5)r_c\leq r\leq r_c$:

$$T(\theta_w,r)=T_\infty+\frac{2q_l''}{k_l}\sqrt{\frac{\alpha_l t}{\pi}}+\frac{q_l''}{k_s}(r_c-r)\cos\theta_w \tag{3}$$

along B-C: for $r_c\leq r\leq(4/3)r_c$:

$$T(\theta_w,r)=T_\infty+\frac{2q_l''}{k_l}\sqrt{\frac{\alpha_l t}{\pi}}-\frac{q_l''}{k_l}(r-r_c)\cos\theta_w \tag{4}$$

along C-D: for $0\leq\theta\leq\theta_w$:

$$T\left(\theta,\frac{4}{3}r_c\right)=T_\infty+\frac{2q_l''}{k_l}\sqrt{\frac{\alpha_l t}{\pi}}-\frac{q_l''}{k_l}\left(\frac{1}{3}r_c\right)\cos\theta \tag{5}$$

along the lower base: for $0\leq\theta\leq\theta_w$:

$$T\left(\theta,\frac{1}{5}r_c\right)=T_\infty+\frac{2q_l''}{k_l}\sqrt{\frac{\alpha_l t}{\pi}}+\frac{q_l''}{k_s}\left(\frac{4}{5}r_c\right)\cos\theta \tag{6}$$

along the centerline ($\theta=0$): for $(1/5)r_c\leq r\leq(4/3)r_c$:

$$\partial T/\partial\theta=0 \tag{7}$$

Introducing the nondimensional variables

$$\Phi=\frac{T-T_\infty}{q_l''r_c/k_l}\quad \eta=r/r_c\quad \hat{t}=\alpha_l t/r_c^2 \tag{8}$$

the equation, initial and boundary conditions, can be stated as

$$\frac{\partial\Phi}{\partial\hat{t}}=\frac{\partial^2\Phi}{\partial\eta^2}+\left(\frac{2}{\eta}\right)\frac{\partial\Phi}{\partial\eta}+\left(\frac{1}{\eta^2\tan\theta}\right)\frac{\partial\Phi}{\partial\theta}+\left(\frac{1}{\eta^2}\right)\frac{\partial^2\Phi}{\partial\theta^2} \tag{9}$$

for $\theta=\theta_w$, $1/5\leq\eta\leq1$:

$$\Phi = 2\sqrt{\frac{\hat{t}}{\pi}} + \left(\frac{k_l}{k_s}\right)(1-\eta)\cos\theta_w \tag{10}$$

for $\theta=\theta_w$, $1 \leqslant \eta \leqslant 4/3$:

$$\Phi = 2\sqrt{\frac{\hat{t}}{\pi}} - (\eta - 1)\cos\theta_w \tag{11}$$

for $0 \leqslant \theta \leqslant \theta_w$, $\eta=4/3$:

$$\Phi = 2\sqrt{\frac{\hat{t}}{\pi}} - \frac{1}{3}\cos\theta \tag{12}$$

for $0 \leqslant \theta \leqslant \theta_w$, $\eta=1/5$:

$$\Phi = 2\sqrt{\frac{\hat{t}}{\pi}} + \frac{4}{5}\left(\frac{k_l}{k_s}\right)\cos\theta \tag{13}$$

for $\theta=0$, $1/5 \leqslant \eta \leqslant 4/3$:

$$\partial\Phi/\partial\theta = 0 \tag{14}$$

Note that in the above model formulation, the cavity is modeled as being surrounded by flat surface. We therefore expect that far from the surface in the ambient liquid, the transient temperature field will be close to that for a large flat surface in the absence of the cavity. We match the computed temperature in the cavity to this field at an arbitrarily chosen distance $r=(4/3)r_c$ outside the cavity to simulate the merger of the temperature field in the cavity with the outer transient field. This is expected to be appropriate in this model because the matching only weakly affects the transient temperature field deeper in the cavity, and the primary objective here is accurate prediction of the temperature variation near the apex of the conical crevice. Note also that to establish the cavity wall boundary conditions, the temperature field in the solid is modeled as ramping up with time in the manner dictated by a 1D conduction transient solution that delivers a nominally uniform heat flux into the liquid in contact with the flat surface.

Although several features of the model are idealized, we adopt them here based on the argument that doing so is representative of typical circumstances during rapid transient heating of a thin metal film on a solid substrate in contact with a liquid. This is consistent with the objective of the model analysis described here, which was to explore whether preferential sites for homogeneous nucleation exist under conditions typical of rapid transient heating processes in applications such as inkjet printing.

Equation (9) with boundary conditions (10)–(14) and initial condition

$$\Phi(\eta,\theta,0) = 0 \tag{15}$$

was solved numerically using a Dufort-Frankel scheme. Derivatives in the conduction equation (9) were converted to finite-difference forms using central differences for first derivatives and split-time central differences for the second derivatives. The resulting finite-difference equation is

$$\begin{aligned}\Phi_{i,j}^{\hat{t}+\Delta\hat{t}} = {} & \frac{\Phi_{i,j}^{\hat{t}-\Delta\hat{t}}}{1+2F_\eta+2F_\theta/\eta_{i,j}^2} \\ & + \frac{2\Delta\hat{t}}{1+2F_\eta+2F_\theta/\eta_{i,j}^2}\left[\frac{\Phi_{i+1,j}^{\hat{t}} - \Phi_{i,j}^{\hat{t}-\Delta\hat{t}} + \Phi_{i-1,j}^{\hat{t}}}{(\Delta\eta)^2}\right. \\ & + \left(\frac{1}{\eta_{i,j}}\right)\frac{\Phi_{i+1,j}^{\hat{t}} - \Phi_{i-1,j}^{\hat{t}}}{\Delta\eta} + \left(\frac{1}{\eta_{i,j}^2\tan\theta_{i,j}}\right)\frac{\Phi_{i,j+1}^{\hat{t}} - \Phi_{i,j-1}^{\hat{t}}}{2\Delta\theta} \\ & \left. + \left(\frac{1}{\eta_{i,j}^2}\right)\frac{\Phi_{i,j-1}^{\hat{t}} - \Phi_{i,j}^{\hat{t}-\Delta\hat{t}} + \Phi_{i,j+1}^{\hat{t}}}{(\Delta\theta)^2}\right]\end{aligned} \tag{16}$$

where

Table 1 Cases considered in model analysis

	I	II	III
θ_w (deg)	18.3	18.3	18.3
r_c (nm)	30	100	30
r_b (nm)	6.0	20	6.0
r_{apex} (nm)	9.6	24	9.6
k_l/k_s	0.00751	0.00751	0.1
k_l (W/m °C)	0.674	0.674	0.674
q_l'' (W/m^2)	2.31×10^8	2.31×10^8	2.31×10^8
T_∞ (°C)	40	40	40
T_{spin} (°C)	306	306	306
$t_r=r_c^2/\alpha_l$ (μs)	0.00523	0.0580	0.00523
$q_l''r_c/k_l$ (°C)	10.3	34.3	10.3
Φ_{spin}	25.9	7.76	25.9
$\Delta\eta$	0.02	0.02	0.02
$\Delta\theta$	0.02	0.02	0.02
$\Delta\hat{t}$	0.00025	0.00025	0.00025
$\hat{t}_{\text{spin}}$	527	47.25	524
t_{spin} (μs)	2.76	2.74	2.74
$\Delta\hat{t}_{\text{FX}}$	4.9	0.55	7.3
Δt_{FX} (μs)	0.026	0.032	0.038
$\Delta\Phi_{\text{FX}}$	0.12	0.041	0.18
ΔT_{FX} (°C)	1.23	1.41	1.85

$$F_\eta = \frac{\Delta\hat{t}}{(\Delta\eta)^2} \quad F_\theta = \frac{\Delta\hat{t}}{(\Delta\theta)^2} \tag{17}$$

This scheme is more stable than an explicit method but can be marched forward in time if the temperature field is known at two previous time steps. To start the Dufort-Frankel scheme, a simple Euler explicit scheme with a very small time step ($0.02\Delta\hat{t}$) was used to march the solution forward one initial time step $\Delta\hat{t}$. The initial condition at $\hat{t}=0$ and the Euler results at $\hat{t}=\Delta\hat{t}$ were then used to start the Dufort-Frankel scheme with time step $\Delta\hat{t}$. The explicit Euler starting scheme used the following finite-difference form of the conduction equation in the starting process:

$$\begin{aligned}\Phi_{i,j}^{\hat{t}+\Delta\hat{t}} = \Phi_{i,j}^{\hat{t}} + \Delta\hat{t}\Bigg[& \frac{\Phi_{i+1,j}^{\hat{t}} - 2\Phi_{i,j}^{\hat{t}} + \Phi_{i-1,j}^{\hat{t}}}{(\Delta\eta)^2} + \left(\frac{2}{\eta_{i,j}}\right)\frac{\Phi_{i,j}^{\hat{t}} - \Phi_{i-1,j}^{\hat{t}}}{\Delta\eta} \\ & + \left(\frac{1}{\eta_{i,j}^2\tan\theta_{i,j}}\right)\frac{\Phi_{i,j+1}^{\hat{t}} - \Phi_{i,j}^{\hat{t}}}{\Delta\theta} \\ & + \left(\frac{1}{\eta_{i,j}^2}\right)\frac{\Phi_{i,j-1}^{\hat{t}} - 2\Phi_{i,j}^{\hat{t}} + \Phi_{i,j+1}^{\hat{t}}}{(\Delta\theta)^2}\Bigg]\end{aligned} \tag{18}$$

Computations using this numerical scheme for conditions associated with rapid transient heating are described in the next section.

Results and Discussion

The model calculations in this study were done for parameters corresponding to transient heating of water at atmospheric pressure and 313.2 K (40°C). This was done to facilitate a comparison of the model predictions with the observations of Rembe et al. [12] for rapid transient heating of water at atmospheric pressure. In their investigation, Rembe et al. [12] used a pseudocinematographic visualization technique to observe the onset of nucleation near a thin film heater between a solid substrate and a reservoir of pure water. The heater was 60 μm square. The film heater was the type used in Hewlett-Packard deskjet printers. Their pseudocinematographic visualization technique required repeated application of power to the heater to collect images of the process at different times. The total power input of 7.5 W was applied for 3 μs. Because the repeated heating is expected to raise the tem-

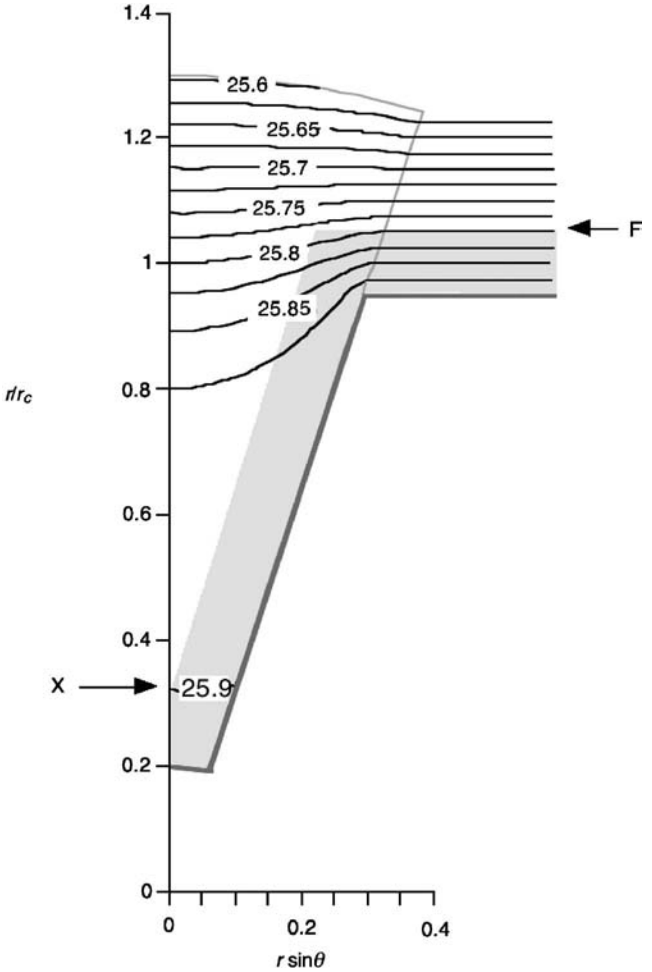

Fig. 5 Dimensionless temperature field $\Phi(\eta,\theta,\hat{t})$ when spinodal condition is reached at point X ($\hat{t}$=527). The crevice sidewall (r_c) is 30 nm and the cone angle is 18.3 deg (case I). The gray region adjacent to the solid surface is the wall-affected layer.

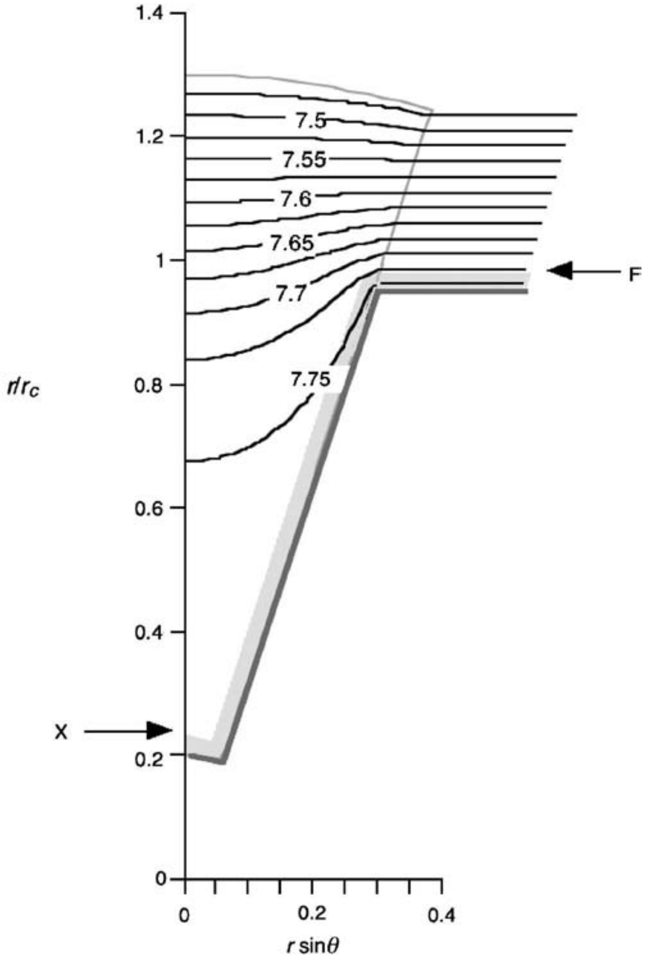

Fig. 6 Dimensionless temperature field $\Phi(\eta,\theta,\hat{t})$ when spinodal condition is reached at point X ($\hat{t}$=47.25). The crevice sidewall (r_c) is 100 nm and the cone angle is 18.3 deg (case II). The gray region adjacent to the solid surface is the wall-affected layer.

perature of the water in the reservoir above room temperature, a bulk water temperature of 40°C was assumed for the comparison here.

Using the properties of water and silicon at 400 K to represent the properties of the solid substrate under the heater and the adjacent water [13,14], the conductivities and thermal diffusivities were estimated to be $k_l = 0.674$ W/m °C, $\alpha_l = 1.72 \times 10^{-7}$ m^2/s, $k_s = 89.7$ W/m °C, and $\alpha_s = 4.76 \times 10^{-5}$ m^2/s. The analysis of Carey and Wemhoff [11] indicates that the heat flux delivered to the liquid during the pulsed-heating experiments was $q_l'' = 2.31 \times 10^8$ W/m^2. The boundary condition parameters in the model calculations in this study were therefore set to levels equivalent to this heat flux input to the liquid.

Initially, the temperature throughout the computational domain and in the adjacent liquid and solid is $T_\infty = 40°$C. As indicated in Fig. 4, a wall-affected region exists immediately adjacent to the solid surface. The analysis of Carey and Wemhoff [11] indicates that for the conditions of interest here, this layer is 3 nm thick (see Fig. 1(*b*)). Once the heat flux input is initiated, the temperature in the liquid adjacent to the surface at point F rises according to Eq. (1). In the solid, the temperature field is presumed to rise so as to sustain the temperature gradient that delivers the required heat flux to the liquid-solid interface at F. The primary objective of this study is to determine where the fluid first achieves the spinodal limit temperature. In terms of dimensionless parameters, the spinodal temperature corresponds to

$$\Phi_{\text{spin}} = \frac{T_{\text{spin}} - T_\infty}{q_l'' r_c / k_l} \tag{19}$$

Here, T_{spin} was taken to be 306°C for water at atmospheric pressure [15]. Note that since the other parameters are fixed, Φ_{spin} will vary with r_c.

Because the spinodal temperature is elevated inside the wall layer, we expect that during the transient heating, it will be first attained just outside the wall layer. The computations were done to determine if this occurs first inside the cone at the apex of the bulk liquid, and if so, how much faster the spinodal temperature is achieved relative to point F outside the wall layer.

The model analysis described above was applied to a variety of transient heating scenarios. The discussion here will focus on the results for the three representative cases listed in Table 1. As indicated in Table 1, the grid size and time step in these cases were set at $\Delta\eta = 0.02$, $\Delta\theta = 0.02$, and $\Delta\hat{t} = 0.00025$. To explore the effect of grid size and time step, some of the simulation calculations were repeated with half the grid spacing ($\Delta\eta = 0.01$, $\Delta\theta = 0.01$) and one-quarter the time step ($\Delta\hat{t} = 0.0000625$). This refinement produced about a 0.2% change in the computed dimensionless temperature values during the transient, and the time to the super-

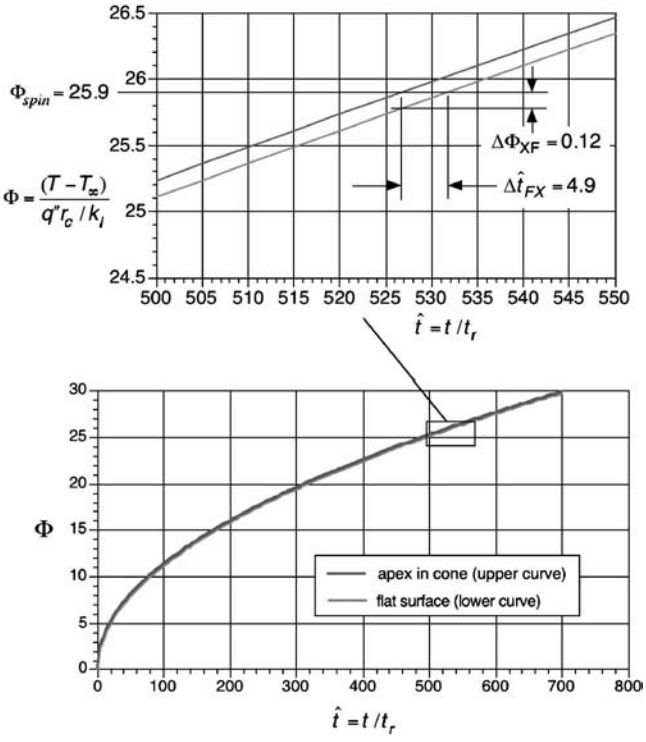

Fig. 7 Variation of dimensionless temperature with dimensionless time ($\hat{t} = t/t_r$) at points X and F. The crevice sidewall (r_c) is 30 nm and the cone angle is 18.3 deg (case I).

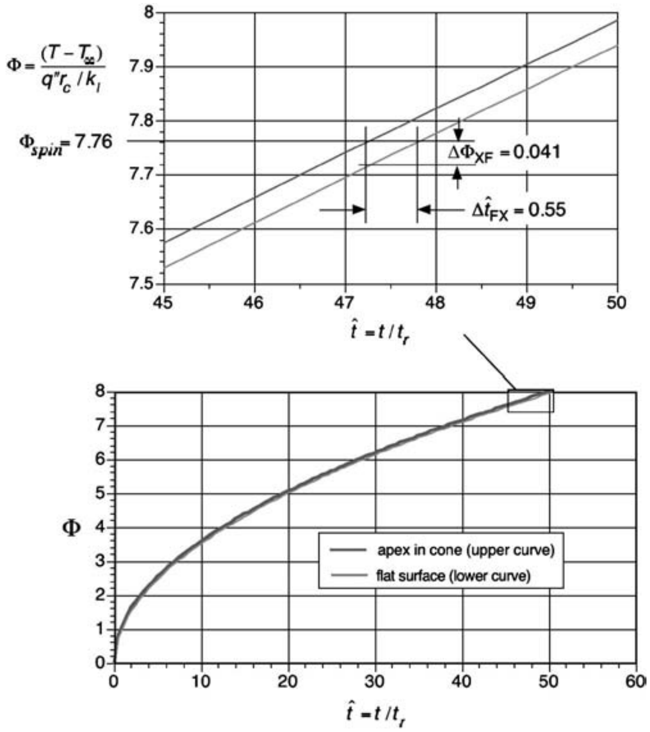

Fig. 8 Variation of dimensionless temperature with dimensionless time ($\hat{t} = t/t_r$) at points X and F. The crevice sidewall (r_c) is 100 nm and the cone angle is 18.3 deg (case II).

heat limit temperature changed by less than 0.7%. These results indicate that for the mesh size and time step shown in Table 1, the computed transient temperature fields are, to a good approximation, independent of mesh size and time step.

The dimensionless temperature field in the liquid at the time that the spinodal condition is first achieved is shown in Figs. 5 and 6 for cone sidewall lengths of 30 nm and 100 nm, respectively. These are for cases I and II in Table 1. Note that for $r_c = 30$ nm, the spinodal condition corresponds to $\Phi_{\text{spin}} = 25.9$, whereas for $r_c = 100$ nm, the spinodal condition corresponds to $\Phi_{\text{spin}} = 7.76$. In both cases, the spinodal condition is first reached at the apex of bulk fluid in the crevice (point X).

By monitoring the temperature rise at points X and F, we determined from the results how much faster the spinodal condition was reached at point X for these cases. Figure 7 shows the time variations of dimensionless temperature (Φ) at these two locations for the 30 nm sidewall case represented in Fig. 5. It can be seen in Fig. 7 that the spinodal condition is reached first at the apex location. This occurs at a dimensionless time $\hat{t}_{\text{spin}} = 527$. As indicated in Table 1, this corresponds to a physical time of 2.76 μs. At that instant, the dimensionless temperature at location F just outside the wall layer is lower by 0.12, which corresponds to a difference of 1.23°C. Similar analysis of the curves in Fig. 7 indicates that an additional 0.026 μs would be required to reach the spinodal temperature outside the wall layer at F.

Analysis of the temperature time variation in Fig. 8 for the larger crevice in case II yielded similar results (see Table 1). For case II, the spinodal condition was again reached first at the apex location at a physical time of 2.74 μs and the temperature outside the wall layer at F was 1.41°C lower at that time. The spinodal condition was not reached at location F outside the layer until 0.032 μs later.

The physical properties in cases I and II were chosen to model the conditions for rapid transient heating of water in the experiments of Rembe et al. [12]. The ratio of conductivities k_l/k_s is very low for these cases. To explore how this ratio affects the results, the analysis was applied to case III in Table 1, which is identical to case I except that k_l/k_s is set to the higher value of 0.1. This corresponds to a much lower conductivity solid surface material. Results for case III are summarized in Table 1. Generally, the results differ only slightly from those for case I, implying that the conductivity change had little impact on the time variation of the temperature field for these conditions.

The results of the conduction transient analysis indicate that when the spinodal condition is first reached, the temperature inside the conical crevice is only about 1°C higher than locations outside the crevice. This might appear too small to make the region inside the conical crevice a preferred nucleation site. However, the kinetic limit nucleation theories generally predict that the rate of critical embryo generation per unit volume increases rapidly with increasing temperature. The kinetic limit theory formulated by Katz and Blander [15] predicts that the rate of formation of embryos of critical size J (number/m^3 s) is given by

$$J = \frac{N_A}{\hat{v}_l}\left(\frac{3\sigma_{lv}}{\pi M}\right)^{1/2} \times \exp\left[\frac{-16\pi\sigma_{lv}^3}{3k_B T(P_{\text{sat}}(T)\exp\{\hat{v}_l[P - P_{\text{sat}}(T)]/RT\} - P)^2}\right] \tag{20}$$

Figure 9 shows the variation of J with liquid temperature predicted by Eq. (20) for water at atmospheric pressure. It can be seen from this plot that near the spinodal temperature (306°C), a liquid temperature change from 306°C to 305°C decreases the embryo production rate per unit volume J by nearly a factor of 1000. For a temperature difference of 1.4°C, J differs by a factor of more than 10^4. This trend suggests that for the 1.4°C higher temperature in the 100 nm crevice predicted in case II, the probability of formation of a critical embryo, per unit volume, is on the order of 10^4 times higher. This analysis implies that despite the small temperature difference in the crevice, homogeneous nucle-

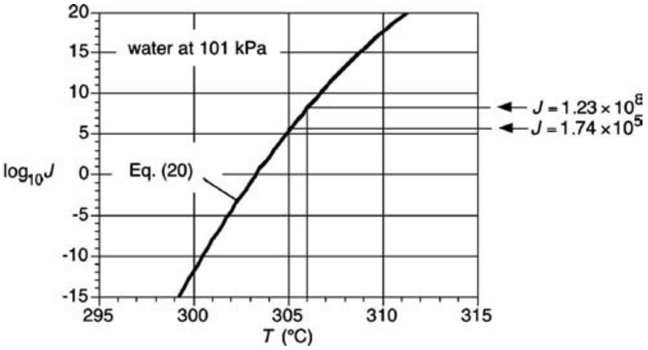

Fig. 9 Variation of embryo generation rate *J* with temperature for water (the units on *J* are number/m^3 s)

ation is more likely to occur first in the conical crevice.

In Table 1, it can be seen that for cases I and II considered here, the flat surface outside the crevice will reach the spinodal limit in 26–32 ns after the apex location inside the crevice. Although this may appear to be an extremely short time interval, the extreme level of superheat at the spinodal can produce substantial bubble growth in short time intervals. The initial growth is expected to be inertia controlled. In the inertia-controlled regime, the bubble radius variation is predicted to have the linear form [16]

$$R = \left\{ \frac{2}{3} \left[\frac{T - T_{\text{sat}}(P_\infty)}{T_{\text{sat}}(P_\infty)} \right] \frac{h_{lv}\rho_v}{\rho_l} \right\}^{1/2} t \tag{21}$$

For water at $T=306°\text{C}$, $h_{lv}=1357$ kJ/kg, $\rho_v=51.2$ kg/m^3, and $\rho_l=699$ kg/m^3. Here, $T_{\text{sat}}=100°\text{C}$ and the slope (dR/dt) in the above linear relation is 191 m/s. This relation predicts that a nucleated bubble can grow to a radius of 1.0 μm in 5.2 ns. This implies that under these conditions, if a bubble nucleates first within the crevice, it may grow to several microns in diameter before nucleation can occur near the flat surface outside the crevice.

Concluding Remarks

Although the model analysis presented here considers an idealized conical crevice geometry, it demonstrates that crevices with simple geometries can be locations where homogeneous nucleation occurs earlier than flat portions of a surface subjected to rapid transient heating. The conditions considered in this study were chosen to be consistent with the water rapid pulse heating experiments done by Rembe et al. [12]. For these conditions, the model analysis predicts first onset of homogeneous nucleation in the crevice at about 2.7 μs, which is close to the first nucleation time reported by Rembe et al. [12] for their experiments. The results of our model analysis demonstrate that first homogeneous nucleation at the apex of a bulk fluid intrusion into a cavity is a plausible explanation for the localized repeatable first nucleation observed in the water rapid pulse heating experiments of Rembe et al. [12], Balss et al. [6], and Avedisian et al. [8]. Although the temperature at the apex in the crevice increases only slightly faster than the temperature adjacent to flat portions of the surface, the extreme sensitivity of the embryo production rate suggests that the onset of nucleation is much more probable inside the cavity. The rapid inertia-controlled bubble growth possible at the high superheat levels in these systems allows a bubble that forms in the crevice to grow to several microns in diameter before onset is likely near flat portions of the surface. Our results for a 30 nm crevice and a 100 nm crevice were very close, suggesting that this type of localized onset could occur over a range of cavity sizes that could exist in the walls of microchannels subject to rapid transient heating.

The results of this investigation indicate that under commonly encountered conditions, the combined effects of wall-fluid attractive forces, conduction heat transfer, nucleation, and bubble growth can result in homogeneous nucleation at preferred sites during rapid transient heating of a liquid. Because this investigation focused on the interaction of these mechanisms, it considered only limited ranges of system parameters, primarily examining those typical of inkjet printing applications. The model analysis clearly indicates that the presence or absence of preferred-site homogeneous nucleation is affected by a variety of system parameters (i.e., crevice geometry, fluid and solid properties, heat flux, and far field subcooling level). Although limited in scope, results of this initial study suggest that preferred-site homogeneous nucleation can occur over substantial ranges of these parameters. A full exploration of how system parameters affect the existence of preferred-site homogeneous nucleation is beyond the scope of this initial investigation. However, a follow-up study is currently underway that will explore how the accuracy and variability of fluid properties and other system parameters affect the presence or absence of preferred-site homogeneous nucleation during transient heating.

Acknowledgment

Support for this research was provided by the National Science Foundation under Grant No. CTS-0456982.

Nomenclature

h_{lv} = latent heat of vaporization per unit mass
J = rate of formation of embryos of critical size
k_B = Boltzmann constant
k_l = liquid thermal conductivity
k_s = solid thermal conductivity
M = molecular mass
N_A = Avogadro's number
P = pressure
P_c = critical pressure
q_l'' = heat flux
R = universal gas constant
t = time
T = temperature
T_c = critical temperature
T_{spin} = spinodal temperature
$\hat{v}_l$ = saturated liquid molar specific volume
z = distance from solid surface
α_l = liquid thermal diffusivity
α_s = solid thermal diffusivity
ρ_l = saturated liquid mass density
ρ_v = saturated vapor mass density
σ = interfacial tension

References

[1] Skripov, V. P., 1974, *Metastable Liquids*, Wiley, New York, Chap. 3 and 6.
[2] Asai, A., 1991, "Bubble Dynamics in Boiling Under High Heat Flux Pulse Heating," ASME J. Heat Transfer, **113**, pp. 973–979.
[3] Andrews, J. R., and O'Horo, M. P., 1995, "High Speed Stroboscopic System for Visualization of Thermal Inkjet Processes," Proc. SPIE, **2413**, pp. 176–181.
[4] O'Horo, M. P., and Andrews, J. R., 1995, "Initial Stages of Vapor Bubble Nucleation in Thermal Ink Jet Processes," Proc. SPIE, **2413**, pp. 182–188.
[5] Lin, L., Pisano, A. P., and Carey, V. P., 1998, "Thermal Bubble Formation on Polysilicon Micro Resistors," ASME J. Heat Transfer, **120**, pp. 735–742.
[6] Balss, K. M., Avedisian, C. T., Cavicchi, R. E., and Tarlov, M. J., 2005, "Nanosecond Imaging of Microboiling Behavior on Pulsed-Heated Au Films Modified With Hydrophilic and Hydrophobic Self-Assembled Monolayers," Langmuir, **21**, pp. 10459–10467.
[7] Avedisian, C. T., Osborne, W. S., McLeod, F. D., and Curley, C. M., 1999, "Measuring Bubble Nucleation Temperature on the Surface of a Rapidly Heated Thermal Ink-Jet Heater Immersed in a Pool of Water," Proc. R. Soc. London, Ser. A, **455**, pp. 3875–3899.
[8] Avedisian, C. T., Cavicchi, R. E., and Tarlov, M. J., 2006, "New Technique for Visualizing Microboiling Phenomena and its Application to Water Pulse Heated by a Thin Metal Film," Rev. Sci. Instrum., **77**, 063706, pp. 1–7..
[9] Israelachvilli, J., 1994, *Intermolecular and Surface Forces*, 2nd ed., Academic, New York, Chap. 11.

[10] Gerweck, V., and Yadigaroglu, G., 1992, “A Local Equation of State for Fluid in the Presence of a Wall and its Application to Rewetting,” Int. J. Heat Mass Transfer, **35**, pp. 1823–1832.

[11] Carey, V. P., and Wemhoff, A., 2005, “Thermodynamic Analysis of Near-Wall Effects on Phase Stability and Homogeneous Nucleation During Rapid Surface Heating,” Int. J. Heat Mass Transfer, **48**, pp. 5431–5445.

[12] Rembe, C., aus der Wiesche, S., and Hofer, E. P., 2002, “Thermal Ink Jet Dynamics: Modeling, Simulation and Testing,” Microelectron. Reliab., **40**, pp. 525–532.

[13] 1972, *Thermophysical Properties of Matter*, Y. S., Touloukian, and C. Y. Ho, eds., Plenum, New York, Vols. 1, 4.

[14] Incropera, F. P., and DeWitt, D. P., 2002, *Fundamentals of Heat and Mass Transfer*, 5th ed., Wiley, New York, Appendix A.

[15] Katz, J. L., and Blander, M., 1973, “Condensation and Boiling: Corrections to Homogeneous Nucleation Theory for Nonideal Gases,” J. Colloid Interface Sci., **42**, pp. 496–502.

[16] Carey, V. P., 1992, *Liquid-Vapor Phase-Change Phenomena*, Taylor & Francis, New York, Chap. 5.

R. Muwanga

I. Hassan[1]
e-mail: ibrahimtt@alcor.concordia.ca

Department of Mechanical and Industrial Engineering,
Concordia University,
Montréal, QC, H3G 1M8, Canada

R. MacDonald[2]
Washington Technology Center,
Seattle, WA 98195-2140

Characteristics of Flow Boiling Oscillations in Silicon Microchannel Heat Sinks

Flow boiling oscillation characteristics in two silicon microchannel heat sink configurations are presented. One is a standard heat sink with 45 straight parallel channels, whereas the second is similar except with cross-linked paths at three locations. Data are presented over a flow range of 20–50 ml/min (91–228 kg/(m^2 s)) *using distilled water as the working fluid. The heat sinks have a footprint area of* 3.5 cm^2 *and contain* 269 μm *wide by* 283 μm *deep reactive ion etching channels. Flow oscillations are found to be similar in characteristic trends between the two configurations, showing a decreasing frequency with increasing heat flux. The oscillation amplitudes are relatively large and identical in frequency for the inlet temperature, outlet temperature, inlet pressure, and pressure drop. Oscillation properties for the standard heat sink at two different inlet temperatures and various flow rates are correlated for different heat fluxes. This work additionally presents a first glimpse of the cross-linked heat sink performance under flow boiling instability conditions.* [DOI: 10.1115/1.2754946]

Keywords: microchannel, boiling oscillations, cross-linked heat sink, boiling instability

Introduction

There is an emerging need for thermal control technologies capable of managing high power densities. This is driven by the electronic needs for both terrestrial and extraterrestrial applications [1,2]. One of the emerging cooling approaches that addresses the increasing miniaturization of electronics is the microelectromechanical system (MEMS) based heat sink. The standard microchannel heat sink consists of a set of microchannels conventionally machined or micromachined into a conducting block. Tuckerman and Pease [3] pioneered this device in the early 1980s using wet etched 50 μm wide and 300 μm deep silicon microchannel heat sinks. Under single-phase conditions flowing deionized water, they were able to demonstrate heat dissipation up to 790 W on a 1 cm^2 chip.

With the recent breakthroughs in MEMS based manufacturing techniques, the microchannel heat sink and similar technologies have become viable options for future thermal management of high-heat flux and ultrahigh-heat flux electronics. Recently, there have been a number of investigations considering radical modifications to the standard straight microchannel heat sink. Among these, single-phase flow studies have considered straight fins [4] and pin fins [5,6], fractal networks [7–9], and cross-linked channels [10–12], all with the aim of increasing the heat transfer while minimizing the pressure drop.

Two-phase flow novel configurations have aimed at increasing heat transfer and minimizing instabilities. Kosar et al. [13] introduced restrictors at the channel inlets to suppress flow boiling oscillations. The restrictors had a diameter six times smaller than that of the channels. They studied the influence of the restrictor length and observed that with increased length the instabilities were less severe. Pressure drop fluctuations were on the order of 2–7 kPa with no restrictors, whereas they were less than 1 kPa with the restrictors. Kandlikar et al. [14] utilized a combination of inlet flow restriction elements and fabricated nucleation sites to stabilize the flow boiling process. The study considered restrictors with 51% and 4% of the flow area, with and without artificial nucleation sites. With the 4% flow area restrictor, no flow reversals were observed and the addition of the fabricated nucleation sites produced the best thermal performance. The penalty of this, however, was an increase in pressure drop of almost double.

Boiling Instabilities in Conventional Size Systems. Boiling instabilities in macrosystems have been extensively studied in the past and may be classified as static or dynamic [15,16]. Static instabilities are those whose cause may be related through steady state laws. During such instability, the fluid may change to another steady state point or oscillate between two steady state points. An example is the Ledinegg instability, which by definition occurs when the pressure gradient with respect to mass flow of the internal flow system is less than that of the pressure supply system. Inertia or other feedback effects cause dynamic instabilities, and the steady state laws are not enough to predict them. These instabilities may be initiated by a static instability. Density waves have low frequencies that are on the order of a particle traveling through the system. Their mechanism is related to delay and feedback between the flow, pressure drop, and density. Other types of dynamic instabilities may include thermal oscillations, which are observed during dryout, and parallel channel instabilities, which are related to interactions between a small number of channels. In this case, various modes of flow redistribution may be observed. A third kind of instability, which occurs as a secondary phenomenon, is the pressure drop oscillation. This type of instability is found to occur when there is a compressible volume upstream of the heated section. Similar to the Ledinegg instability, it occurs just after the minimum in the pressure drop versus mass flow curve. The frequency of oscillation is much lower for the pressure-drop-type instabilities compared to density wave instabilities and is on the order of 0.1 Hz. A comparison of flow stability regions for single, parallel, and cross-connected parallel channels has been summarized by Kakac and Veziroglu [16]. The data were compiled from a number of experiments using a single test facility. This facility consisted of vertical pipe systems with freon-11 as the working fluid and with pipe inner diameters of 7.5 mm (0.295 in.). The study found that for density-wave-type

---

[1] Corresponding author.

[2] Present address: Lund Engineering, 12600 Interurban Ave. S, Tukwilla, WA 98168.

Contributed by the Heat Transfer Division of ASME for publication in the JOURNAL OF HEAT TRANSFER. Manuscript received July 18, 2006; final manuscript received April 13, 2007. Review conducted by Satish G. Kandlikar.

instabilities, a single channel, a parallel channel, and two parallel cross-connected channels all presented a similar performance. For pressure-drop-type instabilities, the most stable system was the four parallel cross-connected channel system. The parallel channel systems with unequal heat inputs showed the smallest stability regions with respect to pressure-drop-type instabilities.

Boiling Oscillations in Parallel Microchannel Systems. Related to microchannel flows, few studies have documented the characteristics of the flow boiling instabilities. Some studies have observed different flow pattern characteristics in the boiling instabilities depending on the imposed conditions and have classified them as such. Wu and Cheng [17] investigated boiling instabilities in eight trapezoidal channels with a hydraulic diameter of 186 μm in a silicon wafer 525 μm thick. They used a microscope and a high-speed camera for bubble visualization and placed thermocouples at the base of the wafer. The authors observed three instability modes consisting of liquid to two-phase alternating flow (LTAF), continuous two-phase flow (CTF), and liquid to two-phase to vapor alternating flow (LTVAF). For the LTAF case, bubbly flow dominated with wall temperature fluctuations of $20-46°$C. The oscillation frequency was 0.065 Hz and was characterized to be of a large amplitude over a long period. Pressure and mass flux oscillations were almost out of phase. With an increase in heat flux and decrease in mass flux, the CTF case was observed. Temperature fluctuations decreased to $7-20°$C, and the pressure and mass flux were almost in phase. Finally, with additional increase in heat flux and decrease in mass flux, the LTVAF case was observed. Wall temperature fluctuations were highest in this case at $66-230°$C, and the pressure and mass fluxes were almost out of phase. These oscillations were also classified as having a large amplitude over a long period. Xu et al. [18] carried out a study of flow boiling instabilities in a copper test section of 26 channels, 300×800 μm^2. Through gradually decreasing the mass flux, they were able to initiate flow boiling instability. Two periodic instabilities were observed and were of large amplitude long period oscillations (LALPOs) and small amplitude small period oscillations (SASPOs). These were accompanied by thermal oscillations with fluctuations of up to 20°C (peak to peak) in the first case and up to 4°C (peak to peak) in the second. The SASPO instability was characterized by bubble growth at the channel exit, followed by the liquid-vapor interface moving upstream. When the interface reached the inlet plenum for a number of channels, the vapor fronts moved forward into the channels. The vapor front growth increased the temperature while decreasing the heat transfer coefficient. The working fluids were water and methanol, and similar behaviors were observed for both fluids. However, due to methanol's lower latent heat, the frequency was lower.

Hetsroni et al. [19] investigated water boiling in 21 isosceles triangle channels with a base of 250 μm and an angle of 55 deg, fabricated in a silicon substrate. At the boiling onset, bubble growth rapidly filled the entire channel cross section and then grew lengthwise both upstream and downstream. The other channels accounted for the liquid that was pushed upstream. An instant later, the bubble was vented from the channel, and a brief period of vapor with liquid droplets commenced. This boiling process was described as "explosive" due to its short time period. The pressure drop amplitude was found to increase with quality, whereas the oscillation frequency in a single channel increased with increasing heat flux. In a recent study by the same authors [20], further characterization of the boiling instabilities, termed explosive boiling oscillations (EBOs), was provided. They found an increase in the amplitude of bulk system parameters, such as the pressure drop and the inlet and outlet fluid temperatures, with increasing heat flux. Additionally, they found a decrease in the frequency of the bulk system with heat flux. This is notably different from the characteristic of individual channels within the same system. Steinke and Kandlikar [21], while studying flow boiling heat transfer in six parallel channels of 214×200 μm^2 in a copper substrate test section, observed flow reversals in individual channels. The fluid used was water, and the channels were slightly trapezoidal. Flow reversals were found to occur during the onset of the annular-slug flow regime. Flow reversals were similarly observed by Balasubramanian and Kandlikar [22], who investigated flow boiling in six parallel copper channels, 990 μm wide and 207 μm deep. The authors noted that while bubble nucleation was the dominant flow pattern (at low surface temperatures), the pressure drop dominant frequency increased with increasing surface temperature. However, with further increase in temperature, the slug flow pattern dominated and the pressure drop dominant frequency decreased. Qu and Mudawar [23] studied boiling in 21 copper channels of dimension 215×821 μm^2, with water as the working fluid. Two oscillation-type instabilities were observed. In the first case, the liquid-vapor interface changed position drastically from close to the exit to close to the inlet. This was accompanied with high pressure drop and temperature fluctuations. The temperature fluctuations reached 15°C and caused a premature critical heat flux (CHF). Installing a throttle upstream of the test section remedied this, and it was classified as a pressure drop oscillation. The second type was a result of installing the throttle valve and was characterized by the liquid-vapor front alternating positions between channels. This was characterized as a parallel channel instability and was accompanied by mild pressure drop and temperature ($<1°$C) fluctuations.

The above show the prevalence of boiling instabilities in parallel microchannel systems. However, compared to conventional size channels, the understanding of their mechanisms and characteristics is still in its infancy. Additionally, boiling oscillations have only been presented for straight standard parallel microchannel systems. The following presents characteristics of boiling instabilities in a cross-linked microchannel heat sink and a standard microchannel heat sink to better understand their mechanisms. The aim of the cross-links is to interrupt any rapidly expanding bubble and prevent it from engulfing the entire channel length up to the inlet.

Test Module Design and Fabrication

The heat sinks have been designed to manage a thermal load of 25 W/cm^2, given a 3.5 cm^2 footprint area, with a maximum temperature of 85°C and under single-phase conditions. This is based on the criterion laid out by Paris et al. [2] for the requirements of future micro-nanospacecrafts. The footprint area is taken as the plan area encompassing the channels (16×21.875 mm^2). Single-phase water was the working fluid, and the maximum available pressure was 34.5 kPa (5 psi). Both the standard and the cross-linked microchannel heats sinks have a measured width and depth of 269 μm and 283 μm, respectively, and the cross-linked design has a measured cross-link width of 269 μm. The fabricated heat sinks consist of a silicon wafer with a SiO_2 insulation layer. A glass cover of 500 μm thickness seals the chamber and is bonded to the silicon base piece containing the channels. The cover has eight 1 mm diameter holes etched for flow inlet and outlet. This glass cover will also allow for future work with flow visualization. A serpentined platinum heating element, 1 mm wide and 186 mm long, is deposited on the backside of the channel base to simulate the heated chip. A schematic of these components is shown in Fig. 1(*a*). Two microchannel schemes are utilized, a standard parallel channel heat sink (STR02) and a cross-linked microchannel heat sink (INT01).

The substrates used for fabricating the heat sinks are (100)-oriented silicon (Si) wafers and 500 μm thick and 350 μm thick Corning 7740 Pyrex wafers. Etching is required to fabricate the glass wafer hole arrangement, and multiple holes are selected to provide an inlet that behaves approximately like a slot. This aims to promote a well distributed flow at the entry. For this process, amorphous silicon deposited in a plasma enhanced chemical vapor deposition (PECVD) reactor (Oxford Instruments, plasma lab

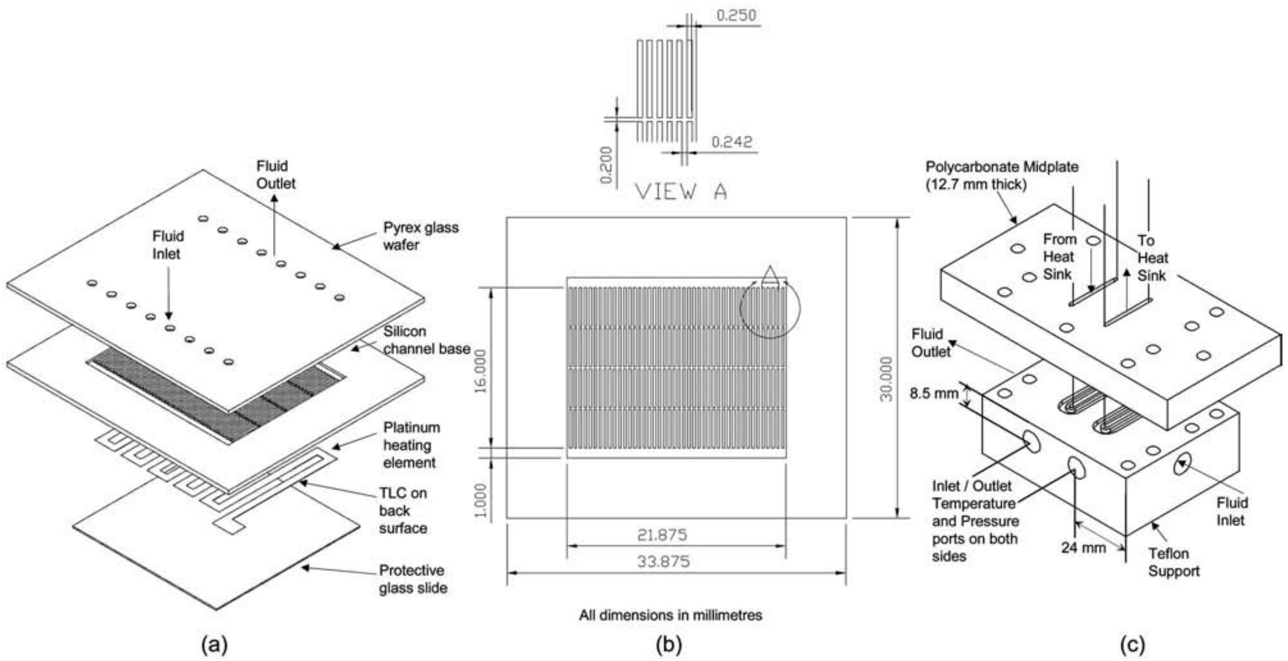

Fig. 1 Microchannel heat sink package configuration

100) is chosen as the mask material and 49% hydrofluoric acid (HF) as the etchant to form the through ports on the Pyrex substrates. After the amorphous silicon is deposited, it is patterned on both sides. The channels are formed in the silicon wafer via deep reactive ion etching (Oxford Instruments ICP 380), as it is a good approach in obtaining uniform vertical sidewalls. Finally, the wafers are bonded using anodic bonding. A summary of this fabrication process is presented in Fig. 2.

A plan view of the heat sink INT01 is shown in Fig. 1(*b*) with nominal dimensions. Heat sink STR02 was similar, expect with no cross-linked paths. The fabricated channel dimensions were optically verified prior to packaging onto the support. Large deviations from the nominal were observed, and the measured values are used in all calculations. A comparison of these dimensions is shown in Table 1. Figure 1(*c*) shows the heat sink support with the inlet and outlet chambers and the pressure and temperature taps. The support was fabricated from Teflon due to its high temperature limits as well as its low thermal conductivity and electrical resistance. The heat sinks were fixed onto the support using a silicone based adhesive with a high temperature limit.

Test Facility and Measurement Methodology

Facility. A schematic of the main components used in the closed loop test facility is shown in Fig. 3. The facility is designed to support experiments using air, FC-72, and distilled water. However, distilled water was used for all the flow boiling data presented in this paper. Flow enters the loop from the main tank and is continuously circulated by a magnetically coupled gear pump. The pump is equipped with a variable speed drive allowing for a flow range up to 300 ml/min, with a maximum pressure of 517 kPa (75 psi). A nutating digital output flowmeter provided by DEA Engineering is used to monitor the flow rate. This meter outputs a 5 V square wave signal at a frequency proportional to the time for the nutator to complete one cycle. The flowmeter has been calibrated using the weighing method, and has a reliable range from 10 ml/min to 250 ml/min. Upstream of the flowmeter is a 15 μm filter, which is used to remove any accumulating particles. In addition, a preheater is located at the inlet of the test section for additional flow temperature control. It consists of a stainless steel tank with a 1500 W stainless steel heating element.

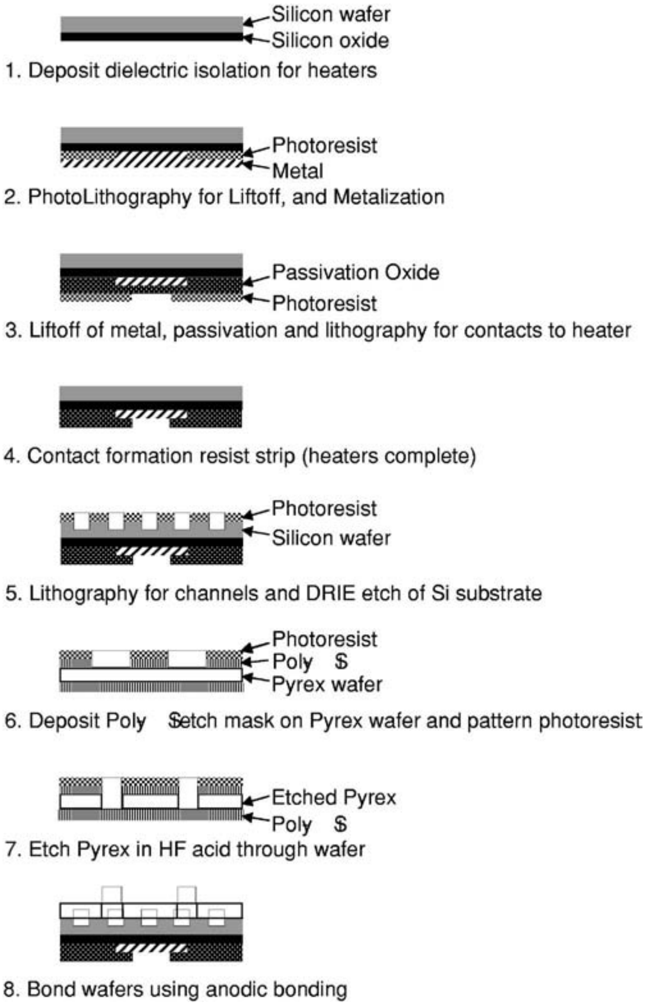

Fig. 2 Microchannel heat sink fabrication process

Table 1 Comparison of design and measured parameters

	Design (μm)	Measured (μm)
Channel width	242	269
Channel depth	300	283
Cross-link width	200	269

Power to this heating element is controlled by a Variac, providing a stable inlet temperature setpoint. At the exit of the test section is a water-cooled heat exchanger, which is used to restore the temperature of the fluid.

The data acquisition hardware consists of National Instrument's SCXI 1000 signal conditioning unit, with the appropriate modules as well as a NI 6052E 16 bit, 333 kHz data acquisition card. Two 1.5 mm diameter type-T (Omega special error limits the material) thermocouples are placed in the heat sink supports to measure the bulk fluid temperature, and their locations are depicted in Fig. 1(*c*). Two pressure transducers track the inlet gage pressure and the differential pressure across the heat sinks. They are Omega model PX02C1 (inlet) with a range of 345 kPa (50 psi) and Omega model PX821 (differential) with a range of 34.5 kPa (5 psi). A Vaisala PTB220 barometer is used to obtain the absolute pressure of the surroundings. The output from these and other sensors is monitored through an automated data acquisition system using the LABVIEW™ software. Power to the serpentined platinum heating element is provided by two BK Precision dc power supplies (model 1623A) operating in parallel mode, each with a voltage range of 0–60 V and a maximum current rating of 1.5 A. The image acquisition system incorporates a three-charge-coupled-device (3-CCD) camera mounted on a 12× zoom traversable microscope system with an external illuminator. It is used to obtain heat sink thermal maps with thermochromic liquid crystals, which can be used to determine local heat transfer characteristics. This is a recently developed method, which has been demonstrated for measurements on microtubes. Further details on this measurement method may be obtained from Muwanga and Hassan [24].

Procedure and Data Reduction. Before commencing the experiments, noncondensables are purged from the fluid through a degassing procedure. This is done by heating the fluid in the preheater tank above 90°C. The fluid is then circulated in the system at a high flow rate for 1 h, allowing the entire fluid to pass through the preheater tank twice. After this, the desired flow rate is set and the preheater is adjusted to obtain the inlet temperature setpoint. Data are obtained at incremental levels of heat flux. Flow boiling measurements for the standard heat sink (STR02) have been obtained at flow rates of 20–50 ml/min $(91-228\ \mathrm{kg/(m^2\,s)})$ and inlet temperatures of 70°C and 80°C. For the cross-linked design (INT01), however, only one flow rate and one inlet temperature are investigated due to difficulties with leakage in the setup. The pressure taps are located at some distance from the channel inlets and exits, and so contain additional pressure drop components due to the inlet and outlet chamber circuitry. These are accounted for through loss factors for area changes and bends and are obtained from Munson et al. [25]. Additional losses will be incurred due to the channel entry and exit and flow acceleration. These are estimated using the methodology outlined by Kays and London [26] for flows in compact heat exchangers. Finally, as the flow at entry is not fully developed, this was also considered. Power to the fluid under single-phase conditions is obtained from an energy balance given by

$$q'' = \frac{Q_{\mathrm{vol}}(\rho_{\mathrm{out}}Cp_{\mathrm{out}}T_{\mathrm{out}} - \rho_{\mathrm{in}}Cp_{\mathrm{in}}T_{\mathrm{in}})}{A_{\mathrm{heated}}} \quad (1)$$

During flow boiling, the heat flux was obtained from the heater power generated and corrected for losses to the environment using a power ratio factor γ. This results in

$$q'' = \frac{(VI)\gamma}{A_{\mathrm{heated}}} \quad (2)$$

Ideally, the power ratio factor γ may be estimated from an energy balance through the estimation of convective losses to the environment and axial conduction losses, as was shown by Hetsroni et al. [19]. However, this requires a measurement of the outer wall temperature, which was not available for the boiling measurements. To alleviate this, the present work estimated this factor by combining Eqs. (1) and (2) under single-phase conditions. For each flow rate, as the heat flux was increased, the power ratio factor reached a limiting value prior to boiling. This limiting value, which ranged from 0.85 to 0.97, for the various flow rates was taken as the power ratio factor under boiling conditions.

Uncertainties are estimated at ±0.57 kPa for inlet gage pressure measurements and at ±0.03 kPa for pressure drop based on instrument specifications, at ±0.7°C for fluid temperature measurement

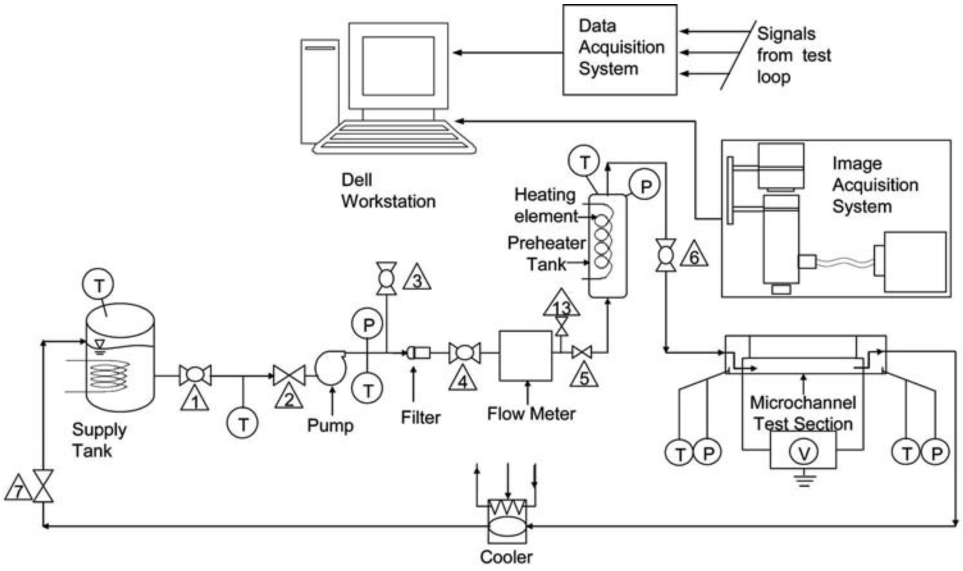

Fig. 3 Test facility

Table 2 Uncertainty estimates for derived parameters

Parameter	Uncertainty
D_h	5.5 μm
G	4.8–12.3%
q''	3.4–6.2%
Re	7.4–27.5%
Bo	7.1–13.4%
We_D and We_L	12.4–24.0% and 12.2–23.9%
N_{sub}	2.4–4.2%
f^*	0.4–2.1%
P^*	1.7–4.7%
T^*	5.3–21.6%

based on manufacturer specifications of the combined measurement system, and at ±2.25 ml/min for the flow rate. Uncertainties for derived parameters have been calculated using methods similar to those described by Kline and McClintock [27] and are presented in Table 2.

Results and Discussion

Figure 4 compares the single-phase pressure drop characteristics between STR02 and INT01, with distilled water as the working fluid. The difference in pressure drop is observed to be negligible over the flow range investigated, and a discernible benefit or detriment of the cross-linked scheme is not observed. A relatively good agreement is observed with the theoretical prediction of fully developed laminar flow given by $f\,\mathrm{Re}=14.25$ for an aspect ratio of ~0.95 [28]. The deviating trend from the theoretical value at the low Reynolds number for the STR02 heat sink is likely due to the sensor's accuracy at measuring the very low pressures. Further, the overall deviation from the theoretical value will be related to the applicability of the entrance and minor loss coefficients utilized. Wall temperature measurements have been obtained under single-phase flow conditions for flowing FC-72. A sample wall temperature mapping is shown in Fig. 5 for the INT01 heat sink and is obtained from unencapsulated liquid crystal measurements. The liquid crystal material is provided by LCR-Hallcrest and has a nominal red start of 40°C with a bandwidth of 10°C. The mapping is a combination of three images at different locations along the heat sink. The thermal map shows a wall temperature rise along the streamwise direction as expected for single-phase flows. There is, however, some minor nonuniformity in the wall temperature downstream of $x/D_h=25$.

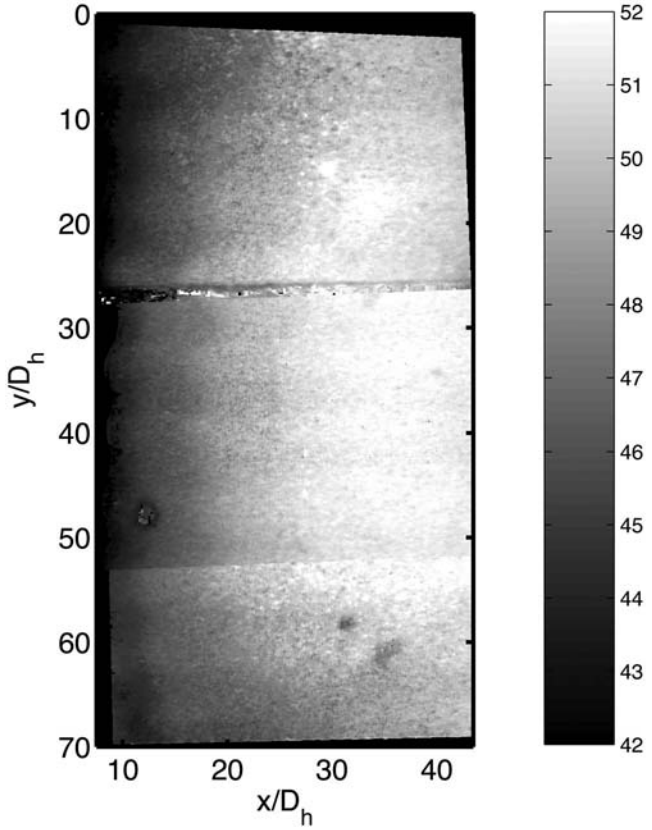

Fig. 5 Wall temperature mapping of heat sink INT01 at Re ~307

The typical inlet pressure trend leading up to a two-phase flow is shown in Fig. 6 for an inlet temperature of 70°C at a flow rate of 30 ml/min. After boiling, the inlet pressure would rise slightly in some cases due to increased vapor generation until instabilities occurred. Figure 6 shows that for degassed fluids, the heat flux at which instabilities occur is similar for both cases at approximately 7.9 W/cm^2. However, for a nondegassed fluid, as shown for the cross-linked design, the onset of flow instabilities occurs earlier and at approximately 66% of the heat flux for the degassed fluid.

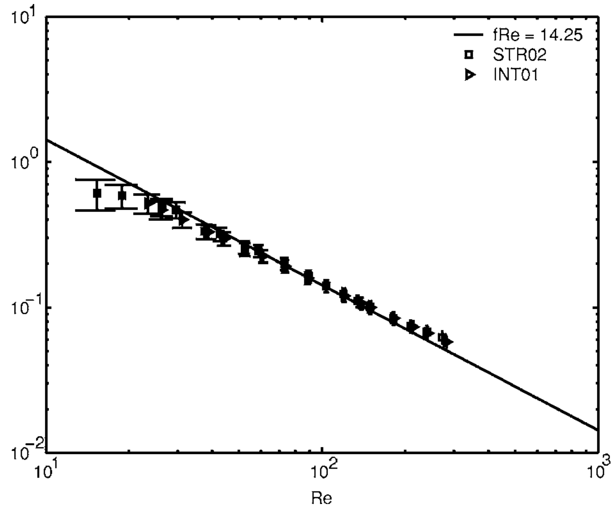

Fig. 4 Friction factor versus Reynolds number, cross-linked and standard heat sink

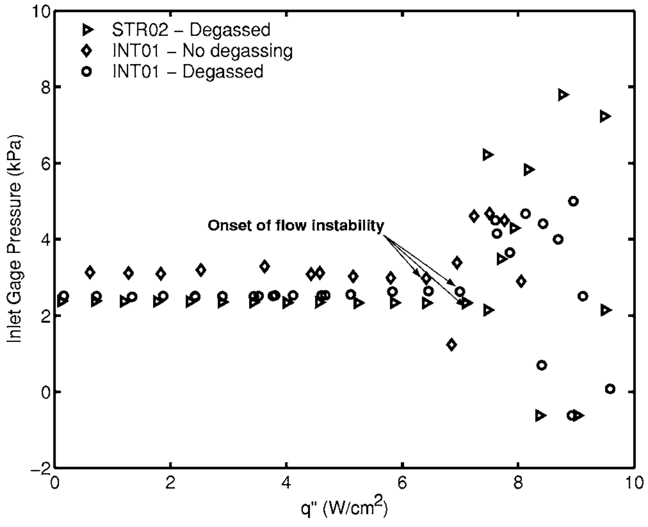

Fig. 6 Inlet pressure versus applied power, $T_{\mathrm{in}}=70°\mathrm{C}$, $Q_{\mathrm{vol}}=30$ ml/min

Table 3 Measurement conditions and stability limits.

Heat sink configuration	T_{in} (°C)	Q_{vol} (ml/min)	G kg/(m^2 s)	Conditions at onset of instability	
				q'' (W/cm^2)	Bo
STR02	70	20	91	4.1	1.958×10^{-4}
		30	140	7.1	2.247×10^{-4}
		40	186	9.7	2.316×10^{-4}
	80	30	140	4.9	1.540×10^{-4}
		40	185	5.5	1.312×10^{-4}
		50	228	7.9	1.538×10^{-4}
INT01	70	30	140	7.0	2.215×10^{-4}

An early onset due to a nondegassed fluid has been observed in prior investigations, and this highlights the importance of utilizing a well prepared fluid for predictability [29]. Additionally, this latter point has recently been reiterated by Chen and Garimella [30], who investigated flow boiling of a degassed and nondegassed dielectric fluid in a microchannel heat sink.

Once the stable threshold was crossed, sustained oscillations in flow parameters were observed. These were relatively periodic fluctuations in various sensors, including the inlet and outlet temperature and the inlet and differential pressure sensors. The identification of the onset of instability was based on the monitoring of the fluctuations of flow parameters, as well as on the observation of the flow in the tubing downstream. A summary of the flow conditions leading to an unstable flow and the boiling oscillation measurement conditions are listed in Table 3. Samples of signal fluctuations during unstable flow boiling, for a given heat flux and flow rate, are presented in Figs. 7–9. They are presented both for the STR02 and INT01 heat sinks. The oscillations were captured at a rate of 5–10 Hz over a 20–50 s span. The time traces show relatively large amplitude oscillations. This is likely due to periodic refilling of the channels, typical of what has been observed by other researchers working with boiling in parallel channel microsystems [19–23]. A characteristic trend in the flow oscillations captured is that the dominant frequency is the same for all the sensors, and they are in phase. This is a relatively low frequency on the order of 10^{-1} Hz. No discernible trends are observed between a pressure time trace versus an inlet or an outlet temperature time trace. The inlet temperature, however, is always observed to oscillate with a smaller amplitude than the outlet temperature. Its amplitude, though, grows more significantly with increased heat flux, and details of these amplitude characteristics are presented later. Through performing a fast Fourier transform on the time traces and parsing for the largest peak, the dominant frequency of the signals is obtained. Figure 10 shows the variation in the inlet temperature oscillation frequencies, comparing both heat sink configurations. For STR02, the frequency is higher than INT01 and decreases with increasing heat flux. For INT01, the

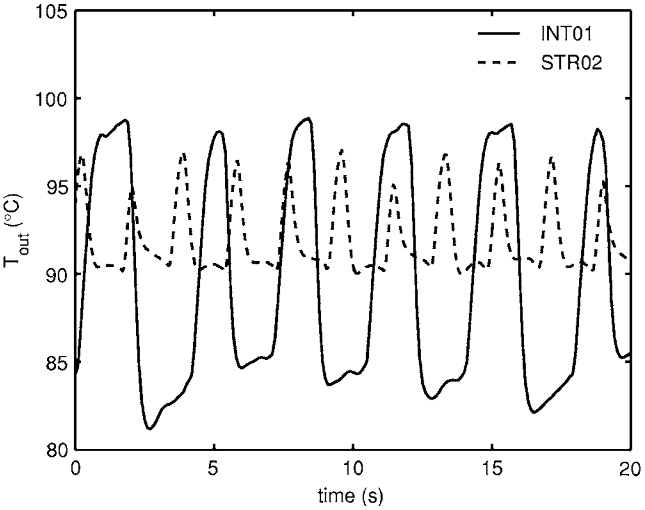

Fig. 8 Outlet temperature sample transient behavior, $q''\sim7.9$ **W/cm^2,** $T_{\text{in}}=70°\text{C}$**,** $Q_{\text{vol}}=30$ **ml/min**

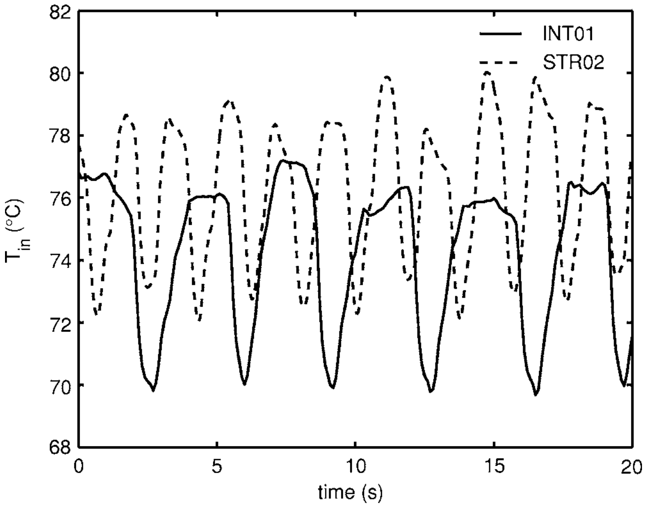

Fig. 7 Inlet temperature sample transient behavior, $q''\sim7.9$ **W/cm^2,** $T_{\text{in}}=70°\text{C}$**,** $Q_{\text{vol}}=30$ **ml/min**

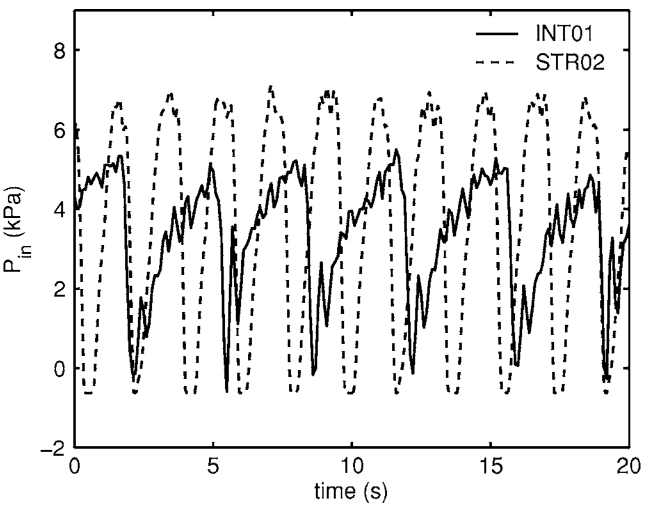

Fig. 9 Inlet pressure sample transient behavior, $q''\sim7.9$ **W/cm^2,** $T_{\text{in}}=70°\text{C}$**,** $Q_{\text{vol}}=30$ **ml/min**

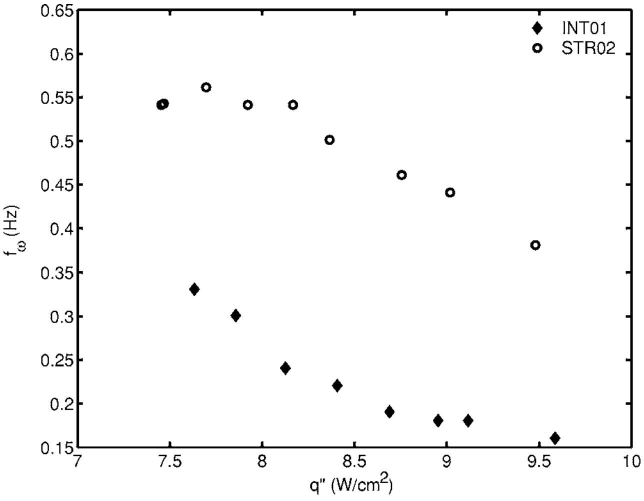

Fig. 10 Inlet temperature oscillation frequency versus power, T_{in}=70°C for different heat sinks at Q_{vol}=30 ml/min

frequency also decreases with increasing heat flux. Figure 11(*a*) shows the variation in frequency for the STR02 heat sink as a function of inlet temperature, flow rate, and heat flux. For a higher temperature, the frequency is lower for the same flow rate, and with a lower flow rate, the frequency is also lower. It is observed that the frequency of oscillations is dependent not only on the heat flux but also on the flow rate and the inlet subcooling. Also included in Fig. 11(*a*) are the frequency data obtained from Hetsroni et al. [20]. The heat sinks in this work contained 13 triangular cross-section channels fabricated in a silicon substrate and with a hydraulic diameter of 220 μm. The mass flux range of the data was 63.3 kg/(m^2 s) to 127 kg/(m^2 s) and the heat flux ranged from 17 W/cm^2 to 32 W/cm^2. Similar trends to the present data are observed in that the frequency decreases with increasing heat flux and lower mass fluxes have lower frequencies. A correlation has been developed to compile these observations. The frequency was nondimensionalized with the heated length and the channel inlet velocity assuming an all liquid flow at entry,

$$f^* = \frac{f_\omega L_{\text{chn}}}{u_{\text{chn,in}}} \tag{3}$$

A number of length scales exist to nondimensionalize the frequency, and they include the boiling length, the full channel length, and the hydraulic diameter. Based on the performance of a number of correlation fit trials, the channel length was chosen, as opposed to the boiling length. The hydraulic diameter is accounted for through the inclusion of the Weber number based on the hydraulic diameter. Since the frequency is a function of the heat flux and subcooling, we may utilize the boiling number as the nondimensional heat flux and the subcooling number (N_{sub}) to account for inlet subcooling. Finally, the number of channels is also included as an independent parameter. Based on these parameters, the following relationship was developed to correlate the data in Fig. 11(*a*):

$$f^* = C_1 \text{Bo}^{C_2} N_{\text{sub}}^{C_3} \text{We}_D^{C_4} N_{\text{chn}}^{C_5} \tag{4}$$

where $C_1=3.383\times10^{-15}$, $C_2=-1.408$, $C_3=4.328$, $C_4=0.144$, and $C_5=-0.137$, or in dimensional form as

$$f_\omega = 3.383(10^{-15})\frac{u_{\text{chn,in}}}{L_{\text{chn}}}\left(\frac{q''}{Gh_{fg}}\right)^{-1.408}\left[\frac{Cp(T_{\text{sat}}-T_{\text{in}})}{h_{fg}}\frac{\rho_f-\rho_g}{\rho_g}\right]^{4.328} \times\left(\frac{G^2D_h}{\sigma\rho_f}\right)^{0.144}(N_{\text{chn}})^{-0.137} \tag{5}$$

Fluid properties in the above are calculated from saturation conditions at the tube exit. Equation (4) fits the data with a standard deviation of 25.4%. Figure 11(*b*) compares the correlation fit with

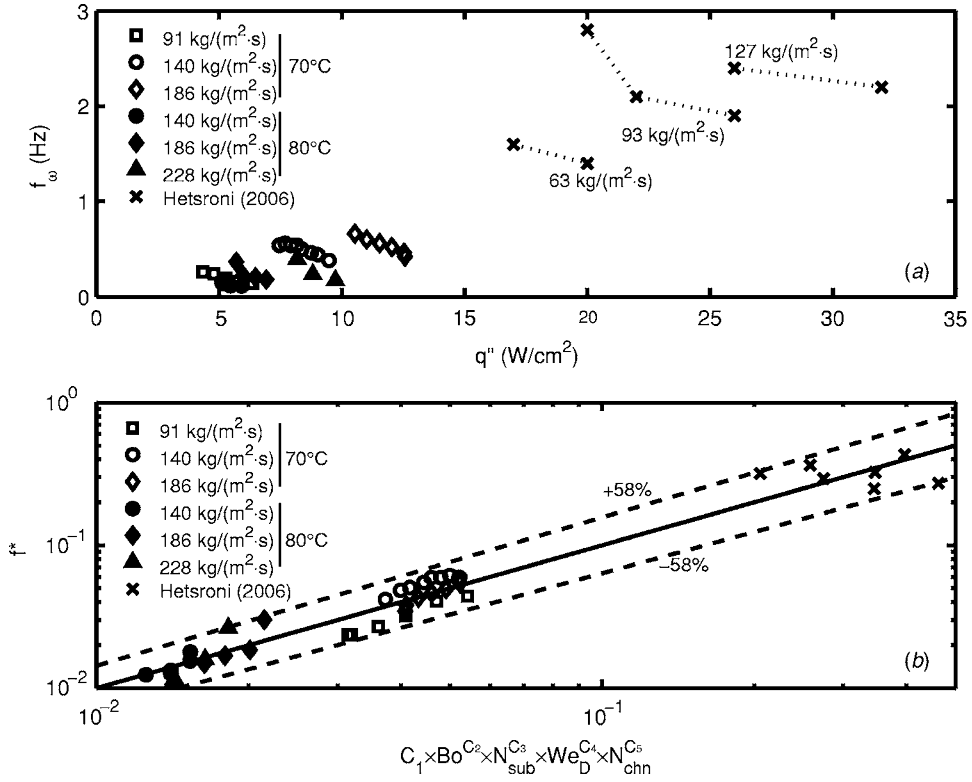

Fig. 11 Inlet temperature oscillation frequency versus power for STR02 at different flow rates and inlet temperatures

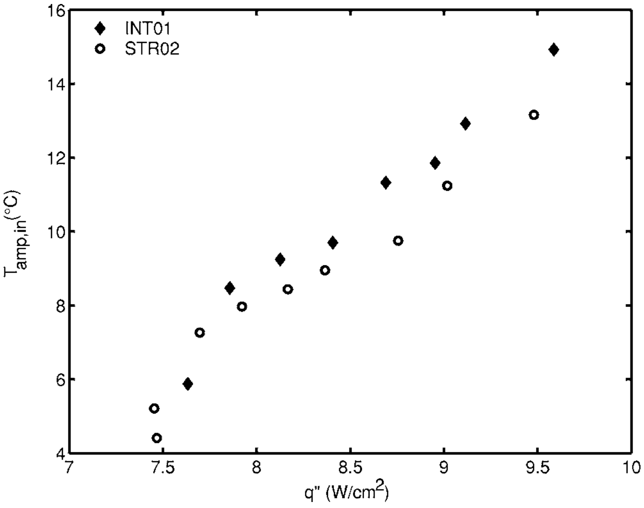

Fig. 12 Inlet temperature oscillation amplitude versus power, $T_{\text{in}}=70°\text{C}$ for different heat sinks at $Q_{\text{vol}}=30$ ml/min

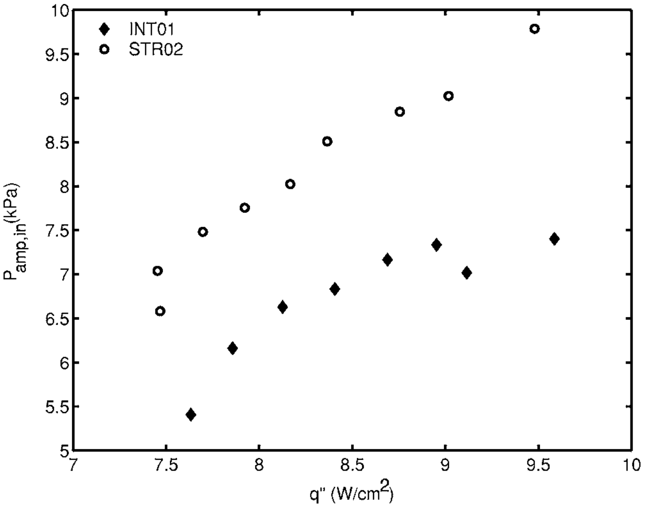

Fig. 14 Inlet pressure oscillation amplitude versus power, $T_{\text{in}}=70°\text{C}$ for different heat sinks at $Q_{\text{vol}}=30$ ml/min

the data and includes the 95% confidence intervals based on the standard deviation. The boiling number exponent shows that f^* is inversely proportional to the heat flux, and hence a decreasing frequency with an increasing heat flux will be obtained. Moreover, the magnitude of the subcooling number exponent is more than double that of the boiling number, suggesting a stronger dependency of the oscillation frequency on the subcooling compared to heat flux.

Figures 12–14 show the variation in the peak to peak amplitude of various sensor signals with increasing heat flux. In all cases (P_{in}, T_{in}, T_{out}), the amplitude increases with increasing heat flux. Fluctuations in the inlet temperature are likely due to flow reversals traveling as far upstream as the inlet plenum chamber. Such observations have been described in some recent studies [19–23]. Comparing the inlet pressure amplitude for heat sinks STR02 and INT01 in Fig. 14, we observe a consistently lower amplitude for INT01. However, looking at the inlet and outlet temperatures, the behavior is opposite, whereby STR02 has a lower amplitude than INT01. Further, the difference in the amplitude is only 1–2°C at the inlet, whereas it is as high as 10°C at the outlet. Such a large variation, if translated to the wall temperature, could be extremely detrimental and will be investigated in future work.

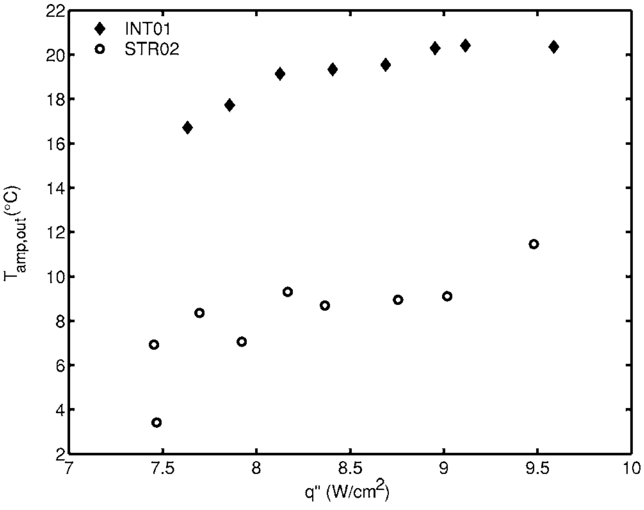

Fig. 13 Outlet temperature oscillation amplitude versus power, $T_{\text{in}}=70°\text{C}$ for different heat sinks at $Q_{\text{vol}}=30$ ml/min

Figure 15 shows the variation of the inlet pressure amplitude for the STR02 heat sink at different flow rates and inlet temperatures. With increased flow rate, the amplitude of the pressure fluctuations increases, but this is also related to the boiling onset and instabilities occurring at a higher heat flux. With decreased inlet temperature, the pressure amplitudes are higher. Overall, the pressure amplitude correlates relatively well with the heat flux, showing an increasing trend. To provide a more universal representation in nondimensional form, the pressure may be nondimensionalized with the liquid density and the inlet velocity, assuming an all liquid flow at entry. This may then be set similar to the frequency case as a function of the boiling number, subcooling number, and Weber number. The following correlation with the fluid properties calculated at saturation conditions at exit was obtained:

$$P^* = \frac{P_{\text{amp}}}{\dfrac{G^2}{\rho_f}} = C_6 \text{Bo}^{C_7} N_{\text{sub}}^{C_8}\, \text{We}_D^{C_9} \tag{6}$$

with the coefficients determined as $C_6=17.600$, $C_7=1.016$, $C_8=0.714$, and $C_9=-0.588$, or in dimensional form as

$$P_{\text{amp}} = 17.600\frac{G^2}{\rho_f}\left(\frac{q''}{Gh_{fg}}\right)^{1.016}\left[\frac{Cp(T_{\text{sat}}-T_{\text{in}})}{h_{fg}}\cdot\frac{\rho_f-\rho_g}{\rho_g}\right]^{0.714} \times\left(\frac{G^2D_h}{\sigma\rho_f}\right)^{-0.588} \tag{7}$$

The correlation fits the data well with a standard deviation of 8.4%. Figure 15(*b*) compares the fit with the experimental points and shows the 95% confidence intervals based on the standard deviation.

The outlet temperature amplitude for the STR02 heat sink for various flow rates and inlet temperatures is presented in Fig. 16(*a*) as a function of the heat flux. In general, the temperature amplitude increases with increasing power, as mentioned previously. The data have been correlated as a nondimensional temperature utilizing the saturation temperature (in kelvin) and set once again as a function of the boiling number and subcooling number. Fluid properties have been calculated at an exit saturation temperature of 373 K, as was done previously. From this, the following is obtained:

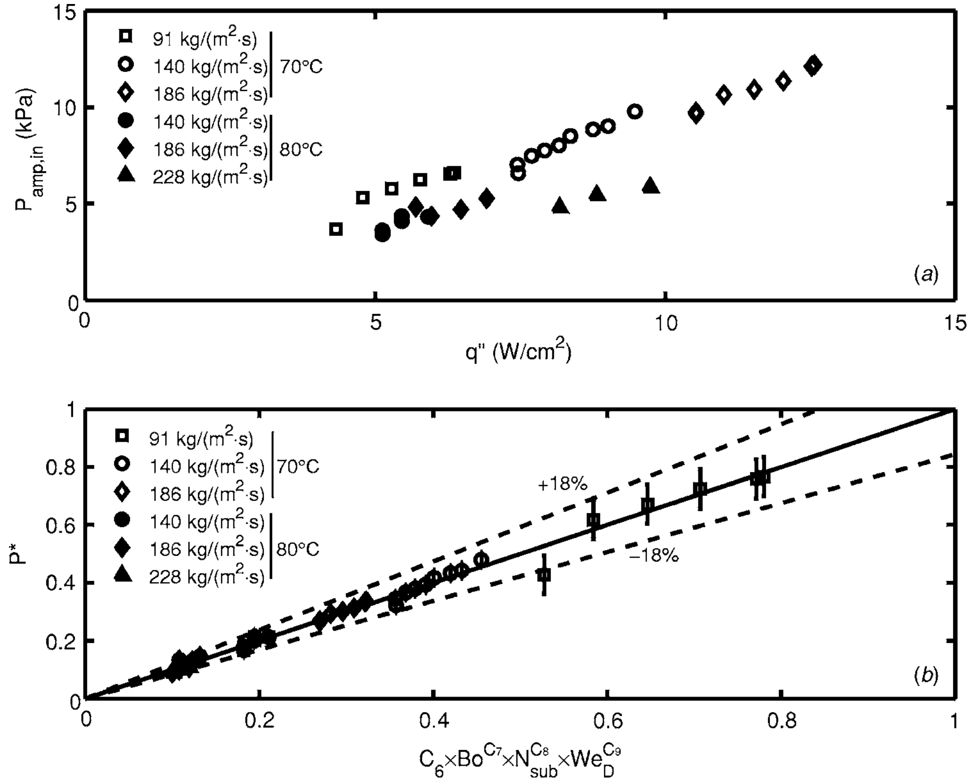

Fig. 15 Inlet pressure oscillation amplitude versus power for STR02 at different flow rates and inlet temperatures

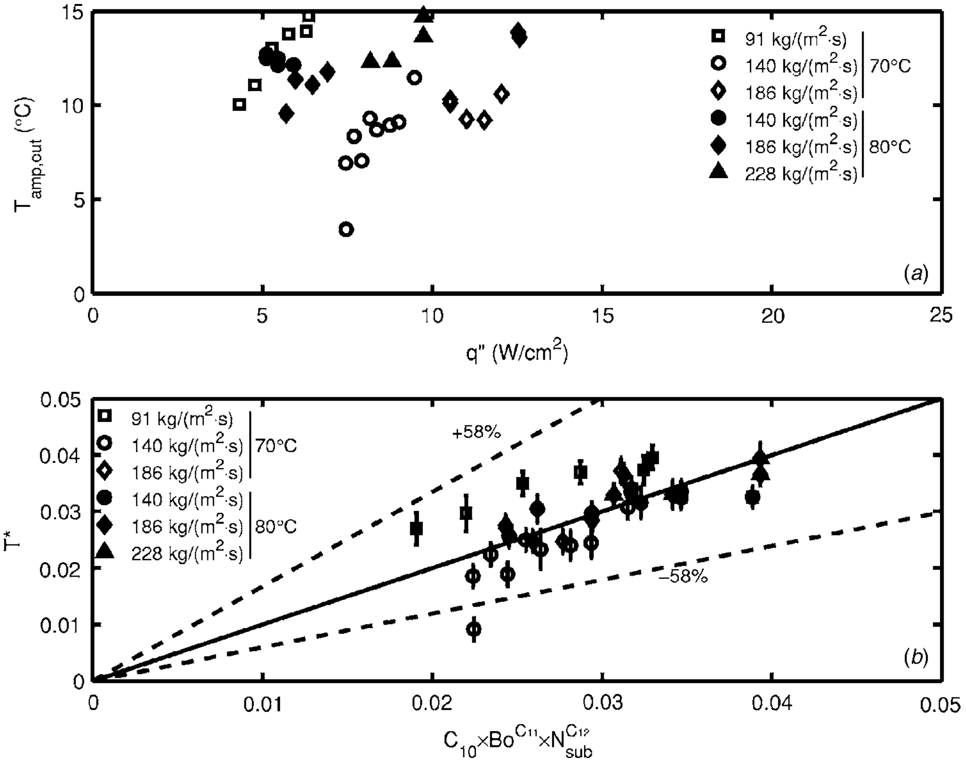

Fig. 16 Outlet temperature oscillation amplitude versus power for STR02 at different flow rates and inlet temperatures

$$T^* = \frac{T_{\text{amp}}}{T_{\text{sat}}} = C_{10}\text{Bo}^{C_{11}}N_{\text{sub}}^{C_{12}} \tag{8}$$

with the coefficients determined as $C_{10}=5.493\times 10^7$, $C_{11}=1.421$, and $C_{12}=-2.169$, or in dimensional form as

$$T_{\text{amp}} = 5.493 \times 10^7 \times T_{\text{sat}}\left(\frac{q''}{Gh_{fg}}\right)^{1.421}\left[\frac{Cp(T_{\text{sat}}-T_{\text{in}})}{h_{fg}}\frac{\rho_f-\rho_g}{\rho_g}\right]^{-2.169} \text{ (in kelvin)} \tag{9}$$

Although there is a large degree of scatter, the correlation (Eq. (8)) fits the data with a standard deviation of 25.5%. Figure 16(*b*) compares the correlation fit with the experimental data and shows the 95% confidence intervals based on the standard deviation. The exponents show that increasing the boiling number and, hence, the heat flux will increase the inlet temperature amplitude, whereas an increased subcooling will have a decreased amplitude.

Although flow visualization was not performed, some conclusions on the type of oscillations may be obtained when compared with other recent findings. The frequency and amplitude data by Hetsroni et al. [20] show trends similar to the present ones, in that the frequency decreases while the amplitude increases with increasing heat flux. Additionally, these authors were able to track the period of oscillations of flow patterns in individual channels. The period of oscillation of the system versus an individual channel from their work has been calculated to range from 5 to 15 times. For the present data the period of oscillation for the system ranged from 1.5 s to 10 s compared to the liquid particle travel time, which was estimated to range from 0.06 s to 0.16 s, for a flow rate of 20–50 ml/min. This ratio of the system's oscillation period to the particle travel time is on the order of ten times and is similar to the range of the data by Hetsroni et al. [20]. These qualitative and quantitative similarities lead to the conclusion that the present oscillation phenomena are EBOs, as described by Hetsroni et al. [19,20] and as also observed by some other researchers [21–23].

A note on the correlations presented follows. According to Yadigaroglu and Bergles [31], density wave oscillation characteristics are governed by the combination of a variety of auxiliary phenomena. These include the heat capacity of the walls, the saturation enthalpy's dependency on the system pressure, the gas phase compressibility, the variation in heat transfer, and the relative velocity between the phases. Although these auxiliary phenomena have been described for density wave oscillations, we expect them to also have some significance during EBOs. The correlations presented are then considered applicable to parallel silicon wafer substrate microchannel systems flowing water with a system pressure of 1 atm and for low mass flux ranges.

Conclusions

Flow boiling oscillations pose a restriction on the realization of MEMS based two-phase flow heat sinks for thermal management in demanding applications for both terrestrial and extraterrestrial applications. This paper has presented the detailed flow characteristics of flow boiling instabilities in two different silicon microchannel heat sinks. One is a straight standard microchannel configuration, whereas the second contains cross-links between the channels. There were similarities in the characteristics of the flow boiling oscillations for both configurations, and these may be summarized as follows.

(i) Both configurations show a decreasing frequency of oscillation with increasing heat flux.
(ii) Flow oscillations for inlet temperature, outlet temperature, and inlet pressure are at the same frequency.
(iii) In both configurations, the peak to peak amplitude for the oscillations increased with increasing heat flux.

The qualitative and quantitative characteristics of these oscillations are similar to the EBOs described in recent literature.

Instability data were presented at two different inlet temperatures and a range of flow rates for the straight standard heat sink. The data showed that with increasing flow rate, the frequency of oscillations increased, whereas with decreasing inlet temperature, the oscillation frequency increased. The frequency and amplitude characteristics of these oscillations for the standard heat sink at two different inlet temperatures have been correlated with the boiling number, the subcooling number, and the weber number. These correlations provide an intuitive means of interpreting the frequency and amplitude characteristics as a function of flow rate, inlet subcooling, and heat flux, combined with a quantitative measure of their relation.

The oscillations had relatively large amplitudes, which—if translated to the wall temperature—could have detrimental effects on the electronic chip being cooled. To the authors' knowledge, this is the first presentation of the influence of cross-links on two-phase flow oscillations in a microchannel system. Future work will investigate further the underlying mechanism of these oscillations and the influence of various cross-link configurations under similar conditions.

Nomenclature

A_{heated} = three-wall heated area
A_{plan} = plan area of channels, m^2 ($3.5\ \text{cm}^2$)
Bo = Boiling number (q''/Gh_{fg})
$C_1 \cdots C_{12}$ = coefficients determined for correlations
Cp = specific heat, kJ/(kg °C)
D_h = hydraulic diameter, 4 × area/perimeter, m
d_{heated} = heated area hydraulic diameter, 4 × area/(2 × height + width), m
f = friction factor
f_ω = frequency, Hz
f^* = nondimensional frequency ($fL_{\text{chn}}/u_{\text{in}}$)
G = mass flux, $\text{kg}/(\text{m}^2\ \text{s})$
$\Delta h_{\text{sub,in}}$ = $Cp(T_{\text{sat}}-T_{\text{in}})$, kJ/kg
I = current, A
INT01 = cross-linked heat sink
k = minor pressure loss coefficients
L = length, m
N_{sub} = Subcooling number $[Cp(T_{\text{sat}}-T_{\text{in}})/h_{fg}][\rho_f-\rho_g/\rho_g]$
P^* = nondimensional inlet pressure amplitude ($P_{\text{amp}}/G^2/\rho_f$)
Q_{vol} = volumetric flow rate, m^3/s
q'' = heat flux, W/m^2
Re = Reynolds number, with respect to the tube inner diameter
STR02 = straight standard heat sink
T = temperature, °C
T^* = nondimensional temperature amplitude ($T_{\text{amp}}/T_{\text{sat}}$)
V = voltage, V
u = velocity, m/s
We_D = Weber number ($G^2D_h/\sigma\rho_f$)
We_L = Weber number ($G^2L_{\text{chn}}/\sigma\rho_f$)
x/D_h = streamwise coordinate
y/D_h = spanwise coordinate

Greek

γ = power ratio factor for heat flux calculation
ρ = density, kg/m^3
σ = surface tension, N/m

Subscripts

amp = peak to peak amplitude
chn = channel parameter

crit = critical heat flux
f = liquid phase
g = vapor phase
in = inlet condition
i = inner wall
out = outlet condition
sat = saturation conditions

References

[1] Jiang, L., Mikkelsen, J., Koo, J., Huber, D., Yao, S., Zhang, L., Zhou, P., Maveety, J. G., Prasher, R., Santiago, J. G., Kenny, T. W., and Goodson, K. E., 2002, "Closed-Loop Electroosmotic Microchannel Cooling System for VLSI Circuits," IEEE Trans. Compon. Packag. Technol., **25**(3), pp. 347–355.

[2] Paris, D. A., Birur, C. G., and Green, A. A., 2002, "Development of MEMS Microchannel Heat Sinks for Micro/Nano Spacecraft Thermal Control," *Proceedings of the International Mechanical Engineering Congress and Exposition* (IMECE), Paper No. IMECE2002–34293, November 17–22, New Orleans, LA.

[3] Tuckerman, D. B., and Pease, R. F. W., 1981, "High-Performance Heat Sinking for VLSI," IEEE Electron Device Lett., **2**(5), pp. 126–129.

[4] Colgan, E. G., Furman, B., Gaynes, M., Graham, W., Labianca, N., Magerlein, J. H., Polastre, R. J., Rothwell, M. B., Bezama, R. J., Choudhary, R., Marston, K., Toy, H., Wakil, J., Zitz, J., and Schmidt, R., 2005, "A Practical Implementation of Silicon Microchannel Coolers for High Power Chips," *21st Annual IEEE Semiconductor Thermal Measurement and Management Symposium*, March 15–17, San Jose, CA, IEEE, Piscataway, NJ, pp. 1–7.

[5] Kosar, A., and Peles, Y., 2006, "Thermal-Hydraulic Performance of MEMS-Based Pin Fin Heat Sink," ASME J. Heat Transfer, **128**(2), pp. 121–131.

[6] Peles, Y., Kosar, A., Mishra, C., Kuo, C., and Schneider, B., 2005, "Forced Convective Heat Transfer Across a Pin Fin Micro Heat Sink," Int. J. Heat Mass Transfer, **48**(17), pp. 3615–3627.

[7] Chen, Y., and Cheng, P., 2005, "An Experimental Investigation on the Thermal Efficiency of Fractal Tree-Like Microchannel Nets," Int. Commun. Heat Mass Transfer, **32**(7), pp. 931–938.

[8] Alharbi, A., Pence, D. V., and Cullion, R., 2004, "Thermal Characteristics of Microscale Fractal-Like Branching Channels," ASME J. Heat Transfer, **126**(5), pp. 744–752.

[9] Pence, D. V., 2002, "Reduced Pumping Power and Wall Temperature in Microchannel Heat Sinks With Fractal-Like Branching Channel Networks," Microscale Thermophys. Eng., **6**(4), pp. 319–330.

[10] Xu, J. L., Gan, Y. H., Zhang, D. C., and Li, X. H., 2005, "Microscale Heat Transfer Enhancement Using Thermal Boundary Layer Redeveloping Concept," Int. J. Heat Mass Transfer, **48**(9), pp. 1662–1674.

[11] Cho, E. S., Koo, J., Jiang, L., Prasher, R. S., Kim, M. S., Santiago, J. G., Kenny, T. W., and Goodson, K. E., 2003, "Experimental Study on Two-Phase Heat Transfer in Microchannel Heat Sinks With Hotspots," *Annual IEEE Semiconductor Thermal Measurement and Management Symposium*, March 11–13, San Jose, CA, IEEE, Piscataway, NJ, pp. 242–246.

[12] Jiang, L., Koo, J. M., Wang, E., Bari, A., Cho, E. S., Ong, W., Prasher, R. S., Maveety, J., Kim, M. S., Kenny, T. W., Santiago, J. G., and Goodson, K. E., 2002, "Cross-Linked Microchannels for VLSI Hotspot Cooling," *Proceedings of the ASME International Mechanical Engineering Congress and Exposition*, Paper No. IMECE2002-39238, November 17–22, New Orleans, LA, pp. 13–17.

[13] Kosar, A., Kuo, C., and Peles, Y., 2006, "Suppression of Boiling Flow Oscillations in Parallel Microchannels by Inlet Restrictors," ASME J. Heat Transfer, **128**(3), pp. 251–260.

[14] Kandlikar, S. G., Kuan, W. K., Willistein, D. A., and Borelli, J., 2006, "Stabilization of Flow Boiling in Microchannels Using Pressure Drop Elements and Fabricated Nucleation Sites," ASME J. Heat Transfer, **128**(4), pp. 389–396.

[15] Bergles, A. E., 1981, "Instabilities in Two-Phase Systems," *Two-Phase Flow and Heat Transfer in the Power and Process Industries*, Hemisphere, Washington, DC, pp. 383–411.

[16] Kakac, S., and Veziroglu, T. N., 1982, "A Review of Two-Phase Instabilities," *NATO Advanced Research Workshop on the Advances in Two-Phase Flow and Heat Transfer, Fundamentals and Applications*, Martinus Nijhoff, The Hague, The Netherlands, Vol. II, pp. 383–411.

[17] Wu, H. Y., and Cheng, P., 2004, "Boiling Instability in Parallel Silicon Microchannels at Different Heat Flux," Int. J. Heat Mass Transfer, **47**(17–18), pp. 3631–3641.

[18] Xu, J., Zhou, J., and Gan, Y., 2005, "Static and Dynamic Flow Instability of a Parallel Microchannel Heat Sink at High Heat Fluxes," Energy Convers. Manage., **46**(2), pp. 313–334.

[19] Hetsroni, G., Mosyak, A., Pogrebnyak, E., and Segal, Z., 2005, "Explosive Boiling of Water in Parallel Micro-Channels," Int. J. Multiphase Flow, **31**(4), pp. 371–392.

[20] Hetsroni, G., Mosyak, A., Pogrebnyak, E., and Segal, Z., 2006, "Periodic Boiling in Parallel Micro-Channels at Low Vapor Quality," Int. J. Multiphase Flow, **32**(10–11), pp. 1141–1159.

[21] Steinke, M. E., and Kandlikar, S. G., 2004, "An Experimental Investigation of Flow Boiling Characteristics of Water in Parallel Microchannels," ASME J. Heat Transfer, **126**(4), pp. 518–526.

[22] Balasubramanian, P., and Kandlikar, S. G., 2005, "Experimental Study of Flow Patterns, Pressure Drop, and Flow Instabilities in Parallel Rectangular Minichannels," Heat Transfer Eng., **26**(3), pp. 20–27.

[23] Qu, W., and Mudawar, I., 2004, "Measurement and Correlation of Critical Heat Flux in Two-Phase Micro-Channel Heat Sinks," Int. J. Heat Mass Transfer, **47**(10–11), pp. 2045–2059.

[24] Muwanga, R., and Hassan, I., 2006, "Local Heat Transfer Measurements in Microchannels Using Liquid Crystal Thermography: Methodology Development and Validation," ASME J. Heat Transfer, **128**(7), pp. 617–626.

[25] Munson, B. R., Young, D. F., and Okiishi, T. H., 2002, *Fundamentals of Fluid Mechanics*, 4th ed., Wiley, New York, pp. 480–489.

[26] Kays, W. M., and London, A. L., 1964, *Compact Heat Exchangers*, McGraw-Hill, New York, pp. 32–33.

[27] Kline, J., and McClintock, F. A., 1953, "Describing Uncertainties in Single-Sample Experiments," Mech. Eng. (Am. Soc. Mech. Eng.), **75**(1), pp. 3–8.

[28] Shah, R. K., and London, A. L., 1978, "Laminar Flow Forced Convection in Ducts," *Advances in Heat Transfer*, Academic, New York.

[29] Steinke, M. E., and Kandlikar, S. G., 2004, "Control and Effect of Dissolved Air in Water During Flow Boiling in Microchannels," Int. J. Heat Mass Transfer, **47**(8–9), pp. 1925–1935.

[30] Chen, T., and Garimella, S. V., 2006, "Effects of Dissolved Air on Subcooled Flow Boiling of a Dielectric Coolant in a Microchannel Heat Sink," J. Electron. Packag., **128**(4), pp. 398–404.

[31] Yadigaroglu, G., and Bergles, A. E., 1972, "Fundamental and Higher-Mode Density-Wave Oscillations in Two-Phase Flow," Trans. ASME, Ser. C: J. Heat Transfer, **94**(2), pp. 189–195.

Internal Condensing Flows inside a Vertical Pipe: Experimental/Computational Investigations of the Effects of Specified and Unspecified (Free) Conditions at Exit

A. Narain[1]
Fellow ASME
e-mail: narain@mtu.edu

J. H. Kurita

M. Kivisalu

A. Siemionko

S. Kulkarni

T. W. Ng

N. Kim

L. Phan

Department of Mechanical Engineering-Engineering Mechanics,
Michigan Technological University,
Houghton, MI 49931

Reported experimental and computational results confirm that both the flow features and heat-transfer rates inside a condenser depend on the specification of inlet, wall, and exit conditions. The results show that the commonly occurring condensing flows' special sensitivity to changes in exit conditions (i.e., changes in exit pressure) arises from the ease with which these changes alter the vapor flow field in the interior. When, at a fixed steady mass flow rate, the exit pressure is changed from one steady value to another, the changes required of the interior vapor flow toward achieving a new steady duct flow are such that they do not demand a removal of the new exit pressure imposition back to the original steady value—as is the case for incompressible single phase duct flows with an original and "required" exit pressure. Instead, new steady flows may be achieved through appropriate changes in the vapor/liquid interfacial configurations and associated changes in interfacial mass, heat-transfer rates (both local and overall), and other flow variables. This special feature of these flows has been investigated here for the commonly occurring large heat sink situations, for which the condensing surface temperature (not heat flux) remains approximately the same for any given set of inlet conditions while the exit-condition changes. In this paper's context of flows of a pure vapor that experience film condensation on the inside walls of a vertical tube, the reported results provide an important quantitative and qualitative understanding and support an exit-condition-based categorization of the flows. Experimental results and selected relevant computational results that are presented here reinforce the fact that there exist multiple steady solutions (with different heat-transfer rates) for multiple steady prescriptions of the exit condition—even though the other boundary conditions do not change. However, for some situations that do not fix any specific value for the exit condition (say, exit pressure) but allow the flow the freedom to choose any exit pressure value within a certain range, experiments confirm the computational results that, given enough time, there typically exists, under normal gravity conditions, a self-selected "natural" steady flow with a natural exit condition. This happens if the vapor flow is seeking (or is attracted to) a specific exit condition and the conditions downstream of the condenser allow the vapor flow a range of exit conditions that includes the specific natural exit condition of choice. However, for some unspecified exit-condition cases involving partial condensation, even if computations predict that a natural exit-condition choice exists, the experimental arrangement employed here does not allow the flow to approach its steady natural exit-condition value. Instead, it only allows oscillatory exit conditions leading to an oscillatory flow. For the reported experiments, these oscillatory pressures are induced and imposed by the instabilities in the system components downstream of the condenser.
[DOI: 10.1115/1.2755063]

Keywords: film condensation, phase-change heat transfer, two-phase flows, interfacial waves

1 Introduction and Background

This paper outlines a fundamental and novel experimental investigation of effects of exit conditions on internal condensing flows. Reported experimental results confirm the existing computational results [1–3] that both the flow features and heat-transfer rates inside a condenser are sensitive to exit conditions and therefore depend on the specification of inlet, wall (particularly condensing surface temperature), and exit conditions. The condensing surface temperature (not heat flux) is assumed to be known (and fixed) or knowable (through consideration of the appropriate conjugate problem). This is true because, geneally, heat is removed from the condensing flow through a wall and put in a large heat sink, which may be a steady coolant flow in contact with the other

---

[1] Corresponding author.

Contributed by the Heat Transfer Division of ASME for publication in the JOURNAL OF HEAT TRANSFER. Manuscript received October 18, 2005; final manuscript received February 10, 2007. Review conducted by Ramendra P. Roy. Paper presented at the 2005 ASME International Mechanical Engineering Congress (IMECE2005), Orlando, FL, November 5, 2005.

side of the wall surface or a suitabe arrangement of thermoelectric coolers. This paper identifies and establishes a multiplicity of steady/quasisteady solutions—and/or oscillatory flows—under different conditions at the exit. Experiments support the existing simulation results [1–3] that have already shown, among other results, the presence of different steady/quasisteady solutions for different steady specifications of the exit condition. The condenser exit condition (for partial as well as full condensation (FC)) is specified by the exit pressure. For partial (incomplete) condensation flows, the specification of the exit pressure is equivalent (see Fig. 6 in Ref. [1]) to the specification of the exit vapor quality, i.e., the ratio of the vapor mass flow rate at the exit to the inlet mass flow rate (see simulation results from Refs. [1–3]). The computational simulations [1–3] for the gravity driven partial condensation cases (such as flows inside a vertical tube) also predict that for a certain set of inlet and wall conditions, even if the exit condition is not specified and a suitable range of exit conditions is available for the flow to choose from, the flow seeks and attains a specific "natural" exit condition (in Narain et al. [1], this situation is also termed natural unspecified steady exit condition due to the presence of an "attractor," i.e., an "attracting" solution). Unfortunately, many planned system designs incorporate a condenser and assume that the condenser will *always* attain a steady flow even if no exit conditions are specified. This is not generally true. The attainment of natural steady flows under unspecified exit conditions occurs more readily (over a larger parameter zone) for gravity driven condensate flows as opposed to shear driven flows (see Ref. [3]). The reported experimental results for gravity driven partial condensation cases under unspecified exit conditions support the computational results—both qualitatively and quantitatively. However, a steady natural exit condition may or may not exist depending on whether or not a steady attractor exists (e.g., as shown in Ref. [3], it does not exist for most slow inlet flow rates in horizontal or zero gravity conditions), and even if an attractor does exist, its realization depends on whether the attracting natural exit-condition value falls within the range of the available steady choices at the exit. In the absence of an *active* specification of a steady exit condition, the available range of steady exit conditions is determined by the components downstream of the condenser as well as the specific nature of the hardware used in the design of the rest of the system (or flow loop). Furthermore, because of the small pressure drops (see Ref. [3] or experimental runs reported here), when a steady natural exit condition is achieved under unspecified conditions or when the specified exit condition is not too far from this natural steady exit value, typically, vapor flows are close to incompressible.

The fact that for partial condensation flows, one can achieve quite different values of average heat-transfer coeffiecients under different realizations of quasisteady flows that correspond to different specifications of exit vapor quality (or pressure) is not surprising—as this follows from a simple overall energy balance. In the context of *boundary value* problems for internal condensing flows, what is new is that our computational and experimental results unequivocally show that the commonly occurring condensing flows are very sensitive to the nature of exit conditions as well as to the changes in exit conditions (due to changes in exit pressure). This sensitivity arises from the ease with which these changes alter the vapor flow field in the interior. Therefore, when only the exit condition is changed from one steady value to another, the changes required for the interior vapor flow toward attaining a new steady flow are such that they do not demand a removal of the new exit pressure imposition—as is the case for incompressible single phase duct flows with only one allowed exit pressure. Instead, for condensing flows, new steady flows are achieved for new exit conditions through appropriate changes in the vapor/liquid interfacial configurations and associated changes in interfacial mass, heat-transfer rates (both local and overall), and other flow variables.

The vertical in-tube internal condensing flows—partial or complete (full)—are investigated here for a downflow configuration. Though numerous in-tube condensation experiments have been done, most of the well-known in-tube vertical downflow experiments done by Goodykoontz and Dorsch [4,5], Carpenter [6], etc., either limited themselves to sufficiently fast flow portions of the duct that do not significantly depend on exit conditions or operated under a particular (natural or otherwise) set of exit conditions (that gets specified or remains unspecified depending on the employed experimental setup). Therefore, results may vary from one experimental system to another. In addition to our group's very early (see Yu [7]) and subsequent [1,2] computational findings on the importance of exit conditions for internal condensing flows, experimental findings of Rabas and Arman [8] also indicated the significance of exit conditions through their observation that the presence or absence of valves at the exit affected some of their in-tube vertical downflow results. Rabas and Arman [8] also pointed out an important fact that in the annular regime, even for a complete condensation vertically downward flow inside a tube (for which, at exit, the condensate is collected in a vapor plenum), the condensing flow is usually annular not only all the way up to the point of FC but also downstream of this point up to the exit; that is, a continuous liquid phase never fills the entire tube. This means that the flow remains annular (or, at most, has a few liquid bridges that encapsulate vapor bubbles) with zero interfacial mass and heat transfer in the segment downstream of the point of FC. Additionally, Rabas and Arman [8] pointed out that in the case of a horizontal in-tube complete condensation for a tube of a certain diameter, the flow regime near downstream and upstream locations of the point of complete condensation (where vapor flow rate is nearly zero) varies from gravity dominated stratified to gravity dominated plug annular—depending on whether the inlet mass flow rate is above or below a certain critical value.

Furthermore, several experimental results and analyses [9–17] indicate that, for certain physical arrangements leading to a specific class of inlet and outlet conditions, transients and instabilities are expected in complete condensation horizontal in-tube internal condensing flows. Since these experiments and the corresponding modeling techniques in the literature [9–17] limit themselves to a particular type of inlet and exit conditions, they do not directly apply to the presence or absence of observed transients and instabilities in other feasible categories of exit-condition specifications.

Since an understanding of internal condensing flows' transients is not entirely possible in the context of traditional two-phase flow analyses based on homogeneous, separated, or drift-flux formulations (see Wallis [18]), more sophisticated averaged model equations of varying degrees of complexities (see, e.g., Lahey and Drew [19]) have been proposed. Despite this, appropriate drift-flux and/or virtual mass force based analyses of Liao et al. [20], Liao and Wang [21], and Wang [22] reported some ability to capture transients in certain internal condensing flows of the type studied by Wedekind and Bhatt [9,12], Wedekind et al. [15], Bhatt and Wedekind [10,11], Bhatt et al. [13], Kobus et al. [16], Kobus [17], Boyer et al. [14], etc. Furthermore, Liao et al. [20] and Liao and Wang [21] also reported difficulties in employing the multidimensional, four field, two-fluid model of Lahey and Drew [19] toward modeling transients and instabilities that occur in internal condensing flow cases of their concern. Other analyses by Wedekind and Bhatt [9,12], Bhatt and Wedekind [10,11], Kobus et al. [16], and Kobus [17] employed the system mean void fraction (SMVF) model, which allows one to ignore the momentum balance equation. These simpler integral analyses have been somewhat successful in capturing some features of the experimentally observed transients and flow oscillations that have been reported [9,11] for certain in-tube horizontal condensing flows involving a complete condensation. In these cases, a fixed pressure tank (plenum) at a sufficiently high pressure pushes vapor through an inlet valve to the inlet of a horizontal condensing section where the

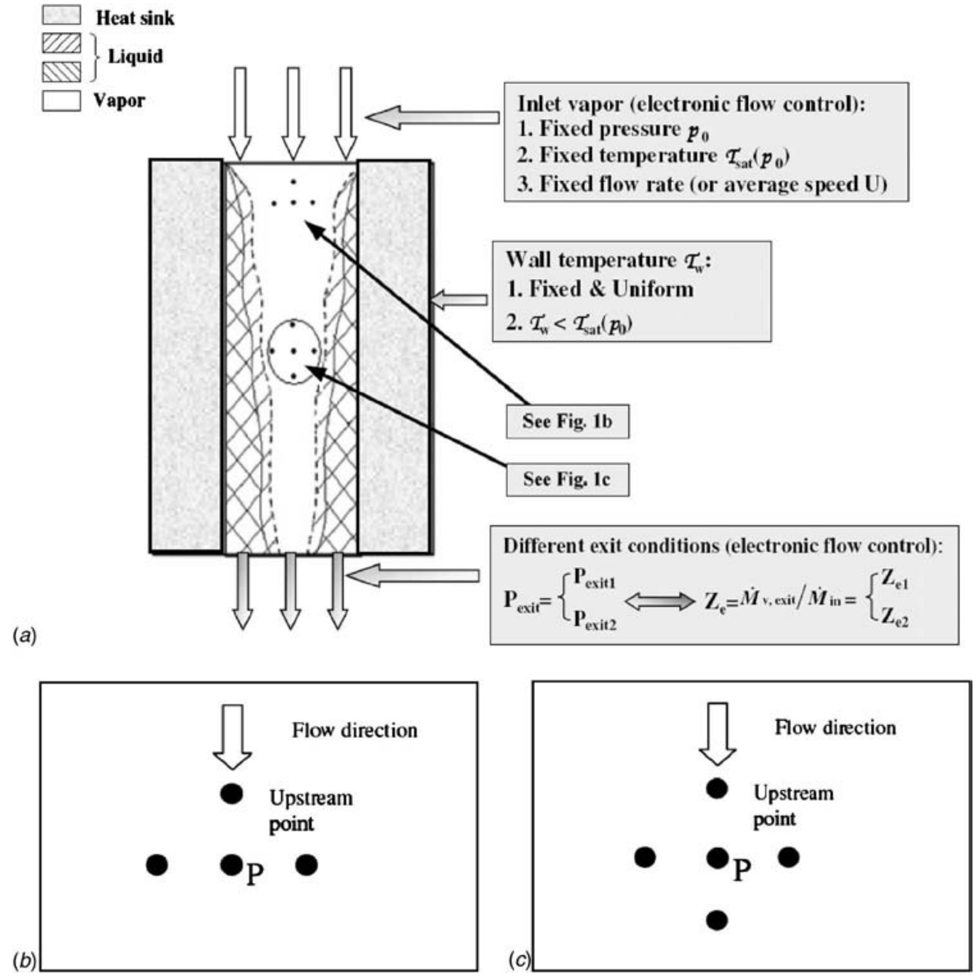

Fig. 1 The schematic for the flow through test-section and exit-condition issues

vapor is fully condensed, and then the liquid flows out of the condenser exit, through an exit valve, to a tank (plenum) at a fixed low pressure.

To understand exit condition issues more clearly, the approach taken here has been to seek an experimental confirmation of key results obtained from employing our fundamental and nearly exact computational technique [1–3] to obtain steady and unsteady simulations for laminar-vapor/laminar-condensate *initial* boundary value problems—in the limited context of separated, quasi-steady annular condensing flows. Therefore, simulation results [1–3] have been central to the development and interpretation of the reported experiments. Fundamentally, the internal condensing flows' exit condition sensitivity arises from governing equations being "elliptic" or requiring "two-way" space coordinates in the flow direction (i.e., the flow variable at a point P is influenced by both upstream and downstream local neighbors, as shown in Fig. 1(c)). However, this sensitivity to exit conditions, or a two-way behavior, is special and does not result from the typical "ellipticity" associated with slow flows and flow reversals (which are, as described in Patankar [23], associated with the changes in the sign of local Peclet numbers). In fact, it is found (for simulations in Refs. [1–3]) that even when vapor and liquid flows are unidirectional (or "one way" or "parabolic") due to local Peclet numbers (which appear in local discretization equations for the velocity components—see Eqs. (5.61)–(5.64) in Ref. [23]) being very large (even greater than 50,000 in both x and y directions), the flows exhibit an elliptic or a two-way behavior leading to a sensitivity to exit conditions. This special sensitivity to exit condition is due to the two-way behavior of the vapor pressure fields (reflected, in the context of our computational methodology [1], by the two-way behavior of the pressure equations given by Eqs. (6.30) and (6.31) in Ref. [23]). These equations for condensing flows are such that the coefficients that multiply the pressures at the locally upstream and downstream neighbors are comparable even for large Peclet numbers (see pressure discretization equations for the SIMPLER procedure in Patankar [23]). Due to this, effects of changes in the exit pressure are felt by the entire vapor flow field.

In the literature, condensing flows have been classified according to whether they are shear dominated or gravity dominated, internal or external, smooth or wavy at the interface, laminar or turbulent in the two phases, etc. It is proposed here that one can only make sense of the vast literature on internal condensing flows if they are also classified in different categories based on the conditions imposed at the inlet and the exit. The following three categories (termed categories I–III) proposed here cover most cases of interest.

(1) Category I (with complete or incomplete condensation under *specified* exit conditions)

- Prescribed or known values of the total inlet vapor mass flow rate $\dot{M}_{in}$ (kg/s), inlet vapor quality, inlet pressure p_{in}, and inlet temperature at all times t. Without loss of generality, one can focus on an all vapor flow (an inlet vapor quality of unity) at the inlet with known values of the total inlet (all vapor) mass flow rate $\dot{M}_{in}$ (kg/s), inlet pressure p_{in}, and inlet temperature (at saturation temperature $T_{sat}(p_{in})$ or at some superheat) at all times t. This

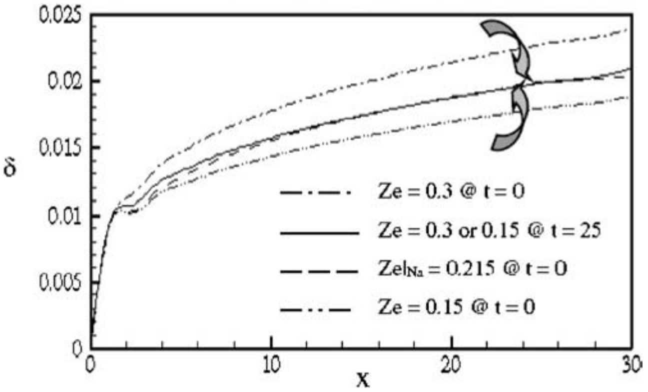

Fig. 2 For tube flow situations specified as in Phan et al. [3] (see their Table 1 and Fig. 2), the figure depicts three steady film thickness profiles for three different exit conditions. The figure also indicates time trends for two sets of $\delta(x,t)$ predictions for $t>0$; one curve starts at $Z_e=0.3$ at $t=0$, and tends, as $t\to\infty$, to the solution for $Z_{e|\mathrm{Na}}=0.215$. The other curve starts at $Z_e=0.15$ at $t=0$ and tends, as $t\to\infty$, to the same $Z_{e|\mathrm{Na}}=0.215$ solution.

means the prescription could be steady or unsteady.

- Prescribed method of cooling leading to known wall temperatures $T_w(x,t)<T_{\mathrm{sat}}(p_{\mathrm{in}})$ for all x locations over which film condensation occurs. Typical wall temperature conditions of interest are steady, but unsteady conditions are relevant to start-up and shutdown.
- Specified or known exit condition. For example, for steady exit conditions, the exit pressure p_e, is a const, which is equivalent, for partial condensation cases, to setting exit mass quality $Z_e\equiv\dot{M}_{\mathrm{vapor@exit}}$ (kg/s)/ $\dot{M}_{\mathrm{in}}$ (kg/s), an appropriate constant where $\dot{M}_{\mathrm{vapor@exit}}$ (kg/s) is the vapor mass flow rate at the exit at time t.

For category I partial condensation flows with steady specified exit conditions, the computational simulations in Fig. 2 (with the flow conditions being the same as specified in Fig. 2 and Table 1 of Phan et al. [3]) show three different steady solutions for three different specified vapor qualities Z_e at the exit (viz., $Z_{e1}=0.15$, $Z_{e2}=0.215$, and $Z_{e3}=0.3$). Some of the experimental investigations of Garimella et al. [24,25] are for flows in this category with an inlet quality $Z_i(<1)$ and an exit quality Z_e specified at values incrementally smaller than Z_i.

(2) Category II (with complete or incomplete condensation under unspecified exit conditions)

- Prescribed or known values of the inlet mass flow rate $\dot{M}_{\mathrm{in}}$ (kg/s), inlet pressure p_{in}, and inlet temperature (at saturation temperature $T_{\mathrm{sat}}(p_{\mathrm{in}})$ or at some superheat) at all times t. Without loss of generality, it is assumed that the flow is all vapor at the inlet.
- Prescribed or known wall temperatures $T_w(x,t)<T_{\mathrm{sat}}(p_{\mathrm{in}})$ for all x locations over which film condensation occurs.
- Exit condition is not specified. However, due to some system hardware limitations and constraints, if only a range of exit pressure conditions is available to the condenser, we still call a flow in the interior of this range a category II flow. A flow at the boundary of this range is, however, not a category II flow.

For category II flows, in Fig. 2, it is computationally shown that if exit vapor quality specification constraints at $Z_{e1}=0.15$ or $Z_{e3}=0.3$ are removed at some time ($t=0$)—and subsequently ($t>0$), one does not specify any exit condition or any restrictions on the available range of exit conditions—this particular incomplete condensation flow seeks its own long-term and steady natural exit vapor quality $Z_{e|\mathrm{Na}}=Z_{e2}=0.215$ and an associated steady natural flow under incompressible vapor conditions. Other simulations for shear driven flows [3] and some experiments reported here under conditions of restricted available range of exit conditions show that the flow in this category may or may not be able to select a quasi-steady flow with a natural exit condition. This is because the unspecified exit condition (category II) cases, though commonly used in applications, are essentially "ill posed" boundary value problems. Therefore, the existence of steady solutions is at the mercy of other factors (such as whether or not an attracting steady solution exists and, if it does, whether or not downstream conditions are conducive to the attainment of this attracting solution). When natural attractors are weak or do not exist, as is the case for some horizontal and zero gravity condensing flows [3], the concave bowl analogy schematic for attractors given in Fig. 9 of Narain et al. [1] needs to be replaced by a bowl shape, which is either weakly concave or completely flat. Furthermore, for category II flows, in Phan et al. [3], the existence of an attractor leading to a long-term steady exit condition was termed differently—it was called a long-term one-way or parabolic behavior. Similarly, non-existence of an attractor (typically an indicator of flows that lie outside the annular regime and are more complex in the sense that they exhibit certain degrees of randomness or indeterminacy) was termed differently in Ref. [3]—it was called a long-term two-way or elliptic behavior.

(3) Category III (complete condensation involving special specified conditions at the inlet and the exit)

Although, technically, this is a special subcategory of fully condensing category I flows, it is listed separately because it typically requires a different experimental setup and hardware facilities. This class has been extensively investigated in the literature [9–16] for oscillatory and unsteady condensing flows.

- In this case, there is a constant pressure reservoir, with a high pressure $p_{\text{tank-in}}$, that feeds the vapor flow $\dot{M}_{\mathrm{in}}(t)$ (at inlet pressure p_{in}, temperature $T_{V\text{-in}}$, and density $\rho_{V\text{-in}}$) into the test section through an inlet valve (with valve coefficient k_i). This requires the inlet pressure p_{in} to satisfy at any time t,

$$p_{\mathrm{in}}\cong p_{\text{tank-in}}-k_i\frac{\dot{M}_{\mathrm{in}}(t)^2}{\rho_{V-\mathrm{in}}}$$

- Also, there is a constant pressure exit tank, with a typically lower pressure $p_{\text{tank-exit}}$ to which the condensate flows through an exit valve of valve coefficient k_e. The exit valve handles an *all liquid* flow because this case is only for complete condensation flows. At the exit of the condenser, the liquid flow rate is $\dot{M}_{\mathrm{exit}}$ at any time t, and the liquid density is $\rho_{L\text{-exit}}$. This requires that the test-section exit pressure p_{exit} satisfy at any time t,

$$p_{\mathrm{exit}}\cong p_{\text{tank-exit}}+k_e\frac{\dot{M}_{\mathrm{exit}}(t)^2}{\rho_{L-\mathrm{exit}}}$$

- Prescribed or known *steady* wall temperatures $T_w(x)<T_{\mathrm{sat}}(p_{\mathrm{in}})$ for all x locations over which film condensation occurs.

The experimental and/or modeling analysis papers of Wedekind and Bhatt [9,12], Bhatt and Wedekind [10,11], Bhatt et al. [13], Kobus et al. [16], Kobus [17], Liao et al. [20], Liao and Wang [21], etc., focused on category III flows for a horizontal condenser.

The experiments and computations in this paper, however, focus only on category I and category II flows. As a result, the flow transients and system instabilities reported in this paper (see Sec. 5), as far as flows within the test section are concerned, are necessarily of different origin. However, at a system level, the experimentally observed flow oscillations' relationship to the better known [11,13] results for category III flows in the downstream auxiliary condenser is also discussed here.

The experimental runs reported here largely involve laminar condensate and turbulent vapor situations with possible vapor compressibility effects for some of the category I flows. Despite this, both qualitative and quantitative comparisons with simulation results based on the laminar-vapor/laminar-condensate methodology given in Refs. [1–3] are possible and are presented here for a feasible subset (within the boundaries for steady annular flows) of experimental runs. This comparison is possible because turbulent vapor often laminarizes in the vicinity of laminar condensate as the condensate is slow and remains laminar approximately up to $\mathrm{Re}_\delta \leq 1800$ (see film Reynolds number Re_δ defined in Phan and Narain [26]). Also, for gravity driven condensate cases considered here, the existence of turbulent vapor zones in the core and entrance zone of the condenser has only a minor second order impact on pressure variations in the condenser. The far field vapor turbulence often tends not to be a significant player because the overall flow features (local and average heat-transfer coefficients) are dominated by interfacial mass and heat-transfer rates, which are dominated by the typically laminar nature of the gravity driven condensate flow and the associated laminar nature of vapor flow in the vicinity of the interface. Because of the above, all experimental runs reported here for partial (or incomplete) condensation cases involving laminar condensate show a very good *qualitative* agreement with the simulations as far as the existence of multiple steady solutions for multiple steady exit conditions (category I) and a natural steady solution for the unspecified exit-condition cases (category II) are concerned. The agreement with simulations, with regard to exit vapor quality and general consistency with overall heat-transfer rates, are also *quantitatively* very good for experimental runs that fit the annular flow assumption for the simulations. It should be noted that, additionally, the accuracy of the employed simulation methodology [1–3] and its quantitative compatibility with a different set of experimental runs (Lu and Suryanarayana [27]) for shear dominated category II flows have also been established (see Ref. [2]). Furthermore, computational results for internal condensing flows are obtained from a simulation tool that has a proven ability (see Phan and Narain [26]) to make good quantitative predictions for wave phenomena and their effects on heat-transfer rates for the benchmark classical problem of Nusselt [28].

The experimental investigation of annular complete condensation cases reported here is less complete and limited to natural steady flows in category II. Computational simulations for these cases are also limited because the flow often condenses completely somewhere within the test section, and the current simulation technique can only approximately cover the zone from the inlet to the point of FC. The simulation tool has not yet been enhanced to automatically identify and handle the exit-pressure-sensitive two-phase annular flow zone—with neglegible interfacial mass and heat-transfer rates—that occurs between the point of FC (whose location itself depends on the exit pressure) and the exit. The reported experiments cover natural FC cases under unspecified exit conditions. The hardware needed to investigate a complete condensation under specified exit conditions (category I flows as well as category III flows) is being developed as an important ongoing area of research.

Thus far, nonexistent accounting of exit-condition categories and exit-condition sensitivities of internal condensing flows is perhaps one of the reasons for the large uncertainities and deficiencies noted by Palen et al. [29] with regard to the poor usefulness of quantitative information available from existing correlations for heat-transfer coefficients.

The experiments reported here involve a single pure working fluid (viz., FC-72 by 3M Corp.) and focus on inlet mass flow rates that correspond to inlet vapor Reynolds numbers in the range of 10,000–40,000 and vapor to wall temperature differences of 3–60°C (i.e., $0 \leq \mathrm{Ja} \leq 0.4$).

2 Experimental Facility

The condenser section, which is of the type shown in Fig. 1(*a*), is typically a part of a closed flow loop. The flow loop, which maintains a steady input pressure (p_{in}) and mass flow rate ($\dot{M}_{\mathrm{in}}$) at the inlet, while maintaining a prescribed steady (and nearly uniform) condensing surface temperature, may be designed to provide different categories of exit conditions. Exit-condition specifications for category I and category II flows defined earlier in Sec. 1 are realized through flow arrangements indicated in Figs. 3 and 4 respectively.

A 0–500 W evaporator/boiler in Figs. 3 and 4 is used to evaporate the working fluid (FC-72). The vapor mass flow rate out of the evaporator, $\dot{M}_{\mathrm{in}}$, is fed into the test section. This mass flow rate is measured by a Coriolis flow meter F_1, and during transients, this value can be controlled by the pneumatically actuated control valve V_1 (shown connected to F_1 in Figs. 3 and 4). Under steady conditions though, the value of $\dot{M}_{\mathrm{in}}$ gets approximately fixed by the net steady electrical heating rate for the evaporator. This is due to the restriction imposed by the evaporator energy balance, viz., $\dot{M}_{\mathrm{in}} \approx \dot{Q}_b / h_{\mathrm{fg}}(p_b)$. Here, $\dot{Q}_b$ is the net heat rate into the evaporator, p_b is the steady evaporator pressure, $T_b \approx T_{\mathrm{sat}}(p_b)$ is the steady evaporator temperature (which is nearly equal to the saturation temperature of the fluid at pressure p_b), and h_{fg} is the heat of vaporization at the liquid/vapor surface pressure p_b in the evaporator. Toward reduction in start-up time to steady state in the evaporator, the liquid flowing in the evaporator is warmed up (between points P′ and B′ in Figs. 3 and 4), so its temperature is nearly equal to the evaporator temperature $T_b \approx T_{\mathrm{sat}}(p_b)$.

The test section is a 0.8 m long, vertical stainless steel (316 SS) tube with 6.6 mm inner diameter and 12.7 mm outer diameter. At the entrance of the test section, the inlet vapor temperature is denoted as $T_{V\text{-in}}$, the inlet pressure is denoted as p_{in}, and the inlet vapor is kept slightly superheated (2–10°C superheat obtained by heating a relevant portion of connecting tubes by a rope heater). A suitable thermocouple and an absolute pressure transducer measure the temperature $T_{V\text{-in}}$ and pressure p_{in}, respectively, of the vapor at the inlet. The dynamic view from an axial boroscope, mounted at the top of the test section shown in Fig. 5, is used to visualize and ascertain the nature of the flow in the first half of the test section. However, because of sharpness and contrast improvements that are needed for better quality images, snapshots and video clips of the flows are not currently included in this paper. They are, however, expected to be available in the near future. We are currently able to use these views to ascertain whether or not annular film condensation begins near the indicated "start of condensation" point in Fig. 5 and to ascertain (and then to ensure) the dryness of the vapor up to the test-section inlet.

The test section (see Fig. 5) is suitably instrumented with various sensors (thermocouples, pressure transducers, etc.). For future work, there is an arrangement to obtain local film thickness data through integration of our recently invented nonintrusive film thickness sensors that utilize the principle of fluorescence and fiber-optic technology (see Ng [30]) and are able to measure the

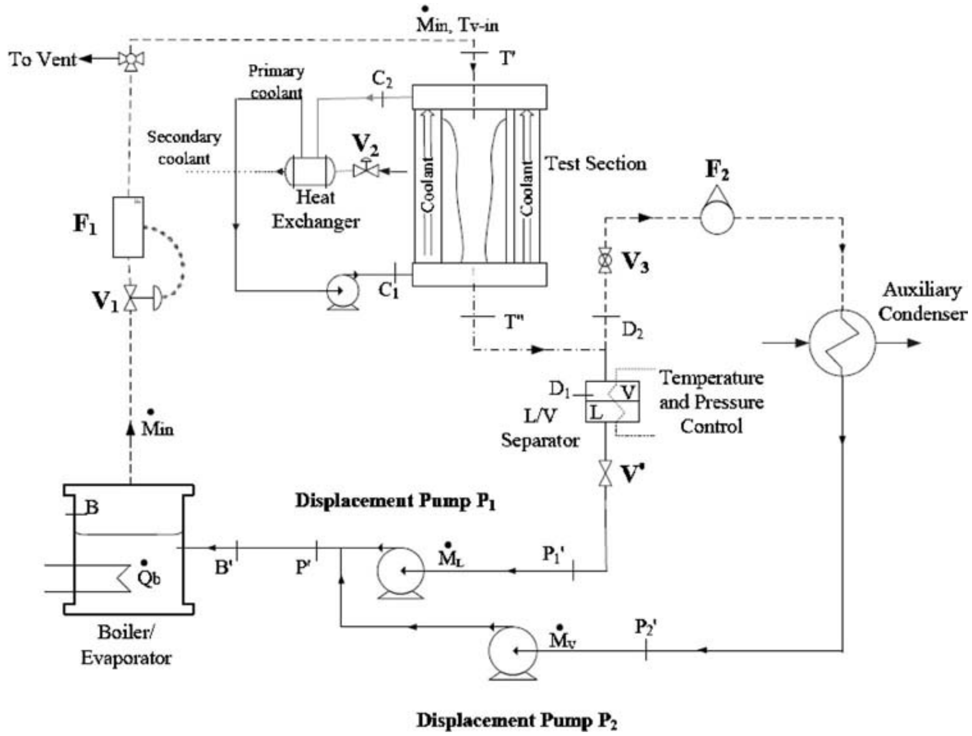

Fig. 3 The schematic of the flow loop for achieving specified exit-condition category I flows for partial condensation cases

"local" time-varying thickness of dynamic liquid films. The technique used for mounting all the sensors is described in detail in Narain et al. [31] and Siemionko [32].

The test section in Fig. 5(*b*) (not shown to scale relative to the outer tube in Fig. 5(*a*)) is centrally aligned in the hollow space of a larger diameter stainless steel (314 SS) tube. This outer tube has an inner diameter of 23.62 mm and an outer diameter of 25.40 mm. The test-section tube is cooled by the flow of cooler water in the annulus formed by the outer surface of the test-section tube and the inner surface of the outer tube. As shown in Figs. 3 and 4, the flow of coolant water is arranged by a separate closed loop consisting of the shell side of the shell-in-tube heat exchanger (the flow is on shell side) and a pump. A separate loop, not shown in Figs. 3 and 4, assures a secondary coolant (cold-water) flow at a steady constant temperature and a steady flow rate through the tube side of the heat exchanger in Figs. 3 and 4. This

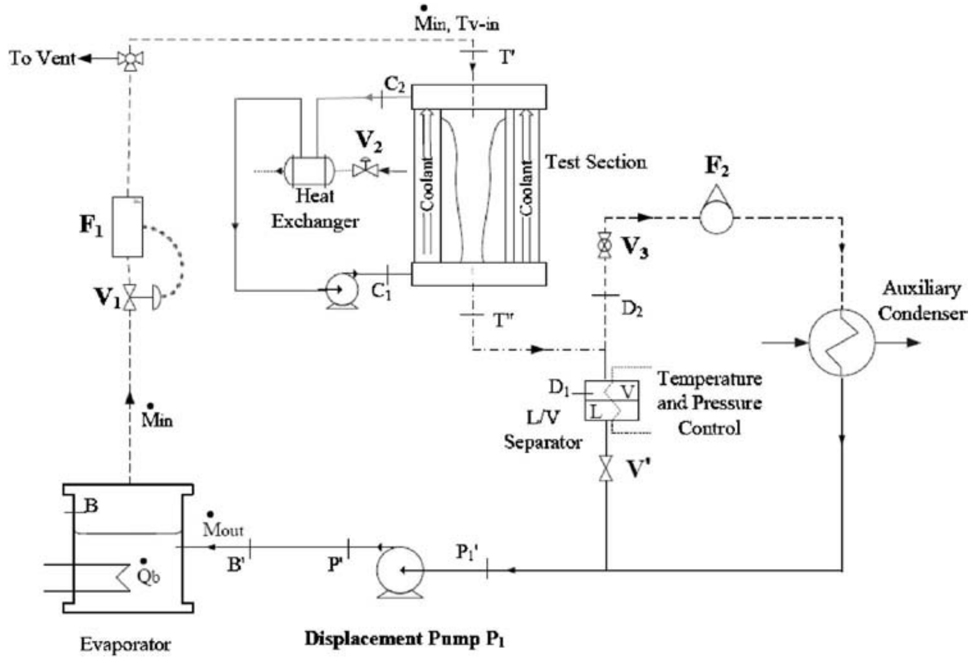

Fig. 4 The schematic of the flow loop for achieving unspecified exit-condition category II flows for partial or FC cases

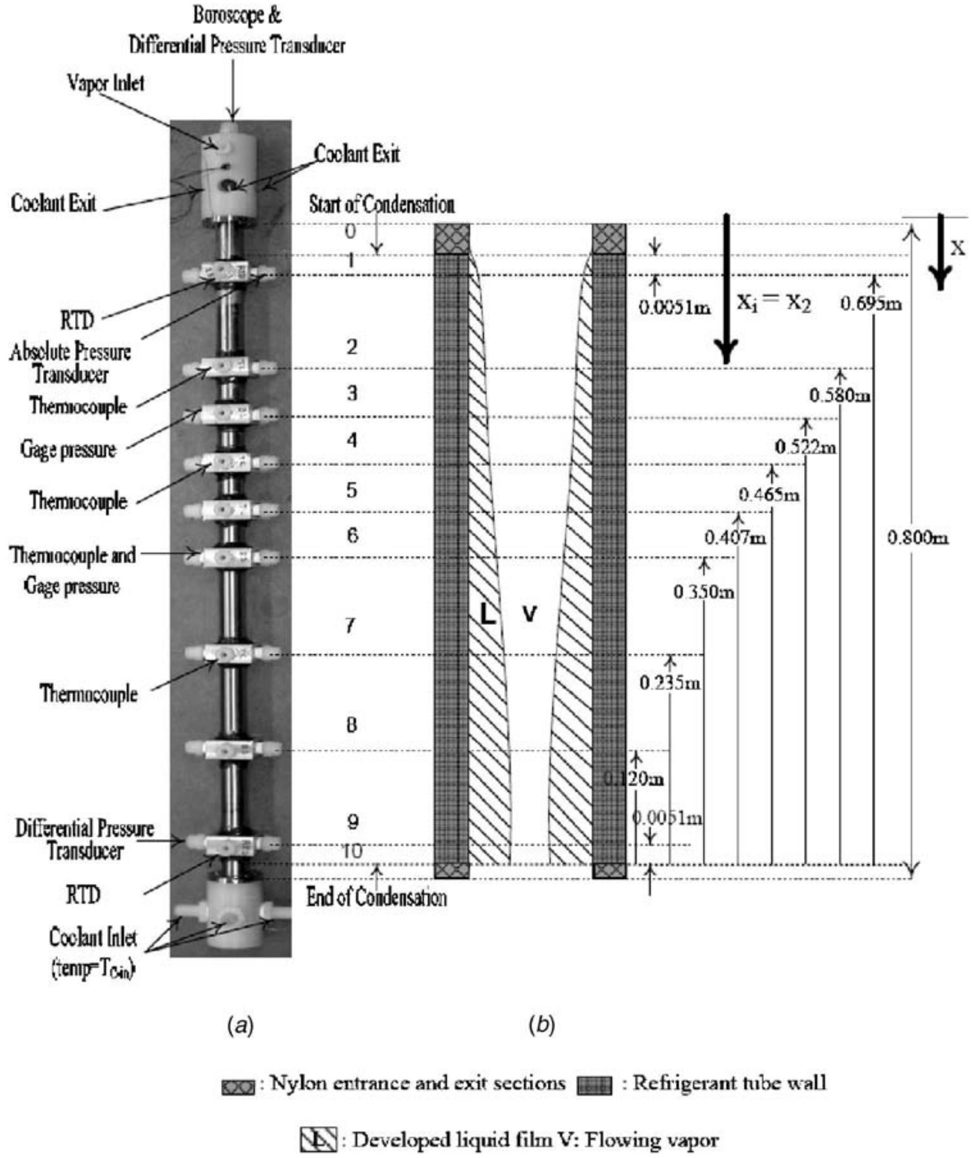

Fig. 5 (***a***) **The photograph of condenser test section.** (***b***) **The test-section schematic (diameters in** (***a***) **and** (***b***) **are not to the same scale). The condensing surface covers the zone** $x_0 \leqslant x \leqslant x_{10}$.

loop (see Kurita [33]) replaces the open drain water loop used in the preliminary experiments. This loop has two chillers in series (one for a coarse control and one for a finer control of temperature), and this provides for a good control of the steady value of temperature $T_{C\text{-in}}$ (marked in Fig. 5(*a*)) at the coolant inlet location in Figs. 3 and 4. This, in turn, enables the repetition of experimental runs regardless of seasonal variations in drain water temperature.

Resistance temperature detectors (RTDs) and type-T thermocouples measure temperatures at different locations of the test section (see Fig. 5) and at other flow loop locations marked by points B, B′, T′, C_1, C_2, D_1, D_2, P_1', P_2', and P′ in Figs. 3 and 4. A barometer measures outside atmospheric pressures. Flow meters at locations marked F_1 (Coriolis meter that directly measures mass flow rate), F_2 (a volume flow rate measuring rotameter), P_1 (volume flow rate meter imbedded in pump P_1), and P_2 (volume flow rate meter imbedded in pump P_2) yield mass flow rates through those locations. Absolute pressure transducers measure pressures at the test-section inlet (location 1 in Fig. 5) and at locations B and D_2 in Figs. 3 and 4. Differential pressure transducers measure pressure differences in the test section (in Fig. 5(*a*), this is between locations 1 and 9, location 3 and outside atmosphere, and location 6 and outside atmosphere). Two electronically controllable displacement pumps, P_1 and P_2 (see Figs. 3 and 4), can pump liquid FC-72 at a steady or unsteady specification of volume or mass flow rates. A pneumatically controlled valve V_1 is used, as needed, to control mass flow rate through F_1. Most of the details of the employed data acquisition system are explained in Narain et al. [31] and Siemonko [32].

For convenience, the system in Figs. 3 and 4 is broken into the following subsystems. (i) Subsystem A is the portion of the flow loop between points P′ and T′ (this portion contains the flow into the evaporator, the evaporator, the flow meter F_1, valve V_1, and the tubing leading the flow into the test section). (ii) Subsystem B is the portion of the flow loop between points T′ and T″ (this portion consists of the test section). (iii) Subsystem C is the portion of the flow loop between points T″ and P′ (this portion consists of the *L*/*V* separator, the two branches of the flow in the liquid line and the auxiliary-condenser line, and the pump or pumps). (iv) Subsystem D is the portion that consists of a primary coolant loop (shown in Figs. 3 and 4 and a secondary coolant loop (not shown here but shown in Kurita [33]). The subsystems A–D defined above are not marked in Figs. 3 and 4, but the definitions introduced here are necessary for later discussions of the experimental results.

Additional details of this experimental facility (in fact, of a similar earlier version), data acquisition, and LABVIEW 7.1 based data processing and instrument control strategies are available in Siemonko [32].

3 Experimental Procedure

Here, we describe the procedure for investigating partial and FC cases under different exit conditions. Note that results from different exit conditions are to be compared for approximately the same inlet mass flow rate $\dot{M}_{\text{in}}$, inlet pressure p_{in}, and temperature difference $\overline{\Delta T}=T_{\text{sat}}(p_{\text{in}})-\bar{T}_w$, where $\bar{T}_w$ is the mean condensing surface temperature. Pure vapor may be allowed to enter the test section with a superheat of 2–10°C. The purging process (see Ref. [32]) ensures that the vapor flowing in the test section is pure over the duration of the experimental run and that noncondensable air in the flow loop has zero to insignificant presence. Note that vapor Jakob numbers $\text{Ja}|_V$ $(\equiv C_p|_V \Delta T_{\text{sup}}/h_{\text{fg}}(p_{\text{in}}))$, where $C_p|_V$ is the specific heat of the vapor and $h_{\text{fg}}(p_{\text{in}})$ is the heat of vaporization at pressure p_{in}, represent the ratio of sensible cooling of vapor to heat of vaporization. Since these numbers are very small $(<1.0\times 10^{-5})$ in comparison to liquid Jakob numbers Ja $(\equiv C_p|_L \cdot \overline{\Delta T}/h_{\text{fg}}(p_{\text{in}}))$, where $C_p|_L$ is the specific heat of the liquid condensate), vapor temperature can be effectively modeled as a steady constant equal to the inlet saturation temperature. The steadiness of $\dot{M}_{\text{in}}$ primarily depends on the constancy of heat supply to the evaporator (which is easily achieved by constant electric heating at a known wattage) and the eventual approximate steadiness of the evaporator pressure p_b. Even if the steady value of p_b changes somewhat for different start-ups, as long as the corresponding evaporator saturation temperature T_b changes negligibly, it is found that the remaining flow loop pressures relative to a single effective boiler pressure are the same for two independent repetitions of the same experimental run (i.e., same $\dot{M}_{\text{in}}$, $\overline{\Delta T}$, $\bar{T}_w$, and Z_e). This is true because all other pressures p are effectively characterized by their pressure differences, $p-p_b$, relative to this pressure p_b. Alternatively, a previously obtained steady value of p_b can be regained by bringing the new evaporator pressure back to roughly this same value by suitably switching the heater on and off under the same steady heating rate or by gradually venting the evaporator from a higher pressure to the desired earlier value of p_b. Both of the above described processes have been used to successfully assess the repeatability of a few representative experimental runs. With regard to constancy of water temperature $T_{C\text{-in}}$ at the coolant inlet for the test section (see Fig. 5) over time, achieving constancy of water temperature and its flow rate in the secondary coolant loop (not shown here) proved to be sufficient.

3.1 Specified Exit Conditions (Category I Flows)

3.1.1 Incomplete or Partial Condensation Flows. For an investigation of partial condensation flows through the test section that involve specified conditions (through a steady and specified exit vapor quality) at the exit, the arrangement in Fig. 3 is used. In this arrangement, the liquid at the exit flows out of the test section at a mass rate of $\dot{M}_L$, goes through the liquid/vapor (L/V) separator, and is pumped by pump P_1 back into the evaporator. Both pumps P_1 and P_2 (displacement pumps made by Masterflex) in Fig. 3 allow a digital control of flow rates. The vapor at the exit flows out of the test section at a mass flow rate of $\dot{M}_V$ and is measured through a volume and mass flow rate measuring rotameter F_2. This vapor then flows through an auxiliary condenser where the vapor is completely condensed into liquid, goes through pump P_2, and then, on its way to the evaporator, merges near point P' (see Fig. 3) with the liquid flowing out of pump P_1.

The control strategy, to achieve a specified steady flow with a prescribed exit vapor quality $(\dot{M}_V/\dot{M}_{\text{in}}\equiv Z_e)$ for a given inlet and wall conditions, is to initially hold valve V_1 open at a fixed level of opening while ensuring (as described in the first paragraph of this section) desired steady values of $\dot{M}_{\text{in}}$, p_b, and $\overline{\Delta T}$. Then, the exit vapor mass rate $\dot{M}_V$ through pump P_2 (or rotameter F_2) is held fixed at a value less than the inlet mass rate $\dot{M}_{\text{in}}$, while the exit liquid mass flow rate $\dot{M}_L$ is varied through pump P_1 at a value given by the tracking equation $\dot{M}_L|_{P_1}=\dot{M}_{\text{in}}-\dot{M}_V|_{\text{rotameter}}$.

As the flow through the evaporator becomes steady, $\dot{M}_{\text{in}}$ becomes steady, and, at that time, we may or may not need to hold this value actively fixed with the help of controllable valve V_1. At this stage, active control of valve V_1 does not achieve much, except that it eliminates some unwanted minuscule drifts in the inlet mass rates. For a given set of inlet $(\dot{M}_{\text{in}}, p_{\text{in}}, T_{V\text{-in}})$ and wall $(\bar{T}_w)$ conditions, different specified steady states are achieved by the above strategy for different values of $\dot{M}_L$. Experimentally achieved examples of specified exit category I partial condensation flows are discussed in the next section.

3.1.2 Complete or Full Condensation Flows. The experimental technique for prescribing different exit pressures in FC cases is important but has not yet been implemented. Typically, one would need to specify different pressures at the exit of the test section, at the L/V separator (see Figs. 3 and 4), which is downstream of the "point of FC." This requires active pressure control at the L/V separator. Fully condensing category I flows achieved in this fashion do, however, become equivalent to category III flows with fixed valve settings (k_i and k_e) introduced in the definition of category III flows. This is part of an ongoing research. Therefore, results for this important case are not reported here.

3.2 Unspecified Exit-Condition Cases (Category II Flows)

3.2.1 Natural Partial Condensation. For obtaining/investigating the existence of a "long-term" and steady natural exit condition for category II flows (under unspecified exit conditions) with all other conditions being kept the same as in a corresponding specified exit-condition case in category I, the flow is required to go through the test section and onwards under the arrangement shown in Fig. 4. Note that this arrangement has a single displacement pump as opposed to the two displacement pumps used in the arrangement of Fig. 3. The approach is to hold values of $\dot{M}_{\text{in}}$, p_b, and $\overline{\Delta T}$ nearly the same as in one of the specified category I cases while the pump P_1 in Fig. 4 is *controlled* such that the mass flow rate through it tracks the equation: $\dot{M}_L|_{P_1}=\dot{M}_{\text{in}}$. If the start-up and other conditions allow, a steady state flow is attained in which, by the exit, the inlet vapor mass flow rate is split, by a natural selection process, into a liquid condensate flow rate $\dot{M}_L|_{\text{Na}}$ and a vapor flow rate $\dot{M}_V|_{\text{Na}}$. Clearly, these values satisfy the equation $\dot{M}_{\text{in}}=\dot{M}_L|_{\text{Na}}+\dot{M}_V|_{\text{Na}}$. Experimentally achieved examples of unspecified exit category II partial condensation flows are discussed in the next section.

3.2.2 Complete or Full Condensation Flows With a Natural Steady State. For achieving FC flows in the test section, valve V_3 in Fig. 3 is shut and the arrangement in Fig. 3 is then used. Here, we choose the controlling temperature difference $\overline{\Delta T}=T_{\text{sat}}(p)-\bar{T}_w$ to become sufficiently large for a fixed inlet mass flow rate to ensure that one achieves, through the indicated procedures for the setup, a steady flow in Fig. 3 with a natural $\dot{M}_V=0$ (an approximate value obtained even if V_3 was to be left open).

Table 1 Experimentally measured data and some key calculated and computed variables for steady states achieved for category II (unspecified exit-condition) partial condensation flows

Run No	$M_{\rm in}$ (g/s)	M_V (g/s)	Z_e exp	Z_e comp	$\bar{T}_W$ (K)	$T_{\rm sat}$ (K)	$\overline{\Delta T}$ (K)	$p_{\rm in}$ (kPa)	p_{x6} (kPa)	$p_{T''}$ (kPa)	Δp (kPa)	$p_{\rm D2}$ (kPa)	ρ_2/ρ_1	μ_2/μ_2	G (kg/m^2 s)	Re	Ja	Pr$_1$	$\dot{Q}_{\rm out}$ (J/s)	$\bar{q}''$ (W/m^2)	$\bar{h}$ (W/m^2 K)
	±0.05	±0.04	±0.04		±1	±0.15	±1	±0.6	±0.6	±0.7	±0.05	±2	±0.0001	±0.0001	±1.5	±900	±0.02	±0.02	±5	±800	±80
1	1.44	0.48	0.33	0.33	320	331.49	11	107.3	109.3	106.5	−0.82	105	0.0085	0.0243	42.1	23,900	0.14	9.61	81	5200	453
2	1.76	1.08	0.62	0.57	317	325.23	8	87.0	86.4	88.0	−0.36	85	0.0070	0.0223	51.5	29,700	0.10	10.11	58	3700	450
3	1.54	0.69	0.44	0.36	323	335.55	12	122.6	116.6	116.1	−0.19	114	0.0097	0.0260	45.0	25,300	0.15	9.21	71	4500	387
4	1.29	0.49	0.38	0.38	320	329.64	10	101.0	102.4	100.8	−2.09	98	0.0081	0.0230	37.7	21,500	0.11	9.69	68	4300	476
5	1.70	0.83	0.51	0.52	324	332.55	9	111.0	112.5	111.0	−0.93	109	0.0089	0.0252	49.6	28,100	0.11	9.37	70	4400	508
6	1.17	0.47	0.40	0.39	320	332.64	13	111.3	NA[b]	111.3	−0.12	109	0.0088	0.0246	34.2	19,325	0.16	9.55	59	3700	298
7	1.31	0.49	0.37	0.37	321	330.85	10	105.0	106.8	104.5	−2.06	102	0.0084	0.0244	38.3	21,700	0.12	9.58	69	4400	462
8[a]	1.93	1.39	0.72	0.72	322	325.55	4	84.6	NA[b]	NA[b]	0.01	NA[b]	0.0071	0.0231	56.4	32,500	0.05	9.85	47	3000	742
9	1.59	1.11	0.69	0.63	328	334.25	6	113.0	NA[b]	NA[b]	NA[b]	NA[b]	0.0094	0.0265	46.5	26,200	0.08	9.07	40	2500	418
10	2.12	1.37	0.64	0.64	320	327.85	8	91.4	NA[b]	NA[b]	−0.10	NA[b]	0.0076	0.0234	62.0	35,500	0.10	9.83	64	4100	503
11	1.30	0.45	0.35	0.38	321	329.29	8	99.8	100.2	99.7	−1.62	97	0.0080	0.0240	38.0	21,700	0.10	9.70	72	4600	537

[a] The error values for this case were greater than the representative error values shown in the column headers due to small $\overline{\Delta T}$ and high relative error associated with its measurement.

[b] NA: The data were not available due to some equipment problem.

For the natural FC case, the valve V$_1$ in Fig. 3 is left open at a fixed opening and pump P$_1$ is controlled to always satisfy, in time, the relation $\dot{M}_L|_{P_1}=\dot{M}_{\rm in}$. If a steady state is achieved, this leads to a natural steady FC flow (i.e., as will be discussed later, if $X_{\rm FC} < L$ in Fig. 9). The word natural is also used here because the use of displacement pump P$_1$ in the arrangement downstream of the test section allows the test-section vapor flow to attain whatever pressure it desires by the test-section exit or by the point of FC. Because of experimental limitations in measuring $X_{\rm FC}$, at present, $X_{\rm FC} < L$ is assured only through a computational simulation. Also, note that because of the unspecified (free) exit condition, this way of achieving steady FC flows is expected to keep vapor density nearly uniform.

4 Experimental Results, Discussions, and Comparisons with Simulations

The column headers in Tables 1–3 indicate accuracies of the values of key *measured* variables obtained through flow loop instruments and sensors. Overall accuracy bounds for the reported calculated variables (such as $\bar{q}''$, $\bar{h}$, etc.) are also shown. The nondimensional numbers Re$_{\rm in}$, $x_e = L/D = 106$, Ja, ρ_2/ρ_1, and μ_2/μ_1 in Tables 1–3 define the flows, and they are defined in Refs. [1–3]. In Tables 1–3, the heat flow rate $\dot{Q}_{\rm out}$ and associated average heat-transfer coefficients $(\bar{h})$ are obtained through the relation $\dot{Q}_{\rm out} \approx \dot{M}_L h_{\rm fg} = \bar{h}(\pi DL)\overline{\Delta T}$. The inlet vapor mass flux G in Tables 1–3 is defined as $4\dot{M}_{\rm in}/(\pi D^2)$.

All (except the Coriolis meter F$_1$) of the instruments' accuracies for measured variables were established after their in-house calibrations with the help of suitable and reliable reference instruments of known resolution and appropriate reference physical conditions (temperature, flow rate, pressure, etc.). The accuracy of the Coriolis meter was established by the vendor support staff at the time of its installation. The error estimates for the calculated variables reported in Tables 1–3 were obtained by well-known standard procedures (see, e.g., Eqs. (3.27) and (3.28) in Ref. [34]). The accuracies of individual calculated variables in a column were taken into account to report maximum values of the errors in the column headers of Tables 1–3. All the individual values of errors were either less than or equal to these reported error values. The error definitions, associated error analyses, and calibration accuracies can be found in Narain et al. [31].

The experimental runs reported in the next section were taken after ensuring that (i) representative runs were repeatable, (ii) the mass flow rates for partial condensation cases added up to satisfy the mass balance, (iii) the overall energy balance for the test section was satisfied, i.e., $\dot{M}_{\rm in}h_{\rm fg} \approx \dot{M}_w C_{\rm pw} \cdot \Delta T_w$, where for a representative FC case, ΔT_w is the rise in the water temperature in the annulus surrounding the test-section, and (iv) various data were reasonable (based on simulation estimates) and consistent with one another. The experimentally obtained partial condensation cases in category II (unspecified exit) are listed in Table 1 with all the essential details, including exit vapor quality Z_e (fourth column) and its value obtained from simulations (fifth column). The corresponding partial condensation flow cases under category I (specified exit-condition cases) are listed in Table 2. The experimental data for category II FC cases are reported in Table 3. The values for pressure drop across the test section were found to be negative for almost all of the cases that have been reported here, indicating that pressure at the exit was greater than that at the inlet. This is because of the typical range of $\dot{M}_{\rm in}$ and $\overline{\Delta T}$ we have been operating in (0.5–2 g/s and 2–12°C, respectively). Further, the magnitude of experimental pressure rise was found to be higher than predictions obtained from the laminar-vapor/laminar-condensate simulation tool employed in this paper. The results and discussions for exit-condition categories I and II are described below, separately, for partial and FC flows.

Table 2 Experimentally measured data and some key calculated variables for steady states achieved for category I (specified exit-condition) partial condensation flows

Run No	M_{in} (g/s)	M_V (g/s)	Z_e exp	$\bar{T}_W$ (K)	T_{sat} (K)	$\overline{\Delta T}$ (K)	p_{in} (kPa)	p_{x6} (kPa)	$p_{T''}$ (kPa)	Δp (kPa)	p_{D2} (kPa)	ρ_2/ρ_1	μ_2/μ_2	G (kg/m^2 s)	Re	Ja	Pr_1	$\dot{Q}_{\text{out}}$ (J/s)	$\bar{p}'$ (W/m^2)	$\bar{h}$ (W/m^2 K)
	±0.05	±0.04	±0.04	±1	±0.15	±1	±0.6	±0.6	±0.7	±0.05	±2	±0.0001	±0.0001	±1.5	±900	±0.02	±0.02	±5	±800	±80
1	1.44	0.52	0.36	320	331.91	12	108.8	110.9	108.0	−1.82	106	0.0087	0.0244	42.1	23,800	0.15	9.59	78	4900	416
2	1.31	0.50	0.38	320	329.16	9	99.4	100.3	99.5	−0.43	98	0.0080	0.0238	38.4	21,900	0.11	9.72	69	4400	505
3	1.34	0.59	0.44	320	328.55	9	97.4	98.4	97.3	−0.32	96	0.0078	0.0236	39.1	22,400	0.10	9.76	64	4100	491
4[a]	1.80	0.64	0.36	323	330.53	8	103.9	105.9	104.4	−0.59	103	0.0083	0.0246	52.6	29,900	0.09	9.50	97	6200	851
5[a]	1.92	1.00	0.52	323	329.64	7	101.0	103.3	101.7	−0.40	100	0.0081	0.0244	56.1	32,000	0.08	9.55	78	4900	771
6	1.20	0.00	0.00	320	332.23	12	110.5	113.2	110.5	−0.80	108	0.0088	0.0245	35.0	19,800	0.16	9.57	101	6400	514
7	1.22	0.44	0.35	320	331.71	12	108.0	110.6	108.0	−0.62	106	0.0086	0.0243	36.6	20,200	0.15	9.62	66	4200	351
8[a]	1.93	1.15	0.60	322	325.21	3	87.15	NA[b]	NA[b]	−1.30	NA[b]	0.0071	0.0231	56.4	32,600	0.04	9.87	67	4300	1174
9	1.61	1.14	0.70	322	332.57	11	111.4	104.6	107.0	−0.87	103	0.0089	0.0250	47.1	26,630	0.13	9.46	35	2200	212
10	1.67	1.37	0.82	322	331.45	10	105.8	98.6	100.8	−0.74	97	0.0085	0.0245	49.0	27,800	0.12	9.57	16	1000	108
11	1.81	1.02	0.56	317	331.48	14	106.8	102.1	NA[b]	−0.58	99	0.0085	0.0237	52.9	30,000	0.18	9.80	54	3400	236
12	1.66	0.60	0.36	318	333.15	15	113.5	108.6	NA[b]	−1.46	106	0.0090	0.0243	48.5	27,400	0.20	9.66	88	5600	363
13	1.71	0.49	0.28	316	331.14	15	108.0	107.9	108.1	−2.10	105	0.0085	0.0237	50.1	28,400	0.19	9.81	103	6500	441
14	1.30	0.65	0.50	320	326.34	6	90.5	92.1	90.5	−1.15	88	0.0073	0.0230	38.0	21,800	0.08	9.90	56	3500	545
15	1.29	0.55	0.43	321	331.63	11	107.7	113.2	110.1	−1.60	107	0.0086	0.0245	37.7	21,400	0.14	9.57	62	3900	366
16	1.31	0.76	0.58	321	331.07	11	105.8	109.1	105.8	−0.95	104	0.0084	0.0243	38.3	21,700	0.13	9.62	46	2900	279
17	1.14	0.88	0.77	319	326.73	8	91.6	92.8	91.9	−0.14	90.4	0.0074	0.0230	33.5	19,300	0.09	9.92	22	1400	186
18	1.39	0.64	0.46	318	329.01	11	98.9	101.3	98.4	−0.65	97.1	0.0079	0.0234	40.6	23,200	0.14	9.85	64	4100	377

[a] The error values for this case were greater than the representative error values shown in the column headers due to $\overline{\Delta T}$ and high relative error associated with its measurement.

[b] NA: The data were not available due to some equipment problem.

Table 3 Experimentally measured data and some key calculated variables for steady states achieved for category II (unspecified exit-condition) FC flows

Run No	M_{in} (g/s)	$\bar{T}_W$ (K)	T_{sat} (K)	$\overline{\Delta T}$ (K)	p_{in} (kPa)	p_{x6} (kPa)	$p_{T''}$ (kPa)	Δp (kPa)	p_{D2} (kPa)	ρ_2/ρ_1	μ_2/μ_1	G (kg/m^2 s)	Re	Ja	Pr_1	$\dot{Q}_{\text{out}}$ (J/s)	$\bar{q}''$ (W/m^2)	$\bar{h}$ (W/m^2 K)
	±0.05	±1	±0.15	±1	±0.6	±0.6	±0.7	±0.05	±2	±0.0001	±0.0001	±1.5	±800	±0.02	±0.02	±5	±500	±26
1	0.69	304	326.93	23	92.3	94.9	90.8	−1.13	89	0.0073	0.0207	20.2	11,600	0.28	10.74	59	3800	165
2	0.70	304	328.46	24	97.2	99.8	95.5	−1.54	94	0.0077	0.0210	20.4	11,700	0.30	10.65	60	3800	156
3	1.01	317	329.67	13	101.1	104.0	100.1	−0.57	99	0.0081	0.0234	29.7	17,000	0.16	9.87	86	5500	438
4	0.86	316	330.20	14	102.8	104.1	101.4	−3.05	99	0.0082	0.0234	25.1	14,300	0.17	9.88	73	4600	331
5	0.96	304	326.95	23	92.4	93.1	90.4	−0.62	89	0.0074	0.0208	28.1	16,000	0.28	10.72	82	5200	230
6	0.75	302	328.61	27	97.6	98.2	95.4	−3.01	92	0.0077	0.0207	22.0	12,500	0.33	10.79	64	4000	151
7	0.62	302	327.17	25	93.0	94.8	91.1	−2.41	89	0.0074	0.0204	18.1	10,400	0.31	10.86	53	3375	133
8	0.63	301	326.97	26	92.4	94.2	90.5	−0.54	90	0.0073	0.0203	18.4	10,600	0.39	10.90	54	3400	134
9	0.48	301	327.07	26	92.8	94.6	90.7	−1.18	90	0.0074	0.0209	14.0	8000	0.32	10.90	41	2600	102
10	0.78	305	341.13	36	146.0	NA[a]	NA[a]	−0.35	129	0.0116	0.0240	22.9	12,700	0.47	9.95	64	4100	112
11	0.97	316	343.27	27	155.8	NA[a]	NA[a]	−0.33	140	0.0127	0.0265	28.3	15,600	0.37	9.25	79	5000	180
12	0.87	300	343.11	43	155.0	NA[a]	NA[a]	−0.14	138	0.0125	0.0236	25.4	14,000	0.57	10.06	71	4500	104
13	0.80	306	342.02	36	150.0	NA[a]	NA[a]	−0.25	136	0.0120	0.0244	23.4	12,900	0.48	9.80	65	4200	115
14	0.80	322	340.69	19	144.1	135.7	140.4	−0.29	143	0.0115	0.0277	23.6	13,000	0.25	9.04	66	4200	228
15	0.99	324	342.32	18	151.4	NA[a]	152.3	−2.05	148	0.0123	0.0279	29.2	16,000	0.24	8.87	81	5200	283
16	1.59	306	333.56	27	115.0	110.5	109.3	−0.24	112	0.0090	0.0225	46.4	26,100	0.35	10.25	133	8400	309
17	0.76	324	337.82	14	131.7	125.7	126.3	−0.23	130	0.0105	0.0266	22.2	12,400	0.18	9.10	63	4000	289
18	1.30	312	331.98	19	109.4	111.4	108.5	−1.32	107	0.0087	0.0231	38	21,500	0.25	10.00	109	6900	350

[a] NA: The data were not available due to some equipment problem.

4.1 Partial Condensation Flows

4.1.1 Specified Exit-Condition (Category I) and Unspecified Exit-Condition (Category II) Cases. For partial condensation, Fig. 6(*a*) shows the attainment of two specified exit-condition case steady/quasisteady flows marked Specified-1 ($t_2 \leq t(\text{min}) \leq t_2 + 20$) and Specified-2 ($t_3 \leq t(\text{min}) \leq t_3 + 30$). The Specified-1 and Specified-2 cases correspond to run 1 and run 18, respectively, in Table 2. The results over time interval $t_4 \leq t(\text{min}) \leq t_4 + 20$ show the experiment's ability to approximately repeat the data for a case that is approximately the same as Specified-1 and is termed as Specified-1 Approx. Following the method described in Sec. 3, Figs. 6(*a*) and 6(*b*) also show, over the time interval $t_1 \leq t(\text{min}) \leq t_1 + 76$, the attainment of a corresponding natural steady exit condition and associated steady flow variables for an unspecified exit-condition (category II) case. This case corresponds to run 1 in Table 1. The Natural-1, Specified-1, and Specified-2 steady states (in Figs. 6(*a*)–6(*c*)) have the same values of $\dot{M}_{\text{in}} \approx 1.40 \pm 0.05$ g/s and $\overline{\Delta T} \approx 11 \pm 1\,^\circ\text{C}$ but different values of $\dot{M}_L$ and $\dot{M}_V$ that satisfy $\dot{M}_L|_1 + \dot{M}_V|_1 = \dot{M}_L|_2 + \dot{M}_V|_2 = \dot{M}_{\text{in}}$. The differences between the Specified-1 and Specified-2 cases are as follows: (i) they have different heat-transfer rates (since energy balance gives $\dot{Q}_{\text{out}} \approx \dot{M}_L h_{\text{fg}}$). The two cases have approximate heat-transfer rates of 78±4 W and 64±4 W and average heat-transfer coefficients of $416 \pm 40\ \text{W/m}^2\,\text{K}$ and $377 \pm 40\ \text{W/m}^2\,\text{K}$, respectively. (ii) The two cases also have different hydrodynamics, the signature of which is clear through corresponding computational simulations and through the difference between experimentally obtained mean values of Δp for the two cases (in Table 2 they are −1.82 kPa and −0.65 kPa, respectively). Furthermore, specified (category I) and unspecified (category II) flows have different dynamic responses to a disturbance (in Figs. 6(*a*)–6(*c*), a disturbance was induced by momentarily shutting or decreasing the opening in the valve V_1 shown in Figs. 3 and 4). The difference in dynamic response is seen by comparing Specified-2 and Natural-1 cases for the transient decay time τ_D associated with the exit vapor flow rate $\dot{M}_V$ in Fig. 6(*a*) or τ_D associated with Δp in Fig. 6(*b*). In Fig. 6(*a*), the rapid shutting or closing of valve V_1 caused the indicated responses in the $\dot{M}_{\text{in}}$ time history. For the Natural-1 case, this response is as shown in Fig. 6(*a*), but a more rapid response for the Specified-2 case is not captured by the resolution of the figure and it is indicated by a dotted line. With regard to dynamic responses to a disturbance, it is clear that the Specified-2 case of Fig. 6(*a*) (though it is farther from a natural case) is more stable than the Natural-1 case because its transient decay time τ_D is much shorter. In other words, natural steady states for unspecified exit conditions (category II) are generally more noise sensitive because the exit in category II cases is not as isolated from flow variation further downstream of it, as is the exit for specified exit-condition cases (category I), and this causes an additional lingering impact of noise arising from the flow variables in the exit zone. Time histories of pressure and temperature values in subsystems A, C, and D for the cases in Figs. 6(*a*)–6(*c*) are not shown here for brevity but are available in Figs. 7(d)–7(e) of Narain et al. [31].

The cases shown in Figs. 6(*a*)–6(*c*) are representative runs taken from a set of partial condensation runs for specified (category I) and unspecified (category II) exit-condition cases in Tables 1 and 2. The data matrix associated with these partial condensation category I and category II cases is best represented by Fig. 7. The test matrix for all partial condensation (including both categories I and II) cases is limited by the system limits and flow regime boundaries indicated on the plane marked by inlet mass flow rate $\dot{M}_{\text{in}}$ and temperature difference $\overline{\Delta T}$ values. Figure 7 shows all the partial condensation cases plotted on the two dimensional plane formed by $\dot{M}_{\text{in}}$ and $\overline{\Delta T}$. These parameters were found to be the key variables controlling the dynamics of the condensing flows in the test section. The typical values for lower and upper limits for the inlet mass flow rate were found to be 1 g/s and 2 g/s, respectively, and those for the $\overline{\Delta T}$ were recorded to be 2°C and 12°C, respectively. The interior shaded zone in Fig. 7 represent $\dot{M}_{\text{in}}$ and $\overline{\Delta T}$ values, for which steady flows were attained for both specified (category I) and unspecified (category II) exit-condition cases. The bounding curve B in Fig. 7 indicates a lower threshold of $\overline{\Delta T}$ such that steady condensing flows attained below that curve (see points marked in Fig. 7) were dropwise patchy—i.e., not annular—on the condensing surface near the inlet. Below this curve, the condensation, as observed from the inlet boroscope, indicates that the flow is no more film annular near the point of onset of condensation as there are wet and dry patches associated with dropwise condensation. This happens because the $\overline{\Delta T}$ value is below a lower threshold. The bounding curve B is partly experimental, and curve C on the right in Fig. 7 is, at present, entirely schematic (i.e., not fully explored by experiments). Curve C represents an expected transition to wispy-annular flows (see Fig. 10.3 in Carey [35]) at very high $\dot{M}_{\text{in}}$ at any $\overline{\Delta T}$. The dotted curve A on the left bottom has been experimentally noticed. It does not represent a flow regime boundary for the test section, as it is a result of the exit pressure oscillations or unsteadiness in the test section imposed by oscillatory or other plug/slug instabilities occurring elsewhere in the system (in this case, in the auxiliary condenser downstream of the test section). An example of such an instability case is discussed in Sec. 5. The bounding curve in the upper left corner of Fig. 7 is marked as curve D. This curve represents a transition from partial condensation to FC. If $\dot{M}_{\text{in}}$ is reduced and $\overline{\Delta T}$ is increased further, computations show that the left side of curve D represents the zone for which the entire vapor coming in condenses inside the test section (i.e., for category II flows, X_{FC} in Fig. 9 starts satisfying $X_{\text{FC}} \leq L$ on the left side of curve D as opposed to $X_{\text{FC}} > L$ on the right side of curve D). Note that Fig. 9 suggests, in accord with computations as well as remarks of Rabas and Arman [8], that this point of FC does not necessarily imply an all liquid phase for $x > X_{\text{FC}}$. It simply means that the zone $x > X_{\text{FC}}$ is such that the average vapor mass flow rate $\dot{M}_V$ is zero and so are the interfacial mass and heat-transfer rates at these locations. Since the area on the left side of curve D represents FC, it is discussed in Sec. 4.1.2.

For a few data points in Fig. 7, the rotameter F_2 data were corrupted by the float's occasional stickiness to the rotameter walls. These cases are marked by unfilled circles in Fig. 7, and all the rest of the good cases (also based on comparisons with computational simulations) are marked by dark filled circles. These dark filled circles representing good partial condensation cases in Fig. 7 are actually the projections on the $\dot{M}_{\text{in}}$-$\overline{\Delta T}$ plane of the points reported in the three dimensional data matrix, which has $\dot{M}_{\text{in}}$, $\overline{\Delta T}$, and Z_e ($\equiv \dot{M}_V/\dot{M}_{\text{in}}$) as the three axes. This three-dimensional data matrix is not shown here for brevity but is shown in Fig. 8(b) of Narain et al. [31], where the figure is able to depict all the cases of category II (unspecified exit) as well as category I (specified exit) partial condensing flows. Each point in Fig. 7 represents, for given values of $\dot{M}_{\text{in}}$ and $\overline{\Delta T}$, a set of data consisting both category I cases and its associated unique natural category II case. There are, however, as seen in Fig. 8(b) of Narain et al. [31], some data sets representing only category I or category II cases. For each data set in Fig. 7 consisting of category I cases and the associated category II case, category I flows were found to be more robust and stable as compared to their associated category II counterparts.

4.1.2 Comparisons With Relevant Computational Results (Partial Condensation). Figure 8 shows the computationally obtained (employing the tools reported in Ref. [3]) steady and noise-free details of local film thickness and heat-flux variations for the specified and unspecified natural cases marked as Specified-2 (run

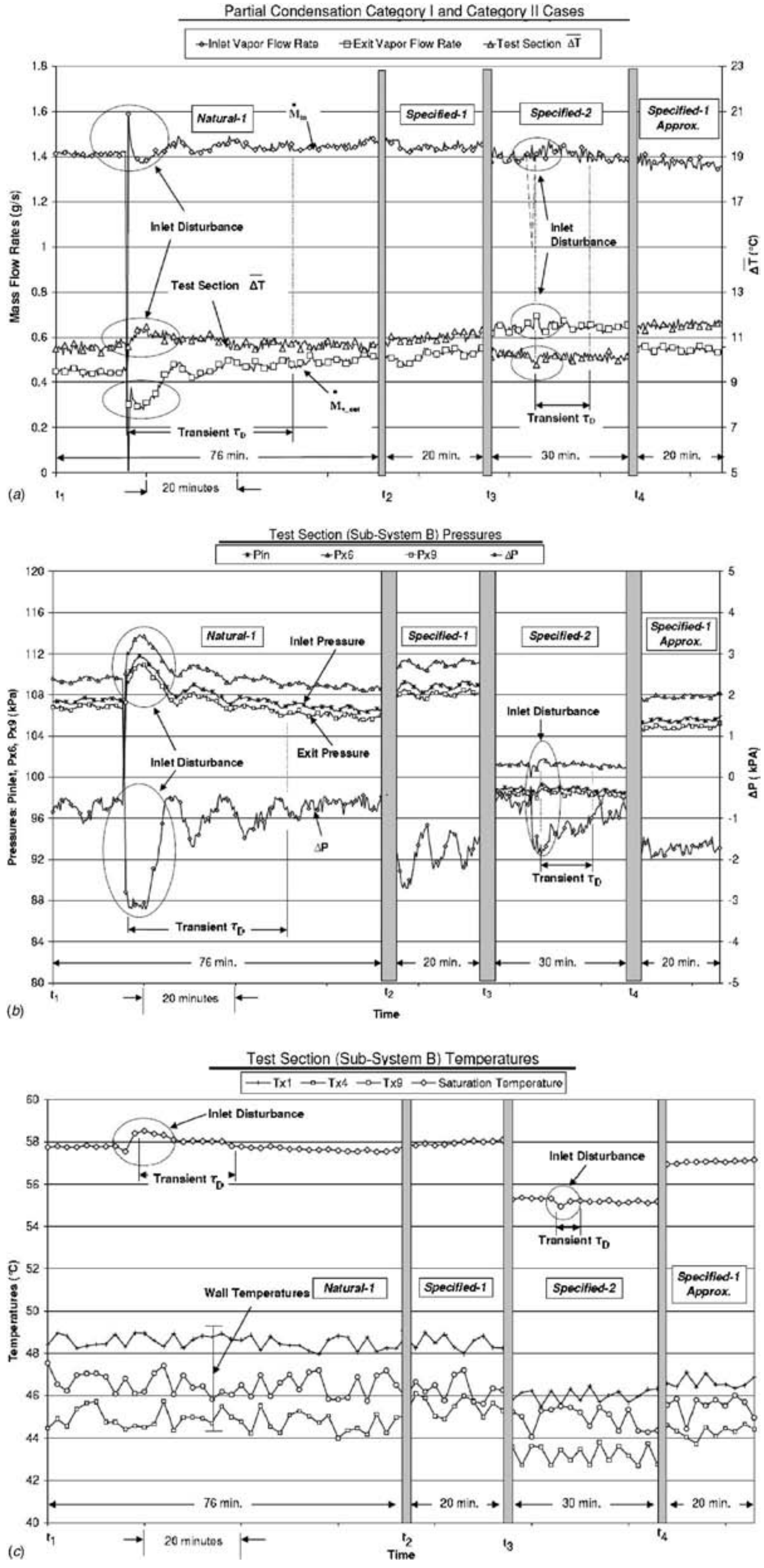

Fig. 6 (*a*) Time history depiction of $\dot{M}_{in}$, $\dot{M}_V$, and $\overline{\Delta T}$ values for multiple steady states of partial condensation cases, viz., Natural-1 (run 1 from Table 1), Specified-1 (run 1 from Table 2), Specified-2 (run 18 from Table 2), and Specified-1 Approx. (*b*). Time history of pressures (along the test section) and Δp values (across the test section) for the cases shown in (*a*) (*c*) Time history of temperature values along the test section (subsystem B) and T_{sat} (p_{in}) for the cases shown in (*a*).

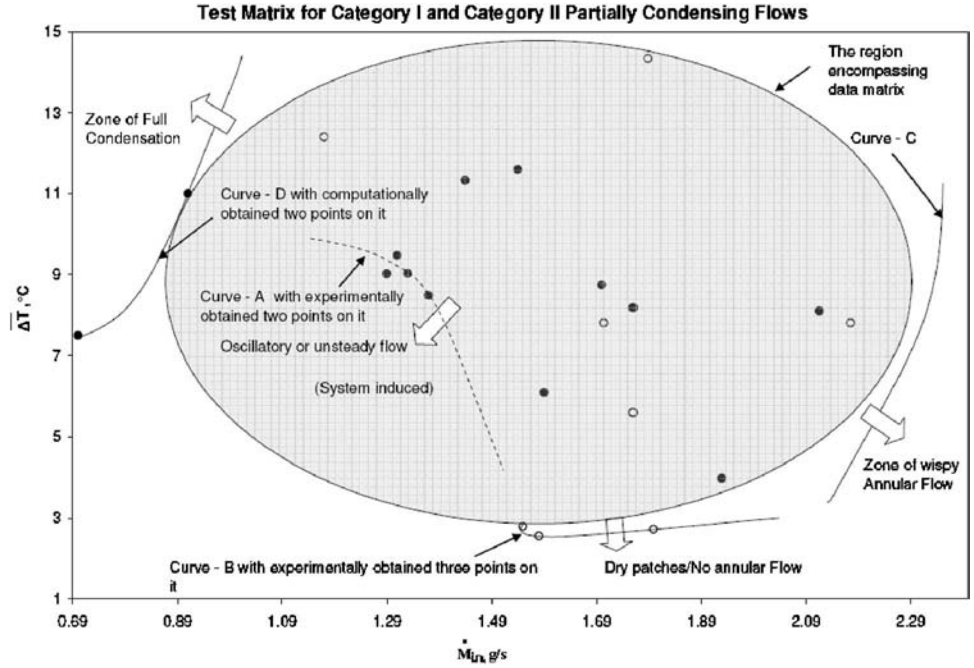

Fig. 7 Two-dimensional test data matrix for category II (unspecified exit condition) partial condensation flow cases and different bounding curves represented on the $\dot{M}_{in}-\overline{\Delta T}$ plane

18 in Table 2) and Natural-1 (run 1 in Table 1) in Figs. 6(*a*)–6(*c*). The variation of vapor quality Z ($\equiv \dot{M}_v/\dot{M}_{in}$ at any x) along the test section can be easily obtained from the graphical results in Fig. 8 from the relation $Z(x) \equiv 1-[(\pi \cdot D)/(\dot{M}_{in}h_{fg})]\int_0^x q''_w dx$.

The exit vapor quality for the Specified-2 case was greater than that of the associated Natural-1 case. As a result, a higher amount of vapor condenses for the Natural-1 case, and this makes the heat-transfer rate $\dot{Q}_{out}$ for the natural case to be on the higher side (see Tables 1 and 2 for details). For all other conditions remaining the same, as observed from the computational results in Fig. 8, this makes the Natural-1 case's liquid film thickness lower and the wall heat flux higher than the values for the Specified-2 case. Such details of representative local variations in film thickness and heat flux are very important and should be more extensively synthesized with experimental results before heat-transfer correlations are developed for suitable categories and subcategories of internal condensing flows. However, reliable experimental information on local spatial variations of these quantities is not expected until later incorporation of film thickness sensors and heat-flux sensors in these experiments. Observe that the computationally obtained prediction of the natural exit vapor quality $Z_e|_{\text{Na comp}}$ (≈ 0.33) for category II flow in Fig. 6(*a*)–6(*c*) is in a very good agreement with the experimentally obtained $Z_e|_{\text{Na Expt}}$ (≈ 0.33) value (see Table 1). In fact, a very good agreement between $Z_e|_{\text{Na comp}}$ and $Z_e|_{\text{Na expt}}$ values was found for all category II cases in Fig. 7, and this is clear from their numerical values in Table 1. Note that a good agreement between experimental and theoretical Z_e values has also been obtained and reported (see Ref. [2]) for a shear driven condensing flow in a channel (category II experiments of Lu and Suryanarayana [27]).

The values of pressure drop Δp (p_{in}-p_{exit}) obtained from simulations for all the category II partial cases were negative and below 50 Pa, indicating that p_{exit} was greater than p_{in} for all the condensation cases in the given $\dot{M}_{in}$ range. This is confirmed by the experimental values of Δp (see Tables 1–3), which are also all negative (except for a very few cases). However, as expected, the magnitudes for experimental values of Δp were found to be greater than those from simulations. The reason behind this is that the simulations assume laminar-vapor/laminar-liquid flows while, in reality, the vapor Reynolds numbers are in the higher range (20,000–30,000), and this makes vapor flows significantly turbulent in the core (see Tables 1–3). The turbulence in the vapor core does not affect the mass transfer across the interface much because the condensate motion is gravity dominated. However, the turbulent vapor core significantly increases Δp values in the vapor domain. Because of this, the values of vapor quality obtained from the simulation are in good agreement with the experiments, but the values of pressure drop Δp obtained from experiments are higher in magnitudes. The predicted pressure drop Δp values do become comparable to experimental values if suitable corrections for vapor turbulence are made. The modifications in the computational procedure needed to account for vapor turbulence are explained in Narain et al. [31].

4.2 Complete or Full Condensation Flows

4.2.1 Specified Exit-Condition Cases (Category I Flows). As mentioned earlier, this case has not been investigated experimentally because the current setup does not have active pressure control strategies for fixing different pressures at the L/V separator, leading to different pressures at the inlet to pump P_1 (point P'_1 in Figs. 3 and 4). However, current computational simulations show that the location of the point of FC shown in the schematic of Fig. 9, is extremely sensitive to exit pressure p_e. For the gravity driven condensate in relatively large diameter tubes, the zone between the point of FC and the point of test-section exit is typically not filled with liquid alone (see the liquid marked by the doubly shaded zone in Fig. 9). Instead, this zone experiences a more complex two-phase flow with nearly zero interfacial mass or heat-transfer rates and nearly *zero average* vapor velocity or average vapor mass flow rate.

4.2.2 Unspecified Exit Condition Cases (Category II Flows). The test matrix (Table 3) for the natural steady FC cases under category II accommodates a range of vapor mass flow rates and temperature difference $\overline{\Delta T}$ values that are shown in Fig. 10. The shaded region in Fig. 10 contains most of the data points obtained for steady FC cases. More details on these cases are given in Table

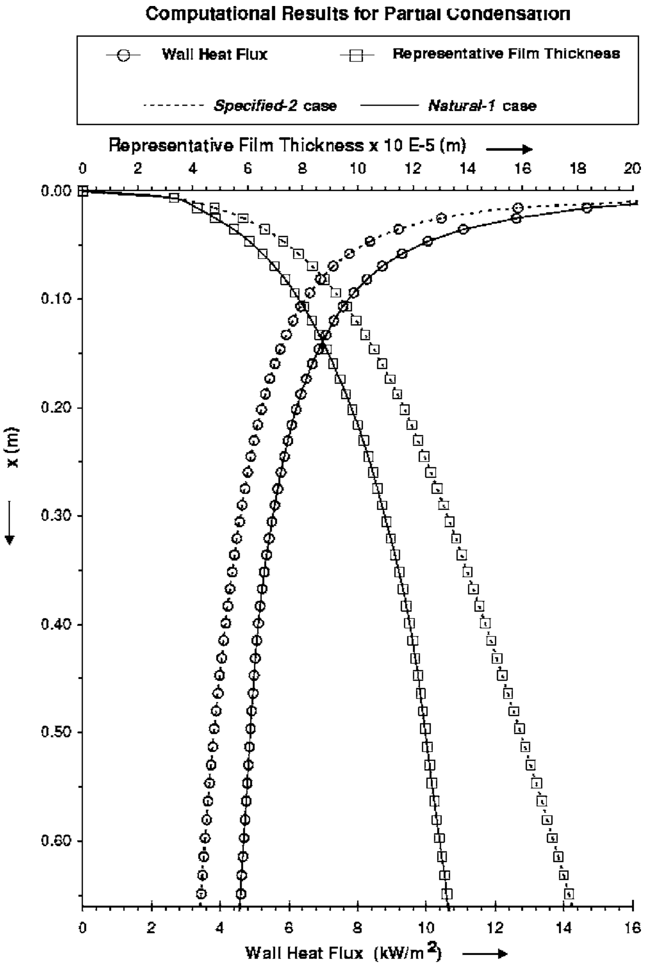

Fig. 8 For the Natural-1 and Specified-2 flow cases in Figs. 6(*a*)–6(*c*), this figure shows the computationally obtained representative film thickness and wall heat-flux variation along the test section. The film thickness and heat-flux values shown have been obtained for smooth interface conditions. In reality, they are modulated by waves due to presence of noise (see Ref. [3]).

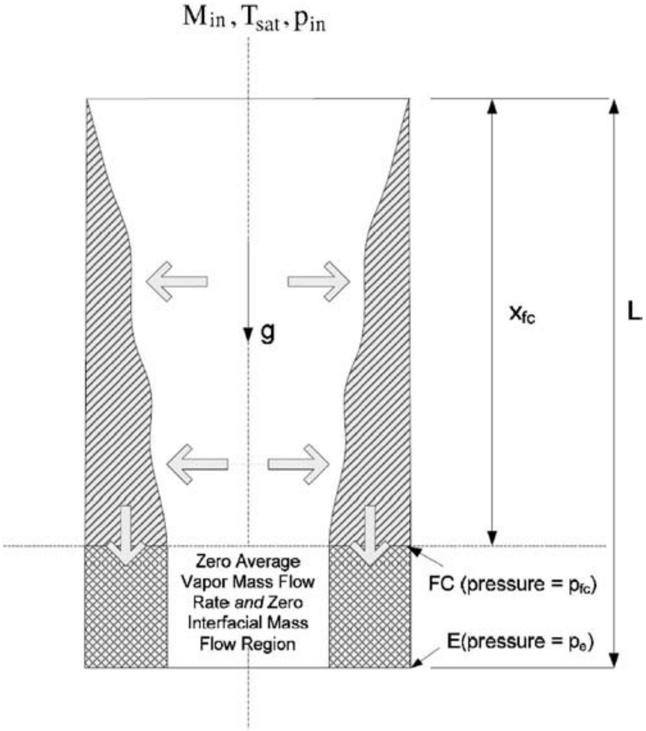

Fig. 9 The schematic of FC showing point of FC and its downstream region with zero interfacial mass and heat transfer.

3 along with the accuracies of measured and calculated variables. For representative FC cases in Table 3, Figs. 11(*a*)–11(*c*) show three steady states: Natural-1 over $t_1 \leq t(\min) \leq t_1+30$ (Table 3, run 1 with $\dot{M}_{\text{in}} \approx 0.69 \pm 0.05$ g/s and $\overline{\Delta T} = 23 \pm 1\,^{\circ}\text{C}$), Natural-2 over $t_2 \leq t(\min) \leq t_2+30$ (Table 3, run 18 with $\dot{M}_{\text{in}} \approx 1.30 \pm 0.05$ g/s and $\overline{\Delta T} = 19 \pm 1\,^{\circ}\text{C}$), and Natural-1 Repeated over $t_3 \leq t(\min) \leq t_3+30$ (run 1 repeated). The mass flow rates for these three and other steady state FC cases are plotted along with their $\overline{\Delta T}$ values in Fig. 10. The steady pressures and temperatures measured at different locations along the test section are plotted in Figs. 11(*b*) and Fig. 11(*c*), respectively. Time histories of variations in temperature and pressure of subsystems A, C, and D for the cases in (Figs. 11(*a*)–11(*c*)) are not shown here for brevity but are available in Figs. 12(d)–12(e) of Narain et al. [31].

The FC cases reported in Table 3 lie in a zone bounded by semischematic curves X and Y, as shown in Fig. 10. These bounding curves, at the present moment, are approximate and schematic in nature, as no more than two points on each of the curves have been obtained by experiments or computations. All FC cases in Table 3 and Fig. 10 are category II cases, and the point of FC lies inside the test section (i.e., $X_{\text{FC}} \leq L$ in Fig. 9). This was verified by simulations performed for each of the FC cases. The curve Y (with two computationally obtained points) depicts the right bound on the test matrix. For cases to the right hand side of this curve, the natural point of FC will lie out of the test section and any steady flow that will be realized will belong to the uninvestigated category I cases dealing with specified FC. If the L/V separator had a natural open vapor outlet (which it does not have because the valve V_3 in Fig. 3 is closed), then curve Y would have represented the transition to partial condensation. Curve X (with two experimentally obtained points), on the left hand side in Fig. 10, represents a system instability that marks a lower left bound on the test matrix. As the mass flow rate decreases below the value given by this curve, there is an experimentally observed instability in the flow, which, in all likelihood, marks the constraining boundary (due to pressure constraints related to saturation pressure in the L/V separator) representing the limited range of available exit pressures to choose from. It can be seen in Fig. 12 that there exists a steady flow for $\dot{M}_{\text{in}} \approx 1.2$ g/s and 0.8 g/s, but as it is reduced to $\dot{M}_{\text{in}} \leq 0.6$ g/s, the schematic curve X (the suggested boundary between steady annular to unsteady plug/slug) in Fig. 10 is crossed from right to left. The inlet mass flow rate never stabilizes for these cases, but the inlet pressure, as shown in Fig. 12, appears to be less erratic. These transition points are evident, for the circled experimental points on curve X, where unsteadiness/spikes of the type shown in Fig. 12 are observed. These unsteady spikes in the inlet flow rate are probably due to the bridges of the liquid that form across the cross section area when X_{FC} becomes significantly smaller than L in Fig. 9 and the desired value of exit pressure falls below the lower bound for allowable exit pressures (the allowed range would typically keep the test-section flow from listening to the downstream vapor pressure restrictions in the L/V separator). These formations may introduce the observed unsteadiness (Fig. 12) in the inlet mass flow rate and inlet pressure.

Although, at present, different boundaries defined in Figs. 7 and 10 are approximate and schematic, some representative full and partial condensation cases on these boundaries have already been obtained (either by experiments or by computations).

The research outlined in this paper mainly focuses on the inte-

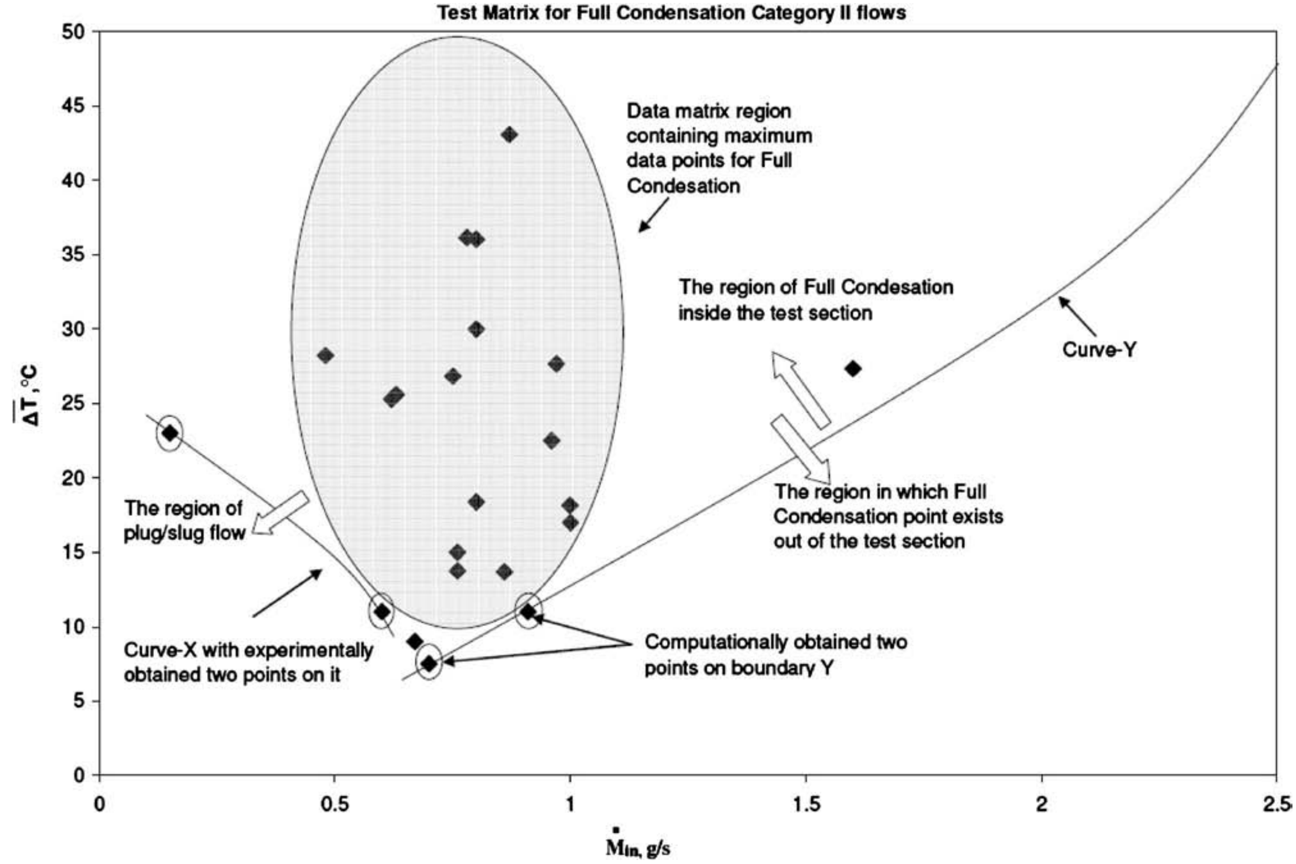

Fig. 10 Two-dimensional test data matrix for category II (unspecified exit-condition) FC case points and different bounding curves represented on the $\dot{M}_{in}-\overline{\Delta T}$ plane

rior region bounded by these curves (see the shaded regions in Figs. 7 and 10), and a careful investigation of the bounding curves and their proper nondimensionalization are a part of future (ongoing) research that awaits more detailed experimental results and better flow visualization.

Even though the exit pressure currently cannot be actively specified for the FC cases, the response of the category II FC cases to disturbances in exit pressure was experimentally ascertained for a number of cases marked in Fig. 10. The exit pressure disturbance was given in the Natural-2 case (see Fig. 11(*a*)) by changing the pressure at the L/V separator (Fig. 3) momentarily. It is seen from Fig. 11(*a*) that although this disturbance died out quickly for the inlet vapor flow rate $\dot{M}_{in}$, the disturbance died out much more slowly for the Δp, which is an indicator of changes in the liquid vapor configuration in the test section. In fact, for all FC cases, the exit pressure disturbance died out in the manner indicated above, showing the generally robust nature of these cases, except for their sensitivity to changes in the exit zone flow variables, as indicated by the Δp response. In fact, even when the aforementioned momentary pressure disturbances in the L/V separator (by injecting liquid through a syringe) was followed by a permanent partial closing of valve V′ in Fig. 3, the same dynamic recovery was observed; however, the recovery time was longer. Also, as seen in Fig. 11(*a*) for the Natural-1 Repeated case, these flows are stable against disturbances in inlet flow rates as well. In this sense, all the category II FC cases in the shaded region of Fig. 10 were found to be robust, pointing to the fact that this experimental procedure is conducive for achieving the steady flow situations associated with the presence of steady attractors for gravity driven condensate flows (see Ref. [1]). It should be noted that the steady flow's robustness is in part a consequence of the appropriate flow loop design whereby the displacement pump P_1 in Fig. 3 continually allows, in the approximate shaded region, the availability of a suitable exit pressure being sought by the flow. This is due to the nature of pump P_1 being "displacement" type and due to its ability to track the inlet mass flow rate $\dot{M}_{in}$. For example, the observed robustness of these fully condensing flows is not at all present in FC cases investigated by others (see, e.g., Ref. [9]) for the earlier described category III flow cases.

4.2.3 Comparisons With Relevant Computational Results (Full Condensation). The simulations for most of the FC cases reported in this paper confirm the fact that the point of FC lies within the test section and almost all the cases lie in the region bounded by the curves X and Y shown in Fig. 10. The simulations performed only up to X_{FC} (with $X_{FC}<L$ in Fig. 9) also predict that the length X_{FC} for FC decreases as the mass flow decreases or the value of $\overline{\Delta T}$ increases. For example, the length of the FC case estimated by the computations for run 11 in Table 3 (with $\dot{M}_{in} \approx 0.97$ g/s and $\overline{\Delta T}=27°\text{C}$) is approximately 0.3 m, while that for run 13 in Table 3 (with $\dot{M}_{in}\approx 0.8$ g/s and $\overline{\Delta T}=36°\text{C}$) is 0.15 m. The computationally obtained steady and noise-free film thickness and local wall heat-flux values for run 12 in Table 3 (with $\dot{M}_{in} \approx 0.87$ g/s and $\overline{\Delta T}=43°\text{C}$) are shown in Fig. 13 over $x \leq X_{FC}$. As seen from Fig. 13, the computationally found length of FC X_{FC} was around 0.2 m. Therefore, results are shown only up to 0.2 m and not up to $L=0.8$ m. As stated earlier, this is because the current simulation methodology cannot simulate the region between X_{FC} and L shown in Fig. 9. Experimental comparisons for these computationally predicted local variations in film thickness and heat-flux values are not currently available but are expected in the near future.

The inclusion of correlations for local or average heat-transfer

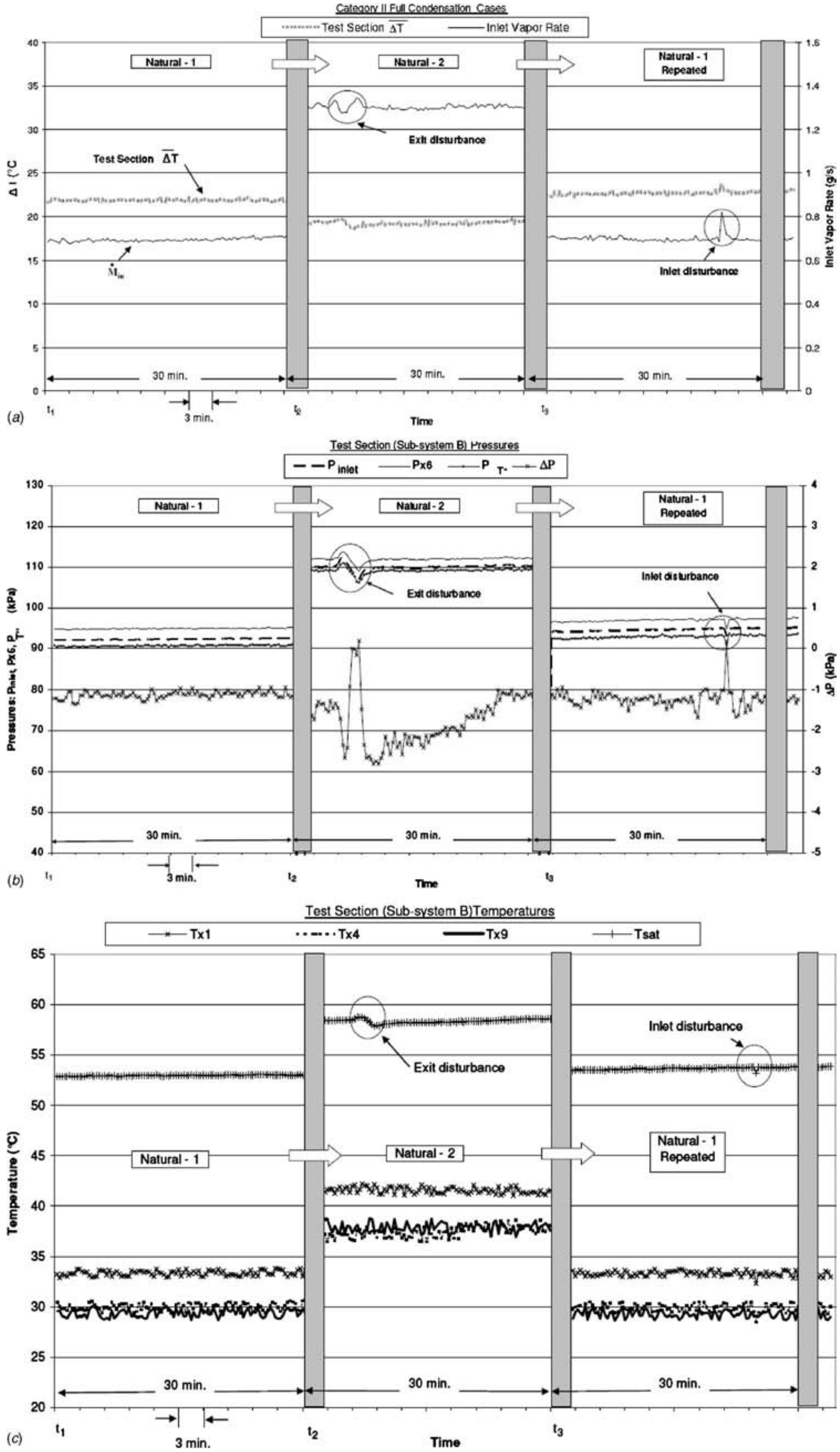

Fig. 11 (*a*) Time history depiction of $\dot{M}_{\text{in}}$ and $\overline{\Delta T}$ values for multiple steady states of FC category II cases, viz., Natural-1 (run 1 from Table 3), Natural-2 (run 18 from Table 3), and Natural-1 Repeated. (*b*) Time history of pressures (along and outside the test section) and Δp values for the cases shown in (*c*) Time history of temperature values along the test section (subsystem B) for the cases shown in (*a*).

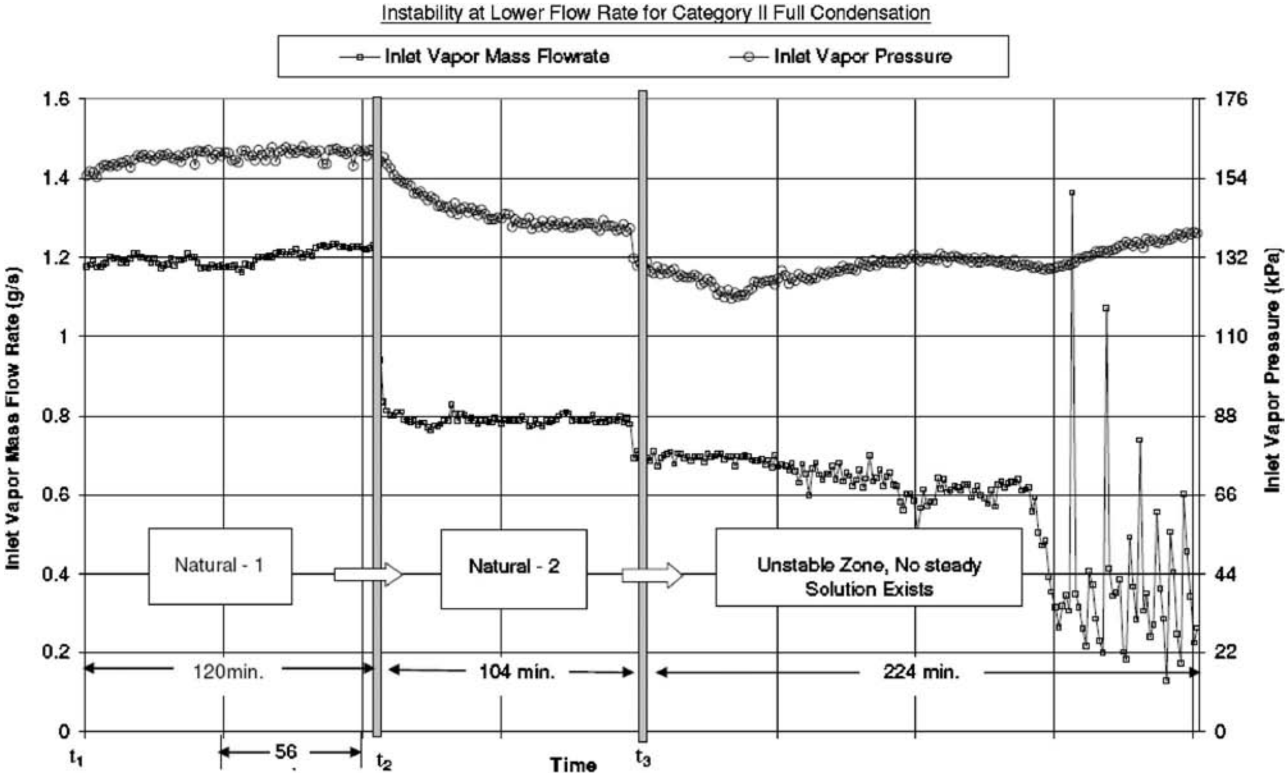

Fig. 12 Time history ($t_3 \leq t\,\text{min} \leq t_3+224$) of mass flow rate and inlet vapor pressure for an attempted unspecified exit-condition (category II) FC case that resulted in instability or transients as the boundary curve X in Fig. 10 is crossed

coefficients is outside the scope of the present paper and is not desirable until a comprehensive synthesis of experimental results and computational results on local film thickness and heat flux becomes available. It should be noted that such data—if obtained without full consideration of the proposed framework of different flow categories, subcategories, and their boundaries—would not be very useful.

5 Results/Comments on Oscillatory System Instabilities

While seeking the natural exit condition for some unspecified exit-condition (category II) partial condensation flows, system instabilities—involving oscillatory flows—of the type shown in Figs. 14(*a*) and 14(*b*) are observed (also see dotted curve A in Fig. 7). The origin of these oscillatory flows appears to be the auxiliary condenser, which sees an approximate category III flow for which, in Fig. 3, the L/V separator is at an approximately fixed high pressure and the merger point P_1' is at an approximately fixed lower pressure. These pressures correspond, respectively, to pressures $p_{\text{tank-in}}$ and $p_{\text{tank-out}}$, which appear in the definition given in Sec. 1 for category III flows. Recall that these fully condensing flows in the auxiliary condenser, unlike the ones studied for the test section, are known (as in Ref. [11]) to become oscillatory under certain conditions. Since details of auxiliary condenser flow data were not obtained (because this component was not the focus of the reported investigations), relating this auxiliary condenser instability to the type of stability boundaries discussed in Ref. [11,13] is outside the scope of this study.

It is clear from Figs. 14(*a*) and 14(*b*) that oscillations in vapor mass flow rate at the exit of the test section impose oscillations on the exit pressure and the pressure drop Δp across the test section, while the inlet vapor mass flow rates remain relatively unaffected. Figure 14(*b*) shows the oscillations in other pressure values and the temperature at the rotameter F_2 (which is nearer to the auxiliary condenser). This, along with the known fact (see Fig. 6 in Ref. [1]) that there is a one to one relation between the exit vapor quality and the exit pressure, indicates an imposition of oscillatory pressures at the exit of the test section.

It suffices here to note that the flow oscillations in the auxiliary condenser can induce an oscillatory exit pressure at the exit of the test-section condenser, and this is the cause, in Figs. 14(*a*) and 14(*b*), of the somewhat reduced level of oscillatory behavior of other test-section flow variables. As a result of the instability in the auxiliary condenser, the dotted curve A in Fig. 7 is merely suggestive of the possible presence of system instabilities. This is because the actual onset of oscillatory conditions has only a very indirect and incomplete relation to the test section $\dot{M}_{\text{in}}$ and $\overline{\Delta T}$ values used in Fig. 7.

The issues regarding the start-up time for the flow loop are discussed in Narain et al. [31] and Kurita [33].

6 Conclusions

This paper experimentally confirms the significance of exit conditions on the nature of quasisteady internal condensing flows and proposes a novel and necessary exit-condition-based categorization of these flows.

In particular, for this gravity driven condensate flow, a way of achieving steady and stable fully condensing flows under unspecified exit-condition cases (category II) is presented. These flows are typically more robust than the fully condensing flows (category III) achieved by a different procedure that has been typically employed and discussed in the existing literature.

The experiments reinforce the simulation results that for partial condensation, multiple steady states, with quite different local and average heat-transfer rates, are often achieved under different exit-condition specifications (category I flows). Therefore, correlations for heat-transfer coefficient (though not developed here) are only meaningful if flow regimes are clearly defined and developed in the framework of proposed exit-condition-based categories.

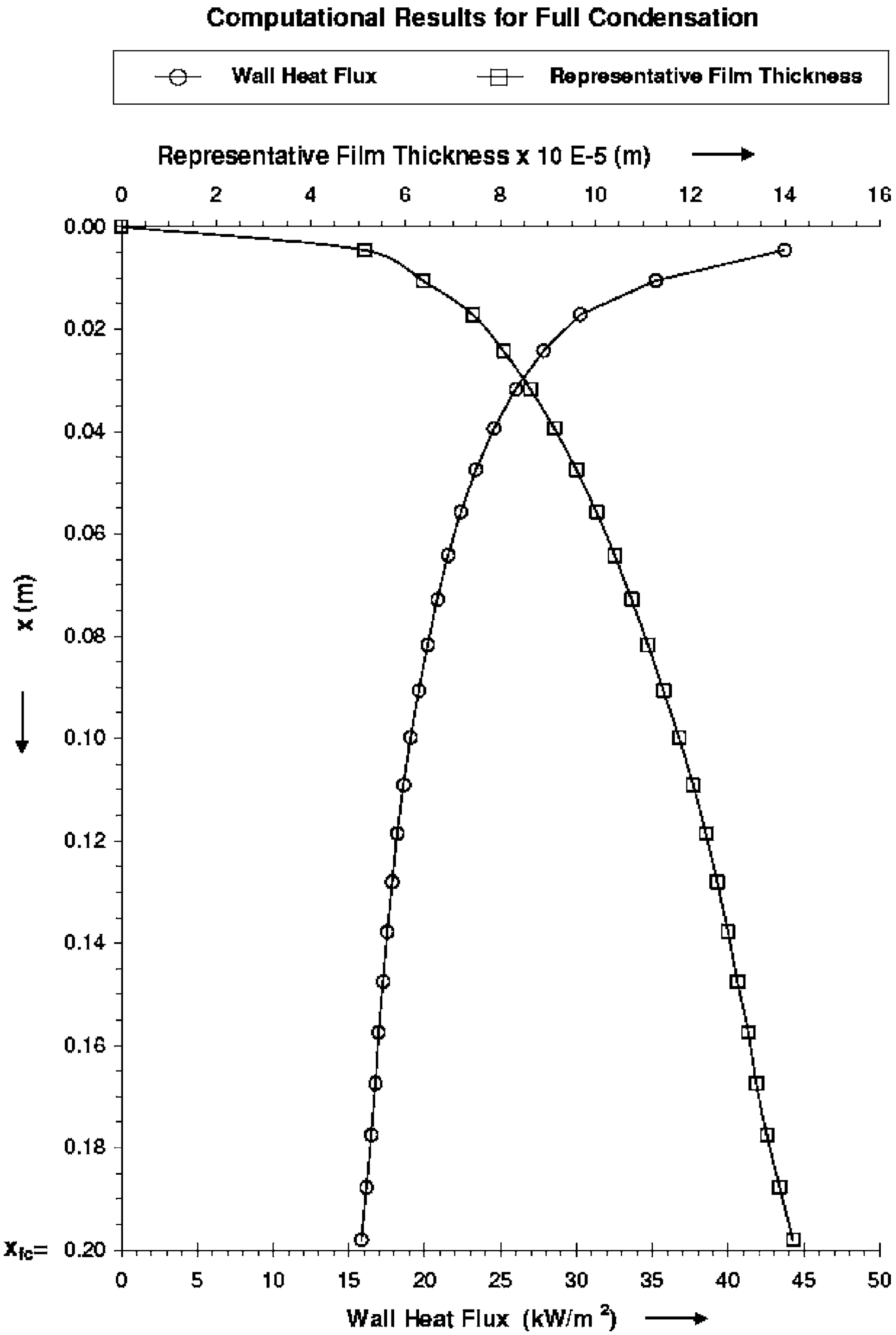

Fig. 13 For a typical category II FC case, this figure shows the computationally obtained representative film thickness and wall heat-flux variation along the test section over $0 \leq x \leq X_{FC}$. The film thickness and heat-flux value shown have been obtained for smooth interface conditions. In fact, they are modulated by waves in the presence of noise (see Ref. [3]). The figure also shows that the length of FC X_{FC}=0.2 m is sufficiently shorter than the test-section length L (=0.7 m).

The existing simulation tool's ability to be quantitatively correct in identifying natural exit conditions for gravity driven partial condensation cases under unspecified exit conditions (category II) is very good, as this is supported by the reported experiments. This agreement adds credibility to the experimental results, simulation tool, and the proposed exit-condition-based categorizations.

The transients in partial condensation experiments establish that the steady flows are definitely more robust under the specified exit condition (category I) operation of condensers. This lends credibility to the simulation result that a steady operation of shear driven condensers (in zero gravity and horizontal configurations) is much more difficult to achieve under unspecified exit conditions (category II). In general, these results suggest that all (partial or complete) specified exit-condition flows (category I flows) with

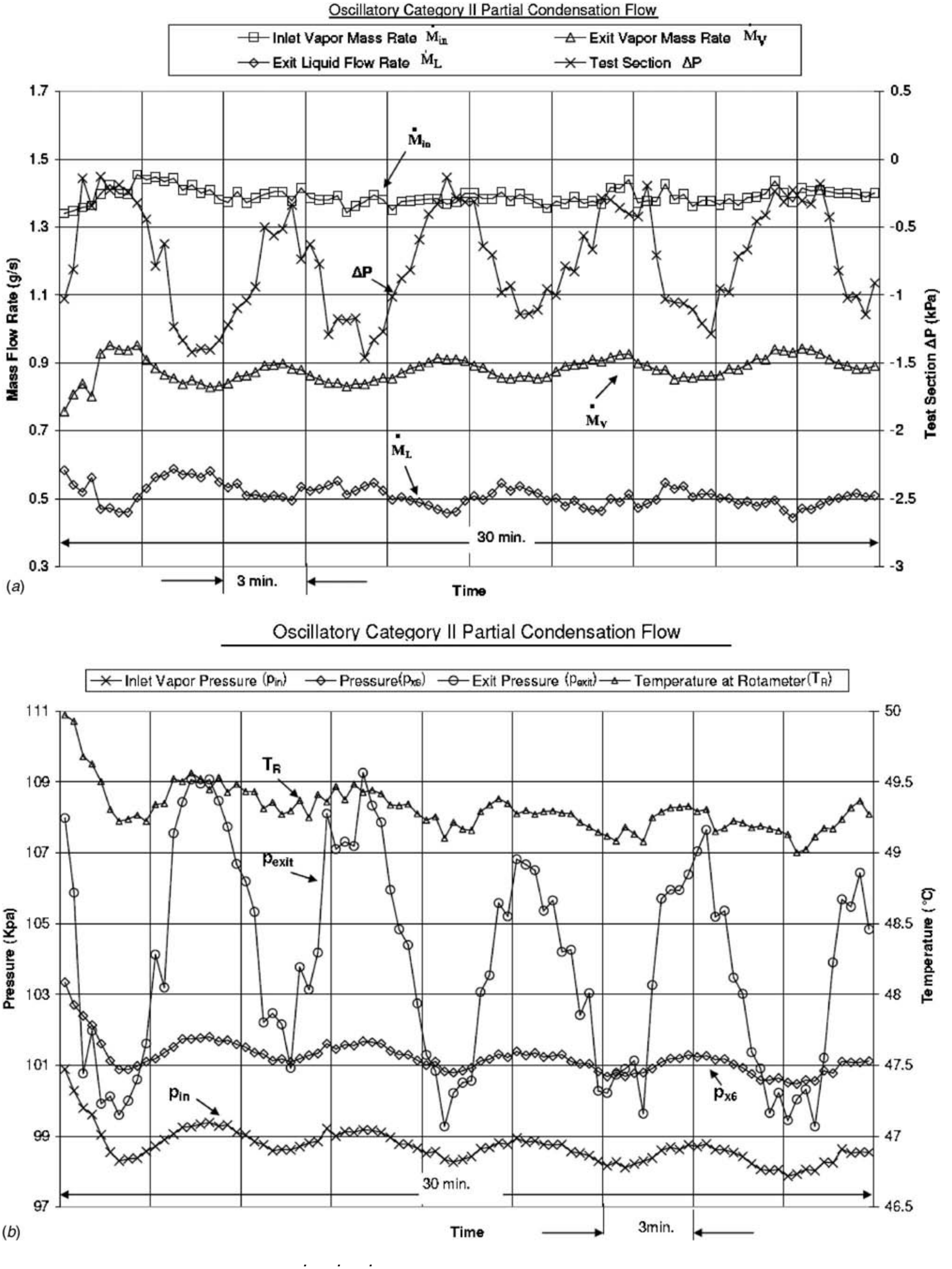

Fig. 14 (*a*) Time history depiction of $\dot{M}_{in}$, $\dot{M}_V$, $\dot{M}_L$, and Δp values for an oscillatory partial unspecified exit-condition case (category II). In Fig. 7, this flow's appearance is indicated by the crossing of the dotted curve A. (*b*) For the case in (*a*), this figure shows the time history depiction of the rotameter temperature T_R and the following pressures: inlet pressure p_{in}, pressure at location 6 in Fig. 5 (p_{x6}), and exit pressure p_{exit}.

properly selected exit pressure values are likely to be more robust and more readily realized than an operation under other arrangements (category II or category III under arbitrarily fixed pressures and valve settings).

Various flow regime and system boundaries for annular category I and category II flows are observed and reported. Though reported preliminary identifications of flow regime boundaries need to be made more definitive, their identifications are clearly important for attaining or ascertaining steady performances of condensers.

The experiments clearly demonstrate the difference between flow regime boundaries and system-instability boundaries and the importance of identifying system-instability boundaries that are specific to individual systems. For example, curve-A in Fig. 7 and curve-X in Fig. 10 represent system instability boundaries that arise from restrictions imposed on the exit pressure by phenomenon occurring in components downstream of the test section.

Acknowledgment

This work was supported by the NSF Grant No. CTS-0086988 and NASA Grant No. NNC04GB52G.

Nomenclature

$C_p|_L$ = specific heat of the liquid condensate, J/(kg K)
$C_p|_V$ = specific heat of the vapor, J/(kg k)
D = inner diameter of the test-section, m
FC = abbreviation for full condensation
G = inlet mass flux, $4\dot{M}_{\text{in}}/(\pi D^2)$, $\text{kg}/(\text{m}^2/\text{s})$
$h_{\text{fg}}(p_{\text{in}})$ = heat of vaporization at pressure p_{in}, J/kg
$\bar{h}$ = average heat-transfer coefficient, $\dot{Q}_{\text{out}}/(\pi DL)$, $\text{W}/(\text{m}^2\ \text{K})$
Ja = condensate liquid Jakob number, $C_p|_L \cdot \overline{\Delta T}/h_{\text{fg}}(p_{\text{in}})$
$\text{Ja}|_V$ = vapor Jakob number, $C_p|_V \Delta T_{\text{sup}}/h_{\text{fg}}(p_{\text{in}})$
k_L = conductivity of condensate liquid, W/(m K)
L = length of the test section, m
$\dot{M}_{\text{in}}$ = vapor flow rate at test-section inlet, g/s
$\dot{M}_L$ = liquid flow rate at test-section exit, g/s
$\dot{M}_V$ = vapor flow rate at test-section exit, g/s
p_b = evaporator (boiler) pressure, kPa
p_{D2} = pressure at the location near the rotameter, kPa
$p_{T''}$ = pressure at a location downstream of the test section, kPa
p_{in} = pressure at the test-section inlet, kPa
p_{exit} = pressure at the test-section exit, kPa
Pr_1 = condensate liquid Prandtl number, $\mu_{1.} C_p|_L/k_L$
p_{xi} = test-section pressures at different locations $x = xi$ $(i=1,2,\ldots)$, kPa
$\bar{q}''$ = average convective heat flux, W/m^2
$\dot{Q}_b$ = net heat rate into the evaporator, W
$\dot{Q}_{\text{out}}$ = net heat rate out of the test section, W
Re = inlet vapor Reynolds number, $4\dot{M}_{\text{in}}/(\pi D\mu)$
T_b = evaporator fluid temperature, °C
T_R = rotameter fluid temperature, °C
$T_{\text{sat}}(p)$ = saturation temperature at pressure p, °C
$T_{s\text{-}xi}$ = condensing surface temperatures at different locations $x=xi$ $(i=1,2,\ldots)$, °C
$\bar{T}_w$ = mean condensing surface temperature, °C
$T_w(x)$ = nonuniform steady condensing surface temperature, °C
$T_{V\text{-in}}$ = vapor temperature at test-section inlet, °C
$T_{C\text{-in}}$ = temperature of the counter-current coolant water flow at the approach to the test section, °C
x = distance along the test section, m
x_e = ratio of test-section length to test-section inner diameter (L/D).
X_{FC} = approximate length needed for full condensation (estimted by computations), m
$\overline{\Delta T}$ = $T_{\text{sat}}(p)\text{-}\bar{T}_w$, °C
ΔT_{sup} = vapor superheat, $T_{V\text{-in}}\text{-}T_{\text{sat}}(p)$ °C
Δp = $p_{\text{in}}\text{-}p_{\text{exit}}$, kPa
Z_e = ratio of exit vapor mass flow rate to total inlet mass flow rate
$Z(x)$ = ratio of vapor mass flow rate to total mass flow rate at any location x along the test section
ρ_2 = density of vapor, kg/m^3
ρ_1 = density of liquid, kg/m^3
μ_2 = viscosity of vapor, kg/(m s)
μ_1 = viscosity of liquid, kg/(m s)
τ_D = transient decay time for disturbances, s

Subscripts

exit = test-section exit
in = test-section inlet
Na = natural steady case
expt = obtained from experiments
comp = obtained from computations

References

[1] Narain, A., Liang, Q., Yu, G., and Wang, X., 2004, "Direct Computational Simulations for Internal Condensing Flows and Results on Attainability/Stability of Steady Solutions, Their Intrinsic T Waviness, and Their Noise-Sensitivity," J. Appl. Mech., **71**, pp. 69–88.

[2] Liang, Q., Wang, X., and Narain, A., 2004, "Effect of Gravity, Shear and Surface Tension in Internal Condensing Flows—Results From Direct Computational Simulations," ASME J. Heat Transfer, **126**(5), pp. 676–686.

[3] Phan, L., Wang, X., and Narain, A., 2006, "Exit condition, Gravity and Surface-Tension Effects on Stability and Noise Sensitivity Issues for Steady Condensing Flows Inside Tubes and Channels," Int. J. Heat Mass Transfer, **49**(13–14), pp. 2058–2076.

[4] Goodykoontz, J. H., and Dorsch, R. G., 1966, "Local Heat Transfer Coefficients for Condensation of Steam in Vertical Down Flow Within a 5/8-Inch-Diameter Tube," NASA Report No. TN D-3326.

[5] Goodykoontz, J. H., and Dorsch, R. G., 1967, "Local Heat Transfer Coefficients and Static Pressures for Condensation of High-Velocity Steam Within a Tube," NASA Report No. TN D-3953.

[6] Carpenter, F. G., 1948, "Heat Transfer and Pressure Drop for Condensing Pure Vapors Inside Vertical Tubes at High Vapor Velocities," Ph.D thesis, University of Delaware.

[7] Yu, G., 1999, "Development of a CFD Code for Computational Simulations and Flow Physics of Annular/Stratified Film Condensation Flows," Ph.D thesis, ME-EM Department, Michigan Technological University.

[8] Rabas, T. J., and Arman, B., 2000, "Effects of the Exit Condition on the Perofromance of In-Tube Condensers," Heat Transfer Eng., **21**(1), pp. 4–14.

[9] Wedekind, G. L., and Bhatt, B. L., 1977, "An Experimental and Theorotical Investigation in to Thermally Governed Transient Flow Surges in Two-Phase Condensing Flow," ASME J. Heat Transfer, **99**(4), pp. 561–567.

[10] Bhatt, B. L., and Wedekind, G. L., 1980, "Transient and Frequency Characteristics of Two-Phase Condensing Flows: With and Without Compressibilty," ASME J. Heat Transfer, **102**(3), pp. 495–500.

[11] Bhatt, B. L., and Wedekind, G. L., 1980, "A Self Sustained Oscillatory Flow Phenomenon in Two-Phase Condensing Flow Systems," ASME J. Heat Transfer, **102**(4), pp. 695–700.

[12] Wedekind, G. L., and Bhatt, B. L., 1989, "Modeling the Thermally Governed Transient Flow Surges in Multitube Condensing Flow Systems With Thermal Flow Distribution Asymmetry," ASME J. Heat Transfer, **111**(3), pp. 786–791.

[13] Bhatt, B. L., Wedekind, G. L., and Jung, K., 1989, "Effects of Two-Phase Pressure Drop on the Self-Sustained Oscillatory Instabilty in Condensing Flow," ASME J. Heat Transfer, **111**, pp. 538–545.

[14] Boyer, D. B., Robinson, G. E., and Hughes, T. G., 1995, "Experimental Investigation of Flow Regimes and Oscillatory Phenomena of Condensing Steam in a Single Vertical Annular Passage," Int. J. Multiphase Flow, **21**(1), pp. 61–74.

[15] Wedekind, G. L., Kobus, C. J., and Bhatt, B. L., 1997, "Modeling the Characteristics of Thermally Governed Transient Flow Surges in Multitube Two-Phase Condensing Flow Systems With Compressibility and Thermal and Flow Distribution Asymmetry," ASME J. Heat Transfer, **119**(3), pp. 534–543.

[16] Kobus, C. J., Wedekind, G. L., and Bhatt, B. L., 2000, "Predicting the Influence of Compressibility and Thermal and Flow Distribution Asymmetry on the Frequency-Response Characteristics of Multitube Two-Phase Condensing Flow Systems," ASME J. Heat Transfer, **122**(1), pp. 196–200.

[17] Kobus, C. J., 2003, "An Investigation Into the Effect of Subcooled Liquid Inertia on Flowrate Induced Frequency-Response Characteristics of Horizontal

Condensing Flow Systems," *Proceedings of the 6th ASME/JSME Thermal Engineering Joint Conference (AJTEC)*, Hawaii, Mar. 16–23.

[18] Wallis, G. B., 1969, *One-Dimensional Two-Phase Flow*, McGraw-Hill, New York.

[19] Lahey, R. T., and Drew, D. A., 2000, "The Analysis of Two-Phase Flow and Heat Transfer Using A Multidimensional, Four Field, Two-Fluid Model," Nucl. Eng. Des., **204**, pp. 29–44.

[20] Liao, N. S., Wang, C. C., and Tien, C. L., 1988, "Analysis of Transient Flow Surge Phenomena in a Single-Tube Condenser," Int. Commun. Heat Mass Transfer, **15**, pp. 257–268.

[21] Liao, N. S., and Wang, C. C., 1990, "Transient Response Characteristics of Two-Phase Condensing Flows," Int. J. Multiphase Flow, **16**, pp. 139–151.

[22] Wang, C. C., and Liao, N. S., 1989, "Transient Response of a Double-Pipe Condenser to Change of Coolant Flowrate," Int. Commun. Heat Mass Transfer, **16**, pp. 325–334.

[23] Patankar, S. V., 1980, *Numerical Heat Transfer and Fluid Flow*, Hemisphere, Washington, D.C.

[24] Garimella, S., Killion, J. D., and Coleman, J. W., 2002, "An Experimentally Validated Model for Two-Phase Pressure Drop in the Intermittent Flow Regime for Circular Microchannels," J. Fluids Eng., **124**, pp. 205–214.

[25] Garimella, S., Killion, J. D., and Coleman, J. W., 2003, "An Experimentally Validated Model for Two-Phase Pressure Drop in the Intermittent Flow Regime for Non-Circular Microchannels," J. Fluids Eng., **125**, pp. 887–894.

[26] Phan, L., and Narain, A., 2007, "Non-Linear Stability of the Classical Nusselt Problem of Film Condensation and Wave Effects," ASME J. Appl. Mech., **74**, pp. 279–290.

[27] Lu, Q., and Suryanarayana, N. V., 1995, "Condensation of a Vapor Flowing Inside a Horizontal Rectangular Duct," J. Heat Transfer, **117**, pp. 418–424.

[28] Nusselt, W., 1916, "Die Oberflächenkondesation des Wasserdampfes," Z. Ver. Deut. Ing., **60**(27), pp. 541–546.

[29] Palen, J. W., Kistler, R. S., and Frank, Y. Z., 1993, "What We Still Don't Know About Condensation in Tubes," in *Condensation and Condenser Design*, J. Taborek, J. Rose, and I. Tanasawa, eds., United Engineering Trustees, Inc. for Engineering Foundation and ASME, New York, pp. 19–53.

[30] Ng, T. N., 2006, "Development and Calibration of a Fluorescence and Fiber-Optics Based Real-Time Thickness Sensor for Dynamic Liquid Films," Ph.D thesis, MEEM, Michigan Technological University.

[31] Narain, A., Kurita, J. H., Kivisalu, M., Siemionko, A., Kulkarni, S., Ng., T., Kim, N., and Phan, L., 2007, "Internal Condensing Flows Inside a Vertical Pipe—Experimental/Computational Investigations of the Effects of Specified and Unspecified (Free) Exit Conditions at Exit," technical Report, available at http://www.me.mtu.edu/~narain/narainpublications1.htm.

[32] Siemionko, A., 2006, "Design, Fabrication, and Operation of a System to Control FC-72 Condensation Inside a Vertical Tube," Ph.D thesis, Chem. Eng. Michigan Technological University.

[33] Kurita, J. H., 2006, "Experimental Investigation of Fully Condensing Downward Vapor Flows in a Vertical Tube—Unspecified (Free) Exit Condition Cases," M.S. thesis, MEEM, Michigan Technological University.

[34] Parratt, L. G., 1961, *Probability and Experimental Errors in Science: An Elementary Survey*, Wiley, New York.

[35] Carey, V. P., 1992, *Liquid-Vapor Phase-Change Phenomena*, Series in Chemical and Mechanical Engineering, Hemisphere, New York.

Quantitative Salt-Water Modeling of Fire-Induced Flows for Convective Heat Transfer Model Development

Xiaobo Yao

André W. Marshall[1]
e-mail: awmarsh@eng.umd.edu

Department of Fire Protection Engineering,
University of Maryland,
College Park, MD, 20742-3031

This research provides a detailed analysis of convective heat transfer in ceiling jets by using a quantitative salt-water modeling technique. The methodology of quantitative salt-water modeling builds on the analogy between salt-water flow and fire induced flow, which has been successfully used in the qualitative analysis of fires. Planar laser induced fluorescence and laser doppler velocimetry have been implemented to measure the dimensionless density difference and velocity in salt-water plumes. The quantitative salt-water modeling technique has been validated through comparisons of appropriately scaled salt-water measurements, fire measurements, and theory. This analogy has been exploited to develop an engineering heat transfer model for predicting heat transfer in impinging fire plumes using salt-water measurements along with the adiabatic wall modeling concept. Combining quantitative salt-water modeling and adiabatic wall modeling concepts introduces new opportunities for studying heat transfer issues in basic and complex fire induced flow configurations. [DOI: 10.1115/1.2754943]

Keywords: fire induced flow, salt-water model, ceiling jet, heat transfer

1 Introduction

The impinging plume is an inevitable flow configuration generated during enclosure fires, such as those occurring in warehouses, hotels, ships, etc. Plumes formed in these fires impinge on ceilings and transport hot toxic fire gases along the ceiling and throughout the enclosure. The interaction of the fire plume with the ceiling plays a major role in critical physical processes of engineering relevance including smoke dispersion, important in toxicity and detection, and heat loading, important in fire-structure interaction and flame spread. The intractable fire environment and diagnostic limitations make it difficult to explore the details of turbulent transport near the ceiling.

Alternatively, salt-water modeling experiments have been used extensively to provide qualitative insight into fire induced flow behavior [1–4]. More recently, quantitative salt-water modeling experiments have shown impressive agreement with real fire induced flow measurements in previous studies [5–12]. This technique has proven to be a useful tool for high fidelity measurement of fire induced flow dynamics in a well controlled, economic way. Generally, salt-water modeling is only able to simulate a fire scenario without consideration of the heat transfer effects. In this study, the quantitative salt-water technique is applied to establish an engineering adiabatic wall heat transfer model, which will be able to predict the convective heat transfer rate from the hot ceiling layer to the ceiling surface.

1.1 Impinging Plume.

The impinging plume can be separated into three regions defined as the plume region (i), the turning region (ii), and the ceiling jet region (iii), as illustrated in Fig. 1. The flow behavior in this configuration is significantly more complicated than in the unconfined fire plume. A number of theoretical and experimental fire studies have been performed to characterize the transport dynamics in the impinging plume configuration. Most notably, Alpert [13] performed an analytical and experimental study developing the theory and associated scaling laws for fire induced ceiling jets. His analysis successfully predicted the maximum temperature distributions in ceiling jets and is widely used in hazard analysis. Based on his analysis, he provided relationships for dimensionless ceiling layer thickness, velocity, and temperature, which compares favorably with measurements. In fact, his analysis revealed that these flow quantities are relatively insensitive to geometric scale. Alpert [13] suggested that credible small-scale fire experiments could be conducted at ceiling heights down to 0.6 m.

Motevalli and Marks [14] conducted small-scale experiments of kinematic and thermal ceiling jet behavior under a heavily insulated ceiling, which generally compared favorably with other ceiling jet data and analysis for $\mathbf{x}_1/H<2$. The velocity and temperature measurements were obtained for unconfined ceiling jets under transient and steady-state conditions. Small fires of 0.5–2.0 kW were produced with a premixed methane-air burner. These measurements represented one of the most detailed studies of unconfined ceiling jets and were in general agreement with large scale data. However, no measurements or analysis of the convective heat transfer rate q'' were performed in this investigation because of the intended adiabatic ceiling boundary condition.

Convective heat transfer from the ceiling jet to the ceiling surface has been studied by Veldman et al. [15]. They conducted experiments to investigate the axisymmetric heat transfer from small-scale fires (1.17 kW and 1.53 kW) under the impinging plume condition. An empirical correlation involving the energy release rate $\dot{Q}$ and ceiling height H was found to correlate measurements of the adiabatic wall temperature and its radial variation in the range of $0\leq\mathbf{x}_1/H\leq 0.7$. A similar correlation for estimating the ceiling heat transfer coefficient h was confirmed by the experimental results. However, their study was limited by the absence of any velocity measurements in both plume and ceiling jet configurations. You and Faeth [16] also conducted a study on heat transfer from an impinging fire plume to a horizontal ceiling. Their measurements were compared with predictions of both differential and integral models where $\mathbf{x}_1/H<1.7$. The integral

---

[1] Corresponding author.

Contributed by the Heat Transfer Division of ASME for publication in the JOURNAL OF HEAT TRANSFER. Manuscript received July 2, 2006; final manuscript received February 23, 2007. Review conducted by Bengt Sunden.

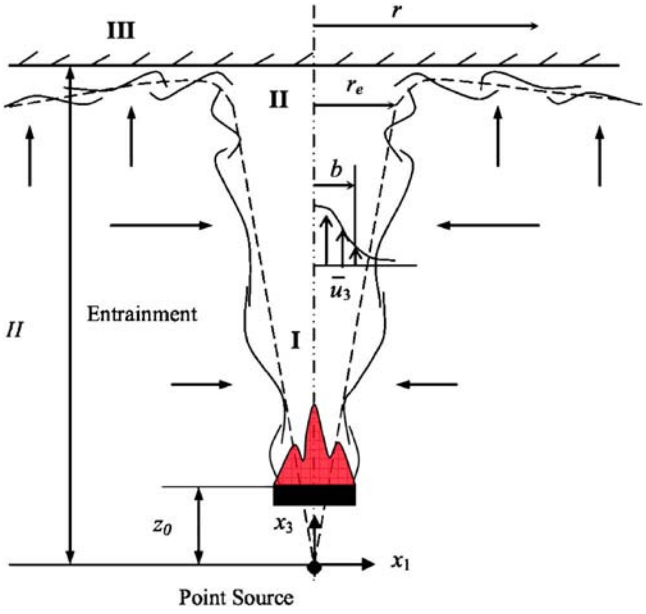

Fig. 1 Schematic of plume and ceiling jet flow for an unconfined ceiling: I, plume region; II, turning region; and III, ceiling jet region

model provided a reasonable prediction of flow properties and ceiling heat fluxes. Their results indicate that entrainment dominates the flow near the ceiling and that wall friction only has a secondary effect on the flow behavior.

Cooper [17–19] developed a heat transfer analysis by using an adiabatic ceiling surface temperature T_{ad} as the reference temperature in Newton's law of cooling. This reference temperature is determined from surface temperature measurements in adiabatic experiments taken at the same conditions as the ceiling heat transfer conditions of interest. The adiabatic ceiling surface temperature helps to remove the ambiguity of selecting an appropriate reference flow temperature to use in heat transfer configurations where there are temperature variations near the surface. By analyzing previous researchers' experimental data, Cooper, [17] similar to Veldman et al., [15] provided correlations for T_{ad} distributions along the ceiling [15,20]. Correlations of the heat transfer coefficient in the turning region and the ceiling jet region of the plume are also provided. Convective heat transfer from the ceiling jet to the ceiling surface has been estimated using correlations of T_{ad} and h in the range of $0 \leq \mathbf{x}_1/H \leq 2.2$.

These fire studies have provided the necessary understanding to predict some of the general transport behavior in fires based on empirical correlations. The results of these investigations have advanced the understanding of fire phenomena and improved the design of fire protection systems. However, detailed measurements in well controlled experiments are required to advance model development. In particular, characterizations of the velocity field in fire plume configurations are notably absent.

1.2 Salt-Water Modeling. The salt-water modeling technique has been used in the fire community primarily as a qualitative tool to explore smoke dispersion in complex geometries [1–4]. Kelly [5] successfully employed this technique quantitatively to determine front arrival times in a multicompartment enclosure. He then compared his measurements with fire dynamic simulator (FDS) simulations. Sangras and Faeth [6] and later Diez et al. [7] used salt-water modeling for a more fundamental investigation. They analyzed the temporal development of round turbulent nonbuoyant starting jets and buoyant starting plumes and thermals theoretically and experimentally. The experiments conducted for the previously mentioned studies involved mixing saline solution with a dye tracer. The tracer allows for visualization of the dispersion dynamics and front movement within transparent enclosures. Some limited quantitative information is available through scaled front arrival times; however, the concentration within the flow cannot be measured.

More recent studies have combined salt-water modeling with planar laser induced fluorescence (PLIF) for measurement of concentration in the flow. Clement [8] used this method for validating the hydrodynamic model within the FDS CFD code. Jankiewicz [9] combined salt-water modeling and PLIF to explore the applicability of these techniques to the prediction of detector response times. He found excellent agreement between dimensionless front arrival times in the salt-water model and the full-scale fire experiments. More impressive quantitative agreement between PLIF salt-water measurements and fire plume measurements has been demonstrated by Marshall and co-workers [10–12] in the unconfined plume and impinging plume configurations.

1.3 Objective. The purpose of this research is to establish a methodology for engineering heat transfer model development in fires using the quantitative salt-water modeling technique. This heat transfer model is developed using salt-water measurements and scaling laws, combined with Newton's law of cooling and the adiabatic wall temperature concept. This model is used to predict the convective heat flux distribution along the ceiling simply from the fire size and ceiling height. Furthermore, the performance of this salt-water based model is evaluated through comparison with actual fire data and earlier models.

2 Experimental Methodology

The quantitative salt-water modeling technique used to characterize turbulent transport and the associated heat transfer near the ceiling of an impinging fire plume requires buoyant scale analysis, advanced laser diagnostics, and buoyancy driven flow experiments. The fundamental scaling theory and the fire/salt-water modeling analogy used in this study are introduced in this section along with some experimental details. Furthermore, the basis of the engineering heat transfer model developed in this study and its connection to the salt-water measurements is presented.

2.1 Fire/Salt-Water Analogy. In salt-water modeling, plumes are created by careful introduction of salt water into fresh water. The salt-water dispersion closely simulates the dispersion of hot exhaust gases (smoke) in a fire plume. For the purpose of analysis, the salt concentration downstream of the source and the exhaust gas temperature downstream of the flame zone in a fire can be thought to behave like passive scalars and are transported by similar turbulent convective and diffusive processes. Proper scaling of the fire and salt-water flows allows for direct comparison of fire measurements and salt-water measurements. The dimensionless mass and momentum transport equations are analogous in the fire and salt-water configurations. Furthermore, the dimensionless energy equation in the fire is analogous to the dimensionless salt mass species equation in the salt-water model. For example, in the fire, the dimensionless energy conservation equation can be expressed as

$$\frac{\partial \theta_T^*}{\partial t^*} + u_i^* \frac{\partial \theta_T^*}{\partial \mathbf{x}_i^*} = \frac{1}{(\mathrm{Gr}_{\mathrm{source}}^{\mathrm{fire}})^{1/3}\,\mathrm{Pr}} \frac{\partial^2 \theta_T^*}{\partial \mathbf{x}_i^* \partial \mathbf{x}_i^*} + \dot{q}^* \tag{1}$$

In the salt-water model, the dimensionless salt mass species equation is given by

$$\frac{\partial \theta_{\mathrm{salt}}^*}{\partial t^*} + u_i^* \frac{\partial \theta_{\mathrm{salt}}^*}{\partial \mathbf{x}_i^*} = \frac{1}{(\mathrm{Gr}_{\mathrm{source}}^{\mathrm{sw}})^{1/3}\,\mathrm{Sc}} \frac{\partial^2 \theta_{\mathrm{salt}}^*}{\partial \mathbf{x}_i^* \partial \mathbf{x}_i^*} + \dot{w}_{\mathrm{salt}}^* \tag{2}$$

Unfortunately, it is impractical to match the Gr between the fire and salt-water flows at reasonable scales for salt-water experiments. The difference in molecular properties between fire gases and water also results in significantly different Pr and Sc. The salt-water model thus behaves like a somewhat distorted model.

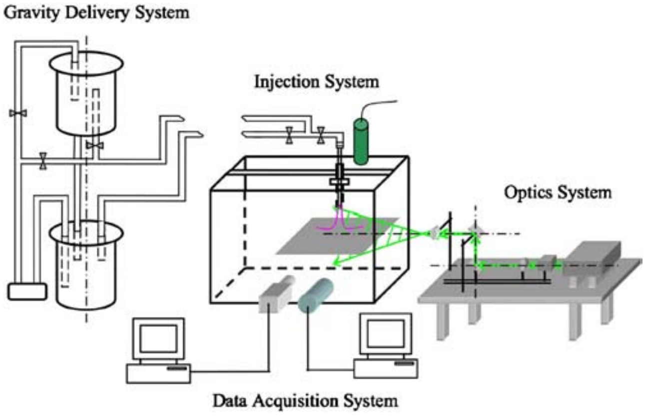

Fig. 2 Quantitative salt-water modeling facility with PLIF/LDV diagnostics; impinging plume configuration shown

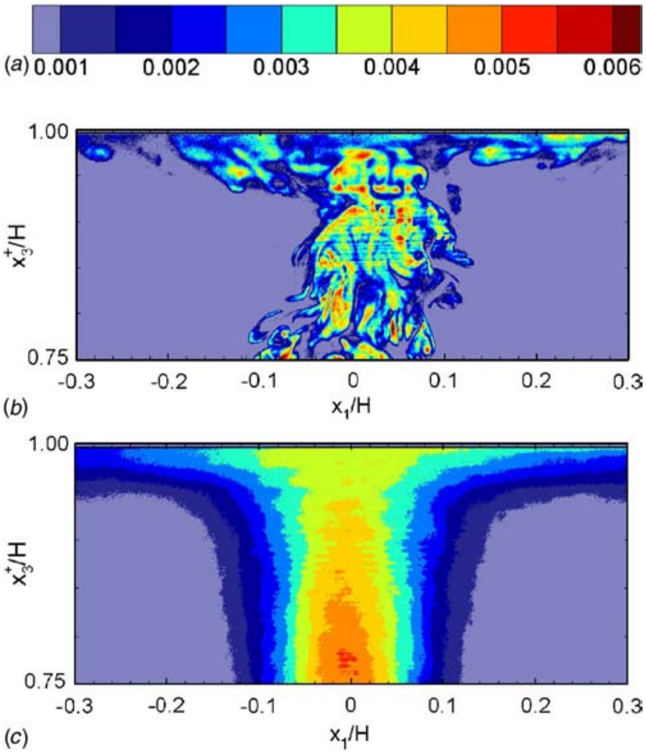

Fig. 3 (*a*) Instantaneous and (*b*) mean PLIF images of dimensionless density difference θ_{sw}

For turbulent flows with associated large Gr, the diffusive terms are small "not close" to the wall and the differences in Gr, Pr, and Sc can be neglected. However, very close to the wall, the velocity gradients become significant and the diffusive terms in the momentum equation may not be negligible. At the same time, previous studies have suggested that frictional or diffusive effects near the ceiling are secondary to entrainment effects potentially making these scaling discrepancies negligible [13]. Subsequent comparisons provided in this study between salt-water and fire measurements will provide insight into the impact of these scaling discrepancies on the fidelity of the analogy. It should also be noted that the impermeable boundary condition results in zero mass fraction gradients at the wall in the salt-water configuration and is analogous to the adiabatic boundary condition in the fire configuration.

2.2 Experimental Facility. As presented in Fig. 2, a large capacity tank ($1.7\times0.9\times1.2$ m^3) was filled with fresh water to provide an ambient environment for the salt-water plume experiments. The saline solution coming from the flow meter was injected into the fresh water through a stainless steel tube with 5.6 mm inside diameter. This source was supplied by a gravity feed system to avoid pump-induced fluctuations in the salt-water plume. An acrylic plate ($610\times610\times12.7$ mm^3) was used as the ceiling in this study. In the PLIF experiments, the plate is painted black to reduce the laser light reflections. On the other hand, a transparent acrylic ceiling is used in velocity measurements to improve the laser Doppler velocimetry (LDV) signal to noise ratio by minimizing scattered light from the solid boundary. Valid measurements could be obtained within about 0.8 mm ($\sim0.004H$) of the ceiling in the PLIF measurements and within about 0.4 mm ($\sim0.002H$) in the LDV measurements.

A 500 mW argon-ion laser was used as the light source in the PLIF measurements. The focusing optics consists of a spatial filter and a cylindrical lens producing a light sheet about 0.5 mm thick. This light sheet was positioned to bisect the plume exciting the fluorescent dye tracer (Rhodamine 6G) in the salt water and making the flow visible. Instantaneous and mean images of the impinging plume are shown in Fig. 3. These images provide a large amount of quantitative concentration data in the flow. Profiles in specific regions of interest (e.g., along the centerline or ceiling) are easily extracted from these images, as shown in Fig. 4(*a*). A Canon EOS D30 digital camera is used in the PLIF impinging plume experiments with a Canon 50 mm ($f/1.4$) lens. It should be noted that a color image is captured by the Canon camera. This color image is converted to a black/white image using a common relationship between red, green, and blue (RGB) luminance and gray level, GL (i.e., GL=0.3red+0.59green+0.11blue). Calibration experiments verified that this conversion method provided the expected linear correlation between GL intensity and dye concentration. The probe volume in the LDV measurements is generated with a SUREPOINT diode laser probe (model 6810, TSI, Inc.) operated in backscatter mode. The laser has a maximum total power of 30 mW and delivers light at 780 nm. The major axis of the beam crossing is 222 μm and the minor axis of the beam crossing is 108 μm when a 350 mm focal length lens is used (the beam crossing angle is 3.97 deg). Additional experimental details can be found in Refs. [12,21].

2.3 Preliminary Validation. Before the salt-water modeling technique was applied to more challenging configurations, it was validated in a canonical unconfined plume geometry. The detailed initial conditions of each experimental case are listed in Table 1. Various buoyancy sources are applied in the PLIF and LDV experiments to validate the scaling theory. Theoretical solutions of the plume characteristics in this configuration and extensive experimental data in actual fires are available for validation of the salt-water modeling measurements and the associated scaling theory [6–10].

It is well known that the centerline mean dimensionless density difference $\bar{\theta}_c$ of the fire plume obeys the $(-5/3)$ power law decay and the centerline mean velocity $(\bar{u}_3)_c$ obeys the $(-1/3)$ power law decay based on the point source theory. Figure 4(*a*) shows excellent agreement between centerline dimensionless density differences taken from the salt-water PLIF measurements, real fire data, and point source plume theory. McCaffrey's plume measurements provided in Fig. 4(*a*) also show the relative strength of the salt-water plume compared to fire plumes [22]. The dimensionless density difference, $\theta_{sw}=\beta_{sw}Y_{salt}$, for salt water is much smaller than $\theta_T=\beta_T\Delta T$ for fire, indicating that the salt-water plumes are relatively weak compared to fire plumes. Figure 4(*b*) shows excellent agreement between the velocity data taken from the LDV measurements and the point source plume theory. Similar to the PLIF salt-water measurements, McCaffrey's plume velocity measurements are also plotted here to emphasize the relative strength

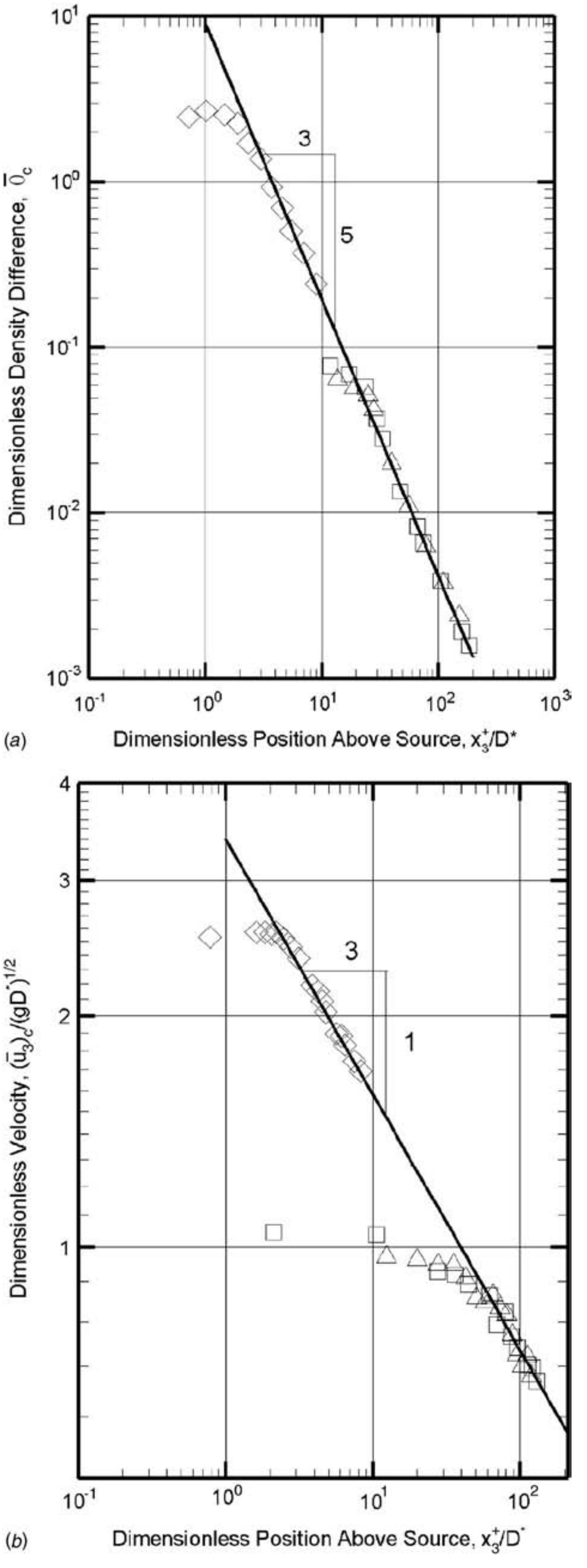

Fig. 4 Dimensionless characteristic density along plume centerline: (*a*) mean profile, $\bar{\theta}_c$. (*b*) Mean profile, $(\bar{u}_3)_c/(gD^*)^{1/2}$; (◇) McCaffrey's plume [22] salt-water model. (△) case 1; (□) case 2; (○) case 3: (—) theory [23].

of salt-water plumes compared to fire plumes [22]. The dimensionless velocity in the salt-water plume is much smaller than that in the real fire plumes, which also demonstrates that the salt water simulates a weak plume. Intensities of fluctuation of the dimensionless density difference and streamwise velocity were also measured with these diagnostics. Although no comparisons were made with turbulence measurements from fires, the salt-water turbulence measurements attained a fully developed turbulent state having values consistent with plume measurements made in weak thermal plumes [11,21,23,24]. This comparison is appropriate because the model is based on and limited to relatively small fires generating weak plumes at the ceiling.

2.4 Engineering Heat Transfer Methodology. Newton's law of cooling provides the heat transfer rate to the ceiling in terms of a convective heat transfer coefficient and the temperature difference between the surface and some characteristic temperature of the fluid, usually the freestream temperature. However, in many complex flow configurations, the fluid temperature is not well defined. A reference temperature is used to calculate the heat transfer. The convective heat transfer is given by

$$q'' = h\Delta T = h(T_{\mathrm{ref}} - T_w) \tag{3}$$

where T_w is the local wall temperature and T_{ref} is the reference temperature. In the limiting case where the wall is perfectly insulated ($q''=0$), it is easy to see that the adiabatic surface temperature T_{ad} provides a reasonable reference temperature. Thus, Eq. (3) is revised as

$$q'' = h(T_{\mathrm{ad}} - T_w) \tag{4}$$

Goldstein et al. [25] have adopted the impingement cooling/heating effectiveness to express the adiabatic wall temperature in dimensionless form. In this study, the same concept has been used with some modification. The effectiveness is defined by

$$\eta = \frac{T_{\mathrm{ad}} - T_0}{T_P - T_0} \tag{5}$$

where T_P is the temperature of the plume at the impinging point and T_0 is the ambient temperature. After substitution of Eq. (5) into Eq. (4), the convective heat transfer rate can be expressed as

$$\dot{q}'' = h[(T_P - T_w) - (1 - \eta)(T_P - T_0)] \tag{6}$$

The salt-water measurements will be used to establish scaling laws for the two important quantities in Eq. (6), the convective heat transfer coefficient h and the effectiveness η, in terms of the radial ceiling location, $\mathbf{x}_1^*$, and global parameters (e.g., H, Pr, and Re_H). A flowchart of the adiabatic wall heat transfer model is provided in Fig. 5. First, PLIF salt-water experiments are conducted to measure the salt mass fraction distributions in the impinging salt-water plume. As mentioned previously, the impermeable ceiling surface in the salt-water model is analogous to an adiabatic wall boundary condition in the actual fire induced flow. Thus, the measured salt-water mass fraction at the ceiling corresponds to the analogous adiabatic surface temperature T_{ad}. A source independent expression for the "adiabatic" effectiveness is given by

$$\eta = \frac{\theta^*_{\mathrm{ad}}(\mathbf{x}^*_1)}{\theta^*_P} \tag{7}$$

where

$$\begin{aligned}\theta^*_{\mathrm{ad}}(\mathbf{x}^*_1) = \theta^*(\mathbf{x}^*_1, \mathbf{x}^*_3 = 1) &= \beta_{\mathrm{sw}}[Y_{\mathrm{salt}}(\mathbf{x}^*_1)](m^*)^{-2/3} \\ &= \beta_T[T_{\mathrm{ad}}(\mathbf{x}^*_1) - T_0](Q^*)^{-2/3}\end{aligned}$$

and

$$\theta^*_P = \theta^*_{\mathrm{ad}}(\mathbf{x}^*_1 = 0)$$

Previous experiments have shown that $\theta^*_P = 11.7$ at the stagnation point [11,21]. The scaling law for this effectiveness is determined

Table 1 Initial experimental conditions in salt water modeling measurements

	Case 1	Case 2	Case 3	Case 4	Case 5
			Experimental configurations and measurements		
Flow configuration	Unconfined plume	Unconfined plume	Unconfined plume	Impinging plume	Impinging plume
Ceiling height H_c (mm)	N/A	N/A	N/A	206	235
Injector diameter D (mm)	5.6	5.6	5.6	5.6	5.6
Measurements	PLIF/LDV	PLIF	LDV	PLIF/LDV	LDV
			Initial flow conditions of salt-water plume		
Volume flow rate $\dot{V}$ (ml/min)	110	165	110	110	110
Salt mass fraction Y_{salt}	0.13	0.13	0.10	0.13	0.10
Injection velocity U_{inj} (mm/s)	74	112	74	74	74

from the analysis of the salt-water PLIF measurements. On the other hand, h used in this study comes from Reynolds analogy where the Stanton number describing wall heat flux is given as

$$\text{St} = \frac{h}{\rho c_p U} = \frac{C_f}{2}\text{Pr}^{-2/3} \tag{8}$$

where ρ is the density, c_p is the specific heat, and U is a characteristic velocity. This quantity is related to viscous wall interactions determined by the friction factor $C_f = \tau_w(\rho U^2/2)^{-1}$. LDV salt-water measurements provide the ability to characterize the velocity near the ceiling and the corresponding wall shear stress τ_w required to determine C_f and ultimately h through Reynolds analogy. The heat transfer coefficient h can also be expressed as functions of $\mathbf{x}_1^*$, H, Re_H, and Pr. Substitution of scaling laws for η and h into Eq. (6) results in an expression for the convective heat transfer rate q'' where

$$q'' = \mathcal{H}(\mathbf{x}_1^*, H, \text{Re}_H, \text{Pr}, T_w) \tag{9}$$

3 Results

A detailed discussion of the adiabatic wall heat transfer model for impinging fire plumes is provided in the following sections. Comparisons between this model and fire experiments are also presented to evaluate the fidelity of the model.

3.1 Effectiveness. The effectiveness distribution from salt-water measurements along the radial coordinate is provided in Fig. 6 along with measurements from actual fire data. The experimental data are reduced to a best-fit function similar in form to the equation used by Veldman et al. [15]

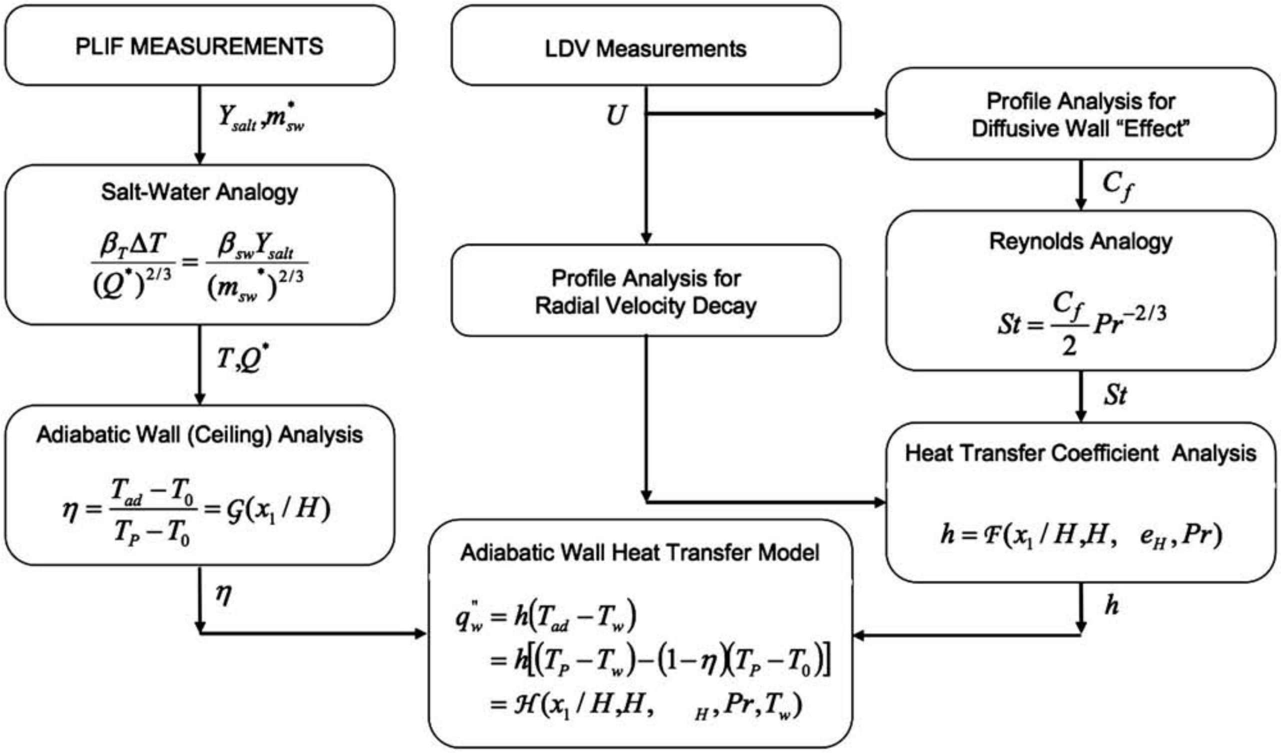

Fig. 5 Adiabatic wall heat transfer model

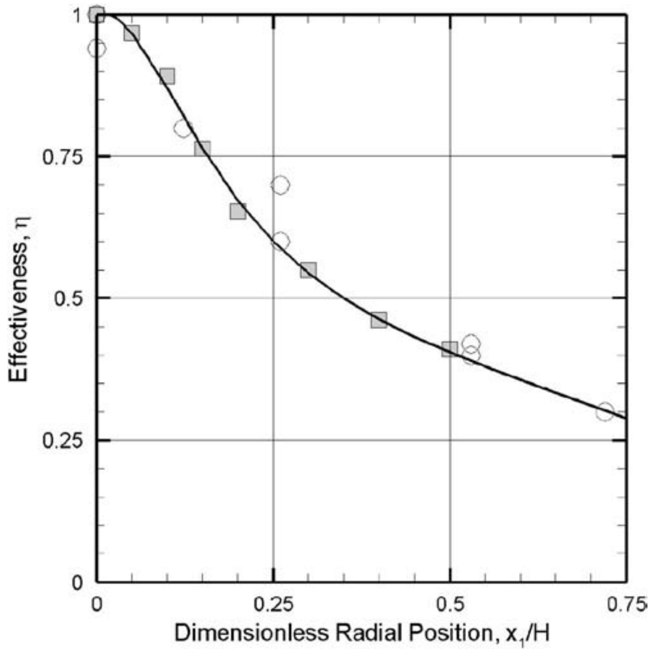

Fig. 6 Distribution of effectiveness η along ceiling: (■) Salt water measurements for case 1; (○) Veldman [15]; (—) curve of Eq. (10).

$$\eta = \frac{-6.67(\mathbf{x}_1^*)^4 + 10.69(\mathbf{x}_1^*)^2 + 1.01}{(\mathbf{x}_1^*)^4 + 27.93(\mathbf{x}_1^*)^2 + 1} \tag{10}$$

where the coefficients are determined from the regression analysis of the salt-water measurements. Figure 6 clearly shows that the expression in Eq. (10) predicts the effectiveness very well. It should be noted that the salt-water measurements are only available from $0 \leqslant \mathbf{x}_1/H \leqslant 0.5$. Beyond this point, the salt-water flow begins to laminarize, making comparisons with fire experiments inappropriate. However, this correlation predicts the fire data well beyond this point. It should be noted that Eq. (10) is applicable in both the impinging region ($\mathbf{x}_1/H < 0.2$) and the ceiling jet region. The expression included in Eq. (10) is completely general for the impinging plume configuration and does not depend on fire size or ceiling height.

3.2 Convective Heat Transfer Coefficient.

Reynolds analogy is used to establish a general expression for h from salt-water model results. Based on the definition of Stanton number, Eq. (8) can be rearranged to yield h in terms of Re_x and Pr as

$$\mathrm{Nu} = \frac{h}{k/\mathbf{x}_1} = \frac{C_f}{2}\mathrm{Re}_x \mathrm{Pr}^{1/3} \tag{11}$$

3.2.1 Friction Wall Interaction, C_f. The friction factor C_f is the key quantity for establishing the scaling law for the heat transfer coefficient. Outside the turning region, a wall jet is formed along the ceiling. This wall jet behavior provides a theoretical basis for calculation of the friction factor [26] directly from velocity measurements along the ceiling. It is reasonable to assume similarity for the mean velocity $\bar{u}_1$ in the ceiling jet [12]. A schematic of the velocity similarity profile in the ceiling jet is shown in Fig. 7, where $\bar{u}_1$ is the temporal mean velocity, u_1' and u_3' are the corresponding fluctuating components of u_1 and u_3, δ_1 is the wall normal location of maximum velocity, and δ_2 is the wall normal location of zero shear stress. The similarity transform variable is defined as $\chi = \mathbf{x}_3/\delta_1$, where $\mathbf{x}_3$ is the wall normal distance from the ceiling and the similarity function $f(\chi)$ is given by $\bar{u}_1/(\bar{u}_1)_{\max}$. Integration across the ceiling jet must be performed in order to obtain the wall shear stress required for determining C_f. Kruka and Eskinazi [26] evaluated the friction coefficient C_f based on the velocity similarity function in the wall boundary layer and determined that

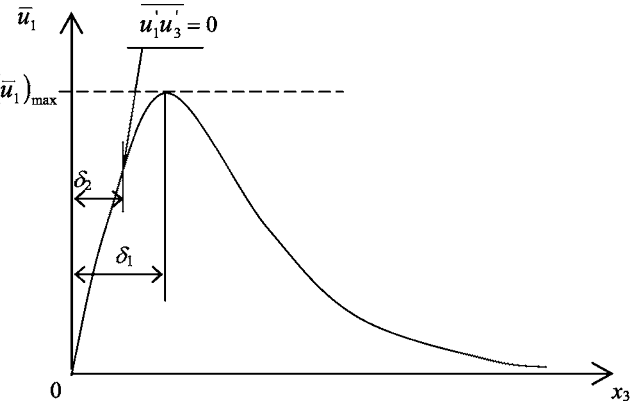

Fig. 7 Velocity similarity profile in the ceiling jet layer

$$C_f = 2c_2[\alpha\psi + (\phi - \psi)(1 - \alpha)] \tag{12}$$

where ϕ and ψ are integrals of the similarity function,

$$\phi = f(\chi_2)\int_0^{\chi_2} f(\xi)d\xi \tag{13}$$

$$\psi = \int_0^{\chi_2} f^2(\xi)d\xi \tag{14}$$

and $\chi_2 = \delta_2/\delta_1$ is the zero shear stress position where $\overline{u_1'u_3'} = 0$. A simple exponential function

$$f(\chi) = \bar{u}_1/(\bar{u}_1)_{\max} = 1.03\chi^{1/n} \tag{15}$$

has been proposed by Patel [27] and Schwarz and Cosart [28] and is also used in this study. The constant c_2 is the ceiling jet growth coefficient for δ_1 so that

$$\frac{\delta_1}{H} = c_2\mathbf{x}_1^* \tag{16}$$

and α is the power law exponent for the velocity decay along the ceiling

$$(\bar{u}_1)_{\max} = c_1 U(\mathbf{x}_1^*)^{-\alpha} \tag{17}$$

These profiles for f, δ_1, and $(\bar{u}_1)_{\max}$ are determined from the salt-water experimental data and provided in Fig. 8. Substitution of $f(\chi) = 1.03\chi^{1/5.707}$, $c_2 = 0.038$, and $\alpha = 0.878$ into Eq. (12) results in

$$C_f = 0.053\chi_2^{1.354} \tag{18}$$

Tailland and Mathieu [29] quantitatively predicted the length scale of $\chi_2 = \delta_2/\delta_1 = 0.55$ in the turbulent boundary layer of a wall jet. Since the salt-water plume is fully turbulent in the ceiling jet layer, Tialland and Mathieu's prediction of χ_2 is applied in this study. Replacing $\chi_2 = 0.55$ in Eq. (18) yields a friction factor $C_f = 0.024$. Previous impinging jet studies have assumed that C_f changes very little in the ceiling layer and can be assumed to be constant [13,30]. The similarity analysis used in this salt-water study yields a similar result. Previous friction factor data of Alpert [13], Veldman et al. [15], and You and Faeth [16] are bounded by the prediction for $C_f = 0.02$ and $C_f = 0.04$. The friction factor measured from the salt-water modeling experiments falls within this bound.

3.2.2 Convective Heat Transfer Coefficient, h. As shown in Eq. (11), the local heat transfer coefficient is a function of local

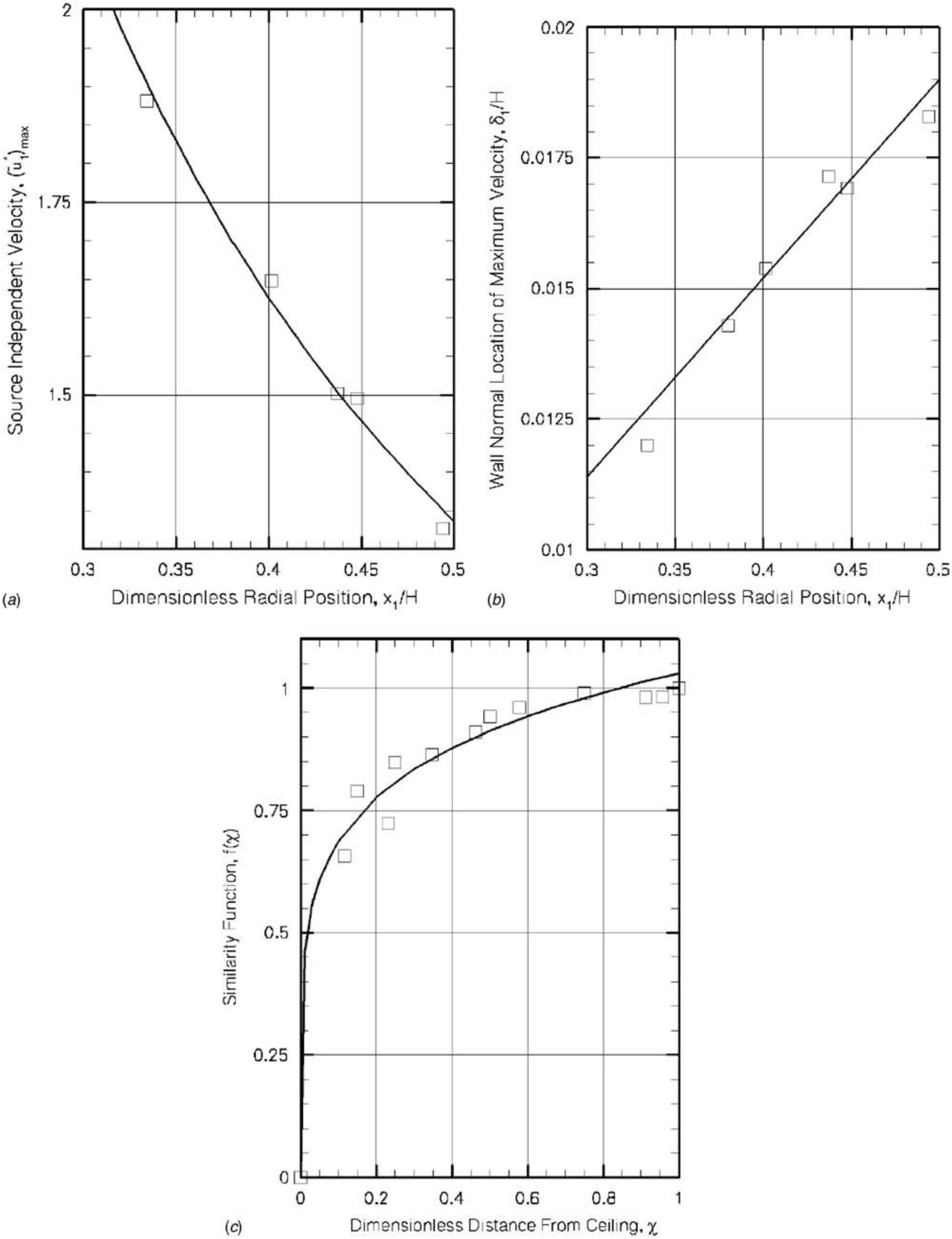

Fig. 8 Scaling laws of distribution of source independent velocity and maximum velocity position. (*a*) $(\vec{u}_1^*)_{max}$; (□) salt-water model; (—) curve of Eq. (17) with $c_1=0.727$, $\alpha=0.878$. (*b*) δ_1/H; (□) salt-water model; (—) curve of Eq. (16) with $c_2=0.038$. (*c*) Similarity function of $f(\chi)$ in boundary layer; (□) salt-water model; (—) curve of Eq. (15) with $n=5.707$.

Reynolds number Re_x. Applying Eq. (17) to the definition of Re_x, the local Reynolds number can be expressed in terms of the characteristic Reynolds number based on the ceiling height, $\mathrm{Re}_H = UH/\nu$, so that

$$\mathrm{Re}_x = c_1 \frac{U\mathbf{x}_1}{\nu}(\mathbf{x}_1^*)^{-\alpha} = c_1\,\mathrm{Re}_H(\mathbf{x}_1^*)^{1-\alpha} \tag{19}$$

This expression is easily coupled with the source based scaling by recognizing that $\mathrm{Re}_H=\mathrm{Gr}_H^{1/3}$ or $\mathrm{Re}_H=(g^{1/2}H^{3/2}/\nu)(Q^*)^{1/3}$. Substitution of Eq. (19) into Eq. (11) and using Pr=0.711 results in an expression for h in terms of Re_H, $\mathbf{x}_1^*$, and H,

$$\mathrm{Nu} = \frac{h}{k/H} = \mathcal{F}(\mathbf{x}_1^*, \mathrm{Re}_H) = 0.00779\,\mathrm{Re}_H(\mathbf{x}_1^*)^{-0.878} \tag{20}$$

Equation (20) has been developed from the salt-water modeling data in the range of $0.3 \leqslant \mathbf{x}_1^* \leqslant 0.5$; however, Eq. (20) should be valid as long as the ceiling jet remains turbulent (which occurs much later in higher Re_H fires).

In the current study, the convective heat transfer coefficient in the plume turning region is taken from impinging jet analysis. For a turbulent impinging jet, the stagnation point heat flux is given by $\mathrm{Nu} \sim \mathrm{Re}_D^{0.8}\,\mathrm{Pr}$ [31,32]. Recognizing that the cross-stream characteristic dimension for the plume is given by the plume radius $b \sim H$ (instead of D), a similar scaling law is used for the impinging plume with Re_H replacing Re_D. Following impinging jet analysis, the Nu along the ceiling can be expressed in terms of the stagnation point value and a radial distribution function:

$$\mathrm{Nu} = \frac{h}{k/H} = 0.711\,\mathrm{Re}_H^{0.8} f_1(\mathbf{x}_1^*, \mathrm{Re}_H) \tag{21}$$

A fourth order polynomial correlation is applied to predict the heat transfer coefficient in the turning region ($0 \leqslant \mathbf{x}_1^* \leqslant 0.2$), where $f_1(\mathbf{x}_1^*, \mathrm{Re}_H)$ is expressed as

$$f_1(\mathbf{x}_1^*, \mathrm{Re}_H) = 0.427 + (2.77\,\mathrm{Re}_H^{0.2} - 21.35)(\mathbf{x}_1^*)^2 - (40.89\,\mathrm{Re}_H^{0.2} - 266.88)(\mathbf{x}_1^*)^4 \tag{22}$$

This expression was derived from the regression analysis of experimental data of Veldman et al. [15]. The polynomial function provides a zero gradient for h at the stagnation point (local maximum) and matches the value and derivative of h at the turning region and ceiling jet interface (i.e., $\mathbf{x}_1/H=0.2$) given by Eq. (20).

The scaling law for the heat transfer coefficient h along the ceiling is then expressed as

$$\frac{h}{k/H} = \begin{cases} 0.711\,\mathrm{Re}_H^{0.8} f_1(\mathbf{x}_1^*, \mathrm{Re}_H) & 0 \leqslant \mathbf{x}_1^* \leqslant 0.2 \\ 0.00779\,\mathrm{Re}_H f_2(\mathbf{x}_1^*) & 0.2 \leqslant \mathbf{x}_1^* \leqslant 5 \end{cases} \tag{23}$$

where

$$f_2(\mathbf{x}_1^*) = (\mathbf{x}_1^*)^{-0.878} \text{ and } \mathrm{Re}_H = (g^{1/2}H^{3/2}/\nu)(Q^*)^{1/3}$$

It should be noted that since Re_H is the characteristic Reynolds number based on the characteristic velocity $U=(gH)^{1/2}(Q^*)^{1/3}$, the heat transfer coefficient is also a function of the dimensionless source strength Q^*. Comparisons of the dimensionless heat transfer coefficient, St=Nu/Re Pr, between Eq. (23) and the mean measurements of Veldman et al. [15] are provided in Fig. 9. Also shown in this figure are two theoretical curves obtained by Alpert [13]. It is worth mentioning that Alpert based h on a mean flow velocity of an assumed Gaussian velocity profile. The mean Gaussian velocity is $1/\sqrt{2}$ times the maximum velocity used in this study; therefore, Alpert's values of h [13] are divided by a factor of $\sqrt{2}$ for the purpose of comparison.

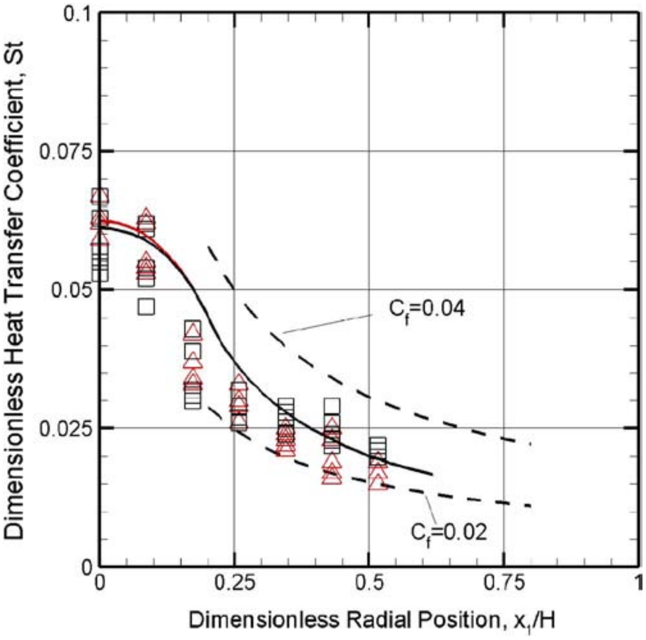

Fig. 9 Heat transfer coefficient along ceiling: (—) Eq. (23) curve for test 1 of Veldman et al. [15]. (—) Eq. (23) curve for test 2 of Veldman et al. C_f=0.024; (---), Alpert's correlation [13]; (■) experiments of Veldman et al. [15] for test 1, H=0.813 m, Q =1.17 kW. (△) experiments of Veldmann et al. [15] for test 2, H=0.584 m, Q=1.17 kW [8].

As shown in Fig. 9, the prediction of h from the salt-water modeling with C_f=0.024 agrees well with the mean measurements of Veldman et al. [15] in both tests and lies within the area bounded by Alpert's theoretical curves for C_f=0.02 and C_f =0.04 [13]. In the turning region, the correlation from Eq. (23) splits into two lines according to the fire configuration (Q^* and H or Re_H). This separation is caused by the different scaling laws for the impingement and ceiling jet regions. Equation (23) stated that $h \sim \mathrm{Re}_H$ in the ceiling layer causing the St predictions to collapse, while $h \sim \mathrm{Re}_H^{0.8}$ in the turning region resulting in slightly different St predictions for the two cases. The differences between the current model and experimental measurements are most apparent at the end of the turning region and beginning of the ceiling jet region, as shown in Fig. 9. The heat transfer coefficient is quite sensitive to small changes in C_f in this region, and additional salt-water data in this region may improve the estimate.

3.3 Adiabatic Wall Heat Transfer Model.

Substitution of Eqs. (10) and (23) into Eq. (6) results in an adiabatic wall heat transfer model

$$\dot{q}'' = h[(T_P - T_w) - (1-\eta)(T_P - T_0)] \tag{24}$$

where

$$\eta = \frac{-6.67(\mathbf{x}_1^*)^4 + 10.69(\mathbf{x}_1^*)^2 + 1.01}{(\mathbf{x}_1^*)^4 + 27.93(\mathbf{x}_1^*)^2 + 1} \qquad \leqslant \mathbf{x}_1^* \leqslant 5$$

$$\frac{h}{k/H} = \begin{cases} 0.711\,\mathrm{Re}_H^{0.8} f_1(\mathbf{x}_1^*, \mathrm{Re}_H) & 0 \leqslant \mathbf{x}_1^* \leqslant 0.2 \\ 0.00779\,\mathrm{Re}_H f_2(\mathbf{x}_1^*) & 0.2 \leqslant \mathbf{x}_1^* \leqslant 5 \end{cases}$$

$$f_1(\mathbf{x}_1^*, \mathrm{Re}_H) = 0.427 + (2.77\,\mathrm{Re}_H^{0.2} - 21.35)(\mathbf{x}_1^*)^2 - (40.89\,\mathrm{Re}_H^{0.2} - 266.88)(\mathbf{x}_1^*)^4$$

$$f_2(\mathbf{x}_1^*) = (\mathbf{x}_1^*)^{-0.878} \quad \mathrm{Re}_H = (g^{1/2}H^{3/2}/\nu)(Q^*)^{1/3} \quad \mathbf{x}_1^* = \mathbf{x}_1/H$$

Guidance is now provided concerning the application of this model. The salt-water model produces weak plumes with small density differences. The salt-water measurements that establish the basis for this model thus limit its applicability to weak fire plumes. This plumelike behavior is assumed at the ceiling, and therefore the fire must be small with respect to the ceiling height. The authors recommend that the model defined in the current study be used for fires having $H_f/H<0.15$.

Scale should also be considered when determining the radial extent for model predictions. The model has been validated out to $\mathbf{x}_1^*=0.7$ using relatively small laboratory fire configurations [15,16]. These small laboratory fires are only weakly turbulent and laminarization may occur at relatively early radial locations, thus limiting the radial extent of relevant data. The radial location where laminarization occurs will depend on Re_H. However, a criterion for determining this location is not yet available. In the absence of laminarization, this model should be valid up to $\mathbf{x}_1^*=5$. Beyond this point, the Richardson number is larger than unity and downstream effects, impossible to include in this model, can alter the ceiling layer behavior [13].

The energy release rate $\dot{Q}$ used in this model is the convective energy release rate $\dot{Q}_c$. In actual fires, the energy released from the source is convected upward $\dot{Q}_c$ and radiated outward $\dot{Q}_r$. Under certain conditions, the radiation heat loss from the flame can be neglected (i.e., if the flame height H_f is relatively small). For instance, in the experiments of Veldman et al. [15], a burner providing a compact flame was used and $\dot{Q}_c=\dot{Q}$. In most fires, flame radiation is significant and the convective energy flux is only a fraction of the total energy release. For example, it was estimated that $\dot{Q}_c\approx 0.8\dot{Q}$ in You and Faeth's experiments [16]. Finally, it should also be noted that the stagnation point θ is defined based on the ceiling height from the virtual point source H. Neglecting the virtual origin will either overpredict θ_P if $(\mathbf{x}_3)_0<0$ or underpredict θ_P if $(\mathbf{x}_3)_0>0$.

Comparisons between the current adiabatic wall heat transfer model and You and Faeth's [16] weak fire plume experiments are provided in Fig. 10. The experimental configurations in You and Faeth's experiments [16] are $\dot{Q}=0.385$ kW, $H_f/H_c=0.15$ and $\dot{Q}=0.24$ kW, $H_f/H_c=0.008$, respectively. The distance between the burner and ceiling is 400 mm. The ceiling temperature is nearly constant and equal to the ambient temperature during experiments. The virtual origins of these experiments are $(\mathbf{x}_3)_0=-17$ mm for case $\dot{Q}=0.385$ kW and $(\mathbf{x}_3)_0=-24$ mm for case $\dot{Q}=0.24$ kW based on Hasemi and Tokunaga's correlations [33]. The thermal radiation is not quantitatively measured but estimated to range from 0% to 20% of the total heat release rate. Convective heat sources are used in the model according to these estimates (i.e., $\dot{Q}_c=\dot{Q}$ and $\dot{Q}_c=0.8\dot{Q}$). As shown in Fig. 10, the estimate for radiation losses significantly affects the model predictions. Figure 10 clearly shows that the convective heat transfer rate is overestimated by neglecting the thermal radiation heat loss. The agreement between the current heat transfer model and measurements is improved when using the upper estimate of $\dot{Q}_c=0.8\dot{Q}$, especially in the turning region. Based on our model comparisons, the differences in the turning region indicate that the thermal radiation heat loss may be even larger than the estimated 20% of the total heat release rate. In fact, Hamins et al. [34] estimate that the radiation heat losses are closer to 30% even for relatively small laboratory scale pool fires.

The adiabatic wall heat transfer model can also be applied to predict the transient heat transfer to the ceiling. Veldman et al. [35] conducted transient experiments in the impinging plume configuration where fixed source strength resulted in ceiling temperature rise. Comparison of the model predictions and the experiments of Veldman et al. [15] are provided in Fig. 10(*b*). The fire strength of test 1 of Veldman et al. [15] is $\dot{Q}=1.17$ kW and the distance between the burner and ceiling is 813 mm. In the measurements of Veldman et al. [15], the flame height of the burner is very small (i.e., $H_f\sim 6$ mm) and the thermal radiation is negligible. The virtual origin of this experimental condition is $(\mathbf{x}_3)_0=-110$ mm, which was extracted from their plume centerline temperature measurements using Heskestad's method [35]. Relatively good agreement has been achieved between the model and experiments at all locations and times, except at the stagnation point where the model underestimates the heat transfer rate. These discrepancies are caused by the stagnation point θ_P used for determining the heat flux in the transient experiments. In the current model, salt-water measurements provide $\theta_P^*=11.7$ when the virtual origin is considered, which is consistently smaller than the measurements of Veldman et al. [15]. More salt-water data and

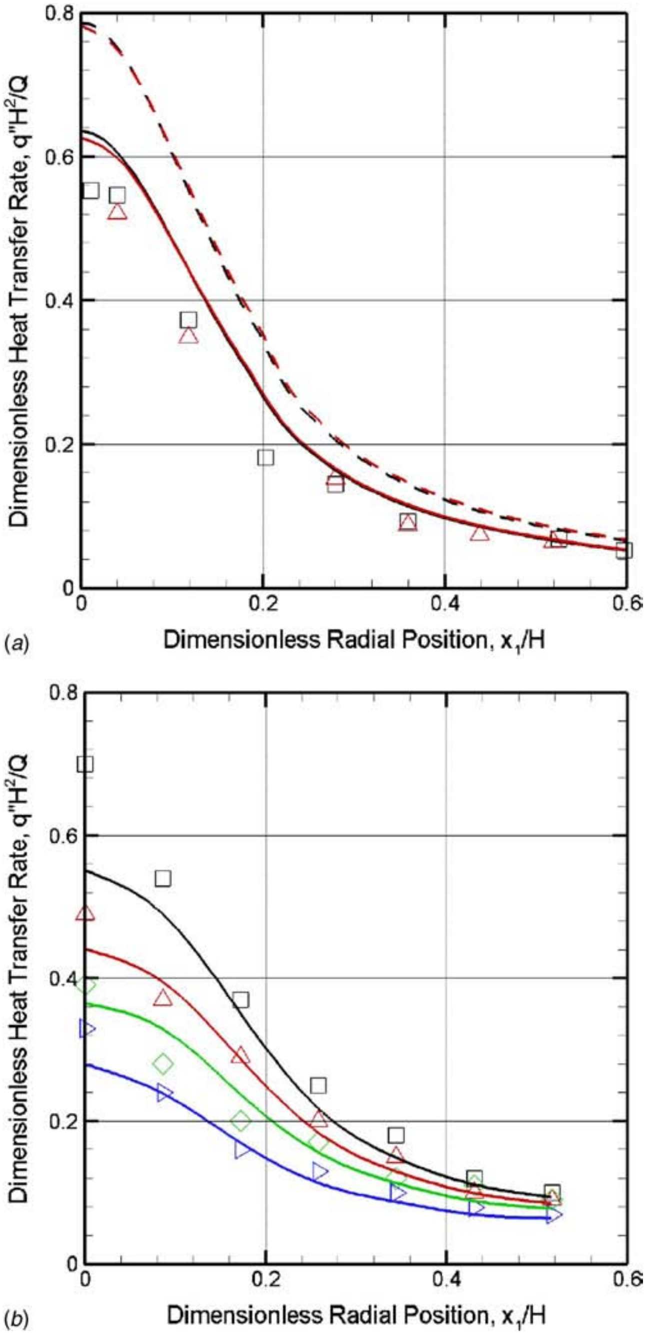

Fig. 10 (***a***) **Heat transfer rate along ceiling radial position between the model and You and Faeth's experiments [16]; (□) $\boldsymbol{Q}$ =0.385 kW, $\boldsymbol{H_f/H_c}$=0.15; (△) $\boldsymbol{Q}$=0.24 kW, $\boldsymbol{H_f/H_c}$=0.08 [9]. (– –) author's model with $\boldsymbol{Q_c=Q}$. (—) author's model with $\boldsymbol{Q_c=0.8Q}$. (*b*) Heat transfer rate along ceiling radial position between the model and experiments of Veldman et al. [15] for test 1, $\boldsymbol{Q}$ =1.17 kW, $\boldsymbol{H_c}$=0.813 m; (□) $\boldsymbol{t}$=1 min, (△) $\boldsymbol{t}$=2 min; (◇) $\boldsymbol{t}$=3 min; (▷) $\boldsymbol{t}$=5 min [8]. (—) authors' model predictions sorted with color.**

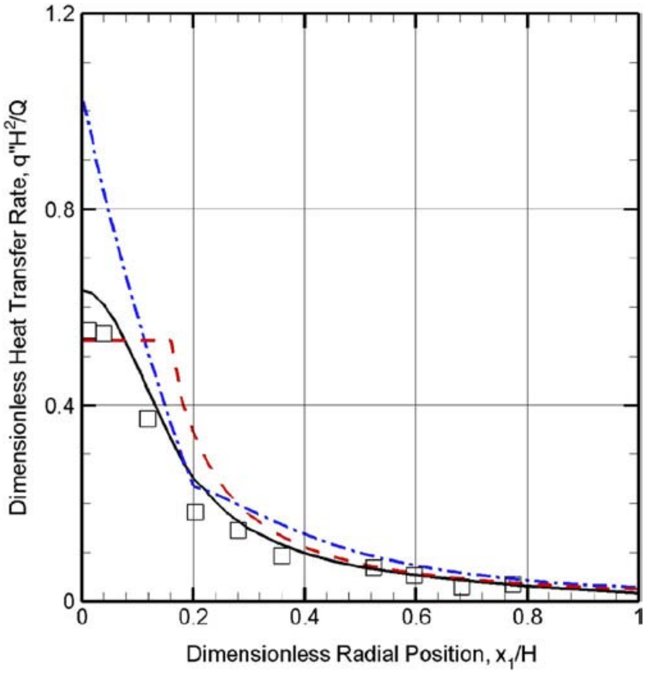

Fig. 11 Comparison of different heat transfer model with You and Faeth's [16] experiment. (□) You and Faeth's [16] experiment [16] of $Q=0.24$ kW, $H_f/H_c=0.08$ [9]; (– –) You and Faeth's correlation [16]; (——) Cooper's model [17] with $Q_c=0.8Q$ [12]; (—) author's model with $Q_c=0.8Q$.

fire data will improve estimation of θ_P. However, good agreement in the ceiling jet region indicates that the influence of θ_P is less important because of the relatively small effectiveness η in this region.

In Fig. 11, various heat transfer models are compared with You and Faeth's [16] steady-state experimental data obtained with $\dot{Q}=0.24$ kW and $H_f/H_c=0.008$. The convective heat source $\dot{Q}_c$ is estimated by $\dot{Q}_c=0.8\dot{Q}$. Cooper's model [17] overpredicts the heat transfer rate in the turning region due to an overprediction of h resulting from the use of a correlation based on laminar impinging jet experimental data. In contrast, the impingement region h in the current study's model is based on the turbulent impinging jet scaling and actual fire data [15]. You and Faeth's correlation [16] provides the correct magnitude of the heat transfer rate at the stagnation point. However, a constant heat transfer rate in the turning region is not in agreement with experimental data. Another limitation of You and Faeth's model [16] is that the ceiling temperature is not included in the correlation. Thus, it can only be used to predict the heat transfer rate at the initial fire stage when the ceiling temperature is uniform and equal to the ambient temperature. The current heat transfer model based on the adiabatic wall concept provides the best agreement with the experimental data. It captures both the peak magnitude and the decay of the heat transfer rate at the ceiling.

The adiabatic wall heat transfer model in Eq. (24) provides a straightforward way to determine the heat transfer rate from the ceiling jet to the ceiling if the ceiling surface temperature is known. Otherwise, the ceiling surface temperature can be predicted from the heat transfer rate to the ceiling. The equations provided in Eq. (24) are well suited for engineering analysis. It should be noted that the current heat transfer model based on the point the source analysis and measurements is only valid for relatively small fires where $H_f/H \ll 1$. The discrepancies between the model predictions and experiments become apparent when compared with the relatively large fire experiments conducted by Veldman et al. [15] and You and Faeth [16]. You and Faeth [16] recommended a Rayleigh number based scaling for these fires.

4 Summary and Conclusions

An engineering level model was established from detailed salt-water modeling measurements and analysis to predict the heat transfer from an impinging plume to a ceiling. This model is based on Newton's law of cooling; however, the model uses an adiabatic ceiling reference temperature basis instead of the ambient temperature. A general expression for this reference temperature is determined from scaling arguments and scalar concentration measurements obtained from analogous impermeable ceiling salt-water experiments. The convective heat transfer coefficient is also determined from scaling arguments in the impinging plume region and a method in the ceiling jet region that combines wall jet similarity analysis with near-wall velocity measurements to determine the friction factor and the corresponding Nusselt number (through the Reynolds analogy). This approach provides an engineering model for convective heat transfer to ceilings in terms of the global characteristics (i.e., Re_H, H, $\mathbf{x}_1/H$, and T_w) providing an easy way to predict the heat transfer rate in both constant ceiling temperature and transient ceiling temperature conditions.

Good agreement between the current model, fire experimental data, and previous analytical models in the impinging plume configuration validated the salt-water based modeling methodology. This model should be used for relatively small fire sources ($H_f/H \ll 1$) where the weak plume salt-water measurements and scaling arguments that form the basis of the model are valid. The authors recommend this model be applied for fires having $H_f/H < 0.15$. Based on the good agreement between the salt-water based ceiling heat transfer models under these conditions, this methodology can now be used to analyze and evaluate the fire and smoke transport dynamics in more complicated geometries.

Acknowledgment

The authors would like to gratefully acknowledge Combustion Science and Engineering, Inc. (CSE) and the Society of Fire Protection Engineers (SFPE) Education and Scientific Foundation for their support of this research. They would also like to thank Sean Jankiewicz for his contributions to this work.

Nomenclature

Y_{salt} = salt mass fraction
T = temperature
H = "ceiling" height above source
H_f = flame height
V = salt-water injection flow rate
$\dot{Q}$ = energy release rate
$\mathbf{x}_i$ = position vector
$(\mathbf{x}_3)_0$ = virtual origin
$\mathbf{x}_i^*$ = dimensionless position, $\mathbf{x}_i/H$
t^* = dimensionless time, $t(g/H)^{1/2}(\zeta^*)^{1/3}$
u_i = velocity
u_i^* = dimensionless velocity, u_i/U
U = characteristic velocity, $(gH)^{1/2}(\zeta^*)^{1/3}$
$\dot{q}'''$ = volumetric energy release rate
$\dot{q}^*$ = dimensionless volumetric energy release rate, $\dot{q}'''H^3/\dot{Q}$
$\dot{w}'''$ = volumetric salt mass release rate
$\dot{w}^*$ = dimensionless volumetric salt mass release rate, $\dot{w}'''H^3/\dot{m}_S$
q'' = convective heat flux to ceiling
h = convective heat transfer coefficient
Pr = Prandtl number
Sc = Schmidt number
Re = Reynolds number

Gr = Grashof number, $g\beta\dot{Q}H^2/\rho_0 c_p \nu^3$ for fire, $g\beta\dot{m}_{\mathrm{salt}}H^2/\rho_0\nu^3$ for salt water
Nu = Nusselt number
St = Stanton Number
C_f = friction factor
Ri = Richardson number

Greek Symbols

β = volumetric expansion coefficient, $1/T_0$ for fire, 0.76 for salt water
ρ = density
θ = density difference, $\beta(T-T_0)$ for fire, βY_{salt} for salt water
θ^* = dimensionless density difference, $\theta(\zeta^*)^{-2/3}$
ζ^* = dimensionless source strength; $Q^*=\beta\dot{Q}/(\rho_0 c_p g^{1/2}H^{5/2})$ for fire, $m^*=\beta\dot{m}_{\mathrm{salt}}/(\rho_0 g^{1/2}H^{5/2})$ for salt water
η = ceiling heating effectiveness, $(T_{\mathrm{ad}}-T_0)/(T_P-T_0)$
δ_1 = wall/ceiling normal location of maximum velocity
δ_2 = wall/ceiling normal location of zero shear stress
χ = similarity variable, x_3/δ_1
χ_2 = dimensionless zero shear stress position, δ_2/δ_1

Subscripts and Superscripts

sw = salt water
T = thermal
w = wall/ceiling
ad = adiabatic
ref = reference
0 = ambient condition
P = stagnation point at ceiling
c = centerline

References

[1] Thomas, P. H., Hinkley, P. L., Theobald, C. R., and Simms, D. L., 1963, "Investigations Into the Flow of Hot Gases in Roof Venting," Fire Research Technical Paper No. 7.

[2] Tangren, E. N., Sargent, W. S., and Zukoski, E. E., 1978, "Hydraulic and Numerical Modeling of Room Fires," California Institute of Technology, Pasadena, CA.

[3] Zukoski, E. E., 1978, "Prediction of Smoke Movement in Buildings," California Institute of Technology, Pasadena, CA.

[4] Steckler, K. D., Baum, H. R., and Quintiere, J. G., 1986, "Salt Water Modeling of Fire Induced Flows in Multi-Compartment Enclosures," *21st Symposium (International) on Combustion*, The Combustion Institute, pp. 143–149.

[5] Kelly, A. A., 2001, "Examination of Smoke Movement in a Two-Story Compartment Using Salt Water and Computational Fluid Dynamics Modeling," MS thesis, University of Maryland, College Park, MD.

[6] Sangras, R., and Faeth, G. M., 1999, "Buoyant Turbulent Jets and Plumes: III. Round Turbulent Nonbuoyant Starting Jets and Puffs and Buoyant Starting Plumes and Thermals," National Institute Standard and Technology Report No. GDL/GMF-99-03.

[7] Diez, F. J., Bernal, L. P., and Faeth, G. M., 2003, "Round Turbulent Thermals, Putts, Starting Plumes and Starting Jets in Uniform Crossflow," J. Heat Transfer, **125**, pp. 1046–1057.

[8] Clement, J. M., and Fleischmann, C. M., 2002, "Experimental Verification of the Fire Dynamics Simulator Hydrodynamic Model," *Fire Safety Science: Proceedings of the 7th International Symposium*, International Association for Fire Safety Science, pp. 839–851.

[9] Jankiewicz, S. P., 2004, "Prediction Smoke Detector Response Using a Quantitative Salt-Water Modeling Technique," MS thesis, University of Maryland, College Park, MD.

[10] Yao, X., Ma, T., Marshall, A. W., and Trouvé, A., 2004, "Mixing and Turbulent Transport in Unconfined and Impinging Plumes," *10th International Fire Science and Engineering Conference: Interflam*, Edinburgh, Scotland, pp. 1233–1244.

[11] Yao, X., and Marshall, A. W., 2005, "Characterizing of Ceiling Jet Dynamics With Salt-Water Modeling," *Fire Safety Science: Proceedings of the 8th International Symposium*, International Association for Fire Safety Science, pp. 927–938.

[12] Yao, X., and Marshall, A. W., 2006, "Quantitative Salt-water Modeling of Fire Induced Flow," Fire Saf. J., **47**, pp. 497–508.

[13] Alpert, R. L., 1971, "Turbulent Ceiling-Jet Induced by Large-Scale Fires," Combust. Sci. Technol., **11**, pp. 197–213.

[14] Motevalli, V., and Marks, C., 1991, "Characterizing the Unconfined Ceiling Jet Under Steady-State Conditions: A Reassessment," *Fire Safety Science: Proceedings of the Third International Symposium*, International Association for Fire Safety Science, pp. 301–312.

[15] Veldman, C. C., Kubota, T., and Zukoski, E. E., 1975, "An Experimental Investigation of the Heat Transfer From a Buoyant Gas Plume to a Horizontal Ceiling: Part 1. Unobstructed Ceiling," National Institute of Standards and Technology Report No. NBS-GCR-77-97.

[16] You, H. Z., and Faeth, G. M., 1981, "An Investigation of Fire Impingement on a Horizontal Ceiling," National Institute of Standards and Technology Report No. NBS-GCR-81-304.

[17] Cooper, L. Y., 1982, "Heat Transfer From a Buoyant Plume to an Unconfined Ceiling," J. Heat Transfer, **104**, pp. 446–451.

[18] Cooper, L. Y., 1993, "Fire-Plume-Generated Ceiling Jet Characteristics and Convective Heat Transfer to Ceiling and Wall Surfaces in a Two-Layer Fire Environment: Uniform Temperature Fire Environment: Uniform Temperature Ceiling and Walls," Fire Science & Technology, **13**, pp. 1–17.

[19] Cooper, L. Y., and Woodhouse, A., 1986, "The Buoyant Plume-Driven Adiabatic Ceiling Temperature Revised," J. Heat Transfer, **108**, pp. 822–826.

[20] Poreh, M., Tsuei, Y. G., and Cermak, J. E., 1967, "Investigation of a Turbulent Radial Wall Jet," ASME J. Appl. Mech., **34**, pp. 457–463.

[21] Yao, X., 2006, "Characterization of Fire Induced Flow Transport Along Ceilings Using Salt-Water Modeling," Ph.D. thesis, University of Maryland, College Park, MD.

[22] McCaffrey, B. J., 1979, "Purely Buoyant Diffusion Flames: Some Experimental Results," Center for Fire Research, National Engineering Laboratory, National Bureau of Standards Report No. NBSIR 79-1910.

[23] Shabbir, A., and George, W. K., 1994, "Experiments on a Round Turbulent Buoyant Plume," J. Fluid Mech., **275**, pp. 1–32.

[24] Pham, M. V., Plourde, F., and Kim, S. D., 2005, "Three-Dimensional Characterization of a Pure Thermal Plume," J. Heat Transfer, **127**, pp. 624–636.

[25] Goldstein, R. J., Sobolik, K. A., and Seol, W. S., 1990, "Effect of Entrainment on the Heat Transfer to a Heated Circular Air Jet Impinging on a Flat Surface," ASME J. Heat Transfer, **112**, pp. 608–611.

[26] Kruka, V., and Eskinazi, S., 1964, "The Wall-Jet in a Moving Stream," J. Fluid Mech., **20**, pp. 555–579.

[27] Patel, R. P., 1962, "Self Preserving Two-Dimensional Turbulent Jets and Wall Jets in a Moving Stream," MS thesis, McGill University, Quebec.

[28] Schwarz, W. H., and Cosart, W. P., 1961, "The Two-Dimensional Turbulent Wall-Jet," J. Fluid Mech., **10**, pp. 481–495.

[29] Tailland, A., and Mathieu, J., 1967, "Jet Parietal," J. Mec., **6**, pp. 103–131.

[30] Phares, D. J., Smedley, G. T., and Flagan, R. C., 2000, "The Wall Shear Stress Produced by the Normal Impingement of a Jet on a Flat Surface," J. Fluid Mech., **418**, pp. 351–375.

[31] Donaldson, C. D., Sendeker, R. S., and Margolis, D. P., 1971, "A Study of Free Jet Impingement. Part 2. Free Jet Turbulent Structure and Impingement Heat Transfer," J. Fluid Mech., **45**, pp. 477–512.

[32] Han, B., and Goldstein, R. J., 2001, "Jet-Impingement Heat Transfer in Gas Turbine Systems," Ann. N.Y. Acad. Sci., **934**, pp. 147–161.

[33] Heskestad, G., 2002, "Fire Plumes, Flame Heiht, and Air Entrainment," in *SFPE Handbook of Fire Protection Engineering*, 2nd ed., DiNenno, P. J., National Fire Protection Association, Quincy, MA, pp. 2–10.

[34] Hamins, A., Konishi, P., Borthwick, P., and Kashiwagi, T., 1996, "Global Properties of Gaseous Pool Fires," *26th Symposium (International) on Combustion*, The Combustion Institute, Pittsburgh, PA, pp. 1429–1436.

[35] Heskestad, G., 1983, "Virtual Origins of Fire Plumes," Fire Saf. J., **5**, pp. 109–114.

S. Han

R. J. Goldstein[1]
e-mail: rjg@me.umn.edu

Department of Mechanical Engineering,
Heat Transfer Laboratory,
University of Minnesota,
Minneapolis, MN 55455

Heat Transfer Study in a Linear Turbine Cascade Using a Thermal Boundary Layer Measurement Technique

An experimental system is designed, constructed, and operated to make local measurements of heat transfer from constant-temperature surfaces in a linear turbine cascade. The system includes a number of embedded heaters and a control system to maintain the turbine blades and end walls in the cascade at a uniform temperature. A five-axis measurement system is used to determine temperature profiles normal to the pressure and suction sides of the blades and to the end wall. Extrapolating these measurements close to the surface, the local heat transfer is calculated using Fourier's law. The system has been tested in the laboratory, and results are shown for the temperature distributions above the surfaces and for the local variations in the Nusselt number on the different surfaces in the cascade. The system can also be used to study the heat and mass transfer analogy as considerable data are available for mass transfer results with similar geometries. [DOI: 10.1115/1.2754972]

Keywords: heat/mass transfer analogy, thermal boundary layer, constant wall temperature, turbine end wall, turbine blade

Introduction

In many heat transfer experiments, a constant wall heat flux boundary condition is used (or approximated) for convenience in the design of the test wall. With such a boundary condition, one only needs to measure the local temperature of the surface using any one of a number of techniques from embedded thermocouples to liquid crystals for IR measurements as well as the local free stream temperature and the measured energy input per unit area. However, studies with this boundary condition often face two difficulties. First, many real systems more closely approximate constant wall temperature rather than constant wall heat flux. In addition, if there are large variations in local heat transfer coefficient, as occurs, for example, in impinging jets or three-dimensional film cooling, wall conduction tends to smooth out the temperature and local heat flux variations, so one does not get a true picture of the heat transport or temperature variation in the flow. Studies with a constant wall temperature surface face the difficulty of maintaining a constant wall temperature in the laboratory if there are large variations in local heat transfer and also the difficulty of measuring the local heat transfer coefficient. In the present study, a number of individual embedded heaters and a specially designed control circuit maintain the temperature of the pressure and suction sides of a model blade as well as the end wall in a cascade at a closely held constant value even though there are large variations in heat transfer coefficient. To measure the local heat transfer rate, we use a thermal boundary measuring technique suggested by Blackwell and Moffat [1]. We measure the local fluid temperature near a surface and, from the linear variation of temperature close to the wall, obtain the local heat flux using Fourier's law. The complex geometry of the turbine cascade requires a special five-axis measurement system, which was designed and constructed in the Heat Transfer Laboratory and used to obtain local heat fluxes and Nusselt numbers on the suction and pressure sides of the blades as well as on the end wall.

End wall heat transfer coefficient distributions were measured by Blair [2] in a large scale turbine cascade. Local heat transfer coefficients were measured using about 150 heaters covering the test section from the leading edge. He showed that the end wall heat transfer is strongly influenced by the existence of a large vortex located in the corner between the end wall and the suction surfaces. A local heat transfer measurement on the end wall and blade surfaces was conducted by Granziani et al. [3]. The measurement was done with two inlet boundary layer thicknesses for a Reynolds number typical in a gas turbine. They found that the secondary flow strongly affects the heat transfer on the end wall and pressure surface of the blade, but does not influence the heat transfer on the pressure surface. They also found that the inlet boundary layer thickness on the end wall has a significant effect on end wall and suction surface heat transfers.

Basis of Measurement

In a fluid flowing over a wall, any turbulent fluctuations, as well as the fluid velocity, approach zero at the wall. In the viscous sublayer, convection effects approach zero and the thermal energy transport in the fluid occurs only by molecular heat conduction. Then, near the wall, the temperature variation is linear and the wall heat flux can be evaluated from the temperature gradient near the wall using Fourier's law,

$$q_w = -k\frac{\partial T}{\partial n} \tag{1}$$

The heat transfer coefficient is obtained from the heat flux, the wall temperature, and the free stream temperature,

$$h = \frac{q_w}{T_w - T_{\text{air}}} = \frac{-k\partial T/\partial n}{T_w - T_{\text{air}}} \tag{2}$$

The local Nusselt number is expressed as

---

[1] Corresponding author.

Contributed by the Heat Transfer Division of ASME for publication in the JOURNAL OF HEAT TRANSFER. Manuscript received August 6, 2006; final manuscript received March 1, 2007. Review conducted by Minking Chyu.

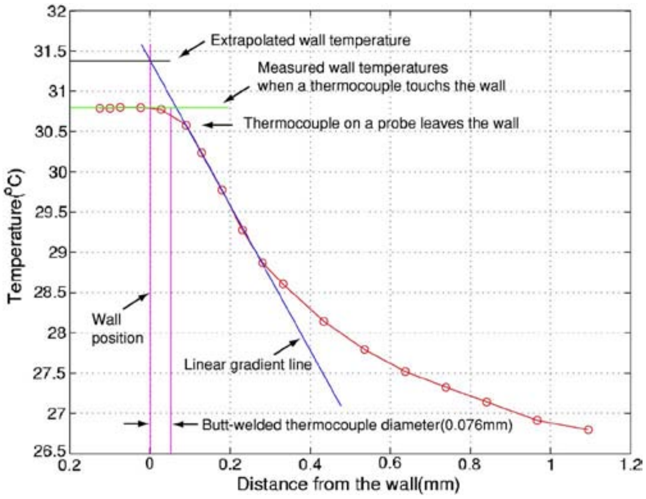

Fig. 1 Typical thermal boundary layer profile

$$
\mathrm{Nu} = \frac{hC_l}{k} = \frac{-C_l \partial T/\partial n}{T_w - T_{\mathrm{air}}} \tag{3}
$$

Considering Eqs. (2) and (3), the precise evaluation of heat transfer coefficients and Nusselt numbers depends on measurements of the temperature in the viscous sublayer region and the wall temperature on the constant temperature wall. With a large thermal gradient in the viscous sublayer region, the temperature measurement by a thermocouple is subject to conduction error. Blackwell and Moffat [1] reviewed temperature measurements using thermocouple probes. They evaluated the performance of different thermocouples against the conduction error and suggested a butt-welded E-type thermocouple.

A sample thermal boundary layer is shown in Fig. 1. Note that the wall temperature is not measured directly by the thermocouple probe. Rather, it should be determined by extrapolation using temperatures in the viscous sublayer. The extrapolation extends until it meets the wall position in the linear conduction region. Finding the exact wall position is critical in determining the wall temperature. Since the temperature is assumed to be measured in the center of the thermocouple junction, the radius of the thermocouple should be considered to decide the wall position. Qiu et al. [4] used a similar butt-welded E-type thermocouple and verified these techniques. They used a constant heat flux plate and measured the heat flux from the probe. A comparison of the input power and local measurement suggested that an uncertainty in the wall heat flux could reach ±7% in their study.

Experimental apparatus

In a turbine cascade, complicated secondary flows occur, as indicated in Fig. 2 by Wang et al. [5]. These flows cause large heat transfer variations along the surfaces, providing a challenge in maintaining a constant wall temperature condition and in measuring local heat transfer to/from the surface. In the present study, new heat transfer experimental facilities are developed to maintain the constant wall temperature condition and measure local heat transfer coefficients on the constant-temperature walls. These consist of a constant-temperature endwall, a constant-temperature blade, three thermal boundary layer probes, a five-axis measurement unit, and a computer-controlled multichannel power supply.

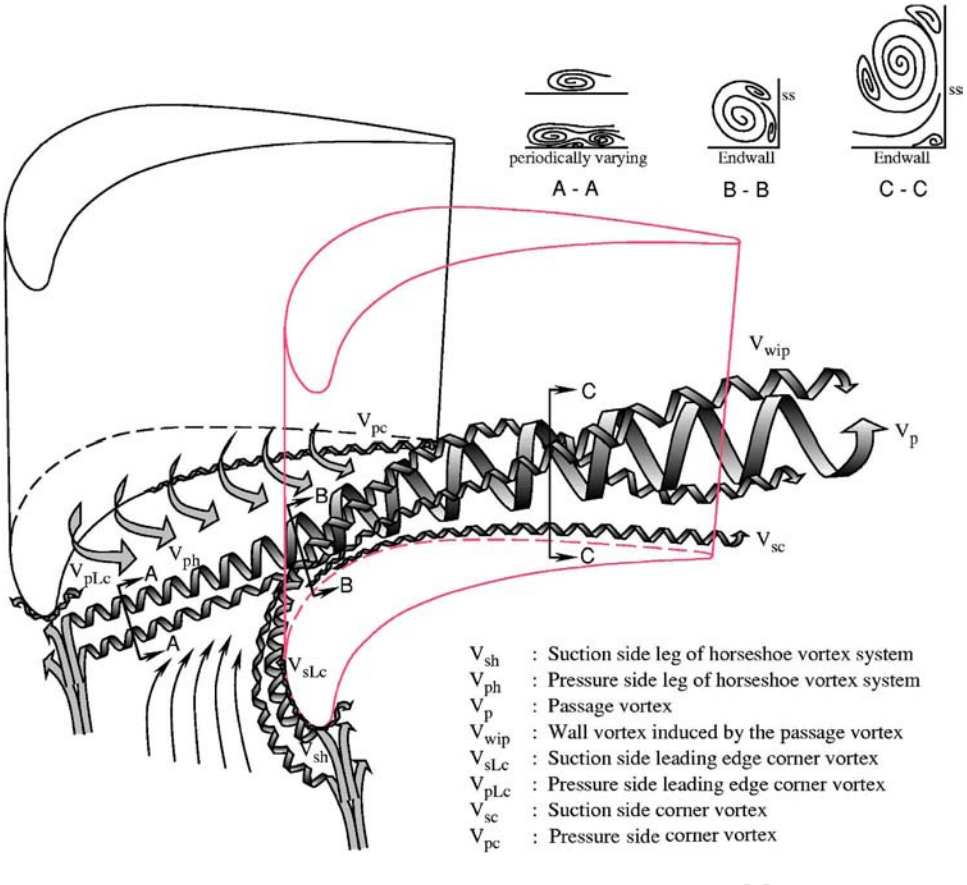

Fig. 2 Vortex model in turbine cascades Wang et al. [5]

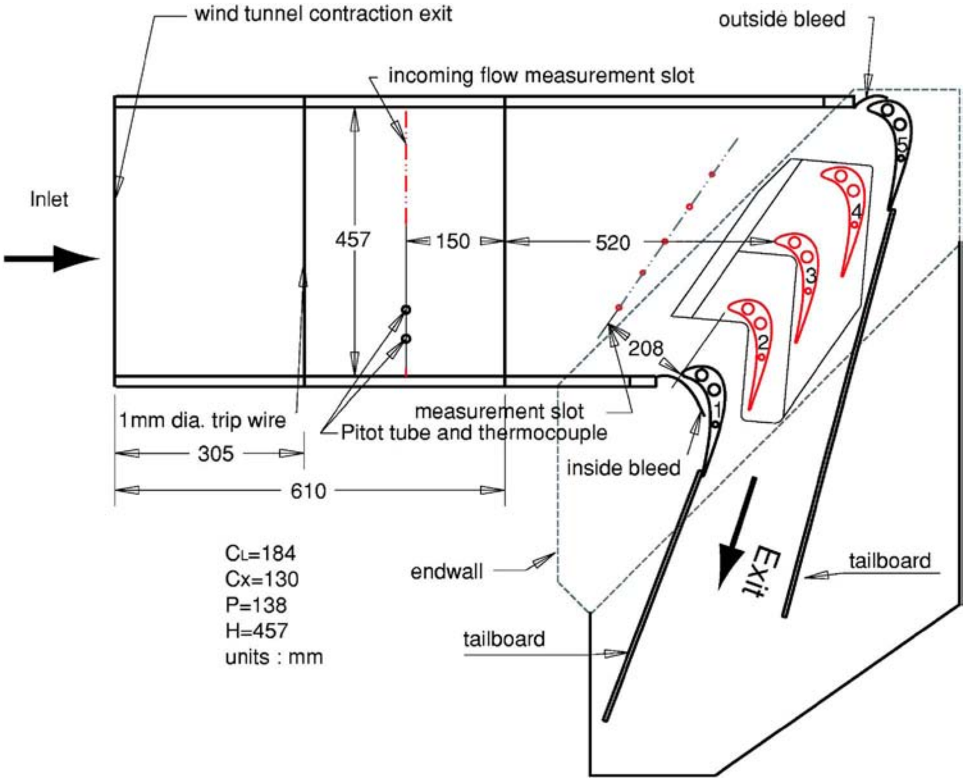

Fig. 3 Test section for the heat transfer experiment

Description of the Test Section

The cascade (Figs. 3 and 4), containing five simulated turbine blades, is connected to a blowing-type wind tunnel. The constant-temperature blade can be installed at any position from the second to the fourth blade. At each position, the height of the constant-temperature blade is adjustable for the investigation of-two- and three-dimensional flow regions. On the end wall, a 1 mm wire trips the incoming flow to provide a turbulent boundary layer. The test section has two adjustable tail boards to help impose periodic flow conditions between the blades. For the end wall surface measurement, a balsa wood plate and two balsa wood blades are put together with the constant-temperature end wall to provide an unheated starting length and to reduce conduction error between the end wall and blades. For the blade surface measurement, one regular end wall cover and aluminum blades are installed, instead of the constant-temperature end wall and the balsa wood blades. The test section is designed to conduct each experiment individually, not simultaneously.

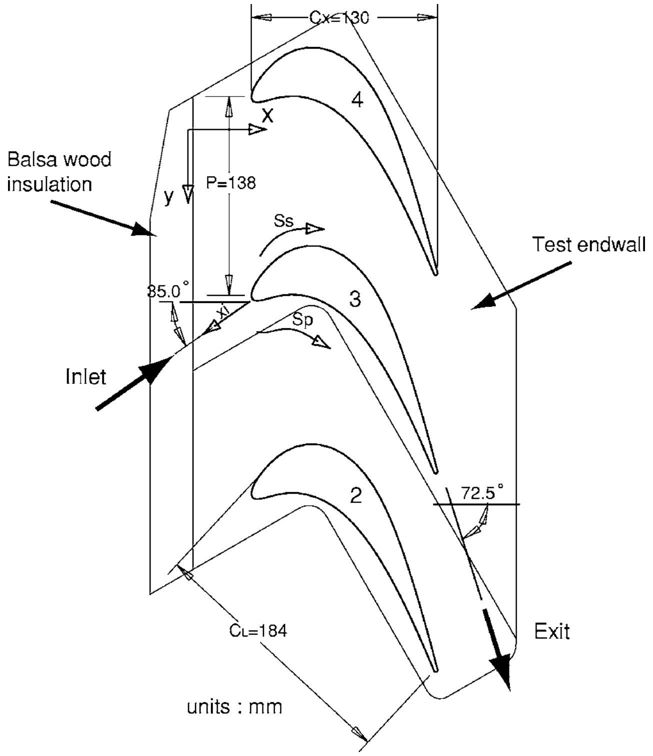

Fig. 4 Blade configuration for the heat transfer experiment

Constant-Temperature End Wall and Blade

The constant-temperature end wall and blade are designed based on numerical analysis with ANSYS. The end wall has 128 strip heaters and 138 E-type thermocouples. Three different heaters are used: $12.8 \times 12.8\ \text{mm}^2$, $38.4 \times 12.8\ \text{mm}^2$, and $192 \times 12.8\ \text{mm}^2$. The selection of the heater depends on the flow characteristic—the two-dimensional flow region uses long strip heaters. Each heater has one E-type thermocouple, except the $192 \times 12.8\ \text{mm}^2$ heaters which have three. The heaters are shown in Fig. 5, with the locations of the thermocouples marked by the plus symbols. The constant-temperature end wall only covers one passage between the third and the fourth blade. Figure 6 shows the cross section of the constant-temperature end wall. It consists of an aluminum plate, Kapton strip heaters, an E-type thermocouple, a balsa wood insulation, and a phenolic insulated plate.

The heat transfer blade has a profile corresponding to a high performance turbine blade in a high pressure stage. The cascade has a blade chord of 184 mm with a solidity of 0.75 and a high turning angle of 107.5 deg (Table 1) A blade with this profile was

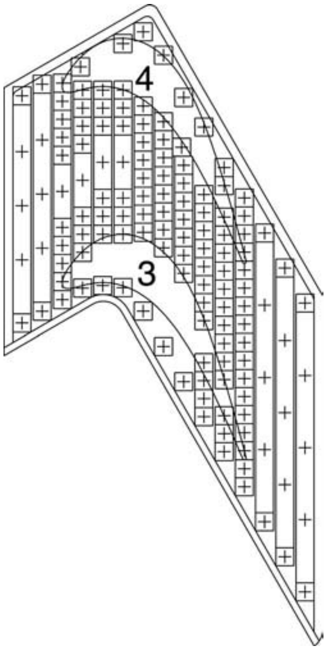

Fig. 5 Constant-temperature end wall with heaters and thermocouples

used by Wang et al. [5] for two-dimensional and three-dimensional measurements without a tip clearance. More detailed information is described in Wang [6].

The blade has 42 cylindrical heaters, three strip heaters (near the trailing edge), and 60 E-type thermocouples on the surface, which is made of copper. Three $\phi\ 7\times 40\ \text{mm}^2$ cylindrical heaters are stacked in the middle holes. Due to space limitations near the trailing edge, three $25.4\times 40\ \text{mm}^2$ strip heaters are used instead of cylindrical heaters. The locations of the heaters and thermocouples are shown in Fig. 7. To reduce the conduction error through the supporting blade, both ends of the blade are connected to insulated blades, which are removable to put the blade near the top end wall. Figure 8 shows the cross section of the blade.

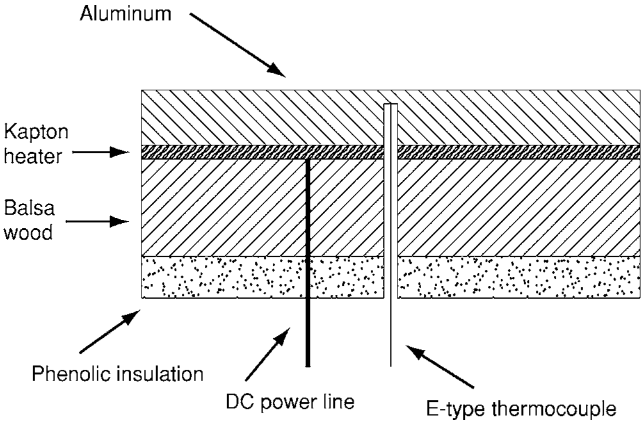

Fig. 6 Typical cross section of the constant-temperature end wall

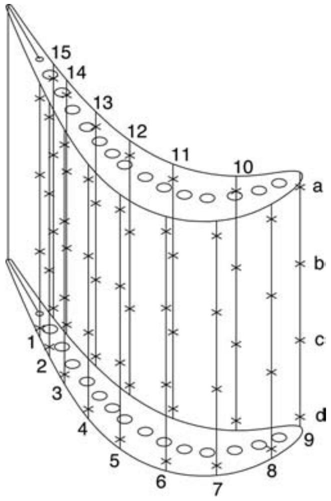

Fig. 7 Constant-temperature blade with heaters and thermocouples

Thermal Boundary Layer Probe

Flow disturbances by the probe can affect the heat transfer measurement. In addition, a strong free stream can dislocate the probe from the expected measurement location by bending and vibration. With large thermal gradients, the probe is subject to conduction error. The current experimental conditions in a simulated turbine cascade include all these issues. Therefore, the thermal probes are designed to reduce flow disturbance to minimize the conduction error and to ensure an accurate measurement location. According to Blackwell and Moffat [1], a ϕ 76 μm E-type thermocouple, which is not relatively sensitive to conduction error compared with other types of thermocouples, can help meet these goals. To minimize flow disturbance and conduction error, the junction of the thermocouple is butt welded by an electrical discharge welding technique. Different probe designs are used for the end wall and the pressure and suction surface measurements. The probes are shown in Fig. 9. The thermocouple supported by two hypodermic needles has an exposed part 14 mm wide and 1 mm high and has a slight curvature, so that the junction touches the wall first. The end wall probe has a straight shape to make movements easy and to guarantee the measurement position. For blade surfaces, the hypodermic needles are bent to reduce flow disturbance, considering the direction of the incoming flow and measurement. A Teflon bar connects between two hypodermic needles to maintain their shape. For the suction surface probe, the probe is bent in a clockwise direction (if observed in Fig. 11) and the diameter of the bent part is 30 mm. The thermocouple exposure is 14 mm wide and 1 mm high. The pressure surface probe is bent in a counterclockwise direction (Fig. 11), and the diameter of the

Table 1 Turbine linear cascade parameters

Chord length of blade (C_l)	18.4 cm	Inlet/exit area ratio of the cascade (AR)	2.72
Axial chord of blade (C_x)	12.96 cm	Area ratio of the contraction	6.25
Pitch of cascade (P)	13.8 cm	Exit Reynolds number ($\text{Re}_{\text{ex}}\times 10^{-5}$ range)	4.5–6.9
Height of cascade (H)	45.7 cm	Highest incoming velocity (U_{in})	25.5 m/s
Aspect ratio (span/chord) (H/C)	2.48	Highest incoming Reynolds number (Re_{in})	290,000
Solidity (pitch/chord) (P/C)	0.75	Highest exit velocity (U_{ex})	69.0 m/s
Blade inlet angle β_1	35 deg	Blade outlet angle (β_2)	−72.49 deg

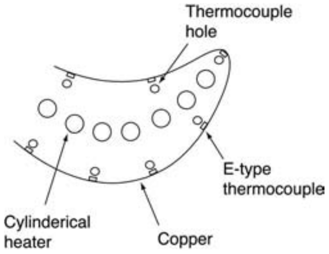

Fig. 8 Typical cross section of the constant-temperature blade

bent part is 25 mm. These probes have different diameters and bending directions to ease measurement and to reduce the interference between the flow and hypodermic needles. In the present experiment, a small Reynolds number ($\approx 2\times 10^5$) is used for the heat transfer measurement due to the long tube design of the probe. The design of the probe determines the maximum Reynolds number (really air speed). If the tube of the probe is shorter and stiffer, higher Reynolds numbers (air speed) are possible.

Five-Axis Measurement Unit for End Wall and Blade

To determine the wall heat flux, the temperature profile in the flow should be measured in a direction normal to the wall with high precision. Figures 10 and 11 show the local heat transfer measurement positions on the end wall and blade. For the end wall measurement, the probe moves into the horizontal end wall vertically and then moves out to measure the temperature profile at each location. For blade measurements, the probe moves along the normal lines from the suction and pressure surfaces to measure the temperature profile in the fluid. As shown in Fig. 11, the alignment of the probe to the wall is difficult due to the curvature of the blade, but it is critical to ensure accuracy. Another issue in the heat transfer measurement is to know the wall location since the accuracy of the extrapolated wall temperature depends on this. Thus, one needs a multiaxis measurement unit to measure temperatures along a line perpendicular to each wall and to find the wall position with high precision. To measure heat flux from both the end wall and blade with one measurement unit, a five-axis measurement unit was developed in the Heat Transfer Laboratory of the University of Minnesota, as shown in Fig. 12. It consists of four unislides (x, y, z, and n) and one rotating table (θ) from Velmex Co., a supporter, and a modified five-axis motion controller. Figure 12 shows a unislide (model MB6030W2J-S8) for the x axis, a unislide (model MB4024P5J-S4) for the y axis, a unislide (model MA2512K1-S2.5) for the z axis, a unislide (model MB2527K1J-S4) for the n axis, and a rotating table (model B4300) for the θ axis. A modified centroid motion controller is used to control the five stepper motors and to find the wall position. Since the screw of the unislide moves 1 mm for 200 steps, it has a resolution of 5 μm. The linear conduction region of a typical thermal boundary layer is about 500 μm at $\mathrm{Re}_{\mathrm{ex}}=2\times 10^5$. Thus, the resolution is three orders of magnitude higher than the thickness of the boundary layer.

For blade heat transfer measurements, four unislides (x, y, z, and n) and one rotating table are used to move the probe. After x and y locate the probe in the measurement positions, the rotating table keeps the n axis normal to blade surfaces and the n-axis unislide moves the attached z-axis unislide holding the probe away from the wall. The z-axis unislide is used to move the probe at different z/C_l positions during each measurement. For end wall heat transfer measurement, only three (x, y, and z) unislides are used. The five-axis system is connected to a supporter to prevent vibrations from the wind tunnel. The probes are attached to the z-axis slide. The probe and wall are connected to an electrical circuit, which would measure 12 V when closed. When the probe touches the wall, it closes the electrical circuit, which is monitored by the motion controller. Since the resolution of the unislide is 5 μm, the wall position is located with a position error in the range of ±2.5 μm.

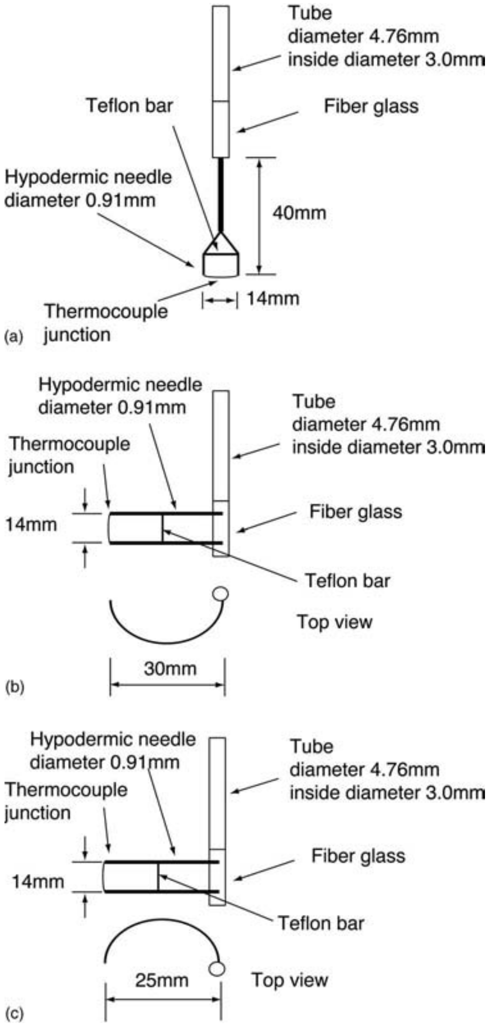

Fig. 9 Thermal boundary layer probe schematic (*a*) for end-wall surface, (*b*) for suction surface, and (*c*) for pressure surface

Computer-Controlled Power Supply

Heat transfer experiments with a constant-temperature condition require a large number of heaters in the system. Each heater needs a thermocouple to measure temperature and a power supply to supply power. The constant-temperature end wall in the current system has 128 heaters and requires 128 individually temperature controls. Therefore, the present apparatus requires a large number of power supplies that are controlled by a computer to ensure the constant-temperature condition. A computer-controlled power supply with 128 output channels is developed with a proportional-integral (PI) control algorithm. It consists of 32 power control

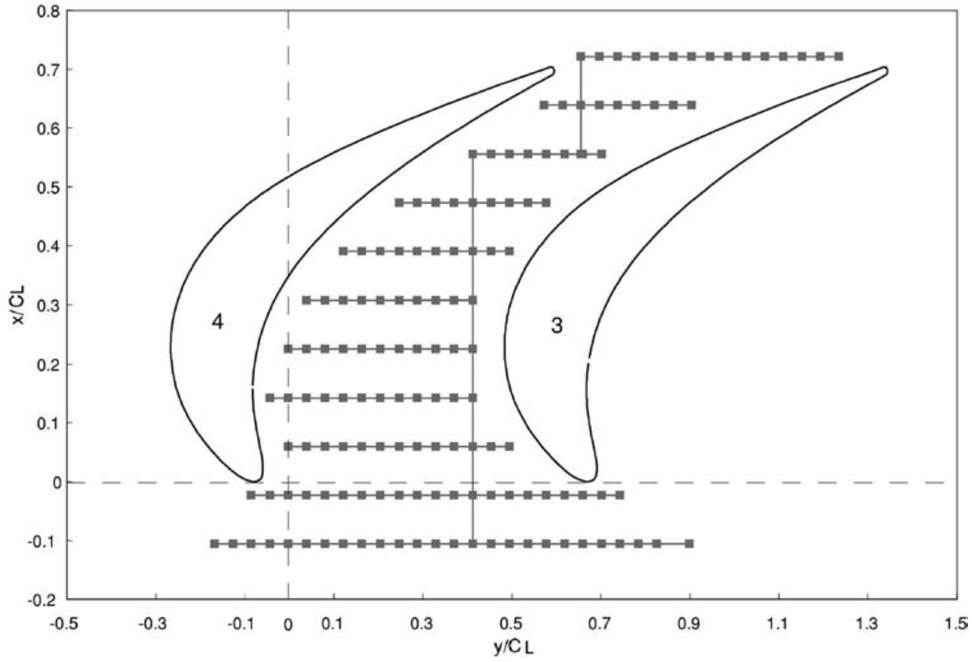

Fig. 10 End wall measurement positions

modules, two +48 V, one +5 V, one −12 V main power supply, and one interface card to a linux PC. Each module comprises four power operational amplifier (OPA544) and one digital potentiometer (X9259). Each board has one dip switch to assign a hardware address. It is controlled through a parallel port in a linux PC and designed to maintain a constant voltage in the four different ranges between 0 V and 40 V in 128 output channels with a 256 step resolution. The power supply includes voltage and current measurement units to evaluate input power during the experiments. For voltage and current measurements, it includes two Fluke 2205A multiplexers, two Keithley 705 multiplexers, one Keithley 196 multimeter, one Keithley 193 multimeter, and one Fluke Y5020 current shunt.

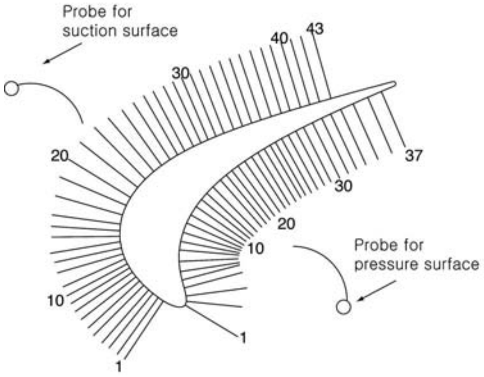

Fig. 11 Blade measurement positions

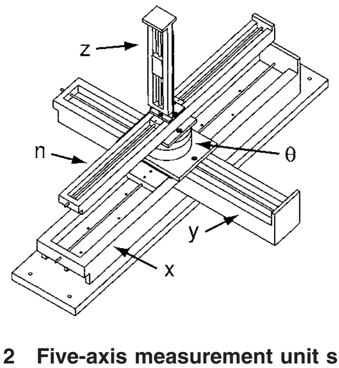

Fig. 12 Five-axis measurement unit sketch

To maintain the constant-temperature condition, the PI control algorithm is used with the computer-controlled power supply. Temperatures from thermocouples are measured by two Keithley 7001 multiplexers and the one Keithley 2000 multimeter, and the PI control algorithm evaluates suitable power for each heater based on measured temperatures. After calculating new power inputs, the power supply adjusts the voltages to each heater. This procedure is repeated for an entire experiment. The temperature control result is shown in Fig. 13. It shows temperatures from 138 thermocouples in the constant-temperature end wall. The room temperature is generally about 18°C and the set temperature is 40°C. The standard deviation of the temperature measurement is less than 0.06°C. These temperatures are only used to maintain and check the constant-temperature wall condition, not to evaluate heat fluxes or Nusselt numbers.

Experimental Procedure

The heat transfer experiment consists of three major steps. The first is to align the five-axis measurement unit to the test section. The second is to provide the constant-temperature condition on the target surface. The final step is to measure the local heat flux from the constant-temperature wall.

To measure the temperature profile from the wall, the five-axis measurement unit should be aligned to the reference points and lines. The alignment process requires a three-dimensional reference to locate the probe in preselected measurement positions. In the test section, the top end wall (aluminum) has a rectangular window for visual observation. Since the rectangular window is parallel to the *x* axis of the test section, it can be used as a reference line. With the top end wall and wall finding technique using the electrical circuit, the five-axis measurement unit can find its position from the reference points and lines. First, a dummy probe

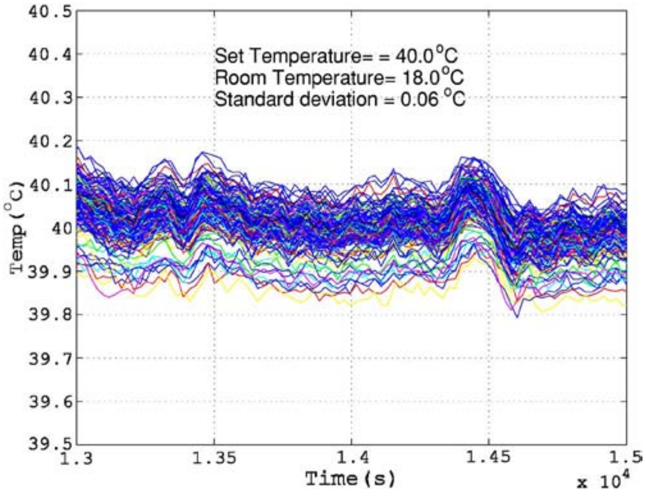

Fig. 13 Temperature variation of 138 thermocouples on the end wall by PI control

connected to the electrical circuit is attached in the z-axis slide and the top end wall is connected to the electrical circuit. When the dummy probe hits the top end wall, the top end wall position will be monitored by the motion controller. Second, the five-axis measurement unit should be level with the top end wall. This can be verified by measuring heights at three different positions on the top end wall. Third, the x axis of the five-axis measurement unit should be parallel to the x axis of the top end wall. To make the five-axis measurement unit parallel to the top end wall, the length should be measured at different x locations. The difference of the length at different x locations shows the degree of misalignment of the measurement unit from the x reference. The five-axis measurement unit should be parallel to the x axis of the top end wall. Fourth, the rotation table should be in its reference angle. The reference angle is parallel to the x axis of the top end wall. It can be aligned using the same method as when aligning the x axis to the x reference line. Finally, the five-axis measurement unit can find one corner of the rectangular window and assign it as its zero reference. After these processes, the five-axis measurement unit is properly aligned to the three-dimensional reference. Taking out the dummy probe, the thermal boundary layer probe is attached to the z axis. Now, it is ready to measure the temperature in the test section.

After aligning the five-axis measurement unit, the constant-temperature end wall or blade is installed in the test section. For the end wall experiment, one balsa wood plate and two balsa wood blades are put together to provide an unheated starting length and to reduce the conduction error between the end wall and the blades. For the blade experiment, the blade is installed on the third cascade position with a regular bottom end wall. Since a heat transfer experiment can take more then 5 h, a double layer ice bath is used to maintain the reference temperature for the 138 thermocouples. After that, all heaters and thermocouples are connected to the power supply. The heat transfer surface temperature is set about 20°C above the room (free stream) temperature. On running the wind tunnel, temperatures are controlled by the power supply and a Linux computer. When the temperatures from heaters reach the set temperature and become stable, the thermal boundary layer measurements start.

When the heat transfer measurement starts, the five-axis measurement unit moves the probe to the proper position and seeks the wall location in 100 μm steps. When the probe touches the wall, the motion controller measures 12 V between the probe and the wall. To find the wall with a high precision, the probe moves 200 μm away from the wall when the probe touches the wall first. It moves against the wall with 5 μm movement and finds the wall again. This process can save measurement time and improve the precision of the wall position. After the wall position is found, the probe move 100 μm against the wall to ensure contact. Then, the five-axis measurement unit starts the temperature measurement from this location with 10 μm increments. After measuring enough points, the five-axis measurement unit moves the probe to another measurement location. The procedure is then repeated in an entire experiment.

Table 2 Heat transfer experimental conditions on a two-dimensional (2D) pressure surface

No.	Run number	Location	$\mathrm{Re}_{\mathrm{ex}}$	U_{ex} (m/s)	z/C_l	Tu (%)
1	P-HT-run1	2D pressure	2.64×10^5	23.6	1.5	0.2
2	P-HT-run2	2D pressure	2.65×10^5	23.5	1.5	0.2
3	P-HT-run3	2D pressure	1.93×10^5	17.2	1.5	0.2

The temperatures in the linear conduction region are used to calculate the heat flux and extrapolated wall temperature. The heat transfer coefficient and Nusselt number are evaluated from the extrapolated wall temperature and heat flux. The uncertainty of the Nusselt number depends on the temperature measurement. Thick and smooth boundary layers reduce the measurement uncertainty to 2%. However, there may be a measurement uncertainty from 4% to 15%, depending on the flow in conditions of the boundary layer at the measurement location. In the boundary layer measurements, the boundary layer thickness is not classified by the Reynolds number since the flow velocity changes as the measurement position goes down in the test section.

Results and Discussion

In a simulated turbine cascade, heat transfer coefficients were measured on the end wall and blade with constant wall temperature conditions. On the end wall, 137 positions selected for heat transfer measurement are shown in Fig. 10. Low (0.2%) and high (8.5%) turblence intensity freestream are used. For the blade, heat transfer coefficients on the pressure surface and suction surface are measured at 37 and 43 locations, respectively (Fig. 11). The measurements are conducted to change z/C_l to know whether the technique is applicable at different spanwise positions. Due to the vibration of the probe, the experiment for a high turbulence intensity is not conducted for the boundary layer on the blade surfaces (Tables 2 and 3).

Thermal boundary layer plots are shown in Figs. 14 and 15. The directly measured wall temperatures in Figs. 14 and 15 are lower than the set temperatures due to the conduction error between the wall and the probe. Therefore, the wall temperature is determined by extrapolating from the measured temperatures in the linear conduction region. The wall position is monitored by the five-axis measurement unit and set to be zero in Figs. 14 and 15. This wall position and linear thermal gradient near the wall evaluate the wall temperature. Therefore, if the wall temperature is properly controlled and the wall position is accurately found, the extrapolated wall temperature should be close to the set temperature. However, the extrapolated wall temperature (44.3°C) is less than the set temperature (45.0°C) by 0.7°C due to the small number of heaters and thermocouples in the blade at the location examined in Fig. 14. Even though the surfaces near the heaters are maintained at the set temperature, the conduction error on the surface slightly lowers the surface temperatures between heaters. Therefore, the

Table 3 Heat transfer experimental conditions on a two-dimensional (2D) suction surface

No.	Run number	Location	Re_{ex}	U_{ex} (m/s)	z/C_l	Tu (%)
1	S-HT-run1	2D suction	2.67×10^5	23.4	1.5	0.2
2	S-HT-run2	2D suction	2.43×10^5	21.7	1.5	0.2
3	S-HT-run3	2D suction	1.77×10^5	15.8	1.5	0.2

true temperature on the wall may be less than the set temperature, and the extrapolated temperature is reasonable. The thermal boundary on the end wall in Fig. 15 is for a set temperature of 40°C, and the room temperature is 18.5°C. The extrapolated wall temperature (39.9°C) is close to the set temperature (40°C) on the wall because the surface temperature on the end wall is controlled by 127 heaters and the conduction error on the surface is negligible. The mainstream temperature is obtained from the probe when it moves out of the conduction region. Since the incoming flow is tripped by a 1 mm trip wire and fully developed, the temperature profile shows fluctuation beyond the conduction region in Fig. 15.

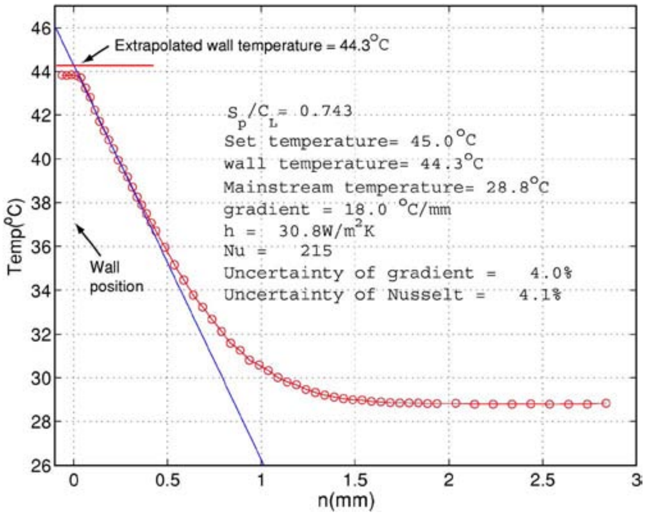

Fig. 14 Thermal boundary layer profile on the blade

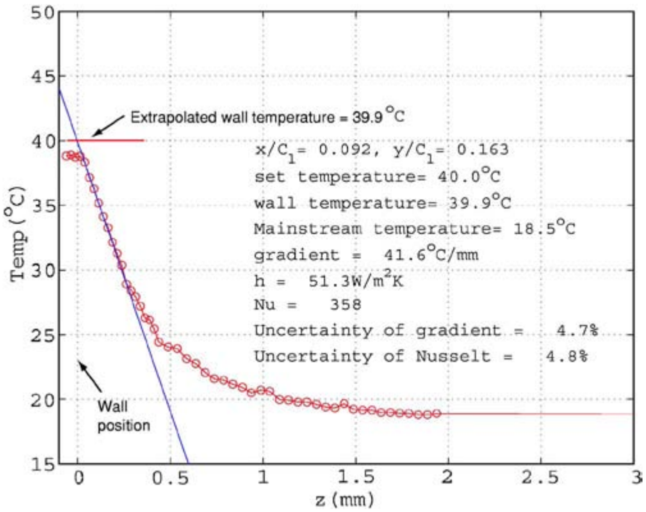

Fig. 15 Thermal boundary layer profile on the end wall

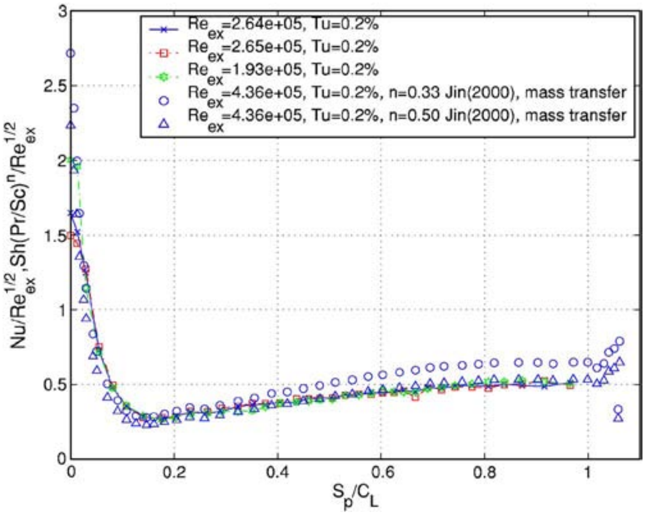

Fig. 16 Normalized Nusselt number and Sherwood number plot on the pressure surfaces

Normalized Nusselt numbers on the pressure and suction surfaces of the blade are shown in Figs. 16 and 17. The heat transfer coefficients are measured at $z/C_l=1.5$ from the top end wall, where the flow is essentially two dimensional over both surfaces. Three Reynolds numbers (2.64×10^5, 2.65×10^5, and 1.93×10^5) are chosen to show the repeatability and the effect of the Reynolds number on the pressure surface heat transfer. Similar Reynolds numbers (2.67×10^5, 2.43×10^5, and 1.77×10^5) are used for the suction surface measurements. These Reynolds numbers are much less than those of the typical turbine operating conditions. Due to the bending and vibration of the probes, these Reynolds numbers are selected for the heat transfer experiments. Figures 16 and 17 show good repeatability on the pressure and suction surfaces, except near the leading edge. In this region near the leading edge, the thermal boundary layer starts and is thin-the linear conduction thickness is 100 μm at $S_P/C_l=0.013$ and $\mathrm{Re}=2.64\times10^5$. On the suction surface, Nusselt numbers are obtained from $S_S/C_l=0.074$ to 1.2. From the stagnation point to $S_P/C_l=0.013$, the thin boundary layer leads to significant conduction errors and poorer repeatability.

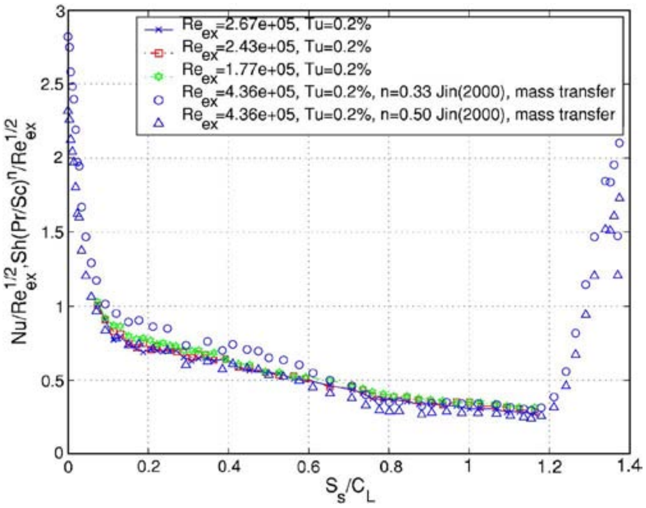

Fig. 17 Normalized Nusselt number and Sherwood number plot on the suction surface

Table 4 Heat transfer experimental conditions on a three-dimensional (3D) pressure surface

No.	Run number	Location	$\mathrm{Re}_{\mathrm{ex}}$	U_{ex} (m/s)	z/C_l	Tu (%)
1	P-HT-run31	3D pressure	2.48×10^5	21.9	0.09	0.2
2	P-HT-run32	3D pressure	2.49×10^5	21.9	0.18	0.2
3	P-HT-run33	3D pressure	2.38×10^5	21.3	0.28	0.2
4	P-HT-run34	3D pressure	2.38×10^5	21.2	0.66	0.2

Jin [7] conducted mass transfer measurements in the same test section with a mass transfer blade and naphthalene sublimation technique. The mass transfer blade had the same profile as the recent heat transfer blade, but Jin [7] used a higher Reynolds number (4.36×10^5) for mass transfer experiments. To validate the heat transfer measurement, the present results are compared with Jin [7] using the heat/mass transfer analogy. The Nusselt number distribution shows a good qualitative agreement with the mass transfer measurements of Jin [7]. For a direct comparison, the Sherwood numbers from Jin [7] are converted by the equation $N=\mathrm{Sh}(\mathrm{Pr}/\mathrm{Sc})^n$ with $\mathrm{Pr}=0.707$ (air) and $\mathrm{Sc}=2.28$ (naphthalene). The Sherwood numbers agrees with the Nusselt numbers, with n varying from 1/3 to 0.5 on both the suction and pressure surface. On the pressure surface, n changes from 1/3 to 0.5 as S_p/C_l moves down to the trailing edge. However, n changes from 0.5 to 1/3 on the suction surface, as S_s/C_l moves down to the trailing edge.

For the three-dimensional boundary layer between the blade surfaces and on the end wall, the heat transfer coefficients are measured at four spanwise positions (z/C_l=0.09, 0.18, 0.28, and 0.66) with the Reynolds number (2.4×10^5). Detailed experimental conditions are presented in Tables 4 and 5. The Nusselt number at the different spanwise measurements are plotted in Figs. 18 and 19. As shown in Wang et al. [5] (Fig. 2), the pressure surface does not experience the complicated secondary flow near the end wall. Therefore, the Nusselt number distributions at the different spanwise locations do not show a significant difference on the pressure side. However, on the suction side, there is a triangular region covered by the passage vortex. Graziani et al. [3] also confirmed these findings in their study. The triangular region is clearly shown in Fig. 19, but a significant fluctuation is shown in the triangle region due to the passage vortex. The trend of the Nusselt number variation is qualitatively similar to that of the Sherwood number variation from Jin [7]. The Nusselt numbers in the region that is covered by the passage vortex show low values due to the limitation of the thermal boundary measurement technique in complicated secondary flows on the suction surface.

For the end wall heat transfer measurement, two experimental conditions are considered—low (0.2%) and high (8.5%) turbulence intensities (Table 6). Since the probe can be bent by a high velocity flow and is sensitive to vibration, a relatively small Reynolds number (2.29×10^5 and 2.56×10^5) is used to reduce measurement uncertainty.

For the end wall, the heat transfer results from the 137 measurement positions between the third and fourth blades in Fig. 10 are shown in Figs. 20 and 21. Due to the shortage of measurement points, the contour plots in Figs. 20 and 21 do not show the detailed secondary flow development. However, the high heat transfer regions near the stagnation points and near the trailing edge are clearly observed.

To compare heat transfer results clearly, the Nusselt numbers are plotted in Figs. 22–24. The dark rectangular boxes represent the blade cross reaction, with P and S indicating the pressure and suction sides, respectively, in Figs. 22–24. Due to the physical size of the probe, the heat transfer measurement cannot include positions very near the pressure and suction walls on the end wall.

Table 5 Heat transfer experimental conditions on a three-dimensional (3D) suction surface

No.	Run number	Location	$\mathrm{Re}_{\mathrm{ex}}$	U_{ex} (m/s)	z/C_l	Tu (%)
1	S-HT-run31	3D suction	2.41×10^5	21.4	0.09	0.2
2	S-HT-run32	3D suction	2.41×10^5	21.4	0.18	0.2
3	S-HT-run33	3D suction	2.41×10^5	21.4	0.28	0.2
4	S-HT-run34	3D suction	2.42×10^5	21.4	0.66	0.2

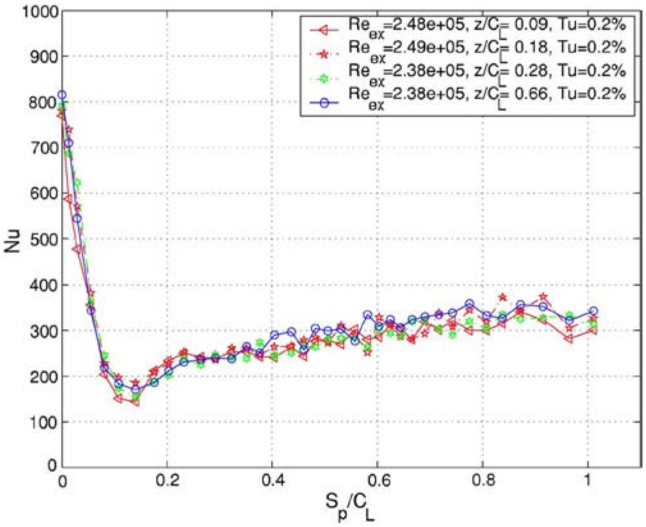

Fig. 18 Nusselt number plot on the pressure surfaces at different z/C_l

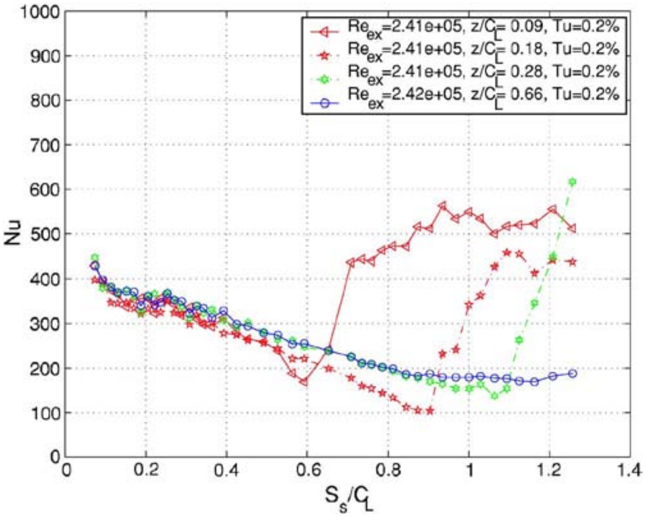

Fig. 19 Nusselt number plot on the suction surfaces at different z/C_l

Table 6 Heat transfer experimental conditions on the end wall

No.	Run number	Trip wire (mm)	$\mathrm{Re}_{\mathrm{ex}}$	U_{ex} (m/s)	Tu (%)
1	HT-run11	1.0	2.56×10^5	21.6	0.2
2	HT-run13	1.0	2.29×10^5	19.6	8.5

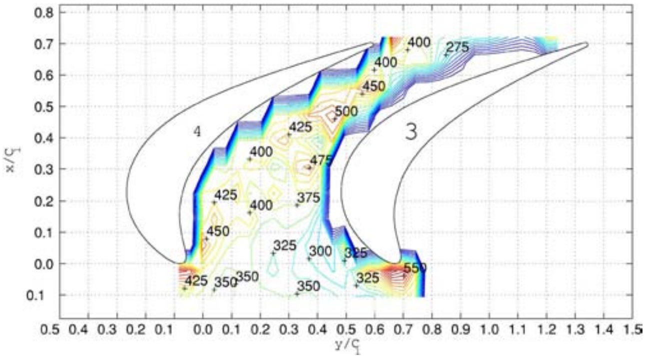

Fig. 20 Nusselt number contour (HT-run11) on the end wall with Re=2.56×10^5 and Tu=0.2%

High Nusselt numbers near the stagnation point are shown at $x/C_l=-0.02$ and $y/C_l=0.7$ in Fig. 22. High Nusselt numbers due to the horseshoe vortex and leading edge corner vortex are observed near the blades at $y/C_l=0.0$ and $y/C_l=0.5$ in the $x/C_l=0.06$ case. The measurement positions can be confirmed in Fig. 10. High Nusselt numbers by the passage vortex are shown at $y/C_l=0.2$ at the $x/C_l=0.22$ case, at $y/C_l=0.3$ at the $x/C_l=0.31$ case, and at $y/C_l=0.5$ at the $x/C_l=0.39$ case. In the absence of measurement near the blade, the plots at $x/C_l=0.47$ do not show the high heat transfer region caused by the passage vortex near the blades, which was shown by Goldstein and Spores [8]. Even though they used different blades and the mass transfer technique, a qualitative comparison show very similar trends in the two studies. For $y/C_1=0.7$ and 1.25 at $x/C_l=0.72$, high Nusselt numbers are shown due to vortex shedding from the trailing edge. Since the thermal boundary layer probe is not good at measuring temperature in the fluctuating three-dimensional flow, the real Nusselt numbers may be higher than the measured values considering the conduction error. The current thermal boundary layer technique has a tendency to indicate lower heat transfer coefficients than the real values in very thin thermal boundary layers or three-dimensional flows. Due to the paucity of the measurement locations, the results with the high turbulence intensity condition do not clearly show differences from those with the low turbulence intensity.

The limitations of this thermal boundary layer technique are the conduction error of the thermocouple and the misalignment of the probe. The conduction error in the thermocouple is significant when the thermal boundary layer is thinner than the physical diameter (76 μm in present study) of the probe. The junction of the probe is in the thin thermal boundary layer, but other parts of the thermocouple are outside of the thermal boundary layer. As the probe moves away from the wall, the conduction error decreases. Misalignment of the probe occurs with a large Reynolds number and a high turbulence intensity. When the Reynolds number is high, the probe is bent and the junction of the butt-welded junction could be off from the measurement position. The high turbulence intensity can increase the measurement uncertainty of this technique. Due to the long probe design, it is sensitive to vibration, which fluctuation in temperature measurement and measurement uncertainty.

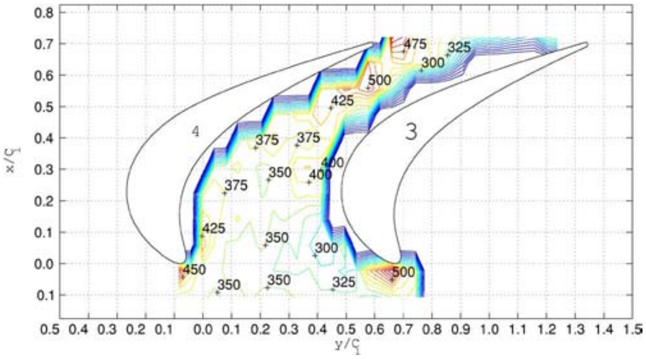

Fig. 21 Nusselt number contour (HT-run13) on the end wall with Re=2.29×10^5 and Tu=8.5%

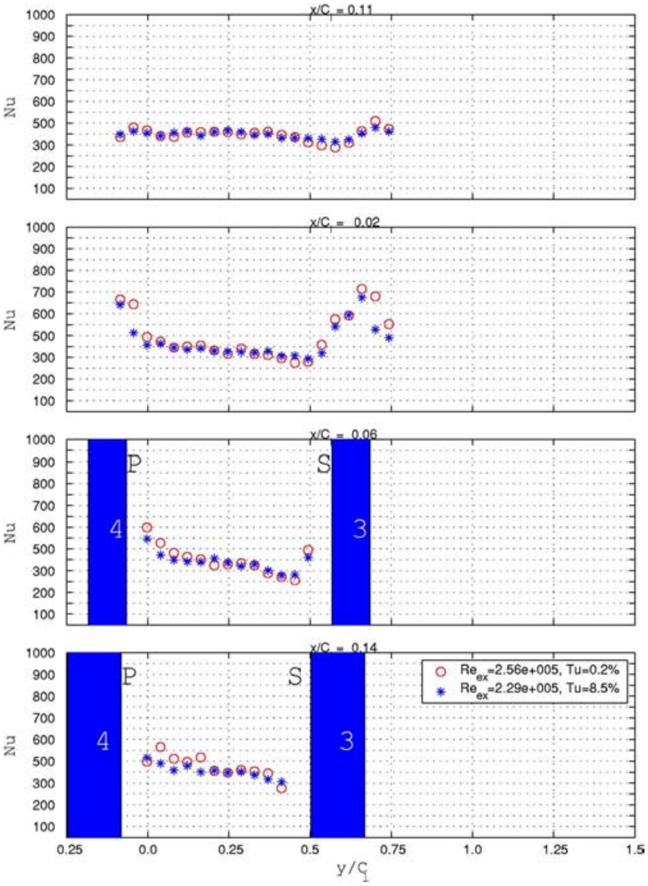

Fig. 22 Nusselt number distribution I on the end wall between blades

Summary and Conclusions

The present paper suggests an improved thermal boundary layer measurement technique and presents experimental heat transfer results in a linear turbine cascade for a heat/mass transfer analogy. A constant wall temperature condition is applied by a computer-controlled power supply using a PI control algorithm. Thermal boundary layer probes measure temperatures in the flow near the end wall and blade surfaces. Due to the versatility of the five-axis measurement unit and the wall finding technique, heat transfer coefficients are successfully evaluated from the thermal gradients and the extrapolated wall temperature. The high heat transfer regions due to the secondary flows are observed by the current technique on both the end wall and the blade surfaces. The fully automated temperature control and measurement system generally guarantees good repeatability and small measurement uncertainty. A smaller diameter thermocouple and a flatter design would reduce the conduction error and improve heat transfer measurements in the boundary layers.

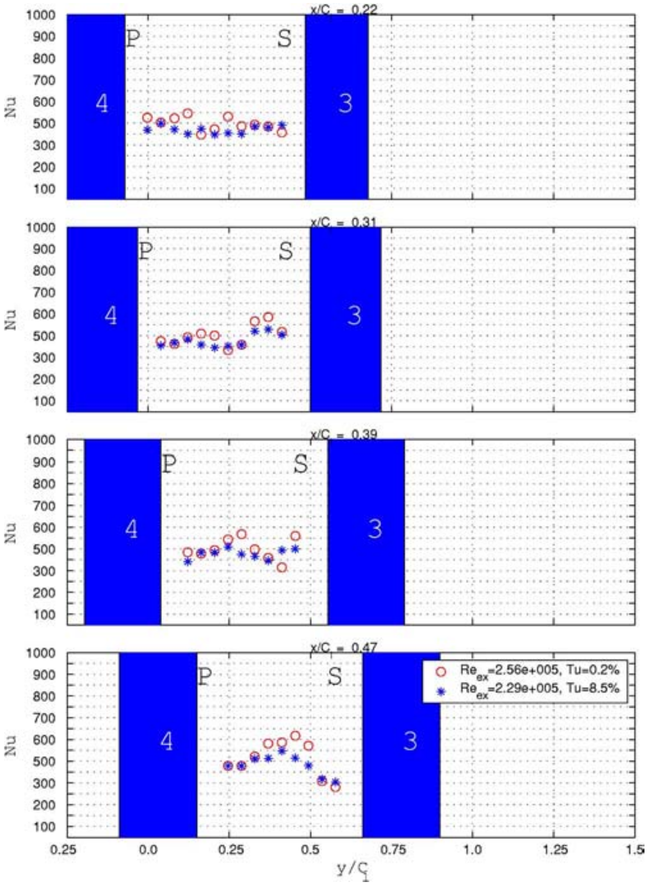

Fig. 23 Nusselt number distribution II on the end wall between blades

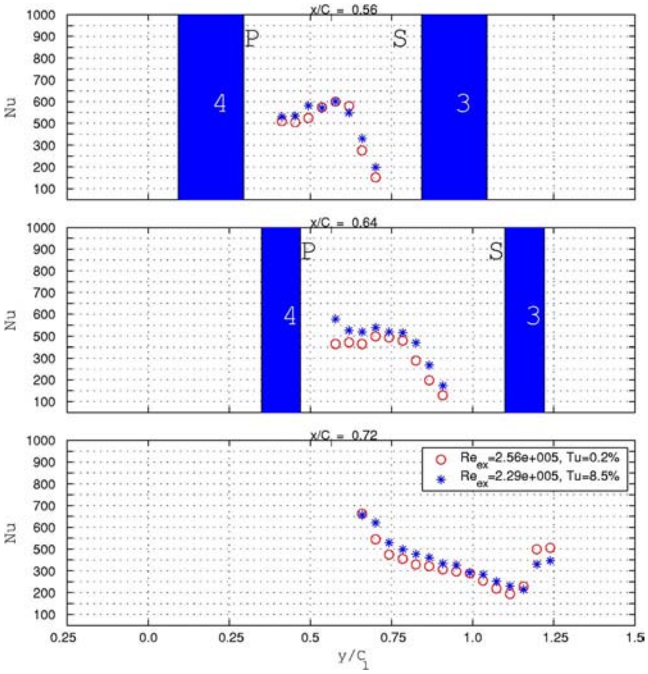

Fig. 24 Nusselt number distribution III on the end wall between blades

Acknowledgment

The authors would like to acknowledge DOE for their support. This research was performed with financial support (02-01-SR096) from the University Turbine System Research Program.

Nomenclature

AR = inlet/exit area ratio of the cascade (2.72)
C_l = characteristic length (184 mm)
c_w = local wall concentration
C_x = axial chord length of blade (130 mm)
d = distance from a blade surface
H = height of blade (457 mm); shape factor of the boundary layer (δ_1/δ_2)
h = convective heat transfer coefficient
n = the distance in the direction normal to the wall
Nu = Nusselt number (Nu=hC_l/k)
P = pitch of blade (138 mm)
p = static pressure
q_w = local wall heat flux
Re$_{\text{ex}}$ = exit Reynolds number ($\rho U_{\text{ex}} C_l/\mu$)
S_p = curvilinear coordinate on the pressure surface (Fig. 4)
S_s = curvilinear coordinate on the suction surface (Fig. 4)
T_w = local wall temperature
T_{air} = free stream temperature
T_{aw} = adiabatic wall temperature
u, v = velocity components
U_∞ = mainstream inflow velocity in wind tunnel
U_{ex} = mainstream exit velocity at the exit of the cascade (ARU_∞)
x = coordinate in the blade chord direction
X_i = coordinate along the inflow direction (Fig. 4)
y = coordinate traverse the blade chord direction
Z = coordinate in the spanwise direction of cascade, Z=0 at the tip

Greek Symbols

k = thermal conductivity of air
δ = boundary layer thickness
ν = kinematic viscosity
β_1 = inlet angle of cascade (35 deg)
β_2 = outlet angle of cascade (72.5 deg)

Subscripts

atm = atmosphere property
st = static property
w = wall property

References

[1] Blackwell, B. F., and Moffat, R. J., 1975, "Design and Construction of a Low Velocity Boundary Temperature Probe," ASME J. Heat Transfer, **97**(2), pp. 313–315.

[2] Blair, M. F., 1974, "An Experimental Study of Heat Transfer and Film Cooling on Large-Scale Turbine Endwalls," ASME J. Heat Transfer, **96**, pp. 524–529.

[3] Graziani, R. A., Blair, M. F., Taylor, J. R., and Mayle, R. E., 1980, "An Experimental Study of Endwall and Airfoil Surface Heat Transfer in a Large Scale Turbine Blade Cascade," J. Eng. Power, **102**, pp. 257–267.

[4] Qiu, S., Simon, T. W., and Ralph, J. V., 1995, "Evaluation of Local Wall Temperature, Heat Flux, and Convective Heat Transfer Coefficient From the Near-Wall Temperature Profile," *Heat Transfer in Turbulent Flows – 1995 ASME IMECE Conference*, N. K. Anand, R. S. Amano, and B. F. Armaly, eds., San Francisco, CA, Vol. 318, pp. 45–52.

[5] Wang, H. P., Olson, S. J., Goldstein, R. J., and Eckert, E. R. G., 1997, "Flow Visualization in a Linear Turbine Cascade of High Performance Turbine Blades," ASME J. Turbomach., **119**, pp. 1–8.

[6] Wang, H., 1997, "Local Mass Transfer Measurement from a Turbine Blade: Influence of High Turbulence With Large Length Scale on Heat/Mass Transfer," Ph.D. thesis, University of Minnesota, July.

[7] Jin, P., 2000, "Local Measurement and Numerical Modeling of Mass/Heat Transfer from a Turbine Blade in a Linear Cascade With Tip Clearance," Ph.D. thesis, University of Minnesota, July.

[8] Goldstein, R. J., and Spores, R. A., 1988, "Turbulent Transport on the Endwall in the Region Between Adjacent Turbine Blades," ASME J. Eng. Gas Turbines Power, **110**, pp. 862–869.

G. Comini
e-mail: gianni.comini@uniud.it

C. Nonino

S. Savino

Department of Energy Technologies,
University of Udine,
Via delle Scienze 208,
33100 Udine, Italy

Numerical Evaluation of Fin Performance Under Dehumidifying Conditions

A numerical model of moist air cooling in compact heat exchangers is presented. The model requires the solution of a coupled problem, since interface temperatures, obtained from the solution of the energy equation in adjacent fluid and solid regions, are used to set the appropriate boundary conditions for the transport equation of water vapor in moist air. The approach is completely general, even if the finite-element method is used for the simulations reported in the paper. The numerical results are favorably compared with the corresponding experimental results concerning the rectangular and wavy fins under dehumidifying conditions. [DOI: 10.1115/1.2755012]

Keywords: finned surfaces, dehumidification, heat transfer, mass transfer, conjugate problems, numerical simulation

Introduction

Simultaneous heat and mass convection occurs in air-cooling systems whenever the exchange surfaces are at a temperature below the local dew point. Typical examples are heat exchangers utilized for summer air-conditioning and process-air dehumidifiers employed in industrial and home appliances. Usually, in these apparatuses, the air-side convection coefficient is much smaller than the convection coefficient for the refrigerating fluid. Thus, on the air side, recourse is often made to fins, which increase the exchange area and reduce the thermal resistance.

When vapor condensation occurs on the fin surfaces, the cooling process requires the removal of sensible as well as latent heat. Because of the industrial importance of heat exchangers operating under dehumidifying conditions, the evaluation of wet fin performances has received a great deal of attention in the literature. In particular, it is worth mentioning the experimental researches of Wang and co-workers, which deal with the design of wet heat exchangers [1–5] as well as with fin performances in both dry and wet conditions [6–9]. The aforementioned studies represent a substantial database. However, the feeling is that designers need further information on fin performances and air-side convection coefficients under dehumidifying conditions [4,5]. The present paper illustrates a numerical procedure that can be used to obtain this kind of information. In general, the modeling of dehumidification processes, which involve adjacent fluid and solid domains, requires the solution of a conjugate conduction and convection problem, since interface temperatures must be calculated at the same time as temperature distributions in the fluid and solid regions. To this aim, it is convenient to solve the energy equation in the whole domain, including the fluid and the solid regions, even if the species conservation equation and the Navier–Stokes equations can still be solved only in the fluid region.

At interfaces between the fluid and the solid regions, we can use the ideal gas relationship to compute the local mass fraction of water vapor corresponding to the saturation pressure at the wall temperature. When interface temperatures are lower than the local dew point, condensation occurs and the saturation value of the mass fraction is utilized as a Dirichlet boundary condition for the species conservation equation. If, on the contrary, interface temperatures are higher than the local dew point, no condensation occurs and we can utilize a Neumann boundary condition (zero normal derivative of the mass fraction) for the species conservation equation.

Our model neglects both the advection velocities induced by vapor condensation and the presence of droplets and liquid films. Neglecting advection velocities is certainly justified by the low rates of mass convection, which characterize standard air-cooling processes [10]. Neglecting the presence of droplets and liquid films implies, in principle, that the condensate is promptly removed from the interfaces. In practice, as shown in the following sections, the assumption can be extended to many situations of technical interest characterized by a good drainage and a relatively low rate of mass convection. On the other hand, designers of compact heat exchangers always devote much effort to the achievement of a good drainage. Retained condensate, in fact, might either be blown away from the apparatus, creating an unwanted fog, or remain on the cooling surface, providing a medium for the growth of bacteria [11,12]. Furthermore, the influence of droplets and liquid films has not been fully established experimentally (see, for example, Refs. [11–14]). The reason is that droplets increase the effective roughness of the exchange surface. Thus, they increase friction factors and heat convection coefficients in turbulent flows, but not in laminar flows, which are rather insensitive to roughness effects. Similarly, liquid films not only increase pressure losses and convection rates by increasing average axial velocities but also bring about additional thermal resistances. The prevailing opinion is that pressure losses are increased by the retained condensate, at least in the presence of liquid films, but it is still unclear whether heat and mass convection coefficients are increased or decreased.

When the presence of liquid films and droplets is neglected, the interface between the air and the solid region is an internal boundary as far as the energy equation is concerned. Therefore, the continuity of temperatures is ensured by the solution of the energy equation on the whole domain, but the additional latent heat flux on surfaces where condensation takes place must still be accounted for. This heat flux affects the temperature distribution on interfaces and, consequently, influences also the boundary condition for the species conservation equation. The already mentioned coupling between temperature and mass concentration fields is, in fact, due to the coupling between conduction and convection.

The proposed model does not rely on a particular numerical technique. However, in this study, we utilize an equal-order finite-element procedure for space discretization and a pseudotransient algorithm to obtain the steady-state solutions [15,16]. The tech-

---

Contributed by the Heat Transfer Division of ASME for publication in the JOURNAL OF HEAT TRANSFER. Manuscript received October 24, 2006; final manuscript received February 13, 2007. Review conducted by Bengt Sunden.

nique used to deal with the pressure-velocity coupling in the Navier–Stokes equations is described in Ref. [17].

The capabilities of the procedure to deal with realistic boundary conditions and complex geometries have already been demonstrated by several simulations of tube-fin exchangers operating under dehumidifying conditions [15,16]. Here, the accuracy and reliability of the methodology are assessed by comparing our numerical results with the experimental results of Wang and coworkers for rectangular [6] and wavy fins [7] under dehumidifying conditions.

Statement of the Problem

The applications considered here refer to an incompressible, laminar flow of moist air treated as a constant property fluid. The heat and mass convection process is governed by the continuity equation, the Navier–Stokes equations, the species conservation equation, and the energy equation. The continuity and the Navier-Stokes equations can be written as

$$\nabla \cdot \mathbf{v} = 0 \qquad (1)$$

$$\rho \frac{\partial \mathbf{v}}{\partial \tau} + \rho \mathbf{v} \cdot \nabla \mathbf{v} = \mu \nabla^2 \mathbf{v} - \nabla p \qquad (2)$$

The species conservation equation can be written as

$$\frac{\partial \omega}{\partial \tau} + \mathbf{v} \cdot \nabla \omega = \mathcal{D} \nabla^2 \omega \qquad (3)$$

where ω is the mass fraction of water vapor in moist air.

In the absence of volumetric heating and of significant viscous dissipation, the energy equation can be written as

$$\rho c_p \frac{\partial t}{\partial \tau} + \rho c_p \mathbf{v} \cdot \nabla t = k \nabla^2 t \qquad (4)$$

In the numerical simulations, the Navier–Stokes equations and the species conservation equation are solved only in the fluid region, while the energy equation is solved in both the fluid and the solid regions. Obviously, in the solution of the energy equation in the whole domain, we must refer to the pertinent thermophysical properties in each region, and we must assume $\mathbf{v}=0$ in the solid region.

To complete the formulation, appropriate conditions must be imposed on the interfaces between the fluid and solid domains and on the external boundaries.

Interface Boundary Conditions

As already pointed out, we disregard the transverse velocity component induced by the condensation process, and we assume that the condensate is promptly removed from the interface. In the absence of advection velocities, we impose the usual no-slip conditions

$$\mathbf{v} = 0 \qquad (5)$$

on all solid walls.

Under the assumption that the condensate is promptly removed, the moist air is always in direct contact with the wall, and the distribution of the interface temperatures t_w obtained from the solution of the energy equation leads to the appropriate boundary condition for the species conservation equation. The implementation is done as illustrated below.

On interfaces where the temperature is lower than the local dew point, we can use the ideal gas relationship to compute the value of the mass fraction of water vapor corresponding to the saturation pressure p_s at the absolute wall temperature T_w

$$\omega_s(t_w) = \frac{p_s(t_w)}{\rho R_v T_w} \qquad (6)$$

In the above equation, R_v is the gas constant for water vapor and the approximate relationship used to evaluate the saturation pressure is [18]

$$p_s(t) = 610.78 \exp\left(17.2694 \frac{t}{t + 238.3}\right) \qquad (7)$$

with the vapor pressure expressed in pascals and the temperature expressed in °C. The relationship

$$\omega = \omega_s(t_w) \qquad (8)$$

obtained from Eqs. (6) and (7) is used as a Dirichlet boundary condition prescribing the distribution of the mass fraction of water vapor.

On interfaces where the temperature is higher than the local dew point, no condensation occurs and we can thus use the Neumann boundary condition

$$\frac{\partial \omega}{\partial n} = 0 \qquad (9)$$

that yields a zero value of the mass flow rate of vapor condensing per unit area ($\dot{m}_v''=0$).

Since the interface temperature is obtained from the energy equation, the continuity of temperature between the fluid and the solid regions is already ensured by the model. On the other hand, on interfaces where condensation takes place, we must account for the latent heat flux

$$q_\lambda'' = \dot{m}_v'' H_{vl} \qquad (10)$$

when we solve the energy equation.

Other Boundary Conditions

At inflow, we prescribe the inlet distributions of velocity, mass fraction, and temperature by imposing

$$\mathbf{v} = \mathbf{v}_i \quad \omega = \omega_i \quad t = t_i \qquad (11)$$

We must also specify suitable conditions at an artificial outflow boundary. These may be represented by the advective boundary conditions written in the form

$$\frac{\partial \mathbf{v}}{\partial \tau} + \bar{u} \frac{\partial \mathbf{v}}{\partial n} = 0$$

$$\frac{\partial \omega}{\partial \tau} + \bar{u} \frac{\partial \omega}{\partial n} = 0$$

$$\frac{\partial t}{\partial \tau} + \bar{u} \frac{\partial t}{\partial n} = 0 \qquad (12)$$

In the above equations, $\bar{u}$ is a constant phase speed, estimated as the average velocity in the direction n orthogonal to the outflow boundary. It must be noted that, in steady-state problems, boundary conditions (12) reduce to the more common zero normal derivative condition for all variables.

On symmetry boundaries, we can impose the boundary condition

$$u_n = \frac{\partial u_\tau}{\partial n} = \frac{\partial \omega}{\partial n} = \frac{\partial t}{\partial n} = 0 \qquad (13)$$

where u_n is the velocity component in the normal direction and u_τ is the velocity component in the tangential direction. The adiabatic boundary condition can be considered a particular symmetry condition for the temperature distribution and can thus be written in the usual form: $\partial t/\partial n=0$. In addition, appropriate thermal boundary conditions must be imposed on the external boundaries of the portion of the domain where only the energy equation is solved.

Finally, it must be pointed out that, in the context of the numerical solution procedure adopted [17], appropriate boundary conditions for pressure are

$$\frac{\partial p}{\partial n} = 0 \tag{14}$$

applied on the whole boundary, with the value $p=0$ specified at least in one point of the domain to fix the pressure level.

Data Reduction

The loss of performance of a finned surface with respect to an unfinned one is characterized by an efficiency which can be defined in different ways. To allow significant comparisons between the present numerical results and the experimental results of interest here [6,7], wet fin efficiencies are evaluated from the enthalpy distributions using the relationship

$$\eta_h = \frac{i(\bar{t}_a, \bar{\phi}_a) - i(\bar{t}_f)}{i(\bar{t}_a, \bar{\phi}_a) - i(t_b)} \tag{15}$$

where $i(\bar{t}_a, \bar{\phi}_a)$ is the enthalpy of the humid air at the average temperature $\bar{t}_a$ and average relative humidity $\bar{\phi}_a$ between inflow and outflow, $i(\bar{t}_f)$ is the saturation enthalpy of the humid air at the average fin temperature $\bar{t}_f$, and $i(t_b)$ is the saturation enthalpy of the humid air at the temperature t_b of the fin base. The dry fin efficiency is calculated from the corresponding expression

$$\eta_d = \frac{\bar{t}_a - \bar{t}_f}{\bar{t}_a - t_b} \tag{16}$$

In some instances, it is convenient to define, for both wet and dry operations, a sensible heat transfer coefficient. With reference to the procedure outlined in Ref. [7], the sensible heat transfer rate is first evaluated as

$$q_a = \dot{m}_a c_{pa} (\bar{t}_{ai} - \bar{t}_{ao}) \tag{17}$$

from the average inflow $\bar{t}_{ai}$ and outflow $\bar{t}_{ao}$ temperatures of the humid air. Then the sensible heat transfer coefficient is calculated from the expression

$$h_0 = \frac{q_a}{\eta_0 A_0 \Delta t_{lm}} \tag{18}$$

where η_0 is the overall fin efficiency, related to the fin surface area A_f, the total heat transfer area A_0, and the dry fin efficiency η_d by the expression

$$\eta_0 = 1 - \frac{A_f}{A_0}(1 - \eta_d) \tag{19}$$

The log-mean temperature difference is expressed as

$$\Delta t_{lm} = \frac{(\bar{t}_{ao} - t_{bo}) - (\bar{t}_{ai} - t_{bi})}{\ln[(\bar{t}_{ao} - t_{bo})/(\bar{t}_{ai} - t_{bi})]} \tag{20}$$

where $\bar{t}_a$ is the average air temperature, and t_{bi} and t_{bo} are the temperatures of the fin base at inflow and outflow, respectively.

Numerical Simulations

As already mentioned, the formulation illustrated here does not rely on a particular numerical technique. However, in the present study, we utilized an equal-order finite-element procedure for space discretization and a pseudotransient algorithm to obtain the steady-state solutions [15,16]. The technique used to deal with the pressure-velocity coupling in the Navier–Stokes equations is described in Ref. [17]. A sequential approach is adopted for the solution of momentum, energy, and species conservation equations. Equal-order interpolation is used in the approximation of velocity components and pressure, while the stabilization of the flow field is achieved by means of a consistent Petrov-Galerkin (SUPG) formulation [19]. The second derivatives of the finite-element solution, necessary for the computation of the SUPG stabilization terms, are approximated as suggested in Ref. [20]. As a first test of the model [10], we considered a boundary-layer solution for the flow of moist air in contact with a cold plate [21]. The comparisons reported in this paper are much more exhaustive, since they are based on the experimental results of Wang and co-workers for rectangular fins [6] and wavy fins [7] under dehumidifying conditions.

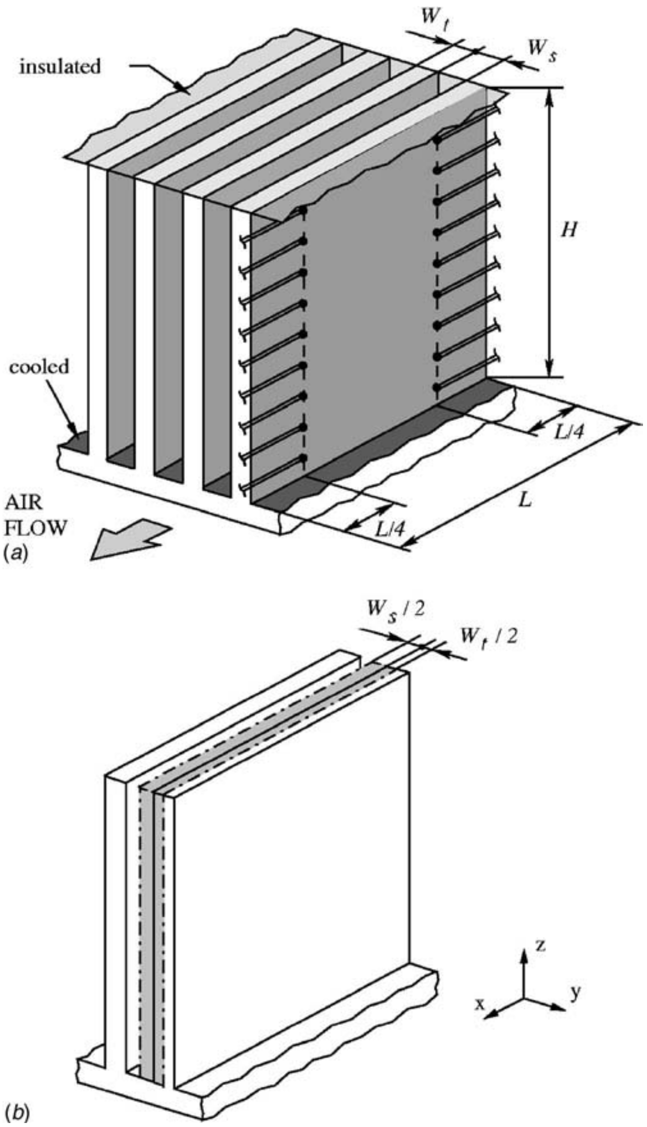

Fig. 1 Rectangular fins: (*a*) geometry (not to scale) and location of thermocouples and (*b*) computational domain

In our analysis, we considered the laminar flow of moist air, treated as an incompressible and constant property fluid. The values of the thermophysical properties used in the calculations were $\rho=1.19\ \mathrm{kg/m^3}$, $\mu=1.84\times10^{-5}\ \mathrm{kg/(m\,s)}$, $\mathcal{D}=2.60\times10^{-5}\ \mathrm{m^2/s}$, $c_p=1.03\ \mathrm{kJ/(kg\,K)}$, $k=2.62\times10^{-2}\ \mathrm{W/(m\,K)}$, and $H_{vl}=2480\ \mathrm{kJ/kg}$. Steady-state solutions were obtained as the final stages of pseudotransient simulations starting from arbitrary initial conditions. Unconditionally stable schemes of the implicit type were used for time integration. Before the final runs, grid and time-step independence were established on the basis of calculations in which the distance between grid points and the time step

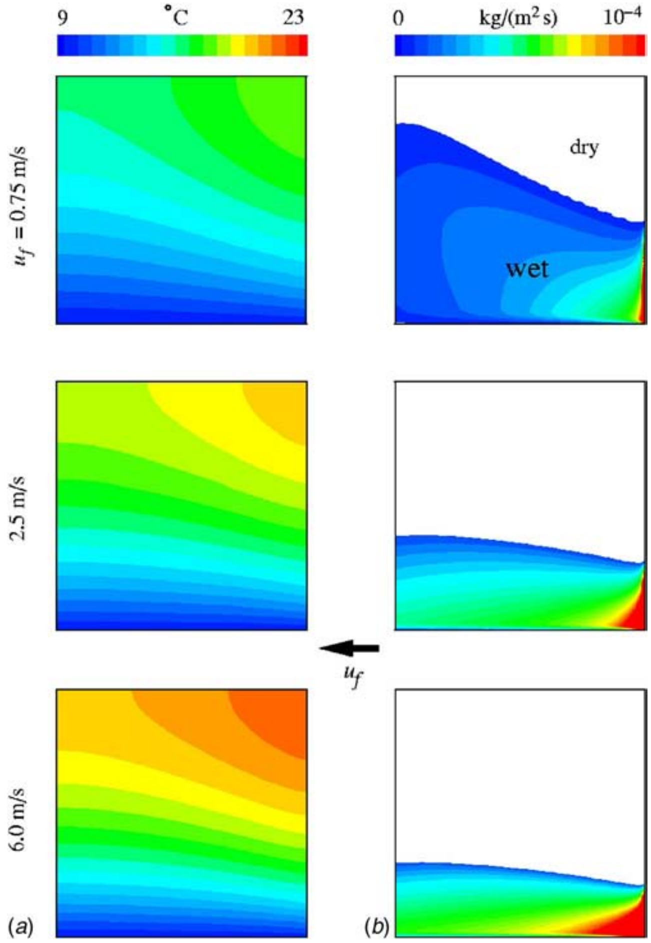

Fig. 2 Rectangular fins in wet conditions at ϕ_i=50% with three different frontal velocities u_f: (*a*) temperature distributions and (*b*) mass flow rates of vapor condensing per unit area of the fin surfaces

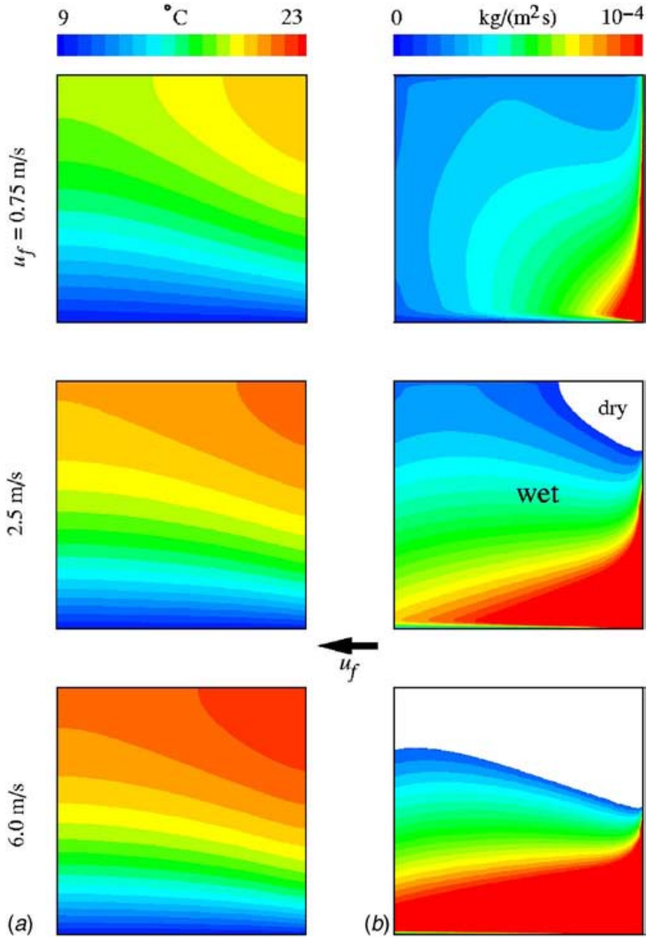

Fig. 3 Rectangular fins in wet conditions at ϕ_i=70% with three different frontal velocities u_f: (*a*) temperature distributions and (*b*) mass flow rates of vapor condensing per unit area of the fin surfaces

were progressively reduced from one simulation to another. When further reductions of distances, or of time steps, led to changes in the average convection coefficients smaller than 1%, the results were considered to be independent of the grid or of the time step, respectively.

Convective Heat and Mass Transfer on Rectangular Fins

The first comparison is carried out with reference to the experiments illustrated in Ref. [6], concerning condensation on rectangular plane fins. The geometry of the test section and the location of the thermocouples are illustrated in Fig. 1(*a*). The thermocouples were positioned near the leading edge at $x/L=0.25$ and near the trailing edge at $x/L=0.75$ of one of the fins, and were vertically spaced at $\Delta z/L=0.1$ intervals [6]. The aluminum alloy 6061, having a thermal conductivity $k=150$ W/(m K), was chosen as the base and fin material, and the height and length of the fins were $H=L=100$ mm. The fin thickness was $W_t=2$ mm, and the fin spacing was $W_s=3$ mm. The experimental conditions were as follows [6].

- In wet tests, inlet dry bulb temperature $\overline{t}_{ai}=27^\circ\mathrm{C}$, base fin temperature $t_b=9^\circ\mathrm{C}$ (uniform), and inlet relative humidity ϕ_i=50%, 70%, and 90%.
- In dry tests, inlet dry bulb temperature $\overline{t}_{ai}=20^\circ\mathrm{C}$, base fin temperature $t_b=35^\circ\mathrm{C}$ (uniform), and inlet relative humidity ϕ_i=70%.

Using the experimental values as boundary conditions, systematic computations were carried out for several values of the frontal velocity u_f in the range $0.3 \leqslant u_f \leqslant 6$ m/s. The corresponding range of Reynolds numbers $\mathrm{Re}=\rho u_i D_h/\mu$ was $180 \leqslant \mathrm{Re} \leqslant 3600$, where D_h is the hydraulic diameter of the flow passages and $u_i=u_f(W_s+W_t)/W_s$ is the inlet velocity. Advantage of existing symmetries was taken in the definition of the computational domain, which is shown in Fig. 1(*b*). The final computational grid consisted of 94,864 nodes and 86,640 eight-node exahedral elements and the time step $\Delta\tau$ used in the final calculations was equal to 0.0001 s.

The distributions of temperature and mass flow rates of vapor condensing per unit area of the fin surface during the wet tests are illustrated in Figs. 2 and 3, where reference is made to the inlet relative humidities ϕ_i=50% and ϕ_i=70%, respectively, and three different frontal velocities u_f. In the white areas, no condensation occurs because the fin temperature is above the local dew point temperature. Elsewhere, the rate of condensation decreases from inflow to outflow, since the decrease of the mass fraction of water vapor in the air stream has a more significant effect than the decrease of fin temperatures. The extensions of the dry and wet portions of the fin, in addition to being correlated to the temperature distributions, are clearly influenced by the frontal velocity of the main flow and the inlet relative humidity. In particular, the decrease of the frontal velocity u_f from 6.0 m/s to 0.75 m/s causes an increase of both the average height and the inclination of the boundary, which separates the dry and wet portions. A similar effect is obtained by increasing the inlet relative humidity

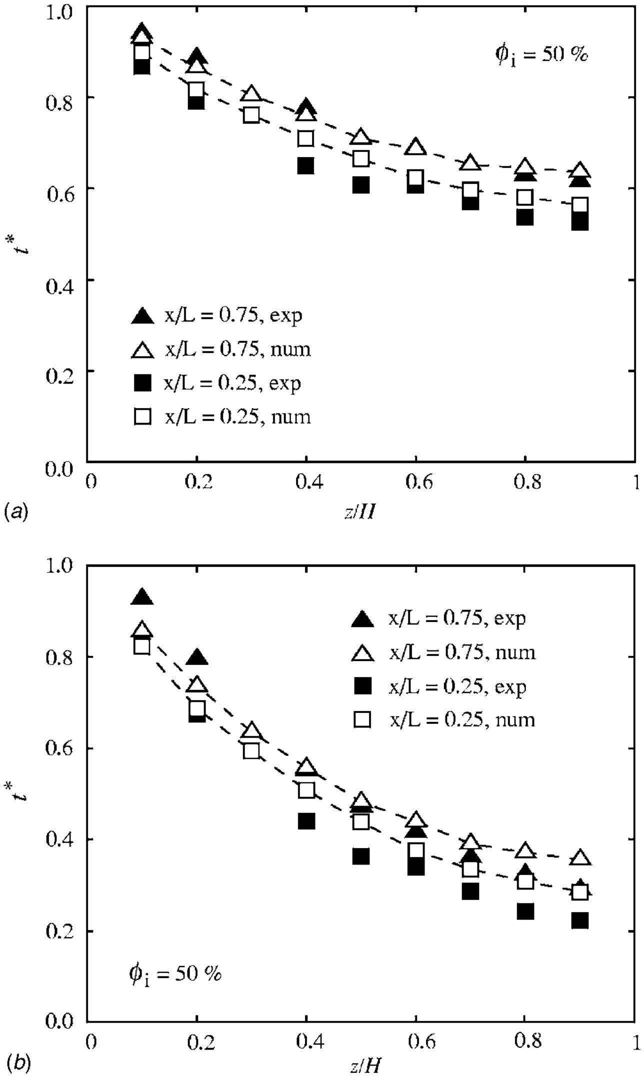

Fig. 4 Rectangular fins in wet conditions at ϕ_i=50%: experimentally [6] and numerically determined values of dimensionless temperatures for (*a*) u_f=0.5 m/s and (*b*) u_f=4.0 m/s

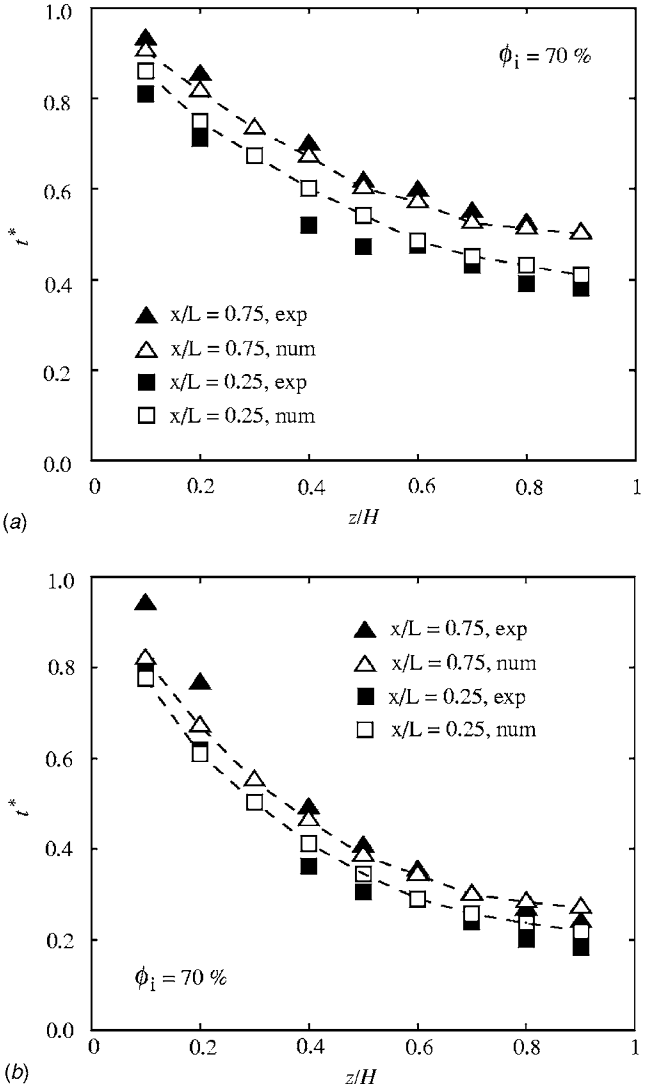

Fig. 5 Rectangular fins in wet conditions at ϕ_i=70%: experimentally [6] and numerically determined values of dimensionless temperatures for (*a*) u_f=0.5 m/s and (*b*) u_f=4.0 m/s

from 50% to 70%. In fact, the dry-wet boundary moves upward and increases its inclination and, at ϕ_i=70% and u_f=0.75 m/s, the whole fin is wet. At ϕ_i=90%, the temperature remains below the local dew point on the whole fin for all frontal velocities. Consequently, the ϕ_i=90% results are of little interest and have not been reported here. We can also add that, from a qualitative point of view, all numerically determined distributions of mass flow rates of vapor per unit area compare favorably with the corresponding visualizations of Lin et al. [6], which cannot be reported here.

More quantitative comparisons can be carried out between computed temperatures and temperatures measured at selected locations [6]. The comparisons illustrated in Fig. 4 concern the ϕ_i =50% case and two frontal velocities: u_f=0.5 and 4 m/s. As can be seen, the agreement is quite good. In particular, the expected trends are confirmed since the dimensionless temperatures $t^*=(t_f-\bar{t}_a)/(t_b-\bar{t}_a)$ near the leading edge, at x/L=0.25, are lower than those near the trailing edge, at x/L=0.75. Analogous results, reported in Figs. 5 and 6, have been obtained also for ϕ_i=70% and ϕ_i=90%.

In Fig. 7, calculated and experimental values of wet and dry fin efficiencies are compared in the whole range of Reynolds numbers considered. The overall agreement is very good. Moreover, the numerical simulations correctly yield wet fin efficiencies consistently lower than the corresponding dry fin efficiencies. In fact, because of the latent heat contribution, total heat transfer rates are higher in wet conditions. Thus, in wet conditions, heat conduction through the fin is less effective in maintaining a low temperature gradient along the fin. Finally, it can be pointed out that both wet and dry efficiencies decrease with the Reynolds number since convection coefficients increase with the Reynolds number, thus increasing heat loads on the fin.

Convective Heat and Mass Transfer on Wavy Fins

The second comparison is carried out with reference to the experiments illustrated in Ref. [7], concerning condensation on wavy fins. Boundary conditions and geometry of the domain, schematized in Fig. 8(*a*), were the same referred to in some of the tests carried out by Lin et al. [7]. Also in this case, the aluminum alloy 6061, having a thermal conductivity k=150 W/(m K), was chosen as the base and fin material. As shown in Fig. 8, the geometry, which consists of several two-wave fins, can be described in terms of height H=100 mm, total length L=150 mm, fin thickness W_t=3.2 mm, fin spacing W_s=2.6 mm, and fin inclination angle β=15 deg. The boundary conditions utilized in the simulations were as follows.

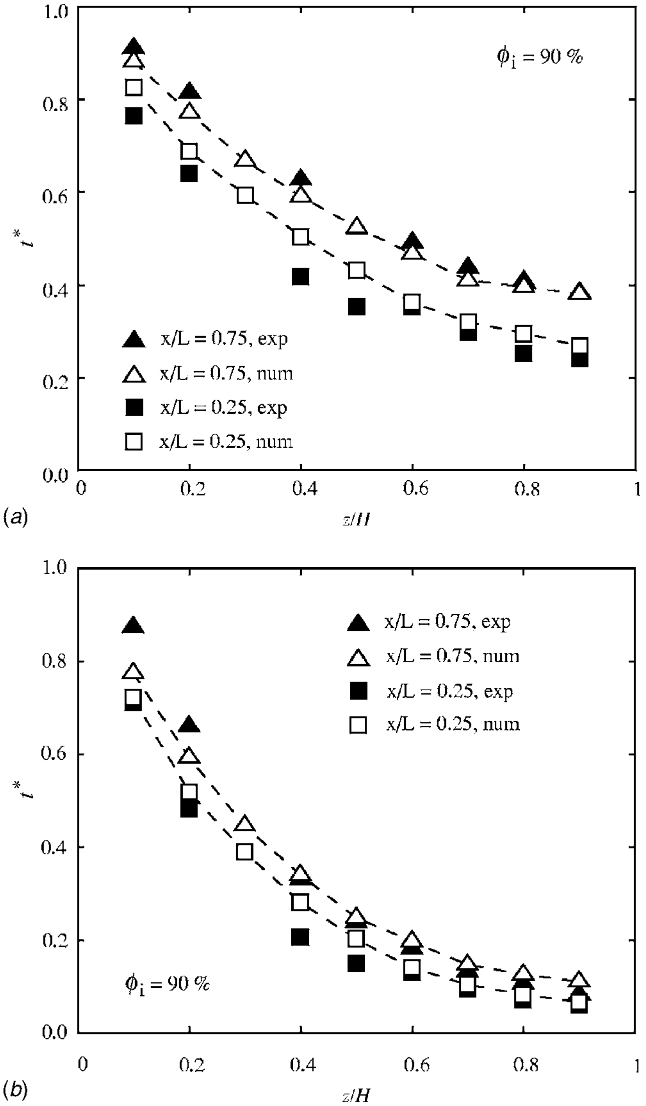

Fig. 6 Rectangular fins in wet conditions at ϕ_i=90%: experimentally [6] and numerically determined values of dimensionless temperatures for (*a*) u_f=0.5 m/s and (*b*) u_f=4.0 m/s

- In wet tests, inlet dry bulb temperature $\overline{t}_{ai}=27°\mathrm{C}$, base fin temperature $t_b=13°\mathrm{C}$ (uniform), and inlet relative humidity $\phi_i=85\%$.
- In dry tests, inlet dry bulb temperature $\overline{t}_{ai}=27°\mathrm{C}$, base fin temperature $t_b=13°\mathrm{C}$ (uniform), and inlet relative humidity $\phi_i=40\%$.

Systematic computations were carried out for several values of the frontal velocity u_f in the range $0.3 \leq u_f \leq 4$ m/s. The corresponding range of Reynolds numbers $\mathrm{Re}=\rho u_i D_h/\mu$ was $220 \leq \mathrm{Re} \leq 2900$.

The computational domain is shown in Fig. 8(*b*). In the imposition of the thermal boundary conditions, advantage was taken of the existing space periodicity in the transverse direction. The final computational grid consisted of 175,440 nodes and 161,280 eight-node exahedral elements and the time step $\Delta\tau$ used in the final calculations was equal to 0.0001 s.

With respect to the experimental measurements, numerical simulations may yield more detailed information on the variables of interest. As an example, the streamlines in the corner regions at the horizontal midplane $z/H=0.5$ are reported in Fig. 9 for two different values of the frontal velocity (u_f=0.3 and 4 m/s). At the lower frontal velocity, there is no recirculation, while at the higher frontal velocity, a flow recirculation region is present at each corner; its size increases from inflow to outflow.

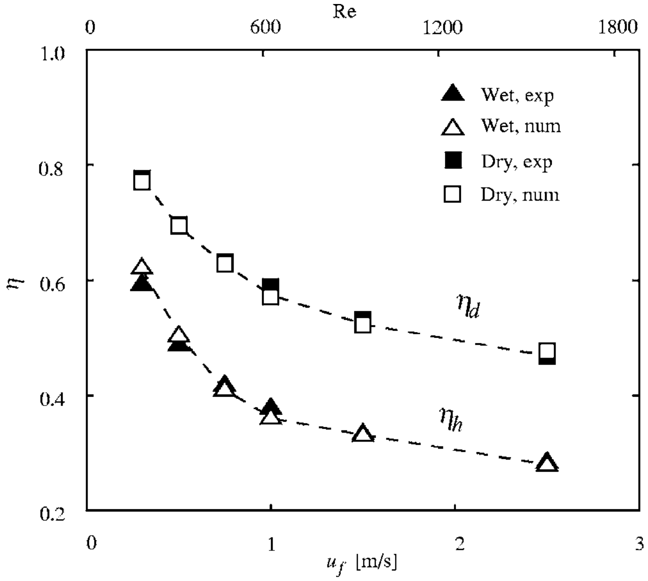

Fig. 7 Rectangular fins: experimentally [6] and numerically determined values of dry (ϕ_i=40%) and wet (ϕ_i=70%) fin efficiencies

The distributions of temperature and mass flow rates of vapor condensing per unit area of the fin surfaces are shown in Fig. 10 for $\phi_i=85\%$ and $u_f=4$ m/s. Once again the numerically determined distribution of mass flow rates of vapor per unit area, in addition to being correlated with the temperature distribution, compares favorably with the corresponding visualization of Lin et al. [7] (not reported here).

On the basis of the available experimental data [7], quantitative comparison can also be carried out between the measured and computed values of the sensible heat transfer coefficient. As can be seen from Fig. 11, the agreement is quite good. It is also worth noting that, as expected, the sensible heat transfer coefficients in wet conditions are higher than in dry conditions. This increase, however, is mainly due to the definition (18), whose denominator includes the fin efficiency (lower in wet conditions).

Conclusions

The modeling of heat and mass transfer under dehumidifying conditions requires the solution of a coupled problem, since interface temperatures, obtained from the solution of the energy equation in adjacent fluid and solid regions, are used to set the appropriate boundary conditions for the transport equation of water vapor in moist air. The energy equation must be solved in the whole domain, and the latent heat flux on the interfaces where condensation occurs must be taken into account. The latent heat flux affects the temperature distribution and, consequently, the mass flow rate of vapor at the interface. Thus, because of the coupling between conduction and convection, the temperature and mass concentration fields become coupled through the boundary conditions. In the examples of application reported here, the governing differential equations have been solved by a finite-element procedure. However, the solution steps have been formulated in a continuous setting, where no reference is made to the particular space discretization technique employed afterward. The accuracy and reliability of the proposed methodology have been demonstrated by means of comparisons with the experimental results concerning rectangular and wavy fins under dehumidifying conditions.

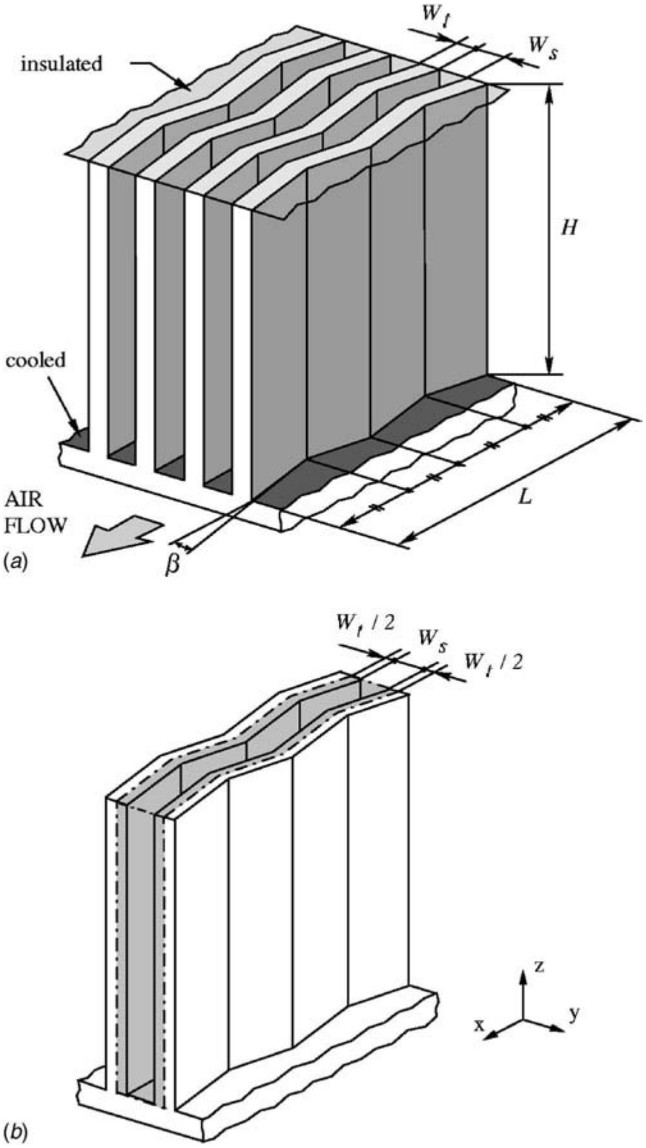

Fig. 8 Wavy fins: (*a*) geometry (not to scale) and (*b*) computational domain

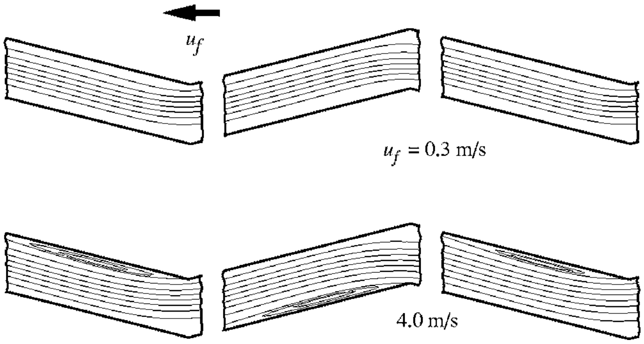

Fig. 9 Streamlines in the corner regions on the horizontal midplane $z/H=0.5$ of wavy fins for two different values of the frontal velocity u_f

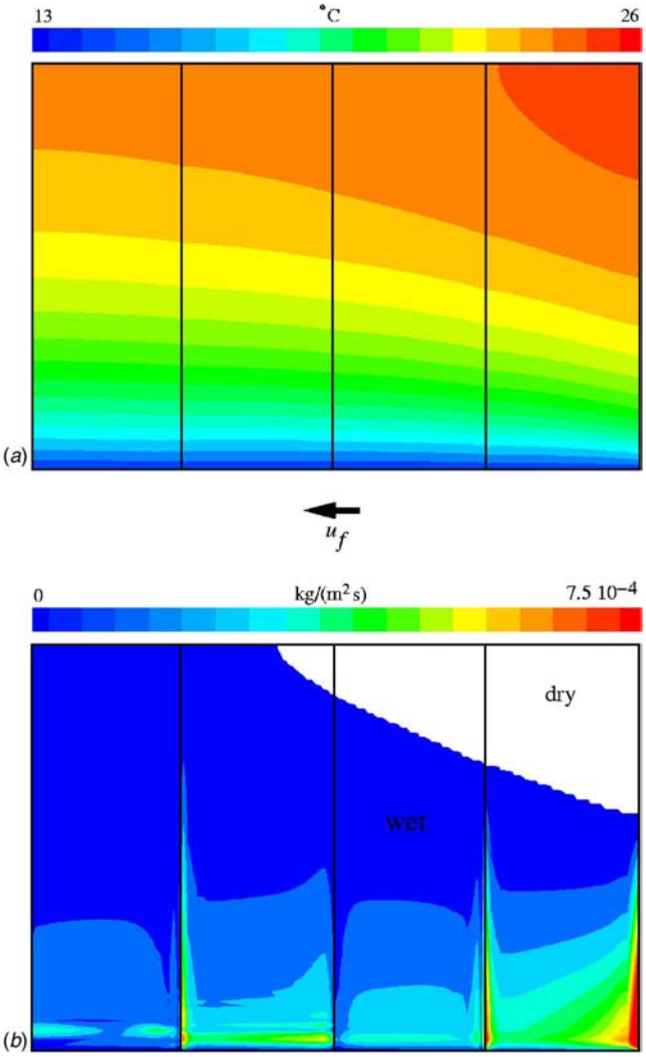

Fig. 10 Wavy fins in wet conditions at $\phi_i=85\%$ and $u_f=4$ m/s: (*a*) temperature distribution and (*b*) mass flow rate of vapor condensing per unit area of the fin surface

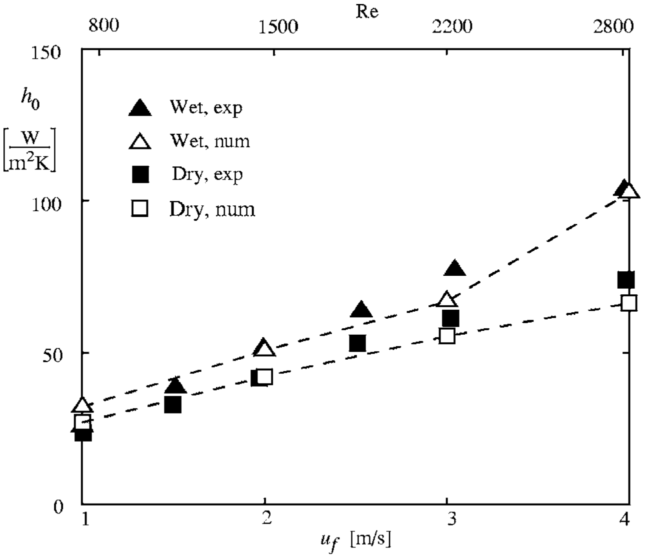

Fig. 11 Wavy fins: experimentally [7] and numerically determined values of dry ($\phi_i=40\%$) and wet ($\phi_i=85\%$) heat transfer coefficients

Acknowledgment

We gratefully acknowledge a personal communication from Professor C. C. Wang concerning the details of his experimental measurements.

Nomenclature

A = area, m^2
c_p = specific heat at constant pressure, J/(kg K)
D_h = hydraulic diameter, m
$\mathcal{D}$ = diffusion coefficient, m^2/s
h_0 = sensible heat transfer coefficient, $\mathrm{W}/(\mathrm{m}^2\,\mathrm{K})$
H = height, m
H_{vl} = latent heat of condensation, J/kg
i = enthalpy of moist air, J/kg
k = thermal conductivity, W/(m K)
L = length, m
$\dot{m}_a$ = mass flow rate of air, kg/s
$\dot{m}''_v$ = mass flow rate of vapor per unit area, $\mathrm{kg}/(\mathrm{m}^2\,\mathrm{s})$
n = outward normal, m
p = pressure, Pa
q = heat flow rate, W
q'' = heat flux, W/m^2
R_v = gas constant, kJ/(kg K)
Re = Reynolds number, $\mathrm{Re}=\rho u_i D_h/\mu$
t = temperature, °C
T = absolute temperature, K
u_f = frontal velocity, m/s
u_i = inlet velocity, m/s
$\mathbf{v}$ = velocity vector, m/s
W = width, m
x,y,z = Cartesian coordinates, m

Greek Symbols

β = angle
η = efficiency
ϕ = relative humidity
ω = mass fraction of water vapor, $\mathrm{kg}_{\mathrm{vapor}}/\mathrm{kg}_{\mathrm{moist\ air}}$
μ = dynamic viscosity, kg/(m s)
ρ = density, kg/m^3
τ = time, s

Superscript

- = average value

Subscripts

a = air
b = base of the fin
d = dry
f = fin
h = wet
i = inlet
o = outlet
n = normal
s = saturation
w = wall
λ = latent
τ = tangential
0 = referred to the total heat transfer area
* = dimensionless value

References

[1] Wang, C. C., Hsieh, Y. C., and Lin, Y. T., 1997, "Performance of Plate Finned Tube Heat Exchangers Under Dehumidifying Conditions," J. Heat Transfer, **119**, pp. 119–117.
[2] Wang, C. C., Lin, Y. T., and Lee, C. J., 2000, "Heat and Momentum Transfer for Compact Louvered Fin-and-Tube Heat Exchangers in Wet Conditions," Int. J. Heat Mass Transfer, **43**, pp. 3443–3452.
[3] Wang, C. C., Lee, W. S., Sheu, W. J., and Chang, Y. J., 2001, "Parametric Study of the Air-Side Performance of Slit Fin-and-Tube Heat Exchangers in Wet Conditions," Proc. Inst. Mech. Eng., Part C: J. Mech. Eng. Sci., **215**, pp. 1111–1121.
[4] Pirompugd, W., Wongwises, S., and Wang, C. C., 2005, "A Tube-by-Tube Reduction Method for Simultaneous Heat and Mass Transfer Characteristics for Plain Fin-and-Tube Heat Exchangers in Dehumidifying Conditions," Heat Mass Transfer, **41**, pp. 756–765.
[5] Pirompugd, W., Wongwises, S., and Wang, C. C., 2006, "Simultaneous Heat and Mass Transfer Characteristics for Wavy Fin-and-Tube Heat Exchangers under Dehumidifying Conditions," Int. J. Heat Mass Transfer, **49**, pp. 132–143.
[6] Lin, Y. T., Hsu, K. C., Chang, Y. J., and Wang, C. C., 2001, "Performance of Rectangular Fin in Wet Conditions: Visualization and Wet Fin Efficiency," J. Heat Transfer, **123**, pp. 827–836.
[7] Lin, Y. T., Hwang, Y. M., and Wang, C. C., 2002, "Performance of the Herringbone Wavy Fin Under Dehumidifying Conditions," Int. J. Heat Mass Transfer, **45**, pp. 5035–5044.
[8] Wongwises, S., and Chokeman, Y., 2004, "Effect of Fin-Thickness on the Air-Side Performance of Herringbone Wavy Fin-and-Tube Heat Exchangers," Heat Mass Transfer, **41**, pp. 147–154.
[9] Wongwises, S., Wang, C. C., and Kuvannarat, T., 2006, "Effect of Fin-Thickness on the Air-Side Performance of Wavy Fin-and-Tube Heat Exchangers Under Dehumidifying Conditions," Int. J. Heat Mass Transfer, **49**, pp. 2587–2596.
[10] Comini, G., and Savino, S., 2006, "Latent and Sensible Heat Transfer in Air-Cooling Applications," *24th UIT National Heat Transfer Conference, Keynote Lecture*, Edizioni ETS, Pisa, pp. 3–12.
[11] Korte, C., and Jacobi, A. M., 2001, "Condensate Retention Effects on the Performance of Plain-Fin-and-Tube Heat Exchangers: Retention Data and Modeling," J. Heat Transfer, **123**, pp. 926–936.
[12] ElSherbini, A. I., and Jacobi, A. M., 2006, "A Model for Condensate Retention on Plain-Fin Exchangers," J. Heat Transfer, **128**, pp. 427–433.
[13] Hu, X., Zhang, L., and Jacobi, A. M., 1994, "Surface Irregularity Effects of Droplets and Retained Condensate on Local Heat Transfer to Finned Tubes in Cross-Flow," ASHRAE Trans., **118**(1), pp. 375–381.
[14] Ramadhyani, S., 1998, "Calculation of Air-Side Heat Transfer in Compact Heat Exchangers Under Condensing Conditions," *Computer Simulations in Compact Heat Exchangers*, B. Sunden and M. Faghri, eds., Computational Mechanics, Southampton, Chap. 6.
[15] Comini, G., Nonino, C., and Savino, S., 2005, "Convective Heat and Mass Transfer under Dehumidifying Conditions," *Progress in Computational Heat and Mass Transfer*, Keynote Lecture Vol. II, R. Bennacer, ed., Editions TEC & DOC, Lavoisier, pp. 711–722.
[16] Comini, G., Nonino, C., and Savino, S., 2007, "Modeling of Coupled Conduction and Convection in Moist Air Cooling," Numer. Heat Transfer, Part A, **51**, pp. 23–37.
[17] Nonino, C., 2003, "A Simple Pressure Stabilization for a SIMPLE-Like Equal-Order FEM Algorithm," Numer. Heat Transfer, Part B, **44**, pp. 61–81.
[18] Padfield, T., 1996, "Equations Describing the Physical Properties of Moist Air," http://www.natmus.dk/cons/tp/atmcalc/atmoclc1.htm
[19] Tezduyar, T. E., and Ganjoo, D. K., 1986, "Petrov-Galerkin Formulations with Weighting Functions Dependent upon Spatial and Temporal Discretization: Applications to Transient Convections-Diffusion Problems," Comput. Methods Appl. Mech. Eng., **59**, pp. 49–71.
[20] Jansen, K. E., Collis, S. S., Whiting, C., and Shakib, F., 1999, "A Better Consistency for Low-Order Stabilized Finite Element Methods," Comput. Methods Appl. Mech. Eng., **174**, pp. 153–170.
[21] Volchkov, E. P., Terekhov, V. V., and Terekhov, V. I., 2004, "A Numerical Study of Boundary-Layer Heat and Mass Transfer in Forced Flow of Humid Air with Surface Steam Condensation," Int. J. Heat Mass Transfer, **47**, pp. 1473–1481.

Natural-Convection Flow Along a Vertical Complex Wavy Surface With Uniform Heat Flux

Mamun Molla
Department of Mechanical Engineering,
University of Glasgow,
Glasgow G12 8QQ, UK

Anwar Hossain
Department of Mathematics,
COMSATS Institute of Information Technology,
Islamabad, Pakistan

Lun-Shin Yao
Department of Mechanical and Aerospace
Engineering,
Arizona State University,
Tempe, AZ 876108

A natural-convection boundary layer along a vertical complex wavy surface with uniform heat flux has been investigated. The complex surface studied combines two sinusoidal functions, a fundamental wave and its first harmonic. Using a method of transformed coordinates, the boundary-layer equations are mapped into a regular and stationary computational domain. The transformed equations can then be solved straightforwardly by any number of numerical methods designed for regular and stationary geometries. In this paper, an implicit finite-difference method is used. The results were readily obtained on a personal computer. The numerical results demonstrate that the additional harmonic substantially alters the flow field and temperature distribution near the surface. The induced velocity normal to the y axis can substantially thicken the boundary layer, implying that its growth is not due solely to the momentum and thermal diffusion normal to the y axis along a wavy surface. [DOI: 10.1115/1.2755062]

1 Introduction

The method of transformed coordinates was originally proposed in Refs. [1–3] as a tool to solve heat-transfer problems in the presence of irregular surfaces of all kinds. Since then, many papers have been published for convection along a wavy surface for different fluids [4–25]. Recently, natural convection along a complex wavy surface consisting of two sinusoidal surfaces with a uniform surface temperature has been investigated [26]. The results show that the additional harmonic substantially alters the flow field and temperature distribution, and thickens the boundary layer; moreover, the total heat-transfer rate for a roughened surface is greater than that for a corresponding flat plate. The current study is motivated by [26], but with uniform wall heat flux, another thermal condition commonly used in heat-transfer studies.

2 Formulation of the Problem

Consider a steady two-dimensional laminar free-convection boundary layer of a viscous incompressible fluid along a semi-infinite vertical complex wavy surface with uniform surface heat flux q_w and T_∞ ambient temperature of the fluid. The boundary-layer analysis outlined below allows an arbitrary $\hat{\sigma}(\hat{x})$, but the detailed numerical work assumes that the surface exhibits a particular sinusoidal-based variation from a flat surface. This complex wavy surface is described by

$$\hat{y}_w = \hat{\sigma}(x) = \hat{a}_1 \sin\left(\frac{2\pi\hat{x}}{L}\right) + \hat{a}_2 \sin\left(\frac{4\pi\hat{x}}{L}\right) \tag{1}$$

where L is the fundamental wavelength associated with the wavy surface, and $\hat{a}_1$ and $\hat{a}_2$ are the fundamental and harmonic amplitudes of the complex wavy surface, respectively.

The geometry of the complex wavy surface and the two-dimensional Cartesian coordinate system are shown in Fig. 1. Under the usual Boussinesq approximation, the flow is governed by the following equations of continuity, momentum, and energy (Eqs. (2)–(5), respectively):

$$\frac{\partial \hat{u}}{\partial \hat{x}} + \frac{\partial \hat{v}}{\partial \hat{y}} = 0 \tag{2}$$

$$\hat{u}\frac{\partial \hat{u}}{\partial \hat{x}} + \hat{v}\frac{\partial \hat{u}}{\partial \hat{y}} = -\frac{1}{\rho}\frac{\partial \hat{p}}{\partial \hat{x}} + \nu\nabla^2\hat{u} + g\beta(T - T_\infty) \tag{3}$$

$$\hat{u}\frac{\partial \hat{v}}{\partial \hat{x}} + \hat{v}\frac{\partial \hat{v}}{\partial \hat{y}} = -\frac{1}{\rho}\frac{\partial \hat{p}}{\partial \hat{y}} + \nu\nabla^2\hat{v} \tag{4}$$

$$\hat{u}\frac{\partial T}{\partial \hat{x}} + \hat{v}\frac{\partial T}{\partial \hat{y}} = \frac{k}{\rho C_p}\nabla^2 T \tag{5}$$

where $(\hat{x},\hat{y})$ are the dimensional Cartesian coordinates, $(\hat{u},\hat{v})$ are the velocity components parallel to $(\hat{x},\hat{y})$, g is the acceleration due to gravity, $\hat{p}$ is the pressure of the fluid, ρ is the density, k is the thermal conductivity, C_p is the specific heat at constant pressure, and $\nu(=\mu/\rho)$ is the kinematic viscosity, where μ is the constant viscosity of the fluid in the boundary-layer region.

The boundary conditions for the present problem are

$$\begin{aligned} &\hat{u} = 0 \quad \hat{v} = 0 \quad q_w = -k(\hat{n}\cdot\nabla\hat{T}) \quad \text{at } \hat{y} = \hat{y}_w = \sigma(\hat{x}) \\ &\hat{u} = 0 \quad T = T_\infty \quad \text{as } \hat{y} \to \infty \end{aligned} \tag{6}$$

where $\hat{n}$ is the unit vector normal to the complex wavy surface.

The following nondimensional variables are introduced:

$$x = \frac{\hat{x}}{L} \quad y = \frac{\hat{y} - \hat{\sigma}(\hat{x})}{L}\mathrm{Gr}^{1/5} \quad u = \frac{\rho L}{\mu}\mathrm{Gr}^{-2/5}\hat{u} \quad v = \frac{\rho L}{\mu}\mathrm{Gr}^{-1/5}(\hat{v} - \sigma_x\hat{u})$$

$$p = \frac{L^2}{\rho\nu^2}\mathrm{Gr}^{-4/5}\hat{p} \quad \theta = \frac{T - T_\infty}{\left(\frac{q_w L}{k}\right)}\mathrm{Gr}^{1/5} \quad \sigma_x = \frac{d\hat{\sigma}}{d\hat{x}} = \frac{d\sigma}{dx} \tag{7}$$

$$a_1 = \frac{\hat{a}_1}{L} \quad a_2 = \frac{\hat{a}_2}{L} \quad \mathrm{Gr} = \frac{g\beta q_w L^4}{k\nu^2}$$

where θ is the dimensionless temperature. The transformed coordinates of (x,y) are not orthogonal, but advantages over solving the problem in the original physical domain are obvious since a regular rectangular computational grid can be easily fitted to the transformed space and the boundary conditions can be rigorously accommodated.

Contributed by the Heat Transfer Division of ASME for publication in the JOURNAL OF HEAT TRANSFER. Manuscript received October 23, 2006; final manuscript received April 25, 2007. Review conducted by Gautam Biswas.

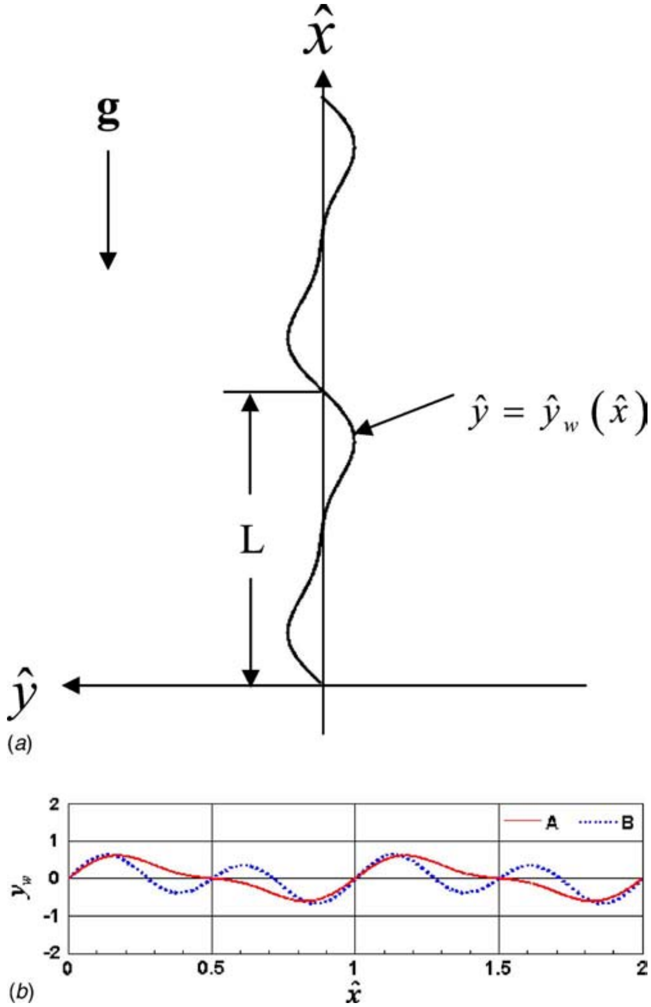

Fig. 1 (***a***)**: Physical model and coordinate system.** (***b***) **Complex wavy surface. Curve A:** $a_1=0.5$, $a_2=0.2$**; curve B:** $a_1=0.2$, $a_2=0.5$.

After introducing the transformations given in Eq. (7) into Eqs. (2)–(5), the following dimensionless governing equations are obtained after ignoring terms of smaller orders of magnitude in Gr, the Grashof number defined in Eq. (7),

$$\frac{\partial u}{\partial x} + \frac{\partial v}{\partial y} = 0 \tag{8}$$

$$u\frac{\partial u}{\partial x} + v\frac{\partial u}{\partial y} = -\frac{\partial p}{\partial x} + \sigma_x \mathrm{Gr}^{1/5}\frac{\partial p}{\partial y} + (1+\sigma_x{}^2)\frac{\partial^2 u}{\partial y^2} + \theta \tag{9}$$

$$\sigma_x\left(u\frac{\partial u}{\partial x} + v\frac{\partial u}{\partial y}\right) + \sigma_{xx}u^2 = -\mathrm{Gr}^{1/5}\frac{\partial p}{\partial y} + \sigma_x(1+\sigma_x{}^2)\frac{\partial^2 u}{\partial y^2} \tag{10}$$

$$u\frac{\partial \theta}{\partial x} + v\frac{\partial \theta}{\partial y} = \frac{1}{\mathrm{Pr}}(1+\sigma_x{}^2)\frac{\partial^2 \theta}{\partial y^2}, \tag{11}$$

where Pr represents the Prandtl number, which is defined as

$$\mathrm{Pr} = \frac{\mu C_p}{k} \tag{12}$$

Equation (10) indicates that the pressure gradient along the y direction is 0 ($\mathrm{Gr}^{-1/5}$), which implies that the lowest order pressure gradient along the x direction can be determined from the inviscid-flow solution. In the present problem, this pressure gradient is zero because there is no externally induced free stream.

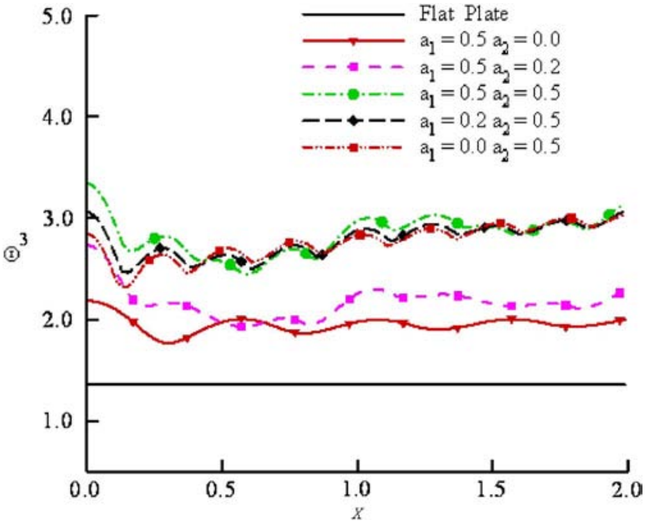

Fig. 2 Surface temperature distribution for Pr=1

Equation (9) further shows that $\mathrm{Gr}^{1/5}\partial p/\partial y$ is 0 (1) and is determined by the left-hand side of this equation. Thus, the elimination of $\partial p/\partial y$ between Eqs. (9) and (10) leads to

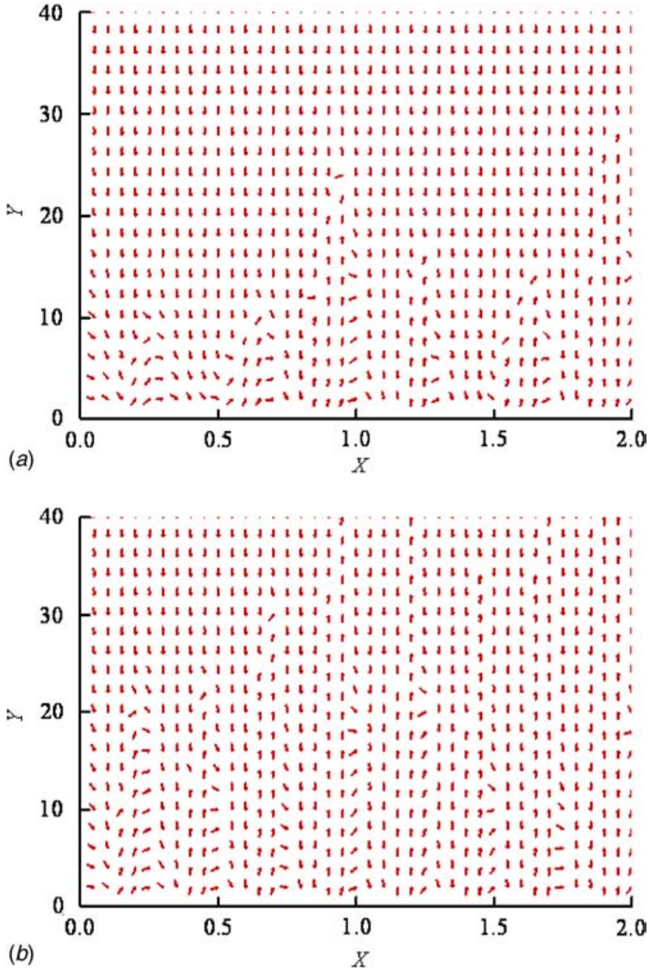

Fig. 3 Velocity vectors for (***a***) $a_1=0.5$, $a_2=0.2$ **and** (***b***) $a_1=0.2$, $a_2=0.5$

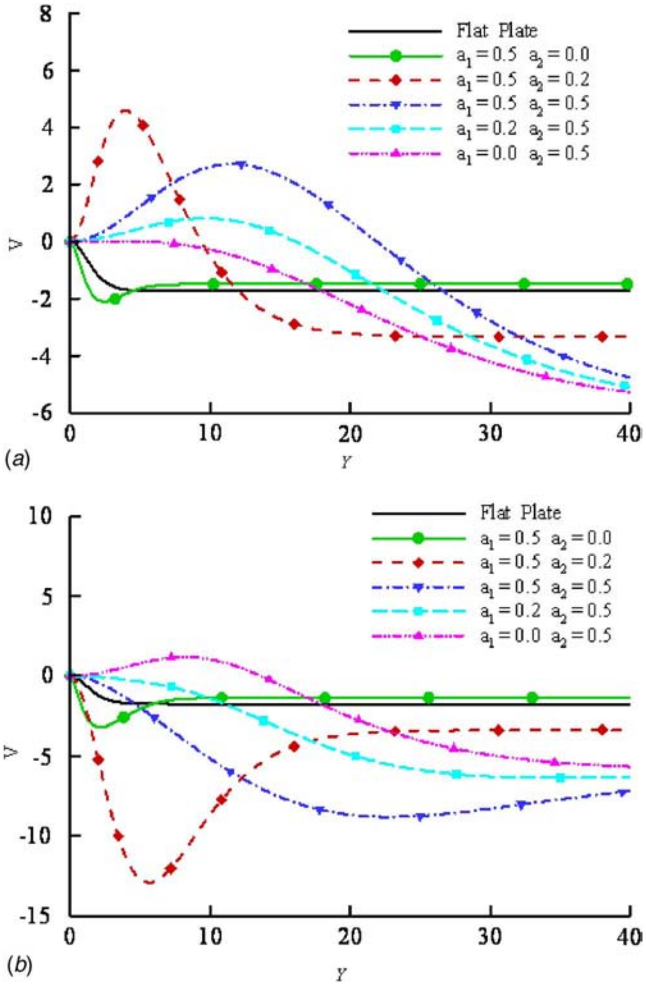

Fig. 4 Normal velocity distribution at (*a*) *X*=0.25 and (*b*) *X* =0.75

$$u\frac{\partial u}{\partial x}+v\frac{\partial u}{\partial y}=(1+\sigma_x{}^2)\frac{\partial^2 u}{\partial y^2}-\frac{\sigma_x\sigma_{xx}}{1+\sigma_x{}^2}u^2+\frac{1}{1+\sigma_x{}^2}\theta \tag{13}$$

The boundary conditions for the present problem turn into

$$u=v=0 \quad \frac{\partial\theta}{\partial y}=-\frac{1}{\sqrt{1+\sigma_x^2}} \quad \text{at } y=0$$
$$u=0 \quad \theta=0 \quad \text{as } y\to\infty \tag{14}$$

Another transformation is used to solve Eqs. (8), (11), and (13)

$$X=x, \quad Y=\frac{y}{(5x)^{1/5}} \quad U(X,Y)=\frac{u}{(5x)^{3/5}}$$
$$V(X,Y)=(5x)^{1/5}v \quad \Theta(X,Y)=\frac{\theta}{(5x)^{1/5}} \tag{15}$$

Using Eq. (15), Eqs. (8), (11), and (13) take the following forms:

$$(5X)\frac{\partial U}{\partial X}+3U-Y\frac{\partial U}{\partial Y}+\frac{\partial V}{\partial Y}=0 \tag{16}$$

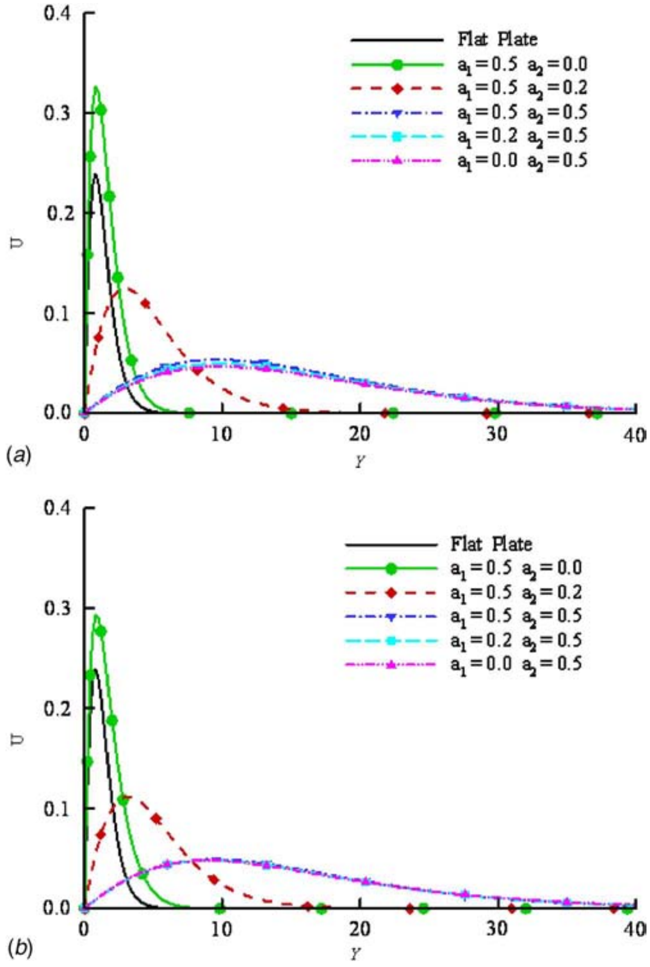

Fig. 5 Tangential velocity distribution at (*a*) *X*=0.25 and (*b*) *X* =0.75

$$(5X)U\frac{\partial U}{\partial X}+(V-UY)\frac{\partial U}{\partial Y}+\left(3+\frac{5X\sigma_x\sigma_{xx}}{1+\sigma_x{}^2}\right)U^2=(1+\sigma_x{}^2)\frac{\partial^2 U}{\partial Y^2}$$
$$+\frac{1}{1+\sigma_x{}^2}\Theta \tag{17}$$

$$(5X)U\frac{\partial\Theta}{\partial X}+(V-UY)\frac{\partial\Theta}{\partial Y}+U\Theta=\frac{1}{\Pr}(1+\sigma_x{}^2)\frac{\partial^2\Theta}{\partial Y^2} \tag{18}$$

The corresponding boundary conditions are

$$U=V=0 \quad \frac{\partial\Theta}{\partial Y}=-\frac{1}{\sqrt{1+\sigma_x{}^2}} \quad \text{at } Y=0 \tag{19a}$$

$$U\to 0 \quad \Theta\to 0 \quad \text{as } Y\to\infty \tag{19b}$$

Now, equations (16)–(18) subject to the boundary conditions (19) are discretized by a central-difference scheme for the diffusion terms and a backward-difference scheme for the convection terms. The resulting implicit tridiagonal algebraic system is solved by a double-sweep technique.

The computation is started at $X=0$, and then marches downstream implicitly. The ordinary differential equations governing the upstream condition at $X=0$ can be obtained by taking the limit of Eqs. (16)–(18) as X approaches zero. The associated boundary conditions are Eqs. (19) with $X=0$. This is, in fact, the similarity solution of a natural-convection boundary layer along a flat plate

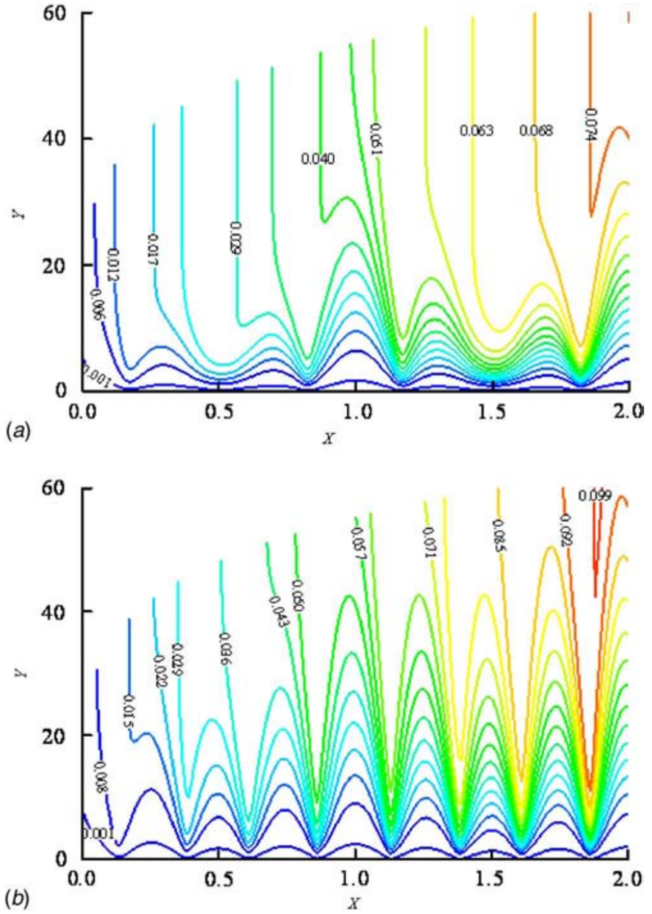

Fig. 6 Streamlines for (*a*) $a_1=0.5$, $a_2=0.2$ and (*b*) $a_1=0.2$, $a_2=0.5$

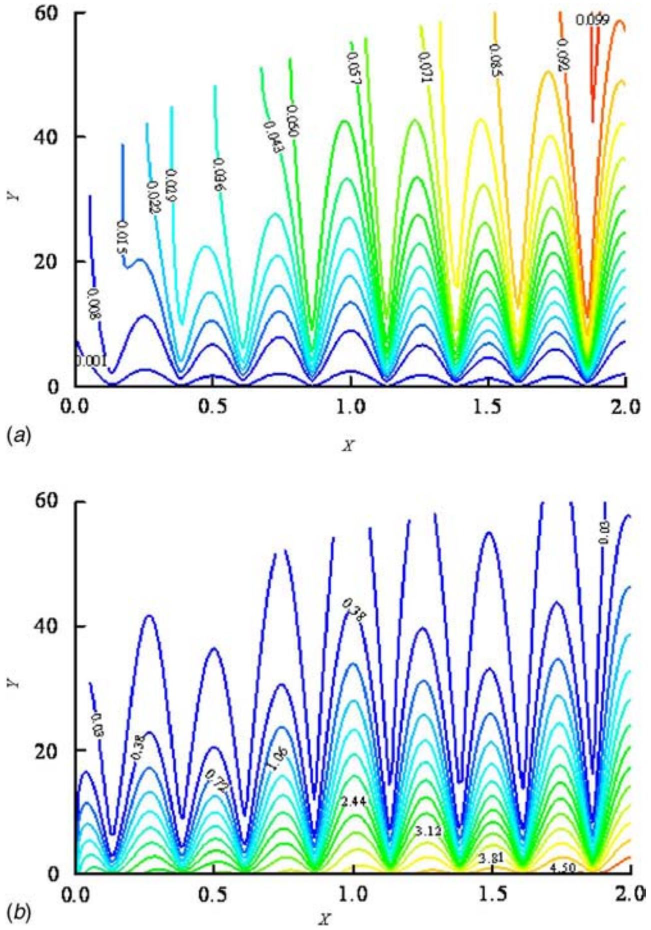

Fig. 7 Isotherms for (*a*) $a_1=0.5$, $a_2=0.2$ and (*b*) $a_1=0.2$, $a_2=0.5$

at a slant angle,$\tan^{-1}\sigma_x$, with the *y* axis. The *Y* and *X* grids are set at 0.01, and the maximum value of *Y* is 80 in the following computations after several test runs for convergence.

3 Results and Discussion

The numerical results are presented for various combinations of the fundamental amplitude a_1 (0.0, 0.2, 0.5) and the harmonic amplitude a_2 (0.0, 0.2, 0.5) of the complex wavy surface. Figure 2 depicts the numerical values of the surface temperature distribution, Θ_w, for different cases of the values of a_1 and a_2. It is shown that the value of the surface temperature is larger when the amplitude of the harmonic wave a_2 increases beyond that of the fundamental wave a_1. Equivalently, the cooling capability of the natural-convection boundary layer is reduced. This is because the thermal boundary layer is thickened by the centrifugal force along the curved surface. The curvature of the harmonic wave is larger; consequently, it induces a larger normal velocity near the surface, as shown in the plot of velocity vectors in Fig. 3 and the distribution of normal velocities in Fig. 4. The effect of thickening of the thermal boundary layer is also clearly confirmed by the plot of the axial-velocity distributions (Fig. 5) and the temperature distributions (Fig. 7). The total heat-transfer rate is proportional to the surface area since the applied thermal boundary condition is a uniform wall heat flux, but the "hot-spot" temperature for a complex wavy surface is higher.

The effects of the fundamental and the harmonic amplitudes on the normal and the tangential velocities at $X=0.25$ and $X=0.75$ are illustrated in Figs. 4 and 5, respectively. It is shown in Fig. 5 that the tangential velocity is larger than that for a flat plate near the crest or trough of a simple sinusoidal wavy surface. On the other hand, increasing values of the amplitude of the harmonic wave of the complex wavy surface retard the fluid motion near the surface but generate more fluid motion away from the surface, resulting in a much thicker momentum boundary layer. This is due to the fact that the complex wavy surface induces a complicated motion normal to the surface, as shown in Fig. 3. From Fig. 5, it is clear that the maximum velocity occurs at the crest of the complex wavy surface, and the additional harmonic of the complex wavy surface substantially alters the flow field and temperature distribution near the surface. The thickness of the thermal boundary layer for a complex wavy surface is consequently much larger than a simple sinusoidal wavy surface. The effect of a larger curvature of a complex surface on natural convection near the surface of constant heat flux on the wall is consistent with what have been found for the case of a constant wall temperature [26].

Figure 6 shows the streamlines for two cases. The complex wavy surface induces a local "approaching and leaving" flow slightly downstream from the trough and slightly upstream of the crest of the complex wavy surface. Such a flow pattern is the mechanism that alters the surface temperature distribution. It is seen that for case (*a*) the value of $\psi_{\max}$ within the computational domain is 0.13; for case (*b*) the value of $\psi_{\max}$ is 0.18. In case (*b*), the harmonic amplitude plays the dominant role since the approaching and leaving flow rate is larger than that for case (*a*). It is interesting to note that the wavelength of the streamline is comparable to that of the shorter wave. This information may have some impact on triggering the boundary-layer transition by "shaping" the leading edge of the plate.

For the above cases, the isotherm pattern is shown in Fig. 7. The temperature distribution increases in the downstream region within the boundary layer, but the temperature distribution is sig-

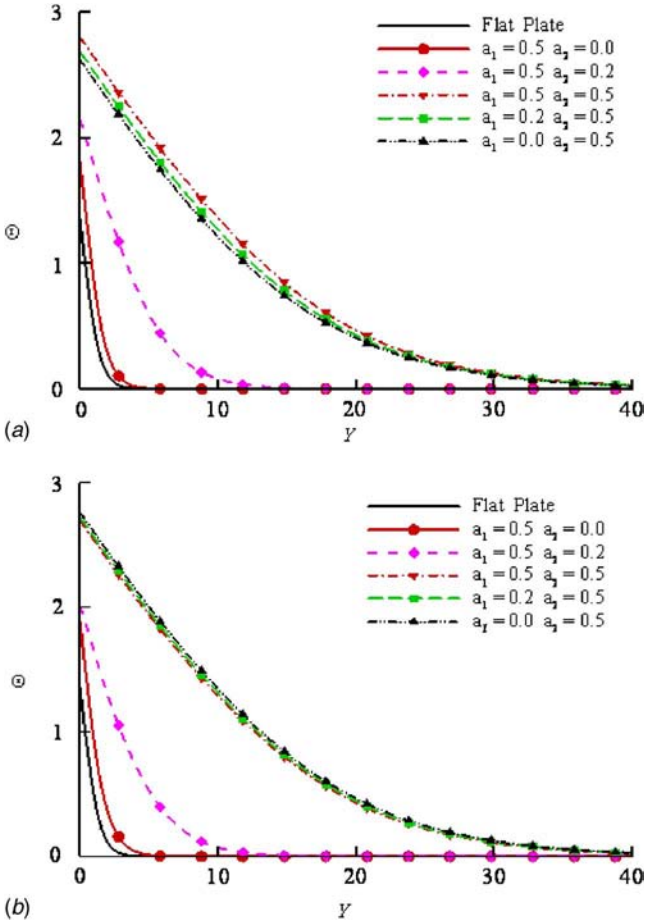

Fig. 8 Temperature distribution at (*a*) $X=0.25$ and (*b*) $X=0.75$ while Pr=1

nificantly higher for case (*b*), where the thickness of the thermal boundary layer is almost twice that of case (*a*). Temperature distributions at $X=0.25$ and 0.75 are plotted in Fig. 8. They show that the temperature distribution is more sensitive to the amplitude variation of the harmonic than the fundamental wave. This is not a surprise and is consistent with the velocity disturbance near the complex wavy surface.

Nomenclature

a_1 = fundamental amplitude of the surface waves
a_2 = harmonic amplitude of the surface waves
C_p = specific heat at constant pressure
g = acceleration due to gravity
L = characteristic length associated with the wavy surface
Gr = Grashof number
p = pressure of the fluid
Pr = Prandtl number
T = temperature of the fluid in the boundary layer
T_∞ = temperature of the ambient fluid
q_w = heat flux at the surface
u,v = the dimensionless x and y components of the velocity
$\hat{u},\hat{v}$ = the dimensional $\hat{x}$ and $\hat{y}$ components of the velocity
$\hat{x},\hat{y}$ = coordinates, defined in Fig. 1(*a*)

Greek symbols

β = volumetric coefficient of thermal expansion
ρ = density of the ambient fluid
ν = kinematic coefficient of viscosity
μ = dynamic coefficient of viscosity
k = thermal conductivity
θ,Θ = dimensionless temperature function
$\sigma(x)$ = surface profile function defined in Eq. (1)

References

[1] Yao, L. S., 1983, "Natural Convection Along a Vertical Wavy Surface," ASME J. Heat Transfer, **105**, pp. 465–468.
[2] Moulic, S. G., and Yao, L. S., 1989, "Natural Convection Along a Wavy Surface With Uniform Heat Flux," ASME J. Heat Transfer, **111**, pp. 1106–1108.
[3] Moulic, S. G., and Yao, L. S., 1989, "Mixed Convection Along Wavy Surface," ASME J. Heat Transfer, **111**, pp. 974–979.
[4] Hossain, M. A., and Pop, I., 1996, "Magnetohydrodynamic Boundary Layer Flow and Heat Transfer on a Continuous Moving Wavy Surface," Arch. Mech., **48**, pp. 813–823.
[5] Hossain, M. A., Alam, K. C. A., and Rees, D. A. S., 1997, "Magnetohydrodynamic Free Convection Along a Vertical Wavy Surface," Appl. Mech. Eng., **1**, pp. 555–566.
[6] Hossain, M. A., and Rees, D. A. S., 1999, "Combined Heat and Mass Transfer in Natural Convection Flow From a Vertical Wavy Surface," Acta Mech., **136**, pp. 133–141.
[7] Hossain, M. A., Munir, M. S., and Pop, I., 2001, "Natural Convection of a Viscous Fluid With Viscosity Inversely Proportional to Linear Function of Temperature From a Vertical Wavy Cone," Int. J. Therm. Sci., **40**, pp. 366–371.
[8] Hossain, M. A., Munir, M. S., and Pop, I., 2001, "Natural Convection of a Viscous Fluid With Variable Viscosity and Thermal Conductivity From a Vertical Wavy Cone," Int. J. Therm. Sci., **40**, pp. 437–443.
[9] Hossain, M. A., Kabir, S., and Rees, D. A. S., 2002, "Natural Convection of Fluid With Temperature Dependent Viscosity From Heated Vertical Wavy Surface," ZAMP, **53**, pp. 48–52.
[10] Molla, M. M., Hossain, M. A., and Yao, L. S., 2004, "Natural Convection Flow Along a Vertical Wavy Surface With Uniform Surface Temperature in Presence of Heat Generation/Absorption," Int. J. Therm. Sci., **43**, pp. 157–163.
[11] Pop, I., and Na, T. Y., 1999, "Natural Convection Over a Vertical Wavy Frustum of a Cone," Int. J. Non-Linear Mech., **34**, pp. 925–934.
[12] Pop, I., and Na, T. Y., 1995, "Natural Convection Over a Vertical Wavy Frustum of a Cone in a Porous Medium," Mech. Res. Commun., **22**, pp. 181–190.
[13] Cheng, C. W., and Wang, C. C., 2000, "Forced Convection in Micropolar Fluid Over a Wavy Surface," Numer. Heat Transfer, Part A, **37**, pp. 271–287.
[14] Jang, J. H., Yan, W. M., and Liu, H. C., 2003, "Natural Convection Heat and Mass Transfer Along a Vertical Wavy Surface," Int. J. Heat Mass Transfer, **46**, pp. 2075–1083.
[15] Jang, J. H., and Yan, W. M., 2004, "Mixed Convection Heat and Mass Transfer Along a Vertical Wavy Surface," Int. J. Heat Mass Transfer, **47**, pp. 419–428.
[16] Jang, J. H., and Yan W. M., 2004, "Transient Analysis of Heat and Mass Transfer by Natural Convection Over a Vertical Wavy Surface," Int. J. Heat Mass Transfer, **47**, pp. 3695–3705.
[17] Wang, C. C., and Chen, C.-K., 2005, "Mixed Convection Boundary Layer Flow on Inclined Wavy Plates Including the Magnetic Field Effect," Int. J. Therm. Sci., **44**, pp. 577–586.
[18] Wang, C. C., and Chen, C.-K., 2002, "Mixed Convection Boundary Layer Flow of Non-Newtonian Fluids Along Vertical Wavy Plates," Int. J. Heat Fluid Flow, **23**, pp. 831–839.
[19] Wang, C. C., and Chen, C.-K., 2001, "Transient Force and Free Convection Along a Vertical Wavy Surface in Micropolar Fluids," Int. J. Heat Mass Transfer, **44**, pp. 3241–3251.
[20] Cheng, C. Y., 2000, "Natural Convection Heat and Mass Transfer Near a Vertical Wavy Surface With Constant Wall Temperature and Concentration in a Porous Medium," Int. Commun. Heat Mass Transfer, **27**, pp. 1143–1154.
[21] Cheng, C. Y., 2000, "Natural Convection Heat and Mass Transfer Near a Vertical Wavy Cone With Constant Wall Temperature and Concentration in a Porous Medium," Mech. Res. Commun., **27**, pp. 613–620.
[22] Kim, E., 1997, "Natural Convection Along a Wavy Vertical Plate to Non-Newtonian Fluids," Int. J. Heat Mass Transfer, **40**, pp. 3069–3078.
[23] Bhavnani, S. H., and Bergles, A. E., 1991, "Natural Convection Heat Transfer From Sinusoidal Wavy Surface," Waerme- Stoffuebertrag., **26**, pp. 341–349.
[24] Tashtous, B., and Al-Odat, M., 2004, "Magnetic Field Effect on Heat and Fluid Flow Over a Wavy Surface With a Variable Heat Flux," J. Magn. Magn. Mater., **268**, pp. 357–363.
[25] Chiu, C.-P., and Chou, H.-M., 1994, "Transient Analysis of Natural Convection Along a Vertical Wavy Surface in Micropolar Fluids," Int. J. Eng. Sci., **32**, pp. 19–33.
[26] Yao, L. S., 2006, "Natural Convection Along a Vertical Complex Wavy Surface," Int. J. Heat Mass Transfer, **49**, pp. 281–286.

Thermal Optimization of an Internally Finned Tube Using Analytical Solutions Based on a Porous Medium Approach

Kyu Hyung Do

Jung Yim Min

Sung Jin Kim

Department of Mechanical Engineering,
Korea Advanced Institute of Science and Technology,
Daejeon 305-701, Korea

The present work deals with thermal optimization of an internally finned tube having axial straight fins with axially uniform heat flux and peripherally uniform temperature at the wall. The physical domain was divided into two regions: One is the central cylindrical region of the fluid extending to the tips of the fins and the other constituted the remainder of the tube area. The latter region including the fins was modeled as a fluid-saturated porous medium. The Brinkman-extended Darcy equation for fluid flow and two-equation model for heat transfer were used in the porous region, while the classical Navier–Stokes and energy equations were used in the central cylindrical region. The analytical solutions for the velocity and temperature profiles were in close agreement with the corresponding numerical solution as well as with existing theoretical and experimental data. Finally, optimum conditions, where the thermal performance of the internally finned tube is maximized, were determined using the developed analytical solutions. [DOI: 10.1115/1.2754866]

Keywords: porous medium approach, internally finned tube, analytical solutions, thermal optimization

1 Introduction

The need for compact and efficient heat transfer equipment has stimulated research efforts in the area of heat transfer augmentation. In order to enhance the rate of heat transfer, finned surfaces have been applied to cooling devices for electronic equipment and compact heat exchangers for many years [1–4]. The apparent advantage of fins is that they increase the heat transfer rate by providing additional surface area. However, fins placed in a tube cause complex flow patterns and increase flow resistance. As the number or the height of fins increases, flow friction increases, thus requiring greater pumping power to sustain a given mass flow rate. Therefore, to design a compact heat exchanger with internally finned tubes, we should optimize the fin geometry by accounting for both flow friction and heat transfer.

In optimizing the thermal performance of an internally finned tube, many previous researchers have relied on experimental and numerical methods. These often involved tedious numerical calculations or extensive laboratory works in order to evaluate the effects of numerous parameters [5–12]. On the other hand, with analytical solutions, identification of important parameters as well as optimization of the thermal performance can be accomplished with ease. This idea has encouraged researchers to turn their attention to the analytical approach for predicting the pressure drop and thermal characteristics in the internally finned tube. Due to the complexity of the flow boundary, there are only a few works that present the analytical solutions for internally finned tubes. Hu and Chang [13] provided analytical solutions for both velocity and temperature in an internally finned tube, assuming zero fin thickness and a constant and uniform heat flux at each fin. Soliman and Feingold [14] presented an analytical solution for the fully developed laminar flow. Soliman [15] obtained an analytical solution for temperature distributions and the Nusselt number by considering fins with finite thermal conductivities, under the assumptions of a circumferentially uniform temperature within the fins and zero heat flux at the tip of the fins. However, these solutions have limited applicability due to various simplifying assumptions employed in their studies. Also, no previous studies have considered the optimal geometry of the fins accounting for both flow friction and heat transfer characteristics.

Because of the complex geometry, fluid flow, and heat transfer characteristics of internally finned tubes, the conventional energy equation cannot be solved analytically without invoking specific assumptions used in the previous studies. As an alternative, a porous medium approach was selected for modeling fluid flow and heat transfer through fins in a channel [16–18]. Srinivasan et al. [19] studied fluid flow and heat transfer through spirally fluted tubes using a porous substrate approach. The model divided the flow domain into two regions, the fluted region and the core region, with the flutes modeled as a porous substrate. Although there is a large difference between the thermal conductivities of the fluid and the internal fins, they used the one-equation model, which treats the flutes and the fluid as a single entity. By contrast, a porous medium approach based on the two-equation model is more appropriate in approaching the problems when the local thermal equilibrium is no longer valid. Recently, Kim et al. [20] presented the analytical solutions for both velocity and temperature profiles in a circular-sectored finned tube using this approach. However, their solutions are applicable only when the fin height equals the tube radius.

The purpose of the present paper is to optimize the fin geometry for enhancing the thermal performance of internally finned tubes with axial straight fins under the fixed pumping power condition. To attain this goal, new analytical solutions, which can accurately predict the velocity and temperature profiles within the tube, are obtained by modeling the internally finned tube as a tube filled partially with a porous medium. The analytical solutions were validated by comparison with the corresponding numerical solutions as well as with existing theoretical and experimental data. Finally, the porous medium formulation was used to perform ther-

---

Contributed by the Heat Transfer Division of ASME for publication in the JOURNAL OF HEAT TRANSFER. Manuscript received May 8, 2006; final manuscript received January 30, 2007. Review conducted by Jamal Seyed-Yagoobi.

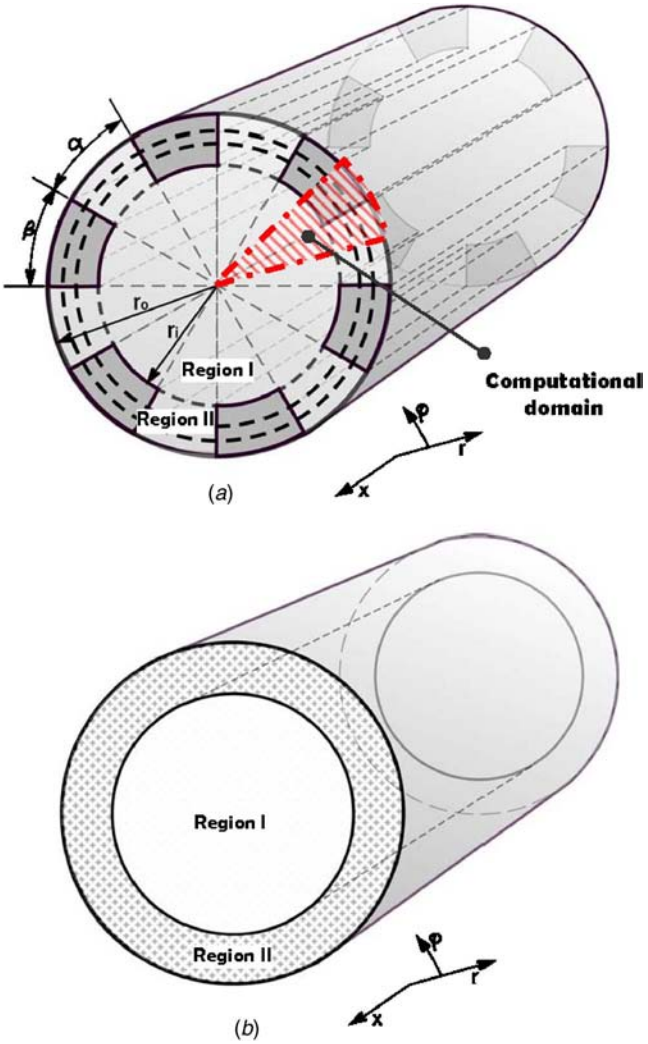

Fig. 1 Schematics of (*a*) an internally finned tube and (*b*) an equivalent porous medium

mal optimization of the internally finned tube. This demonstrates the cost and speed advantage of this type of analytical solution.

2 Mathematical Formulation and Analytical Solutions

The internally finned tube under consideration in this paper is shown in Fig. 1(*a*). The direction of fluid flow is parallel to the tube axis. The entire tube wall is uniformly heated. Axial straight fins with no swirl angle are attached to the inside surface of the tube wall. The flow is assumed to be steady, laminar, and both hydrodynamically and thermally fully developed. All thermophysical properties are assumed to be constant. The physical domain of the internally finned tube is divided into two regions separated by a cylinder of radius r_i, as shown in Fig. 1(*a*) [14,15,19]: Region I is the central cylindrical region extending to the tips of the fins, and region II constitutes the remainder of the tube area, having a periodic structure consisting of fin and fluid, i.e., its solid and fluid phases repeat themselves in a regular pattern, as shown in Fig. 1(*a*). Region II is modeled as an equivalent porous medium [20], as shown in Fig. 1(*b*). Mathematically, this is equivalent to averaging the physical domain in the direction parallel to the wall but perpendicular to the flow direction. For the present system, the representative elementary volume for volume averaging can be visualized as a (dotted) ring, as shown in Fig. 1(*a*). The averaging technique is employed to establish the governing equations for the velocity and temperature fields of the solid (fin) and fluid phases in region II. For fluid flow, the Brinkman-extended Darcy equation is used in place of the Darcy equation in order to account for the boundary effect. Due to the high solid-to-fluid conductivity ratio, the two-equation model for heat transfer, which treats the solid and the fluid as separate entities, is employed. On the other hand, the classical Navier–Stokes and energy equations accounting for variations in the φ and r directions govern the central cylindrical region, region I.

For the convenience of mathematical formulation, we introduce the following dimensionless parameters:

$$\langle U\rangle_j = \frac{\langle u\rangle_j}{r_0^2[-(1/\mu_f)(dp/dx)]} \quad \langle\theta\rangle_j = \frac{\langle T\rangle_j - T_w}{q_w'' r_0/k_f} \quad R = \frac{r}{r_0} \quad \text{for } j = s,f \tag{1}$$

where $\langle\,\rangle_f$ and $\langle\,\rangle_s$ denote a volume-averaged value over the fluid and solid phases in region II, respectively.

Velocity and energy equations are required for each of the three phases: the fluid of region I, fluid of region II, and solid of region II. These equations are expressed in dimensionless form as follows:

Momentum equations,

$$\frac{1}{R}\frac{\partial}{\partial R}\left(R\frac{\partial U}{\partial R}\right) + \frac{1}{R^2}\frac{\partial^2 U}{\partial\varphi^2} = -1 \quad 0 \le R \le R_i^- \tag{2}$$

$$\frac{1}{R}\frac{d}{dR}\left(R\frac{d\langle U\rangle_f}{dR}\right) - \frac{\langle U\rangle_f}{\mathrm{Da}R^2} = -1 \quad R_i^+ \le R \le 1 \tag{3}$$

$$\langle U\rangle_s = 0 \quad R_i^+ \le R \le 1 \tag{4}$$

Energy equations,

$$\frac{1}{R}\frac{\partial}{\partial R}\left(R\frac{\partial\theta}{\partial R}\right) + \frac{1}{R^2}\frac{\partial^2\theta}{\partial\varphi^2} = \frac{2U}{U_m} \quad 0 \le R \le R_i^- \tag{5}$$

$$\frac{1}{R}\frac{d}{dR}\left(R\frac{d\langle\theta\rangle_f}{dR}\right) + \frac{h_l^*}{k_{fe}R^2}(\langle\theta\rangle_s - \langle\theta\rangle_f) = \frac{2\langle U\rangle_f}{U_m} \quad R_i^+ \le R \le 1 \tag{6}$$

$$\frac{1}{R}\frac{d}{dR}\left(R\frac{d\langle\theta\rangle_s}{dR}\right) = \frac{h_l^*}{k_{se}R^2}(\langle\theta\rangle_s - \langle\theta\rangle_f) \quad R_i^+ \le R \le 1 \tag{7}$$

where Da, h_l, k_{se}, and k_{fe} are the Darcy number, the interstitial heat transfer coefficient, and the effective thermal conductivities for the solid and fluid phases, respectively. These parameters are analytically determined as [20]

$$\mathrm{Da} = \frac{\alpha^2}{12} \quad h_l = \frac{\mathrm{Nu}_{i,\infty}k_f}{2r\alpha} \quad \mathrm{Nu}_{i,\infty} = 10 \quad h_l^* = 2rh_l/(\alpha+\beta)$$
$$k_{se} = (1-\varepsilon)k_s \quad k_{fe} = \varepsilon k_f \tag{8}$$

The convection terms on the right-hand side of Eqs. (5) and (6) are derived from the energy balance for the fully developed flow subject to a constant heat flux at the tube wall [21]

$$q_w'' = \rho_f c_f u_m \frac{r_0}{2}\frac{\partial T}{\partial x} = \rho_f c_f u_m \frac{r_0}{2}\frac{\partial\langle T\rangle_f}{\partial x} \tag{9}$$

For region II, the boundary conditions for solving Eqs. (3), (4), (6), and (7) are given by

$$\langle U\rangle_f = \langle U\rangle_s = 0 \quad \langle\theta\rangle_f = \langle\theta\rangle_s = 0 \quad \text{at } R = 1 \tag{10}$$

$$\langle U\rangle_f = U_{fi} = U_i/\varepsilon \quad \langle\theta\rangle_f = \theta_{fi} \quad \langle\theta\rangle_s = \theta_{si} \quad \text{at } R = R_i^+ \tag{11}$$

where U_{fi}, θ_{fi}, and θ_{si} are dimensionless interfacial velocity and temperatures of the fluid and solid phases, respectively. In addition, the boundary conditions for solving Eqs. (2) and (5), which take account of the variations in the R and φ directions, are

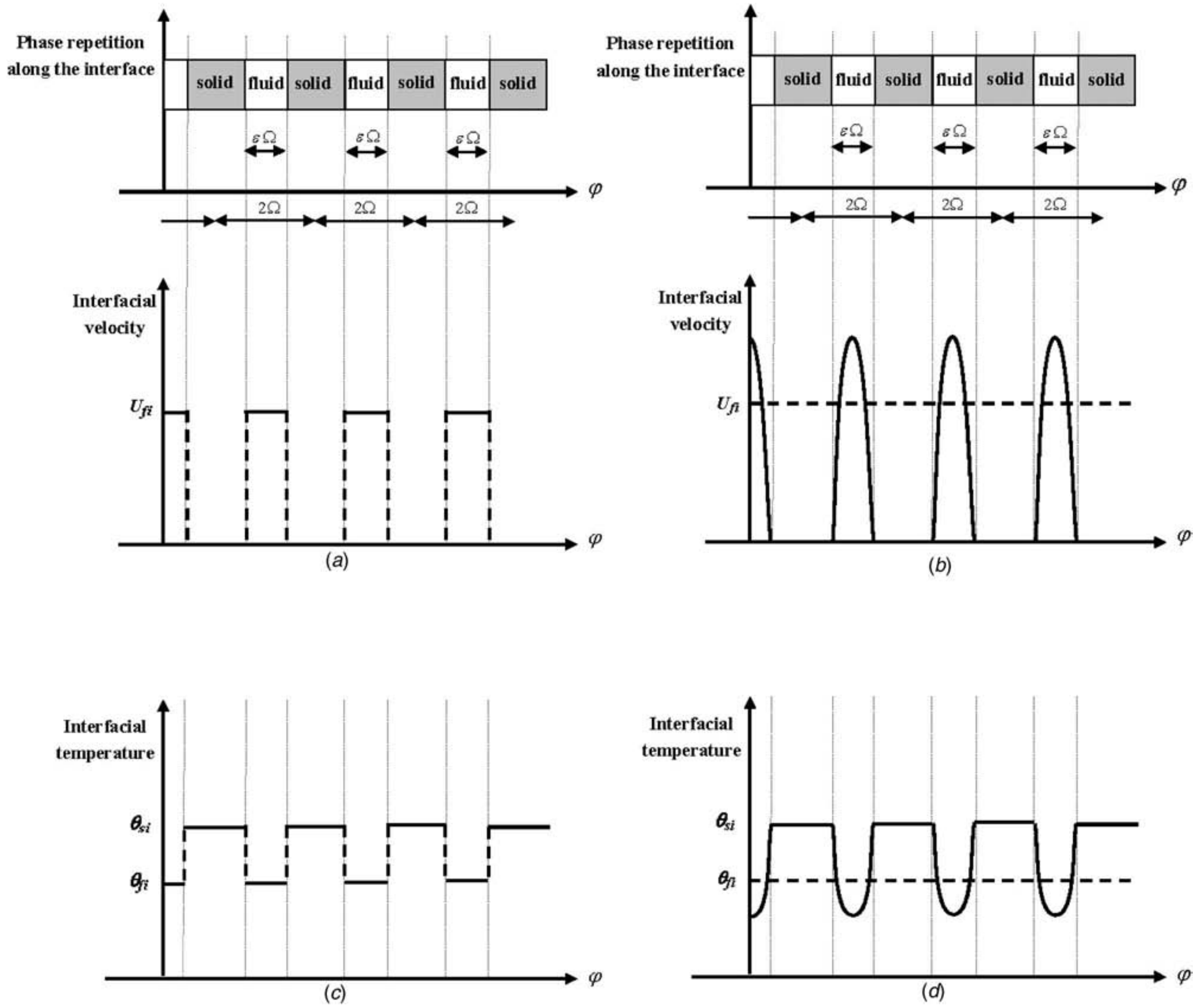

Fig. 2 Distributions along the interface between regions I and II: (*a*) interfacial velocity and (*c*) temperature profiles presented by Min and Kim [22], and (*b*) interfacial velocity and (*d*) temperature profiles used in the present study

$$\frac{\partial U}{\partial R}=0 \quad \frac{\partial \theta}{\partial R}=0 \quad \text{at } R=0 \tag{12}$$

$$\frac{\partial U}{\partial \varphi}=\frac{\partial \theta}{\partial \varphi}=0 \quad \text{at } \varphi=0 \tag{13}$$

$$\frac{\partial U}{\partial \varphi}=\frac{\partial \theta}{\partial \varphi}=0 \quad \text{at } \varphi=\Omega \tag{14}$$

Along the interface between regions I and II, two entities are periodically repeated where the fluid is sandwiched between the adjacent fins. As boundary conditions of Eqs. (2) and (5), the periodic distributions for the interfacial velocity and temperature were expressed in terms of the Fourier cosine series by Min and Kim [22], as shown in Figs. 2(*a*) and 2(*c*). However, the discontinuities of the interfacial velocity and temperature profiles at the intersection between the fin and fluid portions at the interface cause a substantial overshoot near this point, which is known as Gibbs' phenomenon [23]. In order to overcome this problem, a parabolic profile for velocity and a quadratic profile for temperature are suggested in the present study, as shown in Figs. 2(*b*) and 2(*d*): It is assumed that the interfacial velocity over the fluid portion has the parabolic profile and that over the fin portion has zero value; the interfacial temperature over the fluid portion has the quadratic profile and that over the fin portion is θ_{si}. These periodic distributions can be mathematically expressed in terms of the Fourier cosine series as follows:

$$U(\varphi)=U_i\left[1+6\sum_{n=1}^{\infty}A_n\cos\left(\frac{n\pi\varphi}{\Omega}\right)\right] \quad \text{at } R=R_i^- \tag{15}$$

$$\theta(\varphi)=\varepsilon\theta_{fi}+(1-\varepsilon)\theta_{si}+5(\theta_{fi}-\theta_{si})\sum_{n=1}^{\infty}B_n\cos\left(\frac{n\pi\varphi}{\Omega}\right) \quad \text{at } R=R_i^- \tag{16}$$

where

$$A_n=\frac{\sin(\varepsilon n\pi)}{(\varepsilon n\pi)^3}-\frac{\cos(\varepsilon n\pi)}{(\varepsilon n\pi)^2}$$

$$B_n=\frac{3\varepsilon\sin(\varepsilon n\pi)}{(\varepsilon n\pi)^5}-\frac{3\varepsilon\cos(\varepsilon n\pi)}{(\varepsilon n\pi)^4}-\frac{\varepsilon\cos(\varepsilon n\pi)}{(\varepsilon n\pi)^2}$$

Since the interfacial values for U_{fi}, θ_{fi}, and θ_{si} have not been determined, three more conditions are required. Those conditions can be obtained from the continuity of shear stress for the fluid phase and continuity of heat flux for the solid and fluid phases at the interface between regions I and II, as Min and Kim suggested [22].

$$\left.\frac{d\langle U\rangle_f}{dR}\right|_{R=R_i^+}=\frac{1}{\varepsilon R_i\Omega}\int_0^{\varepsilon\Omega}\left.\frac{\partial U}{\partial R}\right|_{R=R_i^-}R_i d\varphi \tag{17}$$

$$k_{fe}\left.\frac{d\langle\theta\rangle_f}{dR}\right|_{R=R_i^+}=\frac{1}{R_i\Omega}\int_0^{\varepsilon\Omega}k_f\left.\frac{\partial\theta}{\partial R}\right|_{R=R_i^-}R_i d\varphi \tag{18}$$

$$k_{se}\left.\frac{d\langle\theta\rangle_s}{dR}\right|_{R=R_i^+}=\frac{1}{R_i\Omega}\int_{\varepsilon\Omega}^{\Omega}k_f\left.\frac{\partial\theta}{\partial R}\right|_{R=R_i^-}R_i d\varphi \tag{19}$$

For the velocity profile in region I, Eq. (2) subject to boundary conditions (BCs) (12)–(15) is solved using the method of separation of variables to yield

$$U(R,\varphi)=-\frac{R^2}{4}+\frac{R_i^2}{4}+U_i\left[1+6\sum_{n=1}^{\infty}\left(\frac{R}{R_i}\right)^{n\pi/\Omega}A_n\cos\left(\frac{n\pi}{\Omega}\varphi\right)\right]$$

$$0\leqslant R\leqslant R_i^- \tag{20}$$

By solving Eq. (3) with BCs (10) and (11), analytical solution for the velocity profile of the fluid phase in region II is obtained as follows:

$$\langle U\rangle_f=C_1R^{1/\sqrt{\mathrm{Da}}}+C_2R^{1/\sqrt{\mathrm{Da}}}+\frac{\mathrm{Da}}{1-4\mathrm{Da}}R^2 \quad R_i^+\leqslant R\leqslant 1 \tag{21}$$

Similarly, for the temperature profile in region I, Eq. (5) subject to BCs (12)–(14) and (16) is solved by using the method of separation of variables as

$$\begin{aligned}\theta(R,\varphi)=\frac{2}{U_m}\Bigg\{&-\frac{R^4}{64}+\frac{R^2}{4}\left(U_i+\frac{R_i^2}{4}\right)-\left(\frac{3R_i^4}{64}+\frac{U_iR_i^2}{4}\right)\\&-6U_i\sum_{n=1}^{\infty}\frac{R_i^2}{4[(n\pi/\Omega)+1]}\left(\frac{R}{R_i}\right)^{n\pi/\Omega}\\&\times\left[1-\left(\frac{R}{R_i}\right)^2\right]A_n\cos\left(\frac{n\pi\varphi}{\Omega}\right)\Bigg\}\\&+\varepsilon\theta_{fi}+(1-\varepsilon)\theta_{si}+5(\theta_{fi}\\&-\theta_{si})\sum_{n=1}^{\infty}\left(\frac{R}{R_i}\right)^{n\pi/\Omega}B_n\cos\left(\frac{n\pi\varphi}{\Omega}\right)\end{aligned} \tag{22}$$

where U_m is the mean velocity defined as

$$U_m=\frac{2}{\Omega}\left(\int_0^{\Omega}\int_0^{R_i}URdRd\varphi+\varepsilon\Omega\int_{R_i}^{1}\langle U\rangle_f RdR\right) \tag{23}$$

Solving Eqs. (6) and (7) with BCs (10) and (11), analytical solutions for temperatures of the solid and fluid phases in region II are obtained as follows:

$$\begin{aligned}\langle\theta\rangle_s=\frac{1}{k_{se}+k_{fe}}\Bigg\{&k_{fe}(C_3R^{\lambda}+C_4R^{-\lambda}+A_1R^4+A_2R^{2+1/\sqrt{\mathrm{Da}}}\\&+A_3R^{2-1/\sqrt{\mathrm{Da}}})+C_5+C_6\ln R+\frac{2k_{fe}}{U_m}\Bigg[\frac{C_1}{(2+1/\sqrt{\mathrm{Da}})^2}R^{2+1/\sqrt{\mathrm{Da}}}\\&+\frac{C_2}{(2-1/\sqrt{\mathrm{Da}})^2}R^{2-1/\sqrt{\mathrm{Da}}}+\frac{\mathrm{Da}R^4}{16(1-4\mathrm{Da})}\Bigg]\Bigg\}\end{aligned} \tag{24}$$

$$\begin{aligned}\langle\theta\rangle_f=\frac{1}{k_{se}+k_{fe}}\Bigg\{&-k_{se}(C_3R^{\lambda}+C_4R^{-\lambda}+A_1R^4+A_2R^{2+1/\sqrt{\mathrm{Da}}}\\&+A_3R^{2-1/\sqrt{\mathrm{Da}}})+C_5+C_6\ln R+\frac{2k_{fe}}{U_m}\Bigg[\frac{C_1}{(2+1/\sqrt{\mathrm{Da}})^2}R^{2+1/\sqrt{\mathrm{Da}}}\\&+\frac{C_2}{(2-1/\sqrt{\mathrm{Da}})^2}R^{2-1/\sqrt{\mathrm{Da}}}+\frac{\mathrm{Da}R^4}{16(1-4\mathrm{Da})}\Bigg]\Bigg\}\end{aligned} \tag{25}$$

By substituting Eqs. (20) and (21) and Eqs. (22), (24), and (25) into Eq. (17) and Eqs. (18) and (19), respectively, the interfacial values for velocity and temperatures can be determined to be

$$U_i=\frac{[2\mathrm{Da}/(1-4\mathrm{Da})]R_i+(R_i/2)+[\sqrt{\mathrm{Da}}/(1-4\mathrm{Da})][R_i^{1/\sqrt{\mathrm{Da}}}/(1-R_i^{2/\sqrt{\mathrm{Da}}})][R_i^{1/\sqrt{\mathrm{Da}}+1}+R_i^{-1/\sqrt{\mathrm{Da}}+1}-(2/R_i)]}{[1/(\varepsilon\sqrt{\mathrm{Da}})][R_i^{1/\sqrt{\mathrm{Da}}}/(1-R_i^{2/\sqrt{\mathrm{Da}}})](R_i^{1/\sqrt{\mathrm{Da}}-1}+R_i^{-1/\sqrt{\mathrm{Da}}-1})-(6/\varepsilon R_i\Omega)\sum_{n=1}^{\infty}A_n\sin(\varepsilon n\pi)} \tag{26}$$

$$\theta_{si}=\frac{n_fm_c-m_fn_c}{n_fm_s-m_fn_s}\quad \theta_{fi}=\frac{n_sm_c-m_sn_c}{n_sm_f-m_sn_f} \tag{27}$$

The detailed expressions for the coefficients are presented in the Appendix.

3 Results and Discussion

3.1 Validation. In order to validate the analytical solutions presented in this study, the analytical solutions for velocity and temperature distributions are compared with the corresponding numerical solutions. The numerical solutions are obtained by solving the Navier–Stokes and classical energy equations for a conjugate heat transfer problem using the control-volume method for the computational domain, as shown in Fig. 1(*a*). The formulation and the numerical method for the conjugate heat transfer problem are very similar to those by Kim et al. [20], and for the sake of brevity are not repeated here. Figure 3 shows the comparison between the analytical solutions and the corresponding numerical solutions for the velocity and temperature distributions, which are averaged along the φ direction. As shown in this figure, the present analytical results are in close agreement with the numerical results with a maximum error of 5%. The analytical results were also compared with two previous results [5,14]. First, the friction factors obtained from the present analytical solutions were compared with experimental data of Watkinson et al. [5] in Fig. 4. The analytical results are shown to be in favorable agreement with the experimental data. Second, the predicted values of the Poiseuille number *f*Re were compared with those calculated by Soliman and Feingold [14]. This comparison is shown in Fig. 5. The

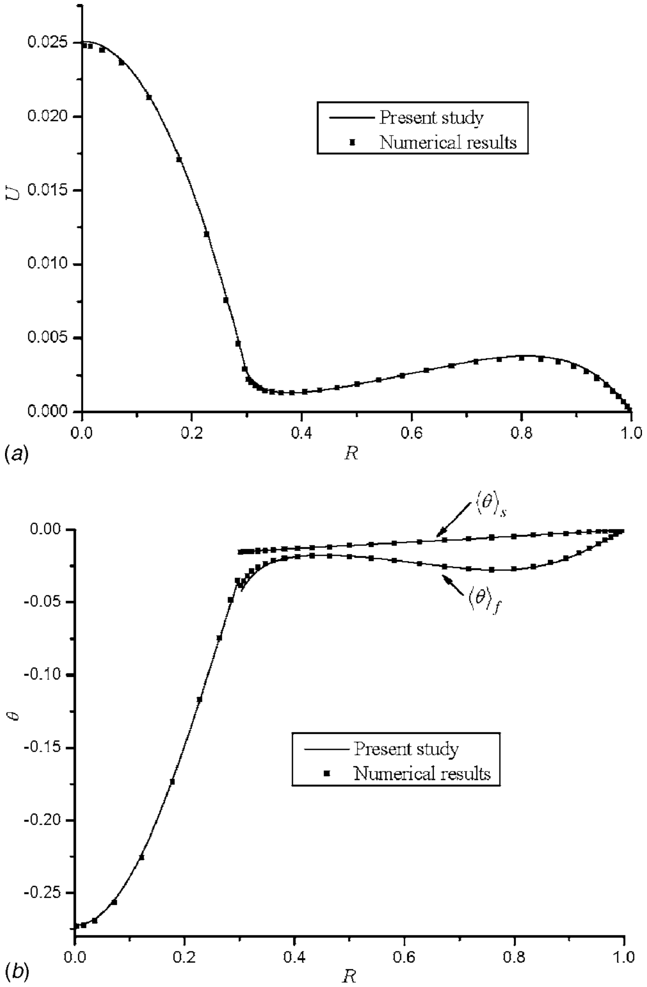

Fig. 3 Comparison of the analytical solutions with the numerical solutions for (*a*) velocity and (*b*) temperature profiles (l=0.7, ε=0.6, N=10, k_s/k_f=100)

discrepancy between the present analytical results and their analytical results is less than 5% for tubes having seven or more fins. Based on these results, the porous medium approach is valid for $N \geqslant 7$ with a maximum error less than 5%. Similar results were presented by Kim et al. [20].

In addition, two limiting cases are considered for validating the present analytical solutions: the finless and full-fin tubes. If the fin height goes to zero, R_i is 1 and U_i, θ_{fi}, and θ_{si} are equal to zero. In this case, Eqs. (20) and (22) reduce to the velocity and temperature profiles for thermally fully developed Hagen–Poiseuille flow with uniform heat flux. When the fin height approaches the tube inner radius, θ_{fi} is equal to θ_{si} and R_i and U_i are zero. In this case, Eqs. (20), (24), and (25) are exactly the same as the analytical solutions for the velocity and temperature profiles reported by Kim et al. [20] for the circular-sectored finned tube. Therefore, the present analytical solutions accurately predict the velocity and temperature distributions for the two limiting cases.

3.2 Discussion on Temperature Distributions. It is obvious that the analytical solutions are helpful for identifying the variables of engineering importance. Equations (22), (24), and (25) show that the variables of engineering importance are the thermal conductivity ratio, the dimensionless fin height ($l=1-R_i$), the number of fins (N), and the porosity (ε), which is the ratio of the angle between the flanks of two adjacent fins to the angle between the centerlines of two adjacent fins.

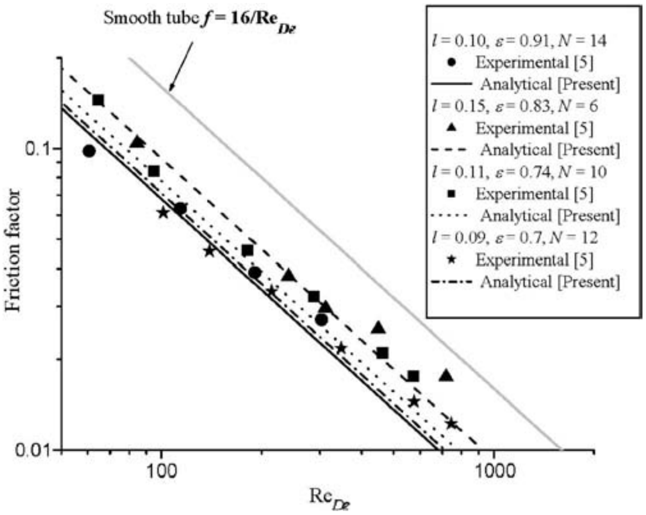

Fig. 4 Comparison of the analytical solutions with the experimental data [5] for the friction factor

As mentioned before, Soliman [15] employed two simplifying assumptions. One is a circumferentially uniform temperature within the fins and the other is zero heat flux at the tip of the fins. In this section, we examine the validity of these assumptions by comparing the averaged solid temperatures in region II. The thermal conductivity ratio is defined as the ratio of thermal conductivity of the solid to that of the fluid. The influence of this ratio on the averaged solid temperatures is shown in Fig. 6. Results from Eq. (24) are compared with the corresponding volume-averaged temperature distributions from the numerical solutions as well as those from Soliman's analytical solutions [15]. The temperature distributions obtained from the present analytical solutions are shown to be accurate in comparison with these numerical solutions to within 3.0% (see Fig. 6). On the other hand, Soliman's

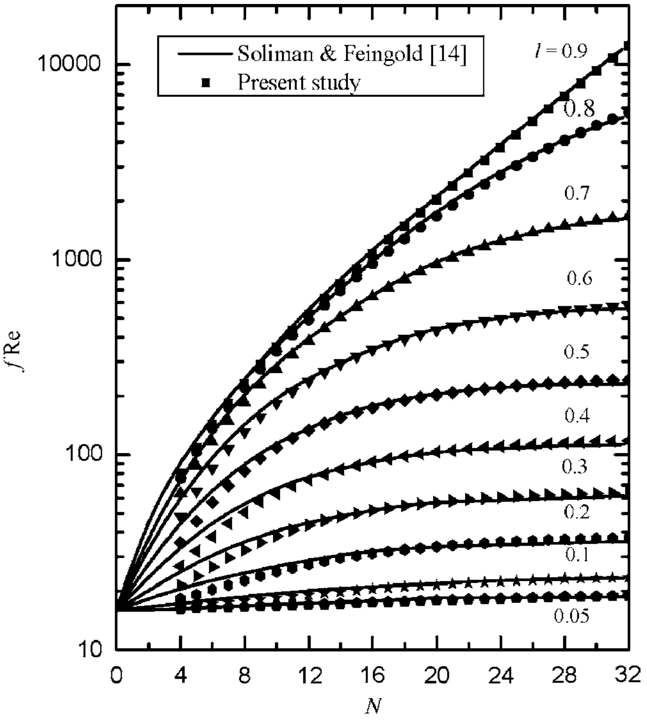

Fig. 5 Comparison of $f\,$Re between the theoretical results [14] and the present results for β=6 deg

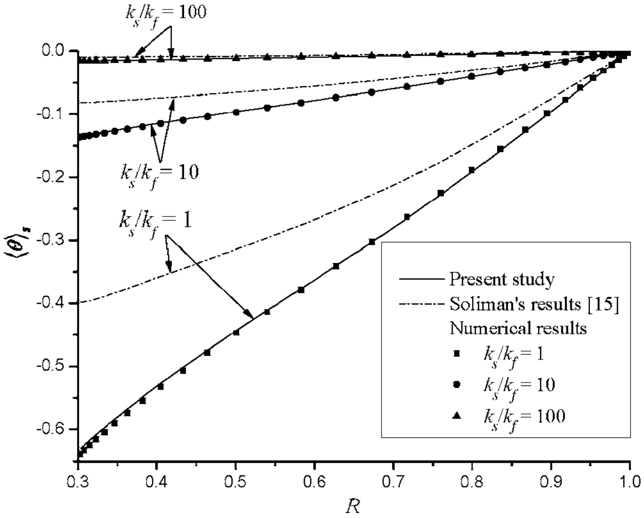

Fig. 6 Effect of the conductivity ratio on the averaged solid temperature profiles ($l=0.7$, $\varepsilon=0.6$, $N=10$)

analytical solutions [15] deviate significantly from the numerical solutions when the thermal conductivity ratio is small. This deviation results from the assumption of a circumferentially uniform temperature within the fins. Even though the solid temperature variation along the circumferential direction increases with the decreasing thermal conductivity ratio, the solid temperature at the intersection between the fin and fluid is dealt with by the averaged solid temperature. Figure 7 illustrates the effect of the number of fins on the averaged solid temperature profiles. In Fig. 7, the averaged solid temperature distribution obtained from Soliman's analytical solution [15] coincides with that obtained from the numerical solution for $N=10$. This indicates that the assumption of zero heat flux at the fin tip is valid. However, for the large number of fins, this assumption is no longer valid. Because the number of fins in region II increases frictional drag, the flow rate in region I increases. As a result, the local heat transfer coefficient at the fin tip increases. Therefore, convection heat transfer between the fin tip and fluid cannot be neglected when the number of fins is larger than 10. Also, because convection heat transfer between the tips of fins and fluid and the temperature variation of the fin along the circumferential direction increase as the porosity or the dimensionless fin height decreases, the difference in the averaged solid temperatures between the numerical results and Soliman's results becomes larger [15].

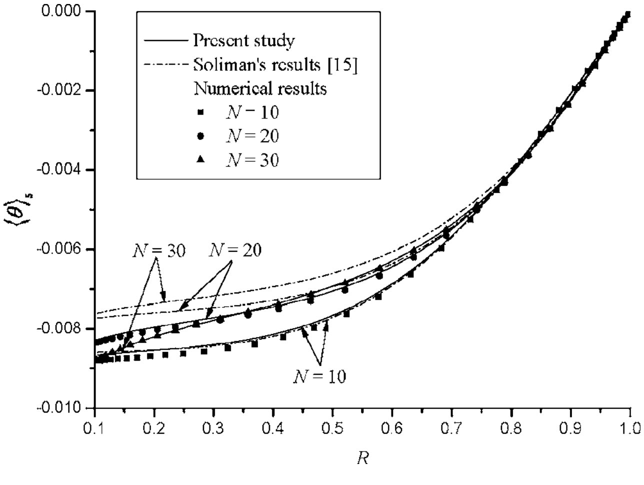

Fig. 7 Effect of the number of fins on the averaged solid temperature profiles ($l=0.9$, $\varepsilon=0.6$, and $k_s/k_f=100$)

Consequently, the simplifying assumptions employed in Soliman's study [15] may lead to significant errors in predicting the temperature distributions of the internally finned tube, as the number of fins increases or the thermal conductivity ratio, the porosity, or the dimensionless fin height decreases. On the other hand, the present analytical solutions presented in this paper agree well with the corresponding numerical solutions over a wide range of parameter values.

3.3 Correction for the Bulk-Mean Temperature. The conventional bulk-mean temperature is calculated by averaging the product of the velocity and temperature distributions over the cross-sectional area. Mathematically, the bulk-mean temperature of an internally finned tube can be written as

$$\begin{aligned} T_m &= \frac{2}{\Omega r_0^2 u_m}\left(\int_0^{r_o}\int_0^{\Omega} uTrd\varphi dr\right) \\ &= \frac{2}{\Omega r_0^2 u_m}\left(\int_0^{r_i}\int_0^{\Omega} uTrd\varphi dr + \int_{r_i}^{r_o}\int_0^{\Omega} uTrd\varphi dr\right) \end{aligned} \tag{28}$$

In order to calculate the bulk-mean temperature shown in Eq. (28), the velocity and temperature variations of the circumferential direction as well as the radial direction are needed. However, in region II, we lost some information, which is the velocity and temperature variations for the fluid phase in the averaging direction, since we adopted the porous medium approach based on the averaging method in this region. In order to compensate the lost information, a correction for the bulk-mean temperature along the averaging direction should be made. We replaced the lost variations of the velocity and temperatures along the averaging direction with the velocity and temperature distributions for the Poiseuille flow between two semi-infinite plates that meet with an angle of α and are subject to a constant heat flux, in the same manner of determining the permeability and the interstitial heat transfer coefficient. It has been shown that this approach devised by Kim and co-workers [18,20] is very successful in compensating the lost information for the averaging. Applying this correction method to the internally finned tube, the corrected dimensionless bulk-mean temperature can be expressed as

$$\begin{aligned} \theta_m = \frac{2}{\Omega U_m}\Bigg\{ & \int_0^{R_i}\int_0^{\Omega} U\theta d\varphi RdR + \varepsilon\Omega\int_{R_i}^{1}\langle U\rangle_f\langle\theta\rangle_f RdR \\ & + \varepsilon\Omega\frac{\alpha(\alpha+\beta)}{2(1-R_i)}\left(\frac{1}{\mathrm{Nu}_{i,\infty}} - \frac{1}{\mathrm{Nu}_\infty}\right)\left[1 - \frac{R_i^2}{U_m}\left(U_i + \frac{R_i^2}{8}\right)\right] \\ & \times\left[\frac{C_1}{3+1/\sqrt{\mathrm{Da}}}\left(1 - R_i^{3+1/\sqrt{\mathrm{Da}}}\right) + \frac{C_2}{3-1/\sqrt{\mathrm{Da}}}\left(1 - R_i^{3-1/\sqrt{\mathrm{Da}}}\right)\right. \\ & \left.\left. + \frac{\mathrm{Da}}{5(1-4\mathrm{Da})}(1 - R_i^5)\right]\right\} \end{aligned} \tag{29}$$

where the value for Nu_∞ is 8.235, which is the Nusselt number based on the bulk-mean temperature for the heat transfer between two semi-infinite plates that meet with an angle of α subject to a constant heat flux.

3.4 Evaluation and Optimization of the Thermal Performance. In order to evaluate the performance of the internally finned tube, a quantitative criterion for performance evaluation is required. There are many kinds of performance evaluation criteria by which an objective function (tube material volume, heat duty, or pumping power) is optimized under the given constraint (pumping power, heat duty, or surface area) [2,24]. In the present study, the thermal resistance and the pumping power are chosen as the objective function and the constraint, respectively, to evaluate the thermal performance of the internally finned tube.

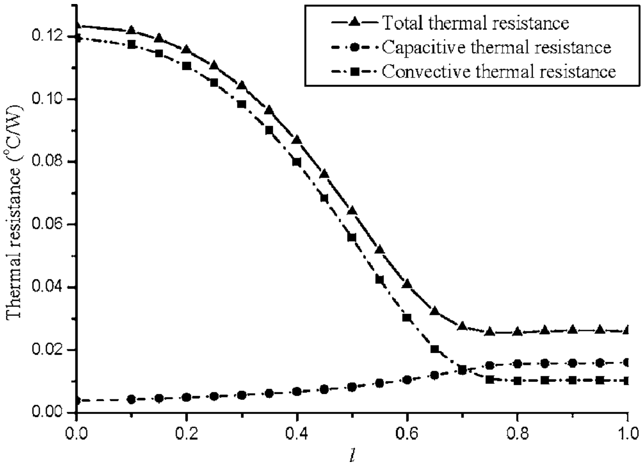

Fig. 8 The variation of the optimized thermal resistances in terms of dimensionless fin height *l* under the condition of the fixed pumping power (D_o=50 mm, *L*=1 m, P.P.=2.0×10^{-5} W)

The total thermal resistance is defined as the temperature difference of the two points of concern per unit heat flow rate [25]. It can be divided into two terms:

$$\zeta_{\text{total}} = \frac{T_{w,\text{out}} - T_{b,\text{in}}}{q} = \zeta_{\text{conv}} + \zeta_{\text{cap}} \tag{30}$$

where the first term on the right-hand side is known as the convective thermal resistance ζ_{conv} and the second term is the capacitive thermal resistance ζ_{cap}. The former is related to heat transfer from the fins to the coolant, and the latter is responsible for the temperature rise of the coolant from inlet to exit. From the definition of the bulk-mean temperature, the convective thermal resistance can be represented by

$$\zeta_{\text{conv}} = \frac{1}{h_{fs}A_{fs}} = \frac{T_w - T_{b,m}}{q''_w L(2\pi r_o)} = -\frac{\theta_m}{2\pi L k_f} \tag{31}$$

where h_{fs} and A_{fs} are the heat transfer coefficient between the fin and the fluid based on the bulk-mean temperature and the surface area between the fin and the fluid, respectively.

From the energy balance, the capacitive thermal resistance can be expressed as

$$\zeta_{\text{cap}} = \frac{1}{\rho_f c_f Q} = \frac{\mu_f L}{\rho_f c_f \Delta p}\frac{1}{U_m \pi r_0^4} \tag{32}$$

Optimization of the thermal performance of the internally finned tube results from the minimization of the total thermal resistance. In minimizing the total thermal resistance, all physical properties of the fluid, tube, and fins were fixed, and the pumping power was used as a constraint. The thermal resistance of the internally finned tube is minimized in the following example using the porous medium analytical solutions. In this example, we demonstrate the cost and speed advantage of the analytical solutions in optimizing the thermal performance of the internally finned tube.

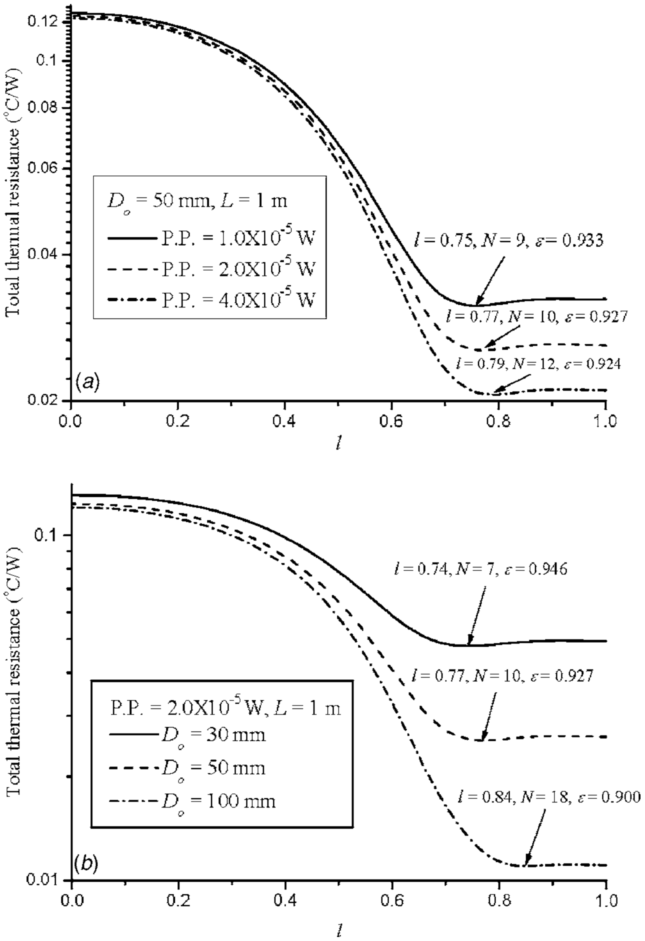

Fig. 9 The effects of (*a*) the pumping power and (*b*) tube diameter on the thermal performance of the internally finned tube

The thermophysical and geometric details of the internally finned tube are listed as follows. The working fluid is water, the material of fins is copper, the length and radius of the tube are 1 and 0.025 m, respectively, and the pumping power is 2.0 $\times 10^{-5}$ W. Figure 8 describes the variation of the total thermal resistance in terms of *l*. Each point marked in this graph represents the minimum value of the total thermal resistance with respect to *N* and ε as a function of *l*. For constant pumping power, the convective thermal resistance decreases while the capacitive thermal resistance increases, as *l* increases. Consequently, there exists an optimal value, which minimizes the total thermal resistance. For a pumping power of 2.0×10^{-5} W, the minimum thermal resistance is about 0.0256°C/W with the optimum conditions, ε =0.93, N=10, and l=0.77. As shown in Fig. 8, the thermal performance of the optimized internally finned tube is enhanced by about 80% compared with that of the unfinned tube (l=0) and 3% compared with that of the optimized circular-sectored finned tube (l=1), respectively. The effects of the pumping power and the tube diameter on the thermal performance of the internally finned tube were also examined. The total thermal resistance increases as the pumping power or the tube diameter decreases due to the fact that the capacitive thermal resistance increases with increasing flow friction (see Fig. 9). As the pumping power or the tube diameter decreases, the optimum geometry shifts toward minimizing flow friction, i.e., toward increasing porosity and decreasing number of fins and dimensionless fin height.

4 Conclusion

In this study, the new analytical solutions for velocity and temperature profiles in the internally finned tube are presented. Based on the analytical solutions, the variables of engineering importance influencing fluid flow and heat transfer in the internally finned tube are identified as the thermal conductivity ratio, the height and the number of fins, and the porosity. It is found that two simplifying assumptions employed in Soliman's study [15] may lead to significant errors in predicting the temperature distributions of the internally finned tube, as the number of fins increases or the thermal conductivity ratio, the porosity, or the dimensionless fin height decreases. On the other hand, the present analytical solutions based on the porous medium approach agree closely with the corresponding numerical solutions, regardless of the variations in these parameters.

In order to optimize the thermal performance of the internally finned tube, the total thermal resistance is minimized for a pumping power. It is shown that there exists an optimum value for the total thermal resistance with respect to the fin height as well as the number of fins and the porosity. Finally, the effects of the pumping power and the tube diameter on the thermal performance of the internally finned tube are examined. As either the pumping power or the tube diameter decreases, the optimum geometry shifts toward minimizing flow friction, i.e., toward increasing porosity and decreasing number of fins and dimensionless fin height.

The thermal performance of the internally finned tube is shown to be optimized with ease by modeling the internally finned tube as a tube filled partially with a fluid-saturated porous medium. The porous medium approach used here could be utilized in analyzing and optimizing the thermal performance of a variety of compact heat exchangers and heat sinks with complex geometry.

Acknowledgment

This work was supported by the Korea Science and Engineering Foundation (KOSEF) through the National Research Lab. Program funded by the Ministry of Science and Technology (No. M10600000224O6J000022410).

Nomenclature

c = specific heat of fluid (J kg^{-1} K^{-1})
Da = Darcy number
D$_o$ = tube diameter (m)
h_l = interstitial heat transfer coefficient (W m^{-2} K^{-1})
k = thermal conductivity (W m^{-1} K^{-1})
l = dimensionless height of fins
L = length of tube (m)
N = number of fins
p = pressure (Pa)
q'' = heat flux (W m^{-2})
Q = volume flow rate (m^3 s^{-1})
r_i = interfacial radius of the tube (m)
r_o = radius of the tube (m)
R = dimensionless radial coordinate
R_i = dimensionless interfacial radius
R_o = dimensionless radius of the tube
T = temperature (K)
u = velocity (m s^{-1})
U = dimensionless velocity, $u/r_0^2[-1/\mu_f(dp/dx)]$

Greek Symbols

α = angle between the flanks of two adjacent fins
β = angle subtended by one fin
ε = porosity, $\alpha(\alpha+\beta)$
Ω = one-half of a period, $(\alpha+\beta)/2$
φ = angular coordinate
λ = dimensionless local heat transfer coefficient, $\sqrt{h_l^*(1/k_{se}+1/k_{fe})}$
μ = viscosity (Pa s)
θ = dimensionless temperature, $T-T_w/q''_w r_0/k_f$
ρ = density (kg m^{-3})
ζ = thermal resistance (°C W^{-1})
$\langle\,\rangle$ = volume-averaged value

Subscripts

e = effective property
f = fluid
i = interfacial property
s = solid
w = wall

Appendix

The expressions for the coefficients appearing in Eqs. (24)–(27) are as follows:

$$C_1 = \frac{R_i^{1/\sqrt{\mathrm{Da}}}}{1-R_i^{2/\sqrt{\mathrm{Da}}}}\left[-\frac{U_i}{\varepsilon}+\frac{\mathrm{Da}}{1-4\mathrm{Da}}(R_i^2-R_i^{-1/\sqrt{\mathrm{Da}}})\right]$$

$$C_2 = \frac{R_i^{1/\sqrt{\mathrm{Da}}}}{1-R_i^{2/\sqrt{\mathrm{Da}}}}\left[\frac{U_i}{\varepsilon}+\frac{\mathrm{Da}}{1-4\mathrm{Da}}(-R_i^2+R_i^{1/\sqrt{\mathrm{Da}}})\right]$$

$$A_1 = \frac{2}{U_m}\left(\frac{\mathrm{Da}}{1-4\mathrm{Da}}\right)\left(\frac{1}{\lambda^2-16}\right) \quad A_2 = \frac{2C_1}{U_m[\lambda^2-(2+1/\sqrt{\mathrm{Da}})^2]}$$

$$A_3 = \frac{2C_2}{U_m[\lambda^2-(2-1/\sqrt{\mathrm{Da}})^2]}$$

$$C_3 = \frac{(\theta_{si}-\theta_{fi})}{R_i^{\lambda}-R_i^{-\lambda}} - \frac{1}{R_i^{\lambda}-R_i^{-\lambda}}[A_1(R_i^4-R_i^{-\lambda})+A_2(R_i^{2+1/\sqrt{\mathrm{Da}}}-R_i^{-\lambda})$$
$$+A_3(R_i^{2-1/\sqrt{\mathrm{Da}}}-R_i^{-\lambda})]$$

$$C_4 = \frac{(\theta_{si}-\theta_{fi})}{R_i^{-\lambda}-R_i^{\lambda}} - \frac{1}{R_i^{-\lambda}-R_i^{\lambda}}[A_1(R_i^4-R_i^{\lambda})+A_2(R_i^{2+1/\sqrt{\mathrm{Da}}}-R_i^{\lambda})$$
$$+A_3(R_i^{2-1/\sqrt{\mathrm{Da}}}-R_i^{\lambda})]$$

$$C_5 = -\frac{2k_{fe}}{U_m}\left[\frac{C_1}{(2+1/\sqrt{\mathrm{Da}})^2}+\frac{C_2}{(2-1/\sqrt{\mathrm{Da}})^2}+\frac{\mathrm{Da}}{16(1-4\mathrm{Da})}\right]$$

$$C_6 = \frac{1}{\ln R_i}\left\{k_{se}\theta_{si}+k_{fe}\theta_{fi}-C_5-\frac{2k_{fe}}{U_m}\left[\frac{C_1R_i^{2+1/\sqrt{\mathrm{Da}}}}{\left(2+\frac{1}{\sqrt{\mathrm{Da}}}\right)^2}+\frac{C_2R_i^{2-1/\sqrt{\mathrm{Da}}}}{\left(2-\frac{1}{\sqrt{\mathrm{Da}}}\right)^2}\right.\right.$$
$$\left.\left.+\frac{\mathrm{Da}R_i^4}{16(1-4\mathrm{Da})}\right]\right\}$$

$$B_1 = \frac{-1}{\ln R_i}\left\{\frac{2k_{fe}}{U_m}\left[\frac{C_1}{\left(2+\frac{1}{\sqrt{\mathrm{Da}}}\right)^2}R_i^{2+1/\sqrt{\mathrm{Da}}}+\frac{C_2}{(2-1/\sqrt{\mathrm{Da}})^2}R_i^{2-1/\sqrt{\mathrm{Da}}}\right.\right.$$
$$\left.\left.+\frac{\mathrm{Da}R_i^4}{16(1-4\mathrm{Da})}\right]+C_5\right\}$$

$$B_2 = \frac{-1}{R_i^{\lambda}-R_i^{-\lambda}}[A_1(R_i^4-R_i^{-\lambda})+A_2(R_i^{2+1/\sqrt{\mathrm{Da}}}-R_i^{-\lambda})+A_3(R_i^{2-1/\sqrt{\mathrm{Da}}}$$
$$-R_i^{-\lambda})]$$

$$B_3 = \frac{1}{R_i^{\lambda}-R_i^{-\lambda}}[A_1(R_i^4-R_i^{\lambda})+A_2(R_i^{2+1/\sqrt{\mathrm{Da}}}-R_i^{\lambda})+A_3(R_i^{2-1/\sqrt{\mathrm{Da}}}$$
$$-R_i^{\lambda})]$$

$$m_s = \frac{k_{fe}k_{se}}{k_{se}+k_{fe}}\left[\frac{1}{R_i\ln R_i}-\frac{\lambda}{R_i^{\lambda}-R_i^{-\lambda}}(R_i^{\lambda-1}+R_i^{-\lambda-1})\right]$$
$$+\frac{5k_f}{R_i\Omega}\sum_{n=1}^{\infty}B_n\sin(\varepsilon n\pi)$$

$$\begin{aligned} m_f = {} & \frac{k_{fe}k_{se}}{k_{se}+k_{fe}}\left[\frac{k_{fe}}{k_{se}}\frac{1}{R_i \ln R_i} + \frac{\lambda}{R_i^{\lambda}-R_i^{-\lambda}}(R_i^{\lambda-1}+R_i^{-\lambda-1})\right] \\ & - \frac{5k_f}{R_i\Omega}\sum_{n=1}^{\infty} B_n \sin(\varepsilon n\pi) \end{aligned}$$

$$\begin{aligned} m_c = {} & \frac{2\varepsilon k_f}{U_m}\left(\frac{R_i^3}{16}+\frac{R_iU_i}{2}\right) \\ & + \frac{6k_f}{\Omega}\frac{U_i}{U_m}\sum_{n=1}^{\infty}\left(\frac{\Omega}{n\pi}\right)\frac{R_i}{(n\pi/\Omega+1)}A_n\sin(\varepsilon n\pi) - \frac{k_{fe}}{k_{se}+k_{fe}}\left\{\frac{B_1}{R_i}\right. \\ & + \frac{2k_{fe}}{U_m}\left[\frac{C_1}{(2+1/\sqrt{\mathrm{Da}})}R_i^{1+1/\sqrt{\mathrm{Da}}} + \frac{C_2}{(2-1/\sqrt{\mathrm{Da}})}R_i^{1-1/\sqrt{\mathrm{Da}}}\right. \\ & \left. + \frac{\mathrm{Da}R_i^3}{4(1-4\mathrm{Da})}\right] - k_{se}\left[\lambda B_2R_i^{\lambda-1} - \lambda B_3R_i^{-\lambda-1} + 4A_1R_i^3\right. \\ & \left.\left. + A_2\left(2+\frac{1}{\sqrt{\mathrm{Da}}}\right)R_i^{1+1/\sqrt{\mathrm{Da}}} + A_3\left(2-\frac{1}{\sqrt{\mathrm{Da}}}\right)R_i^{1-1/\sqrt{\mathrm{Da}}}\right]\right\} \end{aligned}$$

$$\begin{aligned} n_s = {} & \frac{k_{fe}k_{se}}{k_{se}+k_{fe}}\left[\frac{k_{se}}{k_{fe}}\frac{1}{R_i \ln R_i} + \frac{\lambda}{R_i^{\lambda}-R_i^{-\lambda}}(R_i^{\lambda-1}+R_i^{-\lambda-1})\right] \\ & - \frac{5k_f}{R_i\Omega}\sum_{n=1}^{\infty} B_n \sin(\varepsilon n\pi) \end{aligned}$$

$$\begin{aligned} n_f = {} & \frac{k_{fe}k_{se}}{k_{se}+k_{fe}}\left[\frac{1}{R_i \ln R_i} - \frac{\lambda}{R_i^{\lambda}-R_i^{-\lambda}}(R_i^{\lambda-1}+R_i^{-\lambda-1})\right] \\ & + \frac{5k_f}{R_i\Omega}\sum_{n=1}^{\infty} B_n \sin(\varepsilon n\pi) \end{aligned}$$

$$\begin{aligned} n_c = {} & \frac{2(1-\varepsilon)k_f}{U_m}\left(\frac{R_i^3}{16}+\frac{R_iU_i}{2}\right) \\ & - \frac{6k_f}{\Omega}\frac{U_i}{U_m}\sum_{n=1}^{\infty}\left(\frac{\Omega}{n\pi}\right)\frac{R_i}{[(n\pi/\Omega)+1]}A_n\sin(\varepsilon n\pi) - \frac{k_{se}}{k_{se}+k_{fe}}\left\{\frac{B_1}{R_i}\right. \\ & + \frac{2k_{fe}}{U_m}\left[\frac{C_1}{(2+1/\sqrt{\mathrm{Da}})}R_i^{1+1/\sqrt{\mathrm{Da}}} + \frac{C_2}{(2-1/\sqrt{\mathrm{Da}})}R_i^{1-1/\sqrt{\mathrm{Da}}}\right. \\ & \left. + \frac{\mathrm{Da}R_i^3}{4(1-4\mathrm{Da})}\right] + k_{fe}\left[\lambda B_2R_i^{\lambda-1} - \lambda B_3R_i^{-\lambda-1} + 4A_1R_i^3\right. \\ & \left.\left. + A_2\left(2+\frac{1}{\sqrt{\mathrm{Da}}}\right)R_i^{1+1/\sqrt{\mathrm{Da}}} + A_3(2-1/\sqrt{\mathrm{Da}})R_i^{1-1/\sqrt{\mathrm{Da}}}\right]\right\} \end{aligned}$$

References

[1] Bergles, A. E., 1997, "Heat Transfer Enhancement—The Encouragement and Accommodation of High Heat Fluxes," ASME J. Heat Transfer, **119**(1), pp. 8–19.

[2] Webb, R. L., and Kim, N. H., 2005, *Principles of Enhanced Heat Transfer*, 2nd ed., Taylor & Francis, New York.

[3] Kays, W. M., and London, A. L., 1964, *Compact Heat Exchangers*, 2nd ed., McGraw-Hill, New York.

[4] Fraas, A. P., and Qzisik, M. N., 1965, *Heat Exchanger Design*, Wiley, New York.

[5] Watkinson, A. P., Millet, D. L., and Kubanek, G. R., 1975, "Heat Transfer and Pressure Drop of Internally Finned Tubes in Laminar Oil Flow," ASME Paper No. 75-HT-41.

[6] Marner, W. J., and Bergles, A. E., 1978, "Augmentation of Tube-Side Laminar Flow Heat Transfer by Means of Twisted-Tape Insert, Static-Mixers Inserts, and Internally Finned Tubes," *Proceedings of the 6th International Heat Transfer Conference*, Toronto, Hemisphere Pub. Corp., Washington, DC, Vol. 2, pp. 583–588.

[7] Rustum, I. M., and Soliman, H. M., 1988, "Experimental Investigation of Laminar Mixed Convection in Tubes with Longitudinal Internal Fins," ASME J. Heat Transfer, **110**(2), pp. 366–372.

[8] Shome, B., and Jensen, M. K., 1996, "Experimental Investigation of Laminar Flow and Heat Transfer in Internally Finned Tubes," J. Enhanced Heat Transfer, **4**(1), pp. 53–70.

[9] Masliyah, J. M., and Nandakumar, K., 1976, "Heat Transfer in Internally Finned Tubes," ASME J. Heat Transfer, **98**(2), pp. 257–261.

[10] Patankar, S. V., Ivanovic, M., and Sparrow, E. M., 1979, "Analysis of Turbulent Flow and Heat Transfer in Internally Finned Tubes and Annuli," ASME J. Heat Transfer, **101**(1), pp. 29–37.

[11] Rustum, I. M., and Soliman, H. M., 1988, "Numerical Analysis of Laminar Forced Convection in the Entrance Region of Tubes with Longitudinal Internally Fins," ASME J. Heat Transfer, **110**(2), pp. 310–313.

[12] Fabbri, G., 1998, "Heat Transfer Optimization in Internally Finned Tubes Under Laminar Flow Conditions," Int. J. Heat Mass Transfer, **41**(10), pp. 1243–1253.

[13] Hu, M. H., and Chang, Y. P., 1973, "Optimization of Finned Tubes for Heat Transfer in Laminar Flow," ASME J. Heat Transfer, **95**(3), pp. 332–338.

[14] Soliman, H. M., and Feingold, A., 1977, "Analysis of Fully Developed Laminar Flow in Longitudinal Internally Finned Tubes," Chem. Eng. J., **14**(2), pp. 119–128.

[15] Soliman, H. M., 1981, "The Effect of Fin Conductance on Laminar Heat Transfer Characteristics of Internally Finned Tubes," Can. J. Chem. Eng., **59**(2), pp. 251–256.

[16] Koh, J. C. Y., and Colony, R., 1986, "Heat Transfer of Microstructures for Integrated Circuits," Int. Commun. Heat Mass Transfer, **13**(1), pp. 89–98.

[17] Kim, S. J., and Kim, D., 1999, "Forced Convection in Microstructures for Electronic Equipment Cooling," ASME J. Heat Transfer, **121**(3), pp. 639–645.

[18] Kim, S. J., and Hyun, J. M., 2005, "A Porous Medium Approach for the Thermal Analysis of Heat Transfer Devices," *Transport Phenomena in Porous Media III*, D. B. Ingham and I. Pop, eds., Elsevier, New York, pp. 120–146.

[19] Srinivasan, V., Vafai, K., and Christensen, R. N., 1994, "Analysis of Heat Transfer and Fluid Flow Through a Spirally Fluted Tube Using a Porous Substrate Approach," ASME J. Heat Transfer, **116**(3), pp. 543–551.

[20] Kim, S. J., Yoo, J. W., and Jang, S. P., 2002, "Thermal Optimization of a Circular-Sectored Finned Tube Using a Porous Medium Approach," ASME J. Heat Transfer, **124**(6), pp. 1026–1033.

[21] Bejan, A., 1995, *Convection Heat Transfer*, 2nd ed., Wiley, New York, Chap. 12.

[22] Min, J. Y., and Kim, S. J., 2005, "A Novel Methodology for Thermal Analysis of a Composite System Consisting of a Porous Medium and an Adjacent Fluid Layer," ASME J. Heat Transfer, **127**(6), pp. 648–656.

[23] Zill, D. G., and Cullen, M. R., 1992, *Advanced Engineering Mathematics*, PWS, Boston, Chap. 11.

[24] Webb, R. L., and Scott, M. J., 1980, "A Parametric Analysis of the Performance of Internally Finned Tubes for Heat Exchanger Application," ASME J. Heat Transfer, **102**, pp. 38–43.

[25] Knight, R. W., Goodling, J. S., and Hall, D. J., 1991, "Optimal Thermal Design of Forced Convection Heat Sinks—Analytical," ASME J. Electron. Packag., **113**, pp. 313–321.

Spectral Element Approach for Coupled Radiative and Conductive Heat Transfer in Semitransparent Medium

J. M. Zhao

L. H. Liu[1]
e-mail: lhliu@hit.edu.cn

School of Energy Science and Engineering,
Harbin Institute of Technology,
92 West Dazhi Street,
Harbin 150001, P.R. China

A spectral element method is presented to solve coupled radiative and conductive heat transfer problems in multidimensional semitransparent medium. The solution of radiative energy source is based on a second order radiative transfer equation. Both the second order radiative transfer equation and the heat diffusion equation are discretized by spectral element approach. Four various test problems are taken as examples to verify the performance of the spectral element method. The h-and the p-convergence characteristics of the spectral element method are studied. The convergence rate of p refinement for different values of Planck number follows the exponential law and is superior to that of h refinement. The spectral element method has good property to tolerate skewed meshes. The predicted dimensionless temperature distributions determined by the spectral element method agree well with the results in references. The presented method is very effective to solve coupled radiative and conductive heat transfer in semitransparent medium with complex configurations and demands little on the quality of mesh.

[DOI: 10.1115/1.2755061]

Keywords: spectral element method, second order radiative transfer equation, combined mode heat transfer

1 Introduction

The coupled problem of radiative and conductive heat transfer is of considerable practical importance in engineering applications. These applications include, for example, the analysis of heat transfer process in glasses and industrial furnaces or the analysis of thermal performance of porous insulating materials, such as fibers, powders, foams, and so on. The solution of this coupled problem involves the evaluation of radiative heat source and the solution of heat diffusion equation. Due to the inherent complexity associated with radiative transfer, the evaluation of radiative heat source is the main difficulty for the solution of coupled radiative and conductive heat transfer problems in semitransparent medium.

Recently, many numerical methods have been proposed to solve the coupled radiative and conductive heat transfer in semitransparent medium. Viskanta and Grosh [1] analyzed combined radiation and conduction heat transfer between one-dimensional parallel plates filled with absorbing medium using iterative method. Yuen and Wong [2] used a successive approximation technique to solve the combined conductive and radiative heat transfer in one-dimensional absorbing, emitting, and anisotropically scattering medium. Burns et al. [3] analyzed numerically the problem of coupled radiative and conductive heat transfer in one-dimensional absorbing medium using traditional Galerkin finite element method and the Swartz–Wendroff approximation. Yuen and Takara [4] analyzed coupled radiative and conductive heat transfer in two dimensional rectangular enclosure by using a class of generalized exponential integral function. Razzaque et al. [5] employed the finite element method to solve the coupled radiation and conduction in a two dimensional rectangular enclosure filled with gray medium. Kim and Baek [6] studied the coupled radiative and conductive heat transfer in two dimensional rectangular enclosure, in which the central difference scheme was used to discretize the heat diffusion equation and the discrete ordinate method was employed to solve the radiative transfer equation. Sakami et al. [7] solved the coupled radiative and conductive heat transfer in two dimensional complex geometries filled with absorbing, emitting, and scattering medium, in which a modified discrete ordinate approach was applied to solve the radiative transfer equation, while the heat diffusion equation was solved by finite element method. Talukdar and Mishra [8] solved the combined conduction and radiation problem in one-dimensional gray absorbing, emitting, and anisotropically scattering medium using the collapsed dimension method (CDM). Mishra and Lankadasu [9] solved the transient conductive and radiative heat transfer in two dimensional rectangular enclosure filled with absorbing, emitting, and scattering medium, in which the energy equation of the problem is solved with the lattice Boltzmann method (LBM), while the radiative transfer equation is solved using the CDM. Besides that different discretization schemes are often used to solve the heat diffusion equation and the radiative transfer equation, most of these methods are lower order method (first order or second order) and just offer h convergence, i.e., the convergence gained by reducing the element size h or h refinement. As a result, remeshing or refining is often needed in order to gain the wanted accuracy.

The well known radiative transfer equation (RTE), which describes the transport of radiation intensity through an absorbing, emitting, and scattering medium, is one of the first order integrodifferential equations and can be written in Cartesian coordinates as

$$\mathbf{\Omega} \cdot \nabla I + \beta I = \kappa I_b + \frac{\sigma_S}{4\pi}\int_{4\pi} I(\mathbf{r},\mathbf{\Omega}')\Phi(\mathbf{\Omega}',\mathbf{\Omega})d\Omega' \tag{1}$$

where $\mathbf{\Omega}$ is the unit direction vector of radiation, β is the extinction coefficient, κ is the absorption coefficient, σ_S is the scattering coefficient, and Φ is the scattering phase function. The first term

---

[1] Corresponding author.

Contributed by the Heat Transfer Division of ASME for publication in the JOURNAL OF HEAT TRANSFER. Manuscript received October 12, 2006; final manuscript received February 5, 2007. Review conducted by Gautam Biswas.

of the left hand side of Eq. (1) can be seen as a convection term with convection velocity of $\mathbf{\Omega}$. Because of the vanishing of diffusion term, the RTE can be considered as a convection dominated equation. This is the major difference between the RTE and the heat diffusion equation. The solution of the RTE often requires a different solver instead of the one used in the solution of the heat diffusion equation and thus makes it inconvenient in the coupled conduction and radiation analysis. The presence of convection term may cause nonphysical oscillatory of solutions. This type of instability occurs in many numerical methods including finite difference method and finite element method if no special stability treatment is taken. Special stabilization techniques, such as upwinding scheme or artificial viscosity, are often used in finite volume method (FVM) and finite element method (FEM). Besides taking various numerical stabilization schemes, another method to overcome the stability problem is to analytically transform the original RTE into a numerically more stable equation, for example, the second order partial differential equation. One famous transformed equation is the even parity formulation (EPF) of the RTE, which is a second order partial differential equation of the even parity of radiative intensity. It is well known that the second order derivative term have diffusive characteristic and good numerical properties. Cheong and Song [10] examined several spatial discretization schemes in the discrete ordinate solution of the EPF. Fiveland and Jessee [11,12] studied the finite element solution of the EPF. Though the stability of the finite element solution of the second order even parity equation is ensured, numerical results indicate that the solution obtained using the FEM is less accurate as the optical thickness and the wall emissivity are increased.

Recently, Zhao and Liu [13] derived a second order primitive variable radiative transfer equation (SORTE), which is in a form similar to the heat diffusion equation. Numerical results show that the SORTE overcomes most of the drawbacks of EPF and can be effectively applied to solve radiative transfer in absorbing, emitting, and anisotropically scattering medium. The FEM based on the SORTE is numerically stable, efficient, and accurate, and presents a symmetric stiff matrix. It is expected that, based on the SORTE, a unified solver is allowed to stably solve the coupled radiative and conductive heat transfer process in multidimensional semitransparent medium.

Spectral element method, originally proposed by Patera [14] for the solution of fluid problem, combines the competitive advantages of high order spectral method and FEM. Spectral method is preferred because of its exponential convergence characteristics. FEM is attractive because of its highly flexible domain decomposition capability, which is extremely useful for the problem with complex geometries. Spectral element method provides basically two types of refinement scheme to achieve convergence. The most common one is to use smaller size elements in the regions where higher resolution is required, which is called h refinement in literature because the element sizes are usually denoted by h. The second type refinement is the p refinement, in which the number of elements and their sizes are kept the same but the approximation order inside the elements is increased where higher resolution is required. As a result, spectral element method is very flexible for solving the multidimensional problem in complex geometries with higher order accuracy. In recent years, spectral element method has attracted the interest of many researchers in the physics and engineering communities [15–22].

In order to best combine both the advantages of the SORTE and the spectral element approach, in this paper, a spectral element method (SEM) based on the SORTE is developed to solve the coupled radiative and conductive heat transfer in multidimensional semitransparent medium. With application of the advantages of the SORTE, the radiative transfer and the heat diffusion equations are both solved by spectral element approach. Four cases of coupled radiative and conductive heat transfer in semitransparent medium are taken to verify the performance of the presented method.

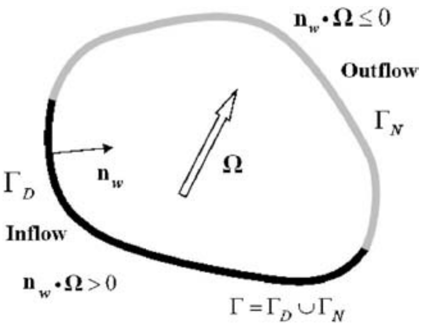

Fig. 1 Schematic of boundary conditions prescription for the SORTE

2 Mathematical Formulation

2.1 Second Order Radiative Transfer Equation. The SORTE was first presented and detailed analyzed in a recent paper [13]. Equation (1) can be written formally as

$$I = \beta^{-1}\left[-\mathbf{\Omega}\cdot\nabla I + \kappa I_b + \frac{\sigma_S}{4\pi}\int_{4\pi} I(\mathbf{r},\mathbf{\Omega}')\Phi(\mathbf{\Omega}',\mathbf{\Omega})d\Omega' \right] \quad (2)$$

Substituting Eq. (2) back into the derivative term of Eq. (1) leads to the second order partial differential equation as follows:

$$-\mathbf{\Omega}\cdot\nabla(\beta^{-1}\mathbf{\Omega}\cdot\nabla I) + \beta I = \beta S - \mathbf{\Omega}\cdot\nabla S \quad (3)$$

where S is the source function defined as

$$S = (1-\omega)I_b + \frac{\omega}{4\pi}\int_{4\pi} I(\mathbf{r},\mathbf{\Omega}')\Phi(\mathbf{\Omega}',\mathbf{\Omega})d\Omega' \quad (4)$$

For the opaque, diffusely emitting and reflecting walls, the boundary conditions are given for both the inflow and outflow boundaries as

$$I(\mathbf{r}_w,\mathbf{\Omega}) = \varepsilon_w I_b(\mathbf{r}_w) + \frac{1-\varepsilon_w}{\pi}\int_{\mathbf{n}_w\cdot\mathbf{\Omega}'<0} I(\mathbf{r}_w,\mathbf{\Omega}') \times|\mathbf{n}_w\cdot\mathbf{\Omega}'^{,m}|d\Omega' \quad \mathbf{n}_w\cdot\mathbf{\Omega} > 0 \quad (5a)$$

$$\beta^{-1}\mathbf{\Omega}\cdot\nabla I(\mathbf{r}_w,\mathbf{\Omega}) + I(\mathbf{r}_w,\mathbf{\Omega}) = S(\mathbf{r}_w,\mathbf{\Omega}) \quad \mathbf{n}_w\cdot\mathbf{\Omega} \leqslant 0 \quad (5b)$$

where ε_w is the wall emissivity, and $\mathbf{n}_w$ is the unit inward normal vector of boundary. A schematic of the prescribed boundary conditions for the SORTE is shown in Fig. 1 for a clear view, where Γ denotes all the boundary of solution domain with $\Gamma=\Gamma_D\cup\Gamma_N$, Γ_D and Γ_N denote the inflow boundary (Dirichlet type) and the outflow boundary (Neumann type), respectively.

The discrete ordinate equation of the SORTE given by Eq. (3) can be written as

$$-\mathbf{\Omega}^m\cdot\nabla[\beta^{-1}\mathbf{\Omega}^m\cdot\nabla I(\mathbf{r},\mathbf{\Omega}^m)] + \beta I(\mathbf{r},\mathbf{\Omega}^m) = \beta S(\mathbf{r},\mathbf{\Omega}^m) - \mathbf{\Omega}^m\cdot\nabla S(\mathbf{r},\mathbf{\Omega}^m) \quad (6)$$

with the following inflow and outflow boundary conditions:

$$I(\mathbf{r}_w,\mathbf{\Omega}^m) = \varepsilon_w I_b(\mathbf{r}_w) + \frac{1-\varepsilon_w}{\pi}\sum_{\mathbf{n}_w\cdot\mathbf{\Omega}'^{,m}<0} I(\mathbf{r}_w,\mathbf{\Omega}'^{,m}) \times|\mathbf{n}_w\cdot\mathbf{\Omega}'^{,m}|w^m \quad \mathbf{n}_w\cdot\mathbf{\Omega}^m > 0 \quad (7a)$$

$$\beta^{-1}\mathbf{\Omega}^m \cdot \nabla I(\mathbf{r}_w,\mathbf{\Omega}^m) + I(\mathbf{r}_w,\mathbf{\Omega}^m) = S(\mathbf{r}_w,\mathbf{\Omega}^m) \quad \mathbf{n}_w \cdot \mathbf{\Omega}^m \leqslant 0 \tag{7b}$$

where $\mathbf{\Omega}^m$ is the discrete angular direction and w^m is the corresponding angular quadrature weight.

2.2 Energy Equation for Coupled Radiative and Conductive Heat Transfer Processes. In the following analysis, Eq. (6) with boundary conditions, Eq. (7), is taken as the model equations to calculate radiative intensity field. When coupled analysis of radiative and conductive heat transfer is needed, an additional equation, namely, heat diffusion equation is required to be solved simultaneously. The energy equation for a steady state coupled conduction-radiation problem can be written as

$$\nabla \cdot [k \nabla T(\mathbf{r})] = \nabla \cdot \mathbf{q}_r(\mathbf{r}) \tag{8}$$

with boundary condition

$$T(\mathbf{r}_w) = \bar{T}(\mathbf{r}_w) \quad \mathbf{r}_w \in \Gamma_T \tag{9a}$$

$$-k\mathbf{n}_w \cdot \nabla T(\mathbf{r}_w) = \bar{q}(\mathbf{r}_w) \quad \mathbf{r}_w \in \Gamma_q \tag{9b}$$

where $\bar{T}$ denotes the temperature distribution on Dirichlet boundary Γ_T, $\bar{q}$ denotes the conductive outflow heat flux distribution at Neumann boundary Γ_q, $\mathbf{q}_r(\mathbf{r})$ is the radiative heat flux, and the $\nabla \cdot \mathbf{q}_r(\mathbf{r})$ is the radiative energy source given by

$$\nabla \cdot \mathbf{q}_r(\mathbf{r}) = \kappa \left[4\pi I_b - \int_{4\pi} I(\mathbf{r},\mathbf{\Omega}) d\Omega \right] \tag{10}$$

2.3 Galerkin Weak Formulation. The discrete ordinate equation of the SORTE (Eq. (6)) weighted by $W(\mathbf{r})$ and integrated over the solution domain after using Gauss divergence theorem leads to

$$\langle \beta^{-1}\mathbf{\Omega}^m \cdot \nabla I^m, \mathbf{\Omega}^m \cdot \nabla W \rangle + (\beta^{-1}\mathbf{\Omega}^m \cdot \nabla I^m, W\mathbf{\Omega}^m \cdot \mathbf{n}_w)_\Gamma + \langle \beta I^m, W \rangle$$
$$= \langle \beta S^m, W \rangle - \langle \mathbf{\Omega}^m \cdot \nabla S^m, W \rangle \tag{11}$$

where $\mathbf{n}_w$ is the inward normal vector of the boundary, Γ denotes the boundary of solution domain ($\Gamma = \Gamma_D \cup \Gamma_N$), Γ_D and Γ_N denotes the inflow boundary, and outflow boundary, as shown in Fig. 1. The operators $\langle \cdot,\cdot \rangle$ and $(\cdot,\cdot)$ are defined as follows:

$$\langle f,g \rangle = \int_V fg dV \quad (f,g)_\Gamma = \int_\Gamma fg dA \tag{12}$$

Assuming the weight function $W(\mathbf{r})$ is zero on the inflow boundary Γ_D, then Eq. (15) can be written as

$$\langle \beta^{-1}\mathbf{\Omega}^m \cdot \nabla I^m, \mathbf{\Omega}^m \cdot \nabla W \rangle + (\beta^{-1}\mathbf{\Omega}^m \cdot \nabla I^m, W\mathbf{\Omega}^m \cdot \mathbf{n}_w)_{\Gamma_N} + \langle \beta I^m, W \rangle$$
$$= \langle \beta S^m, W \rangle - \langle \mathbf{\Omega}^m \cdot \nabla S^m, W \rangle \tag{13}$$

Considering the outflow boundary condition given by Eq. (7*b*), we get

$$(\beta^{-1}\mathbf{\Omega}^m \cdot \nabla I^m, W\mathbf{\Omega}^m \cdot \mathbf{n}_w)_{\Gamma_N} = (S^m - I^m, W\mathbf{\Omega}^m \cdot \mathbf{n}_w)_{\Gamma_N} \tag{14}$$

Substituting Eq. (13) into Eq. (12) leads to the following weak formulation:

$$\langle \beta^{-1}\mathbf{\Omega}^m \cdot \nabla I^m, \mathbf{\Omega}^m \cdot \nabla W \rangle - (I^m, W\mathbf{\Omega}^m \cdot \mathbf{n}_w)_{\Gamma_N} + \langle \beta I^m, W \rangle = \langle \beta S^m, W \rangle$$
$$- \langle \mathbf{\Omega}^m \cdot \nabla S^m, W \rangle - (S^m, W\mathbf{\Omega}^m \cdot \mathbf{n}_w)_{\Gamma_N} \tag{15}$$

The heat diffusion equation (Eq. (8)) is a kind of classical elliptical equation, and its Galerkin weak form is given as

$$-\langle k \nabla T, \cdot \nabla W \rangle = \langle \nabla \cdot \mathbf{q}_r(\mathbf{r}), W \rangle + (\bar{q}, W)_{\Gamma_q}$$
$$= \kappa \langle 4\pi I_b - \int_{4\pi} I(\mathbf{r},\mathbf{\Omega}) d\Omega, W \rangle + (\bar{q}, W)_{\Gamma_q} \tag{16}$$

In the Galerkin weak formulation of SORTE (Eq. (15)) and heat diffusion equation (Eq. (16)), the Neumann type boundary conditions are imposed implicitly, while for imposing the Dirichlet type boundary conditions, the collocation technique [23,24] is employed.

2.4 Spectral Element Approach. The unknown radiative intensity and temperature can be approximated by nodal basis function with Kronecker delta property as

$$I^m(\mathbf{r}) \simeq \sum_{i=1}^{N_{\text{sol}}} I_i^m \phi_i(\mathbf{r}) \tag{17}$$

$$T(\mathbf{r}) \simeq \sum_{i=1}^{N_{\text{sol}}} T_i \phi_i(\mathbf{r}) \tag{18}$$

where ϕ_i is the nodal basis function, I_i^m denotes radiative intensity of direction $\mathbf{\Omega}^m$ at solution nodes i, T_i denotes temperature at solution nodes i, and N_{sol} is the total number of solution nodes. In SEM, the nodal basis function $\phi_i(\mathbf{r})$ is constructed on each element by orthogonal polynomial expansion. In this paper, Chebyshev polynomial expansion is used. The details about building global nodal basis function were described in Ref. [24].

By substituting the approximation of radiative intensity (Eq. (17)) into the Galerkin weak formulation of SORTE (Eq. (15)) and taking the weight function $W(\mathbf{r})$ as nodal basis function $\phi_j(\mathbf{r})$, the spectral element discretization of SORTE can be written in matrix form as

$$\mathbf{K}^m \mathbf{I}^m = \mathbf{H}^m \tag{19}$$

Here, the matrices $\mathbf{K}^m$ and $\mathbf{H}^m$ are defined as

$$K_{ji}^m = \langle \beta^{-1}\mathbf{\Omega}^m \cdot \nabla \phi_i, \mathbf{\Omega}^m \cdot \nabla \phi_j \rangle - (\phi_i, \phi_j \mathbf{\Omega}^m \cdot \mathbf{n}_w)_{\Gamma_N} + \langle \beta \phi_i, \phi_j \rangle \tag{20a}$$

$$H_j^m = \langle \beta S^m, \phi_j \rangle - \langle \mathbf{\Omega}^m \cdot \nabla S^m, \phi_j \rangle - (S^m, \phi_j \mathbf{\Omega}^m \cdot \mathbf{n}_w)_{\Gamma_N} \tag{20b}$$

It can be seen from Eq. (20) that the stiff matrix $\mathbf{K}^m$ is symmetric for every discrete direction.

Similarly, the spectral element discretization of heat diffusion equation can be written in matrix form as

$$\mathbf{MT} = \mathbf{N} \tag{21}$$

Here, the matrices $\mathbf{M}$ and $\mathbf{N}$ are defined as

$$M_{ji} = -\langle k \nabla \phi_i, \cdot \nabla \phi_j \rangle \tag{22a}$$

$$N_j = \kappa \langle 4\pi I_b - \int_{4\pi} I(\mathbf{r},\mathbf{\Omega}) d\Omega, \phi_j \rangle + (\bar{q}, \phi_j)_{\Gamma_q} \tag{22b}$$

2.5 Solution Procedure. The implementation of the SEM for analysis of coupled radiative and conductive heat transfer is carried out according to the following procedure.

(a) Step 1. Mesh the solution domain with N_{el} nonoverlap elements and generate global unique spectral nodes on each element according to the order p of polynomial expansion.
(b) Step 2. Assume initial radiative intensity field and temperature field.
(c) Step 3. Assemble the matrices $\mathbf{M}$ and $\mathbf{N}$ for the discretized heat diffusion equation. Impose Dirichlet boundary condition and solve the discretized equation to update the temperature field. Make under-relaxation on the temperature field as needed.
(d) Step 4. Loop each angular direction for $m = 1, \ldots, M$, and assemble the matrices $\mathbf{K}^m$ and $\mathbf{H}^m$ for the discretized

Table 1 Comparison of dimensionless temperature distributions obtained from different methods

	$N_{plk}=0.01$			$N_{plk}=1.0$		
x/L	SEM	Burns [3]	Nice [25]	SEM	Burns [3]	Nice [25]
0.1	0.9230	0.9206	0.9218	0.9137	0.9137	0.9137
0.2	0.8919	0.8888	0.8913	0.8284	0.8283	0.8288
0.3	0.8680	0.8650	0.8679	0.7427	0.7427	0.7430
0.4	0.8443	0.8415	0.8446	0.6558	0.6558	0.6561
0.5	0.8182	0.8156	0.8189	0.5674	0.5674	0.5677
0.6	0.7859	0.7837	0.7872	0.4772	0.4772	0.4775
0.7	0.7379	0.7361	0.7400	0.3852	0.3853	0.3855
0.8	0.6477	0.6460	0.6502	0.2915	0.2916	0.2918
0.9	0.4570	0.4557	0.4590	0.1964	0.1965	0.1965

SORTE. Impose Dirichlet boundary condition and solve the discretized equation to update radiative intensity field of each direction.

(e) Step 5. Terminate the iteration process if the stop criterion is met. Otherwise go back to Step 3.

In this paper, the maximum relative error 10^{-4} of temperature ($\|T_{\text{new}}-T_{\text{old}}\|/\|T_{\text{new}}\|$) is taken as stopping criterion for the global iteration.

3 Results and Discussion

Computer code is developed based on the numerical method described above. To verify the formulations presented in this paper, three various test cases are selected to verify the performance of the new numerical method for coupled radiative and conductive heat transfer in semitransparent medium. For the sake of quantitative comparison with the benchmark solutions, the integral averaged relative error of SEM solution is defined as

$$\text{relative Error \%} = \frac{\int |\text{SEM solution}(x) - \text{benchmark result}(x)|dx}{\int |\text{benchmark result}(x)|dx} \times 100 \qquad (23)$$

3.1 Case 1: One-Dimensional Nonscattering Gray Medium Between Parallel Black Plates. We consider the coupled radiative and conductive heat transfer in a layer of absorbing-emitting medium between infinite parallel black plates. The medium between the plates is gray and has a constant thermal conductivity and absorption coefficient. The temperatures of the plates are T_0 at $x/L=0.0$, and $T_1=0.1T_0$ at $x/L=1.0$, respectively. The optical thickness of the layer is $\tau_L=\beta L=1.0$. The dimensionless temperature distribution within the layer is determined for different values of Planck number $N_{\text{Plk}}=k\beta/(4\sigma T_0^3)$. This case was considered as a benchmark example and studied by several researchers. The dimensionless temperature distributions obtained using the SEM are shown in Table 1 and compared to the results of Burns et al. [3] and Nice [25] for $N_{\text{Plk}}=0.01$, 0.1, and 1.0. Here, S_8 approximation is used for angular discretization and two elements with tenth order polynomial expansion are used for spatial discretization on each element. The agreement between the different results is quite good. In general, the maximum deviation between these results is less than 0.2%.

The *h*- and the *p*-convergence characteristics of the SEM for the solution of dimensionless temperature distribution for different values of Planck number are studied. Figure 2 shows the *p*-convergence characteristics of the SEM, where two elements are used and the solution obtained with 20th order polynomial is considered as the benchmark solution. Note that the temperature distribution for $N_{\text{Plk}}=0$ is solved as a purely radiation equilibrium problem and without coupling with the heat diffusion equation. It can be seen that the convergence is very fast for different values of Planck number and the convergence rate follows the exponential law. With the increase of Planck number, the convergence rate tends to increase. Figure 3 shows the *h*-convergence characteristics of the SEM. Here, the first order polynomial is used for all the values of Planck number and the same benchmark solution is used for comparison. Similarly, the solution accuracy is better for a relative greater Planck number under the same spatial discretization for the coupled solution. A detailed comparison of the *h*- and the *p*-convergence rate is shown in Fig. 4, where the horizontal coordinate denotes the total number of solution nodes for spatial

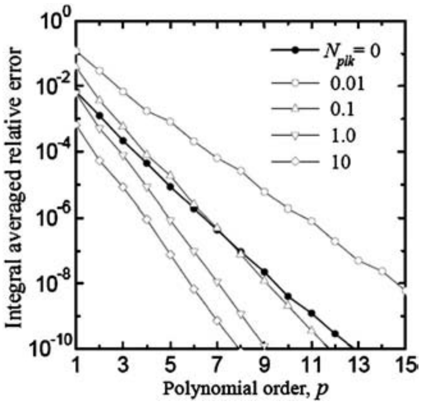

Fig. 2 The *p*-convergence characteristics of the SEM for different values of Planck number

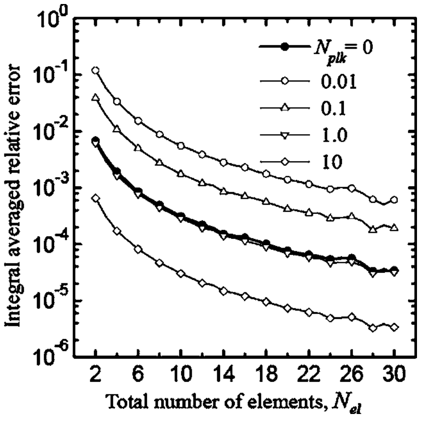

Fig. 3 The *h*-convergence characteristics of the SEM for different values of Planck number

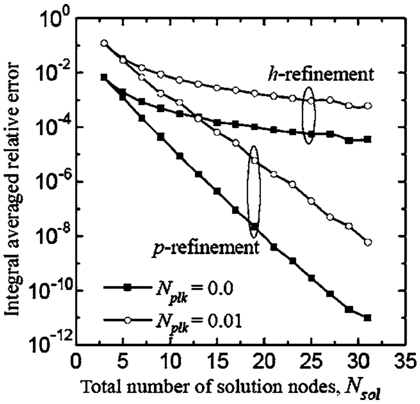

Fig. 4 The *h* and the *p*-convergence rate of the SEM according to total number of solution nodes

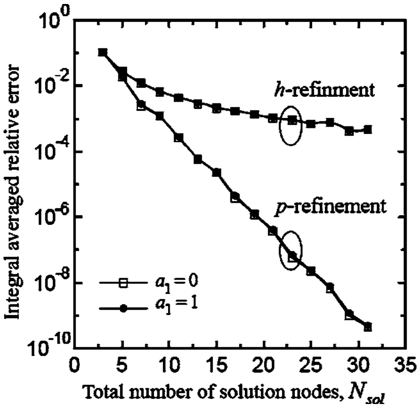

Fig. 6 The *h*- and the *p*-convergence characteristics of the SEM according to total number of solution nodes for different values of anisotropy factor a_1

discretization and only results for $N_{\mathrm{Plk}}=0.01$ and 0 is plotted for clarity. For the one-dimensional problem considered here, total number of solution nodes N_{sol} can be written as a function of the total number of element N_{el} and the order of polynomial expansion p as $N_{\mathrm{sol}}=pN_{\mathrm{el}}+1$. In the h-refinement analysis, the first order polynomial expansion is used and only the number of elements is increased during refining. In the p-refinement analysis, two elements are used and only the order of polynomial is increased during refining. By comparison, it is clearly shown that the convergence rate of p refinement is superior to that of h refinement. This implies that more accuracy of solution can be obtained by p refinement than h refinement under the same computational cost.

3.2 Case 2: One-Dimensional Anisotropically Scattering Gray Medium Between Parallel Black Plates. We consider the coupled radiative and conductive heat transfer in a layer of anisotropically medium between the infinite parallel black plates. The temperatures of the plates are T_0 at $x/L=0.0$, and $T_L=\alpha T_0$ at $x/L=1.0$, respectively. The optical thickness τ_L of the layer is 1.0. The medium has a linear anisotropically scattering phase function: $\Phi(\mu,\mu')=1+a_1(\mu\mu')$. This case was also studied by Tulukdar and Mishra [8] using the CDM. The SEM is applied to this case to study its performance for solution of coupled radiative and conductive heat transfer in scattering media. Here, the S_8 approximation is used for angular discretization and two elements with tenth order polynomial expansion are used for spatial discretization on each element. Figure 5 shows the dimensionless temperature distributions obtained by the SEM for different scattering conditions, namely, isotropically scattering ($a_1=0$) and linear anisotropically scattering ($a_1=1$), and different values of Planck number. By comparison, the results of the SEM agree very well with those obtained by the CDM [8]. Figure 6 shows the h- and the p-convergence curves of the SEM for the solution of dimensionless temperature distribution with $N_{\mathrm{Plk}}=0.01$, $\alpha=0.1$, $\omega=0.5$, and different values of a_1. The solution obtained with two elements and 20th order polynomial is considered as the benchmark solution. For study of the p-convergence characteristics, two elements are used for all p-refinement schemes. For study of the h-convergence characteristics, the first order polynomial is used for all the h-refinement schemes. It can be seen that the convergence rate of p refinement follows exponential law and is superior to that of h refinement when the medium is anisotropically scattering or not.

3.3 Case 3: Two Dimensional Absorbing-Emitting Medium in a Black Enclosure. In this case, we consider the coupled radiative and conductive heat transfer in a two dimensional square gray semitransparent medium enclosed by black walls. The medium is nonscattering and the optical thickness based on the side length L of square enclosure is $\tau_L=\beta L=1.0$. The temperature of the left wall is maintained at $T_{w1}=1000$ K, while the other walls are kept at 500 K. The SEM is applied to solve the dimensionless temperature distribution within the enclosure. The S_8 approximation is used for the angular discretization. The enclosure is discretized uniformly into four quadrilateral elements and sixth order polynomial expansion is used on each element. The dimensionless temperatures distribution along the symmetry line ($y/L=0.5$) are presented in Fig. 7 for three values of Planck number N_{Plk}

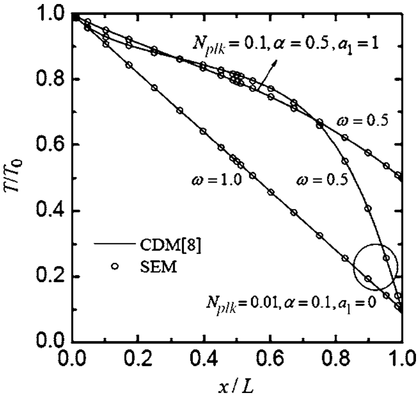

Fig. 5 Dimensionless temperature distributions for different scattering conditions and different values of Planck number

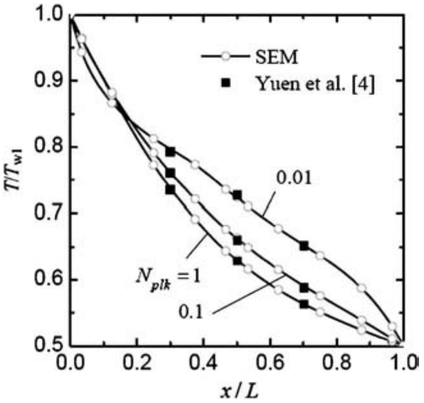

Fig. 7 Dimensionless temperature distribution along the symmetry line ($y/L=0.5$) of the square enclosure

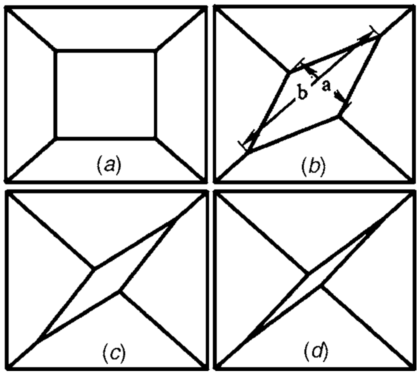

Fig. 8 Skewed meshes with increasing degree of skewness from (*a*) to (*d*)

$=k\beta/(4\sigma T_{w1}^3)$, namely, $N_{\mathrm{Plk}}=0.01$, 0.1, and 1.0, and compared to the results of Yuen and Takara [4]. It can be seen that the results of the SEM agree well with those in reference.

The tolerance for skewed gird of the SEM is tested using this case. The set of skewed mesh with increasing degree of skewness is shown in Fig. 8 from (*a*) to (*d*). As shown in Fig. 8, the degree of skewness s_k is defined as the ratio of the length of diagonal line ($s_k=b/a$) of the center diamond element. By definition, the skewness of the set of meshes from (*a*) to (*b*) is 1.0, 2.6, 5.6, and 11.3, respectively. Here, dimensionless temperature distribution along the symmetry line obtained using the mesh (*a*) of Fig. 8, namely, $s_k=1.0$, which is the least skewed one, with sixth order polynomial expansion on each element is taken as the benchmark solution to verify the results obtained using other meshes. Figure 9 shows the relative deviation between the benchmark solution and those obtained using the skewed meshes. As shown in Fig. 9, the relative deviation increases with the degree of skewness but decreases quickly with the increase of the order of polynomial. This implies that SEM has good property to tolerate the skewed meshes. The ability of tolerance for skewed meshes can be effectively promoted by p refinement. In general, the maximum deviation between these results is less than 0.6%.

3.4 Case 4: Coupled Radiative and Conductive Heat Transfer in a Gray Circular Ring. In this case, the coupled radiative and conductive heat transfer in a circular ring is studied. The configuration of the circular ring is shown in Fig. 10. The radius inner circle (R_1) is half of the radius of the outer circle (R_2). The circular ring is filled with isotropically scattering medium. The wall emissivities of the enclosure are 0.5. The temperature of the inner circle (T_1) and the outer circle (T_2) are kept as 1000 and 100 K, respectively. The optically thickness based on radius of the outer circle is $\tau_L=\beta R_2=2$, and the Planck number is $N_{\mathrm{Plk}}=k\beta/(4\sigma T_1^3)=0.03$. The circular ring is discretized into 60 elements, and S_4 approximation is used for angular discretization. The dimensionless temperature distribution along the radius is solved by the SEM with two different spatial decomposition schemes, namely, a good quality mesh shown in Fig. 10(*a*) and a poor quality mesh shown in Fig. 10(*b*). Figure 11 shows the dimensionless temperature distribution obtained by the SEM for three different scattering albedos, namely, $\omega=0$, 0.5, and 1.0 and compared to the results obtained by Sakami et al. [7] using a

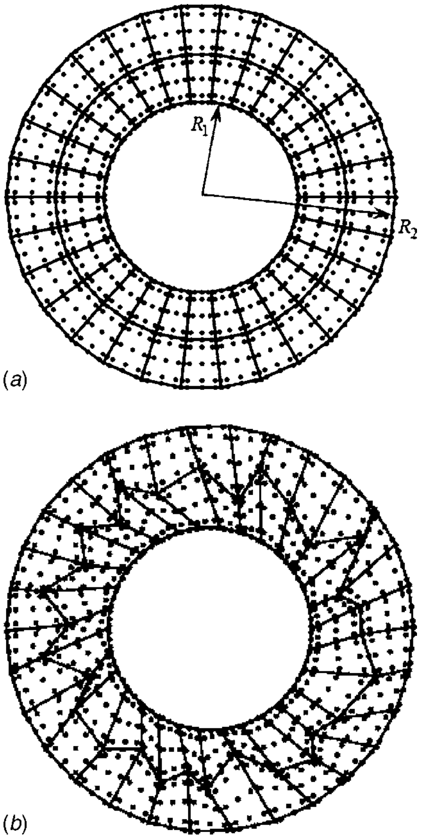

Fig. 10 Configuration and two different mesh decomposition of the circular ring (the dots denotes the spectral nodes of fourth order Chebyshev polynomial expansion): (*a*) good quality mesh (*b*) poor quality mesh

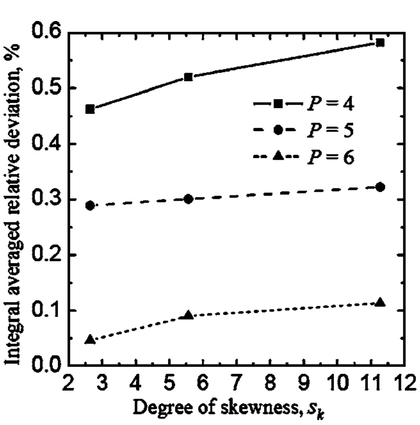

Fig. 9 Relative deviation of the solution from the skewed meshes obtained with different orders of polynomial

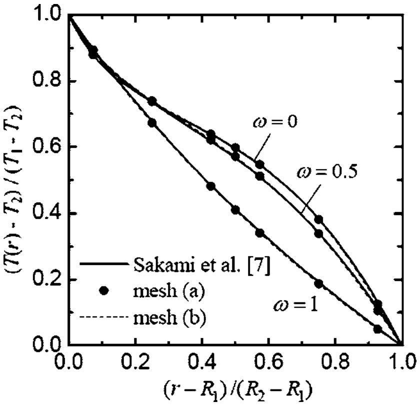

Fig. 11 Dimensionless temperature distributions along the symmetry line of the circular ring for different values of scattering albedo

hybrid DOM and FEM approach. Here, fourth order polynomial expansion is used in each element. By comparison, the results of the SEM using two different mesh schemes agree well with the results of Ref. [7]. The maximum integral averaged relative error is less than 0.5% and the maximum integral averaged relative deviation between the results from the two mesh schemes is less than 0.1%. This demonstrates that the SEM has good accuracy for solving the coupled radiative and conductive heat transfer in semitransparent medium with complex configurations and demands little on the quality of mesh.

4 Conclusions

The highlight of the SORTE is that, it overcomes the nonphysical oscillation of the solutions of RIE when solved by FEM and allows the radiative transfer and the heat diffusion equations to be solved by a unified solver. In this paper, based on the SORTE, a SEM is employed to solve coupled radiative and conductive heat transfer in semitransparent medium, which best combines both the advantages of the SORTE and the spectral element approach. The RTE and the heat diffusion equation are both solved by spectral element approach. The resulting stiff matrices of both the discretized radiative transfer and heat diffusion equations are symmetric. Four various test problems were taken as examples to verify the performance of the presented method. The predicted dimensionless temperature distributions agree well with the benchmark solutions in references. The *h*-convergence and the *p*-convergence characteristics of the SEM are studied. The convergence rate of *p* refinement is very fast for different values of Planck number and follows the exponential law. By comparison, the convergence rate of *p* refinement is superior to that of *h* refinement. The SEM has good property to tolerate skewed meshes and its ability to tolerate skewed meshes can be effectively promoted by *p* refinement. The SEM is very effective to solve coupled radiative and conductive heat transfer in semitransparent medium with complex configurations and demands little on the quality of mesh.

Acknowledgment

The support of this work by the National Natural Science Foundation of China (50425619, 50336010) is gratefully acknowledged.

Nomenclature

a_1 = anisotropy factor
h = element size
$\mathbf{H}$ = matrix defined in Eq. (20*b*)
I = radiative intensity, $\mathrm{W/(m^2\,sr)}$
I_b = Blackbody radiative intensity, $\mathrm{W/(m^2\,sr)}$
k = Thermal conductivity coefficient, W/(Km)
$\mathbf{K}$ = stiff matrix defined in Eq. (20*a*)
L = side length of square enclosure
M = number of discrete ordinate direction
$\mathbf{M}$ = stiff matrix defined in Eq. (22*a*)
$\mathbf{n}$ = unit inward normal vector
$\mathbf{N}$ = right hand side vector defined in Eq. (22*b*)
N_{el} = total number of elements
N_{Plk} = Planck number, $N_{\mathrm{Plk}}=k\beta/(4\sigma T^3)$
N_{sol} = total number of solution nodes
p = order of polynomial expansion
$\mathbf{q}_r$ = radiative heat flux vector
$\bar{q}$ = conductive outflow heat flux at Neumann boundary Γ_q, $\mathrm{W/m^2}$
$\mathbf{r}$ = Spatial coordinate vector
s = degree of element skewness
S = source function defined in Eq. (4)
T = temperature, K
$\bar{T}$ = temperature at the Dirichlet boundary Γ_T, K
V = computational domain
w = weight of discrete ordinate approximation
W = weight function
x,y,z = Cartesian coordinates
β = extinction coefficient $\beta=(\kappa+\sigma_S)$, $\mathrm{m^{-1}}$
ε_w = wall emissivity
ϕ = nodal basis function
Γ = boundary of solution domain
Γ_D = inflow boundary for SORTE
Γ_N = outflow boundary for SORTE
Γ_q = Neumann boundary for heat diffusion equation
Γ_T = Dirichlet boundary for heat diffusion equation
Φ = scattering phase function
μ,η,ξ = direction cosine of radiation direction
κ = absorption coefficient, $\mathrm{m^{-1}}$
σ = Stefan–Boltzmann constant, $\mathrm{W/(m^2K^4)}$
σ_S = Scattering coefficient, $\mathrm{m^{-1}}$
τ_L = optical thickness, $\tau_L=\beta L$
α = temperature ratio, $\alpha=T_L/T_0$
ω = scattering albedo
$\mathbf{\Omega},\mathbf{\Omega}'$ = vector of radiation direction
Ω = solid angle

Subscripts

i,j = spatial node index
w = value at wall
0 = value at $x=0$
L = value at $x=L$

Superscript

m,m' = discrete ordinate direction

References

[1] Viskanta, R., and Grosh, R. J., 1962, "Heat Transfer by Simultaneous Conduction and Radiation in an Absorbing Medium," J. Heat Transfer, **84**, pp. 63–72.
[2] Yuen, W. W., and Wong, L. W., 1980, "Heat Transfer by Conduction and Radiation in a One-Dimensional Absorbing, Emitting and Anisotropically-Scattering Medium," J. Heat Transfer, **102**, pp. 303–307.
[3] Burns, S. P., Howell, J. R., and Klein, D. E., 1995, "Empirical Evaluation of an Important Approximation for Combined-Mode Heat Transfer in a Participating Medium Using the Finite-Element Method," Numer. Heat Transfer, Part B, **27**, pp. 309–322.
[4] Yuen, W. W., and Takara, E. E., 1988, "Analysis of Combined Conductive-Radiative Heat Transfer in a Two-Dimensional Rectangular Enclosure With a Gray Medium," ASME J. Heat Transfer, **110**, pp. 468–474.
[5] Razzaque, M. M., Howell, J. R., and Klein, D. E., 1984, "Coupled Radiative and Conductive Heat Transfer in a Two-Dimensional Rectangular Enclosure With a Gray Participating Media Using Finite Elements," J. Heat Transfer, **106**, pp. 613–619.
[6] Kim, T. Y., and Baek, S. W., 1991, "Analysis of Combined Conductive and Radiative Heat Transfer in a Two-Dimensional Rectangular Enclosure Using the Discrete Ordinates Method," Int. J. Heat Mass Transfer, **34**, pp. 2265–2273.
[7] Sakami, M., Charette, A., and Le Dez, V., 1996, "Application of the Discrete Ordinates Method to Combined Conductive and Radiative Heat Transfer in a Two-Dimensional Complex Geometry," J. Quant. Spectrosc. Radiat. Transf., **56**, pp. 517–533.
[8] Talukdar, P., and Mishra, S. C., 2002, "Analysis of Conduction-Radiation Problem in Absorbing, Emitting and Anisotropically Scattering Media Using the Collapsed Dimension Method," Int. J. Heat Mass Transfer, **45**, pp. 2159–2168.
[9] Mishra, S. C., Lankadasu, A., and Beronov, K. N., 2005, "Application of the Lattice Boltzmann Method for Solving the Energy Equation of a 2-D Transient Conduction-Radiation Problem," Int. J. Heat Mass Transfer, **48**, pp. 3648–3659.
[10] Cheong, K. B., and Song, T. H., 1995, "Examination of Solution Methods for the Second-Order Discrete Ordinate Formulation," Numer. Heat Transfer, Part B, **27**, pp. 155–173.
[11] Fiveland, W. A., and Jessee, J. P., 1994, "Finite Element Formulation of the Discrete-Ordinates Method for Multidimensional Geometries," J. Thermophys. Heat Transfer, **8**, pp. 426–433.
[12] Fiveland, W. A., and Jessee, J. P., 1995, "Comparison of Discrete Ordinates Formulations for Radiative Heat Transfer in Multidimensional Geometries," J. Thermophys. Heat Transfer, **9**, pp. 47–54.
[13] Zhao, J. M., and Liu, L. H., 2007, "Second Order Radiative Transfer Equation and Its Properties of Numerical Solution Using Finite Element Method," Numer. Heat Transfer, Part B, **51**, pp. 391–409.

[14] Patera, A. T., 1984, “A Spectral Element Method for Fluid Dynamics—Laminar Flow in a Channel Expansion,” J. Comput. Phys., **54**, pp. 468–488.
[15] Karniadakis, G. E., and Sherwin, S. J., 1999, *Spectral/hp Element Methods for CFD*, Oxford University Press, New York.
[16] Henderson, R. D., and Karniadakis, G. E., 1995, “Unstructured Spectral Element Methods for Simulation of Turbulent Flows,” J. Comput. Phys., **122**, pp. 191–217.
[17] Hesthaven, J. S., and Gottlieb, D., 1999, “Stable Spectral Methods for Conservation Laws on Triangles With Unstructured Grids,” Comput. Methods Appl. Mech. Eng., **175**, pp. 361–381.
[18] Sherwin, S. J., and Karniadakis, G. E., 1995, “A Triangular Spectral Element Method; Applications to the Incompressible Navier-Stokes Equations,” Comput. Methods Appl. Mech. Eng., **123**, pp. 189–229.
[19] Lee, U., Kim, J., and Leung, A. Y. T., 2000, “The Spectral Element Method in Structural Dynamics,” Shock Vib. Dig., **32**, pp. 451–465.
[20] Giraldo, F. X., 2003, “Strong and Weak Lagrange-Galerkin Spectral Element Methods for the Shallow Water Equations,” Comput. Math. Appl., **45**, pp. 97–121.
[21] Chauvière, C., and Owens, R. G., 2001, “A New Spectral Element Method for the Reliable Computation of Viscoelastic Flow,” Comput. Methods Appl. Mech. Eng., **190**, pp. 3999–4018.
[22] Komatitsch, D., Barnes, C., and Tromp, J., 2000, “Simulation of Anisotropic Wave Propagation Based Upon a Spectral Element Method,” Geophysics, **65**, pp. 1251–1260.
[23] Liu, L. H., 2005, “Meshless Local Petrov-Galerkin Method for Solving Radiative Transfer Equation,” J. Thermophys. Heat Transfer, **20**, pp. 150–154.
[24] Zhao, J. M., and Liu, L. H., 2006, “Least-Squares Spectral Element Method for Radiative Heat Transfer in Semitransparent Media,” Numer. Heat Transfer, Part B, **50**, pp. 473–489.
[25] Nice, M. L., 1983, “Application of Finite Elements to Heat Transfer in a Participating Medium,” *Numerical Properties and Methodologies in Heat Transfer, Proceedings of the Second National Symposium*, Hemisphere, Washington, DC, pp. 497–514.

B. Peng
e-mail: bottlepeng@hotmail.com

Q. W. Wang[1]
e-mail: wangqw@mail.xjtu.edu.cn

State Key Laboratory of Multiphase Flow in
Power Engineering,
Xi'an Jiaotong University,
Shaanxi, Xi'an 710049, China

C. Zhang
Department of Mechanical & Materials
Engineering,
University of Western Ontario,
London, Ontario N6G 5B9, Canada

G. N. Xie

L. Q. Luo

Q. Y. Chen

M. Zeng

State Key Laboratory of Multiphase Flow in
Power Engineering,
Xi'an Jiaotong University,
Shaanxi, Xi'an 710049, China

An Experimental Study of Shell-and-Tube Heat Exchangers With Continuous Helical Baffles

Two shell-and-tube heat exchangers (STHXs) using continuous helical baffles instead of segmental baffles used in conventional STHXs were proposed, designed, and tested in this study. The two proposed STHXs have the same tube bundle but different shell configurations. The flow pattern in the shell side of the heat exchanger with continuous helical baffles was forced to be rotational and helical due to the geometry of the continuous helical baffles, which results in a significant increase in heat transfer coefficient per unit pressure drop in the heat exchanger. Properly designed continuous helical baffles can reduce fouling in the shell side and prevent the flow-induced vibration as well. The performance of the proposed STHXs was studied experimentally in this work. The heat transfer coefficient and pressure drop in the new STHXs were compared with those in the STHX with segmental baffles. The results indicate that the use of continuous helical baffles results in nearly 10% increase in heat transfer coefficient compared with that of conventional segmental baffles for the same shell-side pressure drop. Based on the experimental data, the nondimensional correlations for heat transfer coefficient and pressure drop were developed for the proposed continuous helical baffle heat exchangers with different shell configurations, which might be useful for industrial applications and further study of continuous helical baffle heat exchangers. This paper also presents a simple and feasible method to fabricate continuous helical baffles used for STHXs.

[DOI: 10.1115/1.2754878]

Keywords: *heat transfer, pressure drop, shell-and-tube heat exchanger, continuous helical baffles*

1 Introduction

Heat exchangers are important heat and mass exchange apparatus in oil refining, chemical engineering, environmental protection, electric power generation, et al. Among different types of heat exchangers, shell-and-tube heat exchangers (STHXs) have been commonly used in industries [1]. Master et al. [2] indicated that more than 35–40% of heat exchangers are of the shell and tube type, and this is primarily due to the robust construction geometry as well as easy maintenance and possible upgrades of STHXs. They are widely used as evaporators and condensers. The heat transfer effectiveness of STHXs can be improved by using baffles. Segmental baffles are most commonly used in conventional STHXs to support tubes and change fluid flow direction. Segmental baffles cause the shell-side fluid to flow in a tortuous, zigzag manner across the tube bundles, which can enhance the heat transfer on the shell side. However, there exist many problems associated with the use of segmental baffles [3–5]: (1) high pressure drop on the shell side due to the sudden contraction and expansion of the flow in the shell side, and the fluid impinging on the shell walls caused by segmental baffles; (2) low heat transfer efficiency due to the flow stagnation in the so-called "dead zones," which are located at the corners between baffles and shell wall; (3) low shell-side mass velocity across the tubes due to the leakage between baffles and shell walls caused by inaccuracy in manufacturing tolerance and installation; (4) short operation time due to the vibration caused by shell-side flow normal to tube banks. When the traditional segmental baffles are used in STHXs, higher pumping power is often needed to offset the higher pressure drop under the same heat load. Therefore, it is essential to develop a new type of STHXs using different type of baffles to have higher heat transfer efficiency and lower pressure drop.

The concept of STHXs with helical baffles has been discussed by several researchers [6–12]. The helical baffles in STHXs are shaped approximately as helicoids in order to have the fluid flow in the shell side close to continuous helical flow, which will result in a decrease in pressure drop and an increase in heat transfer in the shell side of the heat exchanger. Productions of STHXs with helical baffles started in 1990s. At present, this type of STHXs is used in many countries, such as USA, Russia, and Japan.

Up to now, nearly all helical baffles used in STHXs are noncontinuous approximate helicoids due to difficulty in manufacturing [13]. Generally, noncontinuous helical baffles are made by four elliptical sector-shaped plates joined end to end. Elliptical sector-shaped plates are arranged in a pseudohelical (noncontinuous helical) baffle system. Each baffle occupies one-quarter of the cross section of the heat exchanger and is angled to the axis of the heat exchanger. The interspace between the two sector plates, as shown in Fig. 1, which is so-called triangle region, leads to great fluid leakage [14]. Therefore, the flow in the shell side is not exactly the perfect helical flow. This will result in a decrease in heat transfer on the shell side of the heat exchanger. Moreover, the fluid flow in the shell side of STHXs becomes more complicated due to the flow leakage in the "triangle region" if noncontinuous helical baffles are used. Block plates can be used to block the flow leakage in this region. However, this will result in difficulty in manufacturing and significant increase in flow resistance. It is clear that the use of continuous helical baffles in STHXs can improve their performance. However, very few research works on STHXs using continuous helical baffles have been reported in

---

[1] Corresponding author.

Contributed by the Heat Transfer Division of ASME for publication in the JOURNAL OF HEAT TRANSFER. Manuscript received May 9, 2006; final manuscript received January 23, 2007. Review conducted by Anthony M. Jacobi.

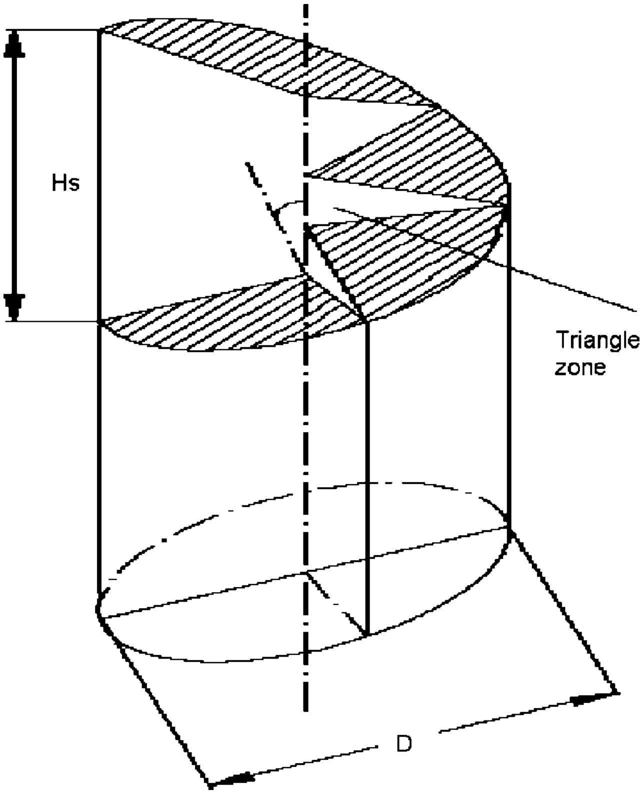

Fig. 1 Sketch of the STHX with noncontinuous helical baffles

open literature. Therefore, the objectives of this study are to develop STHXs with continuous helical baffles and to investigate their performance.

In this work, (1) two different STHXs with continuous helical baffles were designed and tested, (2) a simple and feasible method to fabricate continuous helical baffles used for STHXs was developed, (3) the heat transfer coefficients per pressure drop of the STHXs with continuous helical baffles were compared with those of the STHXs with segmental baffles, and (4) the correlations of Nusselt number and friction factor versus Reynolds number were established.

2 Configuration and Fabrication of the New STHX With Continuous Helical Baffles

Figure 2 shows the sketch of the tube bundle of the STHX where continuous helical baffles were used to have helical flow on the shell side of the heat exchanger. The method proposed in this study to fabricate continuous helical baffles used in STHXs is called the subsection method. In this method, the continuous helicoid was manufactured by linking several sets of helical cycles. One helical cycle was heightened to one screw pitch along the height (axial) direction and was rotated to 2π angle along the circumferential direction, as shown in Fig. 3. Several helical cycles were linked end to end to form a continuous helicoid, as shown in Fig. 2. This method overcame the difficulty in manufacturing a whole continuous helicoid at one time and lowered the manufacture cost significantly.

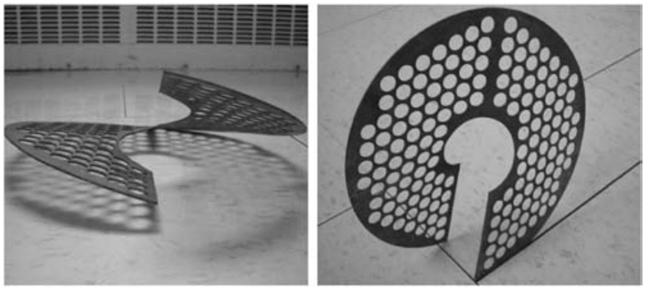

Fig. 3 One helical cycle

One major difficulty related to the manufacturing of continuous helical baffles is the drilling of holes on the baffles. If baffles are drilled the same size holes as the tubes and then later the pitch is varied by stretching the spiral in or out, the tube does not see a round hole but rather an elliptic hole. Then it is impossible to pass a round tube through an elliptic hole. Therefore, a die, as shown in Fig. 4, is used to hold the helical cycle at the required pitch, and then drill holes on the baffles.

Figure 5 shows the tube bundle of the newly designed STHX with continuous helical baffles. Since the configuration of the shell of the heat exchanger also plays a major role on the flow pattern of the shell-side flow in the heat exchanger, it is necessary to investigate the effect of the configuration of the shell of the heat exchanger on the heat transfer coefficient and pressure drop. In this study, two different shell configurations were proposed and tested. The first one is the side-in-side-out model, as shown in Fig. 6(*a*), where the shell-side fluid flows into the heat exchanger from one side on one end and exits from the other side on the other end

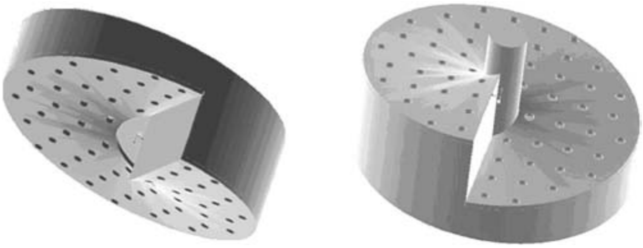

Fig. 4 Dies for drilling

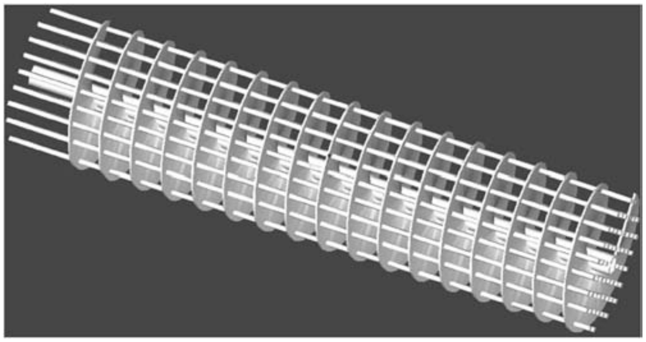

Fig. 2 Sketch of the tube bundle of the STHX with continuous helical baffles

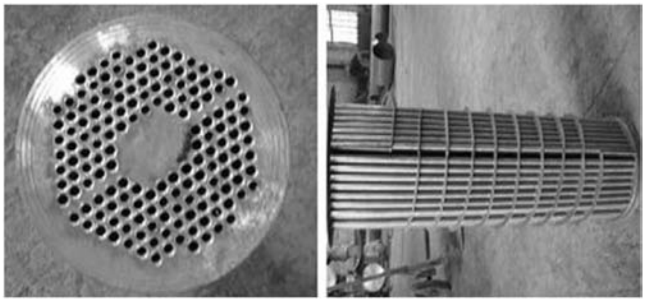

Fig. 5 Tube bundle of the STHX with continuous helical baffles (for CS and CM): (*a*) end view and (*b*) side view

Fig. 6 Shell configurations of the STHXs: (*a*) Side-in-side-out shell for CS and (*b*) middle-in-middle-out shell for CM and SM

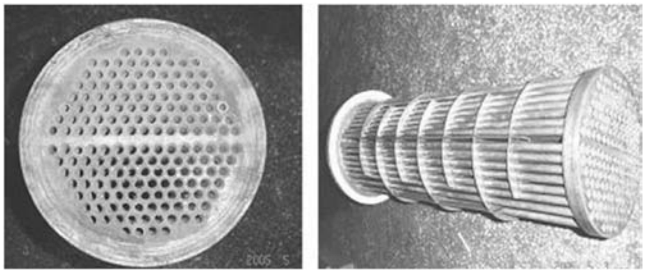

Fig. 7 Tube bundle of the STHX with segmental baffles (for SM): (*a*) end view and (*b*) side view

Table 1 Common geometrical parameters for CS, CM, and SM

Parameter	
Inner diameter of shell	207 mm
Outer diameter of tubes	10 mm
Inner diameter of tubes	8 mm
Arrangement of tubes	Triangle
Effective length of tubes	620 mm
Outer diameter of inlet tube for the tube-side fluid	57 mm
Inner diameter of inlet tube for the tube-side fluid	50 mm
Outer diameter of outlet tube for the tube-side fluid	57 mm
Inner diameter of outlet tube for the tube-side fluid	50 mm
Outer diameter of inlet tube for the shell-side fluid	57 mm
Inner diameter of inlet tube for the shell-side fluid	50 mm
Outer diameter of outlet tube for the shell-side fluid	57 mm
Inner diameter of outlet tube for the shell-side fluid	50 mm
Length of heat exchanger	670 mm

Table 2 Other geometrical parameters for CS, CM, and SM

Heat exchanger	Helical pitch (mm)	Number of baffles	Number of tubes	Diameter of center tube (mm)
CS and CM	48	9	158	48
SM	70	7	176	No center tube

of the heat exchanger. The second one is the middle-in-middle-out model, as shown in Fig. 6(*b*), where the shell-side fluid enters the heat exchanger from the middle on one end and exits from the middle on the other end of the heat exchanger. For the comparison purpose, the STHX with segmental baffles, as shown in Fig. 7, whose shell configuration is the middle-in-middle-out arrangement, was also tested.

For the convenience of discussion, hereinafter, CS refers to the STHX with continuous helical baffles and side-in-side-out shell configuration, CM refers to the STHX with continuous helical baffles and middle-in-middle-out shell configuration, and SM refers to the conventional STHX with segmental baffles and middle-in-middle-out shell configuration. The geometrical parameters of those three heat exchangers are listed in Tables 1 and 2.

3 Experiment

3.1 Experiment Setup. An experiment apparatus was designed and built to study the heat transfer and pressure drop of a STHX. The experiment setup consists of four loops: oil loop, hot water loop, cold water loop, and cooling water loop, as shown in Fig. 8. Tests can be performed for oil-water or water-water heat exchangers. The detailed descriptions of the four loops are given below.

(a) Oil loop. The oil needs to be filtered before the experiment. Therefore, the oil loop contains a filtering loop (not shown in Fig. 8). The heated oil flows from the oil tank (24) into a turbine flowmeter (29), then enters the shell side of the heat exchanger (41) to be tested, and finally returns to the oil tank (24). The pressure was measured by pressure transducers installed at the inlet and outlet of the test section. The heater (25) is an electrical heater with a maximum power of 64 kW. The power input to the heater can be adjusted by a booster. The expansion box (35) is used to prevent pressure builtup in the oil tank. Thermocouples (31-a and 31-b) were installed at the inlet and outlet of the shell side of the test heat exchanger to measure the corresponding temperatures.

(b) Hot water loop. It is similar to the oil loop, but it was not used in this study.

(c) Cold water loop. Cold water flows from the cold water

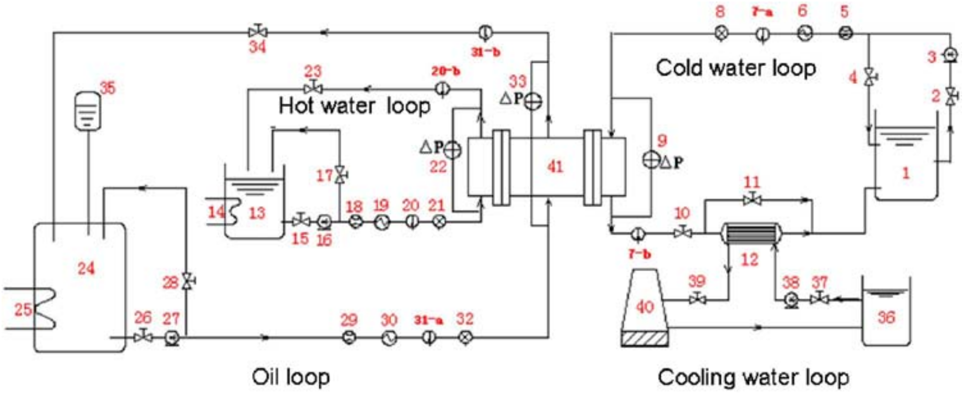

Fig. 8 Experiment setup

tank (1) into a turbine flowmeter (5), then flows through the tube side of the test heat exchanger (41), then flows into the cooling heat exchanger (12), and finally returns to the cold water tank (1). Thermocouples (7-a and 7-b) were installed at the inlet and outlet of the tube side of the test heat exchanger to measure the corresponding temperatures.

(d) Cooling water loop. Cooling water flows from the cooling water tank (36) into the cooling heat exchanger (12), then flows into a cooling tower (40), and finally returns to the cooling water tank (36).

Before testing a heat exchanger, hydraulic pressure tests were performed under 0.6 MPa in the shell side and tube side of the heat exchanger, respectively.

3.2 Data Acquisition. In the experiments, flow rate, temperature, and pressure drop were measured and collected by a data acquisition system. The energy imbalance between the shell side and tube side, which was obtained from the data on the flow rates, and inlet and outlet temperatures of oil and water, was monitored during the experiments and the experimental data were saved and processed when the energy imbalance is less than 8%. Based on the energy balance between the shell side and tube side, the overall heat transfer coefficient of the heat exchanger can be calculated, and then the heat transfer coefficient of the shell side can be obtained using the revised Wilson plot technique described in Ref. [15]. Finally, the correlations between the friction factor (f) and Reynolds number (Re), and Nusselt number (Nu) and Re can be obtained. f, Re, and Nu are defined as follows:

$$f = \frac{\Delta p_o}{(1/2)\rho u^2}\frac{d_o}{l} \tag{1}$$

$$\mathrm{Re} = \frac{u d_o}{\nu} \tag{2}$$

$$\mathrm{Nu} = \frac{h d_o}{\lambda} \tag{3}$$

where Δp_o is the overall pressure drop on the shell side of the heat exchanger, ρ is the density of the oil, l is the effective length of tubes, d_o is the outer diameter of the tube, h is the heat transfer coefficient on the shell side of the STHX, ν is the kinematic viscosity of the oil, λ is the thermal conductivity of the oil, and u is the average velocity based on the characteristic cross-section area A, and it is given as

$$u = \frac{\dot{m}}{\rho A} \tag{4}$$

where $\dot{m}$ is the mass flow rate of the oil and A is the characteristic cross-section area of the STHX. For the STHX with continuous helical baffles and the STHX with segmental helical baffles, the characteristic cross-section areas, A_c and A_s, are given as

$$A_c = \frac{1}{2}\left(1 - \frac{d_{\mathrm{ct}}}{d_{\mathrm{si}}}\right) B d_{\mathrm{si}}\left(1 - \frac{d_o}{S}\right) \tag{5}$$

$$A_s = B d_{\mathrm{si}}\left(1 - \frac{d_o}{S}\right) \tag{6}$$

where B is the helical pitch, which is the distance between the two adjacent baffles, d_{si} is the inner diameter of the shell, d_{ct} is the outer diameter of the central tube, and S is the pitch between the two adjacent tubes, as shown in Fig. 9.

4 Results and Discussion

The experiments were conducted for the three heat exchangers described in Sec. 2, in which cold water flowed in the tube side and hot oil flowed in the shell side of the heat exchangers. Heat was transferred from hot oil to cold water, and the heat from the cold water was carried away by the cooling water.

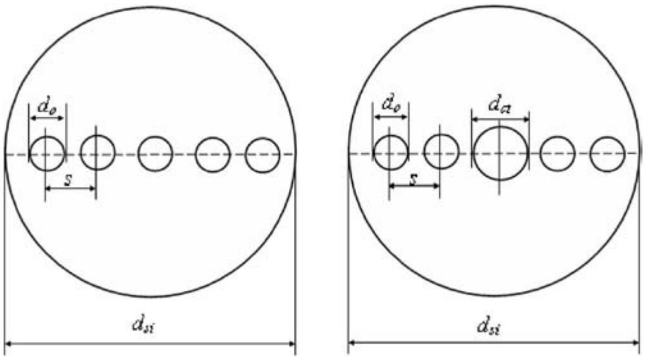

Fig. 9 Illustration of geometric parameters: (*a*) STHX with segmental baffles and (*b*) STHX with helical baffles

4.1 Heat Transfer and Pressure Drop. The variation of the overall pressure drop (Δp_o) with the volumetric flow rate (Q) in the shell side of the heat exchanger is shown in Fig. 10 for the proposed heat exchangers with helical baffles. From Fig. 10, it can be seen that the pressure drop increases with the increase in Q and the difference in the pressure drop between these two heat exchangers for the same volumetric flow rate is very small. The variation of the heat transfer coefficient in the shell side of the heat exchanger (h) with the overall pressure drop (Δp_o) is shown in Fig. 11 for the three heat exchangers to compare their performances. The results indicate that in the low overall pressure drop region, the heat transfer coefficient increases significantly with the increase in the overall pressure drop, while in the high pressure drop region, this increase becomes smaller. For the same overall pressure drop, the difference in the shell-side heat transfer coefficient for all three heat exchangers is very small in the low pressure drop region; however, in the high pressure drop region, the shell-side heat transfer coefficients in CS and CM are higher than that in SM at the same overall pressure drop. The heat transfer coefficient in CS is higher and increases faster with the increase in pressure drop than that in CM. The heat transfer coefficient of the heat exchanger with the side-in-side-out shell design (CS) is about 2% higher than that with the middle-in-middle-out shell design (CM), especially at a high shell-side fluid flow rate. The heat

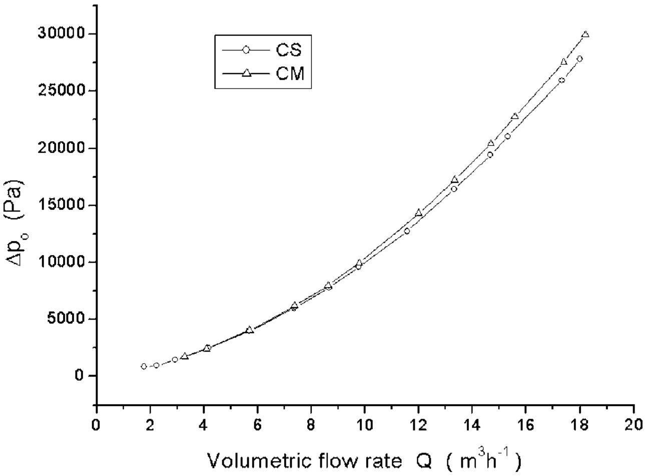

Fig. 10 Overall pressure drop versus volumetric flow rate for helical exchangers

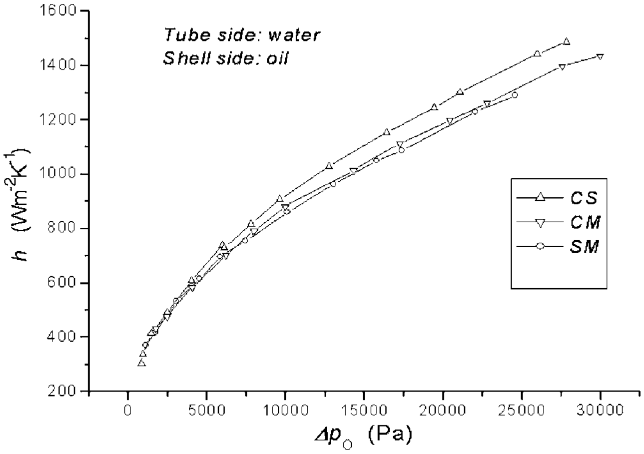

Fig. 11 Heat transfer coefficient versus overall pressure drop

transfer coefficient of the continuous helical heat exchanger with side-in-side-out shell design (CS) is nearly 10% higher than that of the segmental heat exchanger (SM).

The difference in heat transfer coefficients per unit overall pressure drop among those three heat exchangers is due to the different fluid flow patterns in the shell side of the heat exchanger. The flow in the shell side of the heat exchanger with conventional segmental baffles has dead zones because the fluid impacts right onto the wall perpendicularly. The flow in the shell side of the heat exchanger with continuous helical baffles is smooth, rotational, and helical due to the shape of the baffle, which results in an obvious increase in heat transfer coefficient per pressure drop in the heat exchanger. The difference in the shell-side heat transfer coefficients between CS and CM is caused by the difference in the design of the heat exchanger shell. Two reasons account for why the performance of CS is better than that of CM. First, the side-in-side-out design is more effective in forcing the fluid to flow in a helical passage, hence resulting in a higher local heat transfer coefficient. Second, the middle-in-middle-out design causes the fluid to impinge perpendicularly to the shell wall, hence resulting in higher local pressure drop.

4.2 Correlations for Friction Factor and Nusselt Number. The experimental data on the pressure drops under different oil flow rates in the shell side of the heat exchangers were used to obtain the correlation between the friction factor and Reynolds number. The variations of the friction factor f with Reynolds number Re are shown in Figs. 12–14 for CS, CM, and SM, respectively. The data shown in Figs. 12–14 were used to curve fit the correlation between the friction factor and Reynolds number:

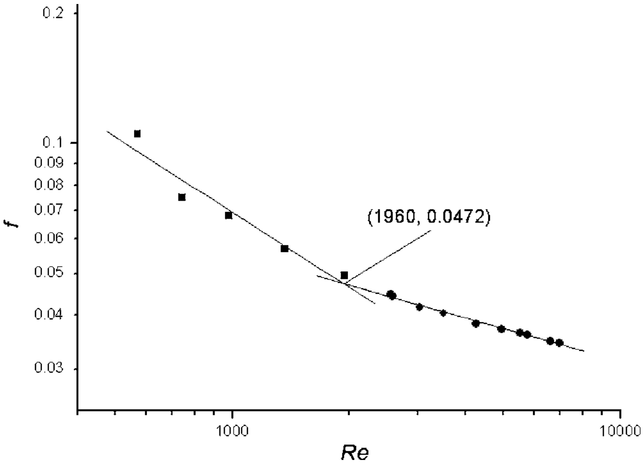

Fig. 12 Friction factor versus Reynolds number for CS

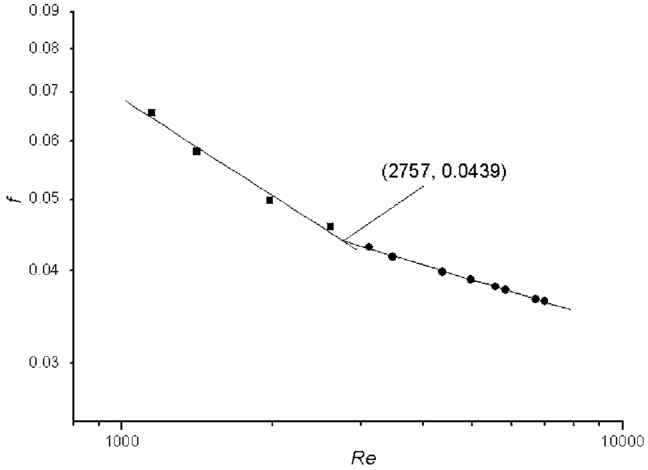

Fig. 13 Friction factor versus Reynolds number for CM

$$f = C_1 \, \mathrm{Re}^{m_1} \tag{7}$$

The constants C_1 and m_1 for different ranges of Reynolds numbers are listed in Table 3.

The experimental data on the heat transfer coefficients under different oil flow rates in the shell side were used to curve fit the correlation between Nusselt number Nu and Reynolds number Re:

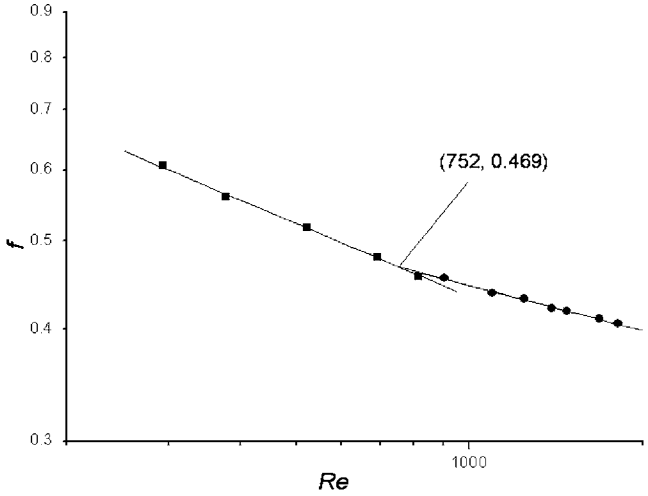

Fig. 14 Friction factor versus Reynolds number for SM

Table 3 Constants in the friction factor correlation (root-mean-square deviation)

Heat exchanger	C_1	m_1	RMSD (%)	Range of Reynolds number
CS	3.76	−0.578	3.12	≤1960
	0.316	−0.251	0.48	>1960
CM	1.40	−0.437	0.80	≤2757
	0.226	−0.206	0.10	>2757
SM	2.79	−0.269	0.10	≤752
	1.41	−0.167	0.35	>752

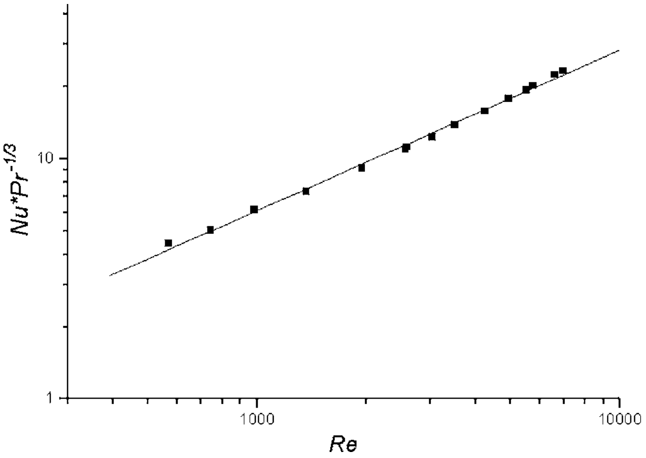

Fig. 15 Nusselt number versus Reynolds number for CS

$$\mathrm{Nu} = C_2\,\mathrm{Re}^{m_2}\,\mathrm{Pr}^{1/3} \tag{8}$$

where Pr is the Prandtl number. The variations of $\mathrm{NuPr}^{-1/3}$ versus Re are given in Figs. 15–17. The corresponding constants C_2 and m_2 in Eq. (8) are given in Table 4.

4.3 Uncertainty Analysis. The uncertainty of the experimental measurements is calculated based on the combination of the bias error limit B and precision error limit P,

$$W = \sqrt{B^2 + P^2} \tag{9}$$

The precision error limit, which can be determined by statistical method, is related to the standard deviation of the measurements. The standard deviation of a variable R, S_R, is given as

$$S_R = \sqrt{\frac{\sum_{i=1}^{n}(R_i - \bar{R})^2}{n-1}} \tag{10}$$

The standard deviation of the mean $\bar{R}$ is related to the standard deviation of R by [16]

$$S_{\bar{R}} = \frac{S_R}{\sqrt{n}} \tag{11}$$

The precision error limit in the mean value can be determined by [16]

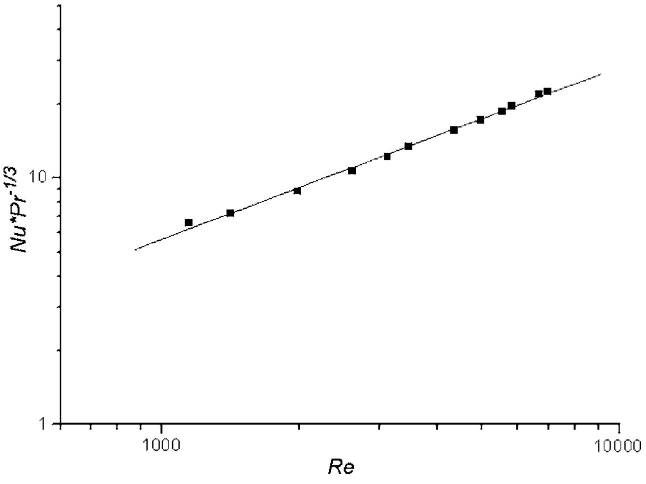

Fig. 16 Nusselt number versus Reynolds number for CM

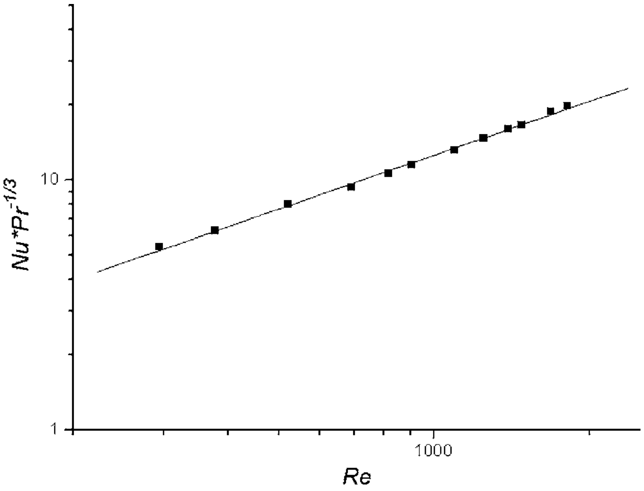

Fig. 17 Nusselt number versus Reynolds number for SM

$$P = tS_{\bar{R}} \tag{12}$$

where t is a function of the confidence level and the degrees of freedom. At a 95% confidence level with a large number of samples (over 30), t=2.0 [16]. The number of samples taken in this experiment is 60. Therefore, the value of t is taken as 2.0. However, the precision error limit for temperature P_T is very small compared to the bias error limit B_T for large number of samples, fast data collection, and good uniformity of the data. Therefore, the uncertainty of the experimental measurements, W_T is dominated by the bias error limit B_T. The accuracy of the measurement system supplied by the manufacturer is used to calculate the bias error limit.

Given a variable R, which is a function of n independent variables $x_1, x_2 \ldots, x_n$,

$$R = f(x_1, x_2, \ldots, x_n) \tag{13}$$

The absolute uncertainty of R can be determined as [16]

$$W_R = \sqrt{\left(\frac{\partial R}{\partial x_1}W_{x_1}\right)^2 + \left(\frac{\partial R}{\partial x_2}W_{x_2}\right)^2 + \cdots + \left(\frac{\partial R}{\partial x_n}W_{x_n}\right)^2} \tag{14}$$

where $W_{x1}, W_{x2} \ldots, W_{xn}$ are the absolute uncertainties of $x_1, x_2 \ldots, x_n$.

Typical uncertainty of the shell-side heat transfer coefficient is about 15.64 W/m^2 K. The maximum and minimum uncertainties for the pressure drop are 155.9 and 190 Pa, respectively.

5 Conclusions

The performance of the proposed STHX with continuous helical baffles has been experimentally investigated in terms of its heat transfer coefficient and pressure drop. The conclusions can be summarized as follows.

(1) Under the same overall pressure drop, the shell-side heat transfer coefficients of heat exchangers with continuous helical baffles (CS and CM) are higher than that of the heat exchanger with segmental baffles (SM), and the heat transfer coefficient of the heat exchanger with the side-in-side-

Table 4 Constants in the Nusselt number correlation

Heat exchanger	C_2	m_2	RMSD (%)
CS	0.0599	0.669	0.20
CM	0.0451	0.699	0.18
SM	0.0889	0.717	0.14

out shell design (CS) is about 2% higher than that with the middle-in-middle-out shell design (CM), especially at a high shell-side fluid flow rate. The heat transfer coefficient of the continuous helical heat exchanger with side-in-side-out shell design (CS) is nearly 10% higher than that of the segmental heat exchanger (SM).

(2) The correlations between Nusselt number and Reynolds number, and friction factor and Reynolds number were developed, with the root-mean-square deviation less than 3.12%.

Acknowledgment

This work was supported by the NSFC Fund for Creative Research Groups (Grant No. 50521604).

Nomenclature

A = area, m^2
A_c = minimum free flow area for the exchanger with continuous helical baffles, m^2
A_s = minimum free flow area for the exchanger with segmental baffles, m^2
B = pitch of baffles, m
B = bias error limit
CS = continuous helical exchanger with side-in-side-out design
CM = continuous helical exchanger with middle-in-middle-out design
C_1, C_2 = constants
d_i = inner diameter of the tube, m
d_o = outer diameter of the tube, m
d_{si} = inner diameter of the shell, m
d_{ct} = diameter of center tube, m
f = friction factor
h = heat transfer coefficient of the STHX, $\mathrm{W/(m^2\,K)}$
l = effective length of the tube, m
$\dot{m}$ = mass flow rate, kg/s
m_1, m_2 = constants
Nu = Nusselt number
P = precision error limit
Pr = Prandtl number
Q = volumetric flow rate, $\mathrm{m^3/s}$
Re = Reynolds number
S = distance between two centers of tubes, m
S_R = standard deviation of a variable R
SM = segmental exchanger with middle-in-middle-out design
t = confidence level
u = characteristic velocity (maximum velocity at minimum free flow area), m/s
W = uncertainty of the experimental measurements

Greek Symbols

ρ = fluid density, $\mathrm{kg/m^3}$
λ = thermal conductivity, W/(mK)
ν = kinematic viscosity, Pa s
Δp_o = overall pressure drop on the shell-side of the exchanger, Pa

Subscripts

c = continuous helical exchanger
s = segmental exchanger

References

[1] Gulyani, B. B., 2000, "Estimating Number of Shells in Shell and Tube Heat Exchangers: A New Approach Based on Temperature Cross," ASME J. Heat Transfer, **122**, pp. 566–571.
[2] Master, B. I., Chunangad, K. S., and Pushpanathan, V., 2003, "Fouling Mitigation Using Helixchanger Heat Exchangers," *Proceedings of the ECI Conference on Heat Exchanger Fouling and Cleaning: Fundamentals and Applications*, Santa Fe, NM, May 18–22, pp. 317–322.
[3] Li, H. D., and Kottke, V., 1998, "Visualization and Determination of Local Heat Transfer Coefficients in Shell-and-Tube Heat Exchangers for Staggered Tube Arrangement by Mass Transfer Measurements," Exp. Therm. Fluid Sci., **17**(3), pp. 210–216.
[4] Reppich, M., and Zagermann, S., 1995, "A New Design Method for Segmentally Baffled Heat Exchangers," Comput. Chem. Eng., **19**, pp. 137–142.
[5] Li, H. D., and Kottke, V., 1998, "Effect of the Leakage on Pressure Drop and Local Heat Transfer in Shell-and Tube Heat Exchangers for Staggered Tube Arrangement," Int. J. Heat Mass Transfer, **41**(2), pp. 425–433.
[6] Doug, S., and Van der Ploeg, H. J., 1997, "Compact Exchanger to Reduce Refinery Fouling," PTQ Autumn, pp. 88–90.
[7] Naim, A., and Bar-Cohen, A., 1996, *New Developments in Heat Exchangers*, Gordon and Breach, Amsterdam, pp. 467–499.
[8] Van der Ploeg, H. J., and Master, B. I., 1997, "A New Shell-and-Tube Option for Refineries," PTQ Autumn, pp. 91–95.
[9] Kral, D., Stelik, P., Van der Ploeg, H. J., and Master, B. I., 1996, "Helical Baffles in Shell-and-Tube Heat Exchangers, Part One: Experimental Verification," Heat Transfer Eng., **17**(1), pp. 93–101.
[10] Stehlik, P., Nemcansky, J., and Kral, D., 1994, "Comparison of Correction Factors for Shell-and-Tube Heat Exchangers With Segmental or Helical Baffles," Heat Transfer Eng. **15**(1), pp. 55–65.
[11] Pekdemir, T., Davies, T. W., Haseler, L. E., and Diaper, A. D., 1994, "Pressure Drop Measurements on the Shell Side of a Cylindrical Shell-and-Tube Heat Exchanger," Heat Transfer Eng., **15**(3), pp. 42–55.
[12] Lutcha, J., and Nemcansky, J., 1990, "Performance Improvement of Tubular Heat Exchangers by Helical Baffles," Chem. Eng. Res. Des., **68**(1), pp. 263–270.
[13] Wang, Q. W., 2004, "Current Status and Development of Shell-Side Heat Transfer Enhancement of Shell-and-Tube Heat Exchangers With Helical Baffles," Journal of Xi'an Jiaotong University, **38**(9), pp. 1–6 (in Chinese).
[14] Zhang, D. J., Wang, Q. W., Zeng, M., and Luo, L. Q., 2005, "Numerical Simulation of Flow Performance in Shell Side of Shell-and-Tube Heat Exchanger With Discontinuous Helical Baffles," 2005, *Proceedings of the Second International Symposium on Thermal Science and Technology*, Beijing, Oct. 23–25, pp. 181–185.
[15] Zhang, Z., Yu, Z., and Fang, X., 2007, "An Experimental Heat Transfer Study for Helically Flowing Outside Petal-Shaped Finned Tubes With Different Geometrical Parameters," Appl. Therm. Eng. **27**(1), pp. 268–272.
[16] Wheeler, A. J., and Ganji, A. R., 2004, *Introduction to Engineering*, 2nd ed., Prentice-Hall, Englewood Cliffs, NJ.

Experimental and Numerical Study of a Stacked Microchannel Heat Sink for Liquid Cooling of Microelectronic Devices

Xiaojin Wei
IBM,
2070 Route 52,
Hopewell Junction, NY 12533
e-mail: xwei@us.ibm.com

Yogendra Joshi
Georgia Institute of Technology,
771 Ferst Drive,
Atlanta, GA 30332
e-mail: yogendra.joshi@me.gatech.edu

Michael K. Patterson
Intel Corporation,
JF1-231,
2111 NE 25th Avenue,
Hillsboro, OR 97124
e-mail: michael.k.patterson@intel.com

One of the promising liquid cooling techniques for microelectronics is attaching a microchannel heat sink to, or directly fabricating microchannels on, the inactive side of the chip. A stacked microchannel heat sink integrates many layers of microchannels and manifold layers into one stack. Compared with single-layered microchannels, stacked microchannels provide larger flow passages, so that for a fixed heat load the required pressure drop is significantly reduced. Better temperature uniformity can be achieved by arranging counterflow in adjacent microchannel layers. The dedicated manifolds help to distribute coolant uniformly to microchannels. In the present work, a stacked microchannel heat sink is fabricated using silicon micromachining techniques. Thermal performance of the stacked microchannel heat sink is characterized through experimental measurements and numerical simulations. Effects of coolant flow direction, flow rate allocation among layers, and nonuniform heating are studied. Wall temperature profiles are measured using an array of nine platinum thin-film resistive temperature detectors deposited simultaneously with thin-film platinum heaters on the backside of the stacked structure. Excellent overall cooling performance ($0.09\,^\circ\mathrm{C/W\,cm^2}$) *for the stacked microchannel heat sink has been shown in the experiments. It has also been identified that over the tested flow rate range, counterflow arrangement provides better temperature uniformity, while parallel flow has the best performance in reducing the peak temperature. Conjugate heat transfer effects for stacked microchannels for different flow conditions are investigated through numerical simulations. Based on the results, some general design guidelines for stacked microchannel heat sinks are provided.*

[DOI: 10.1115/1.2754781]

Keywords: conjugate heat transfer, thermal management, microelectronics, micro-fabrication, microchannel, liquid cooling

1 Introduction

Heat removal has become one of the key design challenges for microelectronics as the total thermal design power (TDP), the local heat flux, and volumetric heat generation rates keep increasing. Extensive efforts have been made to extend the widely used air-cooling technology for high power microprocessors through optimized chip design and layout, development of advanced package materials, and optimized heat sink and air-flow configurations [1,2]. However, it is generally agreed that current air-cooling technology is approaching limits imposed by available cooling area, heat sink and fan sizes, and acoustic noise [3–5]. Advanced liquid cooling technologies employing single-phase or two-phase implementation, such as jet impingement [4,6], evaporative spray [7–9], thermosyphon [3,10], and microchannel cooling [11–15], emerge as alternatives to meet the thermal design challenges.

For single-phase flow in microchannels, cooling capability enhancement is a result of reduced thermal boundary layer thickness and increased heat transfer area to volume ratio. For hydrodynamically and thermally developed laminar duct flow, the heat transfer coefficient is inversely proportional to the hydraulic diameter. As a result, microchannels feature heat transfer coefficients that are orders of magnitude higher than those of macrochannels. This was first demonstrated by Tuckerman [11], where a heat sink, consisting of an array of parallel microchannels, was shown to have a thermal resistance as low as $9\times10^{-6}\ \mathrm{K/W\,m^2}$ for a pumping power of 1.84 W. In a comparative investigation of jet impingement and microchannel cooling, Lee and Vafai [16] reported that for small heat source surfaces, microchannel cooling performs better than jet impingement cooling even if proper treatment is applied for the spent flow after impingement, based on the optimized configuration for both techniques under practical constraints of pressure drop and flow rate.

Successful design of microchannel heat sinks relies on understanding the fundamental characteristics of the flow and heat transfer inside microchannels. Following Tuckerman and Pease's work [11], many efforts have been dedicated to investigate the friction and heat transfer characteristics of microchannels. Several studies [17–25] indicated that these two parameters deviate from the classical theory developed for macrosize channels and the transition from laminar to turbulent flow occurs at a considerably smaller critical Reynolds number. However, there is no consensus on the trend of this deviation among different researchers. For instance, Wu and Little [17] performed tests for flow of gas in trapezoidal microchannels and found the friction factor for laminar flow in microchannel to be generally larger than predicted by the Moody diagram and to be affected by surface roughness. Pfahler et al. [18], however, found the friction factor for microchannels to be smaller than predicted by laminar theory. The reported deviations were attributed to sources, such as microrotational effects of the molecules (Papautsky et al. [21]), flow

---

Contributed by the Heat Transfer Division of ASME for publication in the Journal of Heat Transfer. Manuscript received April 11, 2006; final manuscript received February 23, 2007. Review conducted by Ben Q. Li. Paper presented at the 2004 ASME International Mechanical Engineering Congress (IMECE2004), Anaheim, CA, Nov. 13–19, 2004.

maldistribution in the manifolds (Harms et al. [22]), surface roughness (Mala and Li [23]), electric double layer (Mala et al. [24]), and viscous heating (Tso and Mahulikar [25]).

In contrast, Xu et al. [26] reported that flow characteristics in microchannels with hydraulic diameter of 30–344 μm at Reynolds numbers of 20–4000 agree with predictions based on the Navier–Stokes equations. Qu and Mudawar [27] found good agreement between experiments and numerical simulations based on conventional Navier–Stokes equation for microchannels 231 μm wide and 713 μm deep over Reynolds number range of 139–1672. Liu and Garimella [28] showed that conventional correlations offer reliable predictions for laminar flow characteristics in microchannels over a hydraulic diameter range of 244–974 μm. Recently, Lee and Garimella [29] investigated heat transfer in microchannels made in copper for a Reynolds number range of 300–3500. The widths of the studied channels ranged from 194 to 534 μm, while the depths are five times the widths. In deducing the average Nusselt number, an average wall temperature based on a one-dimensional conduction model was used. For laminar flow, the measured Nusselt number agrees with predictions for thermally developing flow over the entire length of the channel. Kohl et al. [30] developed integrated pressure sensors to measure axial pressure distribution inside a single microchannel for water flow in the range of $4.9 < \mathrm{Re} < 2068$. It was observed that pressure drop for microchannels as small as 24.9 μm in hydraulic diameter can be well predicted by analytical results based on the laminar theory for large channel size. Collectively, these recent works appear to indicate that the pressure drop and transport characteristics for macroscale channels also hold for the microchannels intended for microelectronics cooling.

Analyses have also been conducted for better understanding of the conjugate heat transfer and the effects of several parameters. Phillips [31] provided an analytical model to estimate the thermal resistance of the microchannel heat sink. Weisberg and Bau [32] analyzed a microchannel heat exchanger by numerical simulation of heat transfer in the fluid and the solid substrate. Several assumptions made in the previous research were reexamined by Fedorov and Viskanta [33] who conducted a detailed analysis of the three-dimensional conjugate heat transfer inside microchannels. It was concluded that the temperature gradient near the inlet region is extremely large due to the rapid growth of thermal boundary layer. Vafai and Zhu [34] numerically investigated a two-layered microchannel heat sink with counterflow arrangement. It was found that counterflow arrangement reduces the temperature gradient dramatically compared with single-layered microchannel for the flow condition of $\mathrm{Re}=143.6$. Koo et al. [35] evaluated the thermal performance of a three-dimensional microchannel network for cooling of three-dimensional circuits based on a one-dimensional boiling model. It is predicted that one layer of the microchannel network can remove heat density up to 135 $\mathrm{W/cm^2}$ while maintaining junction temperature within 85°C.

Despite the extensive research in characterizing the flow and heat transfer transport inside microchannels, several issues need to be addressed in order to implement microchannel cooling for microelectronics. Firstly, the pressure drop due to flow friction in a microchannel increases dramatically when the channel size shrinks. To address this issue, manifold microchannel heat sinks were proposed by Harpole and Eninger [36] and numerically studied by Copeland et al. [37]. Compared with a conventional microchannel heat sink, manifold microchannel heat sink features many inlet and outlet manifolds, alternating at a periodic distance along the length of the microchannels. For a fixed overall flow rate, pressure drop for manifold microchannel is significantly smaller. However, there are some concerns about the complexity of the design and fabrication. Another issue, associated with any single-phase cooling technique, is the surface temperature nonuniformity. Along the flow direction, the coolant temperature rises as a result of the heat input. At the same time, the heat transfer coefficients decrease along the flow direction due to the growing boundary layer thickness. In an optimization study, Bau [38] found that reducing the cross-sectional area along the flow direction could dramatically reduce temperature nonuniformity; however, because of flow acceleration, the pressure drop increases considerably. In the numerical work reported by Vafai and Zhu [34], counterflow arrangement was found to reduce temperature gradient dramatically for one flow condition. Fluid distribution into and out of microchannels is another challenge, due to the very limited space. Manifold design is important not only for single-phase microchannel flow but also for two-phase flow inside microchannels, as indicated by Hrnjak [39]. Webb [40] numerically studied the flow distribution in parallel microchannels. It was revealed for the condition studied that the maximum flow rate ratio between parallel channels was 6.5:1 for $\mathrm{Re}=245$ if a parallel manifold is used. This indicates that severe nonuniformity can happen without proper manifold design for microchannels.

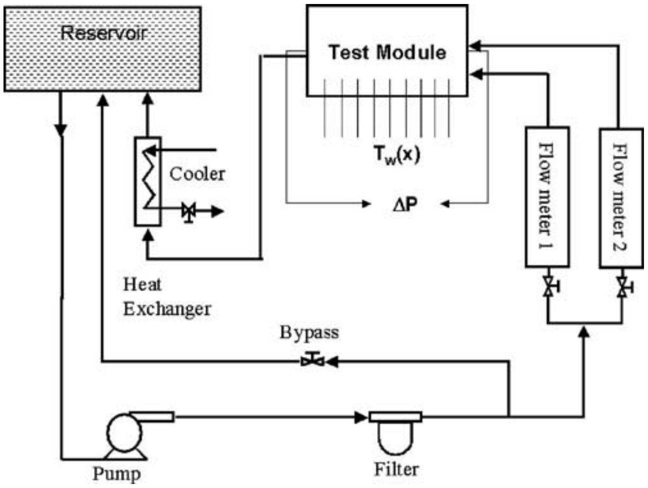

Fig. 1 Schematic of the test flow loop

Stacked microchannel heat sinks were discussed by Wei and Joshi [41]. Several layers of microchannels can be bonded into a stack. For a fixed flow rate, the pressure drop is reduced by a factor almost equal to the number of layers, compared with single-layered microchannels. The thermal performance of stacked microchannel heat sink is affected by aspect ratio, thermal conductivity of base material, and flow rate. A simple thermal resistance analysis found that at fixed pumping power the overall thermal resistance for a two-layered microchannel is 30% less than that of a single-layered microchannel. Stacked microchannel allows coolant flow in opposite directions, which may improve wall temperature uniformity, as also pointed out by Vafai and Zhu [34]. When integrated with manifolds, stacked microchannel can provide uniform fluid flow for the parallel microchannels.

In this study, experiments have been conducted to evaluate the thermal performance of such a stacked microchannel heat sink consisting of two layers of microchannels, two layers of manifolds and one fluid connection layer. All these layers are made of silicon and bonded into a stack through silicon-silicon direct bonding. The flexible design allows either counterflow or parallel flow on the same structure. Results for both configurations over a range of flow rate independently controlled for each layer are reported. Numerical simulations are also performed to study the conjugate heat transfer effects for both parallel and counterflow configurations. Detailed heat transfer information is extracted to understand the experimental results.

2 Experimental Setup and Procedure

2.1 Test Facilities. A schematic of the experimental setup is shown in Fig. 1. A miniature diaphragm pump (overall dimension of $0.01 \times 0.05 \times 0.075$ $\mathrm{m^3}$) drives de-ionized (DI) water from the

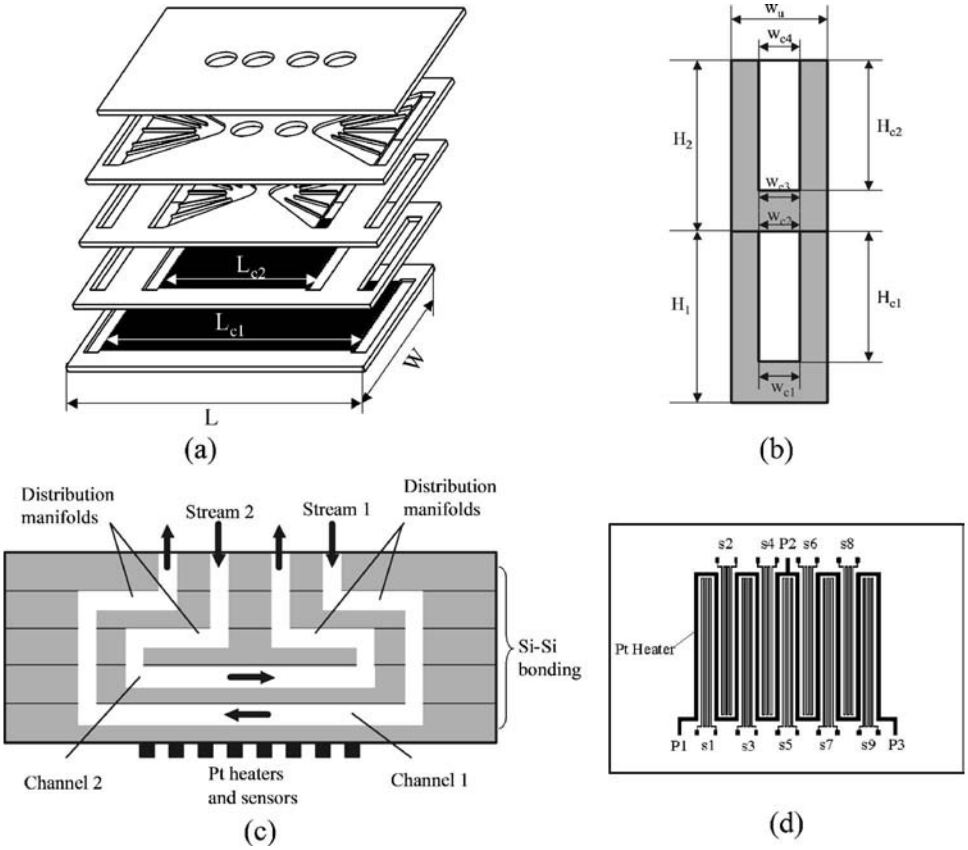

Fig. 2 Schematic of the test module. Dimensions are not drawn to scale. (*a*) Exploded view of the stacked microchannel, (*b*) channel cross section and dimensions, (*c*) Side view of the stacked microchannel, and (*d*) bottom view of the thin-film heaters and temperature sensors.

reservoir through two 8 μm filters and two rotameters to the test module. The cold water picks up the heat from the microchannel heat sink and passes to the external circulating water through a liquid-liquid heat exchanger and rejects the heat to a recirculating chiller. A bypass loop is used to adjust the system flow rate and pressure. Two needle valves control the flow rates through both flow meters. Two differential pressure transducers are used to monitor the pressure drops across the test modules. The inlet and outlet water temperatures were measured using 0.0008 m (0.8 mm) diameter Copper-Constantan (T-type) thermocouples. These thermocouples were inserted into T fittings mounted immediately before the inlet and after the outlet tubings. In this study, a dc power supply with the range of 0–100 V and 0–1 A is used to provide current to the platinum thin-film heaters deposited on the backside of the microchannel heat sink. Temperature profile along the bottom wall of the microchannels stack is measured using the nine thin-film platinum resistive temperature detectors. An Agilent 34970A data acquisition unit is used to collect all the data for further processing.

2.2 Test Module. The test module, illustrated in Fig. 2(*a*), consists of five layers of silicon. Two microchannel layers are at the bottom to provide the cooling. Two manifold layers above the microchannel layers provide fluid distribution. The fifth layer with inlet and outlet ports is for fluid connection. The microchannels, manifolds, and inlet-outlet ports are all fabricated using deep reactive ion etching (DRIE) technique [42]. This technique employs the standard Bosch process [42] in an inductively coupled plasma machine to etch silicon wafers. High aspect ratio features, such as microchannels, can be fabricated. The dimensions of the two layers of microchannels are shown in Table 1 and Fig. 2(*b*). In general, the side profile of the trench fabricated in DRIE depends on the processing parameters as well as on the channel aspect ratio [42]. For certain process parameters, narrow and deep trench tends to be tapered while wide and shallow trench tends to be reentrant [42]. The microchannels fabricated in this study have reentrant shapes. The effects of this shape on the heat transfer have been taken into consideration through numerical modeling of the actual channel geometry. The five layers of silicon populated with respective features are bonded into a watertight stack through silicon-silicon direct bonding. Two separate flow networks are now in place, as shown in Fig. 2(*c*). Both the flow rate and the flow direction into these two networks can be independently controlled. Either counterflow or parallel flow configuration can be conveniently implemented depending on the flow direction.

Thin-film heaters and temperature sensors are deposited on the backside of the microchannel stack to provide heating and sensing, respectively. Figure 2(*d*) shows a layout of the thin-film heaters and sensors. The coarse lines represent heaters, while the fine lines represent resistive temperature sensors. The nine resistive thin-film temperature sensors, s1–s9, measure wall temperature profiles along the flow direction. The heaters, when connected to a dc power supply, simulate the electronic device to be cooled. The

Table 1 Microchannel dimensions $\times 10^3$ (m)

L_{c1}	L_{c2}	w_u	w_{c1}	w_{c2}	w_{c3}
18	10	0.1	0.056	0.054	0.061
w_{c4}	H_{c1}	H_{c2}	H_1	H_2	
0.053	0.284	0.243	0.5	0.5	

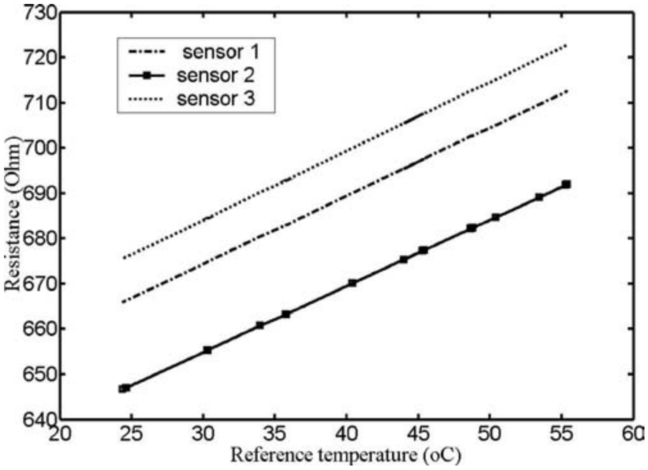

Fig. 3 Typical calibration curves of the resistive sensors

heaters can be connected in three ways. Uniform heating is achieved if one terminal of the dc power is connected to P2, while the other terminal is connected to both P1 and P3. Partial heating is achieved if only P2 and one of P1 and P3 is connected. Fabrication of the heaters and sensors starts with the deposition of a layer of 1.2 μm thick silicon dioxide layer using plasma enhanced chemical vapor deposition (PECVD). Very thin titanium is deposited subsequently as the adhesion layer and finally platinum is deposited to form heaters and sensors. The metal surface is again covered by silicon dioxide to provide insulation. Gold layer is deposited to form bond pads for the final wire bonding to a package.

The temperature sensors were calibrated in an oven against a thermocouple attached to the surface. Figure 3 shows the typical calibration curve. Very good linearity is seen for the range tested. These curves were used to determine the wall temperature according to measured resistance of the sensors.

2.3 Test Procedures and Uncertainty Analysis. A list of controlling parameters for the current experiments is shown in Table 2. A typical test run starts from a degassing process. The trapped air was removed from the loop by running the system continuously for about 1 h. The tested microchannel structure was located at the lowest point of the loop such that air bubble is less likely to be trapped. In the current experiments, the overall flow rate ranges from about 1.38×10^{-6} m^3/s (83 ml/min) to 5.83×10^{-6} m^3/s (350 ml/min). The inlet water temperature was kept uniform at 20°C, as required by the flow meter. For each flow rate, the power input was increased from zero to the maximum output available from the dc power supply. For each test, the temperature and pressure drop were closely monitored. After about 30 min, steady state was typically achieved when the temperature changes are less than 0.2°C within 5 min. Data were subsequently sampled continuously for 1 min at sampling rate of 1 Hz. After each test, an *in situ* flow rate calibration was performed by collecting and weighing the DI water for a certain amount of time.

Table 2 Testing matrix

Parameters	Value
Heating area	Full (1×1 cm^2); upstream (0.5×1 cm^2); downstream (0.5×1 cm^2)
Flow direction	Parallel flow; counterflow
Flow rate ratio between microchannel layer 1 (MC1) and layer 2 (MC2)	1:1; 2:1; 1:2

Error sources for the wall temperature measurement include the calibration uncertainty due to the thermocouple and uncertainties due to the curve fitting for the calibration of the temperature sensors. Any nonuniformity of the calibration oven is assumed not to significantly affect the accuracy of the platinum sensors, as the chip size is much smaller than the chamber. The combined effects result in an uncertainty of ±0.41°C in temperature measurement using the thin-film sensor. The power dissipation is determined from the product of the voltage drop across and the current through the heaters. Voltage input for the heaters were measured across the heater, while the current through the heater is determined by measuring the voltage across a 0.1Ω shunt resistor. For a typical run, this results in a ±0.14% uncertainty in voltage measurement and a ±0.1% uncertainty in current measurement. These uncertainties cause a ±0.2% in power input measurement. It is noted here that actual heat input may be less than the measured value due to the losses to the environment. It was found that the power input measured in this way agreed within 5% of the actual heat transfer rate to the cooling water, which is the product of the flow rate, specific heat, and the water mean temperature rise from inlet to outlet.

As for flow rate measurement, all the measurements were taken at calibration points. Therefore, no data reduction errors were introduced. The bias error due to calibration was estimated to be ±1%. The bias error due to reading is ±0.75 ml/min for all the readings. Combining these errors produces an uncertainty of ±1.8% for 8.3×10^{-7} m^3/s (50 ml/min).

The channel dimensions were measured at 40 locations across the microchannel area using an optical microscope for width measurement and Wyko optical profilometer for depth measurement. The uncertainty due to the microscope width measurement is estimated to be ±0.5 μm. The data scatter in width is around ±3%. For depth measurement, the calibration uncertainty for the Wyko profilometer is ±0.85%. The resulting depth scattering uncertainty is estimated to be ±3%. The combined uncertainty for hydraulic diameter is ±4.4%.

3 Experimental Results and Discussion

Experiments have been conducted for both parallel flow and counterflow arrangements. For each case, both uniform heating and partial heating are tested. As mentioned in the previous section and shown in Fig. 2(*d*), partial heating is made possible by connecting power supply to the electrodes P2 and either P1 or P3, which is referred as upstream heating or downstream heating, respectively. This notation is used throughout the paper assuming the reference stream flows from left to right. For counterflow, the reference stream is the bottom layer. The inlet fluid temperature varies from 20°C to 22°C due to the fluctuation in the chiller operation. Throughout the experiments, flow rate in each layer is controlled independently. Each parallel flow experiment is referenced as PF-*NM*, where *N* represents the relative flow rate in the bottom layer and *M* represents the relative flow rate in the top layer. For example, PF-21 represents the parallel flow condition, where the bottom layer has twice the flow rate as the top layer. Similarly, each counterflow experiment is identified as CF-*NM*. For both parallel and counterflow cases, the interlayer flow ratio is one to one if it is not explicitly specified.

To quantify the overall thermal performance of microchannel heat sinks, historically, a thermal resistance is defined as the maximum temperature difference divided by the heat flux [31]. In the current experiments, the maximum temperature difference is between the maximum wall temperature and the coolant inlet temperature. An on-chip thermal resistance is also defined to describe the across-chip temperature uniformity. This resistance is based on the measured maximum temperature difference over the backside of the chip. Conventionally, a bulk resistance is also defined based on the fluid bulk mean temperature rise along the channel. Convection resistance is defined based on the temperature difference

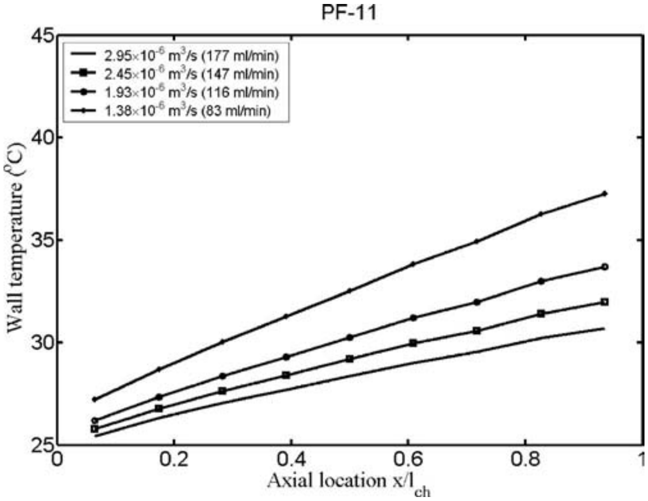

Fig. 4 Wall temperature distribution for parallel flow and uniform heating

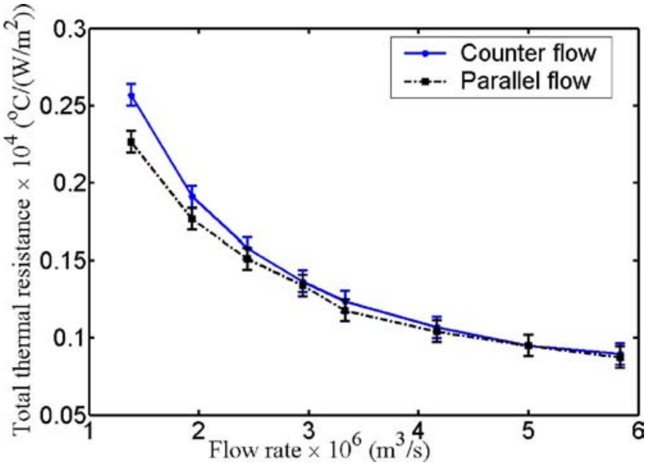

Fig. 6 Total thermal resistances for parallel flow and counterflow with equal flow rate at each of the two microchannels layers

between the average wall temperature and the local bulk resistance. These resistances are defined in the following equations:

$$R_{\text{tot}} = \frac{T_{j,\max} - T_{f,\text{in}}}{Q} \tag{1}$$

$$R_{\text{on chip}} = \frac{T_{j,\max} - T_{j,\min}}{Q} \tag{2}$$

$$R_{\text{bulk}} = \frac{T_{f,\text{out}} - T_{f,\text{in}}}{Q} \tag{3}$$

$$R_{\text{conv}} = \frac{T_{w,m} - T_{f,m}}{Q} \tag{4}$$

3.1 Uniform Heating.

Figures 4 and 5 show the wall temperature distribution along the flow direction for parallel flow and counterflow, respectively, for uniform heating with a heat input of 70 W/cm^2. In both cases, the flow rate for the bottom layer is equal to the top layer. For parallel flow, shown in Fig. 4, along the flow direction, wall temperature increases almost linearly as a result of the uniform heating. The slope decreases as the flow rate increases. For counterflow in Fig. 5, the temperature is more uniform and the maximum temperature exists closer to the middle of the chip along the flow direction. Comparing the results shown in Figs. 4 and 5 reveals that the maximum temperature for counterflow case is higher than for parallel flow. As a result, the overall thermal resistance is higher for counterflow than for parallel flow. This effect on the overall thermal resistance is less significant as the total flow rate increases. Above certain flow rate, this is negligible. As shown in Fig. 6, for large flow rates, the overall thermal resistances for both parallel flow and counterflow are both less than 0.1 °C/(W/cm^2). For counterflow configuration at small flow rates, the fluid temperature rises rapidly such that near the ends of the microchannel the temperature of the hot fluid in one layer is actually higher than the temperature of the adjacent solid regions where cold fluid in the other layer just enters. In these regions, the heat flux is negative as heat flows from liquid to solid. This effect diminishes as flow rate increases. A detailed numerical analysis of this effect is performed in Sec. 3.

Figures 7 and 8 depict the effects of the different flow rate combinations on the overall thermal resistance for parallel flow and counterflow. Clearly, for both flow configurations, the more flow passes through the bottom layer, the lower the overall thermal resistance is.

The total thermal resistance decreases as the total flow rate

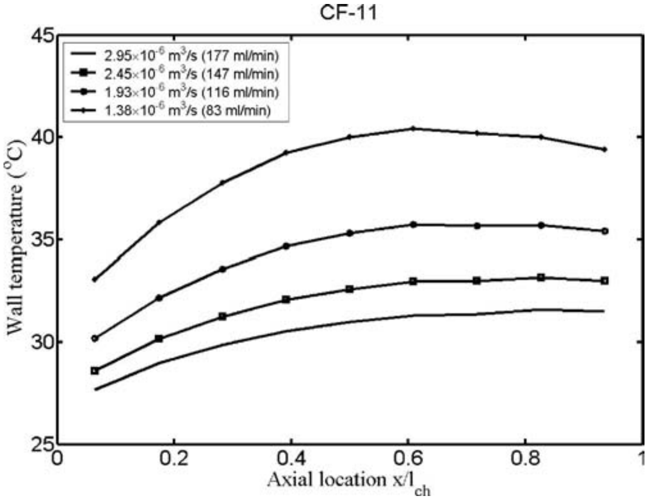

Fig. 5 Wall temperature distribution for counterflow and uniform heating

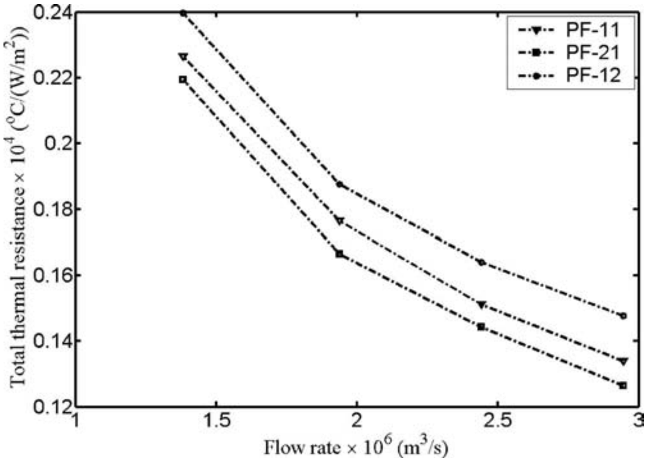

Fig. 7 Total thermal resistances for parallel flow with different interlayer flow rate ratios

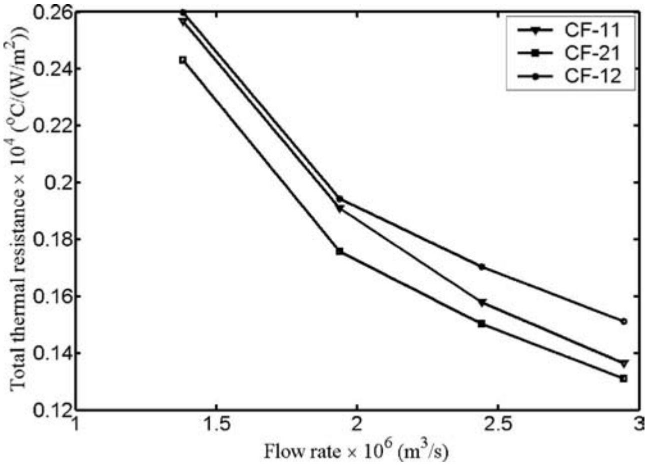

Fig. 8 Total thermal resistances for counterflow with different interlayer flow rate ratios

increases because both bulk resistance and convection resistance decrease. It is interesting to note that the total thermal resistance for counterflow decreases faster than for parallel flow. As a result, at large flow rates, counterflow and parallel flow have almost the same total thermal resistance. For counterflow, increasing flow rate not only reduces the bulk and convection resistances but also reduces the negative heat flow present near the ends of the channel.

Flow rate combinations also affect the temperature uniformity across the chip. Figure 9 shows the on-chip resistances for three interlayer flow rate ratios for both parallel flow and counterflow. As expected, counterflow has significantly smaller temperature nonuniformity than parallel flow. For instance, at the lowest flow rate tested, the temperature nonuniformity for counterflow is 40% less than for parallel flow. For counterflow, contrary to the trend of the total resistance, the on-chip resistances increase when more flow passes the bottom layer. In general, the presence of a reverse temperature gradient at the top layer smoothes out some of the effects of the bottom layer. As less coolant is passed through the top layer, this effect becomes less significant and a steeper temperature profile results. For parallel flow, the trend for on-chip resistances agrees with the total resistances. The on-chip resistance decreases as more flow passes the bottom layer. Interestingly, for counterflow, there is an optimum flow rate combination where the on-chip resistance can be minimized to achieve better chip temperature uniformity. For parallel flow, if pressure drop penalty is not considered, most of the flow should pass the bottom layer to reduce both the total resistance and the on-chip resistance.

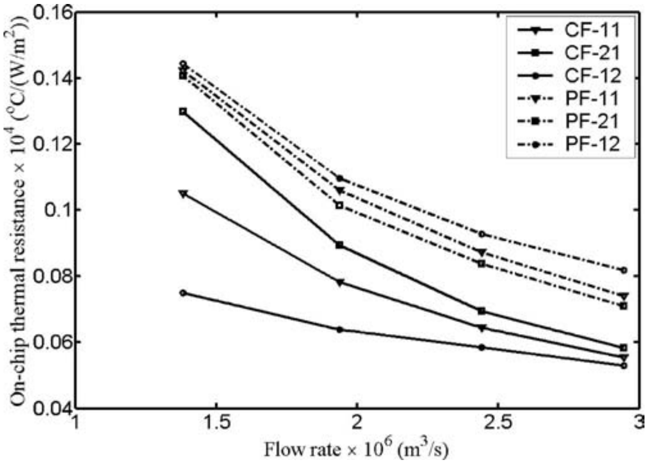

Fig. 9 On-chip thermal resistances for different flow combinations

Table 3 Thermal resistances (°C/W) for different power inputs for counterflow

Flow rate (ml/min)	83	116	147	177
$Q_{\text{input}}=70$ W	0.257	0.191	0.158	0.137
$Q_{\text{input}}=18$ W	0.251	0.181	0.151	0.129

The total thermal resistances for different power input levels are shown in Tables 3 and 4 for counterflow and parallel flow, respectively. For both counterflow and parallel flow, the total thermal resistance increases slightly with increasing power input. As power input increases, coolant temperature also increases. For DI water, the viscosity decreases while the thermal conductivity increases with increasing temperature [11]. This would be beneficial to the convective heat transfer between liquid and solid. On the other hand, thermal conductivity of semiconductors, such as silicon, decreases considerably as the temperature increases [11]. These two effects compete against each other such that the overall thermal resistance is not sensitive to the power input level.

3.2 Partial Heating. Figures 10–15 present the results where only half of the heaters are powered up. For all these cases, equal flow rate is applied to each layer and the total power input is 35 W. Figures 10 and 11 show the measured wall temperature for parallel flow and counterflow, respectively. Only the downstream half heaters are powered up. For both cases, temperature increases along the reference flow direction. Due to conductive heat spreading, the temperature of the upstream walls also increases. This is more evident for counterflow cases. Clearly, parallel flow has a lower peak temperature for the flow rate range studied.

Upstream heating cases are plotted in Figs. 12 and 13. For parallel flow, upstream heating has better temperature uniformity, as well as a smaller peak temperature than for downstream heat-

Table 4 Thermal resistances (°C/W) for different power inputs for parallel flow

Flow rate (ml/min)	83	116	147	177
$Q_{\text{input}}=70$ W	0.226	0.176	0.151	0.134
$Q_{\text{input}}=18$ W	0.223	0.174	0.148	0.133

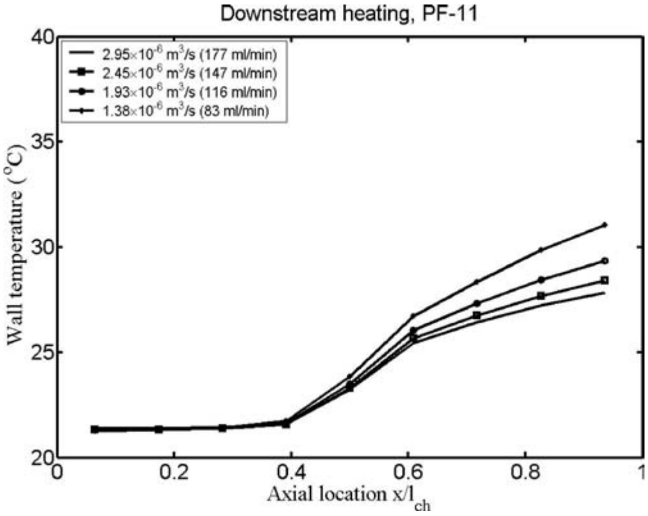

Fig. 10 Temperature distribution for parallel flow with downstream half heating

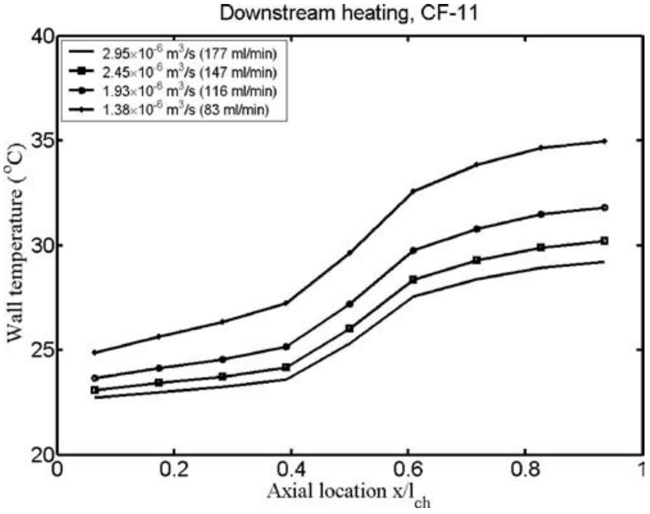

Fig. 11 Temperature distribution for counterflow with downstream half heating

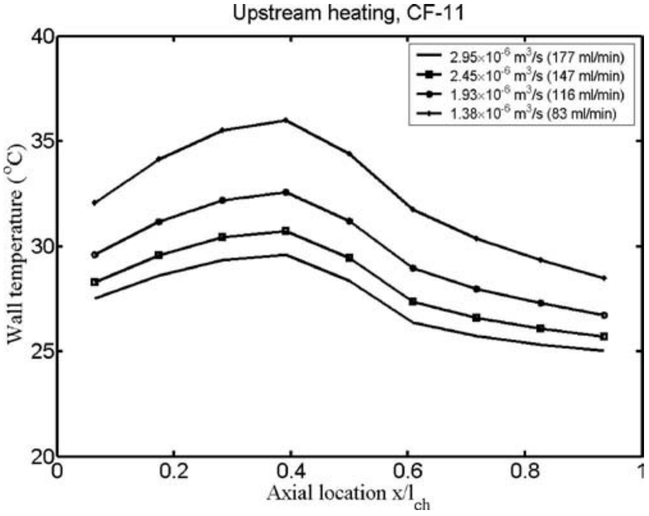

Fig. 13 Temperature distribution for counterflow with downstream half heating

ing. This is because for upstream heating the heat source is localized near the entrance of the channel where the heat transfer is most efficient; whereas for downstream heating the heat source is localized near the exit of the channel where heat transfer coefficient is considerably smaller than entrance region. Similar to the case of downstream heating, the peak temperature for counterflow is higher than for parallel flow.

As expected, the total thermal resistance for half heating is higher than uniform heating as the heat is more localized and the effective heat transfer area is less. Figures 14 and 15 plot the ratio of total resistance for half heating to that of uniform heating for parallel flow and counterflow, respectively. For both cases, the increase in thermal resistance due to half heating intensifies as the flow rate increases. As the liquid flow rate increases, the effective Biot number increases. The conductive heat spreading is reduced, as the convective heat transfer is more efficient. This causes more severe localized heating effects than at lower flow rate conditions. Therefore, for high-end microelectronic cooling applications, in addition to increasing coolant flow rate, it is also important to optimize the heat source locations to minimize localized heating effects. As shown in Fig. 14, for parallel flow, the ratio for upstream heating is lower than the ratio for downstream heating. This is because heat source in upstream heating is closer to the region of high heat transfer coefficient. For counterflow, this ratio is lower for downstream heating than for upstream heating, as shown in Fig. 15. This is possibly due to the less severe negative heat flux for downstream heating than for upstream heating. However, for both counterflow and parallel flow, the difference between downstream and upstream heating is within 5%.

4 Numerical Study of the Conjugate Heat Transfer for Stacked Microchannels

Figure 6 revealed that for low flow rate conditions, the total thermal resistance for parallel flow is considerably smaller than that of counterflow. However, as the flow rate increases the difference decreases, and for certain large flow rates there is virtually no difference between the total thermal resistances of the two flow configurations. To better understand the thermal performance for parallel and counterflow microchannel heat sinks, numerical simulations were conducted to study the conjugate heat transfer effects.

4.1 Modeling Approach. The computational domain, shown in Fig. 16, is essentially a unit cell of microchannel arrays. It includes both solid and fluid regions.

The dimensions of the computational domain can be deter-

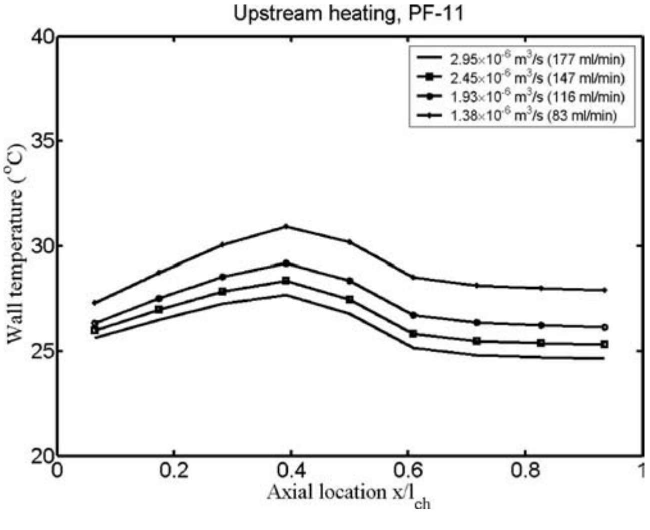

Fig. 12 Temperature distribution for parallel flow with upstream half heating

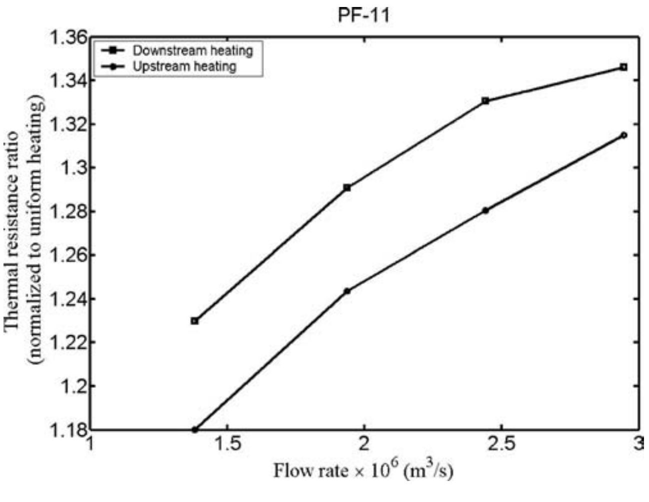

Fig. 14 Increases in thermal resistance for parallel flow cases undergoing localized heating

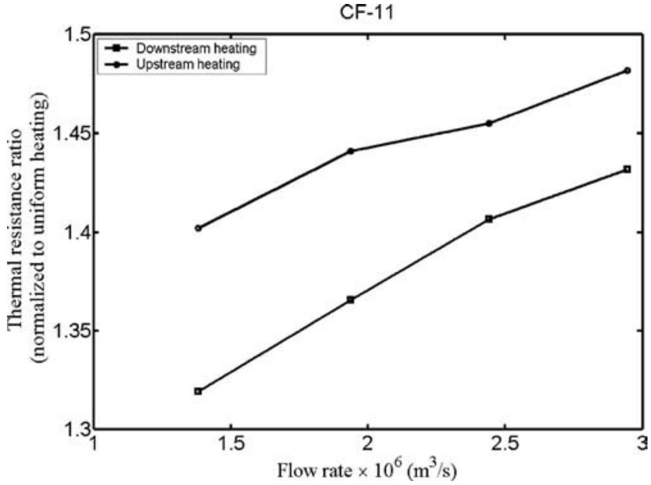

Fig. 15 Increases in thermal resistance for counterflow cases undergoing localized heating

mined from Table 1. A top cover plate with the same thickness as the microchannel layers is added to the computation domain to simulate the effects of the manifold layers above the microchannels.

Conservation equations for mass, momentum, and energy for single-phase laminar flow with conjugate heat conduction were solved using a commercial code (FLUENT). The boundary conditions used for the simulation are described below. At the inlets, uniform velocity and temperature conditions are assumed. These values are taken from experimental results. Outflow conditions are applied at the outlets. Uniform heat flux is applied at the bottom of the silicon structure, and symmetric boundary conditions are applied at the vertical center planes located at the midpoint of the channel width. All other walls are considered adiabatic considering the dominance of the convective heat transfer. Temperature-dependent thermophysical properties are used for water and silicon.

Tables 5 and 6 list the input conditions used for the simulations. For both counterflow and parallel flow conditions, a small flow rate scenario and a large flow rate scenario were considered.

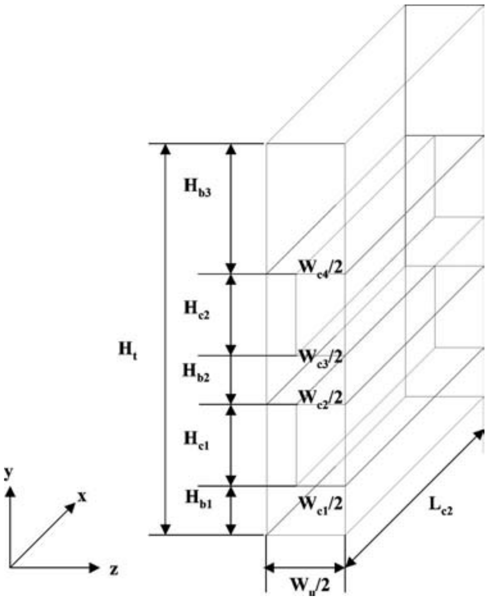

Fig. 16 Domain of computation for numerical modeling

Table 5 Computational conditions for parallel flow

Total flow rate (ml/min)	$T_{f,1}$ (K)	$T_{f,2}$ (K)	V_1 (m/s)	V_2 (m/s)	Heat flux (W/cm^2)
83	294.59	294.26	0.4421	0.5127	71
300	294.56	294.61	1.62	1.83	71

Grid sensitivity study was conducted and a grid system of $40 \times 120 \times 120$ was used finally for all the computations. Further refinement ($40 \times 120 \times 200$) results less than 0.1% changes in the maximum temperature differences on the bottom wall.

To further validate the numerical model, the predicted temperatures are compared with the measurements for the counterflow arrangement at a total flow rate of 1.38×10^{-6} m^3/s (83 ml/min). As shown in Fig. 17, the predictions are generally within 1°C of the measured results, which corresponds to about 5% in terms of overall thermal resistance. Note that there are no data points located exactly at the ends of the channels. Two factors may contribute to the differences. One is the fact that the computational domain covers only the microchannel section. In the model, adiabatic conditions are used at the inlet and outlet cross sections. The actual device includes extra silicon region, which could provide further heat conduction path to the environment. The second factor is that each of the nine measurement points represents the average temperature over a 1 cm × 0.55 mm region. With these in mind, the numerical model is considered sufficiently accurate for this study.

4.2 Modeling Results and Discussion. Figure 18 displays the heat fluxes at the six solid-liquid interfaces for the parallel and counterflow conditions. For both cases, the flow rate is 1.38×10^{-6} m^3/s (83 ml/min). The numbers on the contour lines indicate the heat flux value in kW/m^2. For parallel flow in Fig. 18(*a*), the coolant flows along the positive *x* direction in both layers. For counterflow in Fig. 18(*b*), the coolant flows along the positive *x* direction in the bottom layer and the negative *x* direction in the top layer. For parallel flow, the heat flux at the bottom

Table 6 Computational conditions for counterflow

Total flow rate (ml/min)	$T_{f,1}$ (K)	$T_{f,2}$ (K)	V_1 (m/s)	V_2 (m/s)	Heat flux (W/cm^2)
83	295.55	295.67	0.4421	0.5127	70
300	294.8	294.85	1.62	1.83	71

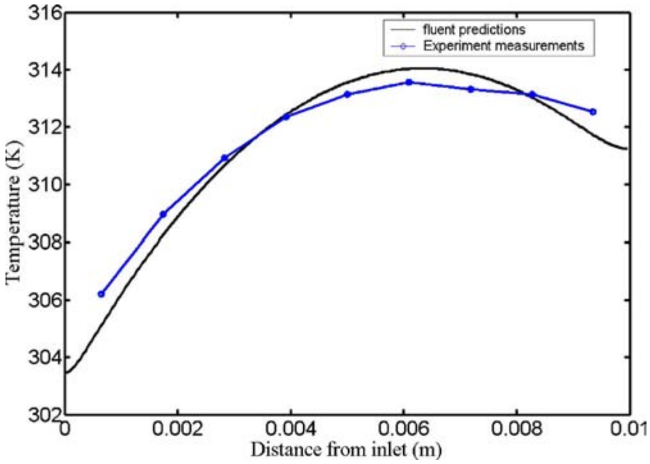

Fig. 17 Wall temperature distribution along the flow direction for counterflow with 1.38×10^{-6} m^3/s (83 ml/min) total flow rate

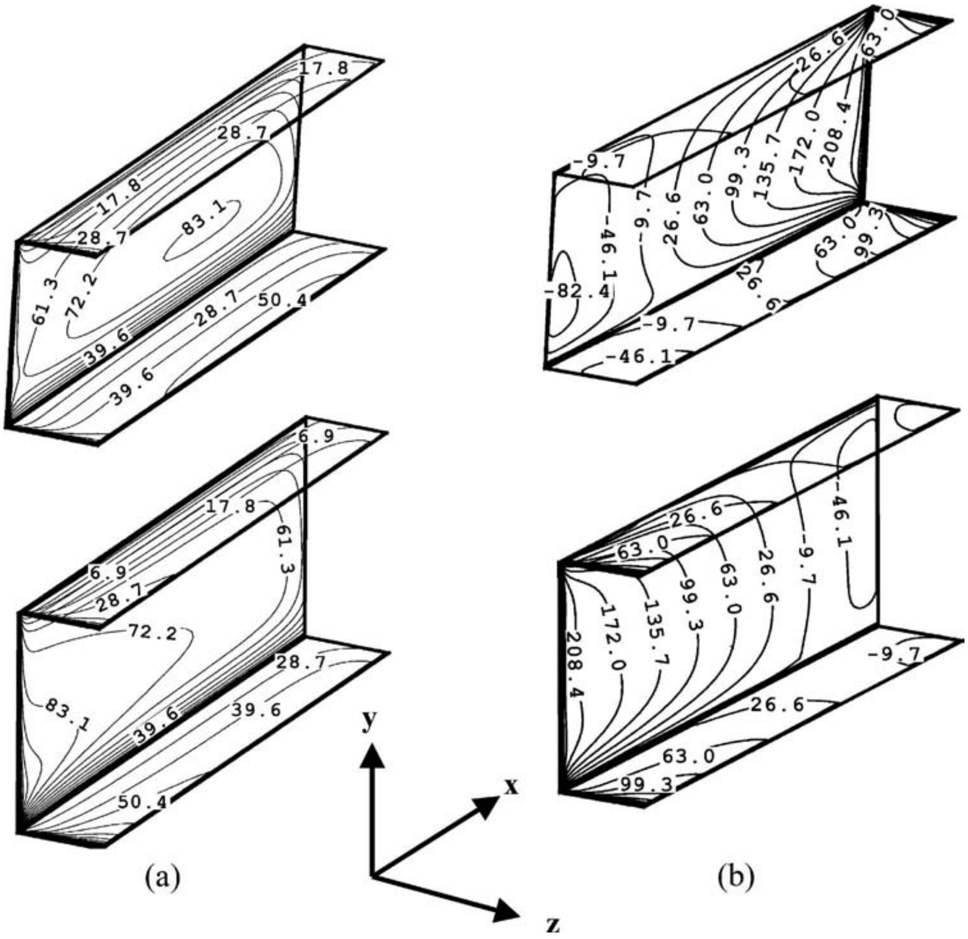

Fig. 18 Heat flux at solid-liquid interfaces in kW/m^2 for a total flow rate of 1.38×10^{-6} m^3/s (83 ml/min). (*a*) parallel flow and (*b*) counterflow.

layer peaks at the entrances for each of the three interface walls. As the flow moves along the *x* axis, the boundary layer thickness increases, and the heat flux decreases rapidly. This is evident from the temperature contours shown in Fig. 19 for different axial locations along the flow directions. The same trend was also reported by Fedorov and Viskanta [33] for a single-layered microchannel. However, the heat flux pattern for the sidewall of the top layer is significantly different. Near the entrance, the heat flux drops initially because of the boundary layer development. After a short distance, it starts increasing. Near the exit (around 7 mm from inlet for the sidewall), it approaches a local maximum after which the heat flux drops again. The fact that heat flux increases along the flow direction for the major portion of the channels is rather surprising. This is the unique feature of stacked microchannels. Heat distribution between different layers of channels varies along the flow directions due to the relative importance of the thermal resistance for each layer. Near the inlet, the bottom layer dominates the heat transfer such that there is much more heat dissipated from the bottom layer than from the top layer. As the flow progresses through the microchannel, the boundary layer thickness for the bottom layer increases. Although the boundary layer thickness for the top layer also grows, the relative importance of the thermal resistance for the bottom layer increases. Therefore, the amount of heat transferred to the top layer increases. As the boundary layers for both layers develop, the relative importance of the thermal resistance for the top layer increases, which causes a reduction in heat flux near the exit. A closer look at the heat flux across the interlayer borders supports this argument, although this is not shown here. For larger flow rates, this effect is even more pronounced, as shown in Fig. 21(*a*).

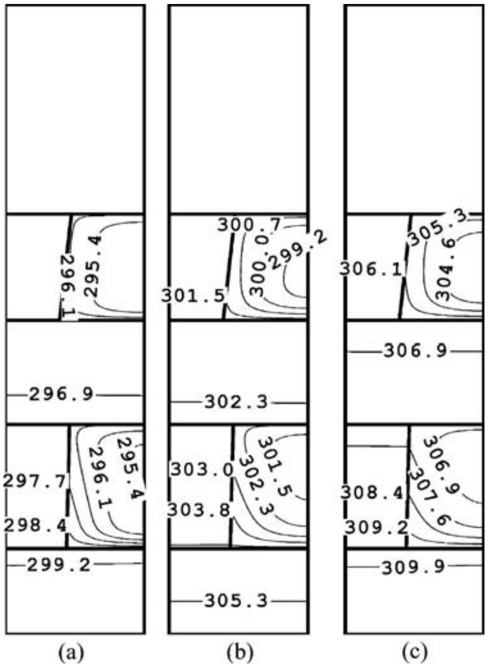

Fig. 19 Temperature contour map (K) for the cross sections (*Z-Y* plane) at different axial positions, parallel flow with total flow rate of 1.38×10^{-6} m^3/s (83 ml/min). (*a*) $x=0.65$ mm, (*b*) $x=5$ mm, and (*c*) $x=9.35$ mm.

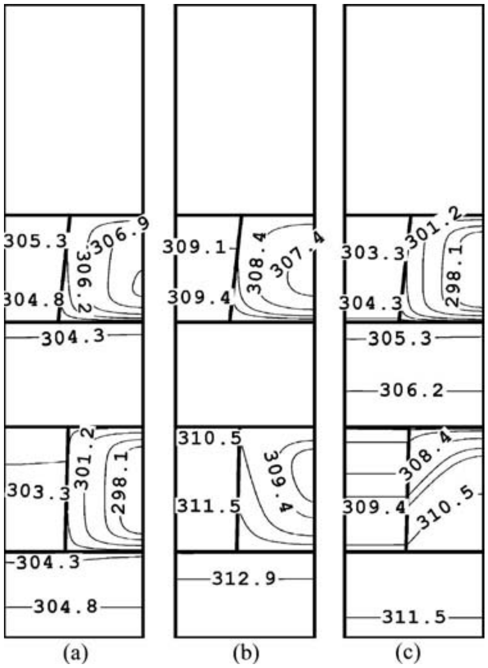

Fig. 20 Temperature contour map (K) for cross sections at different axial positions for counterflow at a total flow rate of 1.38×10^{-6} m^3/s (83 ml/min). (*a*) $x=0.65$ mm, (*b*) $x=5$ mm, and (*c*) $x=9.35$ mm.

The local maximum heat flux at the sidewall is located further away from the inlet (about 9 mm) as the boundary layer develops over longer distance compared to the scenarios of lower flow rate.

Figure 18(*b*) depicts the heat flux across interface walls for the counterflow configuration at a flow rate of 1.38×10^{-6} m^3/s (83 ml/min). The interesting feature is that near the outlets of the channels of both layers the heat flux is negative such that heat is locally dissipated from the heated water to the surrounding cooler silicon. This is because the solid region near the outlets is also cooled by fresh coolant entering the inlets of the other layer. At low flow rates, the temperature of the heated fluid is actually higher than the surrounding solid. An effective heat exchange between the hot fluid and cool fluid exists. This helps to smooth out the temperature gradient as reported in the experimental results in Sec. 4.1. However, the effective heat transfer area is also reduced since not all the channel surfaces are contributing to cooling positively. This has a negative effect on the thermal performance as identified in Fig. 6.

It is interesting to point out that heat flux variations along the flow direction for counterflow are more dramatic than those for parallel flow. Generally, heat flux near the entrance region for counterflow is larger than that of parallel flow. This is true for both small and large flow rate scenarios. Comparing temperature plots in Figs. 19 and 20, the maximum temperature for counterflow is located near the center; whereas for parallel flow it is located at the outlet.

A similar analysis can be performed for the case of a larger flow rate of 5×10^{-6} m^3/s (300 ml/min), as shown in Fig. 21. As previously discussed, for parallel flow, the effect of the heat flow distribution between the microchannel layers is even larger since the boundary layer develops over longer distance. As a result, heat flux in the top layer increases along the flow direction for a larger portion of the channel. For counterflow, the negative heat flux effect near the outlet is much weaker compared to low flow rate scenario. As can be seen from Fig. 21(*b*), only a small portion of the channel experiences a negative heat flux. This is again consistent with the results reported in Fig. 6. Figures 22 and 23 depict the cross-sectional temperature distribution. It is seen that for larger flow rates, the location of the maximum wall temperature is pushed away from the center of the channel length toward the outlet region for the bottom layer.

5 Conclusion

A stacked microchannel heat sink was fabricated using microfabrication techniques to address the limitations of single-layered microchannel heat sinks. Experiments were conducted to study thermal performance of the stacked microchannel structure. The effects of flow direction and flow rate ratio in each microchannel layer were investigated. Both uniform heating and partial heating conditions were evaluated. Numerical simulations were conducted to study the conjugate heat transfer inside stacked microchannels. The main findings and conclusions are presented here.

(a) Stacked microchannel heat sink with two layers of microchannels results in thermal resistance as low as $0.09^\circ\mathrm{C}/(\mathrm{W}/\mathrm{cm}^2)$ for both counterflow and parallel flow configurations. For the flow rate range tested, the counterflow microchannel heat sink has better temperature uniformity. At 83 ml/min, counterflow produces 40% less temperature nonuniformity than parallel flow. For small flow rate range, parallel flow configuration has lower total thermal resistance. At high flow rate, thermal performance for both is indistinguishable.

(b) For both counter- and parallel flow heat sinks, total thermal resistance decreases when more fluid flows through the bottom layer microchannels than through the top layer. However, the pressure drop significantly increases. The flow ratio between the top and bottom layers can be customized to achieve both low pumping power and superior thermal performance.

(c) Partial heating cases have significantly higher total thermal resistance than full heating due to the localization of heat source. For the smallest flow rate tested, thermal resistance for partial heating increases compared to uniform heating by about 20% for parallel flow and 30–40% for counterflow cases. Upstream heating conditions produce fewer penalties in thermal resistances compared with downstream heating conditions for parallel flow. The localized heating effect increases as flow rate increases. Therefore, it is very important to strategically locate the heat sources to minimize the localized heating penalty, especially for high coolant flow rate conditions, which are typical for high-end microelectronic cooling applications.

(d) It is revealed through numerical simulation that for counterflow, heat flux is negative for part of the microchannels if the flow rate is small. This preheating effect effectively reduces the temperature gradient at the price of increasing overall thermal resistance. This effect is less important for flow conditions with larger flow rate. These findings from the numerical simulations agree well with measurements.

(e) The detailed modeling also reveals some unique features of stacked microchannels. For parallel flow, due to the interactions between heat transfer in the top layer and the bottom layer, there exists a local maximum heat flux at the sidewalls of the top layer. This effect is more evident for larger flow rate cases due to the longer boundary layer growth. The unique features of the stacked microchannel need to be carefully assessed before using any existing heat transfer correlations based on idealized conditions.

It is concluded that single-phase liquid cooling using stacked microchannels can achieve excellent cooling performance if proper considerations are given to the unique heat transfer characteristics.

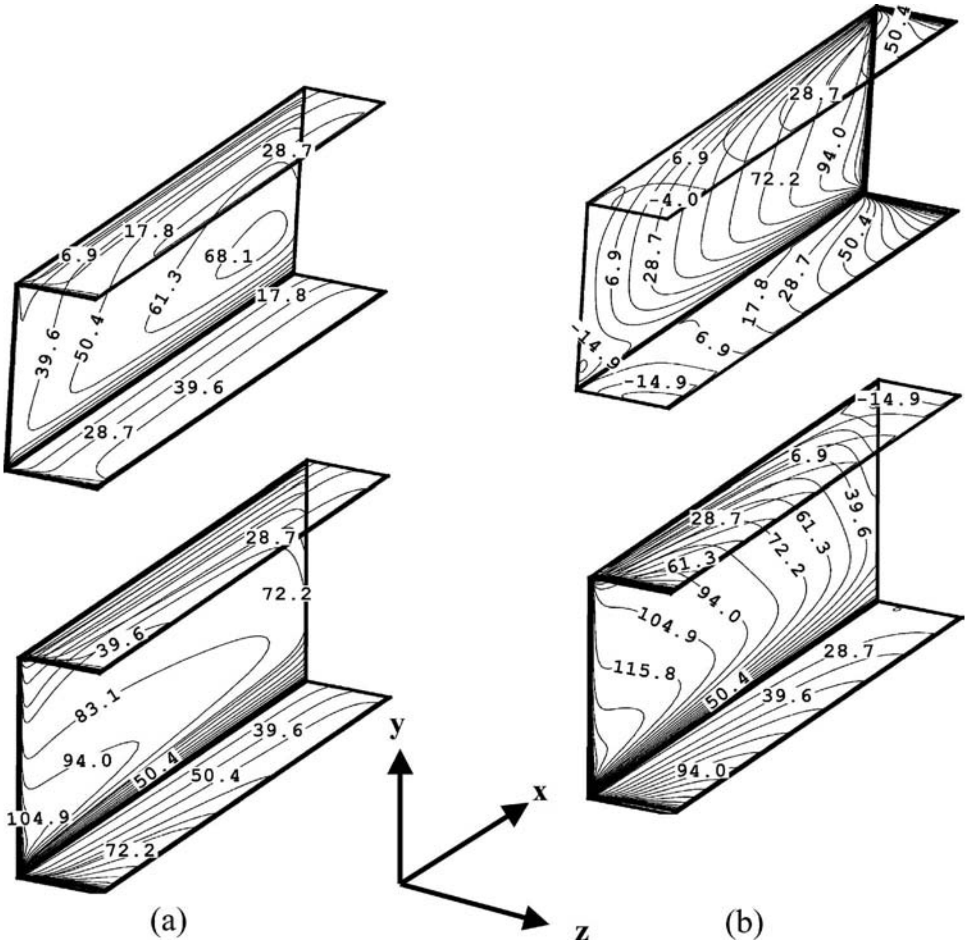

Fig. 21 Heat flux at solid-liquid interfaces in kW/m^2 for a total flow rate of 5×10^{-6} m^3/s (300 ml/min). (*a*) Parallel flow and (*b*) counterflow.

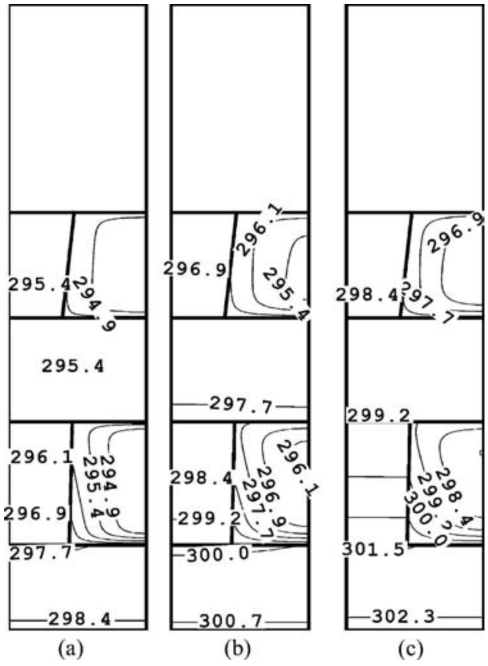

Fig. 22 Temperature contours (K) for the cross sections at different axial positions for parallel flow at a total flow rate of 5×10^{-6} m^3/s (300 ml/min). (*a*) $x=0.65$ mm, (*b*) $x=5$ mm, and (*c*) $x=9.35$ mm.

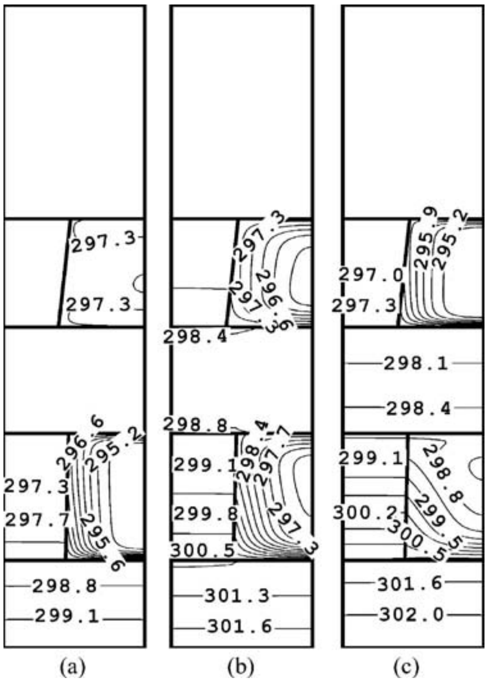

Fig. 23 Temperature contours (K) for the cross sections at different axial positions for counterflow at a total flow rate of 5×10^{-6} m^3/s (300 ml/min). (*a*) $x=0.65$ mm, (*b*) $x=5$ mm, and (*c*) $x=9.35$ mm.

Acknowledgment

The authors acknowledge support for this work under the DARPA Heretic Program through Contract No. N00164-99-C-0039. Additional support was provided by Intel Corporation. Discussions with Dr. Ravi Prasher during the course of some parts of this work are acknowledged.

Nomenclature

CF-11 = counterflow with one flow in bottom layer and one flow in top layer
CF-12 = counterflow with one flow in bottom layer and twice as much flow in top layer
CF-21 = counterflow with one flow in top layer and twice as much flow in bottom layer
H_1 = total thickness of silicon wafer 1, m
H_2 = total thickness of silicon wafer 2, m
H_{c1} = height of channel 1, m
H_{c2} = height of channel 2, m
L_{c1} = length of channel 1, m
L_{c2} = length of channel 2, m
L_{ch} = length of the heater, m
P1, P2, P3 = three electrodes for the heaters
PF-11 = parallel flow with one flow in bottom layer and one flow in top layer
PF-12 = parallel flow with one flow in bottom layer and twice as much flow in top layer
PF-21 = parallel flow with one flow in top layer and twice as much flow in bottom layer
R_{bulk} = bulk thermal resistance due to coolant heating, °C/W
R_{conv} = convective thermal resistance, °C/W
$R_{\mathrm{on\ chip}}$ = on-chip thermal resistance, °C/W
R_{tot} = overall thermal resistance, °C/W
S1–S9 = array of nine thin-film temperature sensors
$T_{f,\mathrm{in}}$ = fluid temperature at the inlet, °C
$T_{f,m}$ = mass average fluid temperature, °C
$T_{f,\mathrm{out}}$ = bulk fluid temperature at the outlet, °C
$T_{j,\max}$ = maximum chip junction temperature, °C
$T_{j,\min}$ = minimum chip junction temperature, °C
T_w = wall temperature distribution, °C
$T_{w,m}$ = mean wall temperature, °C
w_{c1} = bottom width of channel 1, m
w_{c2} = top width of channel 1, m
w_{c3} = bottom width of channel 2, m
w_{c4} = top width of channel 2, m
w_u = unit width of channels, m
x = axial location with reference to the heaters, m

Greek Symbol

ΔP = pressure drop, Pa

References

[1] Sauciuc, I., Chrysler, G., Mahajan, R., and Szleper, M., 2003, "Air-Cooling Extension-Performance Limits for Processor Cooling Applications," *IEEE SEMI-THERM Symposium*, San Jose, CA, Mar. 11–13, pp. 74–81.
[2] Xu, G., Guenin, B., and Vogel, M., 2004, "Extension of Air Cooling for High Power Processors," *Inter Society Conference on Thermal Phenomena*, Las Vegas, NV, Jun. 1–4, pp. 186–193.
[3] Webb, R., 2005, "Next Generation Devices for Electronic Cooling With Heat Rejection to Air," ASME J. Heat Transfer, **127**, pp. 2–9.
[4] Fabbri, M., Jiang, S., and Dhir, V., 2005, "A Comparative Study of Cooling of High Power Density Electronics Using Sprays and Microjets," ASME J. Heat Transfer, **127**, pp. 38–48.
[5] Kandlikar, S., and Grande, W., 2004, "Evaluation of Single Phase Flow in Microchannels for High Flux Chip Cooling—Thermohydraulic Performance Enhancement and Fabrication Technology," *Second International Conference on Microchannels and Minichannels*, Rochester, NY, Jun. 17–19, Paper No. ICMM2004-2321, pp. 67–76.
[6] Womac, D. J., Incropera, F. P., and Ramadhyani, S., 1994, "Correlating Equations for Impingement Cooling of Small Heat Sources With Multiple Circular Liquid Jets," ASME J. Heat Transfer, **116**, pp. 482–486.
[7] Amon, C. H., Yao, S.-C., Wu, C.-F., and Hsieh, C.-C., 2005, "Microelectromechanical System-Based Evaporative Thermal Management of High Heat Flux Electronics," ASME J. Heat Transfer, **127**, pp. 66–75.
[8] Xia, C., 2002, "Spray/Jet Cooling for Heat Flux High to 1 kW/cm^2," *18th IEEE SEMI-THERM Symposium*, San Jose, March 12–14, pp. 159–163.
[9] Heffington, S. N., 2001, "Vibration-Induced Droplet Atomization Heat Transfer Cell for Cooling of Microelectronic Components," *Proceedings of IPACK 01*, Kauai, HI, July 6–13, Paper No. IPACK2001-15567.
[10] Ramaswamy, C., Joshi, Y., Nakayama, W., and Johnson, W., 2000, "Combined Effects of Sub-Cooling and Operating Pressure on the Performance of a Two-Chamber Thermosyphon," IEEE Trans. Compon. Packag. Technol., **23**(1), pp. 61–69.
[11] Tuckerman, D. B., 1984, "Heat Transfer Microstructures for Integrated Circuits," Ph.D. thesis, Stanford University.
[12] Bowers, M. B., and Mudawar, I., 1994, "High Heat Flux Boiling in Low Flow Rate, Low Pressure Drop Mini-Channel and Micro-Channel Heat Sinks," Int. J. Heat Mass Transfer, **37**(2), pp. 321–332.
[13] Garimella, S. V., and Singhal, V., 2004, "Single-Phase Flow and Heat Transport and Pumping Considerations in Microchannel Heat Sinks," Heat Transfer Eng., **25**(1), pp. 15–25.
[14] Wei, X. J., and Joshi, Y. K., 2003, "Optimization Study of Stacked Microchannel Heat Sinks for Microelectronic Cooling," IEEE Trans. Compon. Packag. Technol., **26**(1), pp. 55–61.
[15] Koo, J., Im, S., Jiang, L., and Goodson, K., 2005, "Integrated Microchannel Cooling for Three-Dimensional Electronic Architectures," ASME J. Heat Transfer, **127**, pp. 49–58.
[16] Lee, D.-Y., and Vafai, K., 1999, "Comparative Analysis of Jet Impingement and Microchannel Cooling for High Heat Flux Applications," Int. J. Heat Mass Transfer, **42**, pp. 1555–1568.
[17] Wu, P., and Little, W. A., 1983, "Measurement of Friction Factors for the Flow of Gases in Very Fine Channels Used for Microminiature Joule-Thompson Refrigerators," Cryogenics, **23**(5), pp. 273–277.
[18] Pfahler, J., Harley, J., Bau, H. H., and Zemel, J., 1991, "Gas and Liquid Flow in Small Channels," *Micromechanical Sensors, Actuators and Systems*, D. Cho, R. Warrington, Jr., H. Bau, C. Friedrich, J. Jara-Almonte, J. Liburdy, and A. P. Pisano, eds., ASME New York, 32, pp. 49–60.
[19] Peng, X. F., Peterson, G. P., and Wang, B. X., 1994, "Frictional Flow Characteristics of Water Flowing Through Rectangular Microchannels," Exp. Heat Transfer, **7**, pp. 249–264.
[20] Peng, X. F., Peterson, G. P., and Wang, B. X., 1994, "Heat Transfer Characteristics of Water Flowing Through Rectangular Microchannels," Exp. Heat Transfer, **7**, pp. 265–283.
[21] Papautsky, I., Brazzle, J., Ammel, T., and Frazier, A. B., 1999, "Laminar Fluid Behavior in Microchannels Using Micropolar Fluid Theory," Sens. Actuators, A, **73**, pp. 101–108.
[22] Harms, T. M., Kazmierczak, M. J., and Gerner, F. M., 1999, "Developing Convective Heat Transfer in Deep Rectangular Microchannels," Int. J. Heat Fluid Flow, **210**, pp. 149–157.
[23] Mala, G. M., and Li, D., 1999, "Flow Characteristics of Water in Microtubes," Int. J. Heat Fluid Flow, **20**, pp. 142–148.
[24] Mala, G. M., Li, D., Werner, C., Jacobasch, H. J., and Ning, Y. B., 1997, "Flow Characteristics of Water Through Microchannels Between Two Parallel Plates With Electrokinetic Effects," Int. J. Heat Fluid Flow, **18**, pp. 489–496.
[25] Tso, C. P., and Mahulikar, S. P., 1998, "The Use of the Brinkman Number for Single Phase Forced Convective Heat Transfer in Microchannels," Int. J. Heat Mass Transfer, **41**(12), pp. 1759–1769.
[26] Xu, B., Ooi, K. T., and Wong, N. T., 2000, "Experimental Investigation of Flow Friction for Liquid Flow in Microchannels," Int. Commun. Heat Mass Transfer, **27**, pp. 1165–1176.
[27] Qu, W., and Mudawar, I., 2002, "Experimental and Numerical Study of Pressure Drop and Heat Transfer in a Single-Phase Micro-Channel Heat Sink," Int. J. Heat Mass Transfer, **45**, pp. 2549–2565.
[28] Liu, D., and Garimella, S. V., 2002, "Investigation of Liquid Flow in Microchannels," *Eighth AIAA/ASME Joint Thermophysics and Heat Transfer Conference*, St. Louis, MO, Paper No. AIAA 2002-2776, pp. 1–10.
[29] Lee, P., and Garimella, S. V., 2003, "Experimental Investigation of Heat Transfer in Microchannels," *ASME Summer Heat Transfer Conference*, Las Vegas, NV, Paper No. HT2003-47293, pp. 1–7.
[30] Kohl, M. J., Abdel-Khalik, S. I., Jeter, S. M., and Sadowski, D. L., 2005, "An Experimental Investigation of Microchannel Flow With Internal Pressure Measurements," Int. J. Heat Mass Transfer, **48**, pp. 15518–1533.
[31] Phillips, R. J., 1990, "Microchannel Heat Sinks," *Advances in Thermal Modeling of Electronic Components and Systems*, A. Bar-Cohen and A. D. Kraus, eds., Hemisphere, New York, Vol. 2, pp. 109–184.
[32] Weisberg, A., and Bau, H. H., 1992, "Analysis of Microchannels for Integrated Cooling," Int. J. Heat Mass Transfer, **35**(10), pp. 2465–2474.
[33] Fedorov, A. G., and Viskanta, R., 2000, "Three-Dimensional Conjugate Heat Transfer in the Micro-Channel Heat Sink for Electronic Packaging," Int. J. Heat Mass Transfer, **43**, pp. 399–415.
[34] Vafai, K., and Zhu, L, 1999, "Analysis of Two-Layered Micro-Channel Heat Sink Concept in Electronic Cooling," Int. J. Heat Mass Transfer, **12**, pp. 2287–2297.
[35] Koo, J. M., Im, S., Jiang, L., and Goodson, K. E., 2005, "Integrated Microchannel Cooling for Three-Dimensional Electronic Circuit Architectures," Trans. ASME, Ser. C: J. Heat Transfer, **127**(1) pp. 49–58.
[36] Harpole, G. M., and Eninger, J. E., 1991, "Micro-Channel Heat Exchanger Optimization," *Seventh IEEE SEMI-THERM Symposium*, Scottsdale, AZ, Feb-

ruary 12–14, pp. 59–63.
[37] Copeland, D., Behnia, M., and Nakayama, W., 1996, “Manifold Microchannel Heat Sinks: Isothermal Analysis,” *Proceedings of I-THERM V*, pp. 251–257.
[38] Bau, H. H., 1998, “Optimization of Conduits’ Shape in Micro Heat Exchangers,” Int. J. Heat Mass Transfer, **41**, pp. 2717–23.
[39] Hrnjak, P., 2004, “Developing Adiabatic Two Phase Flow in Headers-Distribution Issue in Parallel Flow Microchannel Heat Exchangers,” Heat Transfer Eng., **25**(3), pp. 61–68.
[40] Webb, R. L., 2003, “Effect of Manifold Design on Flow Distribution in Parallel Micro-Channels,” *IPack’03*, Maui, HI, July, pp. 527–535.
[41] Wei, X. J., Joshi, and Y. K., 2004, “Stacked Microchannel Heat Sinks for Liquid Cooling of Microelectronic Components,” ASME J. Electron. Packag., **126**, pp. 60–66.
[42] Ayon, A. A., Braff, R. A., Bayt, R., Sawin, H. H., and Schmidt, M. A., 1999, “Influence of Coil Power on the Etching Characteristics in a High Density Plasma Etcher,” J. Electrochem. Soc., **146**(7), pp. 2730–2736.

Novel Design of a Miniature Loop Heat Pipe Evaporator for Electronic Cooling

Randeep Singh[1]
e-mail: randeep.singh@rmit.edu.au

Aliakbar Akbarzadeh

Chris Dixon

Energy CARE Group, School of Aerospace,
Mechanical and Manufacturing Engineering,
RMIT University,
P.O. Box 71,
Bundoora, Victoria 3083, Australia

Masataka Mochizuki
Fujikura Ltd.,
1-5-1 Kiba, Koto-ku,
Tokyo 135, Japan

Miniature loop heat pipes (mLHPs) are coming up with a promising solution for the thermal management of futuristic electronics systems. In order to implement these devices inside compact electronics, their evaporator has to be developed with small thickness while preserving the unique thermal characteristics and physical concept of the loop scheme. This paper specifically addresses the design and testing of a mLHP with a flat evaporator only 5 mm *thick for the cooling of high performance microprocessors for electronic devices. A novel concept was used to achieve very small thickness for the mLHP evaporator in which the compensation chamber was positioned on the sides of the wick structure and incorporated in the same plane as the evaporator. This is unlike the conventional design of the flat evaporator for mLHP in which the compensation chamber, as a rule, adds to the overall thickness of the evaporator. The loop was made from copper with water as the heat transfer fluid. For capillary pumping of the working fluid around the loop, a sintered nickel wick with* $3-5$ μm *pore radius and 75% porosity was used. In the horizontal orientation, the device was able to transfer heat fluxes of* $50\ \mathrm{W/cm^2}$ *at a distance of up to* 150 mm *by using a transport line with* 2 mm *internal diameter. In the range of applied power, the evaporator was able to achieve steady state without any temperature overshoots or symptoms of capillary structure dryouts. For the evaporator and condenser at the same level and under forced air cooling, the minimum value of* $0.62°\mathrm{C/W}$ *for mLHP thermal resistance from evaporator to condenser* (R_{ec}) *was achieved at a maximum heat load of* 50 W *with the corresponding junction temperature of* $98.5°\mathrm{C}$. *The total thermal resistance* (R_t) *of the mLHP was within* $1.5-5.23°\mathrm{C/W}$. *At low heat loads, the mLHP showed some thermal and hydraulic oscillations in the transport lines, which were predominately due to the flow instabilities imposed by parasitic heat leaks to the compensation chamber. It is concluded form the outcomes of the present investigation that the proposed design of the mLHP evaporator can be effectively used for the thermal control of the compact electronic devices with high heat flux capabilities.* [DOI: 10.1115/1.2754945]

Keywords: flat evaporator, novel design, electronic cooling, miniature loop heat pipe, mLHP, thermal control

1 Introduction

Compact electronic devices such as notebooks with high performance microprocessors have been developed to meet the extensive data and graphic processing requirements of the end users. Favorably, this has helped to provide superior performance to the electronic equipment but at the same time the thermal management of these high powered electronics is becoming an increasingly challenging task. At present, the waste heat dissipated by the notebook microprocessor is as high as $25-50$ W [1] and is expected to increase further in the coming years. Apart from this, the dense packaging of the high end chipsets with active heating area as small as $1-4\ \mathrm{cm^2}$ gives rise to very high and concentrated heat fluxes. The problem is further complicated by the limitation of the available space and the requirement to maintain the microprocessor temperature below $100°\mathrm{C}$.

In order to design an appropriate thermal solution for the cooling of such compact electronics, a thermal engineer has to deal with both design and performance challenges on the part of the temperature control device [2]. On the design side, the objective is to develop a thermal control device that can be successfully integrated into the limited available space inside the electronic devices such as notebooks while at the same time the performance of the device has to be within the thermal specifications imposed by the chip manufacturer. Two-phase passive cooling systems based on heat pipes and vapor chambers have been invariably used for the thermal management of such compact electronic equipment [3–7]. Such systems have proven to be very efficient cooling devices with ease of integration and design simplicity. Nonetheless, the heat transfer limit of the heat pipe is limited at high heat fluxes due to the considerable pressure losses associated with the liquid flow inside the wick structure that spans the entire length of the pipe. Also, for electronic cooling applications, heat pipes are required to be relatively thin, which imposes an additional limitation on the heat transport capabilities of the device. Different variants of liquid cooling based systems have also been proposed for cooling power saturated microchips [8,9] but these systems pose major reliability and integration issues. In this case, the loop heat pipe can be considered as a potential cooling alternative due to its enhanced design configuration over the conventional heat pipes and passive mode of operation that provide runtime reliability as compared to pump activated systems.

Loop heat pipes (LHPs) are two-phase heat transfer devices that depend on the capillary forces developed in a fine pore wick to circulate the working fluid in the closed loop [10]. A LHP uses the latent heat of evaporation of the working fluid to transfer waste

---

[1] Corresponding author.

Contributed by the Heat Transfer Division of ASME for publication in the Journal of Heat Transfer. Manuscript received May 16, 2006; final manuscript received February 9, 2007. Review conducted by Suresh V. Garimella.

heat from the source to the remotely located heat sink. This can be considered as an enhanced design of heat pipes with spatially and thermally separated liquid-vapor phases, and localized wick structure inside the evaporator section. Such a design approach makes it possible to construct wickless transport lines with least flow resistance and provide efficient heat exchange inside the evaporator by using an efficient system of vapor removal passages. Although primarily developed for space applications, the high heat transport capabilities of these devices have carried them to the forefront of research and development in thermal cooling of consumer electronics.

For the successful use of LHPs in electronics cooling, the performance and design issues related to their miniaturization have to be studied. In this context, different designs of miniature loop heat pipe (mLHP) have been developed by researchers worldwide [11–14]. Generally, the design configuration of these mLHPs is composed of cylindrical evaporator with integral liquid reservoir (also called as compensation chamber). An alternative design of mLHP with a flat evaporator [15–18] has also been successfully designed and tested. In such design, the evaporation section and the compensation chamber (CC) make up the overall thickness of the evaporator. The flat shape provides an optimum design for the mLHP evaporator for ease of integration to the heat source. Most often, the body of the loop is made from stainless steel with a nickel wick and ammonia as the working fluid. However, due to the safety issues associated with the use of ammonia, its use in the consumer electronics is not encouraged. In that respect, water is considered as the most acceptable working fluid. mLHPs based on copper-water have already been developed and tested with satisfactory performance [18–20].

In the design of the mLHP system for electronic cooling, the main restriction is imposed on the total thickness of the flat evaporator, which, as a rule, also includes the CC thickness. It should be noted that the decrease in the thickness of mLHP evaporator is mainly possible by reducing the wick thickness. As a result, the limiting thickness for the evaporator is predominately dictated by the minimum thickness of the capillary structure that guarantees its intended functionalities as a thermal and hydraulic lock. Any decrease in the wick thickness beyond this limit can possibly result in some loss of the thermal performance. This is because the heat locking feature of a wick with smaller thickness is reduced and this results in an increase of heat flow via wick to the CC. Apart from the variables such as vapor saturation conditions, room temperature, geometric characteristics of transport lines, and wick, the saturation temperature of the CC also affects the loop operating temperature to appreciable extent [21]. As a result, increase in the heat leaks to CC tends to increase the mLHP evaporator temperature. It is expected that any attempt of decreasing the evaporator thickness by reducing the thickness of vapor removal channels or CC is also associated with loss in the thermal performance of the device. For the decrease in the evaporator thickness at the expense of the vapor removal channel thickness, the flow resistance and thus the overall pressure losses inside the loop increase. If the overall pressure losses inside the loop exceed the maximum capillary pressure generated by the wick structure, the mLHP will fail to operate. Such a decrease of evaporator thickness is also not possible via thinning of the evaporator wall as this may lead to the deformation of the evaporator heating face under attachment pressure between the evaporator and source face that is required for efficient heat acquisition from the heat source. Any attempt to decrease the CC thickness will reduce the liquid storage capability of the chamber, which may result in poor priming of the wick prior to startup. In addition to this, the potential for bubble formation inside the CC of limited thickness may produce flow blockage and consequently flow instabilities inside the loop. It is seen that numerous performance issues are associated with the downscaling of the evaporator thickness, some of which are discussed above. However, for successful application of the loop system to the cooling of compact and high end electronic equipment, their miniaturization with respect to the evaporator thickness is necessary.

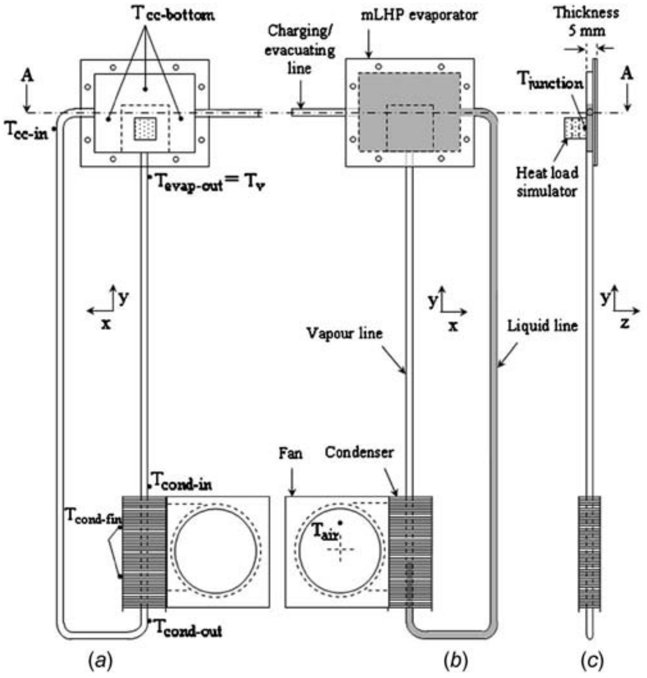

Fig. 1 Schematic of the experimental prototype and test layout for the mLHP. (*a*) Bottom view of the mLHP showing temperature measurement points and the heater location. (*b*) Top view of the mLHP showing different loop components and condenser fan location. (*c*) Side view of the mLHP showing the evaporator thickness and the heater location relative to the evaporator active zone.

The main objective of the present study was to design and test a miniature LHP with an evaporator thickness of 5 mm. A novel concept was used in the design of the mLHP evaporator in which the CC was positioned on the sides of the evaporation zone. The designed mLHP was intended to transfer a maximum of 50 W heat load over a distance of up to 150 mm with the evaporator and condenser at the same horizontal level. The thermal performance of the device was found to be satisfactory and in accordance with the cooling requirements for the high powered and compact electronic devices.

2 Description of Experimental Prototype

The schematic of the mLHP is shown in Fig. 1 and consists of the evaporator structure, finned condenser, vapor line, and liquid line. For the loop evaporator, the design is influenced by the available space inside the electronic equipment. The present study considers laptop computer as a compact electronic equipment and based the design of the mLHP on the space constraints inside it. In this case, the evaporator is rectangular in shape with a planar dimension of 45 mm$(L) \times 35$ mm$(W) \times 5$ mm(T). It is expected that the thickness of the designed mLHP evaporator is lowest among the flat evaporators tested to date. The evaporator body is basically comprised of the evaporator region and an integrated CC. Figure 2(*a*) presents the cross section of the evaporator showing the internal details. The evaporator region is composed of vapor removal channels and a wick structure. It should be noted that in the standard design of the flat evaporator for mLHPs [15,16], the CC is incorporated on the top of the capillary evaporator, which adds to the overall thickness of the evaporator structure. In order to achieve the small thickness of 5 mm, a new evaporator design was developed in which the CC was positioned

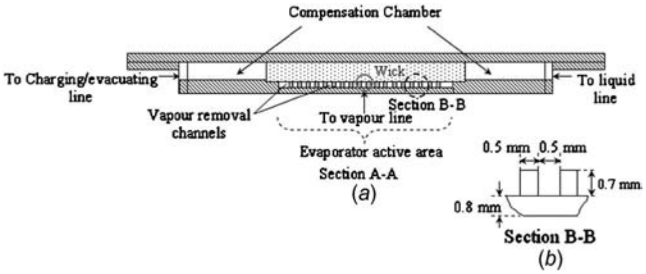

Fig. 2 mLHP Evaporator. (*a*) Cross-sectional details of the mLHP evaporator. (*b*) Sectional view of vapor removal channels.

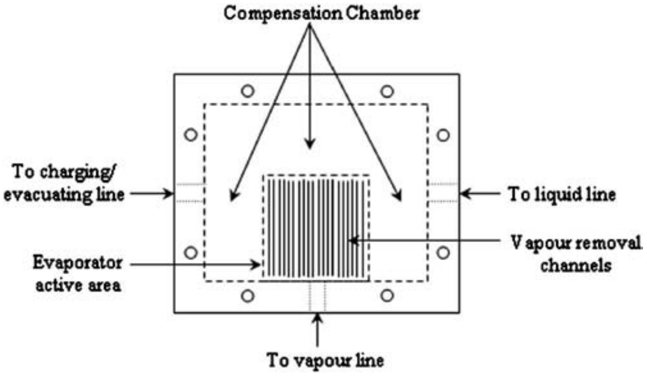

Fig. 3 Planar view of the mLHP evaporator showing the position of the evaporation zone and CC

in the plane of the wick structure, as shown in Fig. 2(*a*). With this approach, it was possible to decrease the evaporator thickness by nearly one-half while preserving the physical concept of the loop scheme.

The CC is thermally and hydraulically linked to the evaporation zone via the capillary structure and principally performs two main functions: (1) It accommodates the extra liquid inventory that is displaced from the evaporator grooves, vapor line, and part of condenser during the loop startup and (2) it promotes the wetting of the wick structure at all times during the cold state as well as normal operation of the loop. To ensure that these tasks are performed properly, special consideration has to be given to the CC with respect to the overall volume and the liquid access to the wick matrix. For the designed mLHP, the volume of the CC was kept equal to the total volume of the loop so that it may be able to accommodate most of the displaced liquid during startup as well as changing heat loads. In the new design, the CC provides liquid access to the wick structure from the three side faces.

Due to the miniature size of the LHP, the pressure loss associated with flow resistance is relatively high. For that reason, it is imperative to use a wick structure with fine pore size that can provide sufficient capillary pressure to keep the working fluid in continuous circulation during loop operation. The function of capillary pump was efficiently performed by a sintered nickel wick with the effective pore radius of 3–5 μm, 75% porosity, and 2.5 mm thick. In addition to capillary pumping, in LHPs, the wick structure is also expected to provide a thermal and hydraulic lock to minimize backconduction of heat and prevent any reverse flow of vapor to the CC via the wick. These functionalities were effectively performed by nickel wick due to its relatively low thermal conductivity and fine pore size. Here, the presence of the liquid inside the small pored wick generates enough capillary pressure to prevent reverse flow of vapor through it. It should be noted that on one side, low thermal conductivity of the wick structure is desirable to reduce the heat leaks to the CC while at the same time, high thermal conductivity is advantageous at the evaporating zone (i.e., wick wall interface) to improve heat transfer process. Such a conflicting situation is best dealt by the nickel wick whose thermal conductivity is neither very low (like plastic wicks) nor very high (like copper wick). Unlike the conventional heat pipe, the capillary structure is localized in the heat acquisition zone of the mLHP evaporator. This allows the transport lines to be made from smooth walled tube that offers low hydraulic resistance to fluid flow and can be easily bent for integration inside the limited available space within the equipment enclosure.

A system of vapor removal passages, as shown in Fig. 3, consisting of 20 microchannels with a rectangular cross section of 0.7 mm depth and 0.5 mm width (Fig. 2(*b*)) were machined on the inside of the evaporator active zone with an area of 22×22 mm^2. The evaporator active zone is the portion of the evaporator where the heat source is actually attached. For the transport lines, copper tubes with an internal diameter of 2 mm were used. Heat load applied at the evaporator was transferred over a distance of 150 mm via the vapor line that was connected to the evaporation zone and lies inline with the system of vapor removal channels. The condensed liquid from the condenser was carried back to the evaporator via the liquid line, 290 mm length, which connects to the CC (Fig. 3).

For rejection of the latent heat transported from the evaporator, a fin-and-tube-type condenser was installed at the end of the vapor line. The condenser was 50 mm in length and 10 mm in thickness. It was provided with external fins measuring 20×10 mm^2 with a thickness of 0.2 mm and fin pitch of 1 mm. The charging of the mLHP was done via a copper line attached to the CC. Water was used as the heat transfer fluid due to its superior heat transfer characteristics and acceptability in electronic cooling. The quantity of water charged inside the loop was such that 50% of the CC should be occupied with the liquid at all times even when the mLHP is not operating. This helps to ensure that sufficient wetting of the wick has been accomplished before startup of the mLHP is initiated. If the wick is improperly wetted, the chances of startup failure and consequential high thermal resistance of the mLHP increase.

The design of the mLHP was performed on the basis of the maximum capillary pressure generated by the porous structure on the working fluid, which depends on the surface tension coefficient (σ_l) of the liquid working fluid and mean effective pore radius (r_{eff}) of the porous structure and is given by Young-Laplace equation [22] as

$$(\Delta P_{\text{cap}})_{\max} = \frac{2\sigma_l}{r_{\text{eff}}} \tag{1}$$

For the proper startup and continuous operation of the mLHP, the capillary pressure developed inside the fine pore wick must be greater than or equal to the total pressure loss incurred by the working fluid inside the loop. This necessary condition for the serviceability of the LHP should be satisfied by the loop design and can be stated in mathematical form as follows:

$$(\Delta P_{\text{cap}})_{\max} \geqslant \Delta P_v + \Delta P_l + \Delta P_g = \Delta P_t \tag{2}$$

The total pressure drop in the loop ΔP_t is the sum of the pressure losses due to vapor flow ΔP_v, liquid flow ΔP_t, and hydrostatic pressure loss due to the tilts of the device in gravity force field ΔP_g.

The pressure drop due to friction losses in liquid or vapor flow through the loop (for laminar or turbulent flows, circular or noncircular pipes, smooth or rough surfaces) is given by Darcy-Weisbach equation [23] as

$$\Delta P = f\frac{L}{D}\frac{\rho V^2}{2} \tag{3}$$

where f, a dimensionless quantity and function of Reynolds number, is the Darcy friction factor. For perfectly smooth pipes/channels, friction factor f is given by

$$f = \frac{64}{\text{Re}} \quad \text{Re} < 2300 \quad \text{(laminar flow)} \tag{4}$$

$$f = \frac{0.316}{\text{Re}^{0.25}} \quad \text{Re} > 2300 \quad \text{(turbulent flow)} \tag{5}$$

The vapor pressure loss in the vapor line is the major resistance that the fluid has to overcome in order to circulate continuously under capillary head.

The pressure drop due to liquid flow through the wick thickness ΔP_w can be determined by Darcy's law of fluid flow through porous media that denotes the effect of applied pressure on the flow rate of fluid for the given physical properties of the porous structure [24] and is given as

$$\Delta P_w = \left(\frac{t_w}{A_w}\right)\left(\frac{\mu_l}{\rho_l h_{lv}}\right)\left(\frac{1}{k_p}\right)Q^{\bullet} \tag{6}$$

where k_p is the permeability of the evaporator wick and describes its ability to transport liquid under an applied pressure gradient. As evident from Eq. (6), pressure losses are magnified for smaller values of permeability.

In the present case, as the testing was done in the horizontal configuration, therefore the hydrostatic resistance due to the tilts of the device in gravitational field was nonexistent.

The effective thermal conductivity of the wick is very important parameter to be considered during the selection of the wick material and design of the capillary evaporator. It is a useful parameter to correctly calculate the wick thickness, which is the most critical factor related to evaporator design. Alexander [25] gives a relation to calculate the effective thermal conductivity k_{eff} of the homogeneous wick structure as

$$k_{\text{eff}} = k_l\left(\frac{k_l}{k_w}\right)^{-(1-\varepsilon)^{\alpha}} \tag{7}$$

where α is the constant equal to 0.59.

3 Testing Method

Figure 1 shows the experimental setup for testing the mLHP prototype. The thermal performance of the mLHP was evaluated by using a heat load simulator with an active footprint of $10 \times 10\ \text{mm}^2$. In this case, the heat simulator imitates a compact microprocessor of the next generation electronics such as notebooks and offers high heat fluxes to carry out rigorous thermal testing of the mLHP. The heat source provided a concentrated heat load to approximately 20% of the evaporator active zone. It can thus be classified as the local heating mode of the mLHP evaporator. The heat simulator was made from a copper block with machined holes in which two cartridge type heaters were inserted. During testing, the source was attached symmetrically to the center of the evaporator active face. The condenser cooling was provided by forced convection of ambient air with an inlet temperature of $(24\pm2)^\circ\text{C}$ that was provided by a centrifugal fan with a volumetric flow rate of $0.1\ \text{m}^3/\text{min}$.

To measure temperature, T-type thermocouples with an accuracy of $\pm0.5^\circ\text{C}$ were installed at different locations along the external surface of the mLHP. Figure 1(a) shows the location of these temperature measurement points. A Keyence Thermo Pro 3000 was used as data acquisition unit to monitor and record readings from these thermocouples during transient as well as steady state operation of the loop. The thermal characteristics of the mLHP were measured on the basis of the junction temperature, saturated vapor temperature, maximum heat capacity, evaporator thermal resistance (R_e), mLHP evaporator to condenser thermal resistance (R_{ec}), and total thermal resistance (R_t) of the device. Thermal resistances were calculated on the basis of relations (8)–(10) given below.

Evaporator thermal resistance

$$R_e = \frac{(T_j - T_v)}{Q^{\bullet}} \tag{8}$$

mLHP evaporator to condenser thermal resistance

$$R_{\text{ec}} = \frac{(T_v - T_c)}{Q^{\bullet}} \tag{9}$$

Total thermal resistance

$$R_t = \frac{(T_j - T_a)}{Q^{\bullet}} \tag{10}$$

In the above equations, T_j is the junction temperature that was measured at the interface of the heater and the evaporator active zone. For measuring the junction temperature, a thermocouple was installed in a fine groove that was machined on the active face of the heat load simulator. Such a groove was difficult to machine on the evaporator surface as the thickness of the wall was very small (i.e., 0.8 mm). In order to quantify the thermal contact resistance between the heater surface and the evaporator heated wall, test was conducted under the same experimental conditions by simulating the interface using copper plate. A copper plate was provided with a thermocouple inside the groove that was machined on it. This plate was then installed between heater and evaporator wall and the contact resistance between the heater and contacting plate surface was determined. As an outcome of this test, the contact resistance was measured to be $0.07-0.1\ \text{cm}^2\ {}^\circ\text{C/W}$. The low values of the contact resistance were achieved by confirming the mating faces to be truly flat and using appropriate thermal fillers and contact pressure. Special care was taken to reproduce the same interface conditions while mounting mLHP evaporator on the heater block. T_v denotes the saturation vapor temperature at the outlet of the evaporator, i.e., $T_{\text{evap-out}}$ in Fig. 1(a). For the determination of the mLHP evaporator to condenser thermal resistance (R_{ec}), evaporator temperature was taken to be equal to the saturation vapor temperature T_v at the evaporator outlet, i.e., $T_{\text{evap-out}}$, and condenser temperature (T_c) was calculated by taking mean of the condenser inlet ($T_{\text{cond-in}}$) and condenser outlet ($T_{\text{cond-out}}$) temperatures. The thermocouple point T_a was suspended in the air to measure the temperature of the ambient air. The heat load $Q^{\bullet}$ input to the mLHP evaporator was controlled and measured by using a wattmeter with an accuracy of ±0.1 W. During the testing, the input power to the heat source was increased in increments of 5 W.

In the calculation of the thermal resistance R, the maximum error can be estimated on the basis of the uncertainty in the measurement of temperature by thermocouple (i.e., $\pm0.5^\circ\text{C}$) and heat load by wattmeter (i.e., ±0.1 W). The errors in the reported values of the thermal resistances were calculated in the entire range of the applied heat load and lie between 1% and 7.8%. The heat simulator and the evaporator body are exposed to the ambient; hence, some part of the applied heat load is lost to the external environment due to the losses associated with natural convection and radiation to the ambient air. A simplified model [23] was designed to calculate these losses and approximated them to be in the range of 7–10% of the input power.

In the experiments, the testing of the mLHP prototype was performed with the evaporator and condenser at the same horizontal level. The effect of the gravity on the device performance was not studied in this phase of experiments. In the tests, the start-up and steady state behavior of the device was studied in detail. Startup of the mLHP was assumed to occur when both the evaporator and the condenser had warmed and the difference between the evaporator outlet and the condenser inlet was less than 1°C. If the

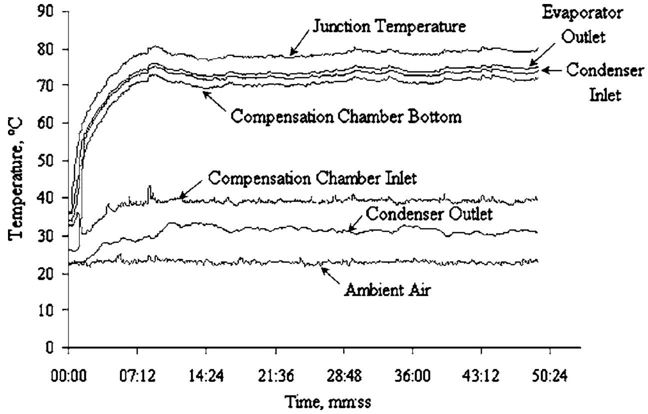

Fig. 4 Startup of mLHP at 20 W input heat load

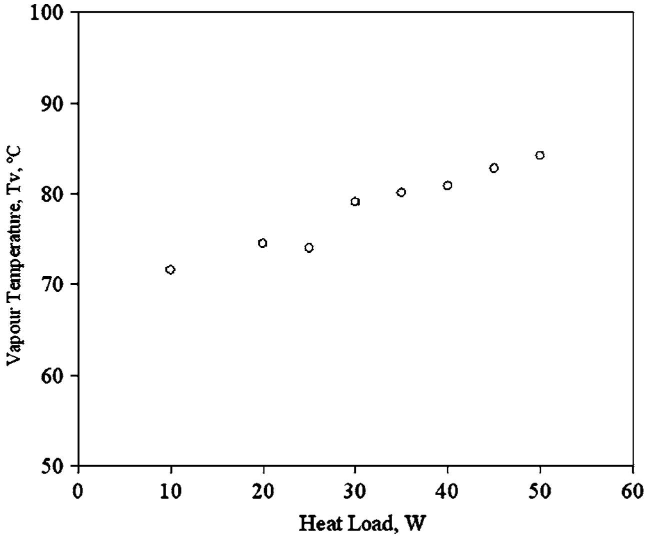

Fig. 5 Head load dependence of the vapor temperature for the mLHP

temperature of the evaporator rises continuously on the initial application of heat load and the condenser does not follow, start-up failure is supposed to occur. Steady state at a given heat load was characterized by the constant temperature of the mLHP evaporator.

4 Results and Discussion

Figure 4 shows the startup of the mLHP for an input heat load of 20 W. As the heat load is applied to the evaporator active zone, an initial rise in the junction temperature is noted. This is followed by the vaporization of the liquid inside the evaporation zone. The resulting vapor displaces the liquid from the vapor removal channels and vapor line around the loop into the CC. In Fig. 4, this is shown by the sudden rise in the temperature first at the evaporator outlet and then at the condenser inlet, due to the vapor flow inside the vapor line. In Fig. 1(*b*), the shaded parts of the mLHP show the portion occupied by the liquid during steady state while the blank portion is filled with vapor. The successful startup of the mLHP is registered by the initiation of the fluid circulation around the loop, which is marked by the stabilization of the temperature at the junction and other points on the mLHP, as shown in Fig. 4. As a necessary condition of loop serviceability, the capillary pressure generated at the liquid-vapor interface of the wick should be equal to or greater than total pressure losses taking place inside the system. It is made possible by self-adjustment of the meniscus curvature at the evaporating face of the wick so that sufficient capillary pressure is generated to keep the fluid in continuous circulation around the loop.

A typical performance curve of the mLHP is shown in Fig. 5, which illustrates the heat load dependence of the saturation vapor temperature. It is observed that the vapor or loop operating temperature presents a rising trend with increasing heat load. The saturation temperature of the mLHP is an outcome of multitude of factors including the heat exchange processes inside the CC and the vapor saturation conditions inside the evaporator. In the mLHP, apart from other variables, the CC temperature also influences the saturation conditions inside the mLHP evaporator due to its thermal and hydraulic linkages with the evaporation zone. It means that any change in the saturation condition inside the CC registers a direct influence on the loop operating temperature. At a particular heat load, the CC temperature is influenced by three main heat transfer processes, i.e., heat exchange between the evaporation zone and the CC due to the conduction through the evaporator walls and wetted wick, heat exchange between the returning subcooled liquid and the CC, and lastly heat exchange between the CC and ambient due to natural convection and radiation losses. For this reason, the condenser should be designed to provide sufficiently subcooled liquid to the CC to be able to counterbalance the effect of the backconducted heat. It should be noted that the volume flow rate of the returning subcooled liquid increases with the input power but at high heat loads, a larger portion of the condenser is acquired by two phase, which reduces the degree of subcooling for the returning liquid. Contrary to this, the parasitic heat leaks from the evaporator to the compensation chamber decrease with increase in input power due to the presence of large liquid inventory inside the CC at high loads. As a result, the saturation temperature of the CC depends on the outcomes of these two competitive processes. At high powers, the vapor mass output by the evaporator also increases that increases the saturation pressure and thus operating temperature. In light of the above discussion, it is expected that the rise in the loop saturation temperature with the applied heat load results as an outcome of heat exchange processes inside the CC and increase in the vapor fraction inside the mLHP at high heat load that increases the loop saturation pressure.

The maximum heat load capacity of the thermal control device is largely limited by the maximum permissible temperature at the heat source. In the electronics cooling applications, the temperature of the silicon microprocessor (i.e., heat dissipating source) should be maintained below $(100\pm5)\,^{\circ}\mathrm{C}$ limit. Using the present design of mLHP, a maximum heat capacity of 50 W was successfully transferred over a distance of 150 mm while maintaining the junction temperature below $98.5\,^{\circ}\mathrm{C}$. Figure 6 presents the plot for the junction temperature with respect to the applied heat load. The high heat transport capacity with the novel evaporator design, which corresponds to a heat flux as high as $50\ \mathrm{W/cm^2}$, clearly confirms the viability of the proposed design for the cooling of compact electronic devices.

The startup of the mLHP is a very complicated phenomenon, which is affected by a large number of factors that include pre startup states in the evaporator and CC, charged liquid inventory, value of applied heat load, heat leaks across the wick, and orientation of the loop. Depending on the pre-start-up fluid distribution inside the evaporator and CC, four different types of startup behavior can result [26]. It was suggested that the condition when liquid-vapor interface is already present inside the evaporation zone is the most favorable for reliable startup of mLHP. When the evaporator is flooded with liquid and an interface is present inside the CC, the startup is most difficult and needs a high heat load to initiate fluid motion. Even if the evaporator is not flooded with liquid, still there exists some minimum value of heat load that is required for the reliable startup of the device without use of any active control. This minimum heat load is associated with the development of the minimum temperature and thus pressure dif-

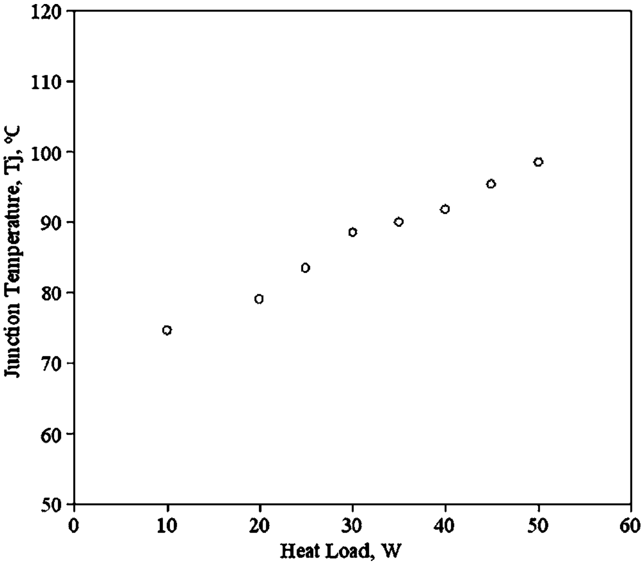

Fig. 6 Interface temperature versus applied heat load

ference across the wick structure that is required for the initiation of the fluid circulation during the startup of the loop. It is difficult to build up such a temperature difference at low heat loads due to heat leaks across the wick structure. Particularly, if the vapor channels are flooded with the liquid charge, a high degree of superheat is required between the evaporator active wall and the liquid to initiate nucleate boiling in the bulk charge. This is necessary for clearing liquid out of the evaporator and vapor line. In the present design of the mLHP, the evaporator body was made of high conductive copper material with an efficient system of vapor removal passages that provide high convective heat transfer. The device was able to startup very reliably for heat loads as low as 10 W.

Figure 7 depicts the startup of the mLHP for 10 W input power. It is evident from the startup trend that the mLHP was able to achieve relatively stable temperature profile for the junction temperature without any major performance issue. However, some temperature oscillations were observed at the evaporator outlet and transport lines. Particularly, at the exit of the vapor line (i.e., condenser inlet) and liquid line (i.e., CC inlet), the extent of the temperature fluctuations was high. These thermal oscillations are expected to be the combined effect of the oscillations in the heat leaks (from the evaporator to the CC) and returning subcooled liquid temperature (from the condenser) at low heat loads [27,28]. From Fig. 7, it is observed that condenser inlet and CC inlet temperature are totally (i.e., 180°C) out of phase while evaporator outlet temperature is more or less in phase with the condenser inlet temperature. If the plot is read along the marker A-B, it is noted that periodic increase in the vapor flow from the evaporator, which is indicated by rise in evaporator outlet temperature, results in the slight drop in the junction and CC body temperature. Here, the increase in the evaporator outlet (and also vapor line) temperature is due to the increased vapor flow inside the vapor line, which brings about its temperature close to the true saturation temperature inside the evaporator. For the same reason, the increased flow rate of the vapor raises the condenser inlet temperature. As a consequence, the flowing vapor displaces some portion of liquid from the condenser to the CC, thereby reducing the CC inlet temperature due to liquid flow through it. Earlier, the high CC inlet temperature was due to the backconduction of heat from the source via evaporator/CC body. The displaced liquid charge inside the CC contributes in the reduction of the CC and evaporator interface (or junction) temperature. As sufficient power is not available to keep adequate mass flow rate of vapor due to the heat leaks across the wick structure, the reverse temperature trend follows, which increases the temperature at CC inlet while at the same time reduces condenser inlet and evaporator outlet temperature, and thus the cycle is repeated and so forth. To some extent, these thermal and hydraulic oscillations are also related to an inadequate charge inside the CC at low heat loads that increase the effect of parasitic heat leaks to the CC [29]. For still lower input powers, it was observed that the amplitude of these resulting oscillations increases further that makes it difficult for the mLHP to achieve steady state operation. It should be noted that the occurrence of these thermal oscillations is the subject of ongoing investigation and has also been observed by other researchers worldwide.

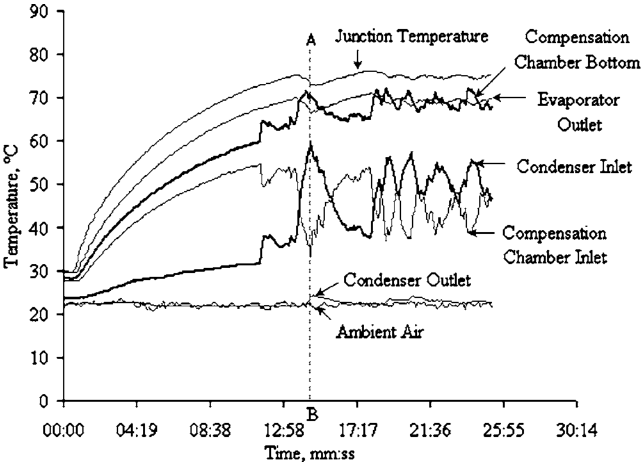

Fig. 7 mLHP startup at 10 W input heat load showing notable temperature oscillations at the evaporator outlet and exit of the vapor and liquid line

In the present design of the mLHP evaporator, the CC is coplanar with the evaporator body and also located in the proximity of the active zone. The bulk quantity of the liquid inside the CC makes contact with the metal wall rather than the wick structure. As a consequence of such design, a major part of the backconducted heat is communicated to the CC liquid through the high conductive copper wall. For that reason, the extent of the parasitic heat loads from the heat source to the CC increases. However, with the sufficient subcooling provided in the condenser to the returning liquid, the mLHP was able to perform satisfactorily in the test range of the applied heat load.

Figure 8 shows the dependence of the mLHP evaporator to condenser thermal resistance (R_{ec}) on the applied heat load. As the input power to the heat source rises from 10 W to 50 W, there was a decrease in the R_{ec} value from 2.47°C to 0.67°C/W. At low heat loads, the thermal resistance is comparatively higher than at high loads. A similar trend was observed for the total thermal resistance (R_t) versus the input power, as presented in Fig. 9. In this case, R_t lies in the range of 5.23–1.5°C/W for 10–50 W input power and is comparable with the thermal resistance of the mLHP prototypes designed by other researchers [30]. The steady decrease in the thermal resistance with the increase in the input heat load is due to the favorable effect of the increase in fluid flow rate at high input power. For low heat loads, the CC is only partially filled with the liquid inventory, which results in low thermal capacity of the CC for the absorption of the heat leaks from the evaporator. As a consequence, the CC temperature rises under the influence of the heat flows from the evaporation zone, which marks the corresponding rise in the evaporator temperature. With the increase in the input heat load, the liquid quantity inside the CC increases, which provides better absorption of the heat leaks from the active zone without any notable temperature rise. In addition, at high heat loads, the volume flow rate of the liquid passing through the CC and porous matrix increases, which re-

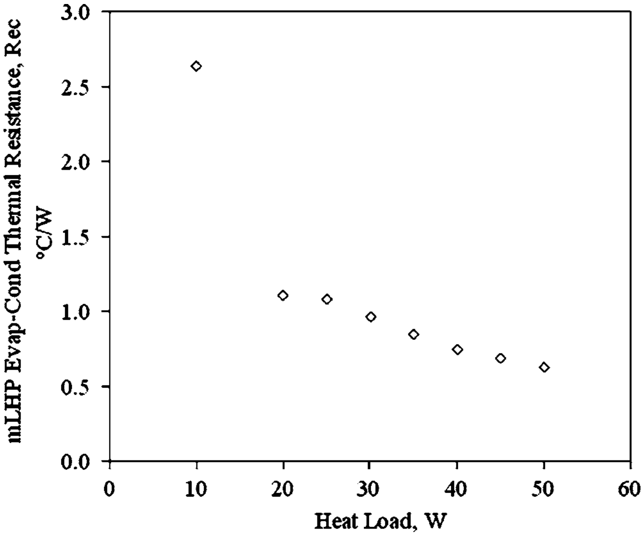

Fig. 8 mLHP evaporator to condenser thermal resistance versus applied heat load

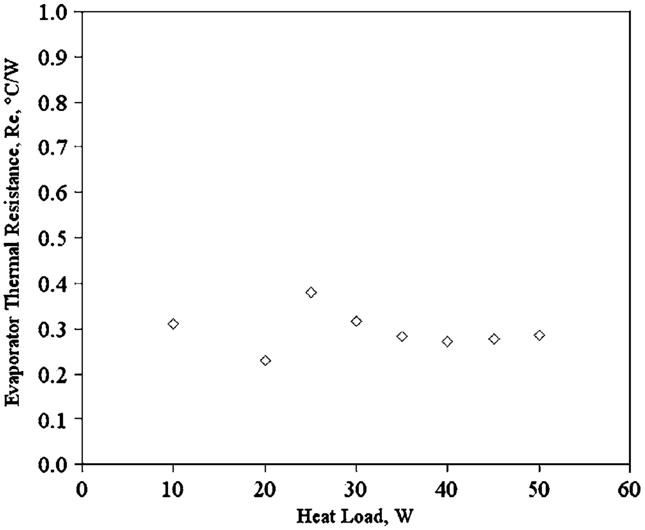

Fig. 10 Evaporator thermal resistance versus applied heat load

duces the fraction of the back heat flow through the wick structure. The improvement in the thermal resistance at the high heat load is also attributed to the increase in the merit number of the water at high temperatures [19,31]. Merit number (M) is used to rank the heat pipe working fluid and defined as the ratio of the product of liquid density ρ_l, liquid surface tension σ_l, and latent heat, h_{iv}, to the liquid viscosity μ_l. It is stated in Ref. [22] as

$$M = \frac{\rho_l \sigma_l h_{lv}}{\mu_l} \tag{11}$$

Also, at higher temperatures, the vapor density and vapor pressure of water increase, which tends to decrease the vapor pressure losses in the vapor line and evaporator grooves and thus the thermal resistance of the mLHP at high heat loads.

The resistance to the heat transfer process from the source-evaporator junction to the working fluid was measured on the basis of the evaporator thermal resistance (R_e), as defined by Eq. (8) and plotted in Fig. 10. In the range of applied heat load, low values for R_e that lie within 0.23–0.38°C/W were obtained. In the current evaporator design, this was made possible by the efficient system of vapor removal channel and high conductive copper material for the evaporator wall that provided minimal resistance to the heat acquisition process.

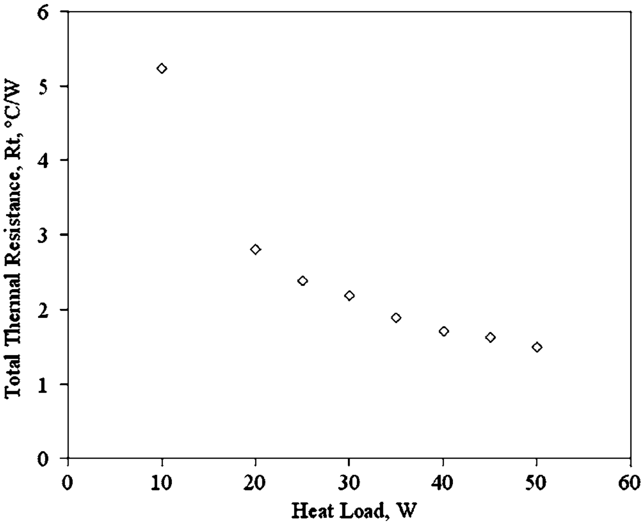

Fig. 9 Total thermal resistance versus applied heat load

5 Conclusions

The study can be summarized as follows:

- A mLHP with a novel design of evaporator of 5 mm thickness was developed for the thermal management of high end microprocessors for compact electronic devices such as slim notebook computers.
- With forced air cooling of the condenser, the device was able to transfer a heat flux as high as 50 W/cm^2 over a distance of up to 150 mm while maintaining the junction temperature below 100°C. At the maximum heat load of 50 W, the junction temperature was 98.5°C.
- For heat load in the range of 10–50 W, the total thermal resistance (R_t) of the mLHP was 1.5–5.23°C/W. The minimum value of 1.5°C/W for R_t was achieved at 50 W. For the mLHP evaporator to condenser thermal resistance (R_{ec}), the corresponding minimum value of 0.62°C/W was obtained.
- The device was able to start up reliably in the range of the applied heat load. However, for low heat loads ($\leqslant$10 W), temperature oscillations were noted in the system. The magnitude of these oscillations was high at the exit of the vapor and the liquid lines. For the junction the temperature fluctuations were minimal and it was possible to achieve virtually steady state conditions. It is expected that the oscillations where they occur are initiated by the combined effect of the fluctuations in the parasitic heat leaks and the temperature of the returning subcooled liquid to the CC at low heat loads.
- For the designed mLHP, the copper-water combination performs very efficiently in the range of the operating temperatures. Water served as an excellent heat transfer working fluid with superior thermal characteristics and acceptability in electronic cooling applications.
- Overall, the new design of the mLHP evaporator showed acceptable thermal performance for high powered chip cooling application. Also, the proposed design can be easily integrated inside the compact enclosure of modern electronic equipment.

Acknowledgment

The authors would like to thank Dr. Yuji Saito, Dr. Thang Nguyen, and Mr. Vijit Wuttijumnong from Fujikura Ltd. Japan for their valuable discussion and technical support throughout the project.

Nomenclature

A = area, m^2
D = diameter, D
f = Darcy friction factor
h_{lv} = latent heat of vaporization, J/kg
k_p = permeability of porous structure, m^2
k = thermal conductivity, W/m K
L = length, m
M = Merit number, W/m^2
$Q^{\bullet}$ = heat load, W
r = pore radius of porous structure, m
R = thermal resistance, °C/W, K/W
t = thickness, m
T = temperature, °C, K
V = velocity, m/s
$(\Delta P_{\text{cap}})_{\max}$ = maximum capillary pressure generated by the wick on liquid, Pa
ΔP = pressure difference, Pa

Greek Symbols

σ = surface tension, N/m
ρ = density, kg/m^3
μ = viscosity, Pa s
ε = porosity,%

Subscripts

a = ambient
cc = compensation chamber
c = condenser
e = evaporator
eff = effective
g = gravity
j = junction
l = liquid
t = total
v = vapor
w = wick

Constant

α = 0.59 (as in Eq. (7))

References

[1] Mochizuki, M., Saito, Y., Nguyen, T., Wuttijumnong, V., Wu, X., and Nguyen, T., 2005, "Revolution in Fan Heat Sink Cooling Technology to Extend and Maximize Air Cooling for High Performance Processors in Laptop/Desktop/Server Application," *Proceedings of the IPACK2005*, San Francisco, CA, ASME Paper No. 73286.

[2] Saucius, I., Prasher, R., Chang, J., Erturk, H., Chrysler, G., Chiu, C., and Mahajan, R., 2005, "Thermal Performance and Key Challenges for Future CPU Cooling Technologies," *Proceedings of the IPACK2005*, San Francisco, CA, ASME Paper No. 73242.

[3] Mochizuki, M., Nguyen, T., Mashiko, K., Saito, Y., Nguyen, Ti., Wuttijumnong, V., and Wu, X., 2004, "Practical Application of Heat Pipe and Vapour Chamber for Cooling High Performance Personal Computer," *Proceedings of the 13th International Heat Pipe Conference*, Shanghai, P. R. China, pp. 23—30.

[4] Moon, S. H., Hwang, G., Yun, H. G., Choy, T. G., and Kang, Y. II., 2002, "Improving Thermal Performance of Miniature Heat Pipe for Notebook PC Cooling," Microelectron. Reliab., **42**, pp. 135–140.

[5] Nguyen, T., Mochizuki, M., Mashiko, K., Sauciuc, I., and Boggs, R., 2000, "Advanced Cooling System Using Miniature Heat Pipes in Mobile PC," IEEE Trans. Compon. Packag. Technol., **23**(1), pp. 86–90.

[6] Xie, H., Aghazadeh, M., Lui, W., and Haley, K., 1996, "Thermal Solutions to Pentium Processors in TCP in Notebooks and Sub-Notebooks," IEEE Trans. Compon., Packag. Manuf. Technol., Part A, **19**(1), pp. 54–65.

[7] Agata, H., Kiyooka, F., Mochizuki, M., Mashiko, K., and Saito, Y., 2004, "Advanced Thermal Solution Using Vapour Chamber Technology for Cooling High Performance Desktop Computer," *Proceedings of the First International Symposium on Micro and Nano Technology*, Honolulu, HI, Paper No. 15331.

[8] Hironori, K., Hitoshi, S., and Takeshi, N., 2005 "High Performance Liquid Cooling Module for Electronic Equipment," Hitachi Cable Review Report No. 24.

[9] Jiang, L., Mikkelsen, J., Koo, J. M., Huber, D., Yao, S., Zhang, L., Zhou, P., Maveety, J. G., Prasher, R., Santiago, J. G., Kenny, T. W., and Goodson, K. E., 2002, "Closed-Loop Electroosmotic Microchannel Cooling System for VLSI Circuits," IEEE Trans. Compon. Packag. Technol., **25**(3), pp. 347–355.

[10] Maydanik, Y. F., and Fershtater, Y. G., 1997, "Theoretical Basis and Classification of Loop Heat Pipes and Capillary Pumped Loops," *Proceedings of the Tenth International Heat Pipe Conference*, Stuttgart, Germany, Keynote Lecture X-7.

[11] Hoang, T. T., O'Connell, T. A., Ku, J., Butler, C. D., and Swanson, T. D., 2003, "Miniature Loop Heat Pipes for Electronic Cooling," *Proceedings of the IPACK2003*, Maui, HI, ASME Paper No. 35245.

[12] Kaya, T., and Ku, J., 2003, "Thermal Operational Characteristics of a Small Loop Heat Pipe," J. Thermophys. Heat Transfer, **17**, pp. 464–470.

[13] Delil, A. A. M., Maydanik, Y. F., and Gerhart, C., 2003, "Development of Different Novel Loop Heat Pipes Within the ISTC—1360 Project," *Proceedings of the 33rd International Conference on Environmental Systems*, Vancouver, Canada, SAE Paper No. 2003-01–2383.

[14] Chu, C. I., Wu, S. C., Chen, P. L., and Chen, Y. M., 2004, "Design of Miniature Loop Heat Pipe," Heat Transfer Asian Res., **33**(1), pp. 42–52.

[15] Singh, R., Akbarzadeh, A., Mochizuki, M., Nguyen, T., and Wuttijumnong, V., 2005, "Experimental Investigation of the Miniature Loop Heat Pipe With Flat Evaporator," *Proceedings of the IPACK2005*, San Francisco, CA, ASME Paper No. 73498.

[16] Chernysheva, M. A., Vershinin, S. V., and Maydanik, Y. F., 2002, "Development and Test Results of Loop Heat Pipes With a Flat Evaporator," *Proceedings of the 12th International Heat Pipe Conference*, Moscow Russia, pp. 134–138.

[17] Delil, A. A. M., Baturkin, V., Fridrichson, Y., Khmelev, Y., and Zhuk, S., 2002, "Experimental Results of Heat Transfer Phenomena in a Miniature Loop Heat Pipe With a Flat Evaporator," *Proceedings of the 12th International Heat Pipe Conference*, Moscow, Russia, pp. 126–133.

[18] Kiseev, V. M., Nepomnyashy, A. S., Gruzdova, N. L., and Kim, K. S., 2003, "Miniature Loop Heat Pipes for CPU Cooling," *Proceedings of the Seventh International Heat Pipe Symposium*, Jeju, Korea.

[19] Maydanik, Y. F., Vershinin, S. V., Korukov, M. A., and Ochterbeck, J. M., 2005, "Miniature Loop Heat Pipes: A Promising Means for Cooling Electronics," IEEE Trans. Compon. Packag. Technol., **28**(2), pp. 290–296.

[20] Singh, R., Akbarzadeh, A., Mochizuki, M., Saito, Y., Nguyen, T., Kiyooka, F., and Wuttijumnong, V., 2006, "Thermal Performance of Miniature Loop Heat Pipe Operating Under Different Heating Modes," *Proceedings of the ITherm 2006*, San Diego, CA, pp. 557–562.

[21] Cheung, K.-H., Hoang, T. T., Ku, J., and Kaya, T., 1998, "Thermal Performance and Operational Characteristics of Loop Heat Pipe (NRL LHP)" *Proceedings of the 28th International Conference on Environmetal Systems*, Danvers, MA, SAE Paper No. 981813.

[22] Dunn, P. D., and Reay, D. A., 1994, *Heat Pipes*, Pergamon, Oxford.

[23] Cengel, Y. A., and Turner, R. H., 2001, *Fundamentals of Thermal-Fluid Sciences*, McGraw Hill, New York, Chaps. 18 and 19.

[24] Faghri, A., 1995, *Heat Pipe Science and Technology*, Taylor & Francis, London.

[25] Alexander, E. G., 1972, "Structure-Property Relationships in Heat Pipe Wicking Materials," Ph.D. thesis, North Carolina State University, Raleigh, NC.

[26] Maydanik, Y. F., Solodovnik, N, and Fershtater, Y., 1995, "Investigation of Dynamic and Stationary Characteristics of a Loop Heat Pipe," *Proceedings of the Ninth International Heat Pipe Conference*, Albuquerque NM, pp. 1002–1006.

[27] Ku, J., Ottenstein, L., Kobel, M., Rogers, P., and Kaya, T., 2001, "Temperature Oscillations in Loop Heat Pipe Operation," AIP Conf. Proc. **552**(1), pp. 255–262.

[28] Chen, Y., Groll, M., Mertz, R., Maydanik, Y. F., and Vershinin, S. V., 2005, "Steady-State and Transient Performance of a Miniature Loop Heat Pipe," *Proceedings of the Third International Conference on Microchannels and Minichannels*, Toronto, Canada, Paper No. 75122.

[29] Mo, Q., Liang, J., 2006, "Operational Performance of a Cryogenic Loop Heat Pipe with Insufficient Working Fluid Inventory," Int. J. Refrig., **29**, pp. 519–527.

[30] Pastukhov, V. G., Maidanik, Y. F., Vershinin, C. V., Korukov, M. A., 2003, "Miniature Loop Heat Pipes for Electronics Cooling," Appl. Therm. Eng., **23**, pp. 1125–1135.

[31] Devarakonda, A., Xiong, D., and Beach, D. E., 2005, "Intermediate Temperature Water Heat Pipe Tests," *Proceedings of the Space Technology and Applications International Forum*, Albuquerque, NM, NASA Report No. TM-2005-213581.

Journal of Heat Transfer

Technical Briefs

The Parametric Study of an Innovative Offset Strip-Fin Heat Exchanger

Clayton Ray De Losier

Sundaresan Subramanian

Valery Ponyavin

Yitung Chen[1]
e-mail: uuchen@nscee.edu

Nevada Center for Advanced Computational Methods,
University of Nevada, Las Vegas,
4505 Maryland Parkway,
P.O. Box 454027,
Las Vegas, NV 89154-4027

Anthony E. Hechanova
Harry Reid Center for Environmental Studies,
University of Nevada, Las Vegas,
4505 Maryland Parkway,
P.O. Box 454027,
Las Vegas, NV 89154-4027

Per F. Peterson
Nuclear Engineering Department,
University of California, Berkeley,
Berkeley, CA 94720-1776

Offset strip-fin heat exchangers have numerous applications throughout various industries because they can provide a large amount of heat transfer area in a small volume. The widespread use of the offset strip-fin design has ensured that there are numerous dimensional variations and shown that changes in dimensional parameters affect performance. It is then important to understand how the geometry of an offset strip-fin heat exchanger can affect its performance. Therefore, an investigation into the parametric effects on the global performance of an innovative high-temperature offset strip-fin heat exchanger was numerically performed in this study, where the numerical solution was obtained through a finite-volume method. Computations were carried out for each of the heat exchanger's geometrical parameters: fin thickness (t)*, fin length* (l)*, channel height* (H)*, spanwise pitch* (p_x)*, and the newly introduced gap parameter* (g)*. Also, the effects of rounding the fins leading and trailing edges were investigated, while the heat exchanger's volume, mass flow rates, and inlet temperatures were kept constant. The results are presented in the form of pressure drops and heat transfer rates, and the coefficient of performance parameter shows that fins with rounded leading and trailing edges outperform fins with rectangular edges.* [DOI: 10.1115/1.2755068]

Keywords: heat exchanger, offset strip-fin, rounded fins, gaps, compact

Introduction

The understanding of offset strip-fin heat exchangers has been extensively investigated in the past, particularly the hydrodynamic and thermal hydraulic effects of fin thickness, fin length, and spanwise pitch of fins with rectangular edges. There are several books [1–4] and numerous experimental and numerical investigations outlining these performance characteristics.

A brief review of experimental works shows that Norris and Spofford [5] were first in the field, and they determined the effects that fin thickness, fin length, and spanwise pitch had on the heat transfer coefficient in an array of staggered strip fins. They also investigated the effect of fin thickness on friction factor. Kays [6] looked at the effects of fin thickness on the heat transfer performance and friction factor in an array of strip-fin surfaces. Shortly after Kays' study, Briggs and London [7] determined the effects that spanwise pitch had on the heat transfer coefficient and pressure drop in a small array of offset rectangular-fin surfaces. Sparrow and Hajiloo [8] later performed an investigation similar to Kays' and determined the effects of fin thickness on the Nusselt number and friction factor in an array of staggered plates. The effect of fin thickness and fin length on a pressure loss coefficient and Nusselt number was studied by Dubrovsky and Vasiliev [9]. Then, Dejong and Jacobi [10] investigated the effects of fin thickness, spanwise pitch, and channel height on the friction factor and Colburn factor in parallel-plate arrays. The idea of investigating the effects of the gap parameter in an array of staggered plates was presented earlier by Mullisen and Loehrke [11], but they failed to provide any data on the matter.

Numerical studies have also been used to present parametric effects in offset strip-fin heat exchangers. Suzuki et al. [12] performed an investigation into the 2D effects of fin thickness, fin length, and spanwise pitch on the heat transfer and pressure loss characteristics in an array of staggered plates. Xi et al. [13] performed an identical investigation with a small array of offset strip fins. Shah et al. [14] compiled a large number of numerical works on offset strip-fin heat exchangers and reported the effects of fin length on the friction factor and Colburn factor. The most recent study, done by Sparrow et al. [15], presented an analysis on a 3D offset strip-fin heat exchanger. But several parameters in the study

---

[1] Corresponding author.

Contributed by the Heat Transfer Division of ASME for publication in the JOURNAL OF HEAT TRANSFER. Manuscript received December 21, 2005; final manuscript received February 12, 2007. Review conducted by Yogesh Jaluria.

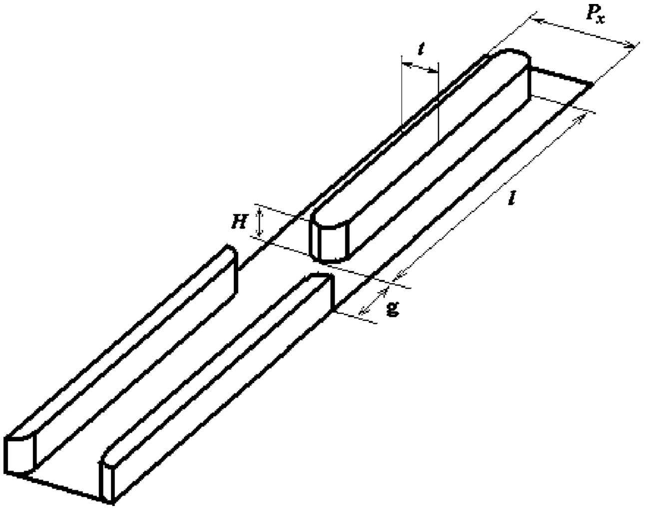

Fig. 1 One channel of the offset strip-fin heat exchanger with rounded fin edges

were lumped into unconventional dimensionless forms, making it extremely difficult to ascertain the effect that a single parameter had on the heat exchanger's performance.

Despite all of this work in the field of offset strip-fin heat exchangers, no one has yet published anything that covers the effects of height, gap, and rounded fin edges. All of the previous works have only covered rectangular-fin edges and displayed the effects of channel height in dimensionless form [10,16–19]. It is then the aim of this study to show the undocumented 3D effects of gap, channel height, and rounded fin edges on the pressure drop values and heat transfer rates in an offset strip-fin heat exchanger, while providing completeness by showing how fin thickness, fin length, spanwise pitch, and rectangular-fin edges also affected performance.

Model

The proposed model for this study employs a liquid silicon impregnated carbon composite (SiC) counterflow offset strip-fin heat exchanger, Fig. 1, which has a physical geometry defined by fin thickness (t), fin length (l), channel height (H), spanwise pitch (p_x), and gap (g). The complete offset strip-fin heat exchanger operates with a liquid to gas arrangement, where the liquid used is a liquid salt, FLINAK (46.5% LiF-11.5% NaF-42% KF), and the gas is helium. On the liquid salt side, an operating pressure of 0.1 MPa and an inlet temperature of 833 K are employed, while the helium side operates at 7 MPa and has an inlet temperature of 1273 K. These operating values as well as the mass flow rates and overall offset strip-fin heat exchanger dimensions are kept constant for each study. The mass flow rates are set at 26 kg/s for the helium side and 64 kg/s for the liquid salt side. Also, the overall dimensions of the offset strip-fin heat exchanger are kept constant at $1 \times 1 \times 0.4\ \mathrm{m}^3$ (height × width × length).

Each fluid is modeled in steady state while using incompressible flow, constant properties, and the appropriate flow regime. Transitional flow is used for the helium side, Re ~ 2500, and laminar flow is used for the liquid salt side, Re ~ 225. The use of constant properties for this model has been shown to have a negligible effect on the results [20]. Only the friction factor on the liquid salt side is affected, with a maximum possible error of 10%, as shown in Ref. [20]. The use of a steady state model for the liquid salt side is justified by Ref. [11], which shows that at Re $=500$, the flow in an offset strip-fin heat exchanger is steady. However, Ref. [11] also shows that unsteady flow starts to set in at Re$=1500$. This would then require the helium side to be modeled in an unsteady state, but this was not feasible due to enormous computational constraints. Currently, it took the 3D model outlined in this paper approximately 96 h to reach convergence, and there were approximately 40 different models run. Running these models using unsteady flow on the helium side would have increased convergence time by at least a factor of 2; thus, it is clear that time constraints made it computationally infeasible to run unsteady simulations.

Governing Equations

The offset strip-fin heat exchanger model presented in this paper is analyzed using FLUENT 6.2, which is a commercially available CFD software that uses the finite-volume method to discretize and solve the governing equations. The first set of equations, Eqs. (1)–(3), is used to define the necessary continuity, momentum, and energy equations, where ρ is the fluid density, μ is the dynamic viscosity, γ is the thermal conductivity, p is the static pressure, T is the temperature, E is the total energy, and δ_{ij} is the Kronecker delta. Equations (1)–(3) are written using a tensor notation; therefore, the x, y, z coordinates are denoted as x_1, x_2, x_3, and the x, y, z velocity components are denoted as u_1, u_2, u_3, where the vector components i, j, k equal 1, 2, 3. Neglecting body forces, the continuity, momentum, and energy equations can be written in the following Cartesian tensor form:

$$\frac{\partial \rho}{\partial t} + \frac{\partial}{\partial x_i}(\rho u_i) = 0 \tag{1}$$

$$\frac{\partial}{\partial t}(\rho u_i) + \frac{\partial}{\partial x_j}(\rho u_i u_j) = -\frac{\partial p}{\partial x_i} + \frac{\partial}{\partial x_j}\left[\mu\left(\frac{\partial u_i}{\partial x_j} + \frac{\partial u_j}{\partial x_i} - \frac{2}{3}\delta_{ij}\frac{\partial u_k}{\partial x_k}\right)\right] \tag{2}$$

$$\frac{\partial}{\partial t}(\rho E) + \frac{\partial}{\partial x_i}[u_i(\rho E + p)] = \frac{\partial}{\partial x_i}\left(\gamma \frac{\partial T}{\partial x_i}\right) \tag{3}$$

The turbulence modeling for the helium side had to compensate for less than fully turbulent flow; therefore, the standard k-ω turbulence model in FLUENT 6.2 was employed [20]. This model is based on the Reynolds averaged Navier-Stokes (RANS) equations, which govern the transport of the average flow quantities [21]. Neglecting the user-defined source terms, the transport equations for the turbulent kinetic energy κ and the specific heat dissipation rate ω can be obtained from Eqs. (4) and (5). With Γ being the effective diffusivity, G the generation of mean velocity gradients, and Y the dissipation of turbulence,

$$\frac{\partial}{\partial t}(\rho \kappa) + \frac{\partial}{\partial x_i}(\rho \kappa u_i) = \frac{\partial}{\partial x_j}\left(\Gamma_\kappa \frac{\partial \kappa}{\partial x_j}\right) + G_\kappa - Y_\kappa \tag{4}$$

$$\frac{\partial}{\partial t}(\rho \omega) + \frac{\partial}{\partial x_i}(\rho \omega u_i) = \frac{\partial}{\partial x_j}\left(\Gamma_\omega \frac{\partial \omega}{\partial x_j}\right) + G_\omega - Y_\omega \tag{5}$$

Numerical Methods

The offset strip-fin heat exchanger modeled in this study was simplified through the use of symmetry planes in the spanwise direction and along the top of the helium and liquid salt channels. It should be noted that at the plane of symmetry, the heat flux and normal velocity component are assumed to be zero; therefore, there is no convective heat flux across that symmetry plane, and the temperature gradients and tangential components of the velocity gradients in the normal direction are set to zero [21]. The uniform velocity inlet and pressure outlet boundary conditions available in FLUENT 6.2 were used at the inlets and outlets of the helium and liquid salt channels. Discretization was then carried out through a first order accurate upwind scheme [21], where cell face values are derived from quantities in the upstream cell, relative to the direction of the normal velocity.

The SIMPLE algorithm [21] and conjugate heat transfer (CHT) were used to solve for the pressure-velocity field and energy equation, where CHT solved the energy equation by taking conduction through the solid SiC material and convection through the fluids into account. No further thermal boundary conditions were required, since the segregated solver calculates the heat transfer directly from the solution in adjacent cells. The solutions were then considered converged once residual values for the continuity, momentum, and turbulence equations reached 10^{-5} and the energy equation reached 10^{-6}.

The mesh used for this study consisted of two regions. One region lied close to the fins, and it consisted of a fine mesh, in order to help capture the effects of vortices and flow separation. A second region between the fins consisted of a coarse mesh due to the relatively uniform flow in those areas. Only one channel of the model was studied in the grid independence study due to the large computational domain required to model the entire offset strip-fin heat exchanger. Three different meshes were chosen: a coarse mesh with 3540 nodes and 2508 hexahedral cells, a fine mesh with 73,182 nodes and 69,954 hexahedral cells, and a normal mesh with 22,419 nodes and 18,392 hexahedral cells. The difference in the results obtained from this study showed that there was no more than a 5% difference in the pressure profiles between the fine and course meshes for the helium channel, and there was an insignificant difference in the pressure profiles for all of the liquid salt channel meshes. A normal mesh was then used throughout the entire offset strip-fin heat exchanger model, since the fine mesh could produce the deteriorating phenomenon of negative volumes.

Results and Discussion

The previously outlined offset strip-fin heat exchanger was numerically modeled in order to determine the effects that any one given parameter would have on the heat exchanger's overall performance. Each parameter was varied a number of times in order to obtain a fairly broad view of the parametric effects, where a corresponding rounded fin edge model was performed for each simulation that employed rectangular-fin edges. The results from the studies using rounded fin edges show that they produce lower pressure drop and heat transfer rates in every case, although the effects are more or less prevalent depending on the case. In general, this can be explained by the fact that rounded fin edges reduce drag due to their aerodynamic shape. This aerodynamic shape also has a difficult time in breaking up the flow, unlike rectangular-fin edges, and allows for greater boundary layer development.

All of the values required to make the previous discovery were obtained after each model simulation was completed. Once the simulations were completed, the temperature and pressure drop results were recorded. The pressure drop values are presented as is, and the temperature results were used to calculate the heat transfer rate Q, Eq. (6), where a is the cross-sectional flow area, c_p is the specific heat, and T_o and T_{in} are the outlet and inlet fluid temperatures, respectively. An energy balance for each case reveals a 2% difference, but this is explained by the negation of radiation, which contributes to approximately 2% of the overall heat transfer.

$$Q = \rho u a c_p (T_o - T_{\text{in}}) \tag{6}$$

The coefficient of performance (COP) values were calculated using Eq. (7), where P is the heat exchanger's overall pumping power. It should be noted that pump efficiency varies from pump to pump, but for all calculations, it is assumed that a pump with an efficiency of 80% is used.

$$\text{COP} = \frac{Q}{P} \tag{7}$$

Spanwise Pitch

The effects of spanwise pitch on pressure drop can be seen in Fig. 2. This is expected because an increase in spanwise pitch creates a larger flow area and allows for a thicker boundary layer to develop. A larger flow area also decreases the flow resistance, allowing the pressure drop values to decrease as the spanwise pitch increases. An increase in spanwise pitch decreases the heat transfer rate at a linear rate, where there is approximately a 3 MW drop across a 3.25 mm increase in spanwise pitch for both liquid salt and helium channels with rectangular edges. The liquid salt and helium channels with rounded fin edges are affected in a similar manner but experience about a 4 MW drop in the same length. Similar effects of spanwise pitch on flow behavior and heat transfer have been seen in both the experimental studies of Refs. [5,7] and in the numerical studies of Refs. [12,13].

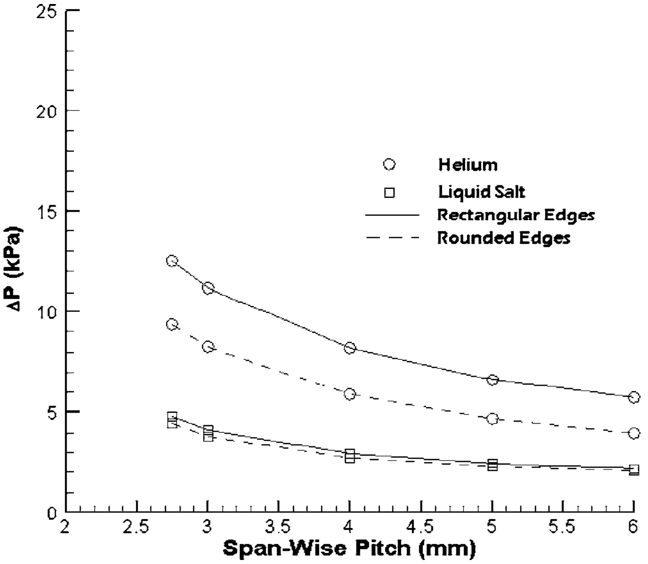

Fig. 2 The effects of spanwise pitch on pressure drop

For an offset strip-fin heat exchanger employing rounded fin edges, the spanwise pitch COP follows a linear trend and doubles across a 3.25 mm increase in spanwise pitch. The rectangular-fin edge results follow the same linear trend but only allow the COP to increase one and a half times across the same range. Also, the COP for the rounded fin edges is 30% higher at a spanwise pitch of 2.75 mm and is 40% higher at a spanwise pitch of 6 mm. Overall, it is highly desirable to have a large spanwise pitch. The reason for this is that the decrease in thermal power as spanwise pitch increases is minimal, while the decrease in pressure drop is more significant. These pronounced decreases in pressure drop values are more prevalent for rounded fin edges; hence, fins with rounded leading and trailing edges outperform fins with rectangular edges.

Fin Length

The experimental studies of Ref. [5] show that a decrease in fin length will decrease heat transfer performance. This is corroborated by the numerical studies of Ref. [12], which also states that a decrease in fin length will result in higher pressure loss coefficients. In the present study, the pressure drop results follow the previously observed behaviors. The pressure drop in the liquid salt channel for both the rectangular and rounded fin edges decreases linearly by approximately 1 kPa across a 10 mm range, and in the helium channel, the linear decrease in pressure drop is approximately 4.5 kPa for the same range. The rounded fin edges also produce lower pressure drops than the rectangular-fin edges in the helium channel, where the pressure drop values for rounded fins are about 35% lower than rectangular fins. It should finally be noted that there is an insignificant change in the heat transfer rate,

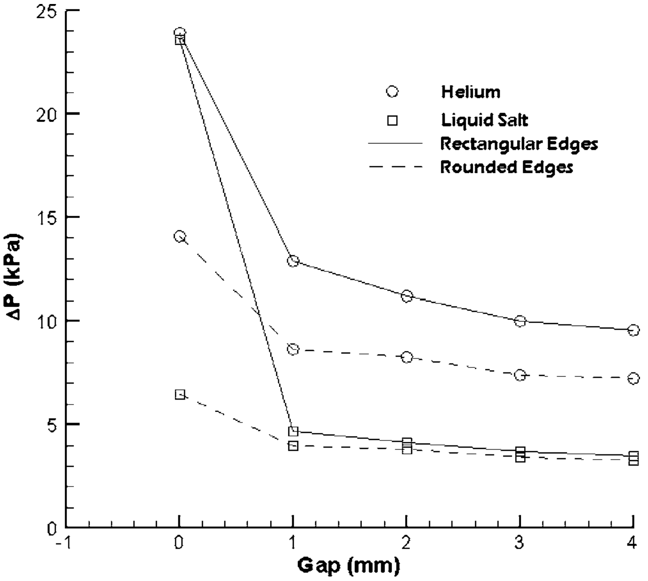

Fig. 3 The effects of gap on pressure drop

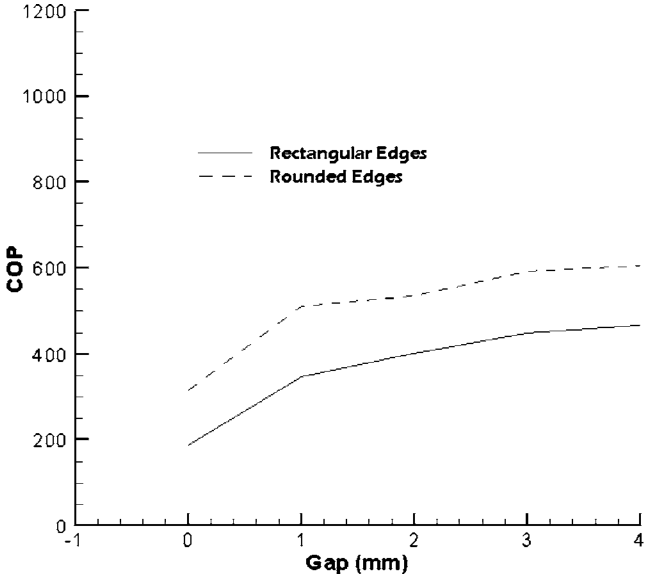

Fig. 4 The effects of gap on the offset strip-fin heat exchanger's coefficient of performance

which can be attributed to the offset strip-fin heat exchanger being long enough to allow the thermal field to become fully developed. The studies of Ref. [12] confirm this analysis.

Both rectangular and rounded fin edges in the studied offset strip-fin heat exchanger yielded a COP that increased by 33% over a 10 mm range; however, the COPs for the rounded fin edges were 40% higher at all fin lengths from 5 mm to 15 mm. The COP values then revealed that longer rounded fins are a superior performer, which is explained by the heat transfer rate remaining fairly constant while the pressure drop decreases with increases in fin length.

Gap

There has been no prior investigation into the effect of gap on the performance of an offset strip-fin heat exchanger, except for Ref. [11]. In Ref. [11], the effect of the studied gap parameter is said to have little effect on the performance of an offset strip-fin heat exchanger. The present study confirms that gap has little effect on the heat transfer rate, since the offset strip-fin heat exchanger is long enough to allow the thermal field to become fully developed. But, it is shown that gap size does significantly affect pressure drop, Fig. 3. The larger gap size should produce lower pressure drops because a gap decreases the amount of flow constriction in each channel. Also, by holding the overall length constant, a larger gap allows for fewer fins in each flow channel and less flow resistance.

The COP for the gap parameter supports the idea that an offset strip-fin heat exchanger with a large gap would be an ideal performer, Fig. 4. A continual decrease in pressure drop as gap increases and a fairly constant heat transfer rate give rise to this behavior. Fins with rounded fin edges still outperform those with rectangular-fin edges, especially in no gap cases. The reason for this is that the rounding of the fin edges not only streamlines the flow but in the no gap cases, it "opens up" the flow channel by eliminating the corners of the rectangular fins.

Channel Height

The present study shows that increases in channel height decrease the heat transfer rate on the helium side, and it has little effect on the liquid salt side, Fig. 5(*a*). A majority of the heat transfer in the liquid salt channel occurs in the spanwise direction due to laminar flow. However, turbulent flow in the helium channels allows for the heat to be transferred equitably in the height and spanwise directions. This means that as the channel height increases, it becomes increasingly difficult to transfer heat to both the top and bottom flow surfaces, which are composed of a poor thermally conductive SiC material. An increase in channel height also leads to reduced pressure drop values in the helium and liquid salt channels, Fig. 5(*b*), since a larger channel height creates a larger free flow area.

A look at the COP for channel height, Fig. 6, reveals that a large channel height is optimum for the helium side, and a small channel height is optimum for the liquid salt side. The heat transfer rate on the helium side does greatly decrease with an increase in channel height, but the pressure drop values decrease at an even greater rate. Small channel heights are the optimum choice on the liquid salt side because the changes in pressure drop are not significant when compared to the changes in the heat transfer rate.

Fin Thickness

The range of the values studied for the effect of fin thickness is smaller than all of the other parameters tested, since there is a large amount of information in the literature about the effects of fin thickness. The study of Ref. [12] states that fin thickness does not have a significant effect on heat transfer when $\mathrm{Re} < 1200$. In the present study, this phenomenon is confirmed when one looks at the low Reynolds number flow of the liquid salt and is further supported by the studies of Ref. [8]. For flows with higher Reynolds numbers, the effects of fin thickness on heat transfer are more pronounced because the narrower flow channels amplify the effects that the turbulent flow has on convective heat transfer. In the helium channel, an increase of 0.25 mm in fin thickness causes the heat transfer rates to increase by approximately 2 MW, where an increase in heat transfer due to increased fin thickness has also been reported by Refs. [6,8,13]. The main reason this occurs is that the low thermal conductivity of the SiC material only accounts for a small percent of heat transfer, while convective heat transfer is responsible for the majority of heat transfer. Pressure drop results in the liquid salt channel reveal that both rectangular and rounded fin edges produce a linear increase of 2 kPa in pressure drop over a 0.45 mm fin thickness range. Results for the helium channel show that the pressure drop for both rectangular and rounded fin edges linearly doubles over a 0.55 mm range, where the rounded fin edges produce pressure drops that are 33% lower than rectangular-fin edges. The main

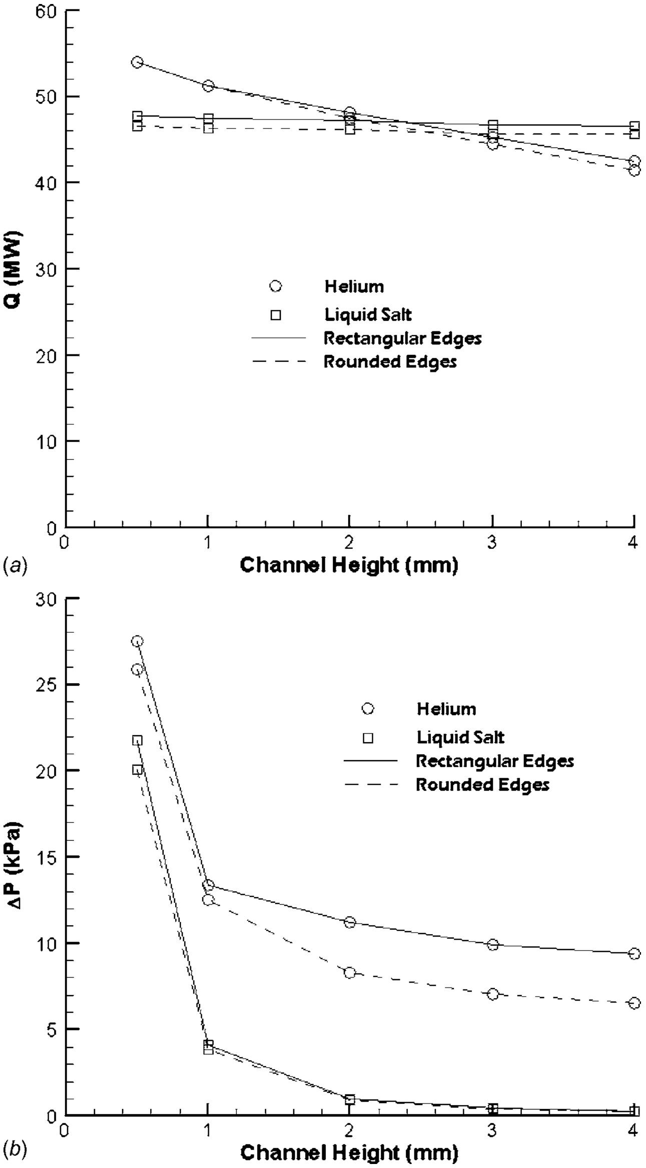

Fig. 5 (*a*) **The effects of channel height on the heat transfer rate.** (*b*) **The effects of channel height on pressure drop.**

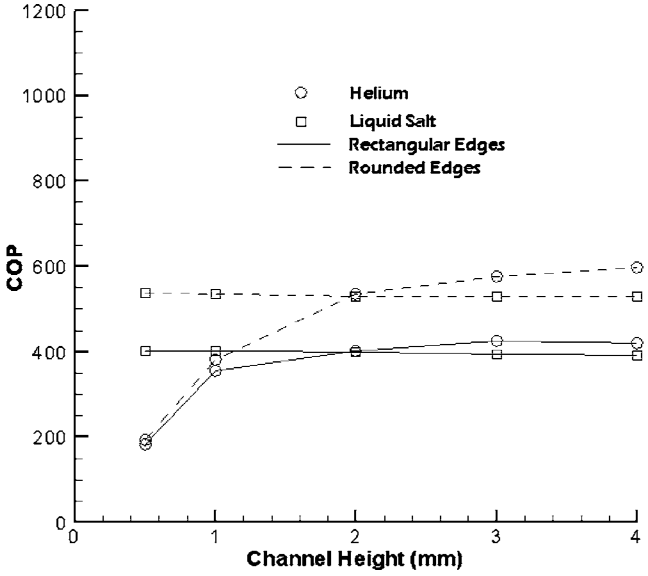

Fig. 6 The effects of channel height on the offset strip-fin heat exchanger's coefficient of performance

contributor to increases in fin thickness causing increased pressure drops is the decrease in free flow area; this phenomenon is also confirmed by the studies of Refs. [6–8,12,13].

The COP for the liquid salt fin thickness turns out to be a horizontal line, since relatively small changes in both pressure drop values and heat transfer rates occur. Hence, any of the fin thicknesses studied would prove to be an acceptable performer. An investigation of the helium side fin thickness reveals that every 0.25 mm increase in fin thickness causes a COP decrease of approximately 200. Thus, a thin fin with rounded edges performs the best due to much lower pressure drop values.

Conclusion

The current study has determined the 3D effects of rounded fin edges and geometric parameters on a high-temperature ceramic offset strip-fin heat exchanger's overall performance, where the effects from the rounded fin edges and geometric parameters are given in the form of pressure drop, heat transfer rate, and COP.

Rounded fins, as opposed to rectangular fins, were shown to produce lower heat transfer rates and pressure drop values in all cases. The COP parameters also revealed that fins with rounded edges are superior performers when compared to fins with rectangular edges. New information on previously ignored parameters, such as channel height and gap, showed encouraging results. The channel height studies revealed that large channel heights produce lower pressure drops in both helium and liquid salt channels, but only the heat transfer rate in the helium channel is significantly affected, where an increase in channel height decreases the heat transfer rate. This leads to a COP biased toward larger channel heights on the helium side and smaller channel heights on the liquid salt side. Gap studies revealed that as the gap increased, the pressure drop values significantly decreased, while heat transfer rates only dipped marginally. Their COP pointed out that larger gaps are preferred; thus, showing that the traditional "nongapped" offset strip-fin heat exchangers should only be considered when building a "gapped" offset strip-fin heat exchanger becomes economically unfeasible to produce.

The behavior of well known parameters, such as fin length, fin thickness, and spanwise pitch in the current gapped offset strip-fin heat exchanger, was performed in the same manner as shown in nongapped. Fin length studies revealed that longer fins reduce pressure drop, while fin length has no effect on the heat transfer rate. Also, spanwise pitch studies showed that large values yielded lower heat transfer rates and pressure drop values. The COP parameters coincided by stating that larger spanwise pitches and fin lengths are preferred. Studies on fin thickness show that thicker fins produce higher pressure drops in both the helium and liquid salt channels. Thus, a thinner fin is preferred in all COP cases because only the heat transfer rate on the helium side is mildly affected by fin thickness.

Overall, the results are specific and could not be used to design an offset strip-fin heat exchanger, but the current study does present previously undocumented results on rounded fins, the gap parameter, and the use of ceramics in offset strip-fin heat exchangers. The results revealed how rounded fin edges and the gap parameter can affect performance. Light has also been shed on how previously understood geometric parameters would behave in conjunction with a new gap parameter. More general studies on the effects of gap, rounded fin edges, and ceramic material in offset strip-fin heat exchangers can now be undertaken since there is an understanding of how these new introductions can affect the typical offset strip-fin heat exchanger.

References

[1] Shah, R. K., and Webb, R. L., 1983, "Compact and Enhanced Heat Exchangers," *Heat Exchangers: Theory and Practice*, Taborek J., Hewitt G. F., and Afgan N., eds., Hemisphere, Washington, DC, pp. 440–444.

[2] Webb, R. L., 1987, "Enhancement of Single-Phase Heat Transfer," *Handbook of Single-Phase Convective Heat Transfer*, Kakac, S., Shah, R. K., and Aung, W., eds., Wiley, New York, pp. 8–10.

[3] Kays, W. M., and Crawford, M. E., 1993, *Convective Heat and Mass Transfer*, 3rd ed., McGraw-Hill, New York, pp. 451–458.

[4] Webb, R. L., 1994, *Principles of Enhanced Heat Transfer*, Wiley, New York, pp. 89–98.

[5] Norris, R. H., and Spofford, W. A., 1942, "High-Performance Fins for Heat Transfer," Trans. ASME, **64**, pp. 489–496.

[6] Kays, W. M., 1960, "The Basic Heat Transfer and Flow Friction Characteristics of Six Compact High-Performance Heat Transfer Surfaces," Trans. ASME: J. Eng. Gas Turbines Power, **82**, pp. 27–34.

[7] Briggs, D. C., and London, A. L., 1961, "The Heat Transfer and Flow Friction Characteristics of Five Offset Rectangular and Six Plain Triangular Plate-Fin Heat Transfer Surfaces," *International Developments Heat Transfer: Proceedings of the Second International Heat Transfer Conference*, Boulder, CO, ASME, New York, pp. 122–134.

[8] Sparrow, E. M., and Hajiloo, A., 1980, "Measurements of Heat Transfer and Pressure Drop for an Array of Staggered Plates Aligned Parallel to an Air Flow," J. Heat Transfer, **102**, pp. 426–432.

[9] Dubrovsky, E. V., and Vasiliev, V. Ya., 1988, "Enhancement of Convective Heat Transfer in Rectangular Ducts of Interrupted Surfaces," Int. J. Heat Mass Transfer, **31**, pp. 807–818.

[10] Dejong, N. C., and Jacobi, A. M., 1997, "An Experimental Study of Flow and Heat Transfer in Parallel-Plate Arrays: Local, Row-by-Row and Surface Average Behavior," Int. J. Heat Mass Transfer, **40**, pp. 1365–1378.

[11] Mullisen, R. S., and Loehrke, R. I., 1986, "A Study of the Flow Mechanisms Responsible for Heat Transfer Enhancement in Interrupted-Plate Heat Exchangers," J. Heat Transfer, **108**, pp. 377–385.

[12] Suzuki, K., Hirai, E., Miyake, T., and Sato, T., 1985, "Numerical and Experimental Studies on a Two-Dimensional Model of an Offset-Strip-Fin Type Compact Heat Exchanger Used at Low Reynolds Number," Int. J. Heat Mass Transfer, **28**, pp. 823–835.

[13] Xi, G., Hagiwara, Y., and Suzuki, K., 1992, "Effect of Fin Thickness on Flow and Heat-Transfer Characteristics of Fin Arrays: An Offset-Fin Array in the Low Reynolds Number Range," Heat Transfer-Jpn. Res., **21**, pp. 1–19.

[14] Shah, R. K., Heikal, M. R., Thonon, B., and Tochon, P., 2000, "Progress in the Numerical Analysis of Compact Heat Exchanger Surfaces," Adv. Heat Transfer, **34**, pp. 363–442.

[15] Sparrow, E. M., Abraham, J. P., and Chevalier, P. W., 2005, "A DOS-Enhanced Numerical Simulation of Heat Transfer and Fluid Through an Array of Offset Fins With Conjugate Heating in the Bounding Solid," J. Heat Transfer, **127**, pp. 27–33.

[16] Wieting, A. R., 1975, "Empirical Correlations for Heat Transfer and Flow Friction Characteristics of Rectangular Offset-Fin Plate-Fin Heat Exchangers," ASME J. Heat Transfer, **97**, pp. 488–490.

[17] Joshi, H. M., and Webb, R. L., 1987, "Heat Transfer and Friction in the Offset Strip-Fin Heat Exchanger," Int. J. Heat Mass Transfer, **30**, pp. 69–83.

[18] Kelkar, K. M., and Patankar, S. V., 1989, "Numerical Prediction of Heat Transfer and Fluid Flow in Rectangular Offset-Fin Arrays," Numer. Heat Transfer, Part A, **15**, pp. 149–164.

[19] Manglik, R. M., and Bergles, A. E., 1995, "Heat Transfer and Pressure Drop Correlations for the Rectangular Offset Strip Fin Compact Heat Exchanger," Exp. Therm. Fluid Sci., **10**, pp. 171–180.

[20] Subramanian, S., Ponyavin, V., De Losier, C. R., Chen, Y., and Hechanova, A. E., 2005, "Design Considerations for Compact Ceramic Offset Strip-Fin High Temperature Heat Exchangers," *Proceedings of the International Conference on Enhanced, Compact, and Ultra-Compact Heat Exchangers: Science, Engineering and Technology*, Whistler, Canada, CHE2005–14, pp. 103–110.

[21] Fluent Inc., 2003, Fluent 6.2 User's Guide, Lebanon, NH.

The Modeling of Viscous Dissipation in a Saturated Porous Medium

D. A. Nield
Department of Engineering Science,
University of Auckland,
Private Bag 92019,
Auckland 1142, New Zealand
e-mail: d.nield@auckland.ac.nz

A critical review is made of recent studies of the modeling of viscous dissipation in a saturated porous medium, with applications to either forced convection or natural convection. Alternative forms of the viscous dissipation function are discussed. Limitations to the concept of fully developed convection are noted. Special attention is focused on the roles of viscous dissipation and work done by pressure forces (flow work) in natural convection in a two-dimensional box with either lateral or bottom heating. [DOI: 10.1115/1.2755069]

Keywords: porous media, natural convection, forced convection, viscous dissipation, pressure work, Boussinesq approximation, scaling

1 Introduction

An examination of the results of the survey presented by Nield and Bejan [1] reveals that in the past few years, there has been a flurry of activity on investigations of the role of viscous dissipation in convection in a porous medium. Some 30 papers on this topic bear publication dates of 2000 or later, while prior to 2000, only a handful of such papers were published. Some of this work is routine, but much is of fundamental importance and several aspects are controversial. Of particular interest are the asymptotic boundary layers and backward boundary layers that exist with natural and mixed convection past vertical walls [2–9], and the changes in fully developed and developing forced convection in channels and ducts [10–16] that result from the viscous dissipation. In this note, various aspects of this work are discussed in turn.

2 Modeling the Viscous Dissipation Term

A prime matter for discussion is the form of the mathematical expression for representing the viscous dissipation in the thermal energy equation. This expression depends on the way in which the drag force is modeled in the momentum equation, which following Eq. (1.18) of Ref. [1] (with a typographical error corrected) is written as

$$\rho\left[\frac{1}{\phi}\frac{\partial \mathbf{v}}{\partial t}+\frac{1}{\phi}\nabla\left(\frac{\mathbf{v}\cdot\mathbf{v}}{\phi}\right)\right]=-\nabla P+\mu_{\text{eff}}\nabla^2\mathbf{v}-\frac{\mu}{K}\mathbf{v}-\frac{c_F\rho}{K^{1/2}}|\mathbf{v}|\mathbf{v} \tag{1}$$

Here, $\mathbf{v}$ is the Darcy velocity, P is the fluid pressure, ρ and μ are the fluid density and viscosity, μ_{eff} is the effective viscosity, and ϕ, K, and c_F are the porosity, permeability, and a Forchheimer coefficient of the porous medium. (Some authors prefer to use $C=c_F/K^{1/2}$. However, c_F is preferred here because it is dimensionless and depends only weakly on the geometry of the porous medium and on the Reynolds number of the flow.) The last three terms of Eq. (1) are the Brinkman, Darcy, and Forchheimer drag terms.

The standard thermal energy equation (compare Eq. (2.3) of Ref. [1]) with local thermal equilibrium assumed and with no energy source term is

$$(\rho c)_m\frac{\partial T}{\partial t}+(\rho c)_f\mathbf{v}\cdot\nabla T=\nabla\cdot(k_m\nabla T) \tag{2}$$

Here, T is the temperature, $(\rho c)_m$ is the heat capacity (per unit volume) of the porous medium, $(\rho c)_f$ is the heat capacity of the porous fluid, and k_m is the thermal conductivity of the porous medium. It appears that Ene and Sanchez-Palencia [17] were the first to introduce an extra term Φ on the right-hand side of Eq. (2) to account for the effect of viscous dissipation, and if the fluid is incompressible, the porous medium is isotropic and Darcy's law holds then

$$\Phi=(\mu/K)\mathbf{v}\cdot\mathbf{v} \tag{3}$$

To see this, note that the average of the rate of doing work by the pressure, on a unit volume of a representative elementary volume (REV), is given by the negative of $\nabla\cdot(P\mathbf{v})=\mathbf{v}\cdot\nabla P$ since $\nabla\cdot\mathbf{v}=0$. Thus, Eq. (3) tells us that in this case, Φ is the power of the drag force. In fact, an argument from first principles given by Nield [18] indicates that Φ should remain equal to the power of the total drag force in more general situations. This means that the Forchheimer drag term should contribute an amount $(c_F\rho/K^{1/2})|\mathbf{v}|\mathbf{v}\cdot\mathbf{v}$ to the viscous dissipation Φ despite the fact that the viscosity μ does not appear explicitly in this expression. The apparent anomaly was resolved by Nield [18] who pointed out that the Forchheimer drag term models essentially a form-drag effect and involves the separation of boundary layers and wake formation behind solid obstacles on the pore scale. The pore scale convective inertial effects contributing to the form drag lead to a substantial modification of the velocity field and, in particular, to an enlargement of the macroscopic region in which pore scale velocity gradients are large. This leads to an increase in the total viscous dissipation (summed over the whole region occupied by fluid) and hence, because of the fundamental equality of viscous dissipation (within a volume) and the power of the drag force (on that volume) to the increase in the drag. Viscosity acts throughout the fluid, and not just at the solid boundaries. The Forchheimer form-drag term arises from the action of viscosity, mediated by the inertial effects affecting the distribution of pressure that also contributes to stress at the solid boundaries. Nield [18] also pointed out that once a division is made into a term linear in the velocity, and one quadratic in the velocity, it is then inevitable, on dimensional grounds, that the Darcy term will appear with the viscosity as a coefficient, whereas the Forchheimer term will not explicitly involve the viscosity. Pertinent to this view of form-drag effects is the work of Narasimhan and Lage (summarized in Ref. [19]) on temperature-dependent viscosity. This work clearly shows changes of dynamic viscosity affecting the total drag, even though the form drag does not carry any explicit relation to the viscosity. As far as the present author is aware, there is now a consensus on how the Darcy and Forchheimer contributions should be modeled. However, how the Brinkman contribution should be modeled is a matter of current controversy. Nield [18] argued that the Brinkman contribution should be the power of the Brinkman drag term, so that the combined Darcy and Brinkman contributions are given by

$$\Phi=(\mu/K)\mathbf{v}\cdot\mathbf{v}-\mu_{\text{eff}}\mathbf{v}\cdot\nabla^2\mathbf{v} \tag{4}$$

In the case of unidirectional flow in a circular tube, this takes the form

---

Contributed by the Heat Transfer Division of ASME for publication in the JOURNAL OF HEAT TRANSFER. Manuscript received August 29, 2006; final manuscript received February 4, 2007. Review conducted by Jose L. Lage.

$$\Phi = \frac{\mu u^2}{K} - \mu_{\text{eff}} u \left(\frac{d^2 u}{dr^2} + \frac{1}{r}\frac{du}{dr} \right) \tag{5}$$

On the other hand, Al-Hadhrami et al. [20] proposed a form which is compatible with an expression derived from the Navier-Stokes equation for a fluid clear of solid material, so that instead of Eq. (5) they would set

$$\Phi = \frac{\mu u^2}{K} + \mu \left(\frac{du}{dr} \right)^2 \tag{6}$$

They correctly noted that in the case where the Darcy number $\text{Da} \to \infty$ (where Da is defined as K/L^2, where L is the characteristic length scale), the expression in Eq. (5) becomes negative and so is physically unrealistic. However, it is the opinion of the present author (expressed in Nield [21]) that the Brinkman equation (with a term involving a constant coefficient μ_{eff}) itself is expected to break down as $\text{Da} \to \infty$. Consequently, one should regard a change in sign of the expression in Eq. (5) as just a warning that one is in uncharted waters. The present author is of the opinion that the equality of the viscous dissipation and the power of the drag, when volume averages are taken, is a fundamental principle. The principle is valid for a Darcy flow. It is also valid for a fluid clear of solid material. It is true that this is not immediately obvious. The argument involves a mathematical identity involving derivatives. When averaging is done over a representative elementary volume, information about these derivatives is lost. This is why for finite values of the Darcy number, Eq. (6) is not consistent with the Brinkman equation. Thus, the situation is that we have two expressions for Φ, one (Eq. (5)) that is based on the Brinkman drag, consistent with the power-of-drag principle but is invalid for infinite Da, and a second one (Eq. (6)) that is valid at infinite Da, consistent with the power-of-drag principle at infinite Da but is not consistent with that principle at finite Da if the Brinkman drag is employed. That inconsistency means that the Brinkman drag assumption is not uniformly valid. The present author concludes that Eq. (6) is not properly based on the Brinkman equation. Rather, it is an ad hoc formula, based on two separate versions of the momentum equation (Darcy and Navier-Stokes), with each version valid for a different Da range.

In their paper on thermally developing forced convection in a circular duct, Nield et al. [12] and Kuznetsov et al. [22] obtained values of the Nusselt number for each of the models of Nield and Al-Hadhrami et al., so in principle these results provide a basis for an experimental test between the two models. However, the differences are significant only at high values of Da and Pe (the Peclet number) and achieving these values in an experiment is likely to be difficult.

Likewise, it should be possible in principle to test whether the Brinkman equation (with a term as written in Eq. (1)) breaks down at large values of the Darcy number by performing numerical simulations of flow past a sparse array of circular cylinders, but again there are practical difficulties. Some preliminary work has been done by Gerritsen et al. [23] that suggests that the Brinkman equation is indeed not uniformly valid as the porosity tends to unity.

3 Scaling Considerations

An important practical consideration is the a priori estimation of whether or not viscous dissipation is important in a particular case. Nield [18] noted that scale analysis, involving the comparison of the magnitude of the viscous dissipation term to the thermal diffusion term, shows that viscous dissipation is negligible if $N_v \ll 1$, where

$$N_v = \frac{\mu U^2 L^2}{K c_P k_m \Delta T} = \frac{\text{Br}}{\text{Da}} \tag{7}$$

where the Darcy number $\text{Da}=K/L^2$ and the Brinkman number Br is defined by

$$\text{Br} = \frac{\mu U^2}{c_P k_m \Delta T} = \text{EcPr} \tag{8}$$

and in turn the Prandtl number Pr and the Eckert number Ec are defined by

$$\text{Pr} = \frac{\mu/\rho}{k_m/(\rho c_P)_f} \tag{9a}$$

$$\text{Ec} = \frac{U^2}{c_P \Delta T} \tag{9b}$$

Here, c_P is the specific heat at constant pressure of the fluid, k_m is the effective thermal conductivity of the porous medium, and U, L, and ΔT are characteristic velocity, length, and temperature scales, respectively. For most situations, the Darcy number is small, so viscous dissipation is important at even modest values of the Brinkman number. These comments have been made on the assumption that the Peclet number Pe is not large, where Pe is defined by

$$\text{Pe} = \frac{(\rho c_P)_f U L}{k_m} \tag{10}$$

If it is large, then the proper comparison is the one between the magnitudes of the viscous dissipation term and the convective transport term. This ratio is of order Ec/DaRe, where the Reynolds number $\text{Re}=\rho UL/\mu$.

For forced convection, the choice of the characteristic velocity is obvious (some mean or maximum value of the forced velocity). However, for natural convection, more care is needed. For the general situation, scale analysis (such as that presented in Sec. 4.3 of Ref. [24]) leads to the estimate

$$U \sim [k_m/(\rho c_P)_f L]\text{Ra}_D^{1/2} \tag{11}$$

and the condition that viscous dissipation becomes negligible becomes $\text{Ge} \ll 1$, where Ge is the Gebhart number defined by

$$\text{Ge} = \frac{g\beta L}{c_P} \tag{12}$$

and Ra_D is the Rayleigh-Darcy number defined by

$$\text{Ra}_D = \frac{\rho g \beta K L \Delta T}{\mu[k_m/(\rho c_P)_f]} \tag{13}$$

The topic of scaling is discussed further in Sec. 6.

4 Forced Convection Problem

When the effect of viscous dissipation is introduced into the classical forced convection problem, some interesting complications arise. Some of these have been discussed by Nield [25]. It is customary to define a Brinkman number Br (like the Nusselt number) in terms of the difference between a bulk mean temperature T_m and a wall temperature T_w. In the case of uniform flux boundaries (the H boundary condition), Br can be readily treated as a constant for the fully developed problem. However, for the uniform-temperature boundaries (the T boundary condition), T_w is a constant but T_m depends on x, and so Br depends on x. One response is to freeze T_m at its value for some representative value of x when determining the value of Br. An alternative response is to declare that in this situation, fully developed flow cannot be treated in isolation but only as a limiting case of the solution of a thermally developing problem with a specified inlet temperature that can be used to define Br.

There are other complications. In the presence of volumetric heating due to the viscous dissipation, and with the wall heat flux depending on the axial coordinate for the case of the T boundary condition, one has to explicitly satisfy the first law of thermodynamics instead of assuming that integration of the local thermal energy equation leads to satisfaction of this law. A further peculiarity with the T boundary condition is that the Nusselt number as usually defined takes one value when $\mathrm{Br}=0$ and another value when $\mathrm{Br}\neq 0$, no matter how small. It appears that the existence of this jump means that the concept of fully developed convection is of limited utility in the situation where viscous dissipation is important.

The situation is further complicated when the viscosity of the liquid varies with temperature. For the T boundary condition with $\mathrm{Br}=0$, the situation is relatively simple, because then the temperature is tending to the wall value throughout the medium as one moves axially downstream, and consequently the Nusselt number tends to that for the constant viscosity case. In other situations, the temperature continually changes as the axial coordinate increases and there is no truly fully developed value of the Nusselt number in a general situation. The effect of viscous dissipation then leads to a new situation that is worthy of further investigation.

The effect of flow work (work done by pressure forces) as well as viscous dissipation was examined by Nield [21]. The magnitudes of these effects are governed by independent parameters, whose ratio involves a parameter N_d defined by

$$N_d = \frac{GK}{\mu U} \tag{14}$$

where G is the magnitude of the applied pressure gradient.

5 Natural Convection Problem

The problem of convection in a two-dimensional laterally heated square cavity (with thermally insulated top and bottom) is of great interest to the computational fluid dynamics community (e.g., see de Vahl Davis [26]) as well as being applicable to a wide variety of practical problems. The case of a porous medium has been discussed by Costa [27]. The corresponding problem with a clear fluid was treated by Costa [28] and Pons and le Quéré [29,30].

Costa [27] concluded that

The unique energy formulation compatible with the first law of thermodynamics informs us that if the viscous dissipation term is taken into account, also the work of pressure forces term needs to be taken into account. In integral terms, the work of pressure forces must equal the energy dissipated by viscous effects, and the net energy generation must be zero. If only the (positive) viscous dissipation term is considered in the energy conservation equation, the domain behaves like a heat multiplier, with a heat output greater than the heat input. …[T]he main ideas and conclusions apply equally for any general natural or mixed convection heat transfer problem.

It is now argued that the statement in the last sentence is incorrect. Rather, Costa's conclusion is specific to natural convection in a laterally heated box and does not apply generally. The argument involves a close examination of the Boussinesq approximation, and to this we now turn.

6 Boussinesq Approximation

A systematic discussion of the validity of the Boussinesq approximation for liquids and gases has been made by Gray and Giorgini [31]. They expressed their result using a velocity scale $(\beta g L \Delta T)^{1/2}$ in the present notation. Using this velocity scale, and the corresponding time scale, the thermal energy equation (Eq. (32) of Ref. [31]) (that represents the thermal energy equation in what they call the extended Boussinesq approximation and what Pons and le Quéré [30] call the thermodynamic Boussinesq equation) can be written as

$$\frac{DT}{Dt} = \frac{1}{(\mathrm{PrRa})^{1/2}}\nabla^2 T - \mathrm{Ge}\frac{T_0}{\Delta T}w + \mathrm{Ge}\left(\frac{\mathrm{Pr}}{\mathrm{Ra}}\right)^{1/2}\Phi \tag{15}$$

Here, the variables are all dimensionless: they are the temperature T, time t, spatial coordinates x, y, and z, vertical velocity component w, and viscous dissipation function Φ. The new dimensionless parameters are the fluid Rayleigh number Ra and the temperature ratio $T_0/\Delta T$, where Ra is defined as

$$\mathrm{Ra} = \frac{\beta g L^3 \Delta T}{\kappa \nu} \tag{16}$$

where β is the isobaric coefficient of volumetric thermal expansion, L is a characteristic length scale that we can take as the height of the enclosure, ΔT is a temperature difference that we can take as $T_h - T_c$, where T_c and T_h are, respectively, the cold and hot wall temperatures, and T_0 is a representative absolute temperature that we can take as the arithmetic mean of T_c and T_h, while κ is the thermal diffusivity and ν is the kinematic viscosity of the fluid. The coefficient of w in Eq. (15), namely, $\mathrm{Ge}T_0/\Delta T$, is Pons and le Quéré's [30] parameter ϕ.

The last term in Eq. (15) represents the effect of viscous dissipation and the second to last term is the largest contribution from the work done by pressure forces (flow work). It is clear that both of these terms will be negligible if Ge is sufficiently small. It is also clear that the ratio of flow work term to the viscous dissipation term is of order $(T_0/\Delta T)(\mathrm{Ra}/\mathrm{Pr})^{1/2}$ and usually this will be large, even for modest values of Ra/Pr, since $T_0/\Delta T$ will commonly be quite large. Thus, in the general situation, one cannot ignore the flow work when the viscous dissipation is important. However, when $(\mathrm{Ra}/\mathrm{Pr})^{1/2}$ is small in comparison with $\Delta T/T_0$, it is the viscous dissipation term that is more important. It is emphasized that the above conclusion applies only when Eq. (15) is applicable. For the case of a liquid, this equation will usually be applicable, but in the case of a gas, another term due to the work of pressure forces, one involving the product of Ge and the parameter $\beta\Delta T$, becomes significant. For air, the Prandtl number equals 0.71 and so the effective Prandtl number Pr is of order unity or smaller, and in a typical CFD calculation, Ra could be 10^6 (or larger) and $T_0/\Delta T$ could be 10 (or larger). In these circumstances, the viscous dissipation will be negligible compared with the flow work.

We interpolate the remark that if all terms are retained in an equation, then altering the velocity scale does not matter. However, when it comes to deciding which terms are negligible (and hence can be ignored), then it does matter. In the thermal energy equation for a natural convection problem, the viscous dissipation term is quadratic in the velocity, while the major flow work term (involving the product of the pressure with a velocity component) is cubic in the velocity (since the pressure itself is quadratic in the velocity). Hence, the velocity scale is critical in deciding which of viscous dissipation or flow work is playing the major role in given circumstances.

For the case of the laterally heated box, the appropriate velocity scale is that based on the thermal conductivity, namely, κ/L, where κ is the effective thermal diffusivity. This is the scaling assumption made by Costa [27]. Now, in place of Eq. (15), we have

$$\frac{DT}{Dt} = \frac{1}{(\mathrm{PrRa})^{1/2}}(\nabla^2 T - \phi w + \mathrm{Eck}\Phi) \tag{17}$$

where the Eckert number Eck is defined as

$$\mathrm{Eck} = \frac{(\kappa/L)^2}{c_p \Delta T} \tag{18}$$

One can get rid of the parameter Pr in Eq. (17) by incorporating it into the time scale (and the corresponding velocity scale), so that then, one has

$$\frac{DT}{Dt} = \frac{1}{\mathrm{Ra}^{1/2}}(\nabla^2 T - \phi w + \mathrm{Eck}\Phi) \tag{19}$$

There is a fundamental difference between the bottom heating and lateral heating cases, as represented by Eqs. (15) and (19), respectively. For the former case, the characteristic velocity, and hence the ratio of the pressure work and viscous dissipation terms, depends on the intensity of the convective flow as measured by the parameter Ra. In the latter case, this ratio does not depend on the intensity of the convective flow. This conclusion is consistent with Costa's conclusion that in the latter case, the ratio for the integrated terms is, in fact, unity.

It is possible to make a further scaling move and incorporate a factor Ra into the velocity scale, which was done by Pons and le Quéré, ending up with

$$\frac{DT}{Dt} = \frac{1}{\mathrm{Ra}^{1/2}}(\nabla^2 T - \phi \mathrm{Ra}^{1/2} w + \mathrm{Ge}\Phi) \tag{20}$$

which can be compared with Eq. (3) in Ref. [30]. It is the opinion of the present author that this move is ill advised because it complicates the discussion unnecessarily, and the more direct approach of Costa [27] is preferable.

A related study is that by Breugem and Rees [32]. They have explicitly derived the volume-averaged Boussinesq equations for flow in porous media with viscous dissipation for the Brinkman model. They introduced a velocity scale on the assumption that the momentum equation is dominated by the balance between the buoyancy force and the Darcy drag force. This yields the velocity estimate

$$U \sim [k_m/(\rho c_P)_f L]\mathrm{Ra}_D \tag{21}$$

They noted that this scale is only appropriate when $\mathrm{Ra}_D \mathrm{Da}/\mathrm{Pr} \ll 1$ and $F \ll 1$, where F is a Forchheimer parameter. It appears to the present author that this means that this scale is applicable to weak natural convection but is generally not appropriate for natural convection problems where the Rayleigh number is large, when one would expect that the expression given in Eq. (11) would be the appropriate velocity scale.

7 Lateral Heating and Bottom Heating

In this section, the difference between natural convection in a box resulting from uniform lateral heating (the de Vahl Davis problem) and that from uniform heating from below (the Rayleigh-Bénard problem) is discussed. In the first case, the basic temperature gradient is horizontal. In the second case, it is vertical, and it is easy to explain what drives the convection. The rate of release of kinetic energy due to the buoyancy force (per unit volume) is proportional to the product of the vertical velocity component w, and the temperature excess θ and $w\theta$ is positive throughout the fluid region. Indeed, the analysis of Chandrasekhar [33] shows that the onset of convection occurs at the minimum temperature gradient at which a balance can be maintained between the kinetic energy dissipated by viscosity and the internal energy released by the buoyancy force. Thus, one can say that convection resulting from a basic vertical temperature gradient is caused by buoyancy.

However, in the case of a basic horizontal temperature gradient, the case is different. Now, when a fluid particle is displaced vertically, no kinetic energy is released since there is no change in basic temperature in that direction. It is only when the fluid particle is displaced at a nonzero angle to both the vertical and the horizontal that kinetic energy is released. This situation occurs in the corners of the box. If one considers a box with two horizontal walls and two vertical walls, with the left-hand one heated and the right-hand one cooled, then the release of kinetic energy is positive in the top left and bottom right corners but negative in the top right and bottom left corners, and by symmetry, the net effect is zero, at least to first order in the small perturbation variables. Thus, it is a glib statement to say that the natural convection is caused by buoyancy in this case. It is obvious that the situation is more subtle.

The approach of Bejan [24] is to consider the box as a closed system and to argue that the only energy exchanges between the system and its surroundings are the heat fluxes through the hot and cold walls (Q_h, positive, and Q_c, negative) and that the first law of thermodynamics requires that $Q_h + Q_c = 0$. It is assumed that gravity plays a passive role and that any additional heating due to viscous dissipation is balanced by work done by pressure forces. As Bejan [24] points out, the cellular flow is the succession of four processes (heating, expansion, cooling, and compression) so that the convection loop is equivalent to the cycle executed by the working fluid in a heat engine. The buoyancy effect due to gravity releases energy that would increase the kinetic energy of the fluid were it not that in a steady state the braking effect of viscosity immediately converts this energy to heat. The net effect of the heat engine is to produce degraded energy in the form of heat. In other words, one has a heat source within the box that has to be taken into account in the energy balance. In other books, Bejan [34,35] discusses a "temperature gap system," in which a would-be Carnot engine has no shaft to the outside but instead dissipates its power, dumping it to one or both of the hot and cold walls. He illustrated this by figures based on the assumption that the system is closed (with respect to mass flow) and isolated and therefore the incoming and outgoing heat fluxes have to be equal.

Thus, the conclusion of Costa [27] is consistent with the explanation of Bejan. Costa's work shows that the following items form a consistent set: (1) zero net release of energy as a result of buoyancy, (2) computations based on equations derived using a diffusive velocity scale, and (3) balancing heat fluxes at the hot and cold boundaries.

However, it should now be clear why his conclusion about the balance between pressure work and viscous dissipation is limited to the case of a laterally heated box. In the case of a bottom heated box, an additional agency, namely, the net kinetic energy released due to the buoyancy force, comes into play. As a result, the velocity scale is changed from a thermal diffusion (conduction) value to one dependent on the Rayleigh number. No longer is there a requirement that the pressure work and viscous dissipation be in balance. Rather, the relative magnitude of these effects depends on the intensity of the convection as measured by the value of the Rayleigh number. For a bottom heated box, the enclosure is closed as far as mass flow is concerned, but energy is exchanged with the outside when uniform temperatures at the bottom and top are maintained at fixed values and the heat fluxes at the bottom and top adjust accordingly. The occurrence of viscous dissipation modifies the energy balance but not in a radical way. The work done by pressure forces also modifies the energy balance but in a way that is not completely tied with the viscous dissipation. For forced convection, the characteristic velocity is again different, and so the roles of pressure work and viscous dissipation are different in this situation, as was noted in Sec. 4 above.

It is worth adding that the result of Chandrasekhar [33] mentioned above can be extended from the Boussinesq case to a non-Boussinesq case. In the case of a compressible fluid, it is known [36] that the main effect of compressibility can be taken into account simply by modifying the definition of the Rayleigh number, replacing the basic temperature gradient by the difference between that basic gradient $\Delta T/L$ and the adiabatic gradient $\beta T_0 g/c_P$ $(=\phi \Delta T/L)$. This implies that at the onset of convection, the viscous dissipation is balanced by the difference between the energy released by buoyancy and the work done by the pressure.

8 Conclusion

In this note, the discussion has ranged over a number of topics, some of which are currently controversial. It is hoped that the discussion will spur further investigations. In particular, the author would like to see an experimental test of the alternative expressions proposed for the viscous dissipation performed. He would also like to see a CFD investigation of natural convection in a square box with both lateral heating and bottom heating, with the computations being done employing the appropriate velocity scales and over the full range of pertinent parameters.

Acknowledgment

My thinking has been greatly stimulated by discussions with my University of Auckland colleague Professor Gordon Mallinson. It was the paper by Mallinson et al. [37] and an associated conference poster presented by Mallinson that stimulated the recent flurry of work on natural convection in a laterally heated square box. I am also grateful for the comments of several other colleagues with whom I have discussed this matter.

Nomenclature

Br = Brinkman number, defined by Eq. (8)
c = specific heat
c_F = Forchheimer coefficient
Da = Darcy number, K/L^2
Ec = Eckert number, defined by Eq. (9*b*)
Eck = Eckert number, defined by Eq. (18)
Ge = Gebhart number, defined by Eq. (12)
K = permeability
k = thermal conductivity
L = length scale
N_d = parameter defined by Eq. (14)
N_v = parameter defined by Eq. (7)
P = pressure
Pe = Peclet number, defined by Eq. (10)
Pr = Prandtl number, defined by Eq. (9*a*)
Ra = Rayleigh number, defined by Eq. (16)
Ra_D = Rayleigh-Darcy number, defined by Eq. (13)
Re = Reynolds number, $\rho UL/\mu$
Q = heat flux
T = temperature
t = time
U = velocity scale
$\mathbf{v}$ = Darcy velocity
w = vertical component of the Darcy velocity
x,y,z = spatial coordinates

Greek Symbols

β = volumetric thermal expansion coefficient
μ = fluid viscosity
μ_{eff} = effective viscosity
ρ = fluid density
θ = perturbation temperature
Φ = viscous dissipation function
ϕ = $\mathrm{Ge}T_0/\Delta T$

Subscripts

c = cold
f = fluid
h = hot
m = bulk, porous medium
w = wall
0 = reference

References

[1] Nield, D. A., and Bejan, A., 2006, *Convection in Porous Media*, 3rd ed., Springer, New York.
[2] Magyari, E., and Keller, B., 2003, "The Opposing Effect of Viscous Dissipation Allows for a Parallel Free Convection Boundary-Layer Flow Along a Cold Vertical Flat Plate," Transp. Porous Media, **51**, pp. 227–230.
[3] Magyari, E., and Keller, B., 2003, "Effect of Viscous Dissipation on a Quasi-Parallel Free Convection Boundary-Layer Flow Over a Vertical Plate in a Porous Medium," Transp. Porous Media, **51**, pp. 231–236.
[4] Magyari, E., and Keller, B., 2003, "Buoyancy Sustained by Viscous Dissipation," Transp. Porous Media, **53**, pp. 105–115.
[5] Magyari, E., and Keller, B., 2004, "Backward Free Convection Boundary Layers in Porous Media," Transp. Porous Media, **55**, pp. 285–300.
[6] Magyari, E., and Rees, D. A. S., 2006, "Effect of Viscous Dissipation on the Darcy Free Convection Boundary-Layer Flow Over a Vertical Plate With Exponential Distribution in a Porous Medium," Fluid Dyn. Res., **38**, pp. 405–429.
[7] Magyari, E., Pop, I., and Keller, B., 2003, "Effect of Viscous Dissipation on the Darcy Forced-Convection Flow Past a Plane Surface," J. Porous Media, **6**, pp. 111–122.
[8] Rees, D. A. S., Magyari, E., and Keller, B., 2003, "The Development of the Asymptotic Viscous Dissipation Profile in a Vertical Free Convective Boundary Layer Flow in a Porous Medium," Transp. Porous Media, **53**, pp. 347–355.
[9] Rees, D. A. S., Magyari, E., and Keller, B., 2005, "Vortex Instability of the Asymptotic Dissipation Profile in Porous Media," Transp. Porous Media, **61**, pp. 1–14.
[10] Nield, D. A., Kuznetsov, A. V., and Xiong, M., 2003, "Thermally Developing Forced Convection in a Porous Medium: Parallel Plate Channel With Walls at Uniform Temperature, With Axial Conduction and Viscous Dissipation Effects," Int. J. Heat Mass Transfer, **46**, pp. 643–651.
[11] Kuznetsov, A. V., Xiong, M., and Nield, D. A., 2003, "Thermally Developing Forced Convection in a Porous Medium: Circular Duct With Walls at Constant Temperature, With Longitudinal Conduction and Viscous Dissipation Effects," Transp. Porous Media, **53**, pp. 331–345.
[12] Nield, D. A., Kuznetsov, A. V., and Xiong, M., 2004, "Effects of Viscous Dissipation and Flow Work on Forced Convection in a Channel Filled by a Saturated Porous Medium," Transp. Porous Media, **56**, pp. 351–367.
[13] Ranjbar-Kani, A. A., and Hooman, K., 2004, "Viscous Dissipation Effects on Thermally Developing Forced Convection in a Porous Medium: Circular Duct With Isothermal Wall," Int. Commun. Heat Mass Transfer, **31**, pp. 897–907.
[14] Hooman, K., and Gorji-Bandry, M., 2005, "Laminar Dissipative Flow in a Porous Channel Bounded by Isothermal Parallel Plates," Appl. Math. Mech., **26**, pp. 587–593.
[15] Hooman, K., Pourshaghaghy, A., and Ejlali, A., 2006, "Effects of Viscous Dissipation on Thermally Developing Forced Convection in a Porous Saturated Circular Tube With an Isoflux Wall," Appl. Math. Mech., **27**, pp. 683–694.
[16] Hooman, K., and Gurgenti, H., 2007, "Effects of Viscous Dissipation and Boundary Conditions on Forced Convection in a Channel Occupied by a Saturated Porous Medium," Transp. Porous Media, in press.
[17] Ene, H. J., and Sanchez-Palencia, E., 1982, "On Thermal Equation for Flow in Porous Media," Int. J. Eng. Sci., **20**, pp. 623–630.
[18] Nield, D. A., 2000, "Resolution of a Paradox Involving Viscous Dissipation and Nonlinear Drag in a Porous Medium," Transp. Porous Media, **41**, pp. 349–357.
[19] Narasimhan, A., and Lage, J. L., 2005, "Variable Viscosity Forced Convection in Porous Medium Channels," *Handbook of Porous Media*, 2nd ed., K. Vafai, ed., Taylor & Francis, New York, pp. 195–234.
[20] Al-Hadhrami, A. K., Elliot, L., and Ingham, D. B., 2003, "A New Model for Viscous Dissipation in Porous Media Across a Range of Permeability Values," Transp. Porous Media, **53**, pp. 117–122.
[21] Nield, D. A., 2004, "Comments on 'A New Model for Viscous Dissipation in Porous Media Across a Range of Permeability Values'," Transp. Porous Media, **55**, pp. 253–254.
[22] Kuznetsov, A. V., Xiong, M., and Nield, D. A., 2003, "Thermally Developing Forced Convection in a Porous Medium: Circular Duct With Walls at Constant Temperature, With Longitudinal Conduction and Viscous Dissipation Effects," Transp. Porous Media, **53**, pp. 331–345.
[23] Gerritsen, M. G., Chen, T., and Chen, Q., 2005, private communication.
[24] Bejan, A., 1984, *Convection Heat Transfer*, Wiley, New York.
[25] Nield, D. A., 2006, "A Note on a Brinkman-Brinkman Forced Convection Problem," Transp. Porous Media, **64**, pp. 185–188.
[26] de Vahl Davis, G., 1983, "Natural Convection of Air in a Square Cavity: A Bench Mark Numerical Solution," Int. J. Numer. Methods Fluids, **3**, pp. 249–264.
[27] Costa, V. A. F., 2006, "On Natural Convection in Enclosures Filled With Fluid-Saturated Porous Media Including Viscous Dissipation," Int. J. Heat Mass Transfer, **49**, pp. 2215–2226.
[28] Costa, V. A. F., 2005, "Thermodynamics of Natural Convection in Enclosures With Viscous Dissipation," Int. J. Heat Mass Transfer, **48**, pp. 2333–2341.
[29] Pons, M., and le Quéré, P., 2005, "An Example of Entropy Balance in Natural Convection, Part 1: The *Usual* Boussinesq Equations," C. R. Mec., **333**, pp. 127–132.
[30] Pons, M., and le Quéré, P., 2005, "An Example of Entropy Balance in Natural Convection, Part 2: The *Thermodynamic* Boussinesq Equations," C. R. Mec., **333**, pp. 133–138.
[31] Gray, D. G., and Giorgini, A., 1976, "The Validity of the Boussinesq Approximation for Liquids and Gases," Int. J. Heat Mass Transfer, **19**, pp. 545–551.
[32] Breugem, W. P., and Rees, D. A. S., 2006, "A Derivation of the Volume-Averaged Boussinesq Equations for Flow in Porous Media With Viscous Dissipation," Transp. Porous Media, **63**, pp. 1–12.
[33] Chandrasekhar, S., 1961, *Hydrodynamic and Hydromagnetic Stability*, Clarendon, Oxford, p. 34.
[34] Bejan, A., 1982, *Entropy Generation Though Heat and Fluid Flow*, Wiley, New York, pp. 35–36.
[35] Bejan, A., 1988, *Advanced Engineering Thermodynamics*, Wiley, New York, p. 136.
[36] Nield, D. A., 1982, "Onset of Convection in a Porous Layer Saturated by an Ideal Gas," Int. J. Heat Mass Transfer, **25**, pp. 1605–1606.
[37] Mallinson, G., Moyle, K., and Norris, S., 2004, "Volumetric Methods for Evaluating Irreversible Energy Losses and Entropy Production With Application to Bioengineering Flows," *Proceedings of the ICHMT International Symposium on Advances in Computational Heat Transfer*, Norway, Apr. 19–24, Paper No. CHT-04-262.